EFFECT OF GEOMETRY, RESPIRATION AND VESSEL

DEFORMABILITY ON FONTAN HEMODYNAMICS:

A NUMERICAL INVESTIGATION

A Thesis

Presented to

The Academic Faculty

by

Tsz Ling Elaine Tang

In Partial Fulfillment

of the Requirements for the Degree

Doctor of Philosophy in the

School of Chemical and Biomolecular Engineering

Georgia Institute of Technology

December 2015

EFFECT OF GEOMETRY, RESPIRATION AND VESSEL

DEFORMABILITY ON FONTAN HEMODYNAMICS:

A NUMERICAL INVESTIGATION

Approved by:

Dr. Ajit P. Yoganathan, PhD, Advisor

Department of Biomedical Engineering

School of Chemical and Biomolecular

Engineering

Georgia Institute of Technology, GA

Dr. Alessandro Veneziani, PhD

Department of Mathematics & Computer

Science

Emory University, GA

Dr. Hang Lu, PhD

School of Chemical and Biomolecular

Engineering

Georgia Institute of Technology, GA

Dr. Pedro J. del Nido, MD

Department of Cardiac Surgery

Boston Children's Hospital, MA

Dr. Doff B. McElhinney, MD

Department of Pediatric Cardiac Surgery

Stanford University Medical Center, CA

Dr. Athanassios Sambanis, PhD

School of Chemical and Biomolecular

Engineering

Georgia Institute of Technology, GA

Date Approved: 08/28/2015

ACKNOWLEDGEMENTS

This has been a long journey. And I sincerely thank everyone who has helped me to make this happen.

I would like to first thank my PhD supervisor, Dr Ajit P. Yoganathan. As a chemical engineer, I am glad to be able to be exposed to the highly translational biomedical engineering world in here in CFML. I also would like to thank my thesis committee members. I need to thank Dr Alessandro Veneziani for the technical guidance and always being very forthcoming when I need advice on numerical simulations. Also thank to his generosity in offering to help with the work being done in this thesis. I also would like to thank Drs Doff B. McElhinney and Pedro del Nido, for all the valuable clinical input I am given in this thesis work. I also need to thank Drs Hang Lu and Athanassios Sambanis for serving on my thesis committee and providing their critical input on my work.

Throughout these years, I am very grateful to be working with many collaborators within and outside Georgia Tech: Mark Luffel and Dr. Jarek Rossignac from the college of Computing at Georgia Tech helping to improve our surgical planning work. Drs Tim Slesnick (CHOA), Kirk Kanter (CHOA), Anne Marie Valente (Boston Children) for all their support and valuable input in our Fontan work. Thank you for our R01 grant collaborators: Drs Mark Fogel, Kevin Whitehead, Bradley Marino for their critical input in my work. Also thank you for Julie Pappas, Ken Gerald, James Bethel, Okan Elci,

Veronica O'Connor and Ravi Doddasomayajula for their assistance in the R01 grant. None of this thesis work would be possible within their assistance.

I would like to express my sincere gratitude to my Fontan team. Whenever I faced frustration with work in these past years, it was having this great Fontan team that kept me going every day. I would like to thank (in no order) Drs Alan Wei, Arvind Santhanakrishnan, Lucia Mirabella, Maria Restrepo and Milan Toma, for not only being my mentors, for all the help in research, grant work and dealing with pressure in lab, but also valuable friends that I made through these years. Especially Dr Alan Wei, my graduation would not be possible without him. Sincere thank you for his support and friendship during the very end of this journey, when things get really hectic. Special thank also goes to Dr Tiziano Passerini for his help in the FSI work in this thesis. Also thanks to Drs Chris Haggerty, Reza Khiabani for laying a lot of ground work for the Fontan team, especially for the earlier part of this thesis. Thanks to Mike Tree and Phillip Trusty for providing critical input into my work, reviewing this thesis, help with grant work, and the positive energy and support that I needed to get this work going. I would like to also thank Huijuan Xu for help with LifeV and reading my thesis. And of course, great UGs: Alex Shou, Feiran Li, Michael Clay and Wenjun Wu. Thank you for all of their contribution. Without them all this thesis would not be possible.

And how could I not thank my fellow awesome CFML-ers? We have been through so much together: exciting research discussions, endless meetings and conference calls, and of course, countless lunch/coffee/ice cream break with many fun conversations. In

addition to the Fontan team, it has been a pleasure to know all the old and current members (alphabetical order): Brian Jun, Charlie Bloodworth, Christine Garcia, Eric Pierce, Ikay Okafor, Jean-Pierre Rabbah, Karthik Srivatsa, Neela Saikrishnan, Prem Midha, Shiva Arjunon, Swetha Rathan, Tausif Salim, Thomas Easley, Timothy Sowers, Vrishank Raghav and anyone I might have missed. Special thanks to many (almost all) of them who helped reviewing this thesis. Thanks for giving me happiness, help and support throughout this journey. Also thanks to Prem Midha for helping me with editing the awesome 20+ videos in this thesis that I could never have done it by myself. Also thanks to the great BME staff: Sandra Maffey, Steven Marzec and Jesus Mata-Acosta, as well as Janice Whatley from ChBE, for all their assistance in the past few years. None of this work would be possible without their pivotal support.

My deepest thanks go to my "sisters" in Atlanta: Swetha Rathan, Yuzhi Kang, Jie Pan, Xiaodan Zhang and Yizheng Chen. Swetha Rathan, she is like my sister in the CFML. Thank you for listening to all my ups and downs throughout these years, and have always been there for me. This would not be possible without her continuous support, especially during the last few months of my PhD. I really have to thank Yuzhi and Jie Pan, not only for giving me a place to stay during the critical time close to my PhD defense, but also their friendship, care and encouragement when I felt frustrated. I am also glad to have Xiaodan Zhang, my roommate for years, whose together we have been through so much. Her support meant so much to me. Yizheng Chen, thank you for always being a good listener when it comes to stress related to grad student life, and

v

showing me the other side of the life other than work. Thank you to my "sisters" for their support throughout these years.

Also big thanks to my "yuntao" gang: Chen Zhang, Wei Mu, Xue Ning, Yang Cai, Boyi Fu, Huayu Li, Weiming Yeh, Pu Gong, Liwei Li, Hongzhi Wang and many others; I am so glad to have met all these amazing friends. Thank you for their care and the fun time we had in the past few years. Adrian Lam, Jeff Wong, Linda Hui, Samantha Lo, Samson Lai, and all other "cooking night" members, hanging out with them always take my mind off from work and I am really glad to be able to meet some of the nicest people I have ever known here. My cool designer friends: Oliver Li, Tom Yang, Tao Yan, Jennifer Cheuk, for all the fun times, and keep reminding me to not just be the practical engineer, but also try to think outside of the box and have fun. A big "remote" thank to my dearest friends in Hong Kong: Kamray Yim, Wini Chan, Apple Chan, Samuel Tang for all the support throughout these crazy years.

Last but probably the most important, my family, for their never-ending support and unconditional love. Even though I did not get to be with them all the time, none of these would been possible without them. I knew getting a doctoral degree outside Hong Kong was never what they pictured my career path would be. I am grateful for my parents for their understanding and faith on me to do what I like. I hope I am making them proud. Thank you to Alfred and Sze, thank you for their constant support and love. I am very thankful to have this family to raise me up to become what I am today.

TABLE OF CONTENTS

LIST OF TABLES

LIST OF FIGURES

xxvii

LIST OF ANIMATIONS

LIST OF SYMBOLS AND ABBREVIATIONS

3D	three-dimensional
AAO	ascending aorta
ACGI	adaptive control grid interpolation
AO	aorta
APC	atriopulmonary connection
AZ	azygos vein
baDI	Beat-averaged deformation index
BSA	body surface area
CFD	computational fluid dynamics
CHB	Boston Children's Hospital
CHD	congenital heart disease
CHOA	Children's Healthcare of Atlanta
CHOP	Children's Hospital of Philadelphia
CI	cardiac index
CMR	cardiac magnetic resonance
CO	cardiac output
DAO	descending aorta
DI	deformation index
EC	extracardiac
FP	Fontan pathway
GFD	global flow distribution
HFD	hepatic flow distribution
HLHS	hypoplastic left heart syndrome
HR	heart rate
IA	intra-atrial
IB	immersed boundary
iPL	indexed power loss
IVC	inferior vena cava
LPA	left pulmonary artery
LSVC	left superior vena cava
LT	lateral tunnel
LV	left ventricle
MRI	magnetic resonance imaging
P	pressure
PA	pulmonary artery
PAVM	pulmonary arteriovenous malformations
PC-MRI	phase contrast magnetic resonance imaging
PFD	pulmonary flow distribution
PI	pulsatility index
PL	power loss

PLE	protein losing enteropathy
Post-stent	after stent implantation
Pre-stent	before stent implantation
PVR	pulmonary vascular resistance
Q	flow
Qs	total systemic flow
RPA	right pulmonary artery
RV	right ventricle
SSFP	steady-state free precession
SV	single ventricle
SVC	superior vena cava
SVHD	single ventricle heart defects
SVR	systemic vascular resistance
TCPC	total cavopulmonary connection
VAT	ventilatory threshold
VENC	velocity encoding
VF	ventricular function
VMTK	vascular modeling toolkit
wPI	Weighted pulsatility index
WU	Wood units

SUMMARY

Single ventricle (SV) congenital heart defects occur in 2 of every 1000 live births in the US. The Fontan procedure, the common palliation of single ventricle heart defect patients, results in the inferior vena cava (IVC) and superior vena cava (SVC) being connected to the pulmonary arteries (PAs) to bypass the right ventricle, completing the total cavopulmonary connection (TCPC). Even though this procedure results in favorable short-term outcomes, Fontan patients are subjected to a series of long-term complications, including reduced exercise capacity and life expectancy. The exact causes of these long-term complications are not clear, but some are attributed to the unfavorable hemodynamics in the TCPC.

Computational fluid dynamics (CFD) is a widely used tool for retrospective and prospective patient study of TCPC hemodynamics. While these studies have improved the understanding of the linkage between TCPC geometric design and the resulting hemodynamics, a systematic study to evaluate the effect of TCPC geometric feature on TCPC hemodynamics on a broad number of patients has not yet been performed. Also, simplifications and assumptions such as steady flow boundary conditions, rigid wall and negligible respiratory effects are often made in CFD modeling of the TCPC.

In this thesis, the impact of geometry, respiration-driven flow, and vessel wall deformability on TCPC hemodynamics will be evaluated and compared. First, the

impact of patient specific geometry will be studied by characterizing the patient specific anatomic features of a large patient cohort of TCPCs obtained from cardiac magnetic resonance (CMR) images. Second, the influence of respiratory-driven flow will be investigated by comparing TCPC hemodynamics simulated using a vessel flow waveform obtained from both free-breathing and breath-held phase-contrast CMR acquisitions. Third, the effect of wall deformability will be studied by comparing TCPC hemodynamics under rigid wall and compliant wall conditions. At the end of this thesis, the impact of patient specific geometry, flow pulsatility, respiration, and wall compliance on TCPC hemodynamics will be discussed.

CHAPTER 1   INTRODUCTION

Single ventricle (SV) congenital heart defects occur in 2 of every 1000 live births in the US. These defects lead to the direct mixing of systemic and pulmonary blood flows in the SV and insufficient blood oxygen saturation for sustaining life. Thus, early surgical correction is required. The Fontan procedure is the final step in a series of palliative surgeries performed in these patients in which the inferior vena cava (IVC) is connected to the pulmonary arteries (PAs) to bypass the right ventricle, completing the Total Cavopulmonary Connection (TCPC). Even though this procedure results in favorable short-term outcomes, Fontan patients are subjected to a series of long-term complications, including reduced exercise capacity and life expectancy. Since the SV has to pump blood for the entire circulation, patients are in a chronic state of systemic hypertension (to compensate for the additional downstream resistance) and pulmonary hypotension (because of the missing sub-pulmonary ventricle). The increased SV workload and the resulting hemodynamics are hypothesized to be major contributors to these long-term complications. Therefore, minimizing TCPC energy dissipation has been one of the goals to optimize its hemodynamics. Pulmonary arteriovenous malformations (PAVMs) are one of the other long-term complications that have been shown to be associated with local TCPC hemodynamics. It has been shown that unbalanced distribution of hepatic blood to the two lungs can increase the risk of PAVMs.

Computational fluid dynamics (CFD) is a widely used method for retrospective and prospective patient studies to explore the TCPC that optimizes hemodynamic efficiency and hepatic flow distribution. While these studies have contributed greatly to the broader understanding of TCPC design and the resulting hemodynamic impacts, possibly confounding simplifications and assumptions are often made. Such simplifications include: idealized geometries, time-averaged flow conditions, rigid vessel walls and neglected respiratory effects. Contrary to these assumptions, studies show that TCPC geometry is highly patient specific. Also, previous studies show that TCPC hemodynamics can be affected by the vessel flow pulsatility. Finally, the TCPC is composed of native, compliant blood vessel tissue. Under the influence of fluid flow, respiration, and other native forces *in vivo wall motion is observed*, which can affect the connection hemodynamics. In order to improve TCPC hemodynamic modeling and physiological understanding, these assumptions must be evaluated.

In this thesis, the impact of geometry, respiration-driven flow, and vessel wall deformability on TCPC hemodynamics will be evaluated and compared. First, the impact of patient specific geometry will be studied by characterizing the patient specific anatomic features of a large patient cohort of TCPCs obtained from cardiac magnetic resonance (CMR) images. These anatomic features will be correlated with TCPC hemodynamics under baseline and exercise flow conditions. Following the identification of the most important geometrical features, the influence of intervention on improving TCPC hemodynamics will be explored. Second, the influence of respiratory-driven flow will be investigated by comparing TCPC hemodynamics simulated using a vessel flow

waveform obtained from both free-breathing and breath-held phase-contrast CMR acquisitions. Third, the effect of wall deformability will be studied by comparing TCPC hemodynamics under rigid wall and compliant wall conditions. At the end of this thesis, the impact of patient specific geometry, flow pulsatility, respiration, and wall compliance on TCPC hemodynamics will be discussed.

For easier interpretation of this thesis, note the definition of the major vessels and regions at the TCPC are defined as follows:
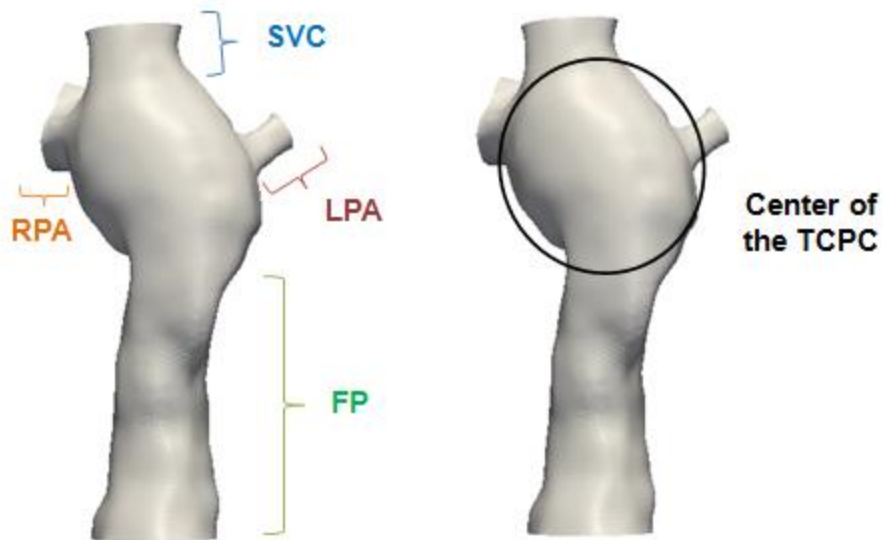
Figure 1.1: Schematic of the definition of regions of the TCPC in this thesis

CHAPTER 2   SPECIFIC AIMS AND HYPOTHESES

The Fontan procedure, the common palliation of single ventricle heart defect patients, results in the inferior vena cava (IVC) and superior vena cava (SVC) being connected to the pulmonary arteries (PAs) to bypass the right ventricle, completing the total cavopulmonary connection (TCPC). Even though this procedure results in favorable short-term outcomes, Fontan patients are subjected to a series of long-term complications, including reduced exercise capacity and life expectancy [1]. The exact causes of these long-term complications are not clear, but some are attributed to the unfavorable hemodynamics in the TCPC. For example, there has been evidence showing the possible link between TCPC energy dissipation and patient exercise tolerance [2]. Also, unbalanced distribution of hepatic blood flow between the lungs has been associated with the risk of pulmonary arteriovenous malformations (PAVMs) [3-5].

Computational fluid dynamics (CFD) is a widely used tool for retrospective and prospective patient study of TCPC hemodynamics. While these studies have improved the understanding of the linkage between TCPC geometric design and the resulting hemodynamics, a systematic study to evaluate the effect of TCPC geometric feature on TCPC hemodynamics on a broad number of patients has not yet been performed. Also, simplifications and assumptions such as steady flow boundary conditions, rigid wall and negligible respiratory effects are often made in CFD modeling of the TCPC. These assumptions need to be evaluated and possibly included to have a more physiologic

4

understanding of TCPC hemodynamics. Although there is no pulsating sub-pulmonary ventricle directly driving the flow in the TCPC, there has been growing evidence showing that cardiac flow pulsatility in the vessels can affect TCPC hemodynamics. Also, it has been clinically observed that the caval vein flow waveform is being affected by respiration; hence respiration can have an impact on TCPC hemodynamics. In addition, the TCPC is composed of compliant native tissue and surgical materials. Under the influence of fluid flow, respiration, patient movement and other possible reasons, wall motion is observed *in vivo*, which can affect the flow dynamics within the TCPC.

The hypothesis of this work is that **TCPC hemodynamic performance can be affected by the connection geometry, respiration and wall deformability.** This hypothesis will be investigated in 3 specific aims (Figure 2.1):
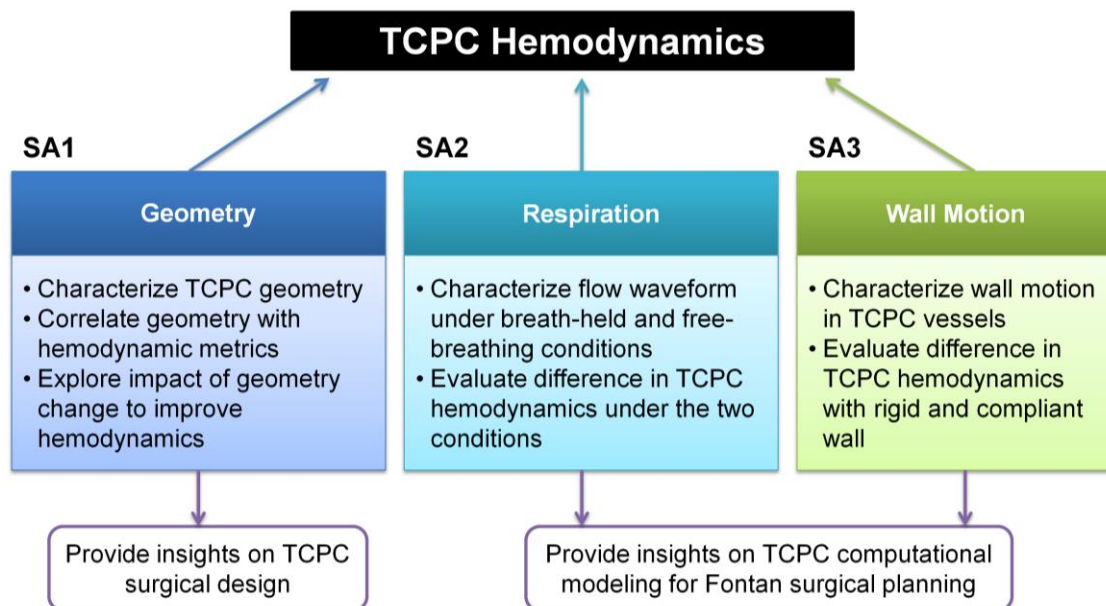
Figure 2.1: Schematic of the specific aims

5

Specific Aim 1: Investigation of the effect of geometry on TCPC hemodynamics. The anatomy of the TCPC is highly patient specific and different geometric features are expected to affect TCPC hemodynamics differently. A systematic evaluation of the impact of TCPC geometric features on TCPC baseline and exercise hemodynamics will be performed in this study. First of all, patient specific TCPC anatomic features will be characterized in a broad patient database from the Georgia Tech Fontan Magnetic Resonance Imaging database. These geometric parameters will then be correlated to baseline hemodynamic metrics (hepatic flow distribution and power loss) and exercise hemodynamic metrics (exercise power loss) simulated with computational fluid dynamics (CFD) to identify geometric parameters that can significantly affect a given hemodynamic metric. Finally, surgical design and intervention to improve TCPC hemodynamics based on the significant geometric parameters will be explored. All these studies will be performed based on the existing numerical framework with steady flow boundary conditions, rigid wall and no respiratory effects to save computational cost in view of the broad patient database to be investigated.

Specific Aim 2: Investigation of the effect of respiration on TCPC hemodynamics. Previous numerical studies have demonstrated the impact of cardiac flow pulsatility on TCPC hemodynamics. Clinically, patient specific vessel flow is often obtained from phase contrast magnetic resonance images (PC-MRI) acquired under breath-held conditions. However, there has been growing evidence that vessel flow is also influenced by respiration. In this specific aim, vessel flow waveforms will be quantified using *in vivo* data acquired under breath-held and free-breathing conditions. TCPC

6

hemodynamic metrics including TCPC power loss will be evaluated using vessel flows obtained from these two conditions to understand the impact of respiration on TCPC hemodynamics.

Specific Aim 3: Investigation of the effect of wall deformation on TCPC hemodynamics. The TCPC is composed of native blood vessel tissues and surgical materials. As a result of the compliance of the blood vessel, the TCPC vessel wall is expected to deform with respect to fluid flow as well as changes in intra-thoracic pressure and exercise. Such characterization of TCPC wall motion is still lacking. For this purpose, the area of TCPC vessel cross section will be quantified and compared under resting breath-hold, resting free-breathing and exercise free-breathing conditions. To gain a better understanding of the importance of vessel compliance on evaluating TCPC hemodynamics, fluid-structure interaction simulations will be performed. TCPC energy dissipation and flow structure will be evaluated and compared with rigid wall simulations. This can help improve the understanding of the importance of including vessel compliance in modeling TCPC hemodynamics.

From Specific Aim 1, the influence of patient specific geometric features on TCPC hemodynamics will be understood, to offer surgeons and cardiologists insights regarding the connection geometries that could result in suboptimal hemodynamics. From the findings of Specific Aims 2 and 3, the relative error contributed by ignoring respiration and vessel compliance will be quantified and compared, which could provide insights on future CFD modeling of TCPC hemodynamics.

CHAPTER 3   Background and Significance

3.1   Normal Cardiovascular System

The cardiovascular system, as part of the circulatory system, is an organ system that permits the transport of oxygen, carbon dioxide, nutrients, waste, hormones and blood cells throughout the body through the circulation of blood. Blood is a fluid that consists of blood cells (red blood cells, white blood cells and platelets) and plasma. The pumping of the heart provides the blood with the driving pressure to circulate to different parts of the body. The cardiovascular circulation can be divided into two primary circuits (Figure 3.1): (i) the pulmonary circulation which allows the movement of blood to and from the lungs, and (ii) the systemic circulation where blood is circulated through the rest of the body.
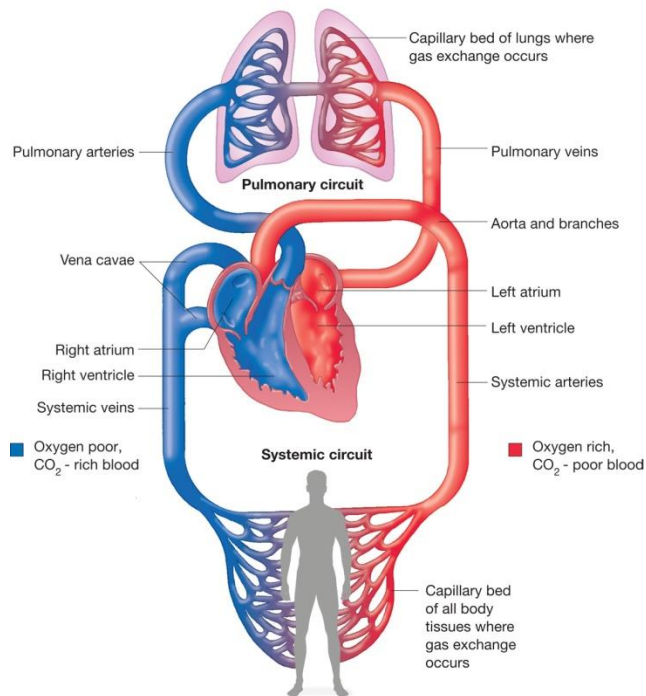
Figure 3.1 Schematic of a normal cardiovascular system (Image credit: http://biology-forums.com/index.php?action=gallery;sa=view;id=8516)

As shown in Figure 3.2, a normal heart has two sides. Each side of the heart contains an atrium and a ventricle; hence a normal heart contains 4 chambers. The ventricles provide the pumping pressure to the blood to circulate through the systemic and pulmonary circulations. The atria facilitate circulation by allowing uninterrupted venous flow to the heart. The septum separates the left and right sides creating two pumps that function in series. There are also 4 heart valves that allow the unidirectional flow of blood: two atrioventricular (mitral and tricuspid) valves and two semilunar (aortic and pulmonary) valves.
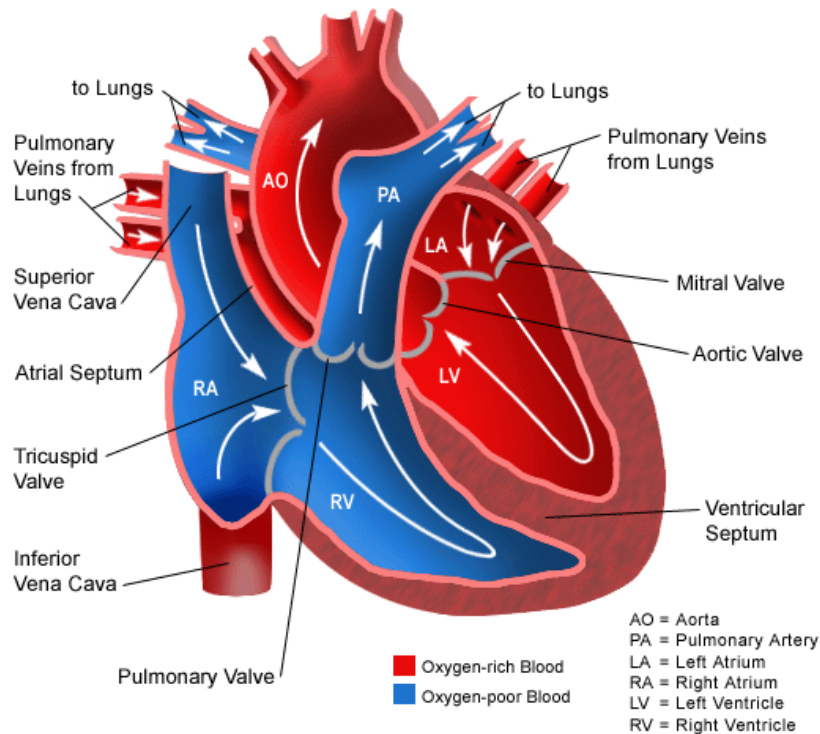
Figure 3.2 Schematic of how blood flows in a normal heart (Image credit: http://seys-science.wikispaces.com/4+How+does+blood+flow+through+our+heart+and+body%3F)

In a normal circulation, oxygenated blood from the lungs enters the left atrium through the pulmonary veins. Since the left ventricular pressure is lower than left atrial pressure, this causes the mitral valve to open. Blood then flows from the left atrium into the left ventricle during diastole. The left ventricle then contracts during systole, and increases the left ventricular pressure. This closes the mitral valve and causes the aortic valve to open. Oxygenated blood then flows to the rest of the body through the aorta. Aortic pressure and left ventricular pressure both decrease. The aortic pressure is higher than left ventricular pressure, forcing the aortic valve to close.

Deoxygenated blood from the systemic circulation flows through the superior vena cava (SVC) and inferior vena cava (IVC) into the right atrium. Right atrial pressure is higher

than right ventricular pressure, which forces the tricuspid valve to open, allowing deoxygenated blood to enter the right ventricle. During systole, the right ventricle pumps the deoxygenated blood through the pulmonary valve to the lungs through the pulmonary arteries.

3.2 Congenital Heart Defects

Congenital heart defects (CHDs) are structural problems that arise from abnormal formation of the heart or major blood vessel(s) during fetal development. These include defects in the heart muscles, heart valves, or the great arteries and veins that are connected directly to the heart, or a combination thereof. CHD is one of the most common severe congenital anomalies [6]. The International Classification of Diseases lists 25 congenital heart defects codes [7], which highlight the variability of congenital heart defects.

Worldwide statistics of CHD patients are reported in van der Linde et. al. [8] CHD accounts for nearly one-third of all major congenital anomalies. Total birth prevalence of CHD has changed over time. It was first reported as 0.6 per 1000 live births in 1930 to 1934, which then increased to 9.1 per 1000 live births after 1995. Over the last 15 years, the incidence stabilized, corresponding to 1.35 million newborns with CHD every year. Asia has highest CHD birth prevalence, with 9.3 per 1,000 live births.

The incidence of CHD in the United States is around 8 per 1000 live births [7]. An estimated minimum of 32,000 infants are expected to be affected by CHDs in the United

States each year [7]. In 2009, congenital cardiovascular defects were the most common cause of infant death resulting from birth defects; 26.6% of infants who died of a birth defect had a heart defect [7]. Table 3-1 shows the incidence of the common CHD in life births in the United States.

Table 3-1 Incidence of CHD in life births in the United States reported in 62 studies published in 1955-2002 [9]

	Incidence per million live births
Bicuspid aortic valve (BAV)	13,556
All CHD (excluding BAV)	9,596
Ventricular septal defect	3,570
Atrial septal defect	941
Patent ductus arteriosus	799
Pulmonary Stenosis	729
Tetralogy of Fallot	421
Coarctation of the aorta	409
Aortic Stenosis	401
Atrio-ventricular Septal Defect	348
Transposition of the Great Arteries	315
Hypoplastic left heart	266
Hypoplastic right heart	222
Ebstein's anomaly	114
Tricuspid atresia	79

The most prevalent CHD worldwide is ventricular septal defect, followed by atrial septal

defect and patent ductus arteriosus (Table 3-2).

Table 3-2 Birth prevalence of CHD subtypes worldwide reported in 114 studies published in
1930-2009 [8]

	Distribution of subtypes within total CHD
Ventricular septal defect	34%
Atrial septal defect	13%
Patent ductus arteriosus	10%
Pulmonary Stenosis	8%
Tetralogy of Fallot	5%
Coarctation of the aorta	5%
Transposition of the Great Arteries	5%
Aortic Stenosis	4%

CHDs are serious conditions that have a significant impact on morbidity, mortality, and

healthcare costs in children and adults. Most CHDs will result in life threatening

situations, such as cyanosis. This means the heart's ability to pump blood to deliver

oxygen to different body parts is being compromised and blood oxygen saturation level

is suboptimal. The cause of congenital heart disease may be either genetic or

environmental, but little is known about the cause of most CHDs. Therefore, there is no

known prevention or cure for these diseases. CHD is also a significant health burden for

children and adults. Almost half of all children and adults with complex CHD who

survived past their infancy have neurological and developmental disabilities. It was

estimated that the total number of adults living with CHD in the United Sates in 2000

was 800,000 [7].In the US, and 1 in 150 adults are expected to have some form of CHD [7].

3.3   Single Ventricle Heart Defects (SVHD)

Single ventricle heart defects (SVHD) are one of the most complex classes of CHD. Instead of having a fully functional four-chambered heart, there is only one functional ventricle to pump blood. As shown in Figure 3.3, in a normal circulation a serial circuit is maintained by having both functional left and right ventricles. In patients with SVHD, there is only one functional ventricle to pump blood to both the systemic and pulmonary circulations in a parallel configuration. The shunts between the left and right heat chambers allow flow mixing of the oxygenated blood from the lungs and deoxygenated blood from the body to mix before leaving the heart. This causes cyanosis in SVHD patients.
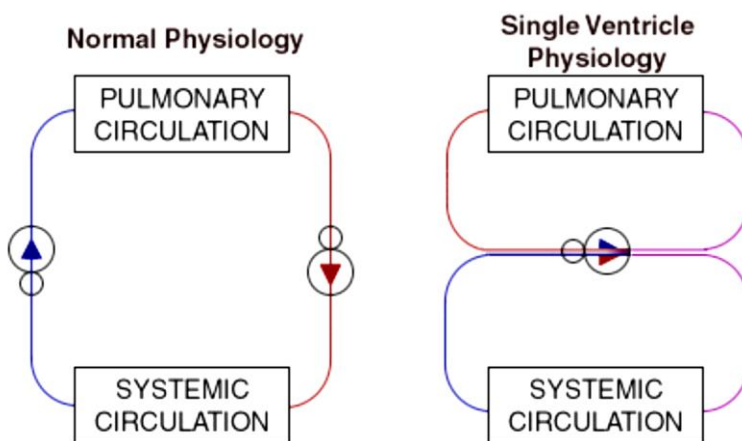
Figure 3.3 Circuit diagram for normal (left) and SVHD (right) physiology; the normal circulation works as a series of the pulmonary and systemic circulation and 2 pumps; the single ventricle physiology is a parallel circuit of pulmonary circulation with a single pump.

The most common forms of CHDs leading to single ventricle physiology include tricuspid or mitral atresia, hypoplastic left or right heart syndrome, transposition of the great arteries and double outlet ventricle.

Though all SVHDs yield some common symptoms, e.g. cyanosis, the patients' anatomy can vary drastically. Other concomitant defects, e.g. ventricular septal defect can also be present. Therefore, different types of repairs may have to be applied for different patients. In the following section, the common forms of SVHD will be described in more detail.

3.3.1 Tricuspid Atresia

Tricuspid atresia (Figure 3.4) is a form of CHD in which there is a complete absence of the tricuspid valve. This leads to a hypoplastic or absent right ventricle. Due to the absence of an atrioventricular connection, an atrial septal defect must be present to maintain blood flow. The presence of a ventricular septal defect allows blood flow from the left ventricle to the pulmonary arteries.
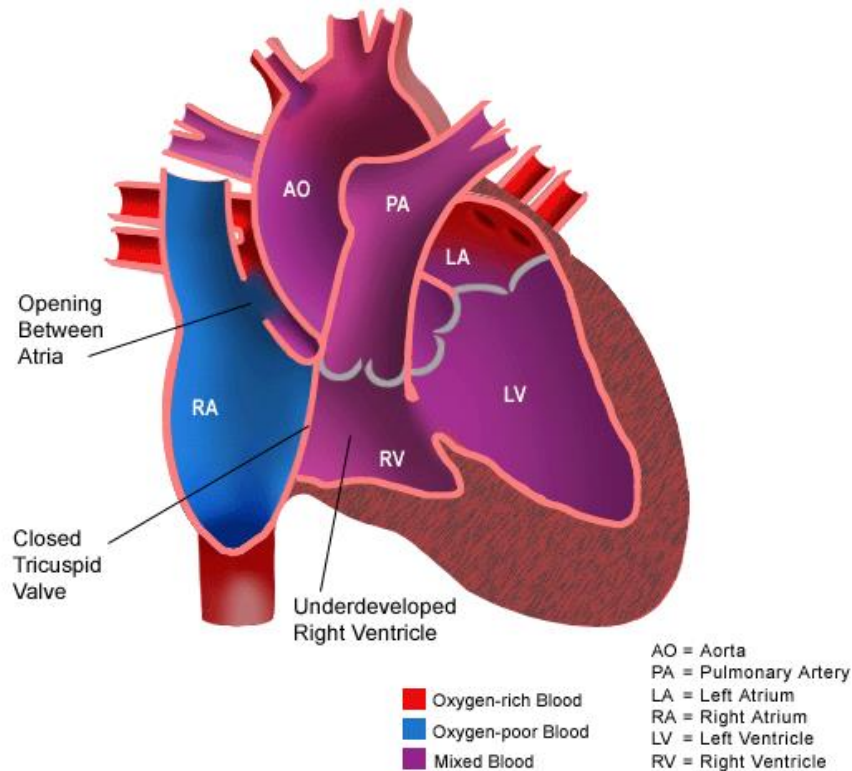
Figure 3.4 Schematic showing the tricuspid atresia (Image credit:
http://www.stanfordchildrens.org/en/topic/default?id=tricuspid-atresia-ta-90-P01819)

3.3.2 Hypoplastic Left Heart Syndrome (HLHS)

Hypoplastic left heart syndrome (HLHS, Figure 3.5) is a severe form of CHD. In these patients, the aorta and the left ventricle are underdeveloped. The aortic and mitral valves are either too small or closed together. Therefore, as blood from the pulmonary veins flow to the left atrium, it must flow through an atrial septal defect to the right atrium and right ventricle. In a normal circulation, the left heart receives oxygenated blood from the lungs and pumps it to the rest of the body. Having underdeveloped left heart severely affects this function. The right ventricle, which is optimized for a lower resistance pulmonary circuit, now must pump blood to both the pulmonary and systemic

circulations. In patients with HLHS, patent ductus arteriosus allows blood from the right

ventricle to pump through the body. This usually closes within eleven days after birth,

severely restricting, and eventually cut off blood flow in HLHS patients. HLHS is a

situation that cannot be sustained for long. It has a 100% mortality rate within the first

year of life if it is not treated properly [10].
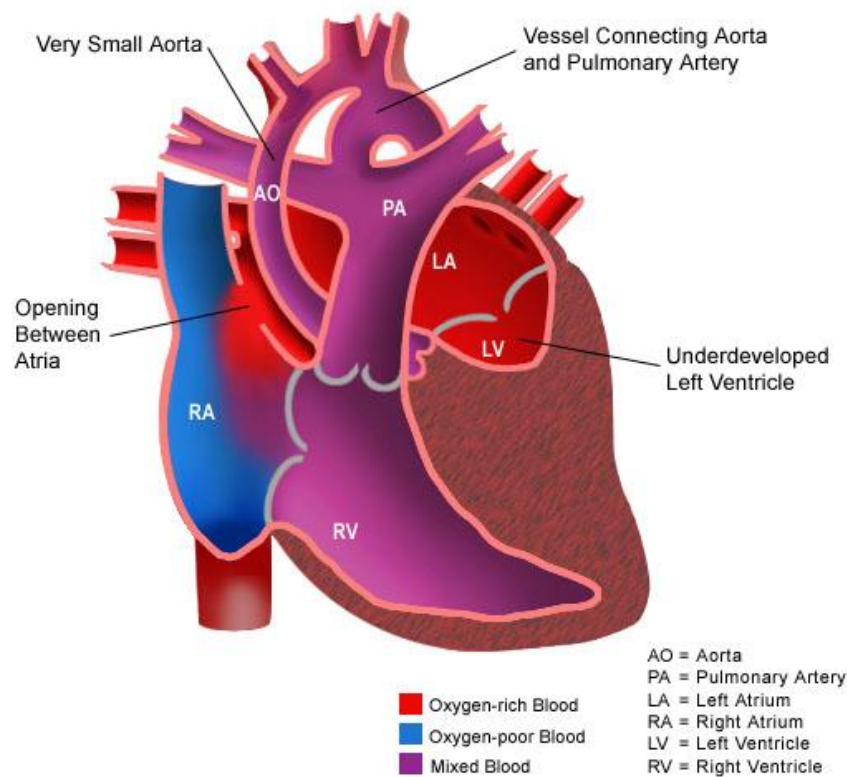
Figure 3.5 Schematic showing the hypoplastic left heart syndrome (Image credit: http://www.stanfordchildrens.org/en/topic/default?id=hypoplastic-left-heart-syndrome-90-P01798)

3.3.3 Surgical Repairs for SVHD
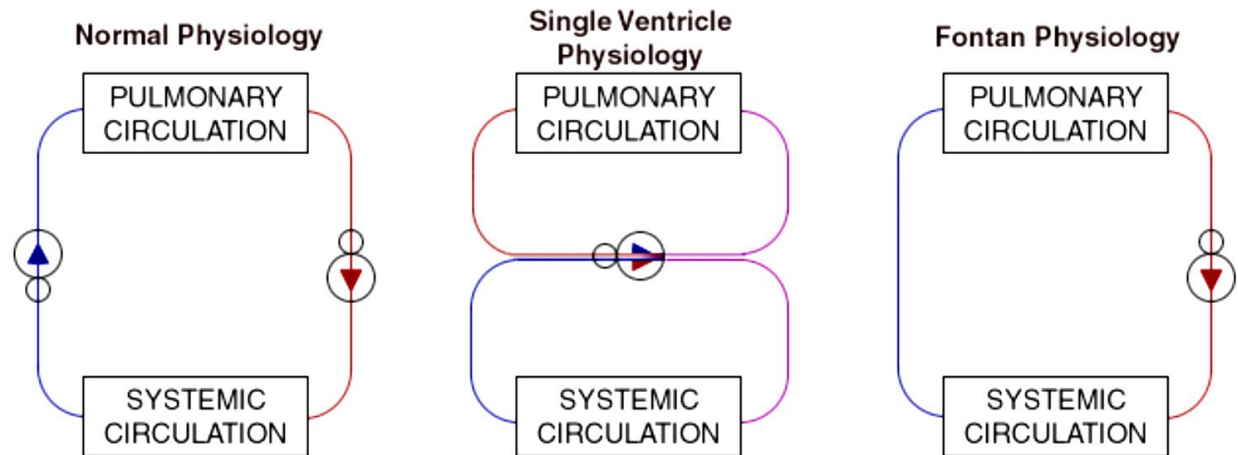
Figure 3.6 Circuit diagram for normal (left), SVHD (middle) and Fontan (right) physiology; the normal circulation works as a series of the pulmonary and systemic circulation and 2 pumps; the single ventricle physiology is a parallel circuit of pulmonary circulation with a single pump; the Fontan physiology is a series of pulmonary and systemic circulation with one pump.

Regardless of the specific nature of the SVHD, the fundamental goal of surgical intervention is to restore the serial connection between the pulmonary and systemic circulations. In 1971, Fontan and Baudet [11] proposed the first surgical palliation of this physiology by connecting the SVC directly to the right pulmonary artery (RPA), and IVC to the left pulmonary artery (LPA), bypassing the right ventricle (Figure 3.6). The introduction of the Fontan procedure restored the serial configuration of the pulmonary and systemic circulations in SVHD patients, avoiding oxygenated and de-oxygenated blood mixing in the single ventricle (as shown in Figure 3.7). However, the original Fontan procedure has a few drawbacks. For example, the IVC-to-LPA and SVC-RPA connection can be problematic if one of the lungs becomes obstructed. Also, hepatic nutrients from the IVC can only reach the LPA, increasing the risk of pulmonary arteriovenous malformations (PAVMs) in the right lungs [3-5]. PAVMs are shunts that form between pulmonary veins and arteries, which can lead to progressive hypoxemia.

The exact mechanism for the PAVMs is not known, however, it has been suggested that ensuring delivery of certain liver-derived protein in the hepatic venous blood to the lungs can prevent PAVMs [12, 13].

In 1973, a modified Fontan procedure, a valveless atriopulmonary connection was introduced by Kreutzer et. al. [14]. The IVC and SVC were left in their native configuration. Instead, an end-to-end anastomosis of the right atrial appendage to the main pulmonary artery was achieved (Figure 3.7). This procedure allowed distribution of hepatic blood to both sides of the lungs. Also the presence of atrial appendage provided atrial contraction pumping force for blood from the IVC to flow to the PAs. However, long-term follow-up showed that patients developed arrhythmias, thrombus and low cardiac output [15-18]. These complications were suggested to be due to the dilated right atrial appendage, which resulted in stagnant blood flow and significant energy dissipation [19].

de Leval et. al. introduced the total cavopulmonary connection (TCPC) as a modified Fontan procedure [20]. In the TCPC, vena cavae (VCs) are directly connected to the pulmonary arteries (PAs) (Figure 3.7), through a series of staged procedures. The benefit of TCPC lies not only on the lower incidence of arrhythmias compared with the earlier atriopulmonary connection (which is achieved by an end-to-end anastomosis of the right atrial appendage onto the main PA) [21], but was suggested also due to its lower energy dissipation rate because of its straight and streamlined design, reducing the workload of the single ventricle. As a result of these modifications, improved patient

management and care, surgical outcomes have increased gradually over the years [22, 23]. Follow-up studies have shown that the TCPC had a more favorable post-operative course, lower mortality and improved outcome [24-26]. The TCPC has become the primary choice of surgical correction for SVHD patients.
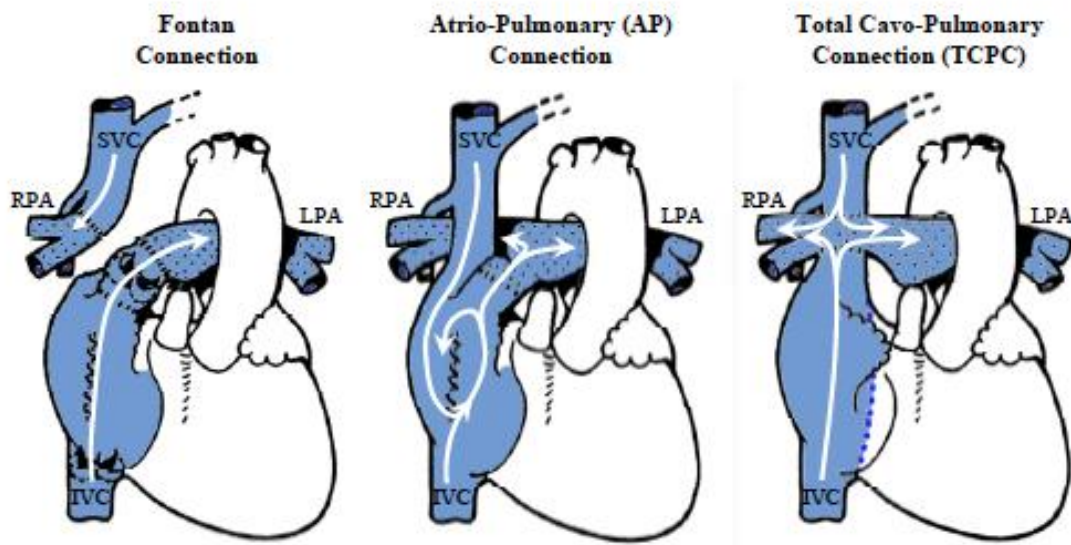
Figure 3.7 Schematic of the 3 versions of the SVHD surgical repair: Fontan connection (left), atriopulmonary connection (AP), and total cavopulmonary connection (right)

In later chapters, unless otherwise specified, "Fontan patients" refers to SVHD patients with a right ventricular bypass, including patients with TCPC. "Fontan circulation" also refers to a single ventricle circulation with Fontan palliation (including original Fontan, atriopulmonary or TCPC).

3.3.4 Total Cavopulmonary Connection (TCPC) – Surgical Procedures

The completion of TCPC is carried out in 3 stages of procedures. A complete right heart bypass is almost impossible to complete at birth, as the pulmonary vascular resistance is high and vessel sizes are too small. The 3-staged procedure allows the patient's body to gradually adapt to the complete right heart bypass.

3.3.4.1   Stage 1: Norwood Procedure

The first stage, Norwood procedure, usually takes place in the first weeks after birth. The main objective of this procedure is to establish unrestricted blood flow from the heart to the aorta, as well as minimal blood flow to the lungs. This ensures proper oxygenation before the patent ductus arteriosus closes. Surgically, this involves the shunting of the systemic to the pulmonary circulation to increase pulmonary blood flow in patients with blocked pulmonary pathway. This is usually achieved by either a Blalock-Taussig (BT) shunt or the Sano procedure (Figure 3.8). For the BT shunt, the right subclavian artery is connected to the right pulmonary artery. For the Sano procedure, the right ventricle is connected to the right pulmonary artery. In patients with HLHS, the reconstruction of the hypoplastic aorta is usually involved as well (as shown in Figure 3.8).
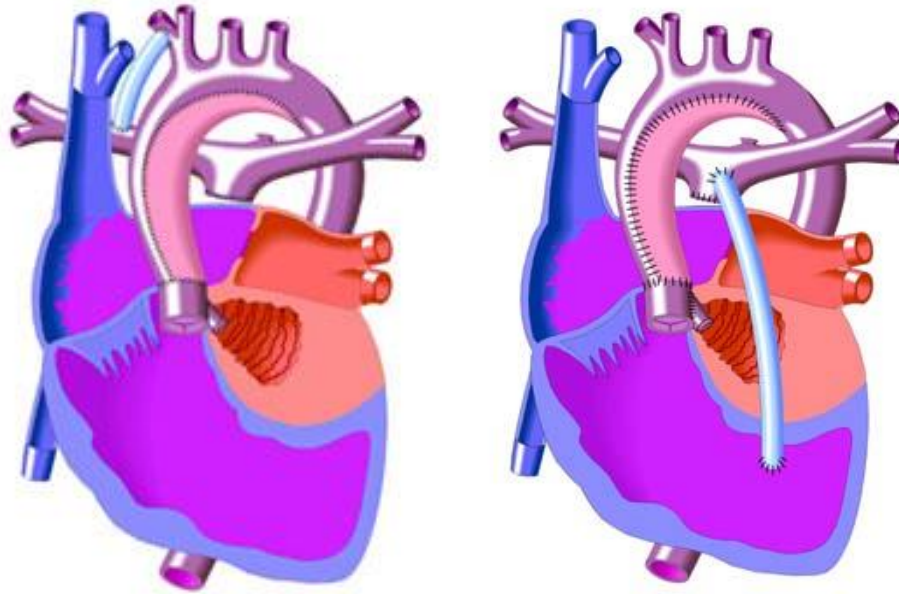
Figure 3.8 Schematic of the Norwood procedure: Blalock-Taussig shunt (left) and Sano procedure (right) (Image credit:: http://congenital.org/hd/?id=norwood-procedure)

3.3.4.2 Stage 2: Superior Cavopulmonary Anastomosis

The second stage, superior cavopulmonary anastomosis is typically performed between 4-12 months of age. This is the first step towards to the separation of the pulmonary and systemic circulations. The native patent ductus arteriosus or the systemic-to-pulmonary shunt created in stage 1 is being removed, hence reducing the ventricular overload.

The SVC is connected to the PAs to direct superior venous return to the lungs. The connection of SVC to the PAs is typically performed using either a bidirectional Glenn (BDG) or a Hemi-Fontan (HF) connection (Figure 3.9). In the BDG connection, the SVC is sutured to the RPA in an end-to-side anastomosis. In the HF connection, the SVC remains in its native configuration and the right atrial appendage is being connected to the PAs.
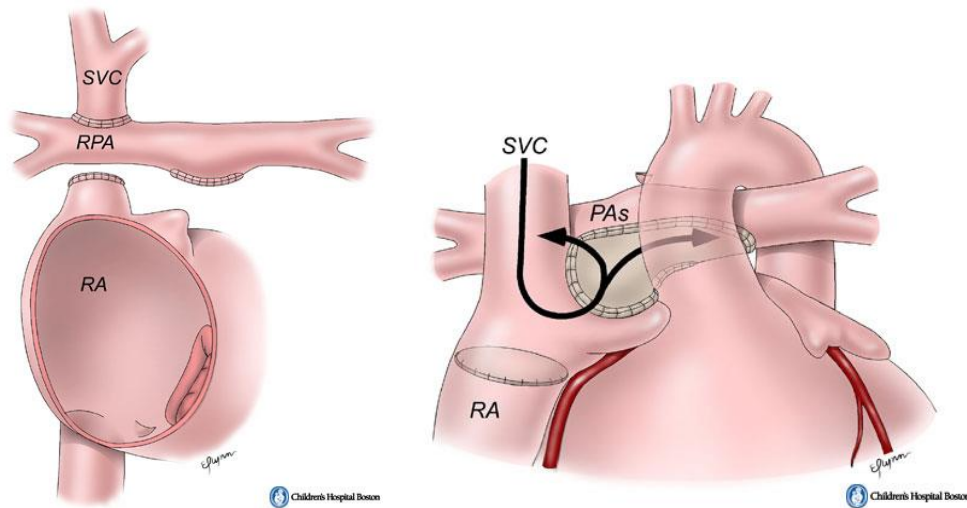
Figure 3.9 Two major options of SVC-to-PAs connection: Bidirectional Glenn (left) and Hemi-Fontan (right) (Image credit: https://apps.childrenshospital.org/clinical/mml/index.cfm?CAT=subtopic&SUBTOPIC_ID=1113)

3.3.4.3   Stage 3: Inferior Cavopulmonary Anastomosis

This final stage involves connecting the IVC to the BDG/HF connection, achieving a complete right ventricle bypass. This is usually performed between 1-5 years of age. It is completed by constructing an intra-atrial (IA) tunnel or using an extra-cardiac (EC) connection from the IVC (Figure 3.10). In all cases, the resulting geometries and constitutive materials can be very different. IA TCPC is more bulgy and compliant at the IA tunnel where vena caval flow mixes and recirculates prior to entering the PAs [20, 27]. EC TCPC is composed of stiffer cylindrical synthetic graft so flow is more streamlined towards the PAs [28].

The optimal choice of IVC connection is unclear, as both connection types offer different advantages and short-comings: The IA tunnels offer growth potential due to the

presence of the right atrial wall. On the other hand, their reconstruction requires opening the right atrium, which increases the risk of arrhythmias [29]. The EC conduits require fewer suture lines and no incision in the atrial wall; however, they do not provide any growth potential and have been associated with conduit stenosis and thromboembolism [30-32].
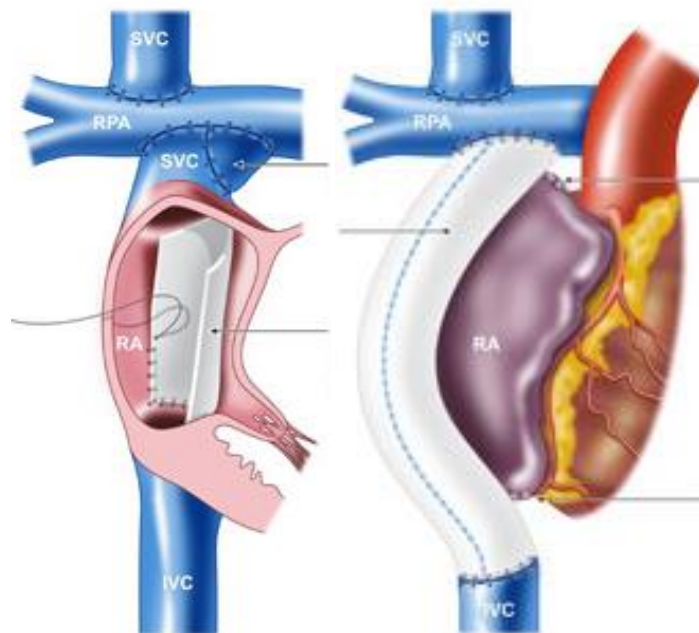
Figure 3.10 Two major types of IVC-to-PAs connection: Intra-atrial tunnel (left) and extra-cardiac graft (right) (Image credit: http://www.fontanregistry.com/fontan-procedure/the-different-forms-of-fontan-procedure.aspx)

3.3.5 Fontan Patient Outcome

In early survivors of Fontan patients, actuarial freedom from death or transplantation was 93.7%, 89.9%, 87.3%, and 82.6% at 5, 10, 15, and 20 years respectively [33]. However, the success of increase in survival rate of these patients does not always follow with a healthy life. Without a normal sub-pulmonary ventricle, these patients

suffer from systemic hypertension due to increased downstream resistance and pulmonary hypotension due to the absence of a second pumping chamber. Various complications arise as a result of this suboptimal hemodynamic state. Types of Fontan failure includes: limited exercise capacity, fatigue, presence of collateral blood flow, ventricular dysfunction, thromboembolism, progressive cyanosis, atrioventricular valve regurgitation, poor cardiac output, arrhythmias, PAVMs, protein losing enteropathy (PLE), liver dysfunction and poor neurodevelopmental outcomes [34]. The causes of many of these complications are not exactly known. It has been suggested that the single ventricle and the TCPC both play important role.

3.3.6 Fontan Physiology

3.3.6.1   Ventricular Function

In the Fontan circulation, the single ventricle performance can be crucial to patient outcome. The single ventricle serves as the sole driving force to blood flow in both systemic and pulmonary circulations. Compared to a biventricular circulation, the single ventricle has to pump blood against increase afterload [35]. Also, the ventricular preload is decreased since the driving force for pulmonary blood flow is reduced [36]. Last but not the least, for patients with HLHS, the morphologic right ventricle may not be well suited for the high pressure systemic circulation, causing ventricle function to deteriorate in time [37]. It has been reported that ventricular hypertrophy is a significant risk factor for death in Fontan patients [38]. Survival rate for single ventricle patients has been reported to be 35% with a decreased ventricular function, compared to 70% in single ventricle patients with normal ventricular function [38]. Another study has shown

that Fontan patients have normal ventricular mass, normal volume, but reduced systolic ventricular function (hence reduced ejection fraction) compared to normal subjects [39]. It has been reported that in the first 1-2 years after Fontan completion, decrease in ventricular mass, volume and ventricular performance was observed [40].

3.3.6.2 *Global Circulation*

With only a single ventricle providing driving force for both pulmonary and systemic circulations, the flow and pressure through the single ventricle circulation can be different from a biventricular circulation. For example, chronic elevation of central venous pressure has been observed in Fontan patients [41]. Liver complications in Fontan circulation have been reported [42, 43]. The exact causes have not been completely understood, but multiple studies have shown that it can be related to central venous hypertension, flow congestion, and impaired cardiac output in the Fontan circulation [42, 44-46].

There has also been growing evidence suggesting that TCPC hemodynamics is relevant to some of the long-term complications of Fontan patients. One of which is PAVMs. Unbalanced distribution of hepatic blood flow between the two sides of lungs has been associated with the risk of PAVMs [3, 5]. Therefore, recent studies have been focusing on improving the hepatic flow distribution to the two sides of the lungs by optimizing the TCPC surgical design [47-49].

3.3.6.3   Exercise Physiology

To evaluate exercise performance in healthy and Fontan subjects, exercise metabolic stress test is often performed. Patients will exercise from rest on a cycle ergometer. Expired gas will be measured during rest and exercise. Oxygen consumption (VO_2), carbon dioxide production (VCO_2), and minute ventilation (VE) are measured on a breath-by-breath basis. Peak VO_2 is defined as the highest VO_2 achieved by the subject, which is a surrogate of exercise performance [50]. Ventilatory anaerobic threshold (VAT) is defined as the VO_2 immediately below the exercise intensity at which pulmonary ventilation increased disproportionally relative to VO_2 [51], which is believed to reflect the onset of anaerobiosis and lactate accumulation. The respiratory exchange ratio (VCO_2/VO_2) is measured, which reflects the type of substrates that are being used by the cells for the production of ATP. Ventilatory equivalent of carbon dioxide (VE/VCO_2) is measured at VAT. This ratio is an index of ventilatory efficiency, which reflects how fast ventilation increases to remove excess CO_2 during anaerobic metabolism. The oxygen pulse (VO_2/heart rate [HR]) is measured at peak VO_2 and indexed to body surface area, which is equal to the product of stroke volume and the arterial-venous oxygen content difference. Since the arterial-venous oxygen content difference at peak exercise varies little among subjects, the oxygen pulse can used as a surrogate for stroke volume at peak exercise [52].

Previous studies in Fontan patients have shown poor exercise performance, including decreased peak VO_2, VO_2 at VAT, peak exercise HR, arterial oxygen saturation and cardiac output compared to healthy subjects [53, 54]. In Paridon et. al. [53], of the 411

Fontan patients, 166 achieved a maximal aerobic capacity. Peak VO_2 was on average 26.3 ml/kg/min. Higher %predicted oxygen pulse at peak exercise was associated with greater %predicted peak VO_2, work rate, and VAT. Adolescence and male gender were related with decreased %predicted peak VO_2. According to Takken et. al. [54], peak VO_2 of Fontan patients were 14.4-32.3 ml/kg/min on average. Peak HR was on average 153±10bpm and average arterial oxygen saturation was 89.5±1.94%. In Fontan patients, due to reduced stroke volume, heart rate response and affected venous return, exercise cardiac output was suboptimal. Also, VAT was below normal values.

Though the exact causes of exercise intolerance are not clearly understood, it is hypothesized that the added TCPC resistance in the circuit and pressure build-up in the venous system plays a role to this SVHD circulation. Due to the complex physiology and hemodynamics in SV patients, recent research has been focusing on investigating the potential linkage between TCPC hemodynamics and SV physiology [55, 56]. Although the clinical importance of TCPC energy dissipation on patient outcome is not clear, there has been growing evidence showing the relevance of elevated TCPC energy dissipation to ventricular performance and exercise performance [57], potentially resulting in limited exercise capacity [2, 58]. Therefore, recent studies aimed at improving the surgical design to minimize TCPC energy dissipation [59-61].

3.3.6.4   *Summary*

In summary, the exact mechanisms for Fontan failure are not clear and likely to be multi-factorial. Based on previous clinical data, we can hypothesize that some of these

complications may be related to the hemodynamics of the TCPC, which is an amenable part in the circulation. Therefore, in this thesis, we will focus on factors affecting TCPC hemodynamics, and how can it be improved with respect to energy dissipation and hepatic flow distribution.

3.4   Previous Investigations of TCPC Hemodynamics

3.4.1 Experimental Investigations

The experimental work performed by de Leval et. al. [20] was one of the very first and important work on studying TCPC hemodynamics. Using an *in vitro* model, they demonstrated the benefit of a TCPC over an atriopulmonary connection by having lower energy dissipation.

The earlier experimental work utilized simplified geometries to parametrically investigate the effect of different geometric parameters on TCPC hemodynamics. Simplified cylindrical tube models were used to study the fluid mechanics in the distinct cross shape geometry of TCPC [59, 61-71]. These studies aimed at ruling out the effect of different geometric parameters on TCPC hemodynamic and design the ideal TCPC with minimized energy loss. It was found that caval offset (distance between IVC and SVC) reduces collision of the incoming caval flow, lowering energy dissipation [59, 61, 63]. Presence of flaring at the connection not only describes the geometry more realistically, but also allows for streamlined flow towards the connection [59] and may reduce energy loss [59, 66]. A few studies also tried to investigate the effect of vessel planarity on

TCPC power loss [65, 69]. With advancement in medical imaging technique, patient-specific anatomies and flow conditions were more widely used recently [72, 73] to account for all these effects. Results were shown to be different from ideal tube models [62]. In the majority of these studies, hemodynamic measurements like flow and pressure were used to measure the energy dissipation across the TCPC. Particle image velocimetry was widely utilized to investigate the flow patterns in the TCPC with both idealized and patient specific TCPC models [64, 72, 73], as well as being used for validation of computational methods [74, 75].

In addition to understanding the impact of TCPC geometry on TCPC hemodynamics, *in vitro* mock setup of the Fontan circulation can also serve as a test bed for implanting medical devices. For example, experimental mock loops have been applied to investigate efficacy of ventricular assist devices in the Fontan circulation [76, 77]. Santhanakrishnan et. al. [78] also used an *in vitro* mock circulation setup to test the placement of a unidirectional valve within the IVC of an idealized TCPC. The results of the *in vitro* modeling suggested that IVC valve placement has the potential to improve hemodynamics in the Fontan circulation by decreasing hepatic venous hypertension and energy loss. Experiment testing allows a novel treatment strategy to be tested for its physics, before being implanted in animal models and patients.

3.4.2 Computational Fluid Dynamics Modeling

Computational Fluid Dynamics (CFD) has been widely used to model 3D blood flow in various cardiovascular applications. This is a valuable tool especially for CHD,

considering the very complex and patient specific anatomy in these patients [74, 79-81]. Compared to the experimental setup, it also allows detailed analysis of flow fields with potentially higher spatial and temporal resolution. Additionally, CFD is faster and cheaper, allowing it to be a great tool for parametric studies of varying conditions.

Earlier CFD studies also investigated idealized geometries to identify geometry parameters that affect TCPC hemodynamics [62, 69, 82-89]. By including 3D anatomy and flow acquired from medical images, patient specific CFD modeling of TCPC hemodynamics has been made possible [80, 90, 91]. For example, Whitehead et. al. [2] have shown the nonlinear increase in power loss in TCPC with increased cardiac output using CFD simulations. Dasi et. al. [92] demonstrated the hemodynamic difference in intra-atrial and extracardiac Fontan pathway with respect to hepatic flow distribution using patient specific anatomy and flow. Haggerty et. al. quantified the TCPC resistance of a large cohort of TCPC patients using CFD modeling [93]. Many of these CFD studies have helped broaden the understanding of the complexity of TCPC hemodynamics. A more detailed discussion of other relevant CFD studies will be presented in Chapter 3.5.

3.4.3 Lumped Parameter Model

Lumped parameter model (LPM) is another mathematical tool that is often used to model Fontan physiology. It is an analog of the electric circuit, in which the cardiovascular circulation is being discretized into compartments with resistance, compliance and inductance. Each compartment can be representing the heart, arterial

and venous system, and capillary beds of an organ or a vessel. These models capture reduced order information about the fluid flow (pressure, flow rate and volume) in a complex multi-compartmental system, and hence are computationally inexpensive compared to 3D CFD models. They are suitable for a system in which spatially resolved details are not important.

LPMs have various cardiovascular applications, and are useful for modeling complex CHD [94]. LPM has been applied for modeling the circulation in the first [95] and second stage [96] of the Fontan palliation, as well as hemodynamics in circulation with transposition of great arteries [97]. Sundareswaran et. al. used an LPM to study the impact of TCPC resistance on the single ventricle circulation under resting and exercise conditions [57]. LPM has also been used for testing the ventricular assist devices on the single ventricle circulation [98]. In more recent years, LPMs have been widely used together with 3D CFD solver to prescribe TCPC boundary conditions [99, 100], as well as relating the TCPC resistance to the hemodynamics of the broader global circulation [101].

3.4.4 Image-based Surgical Planning

Due to the patient specific anatomy and hemodynamics, it is not surprising that a generalized surgical approach may not be optimal for each individual patient. With the use of anatomic and flow information from medical images, as well as CFD solvers, patient specific surgical planning is now possible to allow the surgeon to tailor the surgical design for each patient, especially for the more complex cases. Image-based

surgical planning emerges as a novel technology to allow better visualization of the complex anatomic structures in the patient, as well as being used as a test bed to predict different surgical scenarios.

Image-based surgical planning utilized medical imaging, computer vision and computer-aided design to mimic surgical procedures. Surgeons and clinicians not only can visualize each patient's anatomy, they can also virtually manipulate and test whether a given surgical option is feasible for a given patient. For example, developed through collaborations between Drs. Yoganathan and Rossignac (GT College of Computing), the SURGEM software provides an interface for a user to create virtual surgical connections based on patient-specific anatomies [102]. This allows surgical procedures like baffle connection, or intervention like stent implantation to be virtually implemented, while visualizing patient specific landmarks like heart and surrounding vessels (Figure 3.11).
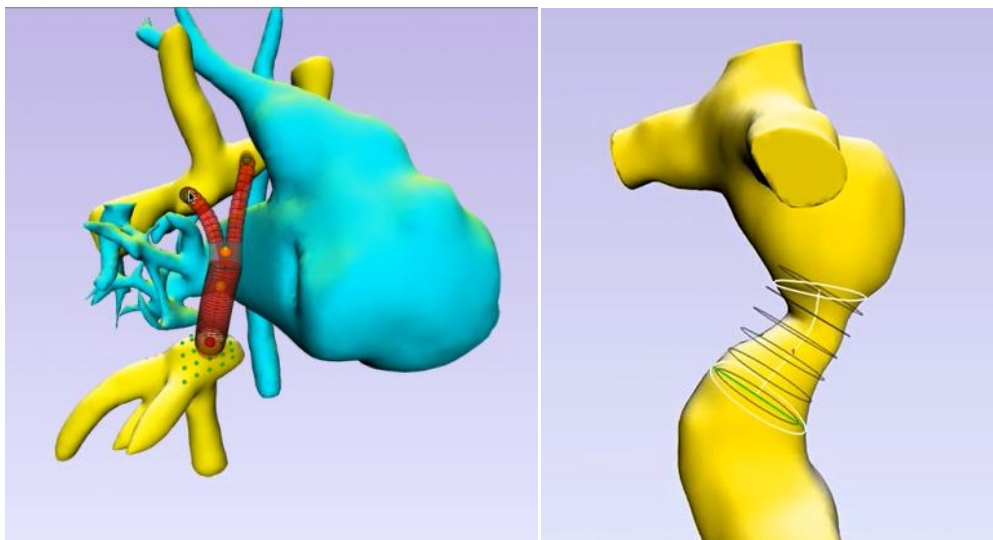
Figure 3.11 Screenshots of SURGEM III: Virtual baffle connection (left) and stent implantation (right). (Left: Yellow - the Glenn connection of the TCPC; Blue – heart and surrounding vessels; Red – virtual baffle; Right: Yellow – TCPC; Black circles – virtual stent)

By including CFD solver in this paradigm, the theoretical hemodynamic outcome of each surgical option can be predicted and compared pre-operatively. Previous studies have applied the surgical planning frameworks at different stages of the Fontan procedure [101, 103-107]. In collaboration with various institutions (mainly The Children's Hospital of Philadelphia, Children's Healthcare of Atlanta and Boston Children's Hospital), our group has applied image-based surgical planning in the third-stage of the Fontan procedure, as well as Fontan re-dos [48, 102, 108-111]. Using CFD solver, our group predicted the hepatic flow distribution of different surgical options for a patient with PAVMs. The best option was implemented in the patient and successfully corrected the patient's PAVMs [48].

One of the virtues of virtual surgery is that novel surgical strategy can be tested before implementation. In the recent decade, a modification to the Fontan procedure, a Y-graft connection, has been proposed (Figure 3.12). This idea was based on the theoretical Optiflo model proposed by Soerensen et. al [112]. The Y-graft connection divides the inferior caval flow to avoid flow collisions and promotes laminar, streamline transition to the pulmonary arteries (PAs). Dr. Kirk Kanter implemented this TCPC modification into his surgical practice, demonstrating surgical feasibility with encouraging short-term results [113, 114]. Furthermore, computational analyses of these patient-specific physiologies demonstrated positive hemodynamic characteristics, such as balanced hepatic flow distribution [115]. Recent work by Yang et. al. also aimed to optimize the Y-graft design for better patient hemodynamic outcome [116].
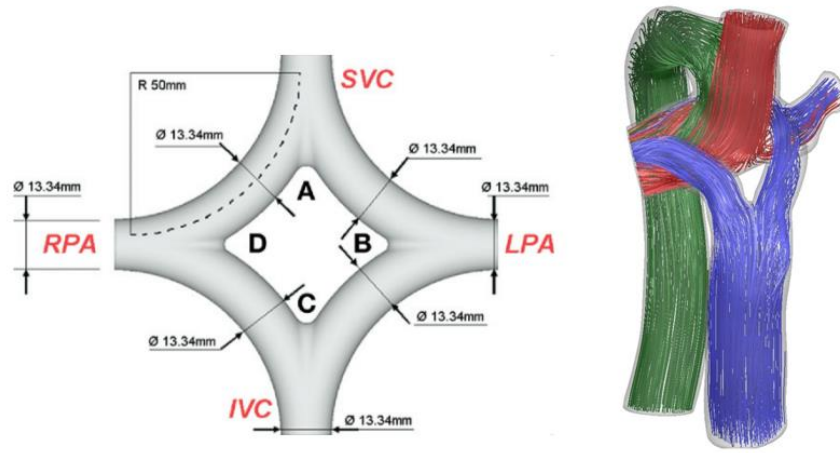
Figure 3.12 The schematic of the theoretical Optiflo connection proposed by Soerensen et. al. [112] (left) and the simulated streamlines in a patient specific Y-graft connection with azygos vein (green streamlines) (right)

In recent years, the image-based surgical planning paradigm has been constantly growing with extended modeling capabilities. For example, multi-scale solver [117] (coupling 3D CFD solver with a reduced-order model like the LPM) has been widely used recently to predict outcome of different surgical and interventional procedures [96, 118-122]. Using a similar paradigm, Mirabella et. al. simulated the effect of fenestration, Fontan revision and anti-pulmonary hypertension drug in a patient diagnosed with complex gastrointestinal disorders [109]. These modeling results offer surgeons and clinicians additional information before operating on the actual patient.

3.5 Computational Modeling: Current Status and Limitations

Computational fluid dynamics (CFD) has gained popularity in recent years to model patient specific TCPC hemodynamics. While it has a lot of advantages, it is still important to keep in mind that it carries various assumptions with regard to the actual physiologic environment. While it would be ideal to include all these complexities in a

single numerical model, it will likely result in a highly complex numerical model, increased computation time and hence hinder clinical applicability. The following sections will describe the different modeling assumptions and review relevant literature.

3.5.1 Flow Pulsatility

Due to the absence of the right ventricle, flow pulsatility in the TCPC is often assumed to be negligible in most studies. However, pulsatility in the IVC and SVC have been clinically reported in Fontan patients [123, 124]. Also, it is questionable whether this assumption is still valid under exercise conditions. DeGroff et. al. performed the first pulsatile *in vitro* experiment using idealized TCPC with different caval offset [125]. In that study, pulsatility was found to lead to power loss increase of up to 67% compared to time-averaged (steady) flow conditions. de Zelicourt et al. [126, 127] has shown that power loss estimation can be different when applying steady and pulsatile boundary conditions for CFD. Using computational model and patient specific flow and geometry, Marsden et. al. showed that energy efficiency across the TCPC decreased with pulsatile flow conditions compared to steady flow [91].

Khiabani et. al. performed the largest scale of pulsatility investigations of the TCPC to date. Using 24 patient specific anatomies and flow data, the power loss across the TCPC was quantified with CFD modeling [128]. A weighted pulsatility index (wPI) was defined to quantify flow pulsatility amplitude from vessel flow waveforms. It was found that flow pulsatility amplitude can strongly affect TCPC power loss. However, there was a minimum wPI threshold, above which the pulsatility effect was significant. When wPI

was less than 30, the difference between pulsatile and steady flow conditions was less than 10%. When wPI was less than 50, the difference between pulsatile and steady flow conditions was less than 20%. Using the Georgia Tech-Children's Hospital of Philadelphia Fontan database, the wPIs of more than 100 TCPC were quantified. It was observed that approximately 30% of these patients have wPI less than 30, and 60% of these patients have wPI less than 50. Therefore, pulsatility can be important for some of the patients with high wPI and should not be neglected in all cases.

3.5.2 Wall Deformability

Another limitation of many computational models of TCPC is the neglect of vessel wall deformability and heterogeneous material properties at the surgical connection that can possibly affect TCPC hemodynamics. Pulsation of fluid flow exerts forces on the deformable vessel wall. In turn, movement of the vessel wall extends or constricts the control volume, altering the fluid flow. Such fluid-structure interaction (FSI) happens in the human bodies, but has not yet been accurately included in most computational models of blood flow. Especially in the case of TCPC, without the normal right pumping chamber, external forces like intra-thoracic pressure, motion of the surrounding single ventricle, may alter TCPC hemodynamics, by acting through the deformable vessel wall. Also, wall motion can be significant during exercise, since vessel flow pulsatility is higher.

The effect of wall motion on TCPC hemodynamics is often modeled computationally in 2 ways: (i) FSI simulation, in which wall material properties are specified and the vessel

wall will deform according to the vessel flow and external pressure, or (ii) prescribed wall motion CFD simulation, where wall motion is prescribed on the wall of the fluid domain. FSI models are numerically complex as it includes fluid and structural models, as well as coupling method to allow the interactions of the two models. Prescribed wall motion CFD simulation using *in vivo* wall motion data includes not only wall compliance, but also any influence on the wall deformation that takes place *in vivo* (e.g. motion of the surrounding ventricle), which is more physiologic. However, this is less suitable for prospective modeling as one cannot always predict how the vessel wall will deform after the surgical connection is being altered.

Bazilevs et al. [129], studied the difference of hemodynamic efficiencies of realistic TCPC geometries with rigid and deformable wall using prescribed wall thickness. This study demonstrated the difference in resting and exercise hemodynamics between rigid wall and FSI analysis. Orlando et al. [88], carried out similar analysis using idealized TCPC model with prescribed material properties and flow rates in the vena cavae, pulmonary arteries and suture lines, after which they established a 10% difference of power loss between the rigid and deformable model. Although a 10% power loss difference in idealized 0 caval offset model may seem negligible, Masters et al. [87] utilized variable caval offset models to demonstrate that modeling FSI in numerical simulations can affect the power loss ranking compared to rigid models (as shown in Figure 3.13). This study highlighted the importance of FSI in TCPC modeling, as caval offset has often been a parameter used to optimize TCPC hemodynamics.
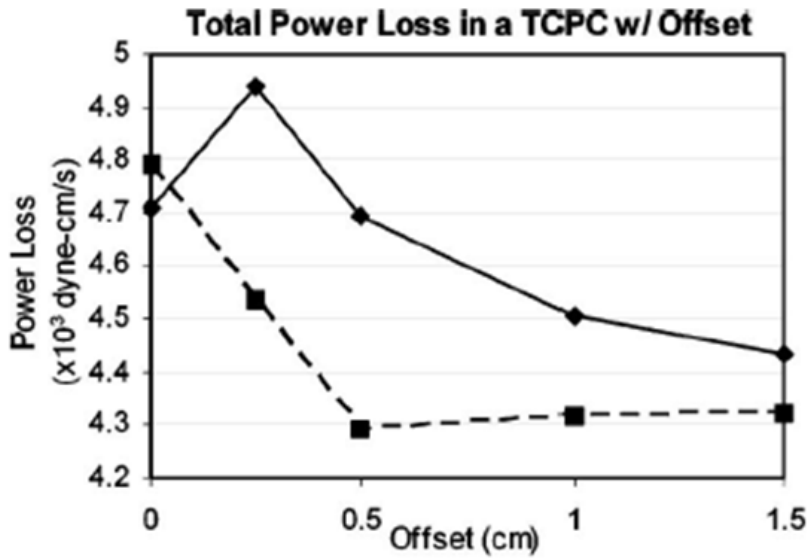
Figure 3.13 Power losses of various offsets TCPC models with rigid (solid line) and compliant (dotted line) simulations from Masters et al. [87]

More recently, using patient specific flow waveforms and anatomies of two patients, Long et. al. performed FSI CFD analysis of the TCPC with varying wall properties [130]. They found that there was little effect of FSI on pressure tracings, hepatic flow distribution, and time-averaged energy efficiency. However, the effect of FSI on wall shear stress, instantaneous energy efficiency, and wall motion was significant. Mirabella et. al. [109] was the first group to study the effect of wall deformability on TCPC hemodynamics with *in vivo* wall motion data. Using cine anatomic magnetic resonance imaging (MRI) data, the magnitude of wall displacement of an intra atrial TCPC was quantified. The *in vivo* wall motion was then prescribed in a CFD model that includes moving domain. The results highlighted the impact of patient-specific wall motion. The largest differences between rigid and moving wall models were observed in measures of energetic efficiency of TCPC as well as in hepatic flow distribution and transit time of seeded particles through the connection.

3.5.3 Respiration

Respiration is another physiologic influence on TCPC hemodynamics that has not been included in most CFD models. Without the presence of a sub-pulmonary ventricle, it has been shown clinically that TCPC vessel flow is affected by respiration. Fogel et. al. have shown that flow in the systemic venous pathway of Fontan patients was phasic to both cardiac and respiration cycle: Approximately 70% of flow was cardiac dependent, and the rest was respiratory [131]. Hsia et. al. reported that Fontan hepatic venous flow (measured with Doppler ultrasonography) depended on respiration more than normal subjects, and was larger in inspiration than expiration [132, 133] . Using real-time MRI, Hjortdal et. al. also observed increased IVC flow during inspiration in Fontan patients [134]. During inspiration, the negative intra-thoracic pressure assists the forward flow in the SVC and the PAs, increasing venous return as compared to expiration.

These effects may have important implications on TCPC hemodynamics that require further investigations. Marsden et. al. simulated TCPC hemodynamics computationally by including respiratory influence in the IVC and SVC flow waveforms. This was done by superimposing patient specific flow waveform of a cardiac cycle with the flow waveform of a respiratory cycle from Hjortdal et. al. [134] Compared with steady flow model, the respiration model has reduced energetic efficiency.

There are several challenges in including respiration in the CFD modeling of TCPC hemodynamics. While previous studies have included respiration by superimposing

respiration flow from literature with patient specific flow of a cardiac cycle, it is not clear whether the respiration flow influence is patient specific. The current methods of assessing TCPC flows clinically are commonly performed at resting breath-held conditions, and respiratory information is not always available. Also, including respiration by the means of augmenting vessel flow represents a simple way to model respiration. However, in addition to change in vessel flow rate, vessel compliance may also come into play. Part of the TCPC is composed of compliant native vessel tissue. The changing intra-thoracic pressure during respiration can deform the vessel wall and affect TCPC hemodynamics. Finally, how respiration affects TCPC hemodynamics during exercise can be different than baseline condition. This can be important when modeling exercise flow in Fontan patients.

3.5.4 Influence of Global Circulation

To understand *in vivo* hemodynamics, patient data from source like MRI, echocardiography and catheterization are often used as flow and pressure boundary conditions for patient specific CFD modeling. However, for prospective modeling these boundary conditions may not necessarily be valid. The TCPC is connected to the global circulation. A specific perturbation to the system, e.g. changing the pressure of the TCPC, will affect the hemodynamics of the rest of the circulation. At the same time, the global circulation, as the source of blood flow to the TCPC, can also affect TCPC hemodynamics. Therefore, it is likely that the boundary conditions of the TCPC will change when any part of the system (the TCPC, the single ventricle or any parts of the circulation) is being altered.

In a clinical standpoint, it is also important to understand the influence of the local TCPC hemodynamics on the global circulation (e.g. ventricular preload and afterload) during surgical planning. As discussed earlier, Fontan patients have reduced ejection fraction compared to normal subject [39]. It can be possible that the local TCPC hemodynamics can be relevant to reduced ventricular function. Optimizing TCPC hemodynamics with respect to ventricular function can be important.

In these scenarios, multi-scale approaches [135] by coupling 3D CFD solver with lower-order representation of the global circulation (e.g. LPM) can be useful. A simple form of such model is by using a Windkessel model at the outlets. This is to model the outlet flows by the downstream pulmonary vasculature's resistance. Marsden et. al. [91] and Mirabella et. al. [109] have utilized this approach to model the relative LPA and RPA flows by prescribing resistance values at the outlets. More recently, LPMs that represent the entire cardiovascular circulation is being coupled to 3D solver, increasing the modeling capabilities of these multi-scale solvers (as discussed in Chapter 3.4.3) [99-101].

While these coupled solvers are useful to understand the impact of TCPC hemodynamics on global circulation, these models require a number of patient specific *in vivo* measurements, which include both flow and pressure data to fit the LPM parameters (e.g. compliance and resistance values). This will require a large amount of clinical data, which is not always easy to obtain. Also, while these models are based on

theoretical relationship of the TCPC and the global vasculature, model validation is still necessary.

3.5.5 Growth and Long-term Remodeling

While virtual surgical planning is aimed to improve patient's hemodynamic outcome, only acute hemodynamic outcome can be modeled. As the patient grows, the hemodynamic outcome may change with time. There are very little data on the serial evolution of patient specific anatomic and hemodynamic changes with time. Especially, the growth potential of an extracardiac conduit compared to the lateral tunnel can be very different. The extracardiac graft is usually performed with a larger graft diameter than the patient's native IVC, so that when the native tissue grows, the extracardiac conduit diameter will be large enough to maintain a uniform diameter pathway [136]. On the other hand, the lateral tunnel is formed partially with native atrial tissue [137], hence is thought to have growth potential [138]. Restrepo et. al. demonstrated that the growth of the Fontan pathway (FP) and TCPC vessels are different with respect to the connection type, and the magnitude of growth is not proportional to somatic growth [139] using patient anatomic data with two serial time points. Using CFD simulations of two serial time points of TCPC patients, the same group of investigators demonstrated the effect of growth on TCPC hemodynamics [140]. It was found that vessel flow increased in time, proportionally to body surface area. And the non-proportional vessel growth contributed to increased energy loss in time. More long-term follow up patient data will help understand the evolution of TCPC hemodynamics and the impact of virtual surgical planning on long-term outcome.

3.6   Summary and Significance of the Proposed Approach

Previous *in vivo*, experimental and computational work has significantly enhanced our understanding of TCPC hemodynamics and SVHDs. The research work proposed here aims to understand the impact of geometry, respiration and wall motion on TCPC hemodynamics, and help to overcome some of the CFD modeling limitations. Clinically, the goal is to identify ways to optimize TCPC hemodynamics to reduce risk of some of the SVHD long-term complications. In a patient specific CFD modeling standpoint, the goal is to quantify the relative error brought by the assumptions in CFD modeling of TCPC hemodynamics, to provide insights for future modeling.

1. **Evaluate the importance of TCPC geometric design on TCPC hemodynamics**

   Even though the Fontan procedure results in favorable short-term outcomes, the patients remain at risk for long term complications [1]. It has been suggested that some of these may be attributed to the unfavorable connection hemodynamics [55]. For example, there has been evidence showing the possible link between TCPC energy dissipation and patient exercise tolerance [2, 57]. Also, unbalanced distribution of hepatic blood flow between the two sides of lungs has been associated with the risk of PAVMs [3, 5]. Since the TCPC design is the factor that is most amenable to surgical manipulation, it has been the focus of a large body of literature. Because of the complex native vessel morphology, vessel growth and difference in surgical techniques, there exists a great variability in the TCPC geometry. This research aims to access the relationship between TCPC geometric

44

parameters (diameters, caval offsets, connection angles) and TCPC hemodynamic outcome (power loss, hepatic flow distribution) using with the largest Fontan MRI database to date. This can potentially provide further insight to surgeons and cardiologists regarding the connection geometries to avoid, and also help in the interpretation of suboptimal hemodynamics relative to the post-operative geometries.

2. **Understand the influence of respiration-driven flow on TCPC hemodynamics**

   Breath-holding or averaged free-breathing segmented phase contrast magnetic resonance imaging (PC-MRI) has been commonly acquired in TCPC patients to evaluate vessel flow, and has been used for the boundary conditions in numerical simulations to evaluate TCPC hemodynamics. However, the impact of ignoring respiration in the evaluation is not fully understood. One of the goals of this thesis work is to evaluate the difference in TCPC hemodynamics under free-breathing and breath-held conditions. With this, we can understand the influence of ignoring respiration effect on vessel flow when evaluating TCPC hemodynamics, and understand the impact of using breath-held PC-MRI acquisition instead of free-breathing. This may also help identify the respiratory phase(s) that affects TCPC hemodynamics positively.

3. **Understand the influence of vessel wall compliance on TCPC hemodynamics**

   Current modeling strategies used to simulate TCPC hemodynamics are mostly based on rigid wall assumption. However, TCPC wall motion is observed *in vivo* and magnitude appears to vary across vessels of the same connection. By quantifying

the wall motion of different vessel types in the TCPC and comparing numerical predictions of hemodynamics with deformable and rigid models, the importance of wall deformability in patient specific modeling will be understood.

4. **Assess the relative importance of modeling assumptions used in the numerical evaluation of TCPC hemodynamics**

While this thesis aims to overcome some of current CFD modeling limitations, including all complexities (pulsatile flow, respiration effect and wall compliance) for all future CFD simulations can be challenging. This is not only due to the increased computational cost due the complexity of FSI models and the increased simulation time for simulating pulsatile breath-held or free-breathing flow (compared to steady simulations); this is also because having all the patient specific data to include all these complexities are not always easy (e.g. real-time MRI to quantify free-breathing flow, having patient specific vessel wall properties). Therefore, this research work aim to quantify the relative influence of pulsatile flow, respiration effect, wall compliance effect on the same patient cases to help understand which is the most important assumption(s) in modeling TCPC hemodynamics.

CHAPTER 4   Materials and Methods

4.1   Overview

This chapter presents all the tools that have been used in this thesis work (illustrated in Figure 4.1). The following sections include:

1. Anatomic CMR image acquisition and image processing to reconstruct patient specific anatomies;

2. Geometric parameter quantification used to characterize patient specific anatomy;

3. Vessel flow CMR image acquisition and image processing to obtain patient specific flow under various conditions), as well as vessel flow and area metrics to characterize vessel flow and area waveform under these conditions:

   - breath-held resting

   - free breathing resting

   - free breathing exercise conditions

4. Exercise stress test protocol to quantify patient exercise performance;

5. Different computational models used in this work for fluid dynamic simulations and hemodynamic metrics computed to characterize TCPC hemodynamics.
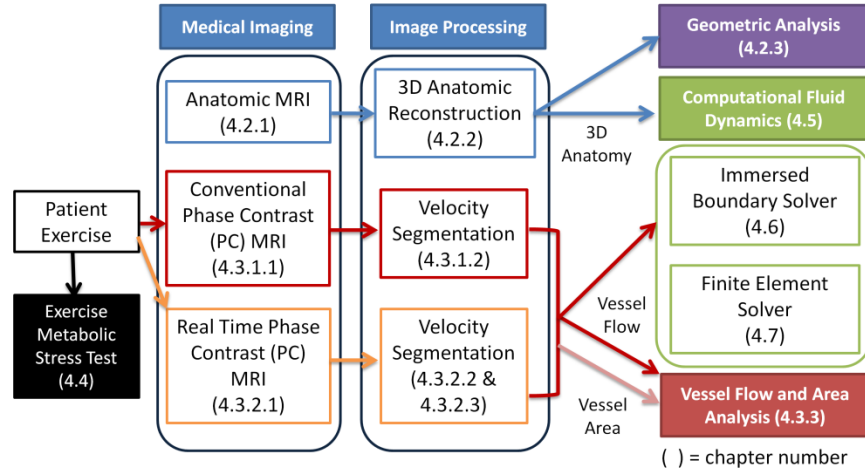
Figure 4.1 Schematic of how patient specific data is used and analyzed in this thesis work

4.2 TCPC Anatomy
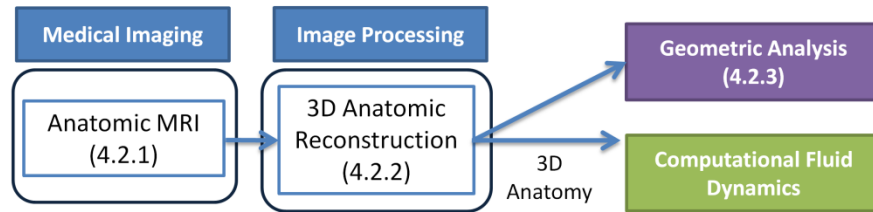
Figure 4.2 Schematic of how anatomic MRI data is used and analyzed in this thesis work

4.2.1 Anatomic Image Acquisition

The anatomic cardiac magnetic resonance (CMR) images in this thesis were mainly acquired with steady-state free precession (SSFP) sequence. With this sequence, lower density tissues (such as soft tissues and airway) will appear black, where as blood will appear in white. To obtain patient specific TCPC anatomy, a stack of anatomic images (typical 40-50) was acquired in the transverse direction spanning the thorax, from right below the confluence of the hepatic veins to the top of the aortic arch (example shown in Figure 4.3). These images have typical in-plane resolution of 0.5-1 mm and slice

thickness of 3-5 mm. In general, smaller voxel sizes were chosen for smaller patients in order to accurately resolve first and second order pulmonary arterial branching; increased number of excitations and oversampling were used to compensate for the decreased signal-to-noise. The CMR image acquisition parameters of each study will be described in each individual specific aim.

(a)   (b)

(c)   (d)
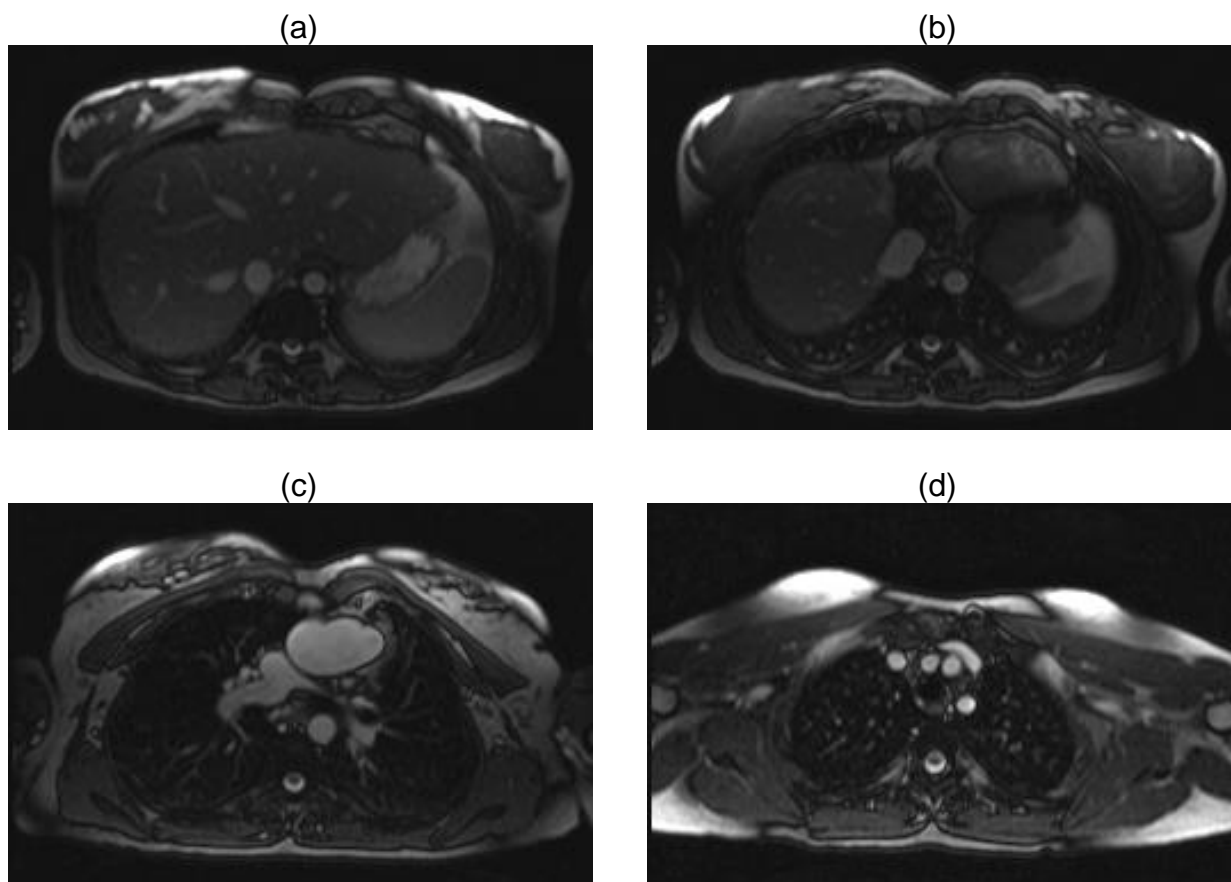
Figure 4.3 Example of transverse anatomic CMR images acquired with SSFP at various locations across the thorax: (a) before the hepatic veins' confluence, (b) across the Fontan pathway, (c) junction with the pulmonary arteries and (d) above the aortic arch

4.2.2 3D Anatomic Reconstruction

TCPC anatomies are complex and patient specific. For patient-specific modeling of the TCPC, 3D *in vivo* anatomies need to be accurately captured from medical images. Previous investigators in our laboratory have developed reconstruction techniques to reproduce 3D geometries using stacks of 2D anatomic images. The reconstruction involves 3 major steps (Figure 4.4):

(i) Interpolation: Due to imaging time constraints, 2D medical images are often sparsely sampled. The transverse CMR images typically have out of plane resolution of 3-5mm, whereas in-plane resolution is usually 0.5-1mm. To obtain isotropic voxel, the transverse CMR images need to be interpolated. Adaptive control grid interpolation (ACGI) was applied to interpolate the CMR images to obtain a stack of images with isotropic size for each volumetric element [141, 142].

(ii) Segmentation: The interpolated images were then segmented to obtain the vessels of interest, using the bouncing ball algorithm [142]. An image intensity threshold was first set for each interpolated image. Based on this threshold, the region of interest was then selected for each image. With the bouncing ball algorithm, adjacent images will also be segmented. This algorithm can handle incomplete vessel edge definitions and has been shown to perform superiorly to other methods [142].

(iii) 3D Reconstruction: A 3D level set surface evolution algorithm was used to extract a set of smooth, coherent surface points from the segmented images, while

transforming the geometry to MRI coordinate system for registration of flow boundary conditions. The contours were imported into Geomagic Studio (Geomagic Inc., NC, USA) for surface fitting. The final volume of interest was extracted by trimming the models at the following positions (example shown in Figure 4.4): (1) IVC/FP: distal to the hepatic veins confluence, (2) SVC: distal to the junction of the SVC and the innominate vein, (3) LPA: proximal to any branching, (4) RPA: proximal to any branching, except in some cases where the upper lope of RPA PC-MRI was acquired separately, the models were trimmed according to the PC-MRI planes.
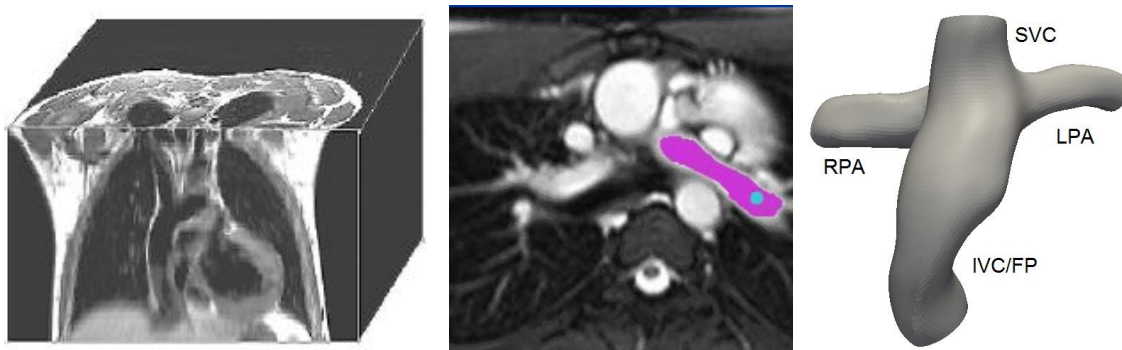
Figure 4.4 Screenshot of the anatomic reconstruction pipeline: Isotropic 3D volume data after ACGI (left), bouncing ball algorithm segmenting vessel of interest (center) and final 3D reconstructed surface (right)

The ACGI and 3D reconstruction methods used in this thesis have been validated for use with the TCPC geometry, demonstrating 0.96% error for PA diameter measurement and 1.77% error on radius curvature [141, 142]. A detailed protocol for the anatomic reconstruction can be found in Appendix A.1.

4.2.3 TCPC Anatomic Characterization

TCPC anatomy is very patient-specific. Since TCPC hemodynamics can be affected by its geometric features, there is a need to quantify these geometric characteristics to better understand the relationship between TCPC geometry and its hemodynamics.

Vascular Modeling ToolKit (VMTK, www.vmtk.org) is an open-source program which allows robust geometric characterization of complex cardiovascular anatomies [143-145]. It was used in this thesis to compute vessel centerlines along the vessels and bifurcation vectors (which contain the location and direction of the point which the centerline starts to bifurcate) at each vessel bifurcation. Each point of the centerline represents the 3D coordinates of the center of the maximum sphere inscribed in the vessel lumen at that point, equipped with the radius of such sphere Figure 4.5. The resulting outputs from the VMTK were processed with a custom Matlab (MathWorks Inc., MA, USA) script to extract geometric parameters. A detailed description of how the VMTK and Matlab scripts can be applied to characterize TCPC geometry is described in Appendix A.2.
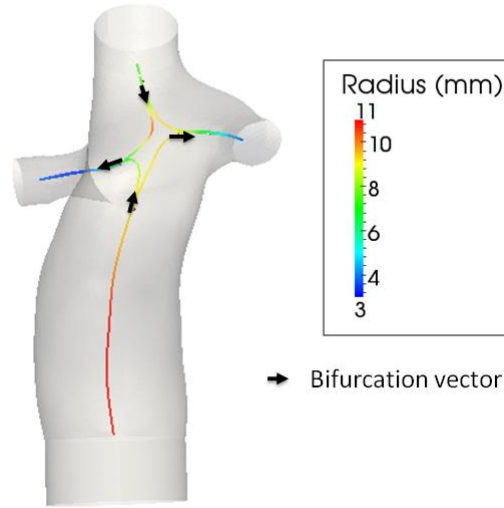
Figure 4.5 Example of vessel centerlines and bifurcation vectors computed with VMTK

4.2.4 Geometric Parameters of Interest

4.2.4.1   Vessel Dimensions

In the geometric characterization of the TCPC in this thesis, a TCPC vessel centerline was defined from the opening of the vessel to a location close to the bifurcation of the vessel. This was computed based on four landmarks obtained in VMTK (Figure 4.6):

- c^A_1 and c^A_2 are the intersections of each centerline with the tube surface of the other branch of the bifurcation;

- c^B_1 and c^B_2 are the centers of the upstream maximal inscribed spheres touching c^A_1 and c^A_2, respectively.
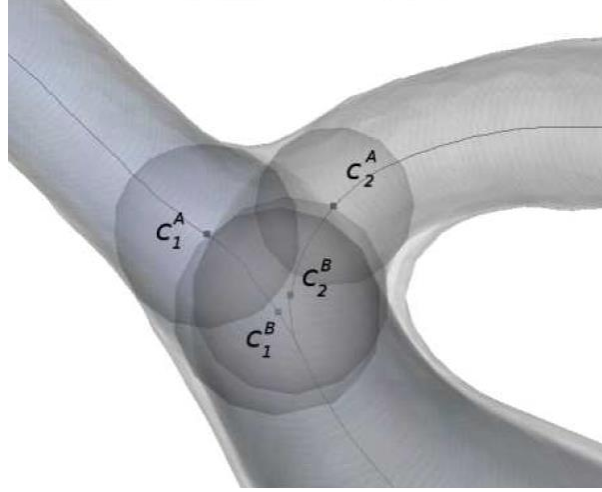
Figure 4.6 Example of landmarks at the vessel bifurcation computed by VMTK [145]

The final vessel centerline was computed by averaging the x, y, z-coordinates and maximum inscribed sphere radius at each point on the centerline along the opening of the vessel to c^B_1 and the centerline along the opening of the vessel to c^B_2.

For each vessel, the minimum, mean, and maximum diameters along the centerline were computed by doubling the maximum inscribed sphere radius. The minimum/maximum diameter ratio (to observe any vessel narrowing) was defined as the ratio of minimum vessel diameter to maximum vessel diameter. Smaller minimum/maximum diameter ratio means a more drastic change in diameter along the vessel. This metric was computed to quantify vessel narrowing for each vessel.

To compare the relative minimum size of the LPA and RPA cross sections, the relative LPA area was defined as follows:

$$Relative\ LPA\ area = \frac{(Minimum\ LPA\ area)}{(Minimum\ LPA\ area)+(Minimum\ RPA\ area)} \quad \text{(Equation 4.1)}$$

54

where each area was computed from the minimum diameter of the respective pulmonary artery (PA) ($\frac{\pi D_{min}^2}{4}$).

4.2.4.2   Vessel Connection Details

Caval offset was defined as the distance between the FP and the (right) SVC or LSVC at the connection. This parameter was computed by extending the length of the FP and SVC bifurcation vectors onto the LPA-RPA centerline, and then calculating the displacement between the points (Figure 4.7). When the FP is to the right of the SVC, the displacement is defined to be negative. VC (vena cava)-PA (pulmonary arteries) offset was defined as the shortest distance between the centerline from FP to SVC and the centerline from LPA to RPA.
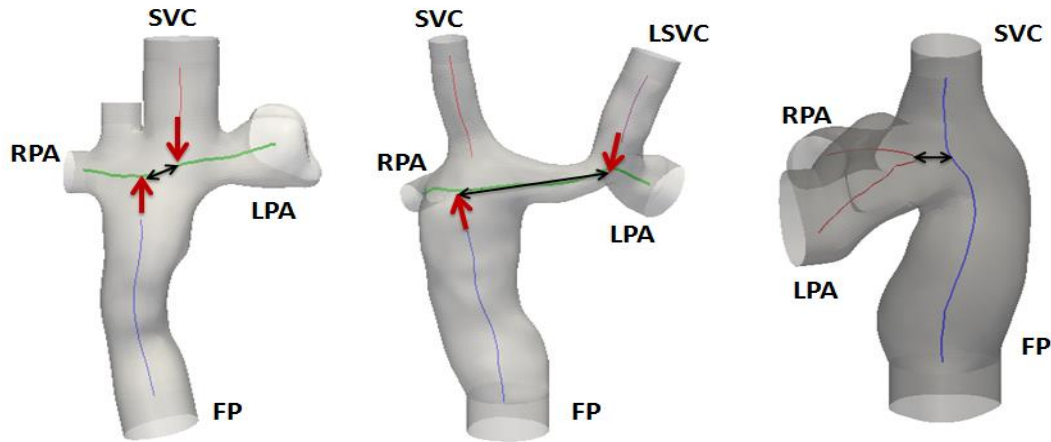
Figure 4.7 Caval offset at the connection (Left: Caval offset with SVC; Middle: Caval offset with LSVC; Right: VC-PA offset)

The 3-dimensional angle θ between any 2 vessels (Figure 4.8) was computed based on the dot product of the two corresponding bifurcation vectors of the vessels involved:

$$\theta = arcos\left(\frac{b_1 \cdot b_2}{\|b_1\|\|b_2\|}\right), 0° \leq \theta \leq 180° \qquad \text{(Equation 4.2)}$$

where b_i=vessel's bifurcation vector. More obtuse (larger) angle corresponds to more streamlined transition between vessels, whereas angle of 180° corresponds to a straight pipe.
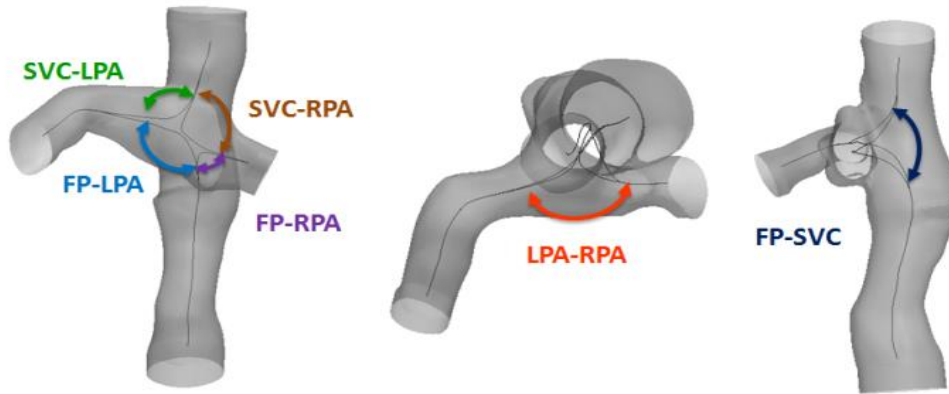
Figure 4.8 Connection angles

To account for differences in patient size, vessel diameters were normalized by the square root of body surface area (√BSA [m]) to obtained diameter in non-dimensional form. The effect of caval offset can be relevant to the diameter of the TCPC vessel. For example, the effect of 10mm caval offset can be different for a patient with FP diameter of 10mm versus a patient with FP diameter of 14mm (illustrated in Figure 4.9). Therefore, caval offsets were normalized by mean FP diameter of each patient instead of BSA, in view of previous convention [59, 61, 146].
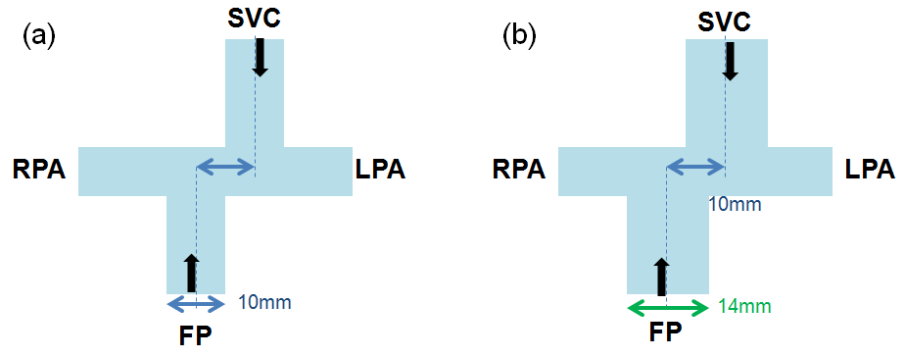
Figure 4.9 Schematic illustrating two TCPC models with the same caval offset magnitude, but different FP and SVC diameters. (a) caval offset magnitude is the equal to FP and SVC diameters, (b) caval offset magnitude is smaller than FP and SVC diameters, so head-on flow collision between FP and SVC is possible.

4.3   TCPC Vessel Flow
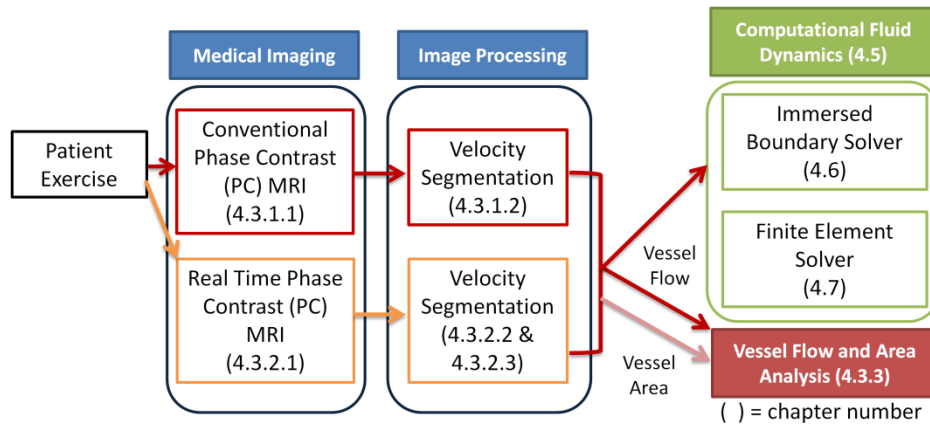
Figure 4.10 Schematic of how phase contrast MRI data is used and analyzed in this thesis work

4.3.1 Conventional Phase-Contrast MRI (PC-MRI)

4.3.1.1   PC-MRI Image Acquisition

Phase contrast magnetic resonance imaging (PC-MRI) was utilized to acquire through-plane velocity profiles at the planes normal to the ascending (AAO) and descending

aorta (DAO), pulmonary arteries and vena cavae (and azygos vein (AZ) if present) over the cardiac cycle. This results in a stack of magnitude images (which show the anatomy) and a stack of phase images (from which velocity maps can be obtained) (example shown in Figure 4.11). The through-plane velocity profiles were obtained by performing a linear transformation of the phase images: the white pixels correspond to the highest values in the encoding direction and the black pixels correspond to the maximum negative values. The brighter the white pixels, the higher the positive velocity values are. The darker the black pixels, the more negative the velocity values are through the acquired plane. The static surrounding structures are represented by a salt-and-pepper noise. For the TCPC, in some patients, the upper lobe branch of the RPA (RUPA) was acquired separately because there is insufficient distance to acquire it with the other branches.

(i) Resting condition: Majority of the conventional PC-MR images studied in this thesis were acquired under resting condition. These acquisitions were mainly performed under breath-held condition, containing 20-30 images (even-spaced in time) that were averaged over multiple cardiac cycles. The encoding velocity was chosen based on the vessel acquired, which could be as low as 60 cm/sec for venous structures and as high as 150 cm/sec for arterial structures.

(ii) Exercise condition: For a subset of patients studied in this thesis, exercise PC-MR images were also available at the AAO, DAO and SVC. FP images under exercise condition were not available in most patients since the motion of the FP during exercise hindered an accurate quantification of vessel flow. These patients were all prospectively

enrolled at Children's Hospital of Philadelphia. Patients included had a minimum age of 12, had the TCPC as the only source of pulmonary flow, and were able to perform a metabolic exercise stress test using a stationary cycle ergometer. After the resting CMR acquisition, the patients were slid partially out of the bore of the MRI machine. Lower limb exercise using an MRI-compatible supine bicycle ergometer (Lode BV, Groningen, the Netherlands) was performed which allows RPM-independent workload ranging from 10 to 250 W. The workload was set initially at 20 W. It was then increased at a rate of 20 W/min progressively to obtain heart rate (HR) corresponding to the HR at ventilatory anaerobic threshold (VAT) during the exercise stress test. After that, the patients were returned to the isocenter of the magnet for imaging within 10 seconds. HR was monitored continuously. PC-MRI across the SVC, AAO and DAO were acquired separately as 3 separate velocity maps. The patients repeatedly exercised to return to the target HR (HR at VAT) for each acquisition. The images were acquired at free-breathing and the velocity maps were averaged. Typically 20-30 phases were acquired per cardiac cycle, with encoding velocity ranges 100-350 cm/s for the aorta and 60-250 cm/s for the SVC. The study lasted approximately 90 minutes with the patient lying spine.
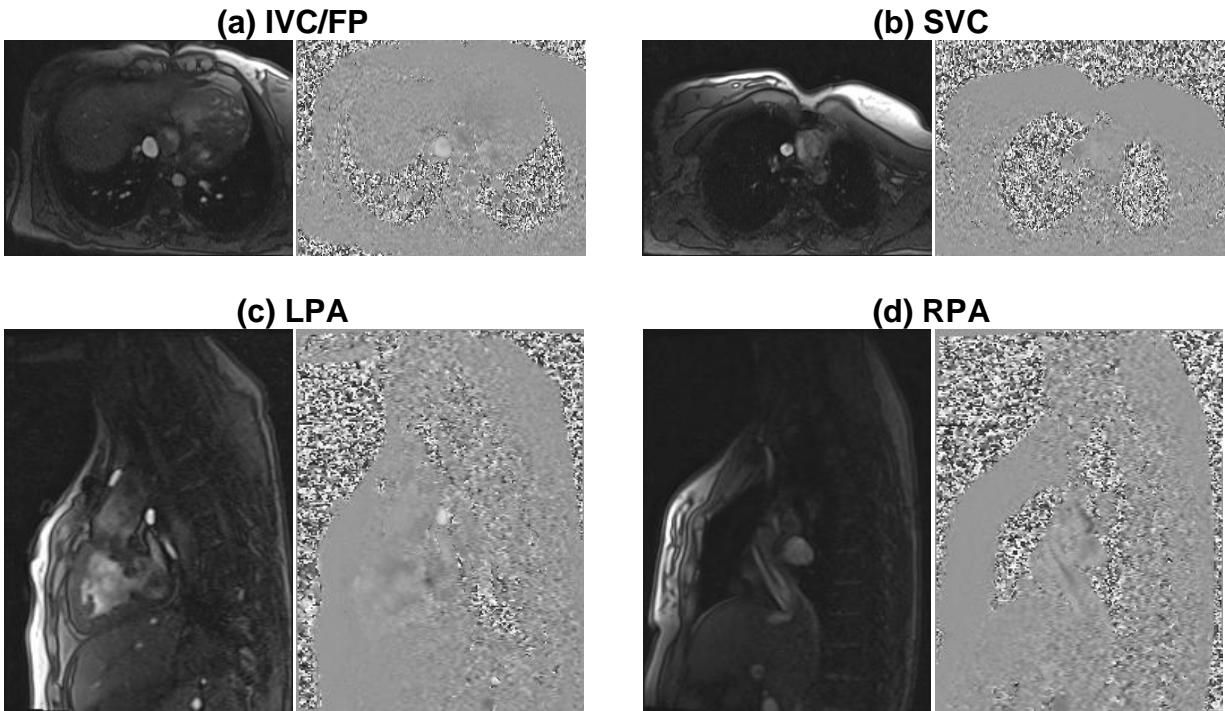
Figure 4.11 Example of resting PC-MRI images at the (a) IVC/FP, (b) SVC, (c) LPA and (d) RPA. The black and white image on the left shows the magnitude image, and the adjacent grey image is the corresponding phase image.

4.3.1.2   *Velocity Segmentation*

The methodology developed for velocity segmentation employs parametric active contours with Gradient Vector Flow (or snakes), where the user specifies an initial contour that evolves under the influence of internal and external energy fields to precisely sit on the vessel border [147]. Flow artifacts, introduced by air in the lungs, are eliminated with an adaptive median filtering approach, where spurious noise vectors are automatically removed close to the vessel border. Validation against manual segmentation demonstrated an excellent agreement between the two methods with less than 1% difference in resulting flow rates [148]. The velocity within the segmented area

was then integrated over the area to obtain flow rate. A detailed protocol for velocity segmentation of conventional PC-MRI is described in Appendix A.3.

4.3.2 Real Time (RT) PC-MRI

In accessing TCPC vessel flow under resting conditions, majority of the image acquisition was performed under breath-held (BH) conditions. For exercise conditions, even though image acquisition was performed under free-breathing condition, phase contrast images were still averaged over multiple cardiac cycles. Therefore, the influence of expiration and inspiration on flow was masked by the averaging. With the advancement of image acquisition and processing techniques, real time PC-MRI (RT PC-MRI) allows a detailed analysis of respiratory effects on TCPC flow under rest and exercise conditions. Here, an overview of processing RT PC-MR images is presented, whereas a detailed protocol is described in Appendix A.4

4.3.2.1   Real Time PC-MRI Image Acquisition for resting and exercise conditions

The real-time PC-MR imaging protocols for resting free-breathing and resting breath-held (at the end of expiration) conditions are the same. The RT PC-MR images were acquired with an echoplanar (EPI) sequence utilizing shared velocity encoding [149]. The acquisition protocol consists of through-plane PC-MRI across the IVC/FP, SVC, AAO and DAO for at least 10 seconds to capture multiple respiratory cycles under free-breathing condition (FB). Approximately 20 frames were acquired per second, resulting in a series of about 200-300 PC-MR images for each vessel for resting conditions.

For exercise RT PC-MRI acquisition, the patient was slid partially out of the bore of MRI machine. The MRI-compatible supine bicycle ergometer was used to allow patient performing RPM-independent workload. The workload was set initially at 20 W. It was then increased at a rate of 20 W/min progressively to obtain HR corresponding to the HR at ventilatory VAT during the exercise stress test. Exercise was then suspended and the patient was automatically returned to the isocenter of the magnet for imaging. Using this method, RT PC-MRI measurements of the AAO, DAO, IVC/FP, and SVC were acquired with repeated exercise performed in between for the patient to return to the target heart rate. About 200 images PC-MR images were acquired for about 10 seconds under exercise conditions.

4.3.2.2   *Velocity Segmentation for RT PC-MRI Images for resting and exercise conditions*

Since the RT image series contains more than 200 images for each vessel, the previously described velocity segmentation method is not the feasible as it is not suited for segmenting a large number of images. A semi-automatic protocol for segmenting RT PC-MRI was developed using the open-source software Segment [150-152]. The vessel of interest is first selected on the image slice. Encoding velocity values are then used as verification for the instantaneous flow velocity in the selected region. Any velocity value exceeding the encoding velocity is automatically unwrapped in the Segment software. Velocity values are then integrated over the region of interest to calculate the associated flow rate in Segment. Segment also allows for automatic propagation of

region of interest to adjacent slices or the entire imaging sequence, which increases the ease in segmenting a large image series like RT-MR images.

4.3.2.3   Obtaining Respiratory and Cardiac Cycle Durations

It is hypothesized that under FB conditions, vessel flow is influenced by respiration and cardiac pulsation, whereas under BH conditions, vessel flow is only affected by cardiac pulsation. To understand the influence of each effect, the durations of respiratory cycle and cardiac cycle need to be tracked simultaneously with the vessel flow.

Time points of inspiration and expiration can be determined by tracking the chest wall motion on the same magnitude images. Using Segment, the thoracic cavity area was segmented and the temporal variation in cross sectional area was tracked. Through the change in the chest wall area, time points of inspiration and expiration can be identified (Figure 4.12). Credit for development of this protocol belongs to Dr Reza Khiabani.
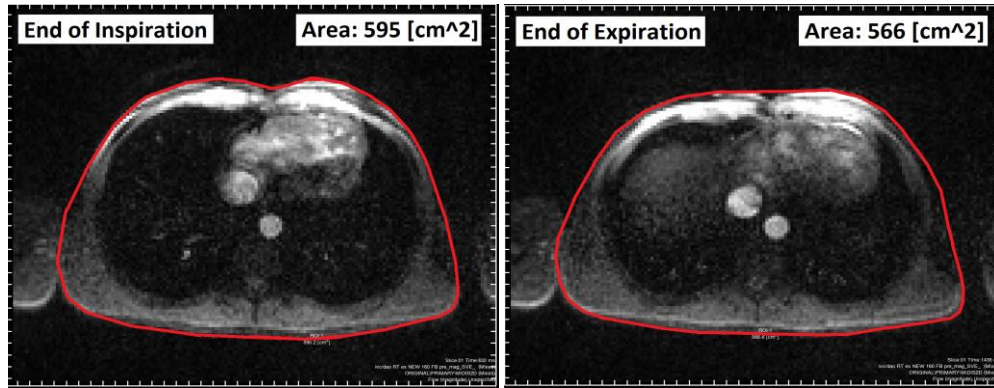
Figure 4.12 Example segmented chest wall cavity using the Segment software. As shown in the figure, change in chest wall area during inspiration and expiration can be traced
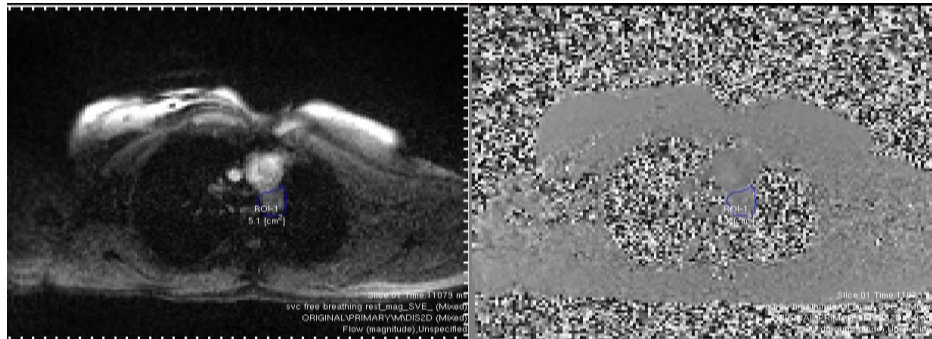
Figure 4.13 Example of the segmented descending aorta on the same slice of the SVC image series

Due to the PC-MRI slice location and orientation, DAO vessel is also acquired on the same image slice of the FP acquisition. AAO (and DAO for some cases) is also acquired on the same image slice of the SVC acquisition. By using the velocity segmentation protocol for segmenting flow data with Segment, AAO/DAO flow waveform can be obtained (Figure 4.13). Time points of diastole and systole of the AAO/DAO flow waveform can then be used to help identify the cardiac cycle from the RT PC-MR images of the FP and SVC. Therefore, the duration of cardiac cycle can also be traced simultaneously with the flow waveform of the vessel of interest (FP/SVC).

One caveat with segmenting AAO/DAO flow on the FP/SVC slices is that the encoding velocities for FP/SVC slices are general lower than for what DAO/AAO acquisitions require. However, the goal here is to obtain an approximate duration of a cardiac cycle along with IVC/SVC vessel flow, rather than the actual DAO/AAO flow rates in time.
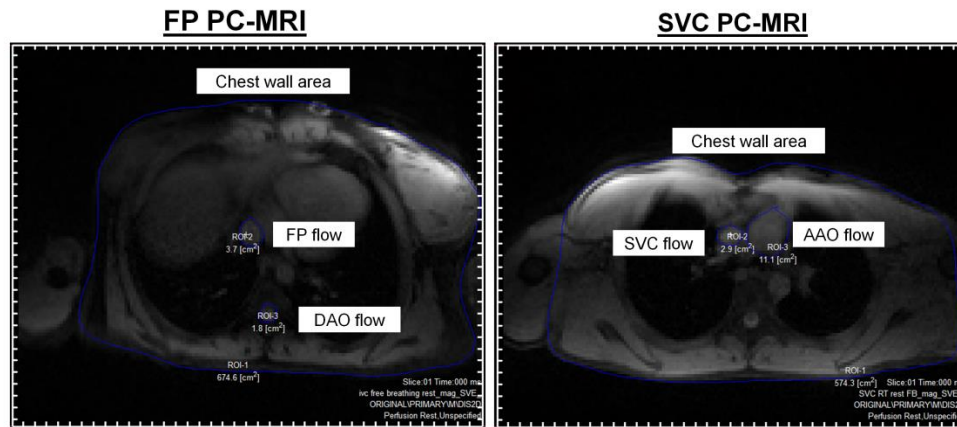
Figure 4.14 Example of how vessel flow, cardiac cycle and respiratory cycle can be tracked simultaneously on the same FP image and the same SVC image

Using the above protocol, vessel flow (FP/SVC), aortic flow curve and chest wall area waveform could be segmented from the same image series, so that vessel flow, cardiac cycle and respiratory cycle can be tracked simultaneously on the FP/SVC slice (illustrated in Figure 4.14). Figure 4.15 shows an example of the segmented flow waveform from FB and BH RT PC-MRI of the same vessel, along with the traced chest wall area (for FB) and descending aorta flow (both FB and BH). The respiration and cardiac cycle can be easily identified using the described methodology.
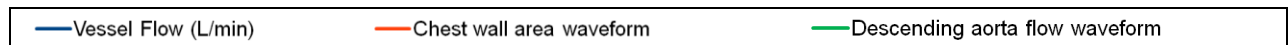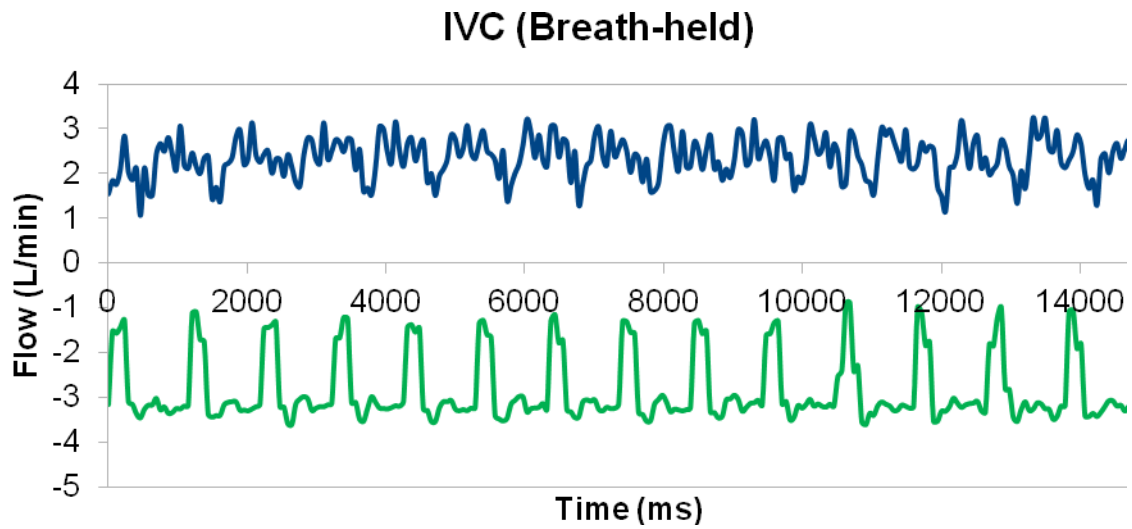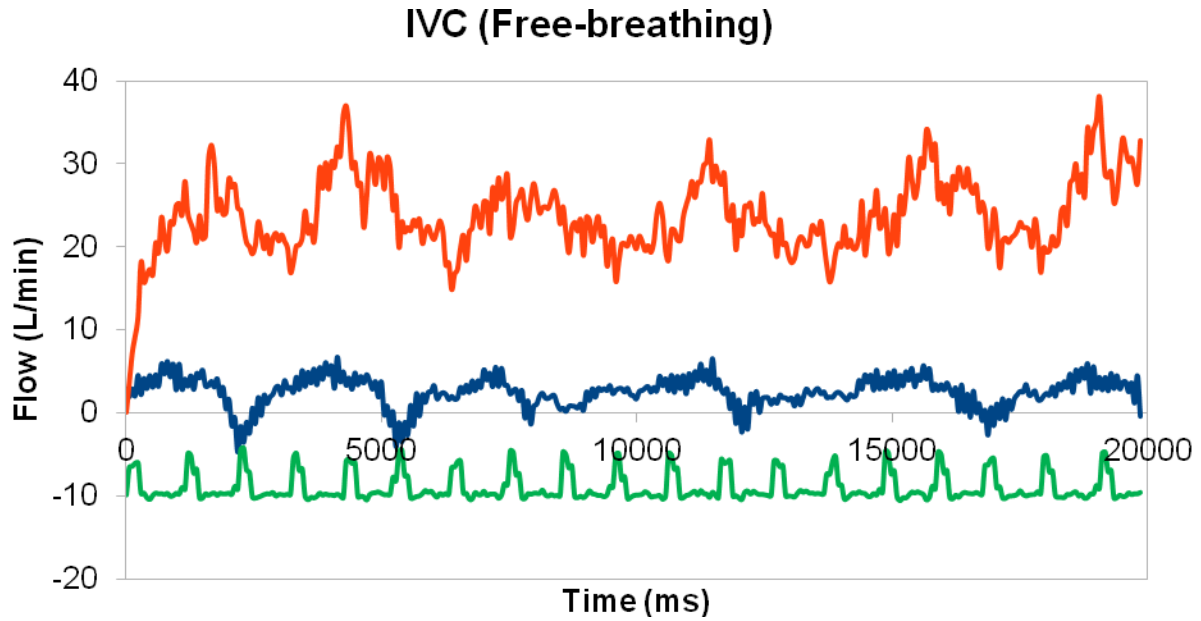
Figure 4.15 Example of the resting FB (top) and BH (bottom) flow waveforms of the IVC for the same patient segmented from RT PC-MRI. Respiratory and cardiac cycles were traced simultaneously using the segmented chest wall area and descending aorta flow waveforms

4.3.3 *In Vivo* Vessel Flow and Area Metrics

Based on the segmented *in vivo* flow and vessel area waveforms, several relevant metrics were computed to better understand patients' functional status, as well as used to correlate with simulated hemodynamic metrics:

(i) Cardiac Index: Computed as total cardiac output divided by patient's body surface area (BSA, m^2), where cardiac output was obtained by segmenting PC-MRI images across the AAO. It describes the volume of blood being pumped by the heart.

(ii) Pulmonary flow distribution (PFD): This was defined as the flow distribution of the total systemic return to the left and right lung. It was calculated as:

$$\%PFD(LPA) = \frac{Q_{LPA}}{Q_{LPA}+Q_{RPA}} \times 100\% \qquad \text{(Equation 4.3)}$$

where %PFD(LPA) is the percentage of total pulmonary flow leaving through the LPA, Q_i is the flow rate of the specific vessel i (LPA or RPA). This was also referred as global flow distribution in previous work.

To quantify the magnitude of flow pulsatility under different conditions, the following metrics were also computed:

(iii) Pulsatility Index (PI): PI was computed to quantify the amplitude of flow pulsations (cardiac pulsation-driven or respiratory-driven) at each vessel:

$$PI = \frac{Q_{max}-Q_{min}}{Q_{mean}} X100\% \qquad \text{(Equation 4.4)}$$

where Q_{mean} is the time-averaged flow rate over one respiratory or cardiac cycle, and Q_{min} and Q_{max} are the minimum and maximum instantaneous flow rates within the same cycle.

(iv) Weighted Pulsatility Index (wPI): In order to characterize the overall vessel flow pulsatility in the TCPC, a weighted flow pulsatility index (wPI) [153] was defined as:

$$wPI = \sum_{i=1...n} PI_i \times c_i \qquad \text{(Equation 4.5)}$$

$$c_i = \frac{Q_i}{\sum_{i=1...n} Q_i} \qquad \text{(Equation 4.6)}$$

where n is the total number of inlet vessels and c_i is the flow split of vessel i, Q_i is the time-averaged vessel flow of inlet i.

To quantify the magnitude of vessel area change of different vessel under different conditions, the following metric was also computed:

(v) Deformation Index (DI): DI was computed to quantify the amplitude of cross sectional area change at each vessel:

$$DI = \frac{A_{max} - A_{min}}{A_{mean}} X 100\% \qquad \text{(Equation 4.7)}$$

where A_{mean} is the time-averaged vessel cross sectional area over one respiratory or cardiac cycle, and A_{min} and A_{max} are the minimum and maximum instantaneous vessels cross sectional areas within the same cycle.

4.4   Exercise Stress Test Protocol

For patients enrolled in the exercise CMR study, they first completed a routine maximal metabolic exercise stress test using a ramp cycle protocol [154]. Firstly, pulmonary function was evaluated prior to the exercise study using standard methods for spirometry, lung volumes, and conductance as outlined by the American Thoracic Society [155]. Forced expiratory volume (air exhaled during a forced breath) in one second and forced vital capacity (total amount of air forcibly exhaled after taking the deepest breath) were measured.

After resting spirometry, the patients exercised to maximal volition (respiratory exchange ratio (ratio between the amount of cardiac dioxide produced and oxygen consumed in one breath) >1.10) using an electronically braked cycle ergometer (SensorMedics, Yorba Linda, CA). Patients first pedaled for 3 minutes in an unloaded state followed by a ramp increase in work-rate to maximal exercise. Cardiac rhythm was monitored continuously throughout the study with 12-lead ECG (Marquette Case-8000, Milwaukee, WI) measurements. Systemic arterial oxygen saturation (SaO_2) was monitored continuously by pulse oximetry.

Metabolic data were obtained throughout the exercise study using a metabolic cart (SensorBiomedics V29, Yorba Linda, CA). Parameters measured included minute oxygen consumption (VO_2), minute carbon dioxide production (VCO_2), oxygen pulse (O_2P), maximal ventilation, and respiratory exchange ratio. Ventilatory anaerobic threshold (VAT), the point during exercise at which pulmonary ventilation becomes

69

disproportionately high with respect to oxygen consumption (which is believed to be the onset of anaerobiosis and lactate accumulation), was measured by the V-slope method [156].

4.5 Computational Fluid Dynamics (CFD) Overview

Throughout this thesis, two types of CFD solvers were used (illustrated in Figure 4.16). An immersed boundary method solver was used to investigate the relationship between geometry and TCPC hemodynamics under rigid wall and time-averaged boundary conditions (both inlets and outlets). This solver (described in Chapter 4.6) was developed by de Zelicourt et. al. [75, 157, 158] in 2010 and has been applied in most patient cases in the Georgia Tech Fontan database. More recently, to increase the complexity of our computational model, namely to include Windkessel outlet boundary condition, as well as fluid-structure interaction capability, an open source Finite Element Library implemented in C++, LifeV (www.lifev.org) was applied. More details of the LifeV solver are described in Chapter 4.7.
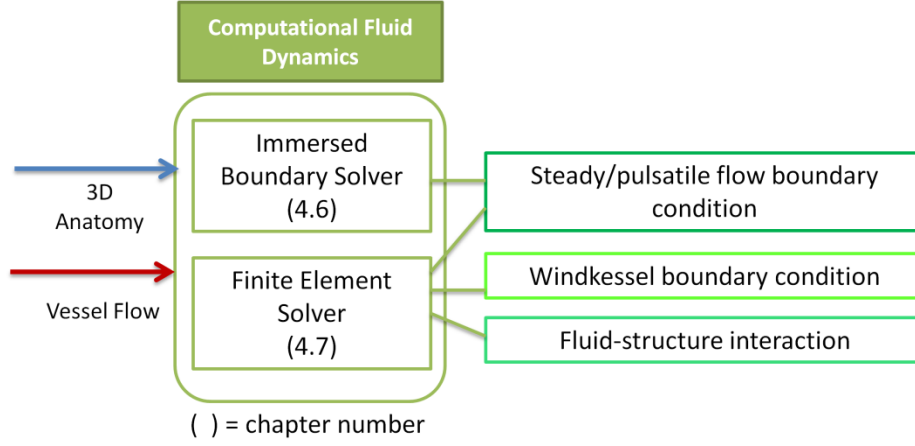
Figure 4.16 Schematic of the CFD methodology utilized in this work

For both the immersed boundary and finite element solver, to solve for the blood flow field within the TCPC, the incompressible viscous Navier-Stokes equations were being solved in a spatial domain (Ω_f) over time interval of interest (t_0, T):

$$\rho_f \left(\frac{\partial u}{\partial t} + (u \cdot \nabla)u \right) - \nabla \cdot \sigma_f = g_f \qquad \text{in } \Omega_f \times (t_0, T) \qquad \text{(Equation 4.8)}$$

$$\nabla \cdot u = 0 \qquad \text{in } \Omega_f \times (t_0, T) \qquad \text{(Equation 4.9)}$$

where ρ_f represents fluid density, u is fluid velocity and g_f is body force (which is zero in the simulations performed in this thesis). σ_f is Cauchy stress tensor. For Newtonian fluid:

$$\sigma_f(u, p) = -pI + 2\mu_f \epsilon(u) \qquad \text{(Equation 4.10)}$$

Where p represents fluid pressure, μ_f is fluid dynamic viscosity, $\epsilon(u)$ is the strain tensor:

$$\epsilon(u) = (\nabla u + (\nabla u)^T)/2 \qquad \text{(Equation 4.11)}$$

4.6   CFD Solver – Immersed Boundary Method

To simulate patient specific hemodynamics, a validated CFD solver based on immersed boundary method was developed by de Zelicourt et. al. [75, 157, 158]. This solver was specifically tailored to handle the complex anatomies and flow present in the TCPC. It is based on the assumption of incompressible Newtonian fluid. The current version of this solver can handle prescribed pulsatile flow boundary conditions at the inlets and outlets. A detailed protocol of using this solver is described in Appendix A.5.

4.6.1 Numerical Method

4.6.1.1   Solver Description

The solver is based on hybrid Cartesian sharp-interface immersed boundary method of Gilmanov and Sotiropoulos [159]. The external surface of the fluid domain is meshed with unstructured triangular elements and registered within a structured Cartesian grid. The grid cells are classified into three types (Figure 4.17): (i) fluid cells internal to the boundary, (ii) wall cells external to the boundary and (iii) immersed boundary (IB) cells immediately interior to the wall. The Navier-Stokes equations are discretized and solved in the fluid cells. The velocities at the IB cells are reconstructed based on a rigid no-slip condition assumption on the wall. The wall nodes are excluded from the computation, since the cardiovascular geometries used in this application are small compared to the overall Cartesian grid.
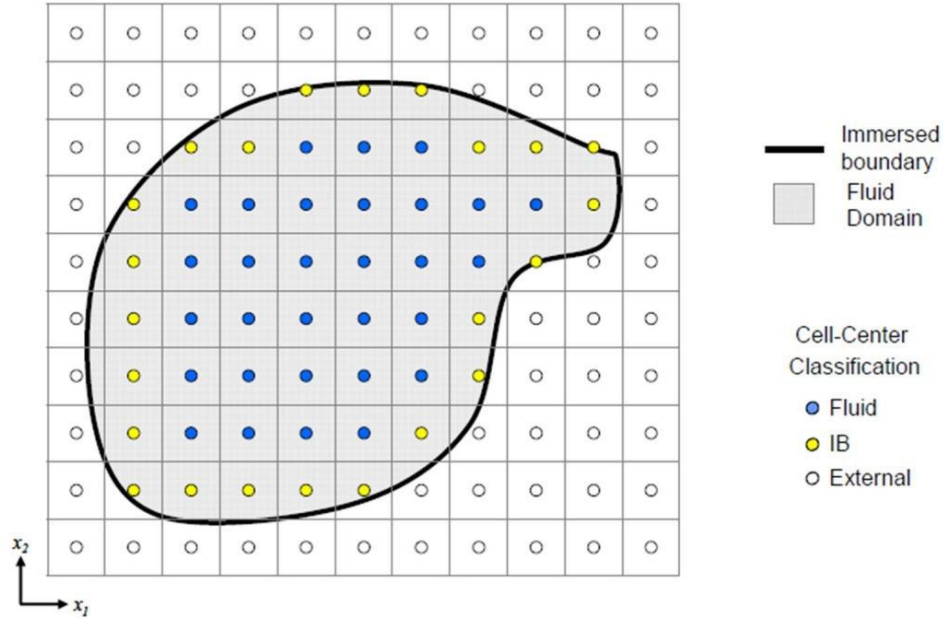
Figure 4.17 Two-dimensional representation of Cartesian grid cell classification with respect to the immersed boundary. External (Wall) cells (white) are external to the boundary. Immersed boundary (IB) cells (yellow) are internal and immediately adjacent to the boundary. Fluid cells (blue) are entirely enclosed by the boundary and IB cells [157]

4.6.1.2   Spatial Discretization

The spatial derivatives are computed using a central differencing scheme:

$$\frac{du_i}{dx} = \frac{u_{i+1} - u_{i-1}}{2\Delta x} \qquad \text{(Equation 4.12)}$$

where i is the cell index and Δx is the spacing between cell centers.

However, oscillations can be present in the pressure field when the pressure and velocity data are considered in the same grid location and symmetric differencing operators are used. This is because P_i is dependent on u_{i-1} and u_{i+1}, which depend on P_{i-2}, P_i, and P_{i+2}. Therefore, the adjacent grid points are de-coupled and may evolve independently of each other. This can be solved by either applying artificial damping

terms or the use of a staggered grid arrangement (i.e. storing pressure at the cell centers and velocities at the faces), as shown by Figure 4.18. In this immersed boundary solver, a hybrid staggered/non-staggered formulation is used [159]: The boundary conditions are imposed on a non-staggered layout, whereas the velocity are mapped to their staggered cell face locations. The Navier-Stokes equations are then solved in the staggered configuration.
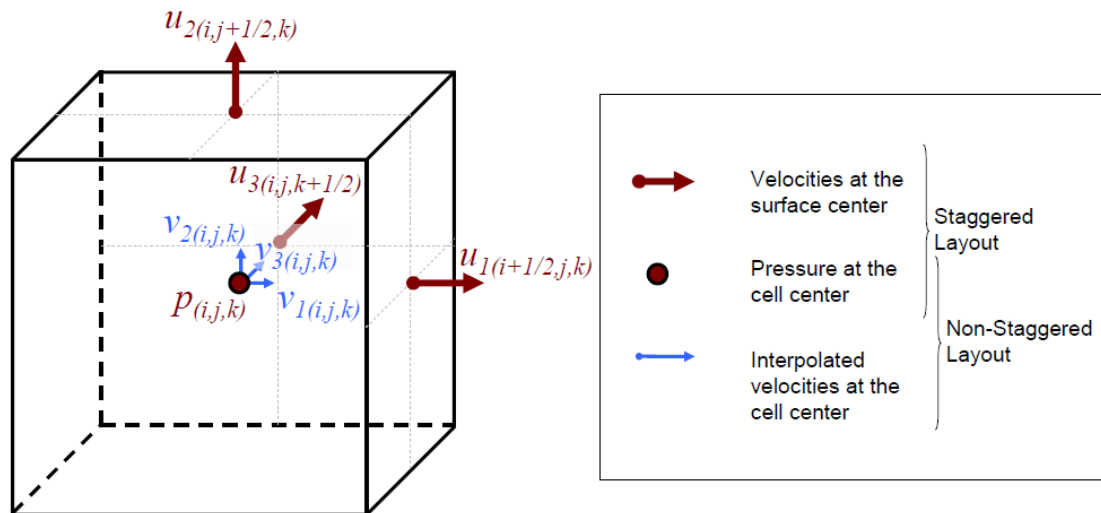
Figure 4.18 Representation of the hybrid Staggered/non-Staggered variable storage scheme. Pressure (P) values are stored at cell centers while velocities (u) are stored at cell face centers. In the boundary condition prescription, velocities are interpolated to the cell center (v) to maintain uniformity with the imposed pressure [157]

4.6.1.3   Temporal Discretization

Fractional-step integration method is used for time advancement [160]. This consists of three steps:

(i)   Prediction step, which fluid equations are solved;

(ii) Pressure correction step, which iteratively solves the pressure correction term based on the velocity field obtained in step (i);

74

(iii) <u>Projection step</u>, which enforces continuity and advances the predicted variables in time.

The prediction is performed using a 4th order explicit Runge-Kutta method to obtain the immediate velocity prediction (u*):

$$\frac{u_i^* - u_i^n}{\Delta t} = -u_j^n \frac{\partial u_i^n}{\partial x_j} - \frac{1}{\rho} \frac{\partial P^n}{\partial x_i} + v \frac{\partial^2 u_i^n}{\partial x_j \partial x_j} \qquad \text{(Equation 4.13)}$$

The pressure (P^n) is the known pressure field from time n and only u* is advanced in time through that calculation. Since u* is not divergence free, a correction is applied to project the result back to the divergence free space. Therefore, the incremental pressure field must be resolved. Incremental pressure δP, is related to u* as:

$$\nabla^2(\delta P) = \frac{3}{2\Delta t} \nabla(u^*) \qquad \text{(Equation 4.14)}$$

To solve efficiently the Poisson equation, the Flexible Generalized Minimal Residual (FGMRES) solver with multi-grid preconditioner was used [157, 161]. Then P_{n+1} and u_{n+1} are computed as:

$$P^{n+1} = P^n + \delta P \qquad \text{(Equation 4.15)}$$
$$u^{n+1} = u^* - \frac{3}{2\Delta t} \nabla(\delta P) \qquad \text{(Equation 4.16)}$$

4.6.2 Boundary Conditions

The current version of the IB solver assumes rigid wall and no-slip boundary condition at the vessel wall. Flow boundary conditions are utilized at the inlets (with prescribed velocity profile) and the outlets.

4.6.2.1   Treatment of Velocities at the Immersed Boundaries

Velocities at the IB cells are not calculated from the Navier-Stokes equations. Instead, they are reconstructed based on the wall normal vector and proximal fluid cell velocity (Figure 4.19). The normal vector $(\overrightarrow{n_f})$ from the center (F) of the closest triangular surface mesh element ("s") connects the IB cell center (G) to its respective fluid element (H). The value at G is reconstructed via quadratic interpolation of values at H and F (which is zero due to no-slip boundary condition).
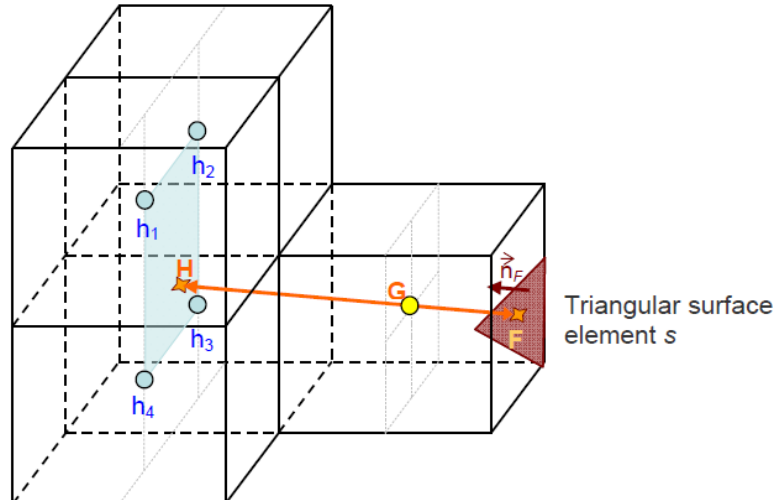
Figure 4.19 Reconstruction of the solution at an IB-cell center (G) by interpolating between its projection onto the closest immersed-boundary and fluid elements (points F and H, respectively) along the local normal to the immersed-boundary. The light gray lines are provided for sole visual display to help localize the centers of the fluid and IB cells [157].

4.6.2.2   Inlet Boundary Conditions

Dirichlet velocity boundary conditions were applied at the inlets. Flow condition can be imposed as either a flat velocity profile or a parabolic velocity profile. Usually flat velocity (plug-like) profile is preferred based on previous work [157]. Either time-averaged or pulsatile flow boundary conditions can be prescribed. For pulsatile flow boundary conditions, flow waveform of a cardiac cycle is usually applied. The PC-MRI-derived

76

flow data have very few data points compared to the temporal resolution needed for CFD. Fourier decomposition is performed on the measured flow curve to increase the temporal sampling for pulsatile simulations.

4.6.2.3   Outlet Boundary Conditions

At the outlets, flow boundary conditions were enforced to ensure mass convergence. Outlet flow rate is imposed as ratio of the outlet flow rate scaled to the total inlet flow:

$$\boldsymbol{Q_{outlet}} = \frac{Q_{outlet}}{\sum_{i=1}^{n} Q_i} \times \boldsymbol{Q_s} \qquad \text{(Equation 4.17)}$$

where Q_{outlet} is the flow rate of the outlet of interest, Q_i is the flow rate of each outlet, n is the total number of outlet and Q_s is the total inlet flow rate.

The velocities extrapolated at the outlet cell faces (v_G) were scaled to enforce the prescribed flow rate and ensure mass conservation:

$$\overrightarrow{v_G} = \overrightarrow{v_G} + \Delta Q \cdot \overrightarrow{n_f} \qquad \text{(Equation 4.18)}$$

where ΔQ is the difference between the desired flow rate (Q_0) and the current flow rate:

$$\Delta Q = Q_0 - \sum_{G \in Outlet} \overrightarrow{v_G} \cdot \overrightarrow{n_f} \qquad \text{(Equation 4.19)}$$

4.6.3 Mesh Preparation

The 3D surface of the reconstructed patient specific anatomy prepared as described in Chapter 4.2.2 was loaded into Gambit (ANSYS, Inc., PA, USA) for meshing. Vessel extensions of 10 mm and 50 mm were added to the inlets and outlets respectively, normal to the cross sections, to ensure flow stability. This was also to minimize

recirculations at the boundaries and reduce the effect of the prescribed inlet velocity profile on TCPC hemodynamics. The TCPC and the extended surface together was then meshed with unstructured triangular elements, which was then be read by the solver pre-processor. The pre-processor first read in the triangular mesh with 2D elements. The Cartesian grid node density was then specified (typical 0.02 times of the IVC diameter of each patient, which has been shown to be mesh independent [162]) and the immersed boundary was registered with the structured Cartesian grid. The nodes in the Cartesian grids were then classified into fluid, wall and immersed boundary nodes. A second mesh without flow extensions was created in GAMBIT as well. After the CFD simulation reached convergence (residuals of the Poisson solver decrease by 8 orders of magnitude), the TCPC domain was post-processed with this mesh to obtain the fluid domain without flow extensions.

4.6.4 Flow Field Analysis

Using the fluid domain without flow extensions, both qualitative and quantified analysis can be performed. For qualitative analysis, the flow field can be visualized using a semi-automatic macro developed with Tecplot 360 (Tecplot, Inc., Bellevue, Washington) (Appendix A.5.2.5.2.). For quantitative analysis, power loss and hepatic distribution were usually quantified (as defined in Chapter 4.8). A detailed description of computing these metrics with this immersed boundary solver results is described in Chapters A.5.2.5.3 and A.5.2.5.4.

4.7 CFD Solver - Finite Element Method

To include more modeling complexities in the simulation of TCPC hemodynamics, finite element method solver LifeV (www.lifev.org) was applied in this work. The main features utilized in this work from the LifeV library are (i) three-element Windkessel model coupled to the 3D Navier-Stokes solver (for specific aim 2 and 3) and (ii) fluid-structure interaction (FSI) model (for specific aim 3). The Navier-Stokes solver is based on the assumption of incompressible Newtonian fluid. The FSI solver is presented in Passerini et. al. and has been validated with experimental data [163]. The structural model is based on the assumption of linear elastic model. The moving fluid domain in the FSI solver is based on arbitrary Lagrangian–Eulerian (ALE) mapping. A detailed protocol of using the LifeV solver is described in Appendix A.6.

4.7.1 Numerical Method – Navier-Stokes Solver

4.7.1.1 Temporal Discretization

Backward differentiation formula of the order of 2 is used for temporal discretization [164]. The convective term is linearized by an extrapolation formula of the same order. For the given time interval of interest (t_o, T), $t^n = t_o + n\Delta t$, with $n = 0, \ldots, N_T$ and $T = t_o + N_T \Delta t$. Given u^n, the Navier-Stokes and continuity equations are discretized in time as follows to solve for (u^{n+1}, p^{n+1}) in the system:

$$\rho_f \frac{3u^{n+1} - 4u^n + u^{n-1}}{2\Delta t} + \rho_f (2u^n - u^{n-1}) \cdot \nabla u^{n+1} - \nabla \cdot \sigma_f(u^{n+1}, p^{n+1}) = 0 \quad \text{in } \Omega_f$$

(Equation 4.20)

$$\nabla \cdot u^{n+1} = 0 \quad \text{in } \Omega_f \text{ (Equation 4.21)}$$

4.7.1.2   Spatial Discretization

The fluid domain is discretized in space with finite element method with tetrahedral elements [165]. Linearization and discretization results in the following system of algebraic linear equations:

$$\rho_f \frac{3}{2\Delta t} M u^{n+1} + \mu_f K u^{n+1} + \rho_f N u^{n+1} + B^T p^{n+1} = b_u^{n+1} \qquad \text{(Equation 4.22)}$$

$$B u^{n+1} = 0 \qquad \text{(Equation 4.23)}$$

Where u^{n+1} and p^{n+1} are the arrays of nodal values for velocity and pressure respectively. The array b_u^{n+1} account for the contributions of solution at the previous time steps and the contribution that the boundary nodes give to the internal fluid nodes. M is the mass matrix and K is the diffusion matrix. N is the matrix associated with the discretization of the convective term. B is the matrix associated with the discretization of the operator $(-\nabla \cdot)$.

Let $C = \rho_f \frac{3}{2\Delta t} M + \mu_f K + \rho_f N$, equations 4.22 and 4.23 can be re-written as:

$$A x^{n+1} = b_f^{n+1} \qquad \text{(Equation 4.24)}$$

where $A = \begin{bmatrix} C & B^T \\ B & 0 \end{bmatrix}$, $x^{n+1} = \begin{bmatrix} u^{n+1} \\ p^{n+1} \end{bmatrix}$, $b_f^{n+1} = \begin{bmatrix} b_u^{n+1} \\ 0 \end{bmatrix}$

Equations 4.24 was solved at each time step t_{n+1} using left preconditioned Generalized Minimal Residual (GMRES) method [166-169]. An upper-triangular variant of the pressure corrected Yosida splitting [170, 171] was used as preconditioner (P):

$$P = \begin{bmatrix} C & B^T \\ 0 & S(S + BH(\mu_f K + \rho_f N)HB^T)^{-1}S \end{bmatrix}, \quad H = \frac{2\Delta t}{3\rho_f}M^{-1}, \quad S = -BHB^T \quad \text{(Equation 4.25)}$$

P is also an approximation of the U factor in the exact block LU factorization of matrix A.

$$A = LU, \quad L = \begin{bmatrix} I & 0 \\ BC^{-1} & I \end{bmatrix}, \quad U = \begin{bmatrix} C & B^T \\ 0 & -BC^{-1}B^T \end{bmatrix} \quad \text{(Equation 4.26)}$$

4.7.1.3 *Three-Element Windkessel Model*

To simulate patient specific hemodynamics in the TCPC, proper patient specific boundary conditions have to be defined at the inlets, outlets and the vessel wall. In many cases, patient specific information of flow distribution and pressure field are not completely known and cannot be prescribed at the outlets. In these situations, reduced order models (e.g., 0D or lumped parameters models) can be utilized to model flow and pressure downstream of the fluid domain. These models can be coupled to the 3D CFD model as outlet boundary conditions [119, 120, 172, 173].

In LifeV, 3-element Windkessel boundary condition has already been implemented as a possible choice of outflow boundary condition. The downstream resistances (R) and

compliance (C) were prescribed and applied as boundary conditions [174] (as illustrated in Figure 4.20).
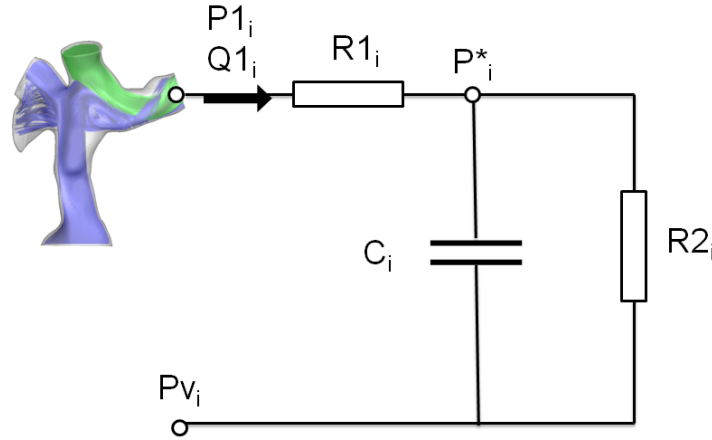
Figure 4.20 Schematic representing the 3-element Windkessel model as outlet boundary conditions of the CFD simulations of the TCPC. "i" denotes the specific outlet, P1 denotes outlet pressure, Q1 represents outlet flow rate, P* denotes the pressure at the junction of the compliance and distal resistance, C is the capacitance, Pv is the downstream pressure (left atrial pressure in the case of TCPC), R1 and R2 are the proximal and distal resistances respectively

Using the analogy of electric circuits, the governing equations of the 3-element Windkessel model for each outlet are as follows:

$$\frac{dP^*}{dt} = -\frac{1}{R_2 C}(P^* - P_v) + \frac{1}{C}Q_1 \qquad \text{(Equation 4.27)}$$

$$P_1 = P^* + R_1 Q_1 \qquad \text{(Equation 4.28)}$$

After arrangement, the above equations can be combined into a single equation:

$$P_1 + CR_2 \frac{dP_1}{dt} = (R_1 + R_2)Q_1 + R_1 R_2 C \frac{dQ_1}{dt} + P_v \qquad \text{(Equation 4.29)}$$

In LifeV, this ordinary differential equation is solved analytically at each time step t:

$$P_1(t) = P_1(0) + \left\{ \int_0^t \left[P_v + (R_1 + R_2)Q_1(s) + R_1 R_2 C \frac{dQ_1(s)}{ds} \right] exp\left(\frac{s}{R_2 C}\right) ds \right\} exp\left(-\frac{t}{R_2 C}\right)$$

(Equation 4.30)

where $P_1(0)$ is the initial pressure at the outlet, which is zero in this thesis.

Using simple trapezoidal rule, a first order approximation of the derivative of Q1 is being applied:

$$\frac{dQ_1(s)}{ds} = \frac{Q_1(t_{n+1}) - Q_1(t_n)}{t_{n+1} - t_n} \qquad \text{(Equation 4.31)}$$

In the Georgia Tech Fontan database, majority of the patient data at the LPA and RPA were available in the form of vessel flow waveform obtained from PC-MRI data. By using the pulmonary vascular resistance (PVR) from patient specific data or literature value, the relative total resistances of the left and right lungs can be computed as follows:

$$R_{LPA} = \frac{Q_{LPA} + Q_{RPA}}{Q_{LPA}} \times PVR \qquad \text{(Equation 4.32)}$$

$$R_{RPA} = \frac{Q_{LPA} + Q_{RPA}}{Q_{RPA}} \times PVR \qquad \text{(Equation 4.33)}$$

where R_{LPA} and R_{RPA} are the total vascular resistance at the left and right lung respectively, Q_{LPA} and Q_{RPA} are the time-averaged vessel flow rates at the LPA and RPA respectively.

4.7.1.4 Large Eddy Simulation

Average Reynolds number (Re) of flow in the FP of the TCPC typically ranges from 700 to1600 under resting breath-hold conditions. However, under certain conditions like exercise and free-breathing, peak Re at the FP can be moderately high (Re=2000-4000). For moderately large Reynolds number, the effects of flow disturbances cannot be neglected. The largest characteristic space scale at which the viscous forces dissipate energy (Kolmogorov scale, η) is expressed by the following empirical relationship:

$$\eta = Re^{-3/4}L \qquad \text{(Equation 4.34)}$$

where L is the characteristic length.

To model moderately high Reynolds number, direct numerical simulation should be used, but is often associated with high computational cost since a fine space discretization and a fine time discretization is required to resolve flow at the Kolmogorov scale. If the mesh is too coarse, it will fail to resolve the Kolmogorov scale, leading to nonphysical computed velocities. A possible solution to this problem is to introduce a filter of the velocity to convey the energy loss at the unresolved scale to resolved scales. A Large Eddy Simulation (LES) approach that relies on a space average formulation of the Navier-Stokes equations can be applied [175]. One type of LES model, "Leray model", couples the Navier-Stokes equations with a differential filter [176, 177]. The model is governed by the Navier Stoke equations and the following equations:

$$\rho_f \left(\frac{\partial u}{\partial t} + (\bar{u} \cdot \nabla) u \right) - \nabla \cdot \sigma_f = g_f \quad \text{(Equation 4.35)}$$

$$\nabla \cdot u = 0 \quad \text{(Equation 4.36)}$$

$$-2\delta^2 \nabla \cdot (a(u) \nabla^s \bar{u}) + \bar{u} + \nabla\lambda = u \quad \text{(Equation 4.37)}$$

$$\nabla \cdot \bar{u} = 0 \quad \text{(Equation 4.38)}$$

Where $\bar{u}$ is the filtered velocity, δ is the filtering radius (radius of the neighborhood

where the filter extracts information from the unresolved scales), λ is a Lagrange

multiplier to enforce the incompressibility constraint for $\bar{u}$, a($\cdot$) is a deconvolution-based

indicator function, which is a scalar function such that:

a(u) = 0 where the velocity u does not need regularization

a(u) =1 where the velocity u does need regularization

More detail related to the indicator function can be found at Bertagna et. al. [176] A

three-step algorithm called evolve-filter-relax (EFR) [178] was implemented [176, 177]:

(i) Evolve: Find the intermediate velocity and pressure (v^{n+1}, q^{n+1}), such that

$$\rho \frac{1}{\Delta t} v^{n+1} + \rho u^* \cdot \nabla v^{n+1} - 2\mu \Delta^s v^{n+1} + \nabla q^{n+1} = b^{n+1} \quad \text{(Equation 4.39)}$$

$$\nabla \cdot v^{n+1} = 0 \quad \text{(Equation 4.40)}$$

where u^* is an approximation of the end-of-step velocity u^{n+1} based on previous time

steps solutions

(ii) Filter: Find ($\bar{v}^{n+1}$, λ^{n+1}), such that

$$-2\delta^2 \nabla \cdot (a(v^{n+1})\nabla^s \bar{v}^{n+1}) + \bar{v}^{n+1} + \nabla \lambda^{n+1} = v^{n+1} \quad \text{(Equation 4.41)}$$

$$\nabla \cdot \bar{v}^{n+1} = \nabla \cdot v^{n+1} = 0 \quad \text{(Equation 4.42)}$$

(iii)Relax: Set

$$u^{n+1} = (1 - \chi)v^{n+1} + \chi \bar{v}^{n+1} \quad \text{(Equation 4.43)}$$

$$p^{n+1} = (1 - \chi)q^{n+1} + \chi \lambda^{n+1} \quad \text{(Equation 4.44)}$$

where $0 \leq \chi \leq 1$ is a relaxation parameter.

4.7.2 Numerical Method – Fluid-Structure Interaction Model

To simulate blood flow in a deformable vessel, the mechanical behavior of the moving vascular structure and its interactions with the blood flow needs to be characterized. Various algorithms of FSI formulations are present and have been applied in cardiovascular applications [179]. In the FSI solver of LifeV [180], the moving domain of the fluid problem is stated in an Arbitrary Lagrangian-Eulerian (ALE) framework, which combined the advantages of classical Lagrangian and Eulerian formulations [181, 182]. The ALE map is used to describe the fluid domain and displacement (d_f) is computed as a harmonic extension of the structural displacement ($d_s|\Gamma_0$), from the FS interface Γ_0 to the internal of the fluid reference domain Ω^f_0. The fluid problem is composed of the incompressible Navier-Stokes equations written in ALE form and the structural problem describes the vessel wall dynamics through a linear elastic model.

4.7.2.1   Fluid Model

The same Navier-Stokes solver (Chapters 4.7.1) is used to solve the fluid equations in the fluid-structure interaction model. Features like 3-elements Windkessel model are still applicable in the coupled fluid-structure interaction model.

4.7.2.2   Structural Model – Governing Equations

The motion of the structure with respect to a given material reference configuration Ω_s is governed by the elastodynamics equation:

$$\rho_s \frac{\partial^2 d}{\partial t^2} - \nabla \cdot \Sigma_s (d) = g_s \qquad \text{in } \Omega_s \times (t_0, T) \qquad \text{(Equation 4.45)}$$

where ρ_s represents structure density, d is the structural displacement field, g_s is the body force.

The structure is assumed to be linearly elastic for simplification:

$$\Sigma_s (d) = 2\mu_s \epsilon(d) + \lambda_s (\nabla \cdot d) I \qquad \text{(Equation 4.46)}$$

Where $\epsilon(d) = (\nabla d + (\nabla d)^T)/2$ is the strain tensor, μs and λs are Lamé constants, which are related to Young's modulus E and Poisson ratio v_s:

$$\mu_s = \frac{E}{2(1+v_s)} \qquad \text{(Equation 4.47)}$$

$$\lambda_s = \frac{E v_s}{(1+v_s)(1-2v_s)} \qquad \text{(Equation 4.48)}$$

4.7.2.3   Structural Model – Temporal Discretization

The elastodynamics equation (equation 4.45) is discretized according to the generalized-α schemes [183].

$$\rho_s a^{n+1} - \nabla \cdot \sigma_s(d^{n+1}) = 0 \qquad \text{(Equation 4.49)}$$

$$d^{n+1} = d^n + \Delta t v^n + \Delta t^2 \left(\beta a^{n+1} + (\tfrac{1}{2} - \beta) a^n \right) \qquad \text{(Equation 4.50)}$$

$$v^{n+1} = v^n + \Delta t (\gamma a^{n+1} + (1 - \gamma) a^n) \qquad \text{(Equation 4.51)}$$

where v^n and a^n are proper approximations of the structure velocity and acceleration at time t^n. For second order accuracy, $\beta=1/4$ and $\gamma=1/3$. To avoid high frequency oscillations of the numerical solutions, the asymptotic spectral radius ρ_∞ ($0 \leq \rho_\infty \leq 1$) is included in the discretization:

$$a^{n+1-\alpha_m} = (1 - \alpha_m(\rho_\infty))a^{n+1} + \alpha_m(\rho_\infty)a^n, \qquad 0 \leq \alpha_m(\rho_\infty) \leq 1 \qquad \text{(Equation 4.52)}$$

$$d^{n+1-\alpha_k} = (1 - \alpha_k(\rho_\infty))d^{n+1} + \alpha_k(\rho_\infty)d^n, \qquad 0 \leq \alpha_k(\rho_\infty) \leq 1 \qquad \text{(Equation 4.53)}$$

$$\rho_s a^{n+1-\alpha_m} - \nabla \cdot \sigma_s(d^{n+1-\alpha_k}) = 0 \qquad \text{(Equation 4.54)}$$

According to previous study [184], parameter choice of $\alpha_m=-1$ and $\alpha_k=0$, $\gamma=3/2$ and $\beta=1$ results in excellent stability properties and second order accuracy in time.

4.7.2.4   Structural Model – Spatial Discretization

The structural domain is discretized in space with Galerkin finite element procedure. The linearization and discretization results in the following system to solve for v^{n+1}:

$$Dv^{n+1} = b_s^{n+1} \qquad \text{which } D = \rho_s \frac{1-\alpha_m}{\gamma \Delta t} M_s + (1 - \alpha_k)\frac{\beta}{\gamma}\Delta t K_s \qquad \text{(Equation 4.55)}$$

Where v is the array of nodal values for structure velocity, M_s is the mass matrix and K_s is the stiffness matrix, b_s is the array to account for the contribution of the solution at previous time steps and boundary conditions.

4.7.2.5   Fluid-Structure Coupling

Two-way fluid-structure interaction was utilized in the FSI solver. Pulsation of fluid flow exerts forces on structural wall, in turn, movement of the structure extend or constrict the control volume and allow more or less room for fluid flow. Let $\Gamma(t)$ be the fluid-structure interface. The FSI problem is coupled by two conditions:

Continuity of velocity: $u = v$ on $\Gamma(t)$, $t_0 < t \leq T$ (Equation 4.56)

Continuity of stress: $\sigma_f n = \sigma_s n$ on $\Gamma(t)$, $t_0 < t \leq T$ (Equation 4.57)

where n is the outward normal for the fluid domain, σ_s is the structure Cauchy stress tensor

Two different approaches are applied for the structural and fluid subdomains. The structural domain is described with Lagrangian mapping. The fluid domain is described with arbitrary Lagrangian-Eulerian (ALE) mapping [185, 186], which means it kinematics is only required to comply by that of the fluid-structure boundary, which results in the coupling with the structural model. The position in reference fluid domain $\hat{\Omega}_f$ is defined as $\dot{x}_f$ and the domain velocity w is calculated by:

$$w(x_f, t) = \frac{\partial x_f}{\partial t}\Big|_{\dot{x}_f}$$ (Equation 4.58)

By including the fluid domain velocity, the incompressible Navier-Stokes equations are then re-written in ALE formulation:

$$\rho_f \frac{\partial u}{\partial t}\Big|_{\dot{x}_f} + \rho_f(u - w) \cdot \nabla u - \nabla \cdot \sigma_f = 0 \qquad \text{in } \Omega_f(t) \qquad \text{(Equation 4.59)}$$

$$\nabla \cdot u = 0 \qquad \text{in } \Omega_f(t) \qquad \text{(Equation 4.60)}$$

The coupling conditions (equations 4.56 and 4.57) can be re-written as follows:

$$r_f u + \sigma_f n = r_f v + \sigma_s n \quad \text{on } \Gamma(t) \quad \text{(Equation 4.61)}$$

$$r_s u + \sigma_f n = r_s v + \sigma_s n \quad \text{on } \Gamma(t) \quad \text{(Equation 4.62)}$$

where $r_f > 0$ and $r_s > 0$ are constants.

At every time step (t^{n+1}), the coupled FSI problem can be written as:

$$A_{fs} x_{fs}^{n+1} = b_{fs}^{n+1} \quad \text{(Equation 4.63)}$$

$$A_{fs} = \begin{bmatrix} C + r_f R_f & T_{fs} & B^T \\ T_{su} & D + r_s R_s & T_{sp} \\ B & 0 & 0 \end{bmatrix}, \qquad x_{fs}^{n+1} = \begin{bmatrix} u^{n+1} \\ v^{n+1} \\ p^{n+1} \end{bmatrix}, \qquad b_{fs}^{n+1} = \begin{bmatrix} b_u^{n+1} \\ b_s^{n+1} \\ 0 \end{bmatrix}$$

(Equation 4.64)

where the boundary mass matrices R_f and R_s and the coupling matrices T_{fs}, T_{su} and T_{sp} are from the discretization of coupling equations 4.61 and 4.62.

For preconditioning, an inexact LU block factorization of the matrix A_{fs} was considered [185, 186]. The approximated U factor is:

$$\hat{U}_{fs} = \begin{bmatrix} C + r_f R_f & T_{fs} & B^T \\ 0 & \hat{\Sigma}_s & T_{sp} \\ 0 & 0 & \hat{\Sigma}_p \end{bmatrix} \quad \text{(Equation 4.65)}$$

Where $\hat{\Sigma}_s$ and $\hat{\Sigma}_p$ are approximations of the structure Schur complment (Σ_s) and pressure (Σ_p) Schur complement:

$$\Sigma_s = D + r_s R_s - T_{su}(C + r_f R_f)^{-1} T_{fs} \quad \text{(Equation 4.66)}$$

$$\Sigma_p = -B(C + r_f R_f)^{-1} B^T + B(C + r_f R_f)^{-1} T_{fs} \Sigma_s^{-1} T_{su}(C + r_f R_f)^{-1} B^T$$

$$-B(C + r_f R_f)^{-1} T_{fs} \Sigma_s^{-1} T_{sp} \qquad \text{(Equation 4.67)}$$

For Σ_s, it is approximated by $(C + r_f R_f)^{-1} \approx H$, where H was defined in equation 4.25, which gives:

$$\widehat{\Sigma}_s = D + r_s R_s - T_{su} H T_{fs} \qquad \text{(Equation 4.68)}$$

For Σ_p, the pressure corrected Yosida preconditioner in Chapter 4.7.1.2 is modified as follows:

$$\widehat{\Sigma}_p = S(S + BH(\mu_f K + \rho_f N + r_f R_f) H B^T)^{-1} S \qquad \text{(Equation 4.69)}$$

The preconditioned system $\widehat{U}_{fs}^{-1} A_{fs} x_{fs}^{n+1} = \widehat{U}_{fs}^{-1} b_{fs}^{n+1}$ was solved with GMRes method. The position of the fluid domain was extrapolated from the previous time step. The non-linearity induced by the fluid convective term was solved with Picard iterations.

4.7.3 Mesh Preparation

The 3D surface of the reconstructed patient specific anatomy prepared as described in Chapter 4.2.2 was loaded into GAMBIT/ANSYS Workbench (ANSYS, Inc., PA, USA) for surface meshing with unstructured triangular elements. Gmsh [187] was used to prepare volume meshes for both fluid and structural simulations based on the surface mesh. Gmsh preserves the nodes of the input surface mesh when creating a 3D volume mesh. This is important since for FSI simulations, the fluid and structural domain need to share common nodes at the fluid-structure interface. Tetrahedral elements were created in the fluid domains while maintaining the nodes at the input surface. For the structural mesh, the input surface mesh was extruded based on the normal of each element on the surface mesh. The thickness and number of layers was specified in

Gmsh. Examples of a fluid mesh and a structure mesh created by Gmsh is illustrated by

Figure 4.21.

(A)

(B)   *(C)*
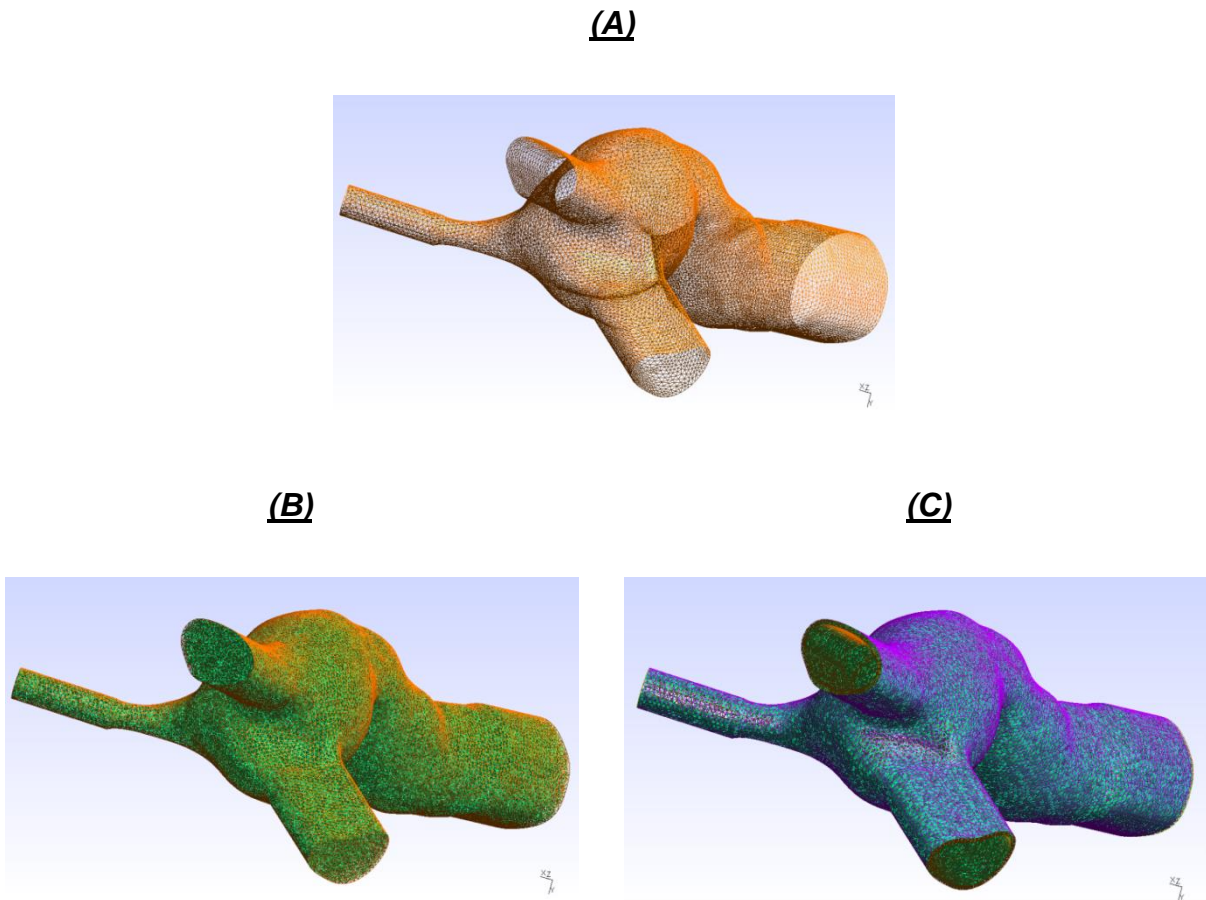
Figure 4.21 Examples of volume meshes created with Gmsh: (a) original input surface mesh created with GAMBIT/ANSYS Workbench, (b) fluid volume mesh and (c) structure volume mesh created from Gmsh

4.7.4 Flow Field Analysis

During the simulation, flow rate and average pressure at each boundary was output to a

text file. Therefore, unlike the IB solver, additional post-processing was not necessary

to obtain these values. For qualitative analysis, the flow field can be visualized, probed and processed using ParaView software (Kitware Inc., Clifton Park, NY, USA). Particle tracking was performed with ParaView. Using in-house codes, hepatic flow distribution and particle washout time (defined in Chapter 4.8) can be computed from the particle tracking results. A detailed description of computing these metrics based on particle tracking is described in Appendix A.6.2.5.2.

4.8   Hemodynamic Metric

(i) Pressure Drop: Pressure drop was computed as the difference between the average pressure values at inlets and outlets of CFD domain.

(ii) Energy Dissipation: TCPC energy dissipation was defined as the energy loss of the blood after flowing through the TCPC domain, under a control volume energy balance assumption. This metric is considered important as elevated energy loss through the TCPC is hypothesized to result in an inefficient single ventricle circulation. TCPC Power loss ($\dot{E}_{Loss}$) was defined as:

$$\dot{E}_{Loss} = \sum_{inlets}\int_A (p + \frac{1}{2}\rho v^2)v \cdot dA - \sum_{outlets}\int_A (p + \frac{1}{2}\rho v^2)v \cdot dA \qquad \text{(Equation 4.70)}$$

where p is the static pressure relative to the FP measured from CFD, ρ is the blood density, A is area of the inlet/outlet, and v the velocity.

To account for the difference in patient flow and patient size, the TCPC power loss was normalized in two ways:

(a) TCPC Resistance: TCPC resistance refers to the resistance that must be overcome to push blood through the TCPC. In order to compare the energy loss in the TCPC with clinical measures like PVR and systemic vascular resistance (SVR), TCPC power loss was also normalized to obtain energy loss in the unit of flow resistance (pressure drop / flow rate). A TCPC power loss-based pressure drop was first evaluated as $\Delta P_{TCPC} = \frac{\dot{E}_{Loss}}{Qs}$, which was then normalized by flow to obtain TCPC resistance $= R_{TCPC} = \frac{\Delta P_{TCPC}}{Qs/BSA}$. This is usually computed in the unit of Wood Units $(WU = \frac{mmHg}{L/min})$.

(b) Indexed Power Loss (iPL): iPL is the non-dimensional energy dissipation through the TCPC, which is also a measure of the resistance of the connection. $\dot{E}_{Loss}$ is normalized by flow and patient body surface area (BSA) to calculate the indexed power loss (iPL,$=\frac{\dot{E}_{Loss}}{\rho Qs^3/BSA^2}$) [188], where Qs is the total systemic return and ρ is blood density $= 1060kg \ m^{-3}$. This is a dimensionless metric and is used throughout this thesis.

(iii) Hepatic Flow Distribution (HFD): HFD is calculated from the post-processing of CFD simulation, by the following equation:

$$\% HFD(LPA) = \frac{Q_{FP-LPA}}{Q_{FP-LPA} + Q_{FP-RPA}} \quad \text{(Equation 4.71)}$$

where %HFD(LPA) is the percentage of FP flow leaving through the LPA, Q_{FP-LPA} and Q_{FP-RPA} are the computed flow rate from FP to LPA and RPA, respectively.

For steady flow simulations, HFD is computed by seeding streamtraces across the FP cross-section and quantifying the total flux of the streamtraces exiting from the FP through the LPA and RPA. For pulsatile flow simulations, it is computed by seeding particles across the FP cross-section and quantifying the total flux of the particles exiting from the FP through the LPA and RPA through particle tracking.

(iv) Particle Washout Time (WOT): This was defined as the number of cardiac cycles (or respiratory cycles) necessary for the 95% of the massless particles injected from the IVC during the first cycle to leave the fluid domain [109]. This is computed from the particle tracking using ParaView 3.14.1 (www.paraview.org).

4.9   Chapter Summary

To help with the interpretation of the upcoming chapters, the following outlines which of the previously mentioned tools were being applied for each specific aim (SA).

- SA1: Anatomic image acquisition and reconstruction, TCPC anatomic characterization, conventional PC- MRI, exercise stress test protocol, immersed boundary method solver

- SA2: Anatomic image acquisition and reconstruction, conventional PC-MRI and RT PC-MRI, LifeV finite element solver (Navier-Stokes flow solver)

- SA3: Anatomic image acquisition and reconstruction, conventional PC-MRI and RT PC-MRI, LifeV finite element solver (fluid-structure interaction solver)

CHAPTER 5   Specific Aim 1: Investigation of the Effect of Geometry on TCPC Hemodynamics

5.1   Overview

Since the first introduction of the Fontan procedure, survival rate of single ventricle patients has increased.   However, patients still suffer from various long-term complications (e.g. limited exercise capacity, pulmonary arteriovenous malformations, and venous hypertension) [1]. Though the exact causes of these complications are not clear, many of them are attributed to the adverse hemodynamic environment in the TCPC and the single ventricle circulation. For example, high energy loss has been associated with poor exercise performance [189]. Unbalanced distribution of hepatic factors to the two sides of the lungs has been shown to increase the risk of pulmonary arteriovenous malformations [3, 5, 48]. TCPC anatomies are complex and patient-specific, and have been shown to affect the connection hemodynamics. Therefore, recent studies have been focusing on optimizing the geometric configuration to improve TCPC hemodynamic performance.

Geometric alterations of the TCPC to minimize energy dissipation have been widely studied in idealized geometries [27, 59, 61, 69, 112]. Earlier studies have emphasized the benefit of having caval offsets to reduce caval flow collision and therefore lower TCPC power loss [59, 61]. It has also been shown that small vessel diameter can elevate TCPC energy dissipation [69]. Using patient-specific geometry, Dasi et. al.

[190], for the first time, have shown that there existed a strong inverse correlation between minimum PA area and TCPC energy dissipation with 22 Fontan patient models. Routing balanced distribution of hepatic blood flow to both lungs has been shown to be important for palliation of PAVM in SV patients [3-5, 47, 191]. While these findings have provided significant insights on possible ways to improve TCPC hemodynamics, it is important to note that TCPC anatomy has great patient-specificity. Investigations with a large patient cohort to compare the relative effect of geometric alterations for a specific hemodynamic outcome are still lacking.

With the patient enrollment of National Heart, Lung, and Blood Institute Grants HL67622 and HL098252, as well as the data residing in the Georgia Tech Fontan MRI database, a cohort of Fontan patient MRI data are available for a geometric characterization and statistical analysis. The objectives of this specific aim are to utilize such patient data to: (a) characterize the geometric features of TCPC anatomy; (b) identify the geometric features that are most relevant for a given hemodynamic outcome; and (c) investigate the impact of intervention to improve hemodynamic outcome based on the TCPC geometric characteristics.

The basic outline for this chapter is as follows (Figure 5.1). First, the geometric features of a cohort of TCPC will be quantified (Chapter 5.2, Specific Aim 1(a)). Then, these geometric features will be statistically correlated to the baseline hemodynamic metrics (cardiac index, TCPC power loss, pulmonary and hepatic flow distributions) to identify significant geometric predictors (Chapter 5.2, Specific Aim 1(a)). Next, for patients who

have performed the exercise cardiac magnetic resonance (CMR) protocol, their geometric features will be statistically correlated to the TCPC power loss during exercise (Chapter 5.3, Specific Aim 1(b)). Finally, the effect of stent implantation on reducing TCPC power loss will be investigated on a cohort of patients with lateral tunnel (LT) stenosis (Chapter 5.4, Specific Aim 1(c)).
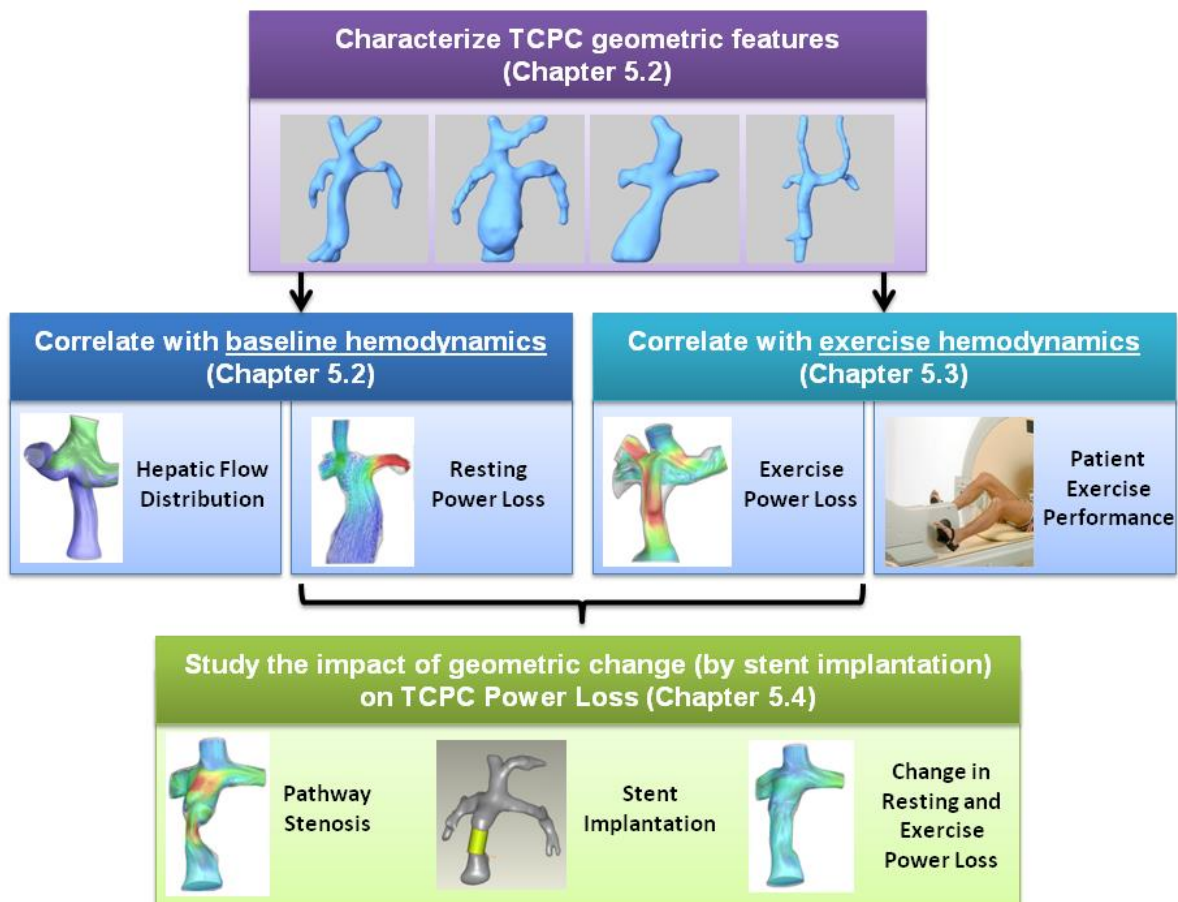
Figure 5.1 Schematic of Specific Aim 1

5.2   Specific Aim 1(a): Geometric Correlation with Baseline Hemodynamics

Improving TCPC geometric design for better TCPC hemodynamic outcome has been the focus of a large body of literature. Previous studies have shown that geometric parameters, such as diameter, caval offset, and vessel flaring can affect the TCPC hemodynamics [27, 61, 192, 193]. Because of the complex native vessel morphology, vessel growth and difference in surgical techniques, there exists a great variability in the TCPC geometry. For example, the IVC anastomosis is currently performed using two approaches [60]. The intra atrial pathway usually forms a bulge, which promotes flow recirculation and mixing within the FP [27, 194, 195]. The extracardiac conduit has more uniform cross sectional area along the vessel which results in a more streamlined flow [196]. Such variability can in turn translate to differences in flow dynamics within the systemic venous pathway [47, 197]. All these studies suggested the key role played by TCPC geometry in the resulting hemodynamics.

The hypothesis of this study was that significant correlations exist between certain TCPC geometric features and hemodynamics such as power loss, cardiac index and flow distribution (presented by Figure 5.2). These relationships were investigated within a patient cohort in order to give the surgeon information to optimize flow dynamics by shaping the systemic venous pathway appropriately.
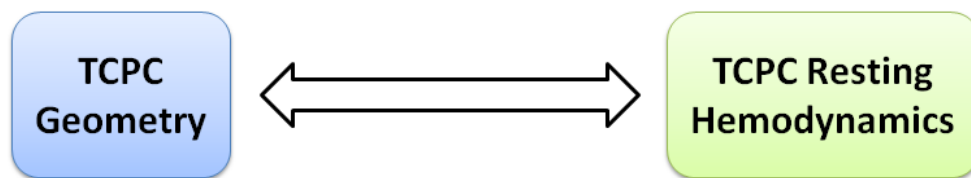
Figure 5.2 Schematic representing the hypothesis of SA1(a)

5.2.1 Patient Cohort

One hundred and thirty one consecutive single ventricle patients with a TCPC were selected from the Georgia Tech–Children's Hospital of Philadelphia Fontan database. Prospective cardiac magnetic resonance (CMR) data were acquired between 2002 and 2012. The study was approved by the institutional review boards (IRB) of both institutions. Patient data were collected with informed consent. Cases with severe CMR artifacts, diagnosis of Ebstein's anomaly, atriopulmonary connections, left SVC (LSVC) to coronary sinus to systemic venous pathway connection, and bifurcated Fontan Y-graft were excluded. A total of 108 patients were included (Table 5-1). Full list of patient IDs are listed in Appendix A.7.1.1.

Table 5-1 Demographic details of the 108 patients analyzed

Patient characteristics	Mean ± standard deviation
Age (years)	10.2 ± 6.8
Body surface area (m^2)	1.12 ± 0.45
Gender (M/F)	63/45
IVC connection type (IA/EC) [†]	67/41
HLHS vs. non-HLHS [‡]	40/68

† IA – Intra-atrial, EC- Extra-cardiac. ‡ HLHS- Hypoplastic left heart syndrome

5.2.2 CMR Acquisition

For each patient, steady state free precession (SSFP) CMR images were acquired in the transverse plane using a Siemens Avanto 1.5 Tesla whole-body MRI scanner (Siemens Medical Systems, Malvern, PA) (acquisition parameters summarized in Table

5-2). The CMR images were acquired with 3 excitations every other heartbeat at end-diastole under breath-hold conditions. In general, smaller voxel sizes were chosen for smaller patients to accurately resolve first and second-order pulmonary arterial branching. To compensate for the signal-to-noise loss, 1 to 2 additional excitations were added, and oversampling was increased to 50%. PC-MRI was utilized to acquire through-plane velocity profiles across the aortic valve, the vena cavae, LPA, and RPA over a cardiac cycle under breath-hold conditions.

Table 5-2 Summary of CMR acquisition parameters

Transverse CMR	
No. of slices	30 – 65
Matrix (pixel)	84 – 254 X128 - 384
Spatial resolution (mm)	0.547 - 1.875
Slice thickness (mm)	3 – 5
Echo time (ms)	1.10 - 1.96
PC-MRI	
Encoding velocity (cm/s)	$60 – 150^{\dagger}$
No. of phases	13 – 30

† As low as 60 cm/s for venous structures and as high as 150 cm/s for arterial structures.

5.2.3 Metrics of Interest

5.2.3.1   Geometry

The transverse CMR images were interpolated to obtain a stack of images with isotropic voxels, which were segmented to select the TCPC anatomies using the image processing tools described in the method section (Chapter 4.2.2). Centerlines and

bifurcation vectors were computed to calculate minimum, mean, maximum diameters of each TCPC vessel, ratio between minimum and maximum diameters of each vessel (to quantify vessel narrowing), relative LPA area, angle between vessels present, and caval offsets (Chapter 4.2.3 and 4.3.4). To account for differences in patient size in the cohort, vessel diameters were normalized by the square root of body surface area ($\sqrt{BSA}$ [m]). Caval offsets were normalized by mean FP diameter of each patient instead of BSA, in view of previous conventions [59, 61, 146].

5.2.3.2   Hemodynamics

Patient-specific flow conditions were obtained by segmenting PC-MRI images at each vessel's cross section (Chapter 4.3.1), which were then cycle-averaged. Cardiac index (CI) was calculated by dividing the mean aorta flow rate by each patient's BSA. Pulmonary flow distribution (PFD) was calculated as:

$$\%\text{PFD(LPA)} = \frac{Q_{LPA}}{Q_{LPA}+Q_{RPA}} \times 100\% \qquad \text{(Equation 5.1)}$$

where %PFD(LPA) was the percentage of total pulmonary flow leaving through the LPA, Q_i is the flow rate of the specific vessel i. Patient-specific TCPC 3D flow dynamics were also evaluated using the in-house immersed boundary solver (Chapter 4.6) with time-averaged flow boundary connections from PC-MRI. Due to CMR resolution, the sum of inlet flows from PC-MRI may not be exactly equal to sum of outlet flows. Therefore, actual flow rates of the vena cavae were used as inlet boundary conditions, and the flow splits of the LPA and RPA were prescribed as outlet boundary conditions. Among the parameters of interest were: (i) iPL (at rest) and (ii) percentage HFD to LPA (%HFD(LPA)) (as defined in Chapter 4.8).

5.2.4 Statistical Methods

Statistical analysis was performed using IBM SPSS Statistics (version 20, IBM Corporation, Armonk, New York). Paired-samples t-test and repeated-measures ANOVA were used to compare geometric parameters among vessel types. Wilcoxon signed-rank test and Friedman test were used for non-normal data (tested by Shapiro-Wilk test). Bivariate Pearson's correlation was carried out first to look for trends between the geometric variables and hemodynamic endpoints. The significant variables were selected and multiple linear regression (MLR) of the hemodynamic endpoints was performed, using forward stepwise procedures. Standardized coefficients were reported to compare the relative importance of each independent variable. In all analyses, p-value ≤ 0.05 was considered significant (two-tailed). All models were screened for outliers (standardized residual not within ± 2) and influential observations (Cook's distance > 0.04). Outliers and influential observations were reviewed and all calculations were verified.

5.2.5 Cohort Geometric Characterization

The full lists of the computed geometric variables and hemodynamic results of the patients in this cohort (N=108) are presented in Appendix A.7.1.1. The average geometric features of 108 TCPCs are presented in Table 5-3 (represented by mean $\pm$ standard deviation (SD)). The FP had the largest average diameter compared to other vessels (p<0.001), but also the highest minimum and mean diameter variability (SD = 3.8 mm/m). Comparing the LPA and RPA, LPA diameters were observed to be smaller

than the RPA on average (minimum: p<0.001; mean: p<0.001; maximum: p=0.02). Of particular note is the lower value for the minimum/maximum diameter ratio at the LPA, which implied that LPA diameter was less uniform than the RPA (p<0.001), and different degrees of vessel narrowing were observed.

There was great variation among patients in terms of caval offset. The population offset magnitude average was 0.24 ± 0.36 times the mean FP diameter of each patient, and the maximum magnitude was 2.21 times the mean FP diameter.

Table 5-3 Cohort summary of geometric characteristics (N=108)

Normalized vessel diameter (mm/m)				
	Minimum	Mean	Maximum	Minimum/maximum diameter ratio (mm/mm)
FP	15.4 ± 3.8	18.2 ± 3.8	21.5 ± 3.6	0.72 ± 0.12
SVC	12.4 ± 2.6	14.1 ± 2.7	16.5± 3.0	0.76 ± 0.12
LPA	8.0 ± 2.2	11.0 ± 2.2	16.4 ± 3.9	0.51 ± 0.18
RPA	10.0 ± 2.1	12.0 ± 2.2	15.6 ± 3.5	0.66 ± 0.16
RUPAɫ (N=36)	6.3 ± 1.4	7.6 ± 1.9	9.7 ± 3.4	0.70 ± 0.20
LSVC (N=15*)	9.0 ± 3.0	10.5 ± 3.2	12.4 ± 3.6	0.73 ± 0.14
AZ (N=5)	8.8 ± 1.4	10.7 ± 2.1	14.2 ± 1.3	0.62 ± 0.10
Relative PA cross sectional area				
Relative LPA area				0.39 ± 0.15
Caval offset (normalized by mean FP diameter)				
Caval offset with SVC (mm/mm)	Offset			0.08 ± 0.43
	Magnitude			0.24 ± 0.36
	VC-PA			0.25 ± 0.22
Caval offset with LSVC (N=15*) (mm/mm)	Magnitude			1.86 ± 0.83
Angle between vessels (degrees)				
FP-LPA				109 ± 16
FP-RPA				87 ± 15
SVC-LPA				106 ± 15
SVC-RPA				100 ± 15
FP-SVC				133 ± 19
LPA-RPA				108 ± 27
LSVC-SVC (N=15*)				57 ± 22
LSVC-FP (N=15*)				131 ± 19
LSVC-LPA (N=15*)				103 ± 19
LSVC-RPA (N=15*)				125 ± 17

ɫ RUPA = Upper lobe of right pulmonary artery
* Among these patients, 4 also have azygos vein (AZ)

In the entire cohort, FP-LPA angle was significantly larger than FP-RPA angle (p<0.001) and SVC-LPA angle was significantly larger than SVC-RPA angle (p=0.009). For cases with the four typical TCPC vessels (FP, SVC, LPA and RPA; N=92; patient ID listed in Appendix A.7.1.1), it was observed that the SVC anastomosis was generally more symmetric with respect to the pulmonary arteries (no significant difference between SVC-LPA and SVC-RPA angle, p=0.566), while difference between FP-LPA and FP-RPA angles remained significant (p<0.001). This highlighted the asymmetry of IVC anastomosis compared to the more symmetric alignment of the SVC anastomosis to the PA in these cases.

Hemodynamic findings from PC-MRI segmentation and CFD analysis are presented in Table 5-4 (detailed results listed in Appendix A.7.1.1). There was a significant correlation between %PFD(LPA) and %HFD(LPA) (r=0.396, p<0.001) and between cardiac index and the natural logarithm of iPL (r=-0.366, p<0.001) from Pearson's correlations.

Table 5-4 Cohort summary of hemodynamics under resting conditions (N=108)

	Mean	Standard Deviation	Median
Cardiac Index (L/min/m^2)	3.55	0.97	3.53
iPL	0.031	0.028	0.022
%PFD(LPA)	43	12	42
%HFD(LPA)	42	22	44

5.2.6 Correlations between Geometric Parameters and TCPC Hemodynamics

Due to the skewness of the offset magnitude data (skewness=3.96±0.23), 4 cases with discrete caval offset magnitude (CHOP_M7, CHOP025A, CHOP035A, CHOP057A; Figure 5.3) were outliers and were excluded in subsequent statistical correlations, resulting in a final patient population of 104 (skewness=1.172). Detailed results of statistical analysis are presented in Appendix A.7.2.
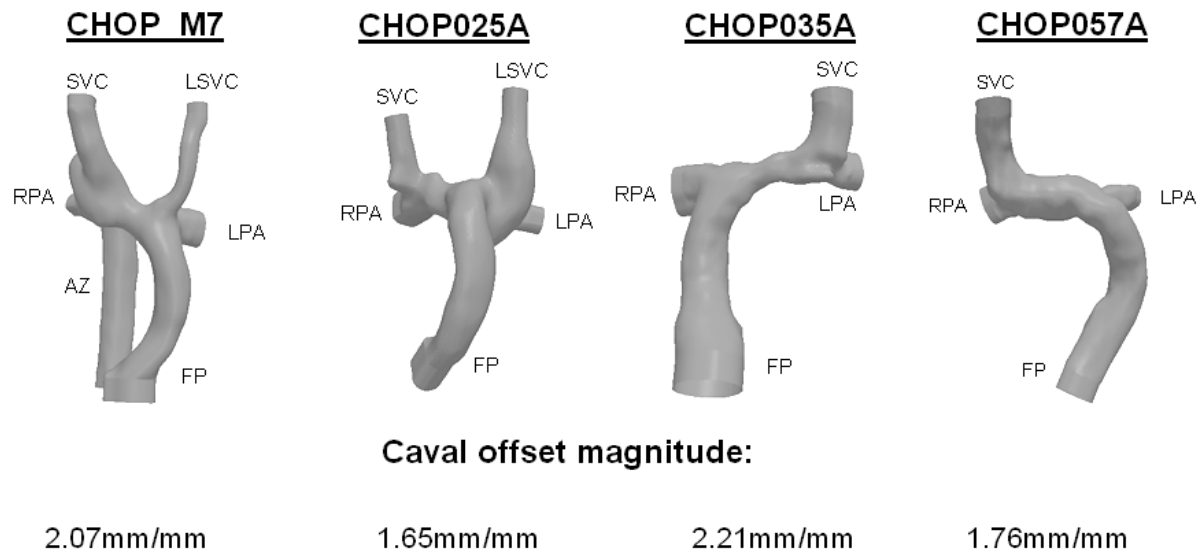
Figure 5.3 Outlier cases of caval offset magnitude

Multiple regression of iPL (N = 104; R^2 adjusted = 0.670)

Dependent variable	Representative cases	
Normalized Minimum FP diameter (minFP) $y = 9.8206x^{-2.274}$ Independent variable used for MLR: (minFP)$^{-2.274}$ $\beta = 0.657$; $r = 0.730$; $p < 0.001$	**CHOP032A** minFP:8.34 mm/m iPL: 0.120	**CHOP080A** minFP:7.54 mm/m iPL: 0.106
Normalized Minimum LPA diameter (minLPA) $y = 0.4214x^{-1.492}$ Independent variable used for MLR: (minLPA)$^{-1.492}$ $\beta = 0.324$; $r = 0.496$; $p < 0.001$	**CHOP026A** minLPA:4.90mm/m iPL: 0.072	**CHOP_M11p** minLPA: 4.05mm/m iPL:0.076
Normalized Minimum RPA diameter (minRPA) $y = 1.4986x^{-1.893}$ Independent variable used for MLR: (minRPA)$^{-1.893}$ $\beta = 0.161$; $r = 0.254$; $p = 0.01$	**CHOP088A** minRPA:6.74mm/m iPL: 0.070	**CHOP072A** minRPA:6.21mm/m iPL: 0.101

β = Standardized coefficient; r = partial correlation

Velocity (cm/s): 5 15 25 35 45

Figure 5.4 Significant correlations between iPL with normalized minimum FP, LPA and RPA diameters and representative cases for each independent predictor (β = Standardized coefficient; r = partial correlation)

5.2.6.1 Indexed Power Loss (iPL)

It was found that there existed a power law relationship between iPL and normalized minimum vessel diameter (Figure 5.4). Therefore, the normalized diameters were transformed to their respective exponents (e.g. normalized minimum FP diameter was powered with -2.274) for MLR. For each vessel, the strongest correlations existed between iPL and powered normalized minimum diameters. From MLR, only normalized minimum vessel diameters of FP, LPA and RPA were identified as independent predictors. The strongest predictor was normalized minimum FP diameter, which carried the majority of TCPC blood (59±15% of total systemic return on average). In addition, the majority of patients with low minimum FP diameter in this cohort had an intra atrial connection (Figure 5.4). Among the PAs, LPA (smaller diameter on average) was a more significant predictor of iPL.

5.2.6.2 Cardiac Index

Consistent with the trend between iPL and CI, and between iPL and minimum FP diameter, significant positive correlation between CI and normalized minimum FP diameter was observed (standard coefficient=0.347; r=0.355, p<0.001). Also, positive significant correlation between CI and SVC minimum/maximum diameter ratio (standard coefficient=0.215; r=0.229, p=0.02) was observed. Overall R-squared value of this correlation is 0.2.

5.2.6.3   Pulmonary Flow Distribution

From bivariate analysis of %PFD(LPA) and LPA/RPA geometrical variables, significant positive correlation was found between %PFD(LPA) with normalized minimum (r=0.356, p<0.001) and mean (r=0.226, p=0.021) LPA diameter, LPA minimum/maximum diameter ratio (r=0.345, p<0.001) and relative LPA area (r=0.519, p<0.001). %PFD(LPA) also correlated negatively with normalized minimum (r=-0.285, p=0.003) and mean (r=-0.288, p=0.003) RPA diameter. It was found by MLR that relative LPA area was the only independent predictor for %PFD(LPA) (Figure 5.5).

Multiple regression of %PFD(LPA) (N = 104) R^2= 0.27
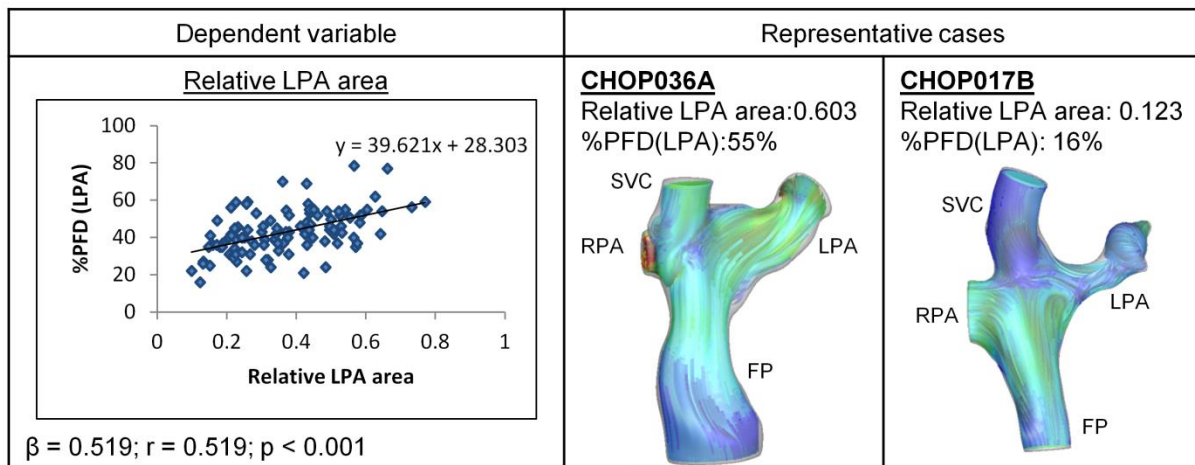
Figure 5.5 Significant correlation between %PFD(LPA) with relative LPA area and representative cases (β = Standardized coefficient; r = partial correlation)

5.2.6.4   Hepatic Flow Distribution

To exclude the influence of any additional vessel(s) such as AZ and LSVC, correlations of %HFD(LPA) were carried out only on cases with the four typical TCPC vessels (FP, SVC, LPA and RPA; N=90, listed in Appendix A.7.1.1). From bivariate analysis, significant positive correlation was found between %HFD(LPA) and %PFD(LPA) in this subset of patients. %HFD(LPA) correlated positively with normalized mean LPA diameter (r=0.240,p=0.023) and negatively with RPA minimum/maximum diameter ratio (r=-0.222,p=0.035), which could be explained by the correlation between %PFD(LPA) and relative LPA/RPA minimum size.

Of the geometric variables, normalized caval offset with SVC correlated most significantly with %HFD(LPA). When the FP was connected to the left relative to the SVC, higher flow from the FP coursed through the LPA than the RPA as a result of proximity. Also, significant correlations were found between %HFD(LPA) and connection angles. FP-LPA angle (angle between FP and LPA) correlated positively with %HFD(LPA), negatively with SVC-LPA angle and positively with SVC-RPA angle. From multiple regression, %HFD(LPA) varied significantly with normalized caval offset with SVC, %PFD(LPA), followed by angle between the FP and SVC (Figure 5.6). An example showing the influence of FP-SVC angle on %HFD(LPA) is illustrated by Figure 5.7.

Multiple regression of %HFD(LPA) (N = 90; R^2 adjusted = 0.649)

Dependent variable	Representative cases

Normalized caval offset with SVC (offset)

$y = 63.724x + 40.248$

Right of SVC — Left of SVC

Normalized caval offset with SVC (mm/mm)

β = 0.595; r = 0.713; p < 0.001

CHOP191A
Offset:0.53
%HFD(LPA):65%
%PFD(LPA):45%

CHOP052B
Offset: -0.52
%HFD(LPA): 21%
%PFD(LPA):44%

%PFD (LPA)

$y = 0.9961x + 1.8185$

β = 0.466; r = 0.624; p < 0.001

CHOP054A
%PFD(LPA): 21%
%HFD(LPA): 17%

CHOP004B
%PFD(LPA): 56%
%HFD(LPA): 71%

Angle between FP and SVC (FP-SVC angle)

$y = -0.3167x + 85.551$

Angle between FP and SVC (°)

β = -0.209; r = -0.336; p = 0.001

CHOP063A
FP-SVC angle: 127°
%HFD(LPA):71%

CBF069
FP-SVC angle: 160°
%HFD(LPA):10%

β = Standardized coefficient; r = partial correlation;
Green: flow originated from SVC; Blue: flow originated from FP

Figure 5.6 Significant correlations between %HFD(LPA) with normalized caval offset, %PFD(LPA) and FP-SVC angle and representative cases for each independent predictor (β = Standardized coefficient; r = partial correlation)

114
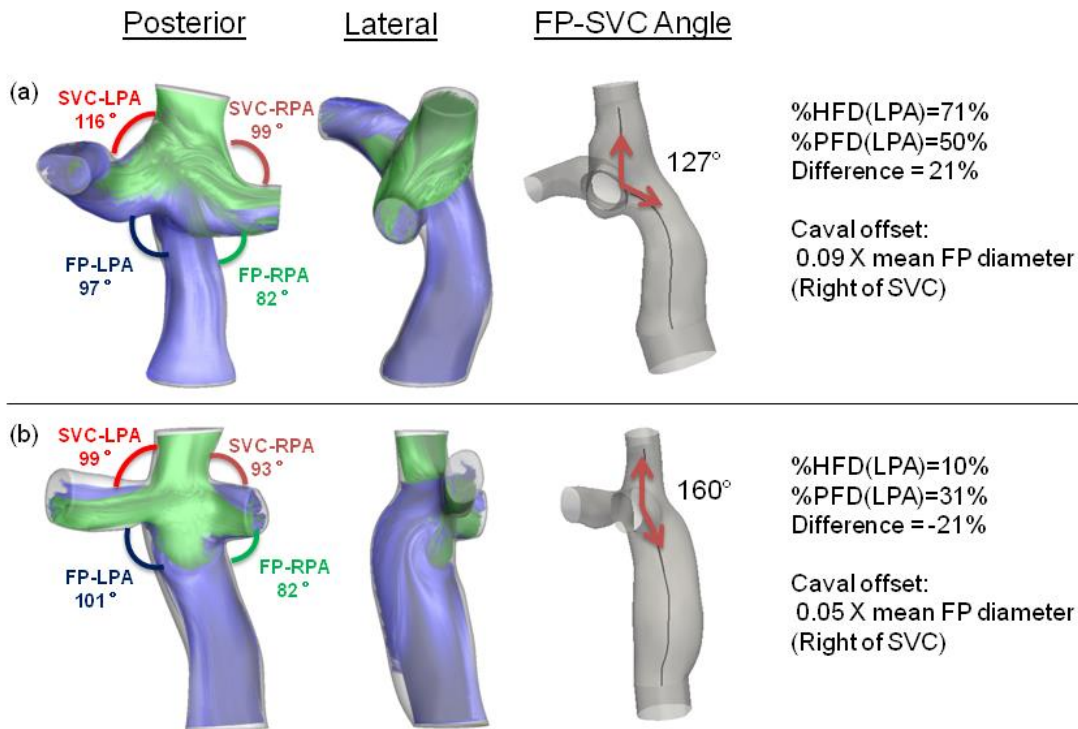
Figure 5.7 Angulation of FP away from SVC prevents recirculations at the FP-SVC junction. Labels on figure represent angles between the TCPC vessels: (a) CHOP063A was connected anteriorly towards the PAs, resulting in a small FP-SVC angle, (b) CBF069 (CBF= cerebral blood flow cohort from CHOP) had a large FP-SVC angle that almost resembled a straight pipe

5.2.7 Discussion

5.2.7.1 Impact of Geometry on Resting Energy Dissipation
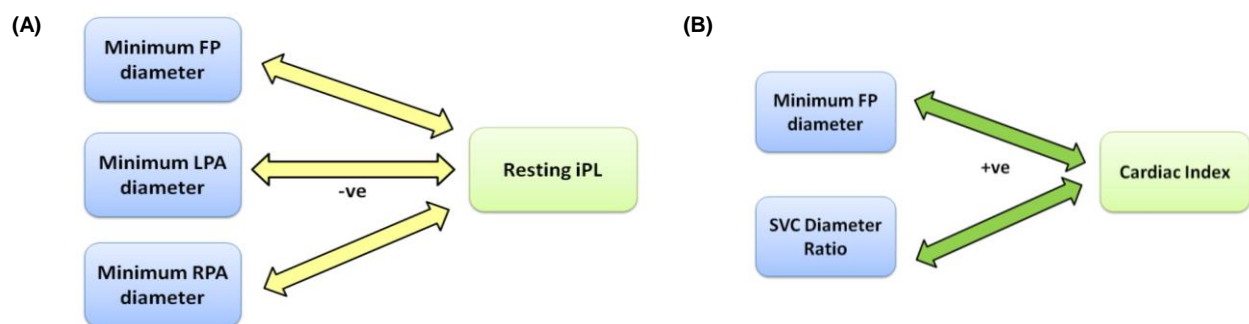
Figure 5.8 Schematic representing the significant independent predicators of (a) resting iPL and (b) cardiac index. "-ve" (yellow arrow) denotes a negative correlation and "+ve" (green arrow) denotes a positive correlation

115

The significant independent predictors of resting iPL and cardiac index are shown in Figure 5.8. In this patient cohort, the effect of minimum vessel size manifested as the most important geometric parameter for resting iPL. Even when the average LPA diameter was smaller than that of the FP, the correlation between minimum FP diameter and iPL at rest was the most significant, followed by minimum LPA and RPA diameters. This could be due to the fact that FP carried higher blood flow, which further elevated energy loss when the diameter was small. On the other hand, caval offset was not significantly correlated to resting iPL in this cohort, in spite of previous findings [59, 61]. This indicates that it may not be of critical importance compared to vessel diameter in order to minimize power loss.

5.2.7.2   Factors Affecting Resting Hepatic Flow Distribution
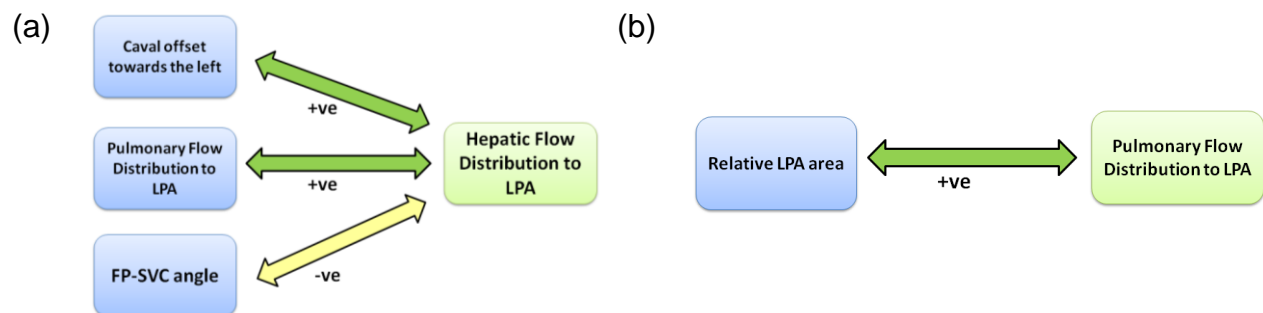
Figure 5.9 Schematic representing the significant independent predicators of (a) %HFD(LPA) and (b) %PFD(LPA). "-ve" (yellow arrow) denotes a negative correlation and "+ve" (green arrow) denotes a positive correlation

The significant independent predictors of %HFD(LPA) and %PFD(LPA) (or global flow distribution (GFD)) are shown in Figure 5.9. Avoiding unbalanced distribution of hepatic flow to both lungs has been shown to be important for palliation of PAVMs in SV patients [3-5, 191]. Another study by Dasi et al. has shown that %HFD(LPA) was

strongly correlated with caval offset in extra cardiac patients (N=5), and with %PFD(LPA) in intra atrial patients (N=5) [47]. In the current cohort as a whole, normalized caval offset (with SVC) was most significantly correlated with %HFD(LPA), which agreed with the previous study. This emphasizes again the need to consider the relative displacement between FP and SVC in the staged procedures (whether the FP is connected to the left or the right of the SVC).

Another significant variable for HFD was the angle between FP and SVC. From the cohort geometric characterization, FP was generally connected towards the left (FP-LPA angle > FP-RPA angle) favoring HFD to the LPA, but it was not the case with SVC (SVC-LPA angle ≈ SVC-RPA angle, meaning that SVC was connected relatively symmetric respect to the PAs, not connected towards a particular PA). When the angle between FP and SVC was large (close to 180°), the FP and SVC flows were directly opposed and subject to collisions. This likely resulted in more recirculation, negating the preference of the FP flow towards the LPA. As shown in Figure 5.7, both cases had low caval offset magnitudes and FP pointing towards the left, but CHOP063A was connected anteriorly towards the PAs, resulting in a small FP-SVC angle. Therefore, hepatic blood from FP still flows preferably towards the LPA since FP-LPA angle > FP-RPA angle, resulting in %HFD(LPA) of 71%. On the other hand, CBF069 (CBF = cerebral blood flow cohort from CHOP) had a large FP-SVC angle that almost resembled a straight pipe. Therefore, FP and SVC blood collided and mixed before leaving through the PAs. Even though FP-LPA angle was larger than FP-RPA, the %HFD(LPA) was still only 10%. These findings suggest that whereas caval offset

117

remains the most important geometric determinant of HFD, in cases where caval offset is constrained (e.g., by surrounding structures) and PFD is unbalanced, FP should not be angled only towards the desired side of the lungs (left or right, on the basis of the patient-specific circumstances). The relative angle with the SVC should also be considered to avoid head-on collisions and reduce caval flow mixing.

5.3 Specific Aim 1(b): Geometric Correlation with Exercise Hemodynamics

Previous studies in Fontan patients have shown poor exercise performance, including decreased peak oxygen consumption, oxygen consumption at ventilatory anaerobic threshold (VAT), peak exercise heart rate (HR), arterial oxygen saturation and cardiac output compared to healthy subjects [53, 54]. Due to the complex physiology and hemodynamics in SV patients, recent research has been focusing on investigating the potential linkage between TCPC hemodynamics and SV physiology [55, 56]. TCPC anatomy varies significantly between patients, and has been shown to be closely related to TCPC energy loss. Under baseline conditions (i.e. resting), it has been shown that vessel diameters were inversely correlated to TCPC energy dissipation [198]. Though the clinical importance of TCPC energy dissipation on patient outcome is not clear, there has been growing evidence showing the relevance of elevated TCPC energy dissipation to ventricular performance and exercise performance [57], potentially resulting in limited exercise capacity [2, 58].

The hypothesis of this sub aim is that TCPC geometry, TCPC hemodynamics and patient exercise performance are interlinked (represented by Figure 5.10). Understanding these relationships in Fontan patients may help develop ways to improve patient exercise performance and quality of life by optimizing TCPC surgical design.
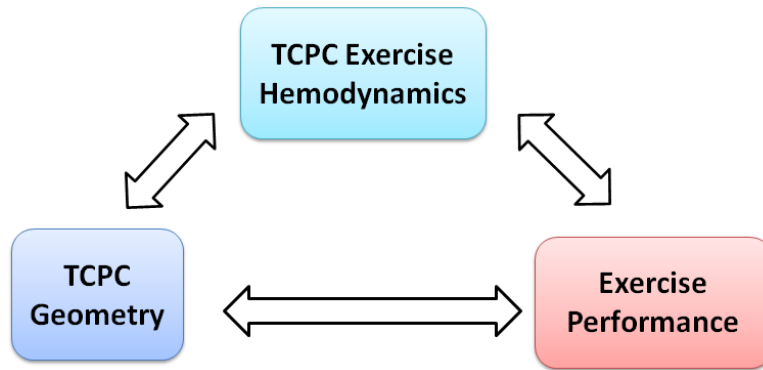
Figure 5.10 Schematic representing the hypothesis of SA1(b)

5.3.1 Patient Cohort

Patients who underwent TCPC palliation were prospectively enrolled at Children's Hospital of Philadelphia to evaluate the relationship between hemodynamics, anatomic features and exerciser performance. Patients included had a minimum age of 12 years old, had the TCPC as the only source of pulmonary blood flow, and were able to perform a metabolic exercise stress test using a stationary cycle ergometer. Patients with pacemaker or implanted metal that precluded image acquisition were excluded. Fifty-two consecutive patients were included. Two patients with CMR image artifacts and one patient with a large baffle leak were excluded from this study, resulting in a total of 49 consecutive patients. The study was approved by the IRBs at Georgia Tech and Children's Hospital of Philadelphia. Patient data were collected with informed consent. Patient demographic and anatomic data are summarized in Table 5-5. Full list of patient IDs are listed in Appendix A.7.3.1.

Table 5-5 Demographic information of patients included in the exercise study (N=49)

	Mean ± standard deviation
Age	19.2 ± 5.6
Body surface area (m2)	1.66 ± 0.21
Gender (male/female)	27/22
IVC connection type (intra-atrial /extra-cardiac)	35/14
Left / right / mixed ventricle	18/25/6

5.3.2 Exercise Stress Test Protocol

As described in Chapter 4.4, Enrolled patients first completed a routine maximal metabolic exercise stress test using a ramp cycle protocol. Maximal minute oxygen consumption (VO_2), as well as heart rate (HR), work rate, and VO_2 at VAT were obtained using a metabolic chart (SensorBiomedics V29, Yorba Linda, CA). VAT was measured using the V-slope method.

5.3.3 CMR Acquisition

After the metabolic stress test, the baseline and exercise CMR studies were performed. The anatomic images acquisition was performed under baseline conditions and the protocol was the same as described in Chapter 4.3.1. PC-MRI was utilized to acquire through-plane velocity profiles across all the TCPC vessels, the aortic valve and descending aorta (DAO) over the cardiac cycle under resting breath-held condition.

Table 5-6 Summary of CMR acquisition parameters

		Range
Transverse CMR	**No. of slices**	38 - 75
	Matrix (pixel)	126 - 168 X 192 - 256
	Spatial resolution (mm)	1.055 - 1.719
	Slice thickness (mm)	3 - 5
	Echo time (ms)	1.1 - 1.44
Phase-contrast CMR (Exercise)	**Encoding velocity (cm/s) – descending aorta**	100-350
	Encoding velocity (cm/s) – superior caval vessels	60-250
	No. of phases	20-30
Phase-contrast CMR (Rest)	**Encoding velocity (cm/s) – pulmonary arteries**	60-180
	No. of phases	20-32

After the baseline CMR acquisition, the patients were slid partially out of the bore of the MRI machine. Lower limb exercise using an MRI-compatible supine bicycle ergometer (Lode BV, Groningen, the Netherlands) was performed which allowed RPM-independent workload ranging from 10-250 Watt. The workload was set initially at 20 Watt. It was then increased at a rate of 20 Watt/min progressively to obtain HR at VAT (determined during the exercise stress test). After that, the study subject was returned to the isocenter of the magnet for imaging within 10 seconds. HR was monitored

continuously. PC-MRI across the SVC, ascending aorta and descending aorta were acquired as 3 separate velocity maps. The patients repeatedly exercised to the target heart rate (heart rate at VAT) for each acquisition. The images were acquired with free-breathing and the velocity maps were averaged. The study lasted approximately 90 minutes with the patient lying supine. The CMR acquisition parameters are summarized in Table 5-6.

5.3.4 Metrics of Interest

5.3.4.1 Geometry

The anatomic image processing pipeline was similar to those involved in Chapter 5.2, as described in the method section (Chapter 4.2.2). Centerlines and bifurcation vectors were computed from VMTK to calculate minimum, mean, maximum diameter of each TCPC vessel, ratio between minimum and maximum diameter of each vessel (to quantify vessel narrowing), angle between vessels present, and caval offsets (Chapter 4.2.3 and 4.2.4). To include the influence of minimum diameter of different vessels, TCPC diameter index was computed by averaging the normalized minimum diameter of any connection vessel present (including LSVC, AZ and RUPA if present). In this way, influence of narrowing/stenosis at different vessels can be captured with one variable.

$$TCPC\ diameter\ index = \frac{\sum_{i=1}^{n}(Minimum\ vessel\ diameter)}{n\cdot\sqrt{BSA}}$$ (Equation 5.2)

where n = number of vessels present at the TCPC, BSA = body surface area (m^2)

To account for differences in patient size in the cohort, vessel diameters were normalized by the square root of body surface area ($\sqrt{BSA}$ [m]). Caval offset magnitude and VC-PA offset were normalized by mean FP diameter.

5.3.4.2 Hemodynamics

Patient-specific flow conditions were obtained by segmenting PC-MRI at each vessel's cross section (Chapter 4.3.1), which were then cycle-averaged. iQs at VAT (defined as total system return (Qs) at VAT, normalized by patient body surface area) was computed from time-averaged vessel flow rate obtained from PC-MRI data.

Patient-specific TCPC 3D flow dynamics were also evaluated using the in-house immersed boundary solver (Chapter 4.6) with time-averaged flow boundary connections from PC-MRI. Diaphragm motion during exercise made positioning the FP flow plane unreliable; therefore exercise DAO flow rate was substituted for exercise FP flow rate both for calculation of iQs and flow boundary conditions of CFD. Since the patient's motion during exercise affected the flow measurements with PC-MRI, the LPA/RPA flow ratio was taken from the baseline data and used as outflow boundary conditions for CFD.

5.3.4.3 Exercise Performance

Minute oxygen consumption at VAT (VO_2 at VAT), as well as work rate at VAT were correlated with TCPC geometric parameters and exercise hemodynamics.

5.3.5 Statistical Methods

Statistical analysis was performed using IBM SPSS Statistics (version 22, IBM Corporation, Armonk, New York). Bivariate Pearson's correlation was carried out to assess correlations between geometric variables and iPL at VAT. The significant geometric variables were selected, and MLR was performed using forward stepwise procedures to identify the independent geometric predictor of iPL at VAT. The independent geometric predictors and iPL at VAT were correlated with exercise stress test parameters using Pearson's correlation. Fisher's z-transformation was used to assess the significance of the difference between the two correlation coefficients found between different age groups. Student's t-test (or Mann–Whitney test) was used to compare geometric parameters, iPL at VAT and exercise parameters among different age groups (normality tested by Shapiro-Wilk test). For all analyses, p-value ≤ 0.05 (two-tailed) was considered significant.

The lists of the computed geometric variables, total systemic return, iPL at VAT and exercise performance of the patients in this cohort are presented in Appendix A.7.3.1.

5.3.6 Correlations between TCPC Geometry and Energy dissipation at VAT

For the entire cohort, iPL at VAT was inversely correlated to normalized minimum FP diameter (r=-0.6643, p<0.001) and normalized minimum pulmonary artery diameter (r=-0.4694, p<0.001). iPL at VAT was also significantly correlated to caval offset magnitude (r=0.356, p=0.012) and connection angle between FP and SVC (r=-0.340, p=0.017). Figure 5.11 shows patients with low normalized minimum FP and pulmonary artery

diameters in this cohort. It was observed that regions with vessel narrowing also corresponded to regions with higher velocity magnitude in the connection at VAT.
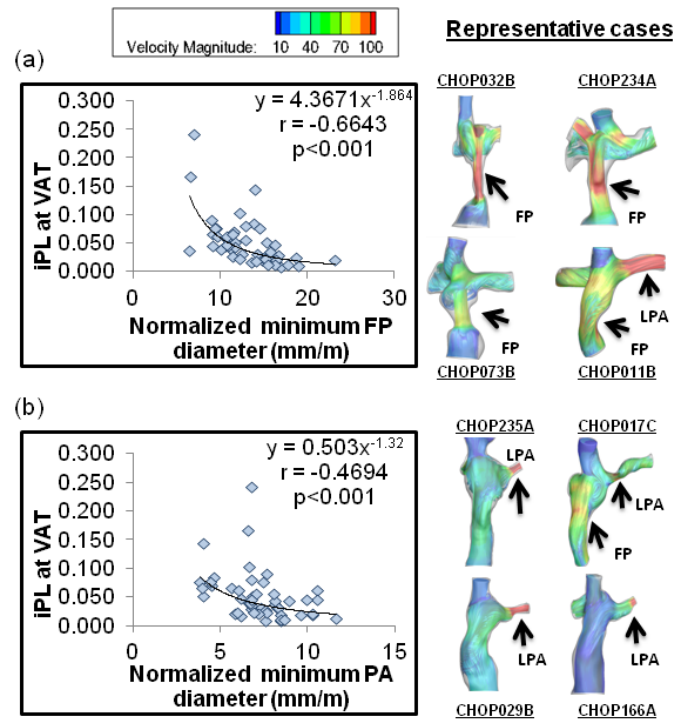
Figure 5.11 Significant inverse correlations between iPL at VAT with: (a) normalized minimum FP diameter, (b) normalized minimum pulmonary artery (PA) diameter, along with 8 example patient anatomies with stream traces color-coded by velocity magnitude. High velocity flow through the vessel narrowing was observed. (r is shown instead of R^2 to show whether the correlation is positive or negative)

An inverse correlation was observed between TCPC diameter index (which included the influence of vessel narrowing of all vessels present) and iPL at VAT (r=-0.7880, p<0.001,Figure 5.12). From the regression of all significant geometric variables, it was found that TCPC diameter index was the only geometric predictor of iPL at VAT.

126
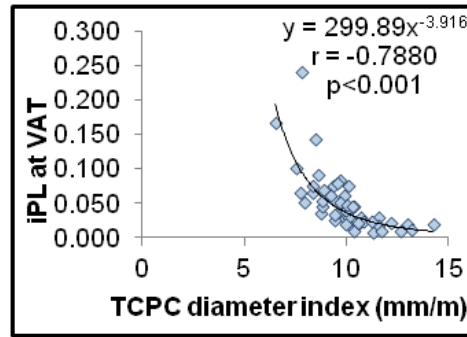
Figure 5.12 Significant inverse correlations between iPL at VAT with TCPC diameter index in the patient cohort (N=49)
(r is shown instead of R^2 to show whether the correlation is positive or negative)

5.3.7 Factors Correlating with Exercise Stress Test Performance

5.3.7.1 Cohort Correlations

The correlations between patient age, exercise stress test results, iPL at VAT, TCPC diameter index and iQs at VAT are summarized in Table 5-7 for 47 patients (2 of the 49 patients did not complete the entire metabolic stress test protocol). A significant negative correlation was observed between patient age with VO_2 at VAT and work at VAT (orange text in Table 5-7). Inverse correlations were observed between iPL at VAT and VO_2 at VAT, and between iPL at VAT and work at VAT (blue text in Table 5-7). The correlation between TCPC diameter index and VO_2 at VAT was not significant and there was a weak positive correlation between TCPC diameter index and work at VAT (green text in Table 5-7). Significant positive correlations between iQs at VAT and VO_2 at VAT, between iQs at VAT and work at VAT were observed (purple text in Table 5-7).

127

Table 5-7 Bivariate correlations between patient age, exercise stress test results, iPL at VAT, TCPC diameter index and iQs at VAT (N=47)

Variable		Age	VO2 at VAT	Work at VAT/weight	iPL at VAT	TCPC diameter index	iQs at VAT
Age	r	--	-0.4569†	-0.2884	0.1127	0.2256	0.2744
	p	--	0.001*	0.05*	0.45	0.13	0.06
VO2 at VAT	r	-0.4569†	--	0.8018	-0.3734†	0.2128	0.2950
	p	0.001*	--	<0.001*	0.01*	0.15	0.04*
Work at VAT/weight	r	-0.2884	0.8018	--	-0.2902†	0.2885	0.4317
	p	0.05*	<0.001*	--	0.05*	0.05*	0.002*
iPL at VAT	r	0.1127	-0.3734†	-0.2902†	--	0.7892†	0.1273
	p	0.45	0.01*	0.05*	--	<0.001*	0.39
TCPC diameter index	r	0.2256	0.2128	0.2885	0.7892†	--	0.014
	p	0.13	0.15	0.05*	<0.001*	--	0.93
iQs at VAT	r	0.2744	0.2950	0.4317	0.1273	0.014	--
	p	0.06	0.04*	0.002*	0.39	0.93	--

r = correlation coefficient (r is shown instead of R^2 to show whether the correlation is positive or negative)

* $p \leq 0.05$ † Nonlinear correlations

In view of the confounding effect of age on exercise stress test performance, these correlations were further studied by separating the patient cohort into two age groups: (i) Adolescents (age 12-18, N=26), and (ii) Adults (age > 18, N=21). Significant difference in iPL at VAT (p=0.016) and VO_2 at VAT (p=0.009) were found between the two groups (detailed results in Appendix A.7.4). Detailed results of statistical correlations within each age group are summarized in Appendix A.7.5.

5.3.7.2   Adolescents

There were significant negative correlations between iPL at VAT with VO_2 at VAT (Figure 5.13(a)(i)) and work at VAT (Figure 5.13(b)(i)). Consistent with the correlation between iPL at VAT and TCPC diameter index, there were positive correlations between TCPC diameter index with VO_2 at VAT (Figure 5.13 (c)(i)) and work at VAT (Figure 5.13(d)(i)). Correlations between iQs at VAT with VO_2 at VAT, between iQs at VAT with work at VAT were not statistically significant. There were no significant correlations between patient age with VO_2 at VAT, work at VAT and iQs at VAT (Figure 5.13(e)(i)) within this patient group.
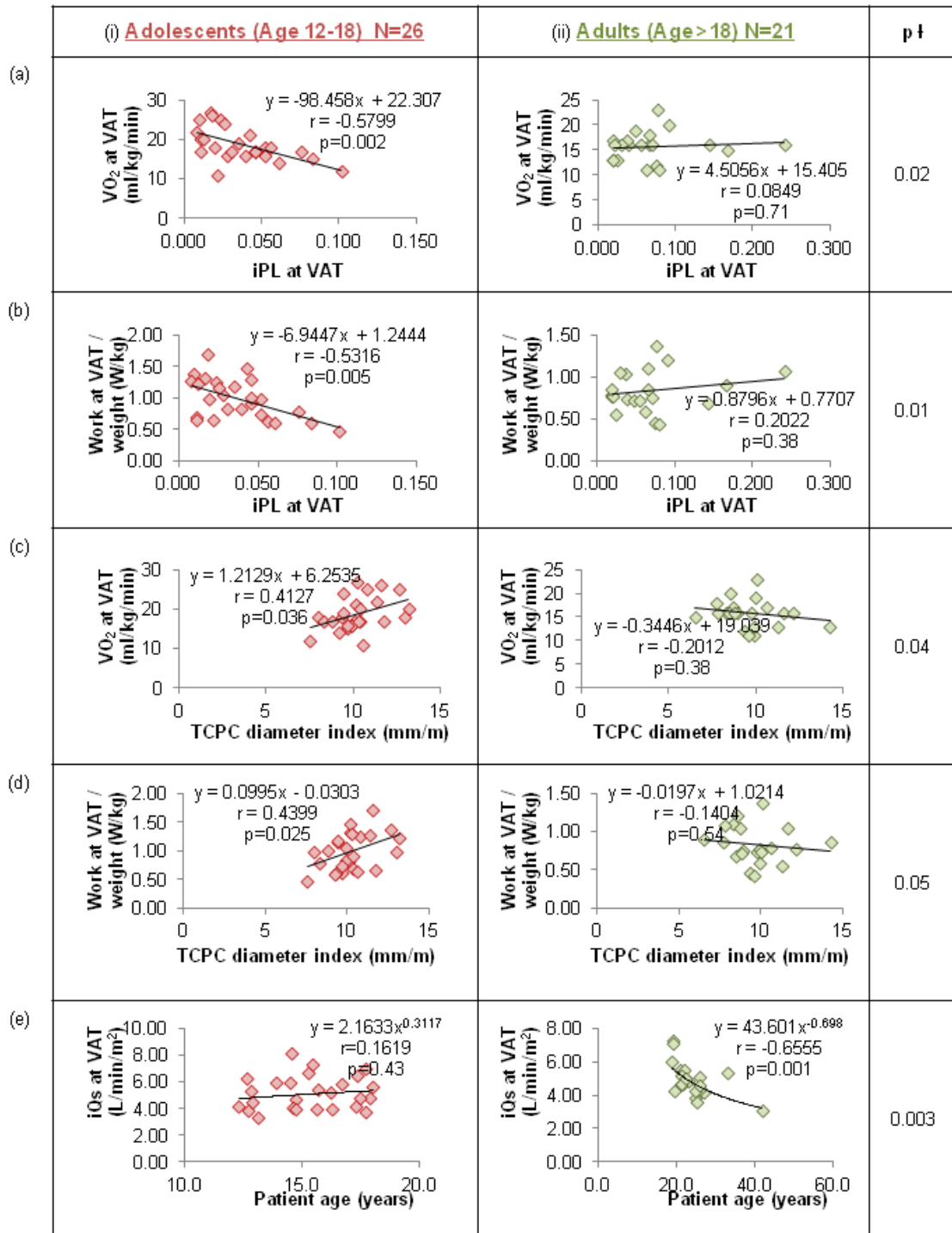
Figure 5.13 Correlations between (a) VO_2 at VAT and iPL at VAT, (b) work at VAT and iPL at VAT, (c) VO_2 at VAT and TCPC diameter index, (d) work at VAT and TCPC diameter index, (e) iQs at VAT and patient age for (i) adolescent and (ii) adult groups. (r is shown instead of R^2 to show whether the correlation is positive or negative)

130

5.3.7.3   Adults

In this subgroup, there were no significant correlations between iPL at VAT with VO_2 at VAT (Figure 5.13(a)(ii)) and work at VAT (Figure 5.13(b)(ii)), as well as between TCPC diameter index with VO_2 at VAT (Figure 5.13(c)(ii)) and work at VAT (Figure 5.13(d)(ii)). The inverse correlations between patient age with iQs at VAT (Figure 5.13(e)(ii)) and with VO_2 at VAT (Figure 5.14(a)) were significant, but not for work at VAT (Figure 5.14(b)). Significant positive correlations between iQs at VAT with VO_2 at VAT (Figure 5.14(c)) and work at VAT (Figure 5.14(d)) were observed.
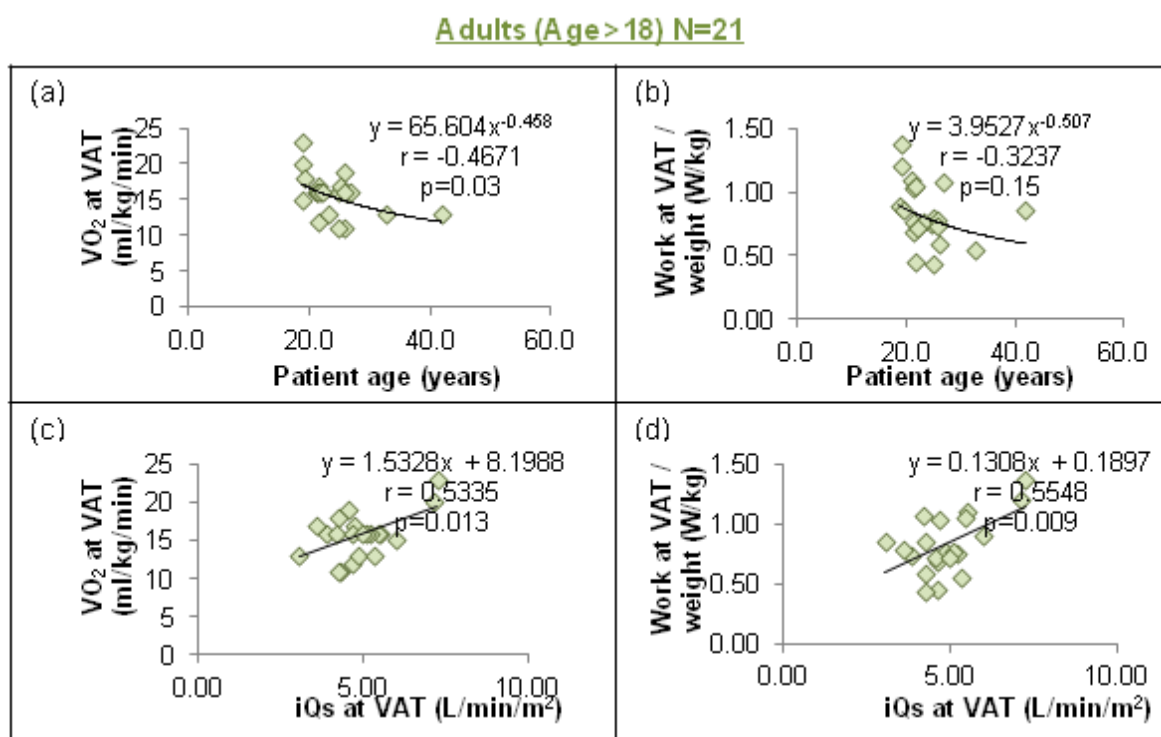
Figure 5.14 Graphs illustrating (a) significant inverse correlation between VO_2 at VAT and age, (b) non significant correlation between work at VAT and age, (c) significant positive correlation between VO_2 at VAT and iQs at VAT, (d) significant positive correlation between work at VAT and iQs at VAT in the <u>adult</u> group (age >18, N=21). (r is shown instead of R^2 to show whether the correlation is positive or negative)

5.3.7.4   Adolescents vs. Adults

To evaluate the significance of the difference in correlation between the two groups, Fisher's z-transformation was applied. Significant differences in correlation coefficients between the two age groups were found in correlations between iPL at VAT and VO_2 at VAT (p= 0.02, Figure 5.13(a)), and between iPL at VAT and work rate at VAT (p=0.01, Figure 5.13 (b)). Significant differences in correlation coefficients were also found in correlations between TCPC diameter index and VO_2 at VAT (p=0.04, Figure 5.13 (c)), and between TCPC diameter index and work rate at VAT (p=0.05, Figure 5.13 (d)). A significant difference in correlation coefficients was observed in the correlation between iQs at VAT and patient age among the two groups (p=0.003, Figure 5.13 (e)). No significant differences in correlation coefficients were found between iQs at VAT and VO_2 at VAT, and between iQs at VAT and work rate at VAT among the two groups.

5.3.8 Discussion

5.3.8.1   Impact of Geometry on Exercise Hemodynamics
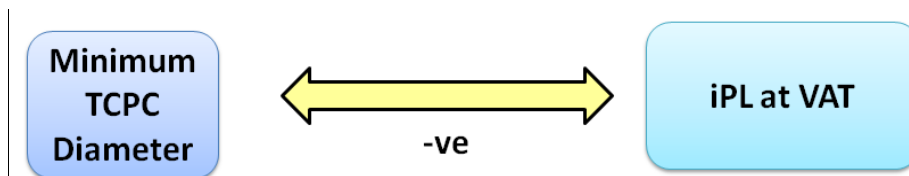
Figure 5.15 Schematic representing the significant independent predicator of iPL at VAT. "-ve" denotes a negative correlation

The significance correlation between TCPC geometric variable and iPL at VAT was illustrated in Figure 5.15. In this Fontan patient cohort with exercise data, it was observed that minimum FP diameter and minimum PA diameter were negatively correlated with iPL at VAT. Since FP carries the bulk of the total systemic venous return

on average (73±14%) during exercise, it is not surprising that vessel narrowing at FP was associated with high iPL at VAT. A previous study has shown that the obstruction of cavopulmonary pathway was mainly observed in the Fontan pathway and the LPA in extra-cardiac Fontan patients [199]. In this cohort, the presence of FP and PA narrowing were prevalent, also resulting in higher iPL at VAT (Figure 5.11). Therefore, a compounded index, accounting for vessel narrowing at all the TCPC vessels (which we defined as the TCPC diameter index) was found to be the only independently significant predictor of iPL at VAT, among the parameters investigated in this study. This highlights that TCPC diameter index is the primary geometric determinant of iPL at VAT. Even though previous studies have shown the effect of caval offset magnitude on TCPC power loss [59], it was of lesser importance in this cohort. This was mainly due to the dominant effect of vessel stenosis on TCPC power loss.

5.3.8.2   Relevance to Fontan Exercise Physiology

Given the close relationship between TCPC diameter index and iPL at VAT, it is important to investigate the clinical importance of this correlation with patient exercise performance. Firstly, it is important to understand the influence of TCPC energy dissipation on exercise performance. In the single ventricle circulation, a low pulmonary vascular resistance (PVR) is essential to achieve the increase in cardiac output required during exercise, and is therefore important for exercise performance [200]. PVR for Fontan patients was previously reported as $2.8±0.9 mmHg/(L/min/m^2)$ during peak exercise conditions [58]. In this cohort, it was found that TCPC resistance at VAT was on average $0.57±0.48 mmHg/(L/min/m^2)$, and could be as high as $2.23 mmHg/(L/min/m^2)$

(for the patient with the lowest TCPC diameter index, 10.8mm/m). Given that this is comparable in magnitude with PVR at peak exercise, it is clear that TCPC resistance is not negligible in all patients and can contribute or even become the dominant factor in the ability to increase pulmonary blood flow that is required for effective exercise.

5.3.8.3   Age-Related Differences of Fontan Exercise Performance

Khiabani et. al. [189], for the first time, established negative correlations between iPL at VAT with minute oxygen consumption and work rate at VAT with a subset of the patients (N=30, 19 adolescents and 11 adults) included in this study. In this cohort with more patients, only fair correlations between iPL at VAT with the two exercise stress test parameters were observed. This was due to the confounding effect of patient age on exercise capacity. Consistent with the findings in Giardini et al. [201], patient exercise performance was negatively correlated to patient age. Due to the confounding effect of age on patient exercise, the patients were divided into two age groups.

In the adolescents group, patient age, as well as iQs at VAT did not play a significant role in exercise performance. Based on the correlations between TCPC diameter index, iPL at VAT and exercise performance (as illustrated in Figure 5.16), we presume that local geometry and hemodynamics are important to exercise performance. The negative correlations between iPL at VAT with exercise performance, as well as the positive correlations between TCPC diameter index with exercise performance, suggests that eliminating vessel stenosis or stimulating vessel growth (increasing diameter) within the

TCPC, may minimize TCPC energy dissipation during exercise, thereby allowing adolescents to have improved exercise capacity.
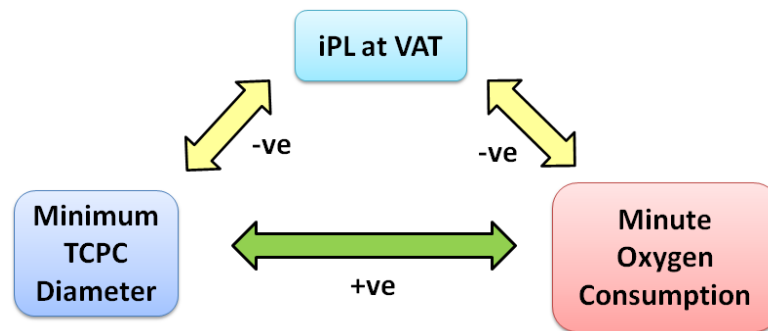
Figure 5.16 Schematic representing the significant relationships between minimum TCPC diameter, iPL at VAT and minute oxygen consumption in adolescents. "-ve" (yellow arrow) denotes a negative correlation and "+ve" (green arrow) denotes a positive correlation.

On the other hand in the adult patients, the inverse correlations between patient age with exercise performance and iQs at VAT, as well as the positive correlation between iQs at VAT and exercise performance, suggest that the deteriorating iQs at VAT with age could be the reason why exercise capacity was reduced as the adult patients grow older. This population tends to be physically more limited and the contribution of declining cardiac function to the variance in aerobic capacity is more significant [53, 201, 202]. Thus, there is less ability in this adult population for the peripheral muscle oxygen extraction to compensate for the lower iQs at VAT. This would explain the positive correlation of iQs at VAT and exercise performance seen in the adult but not in the adolescent population. TCPC vessel diameter and energy dissipation did not appear to be significant factors in adult patients' exercise performance.

This study for the first time establishes the age-related differences in Fontan exercise performance with respect to TCPC geometry and hemodynamics. It shows the relevance of local TCPC geometry and hemodynamics to exercise performance in adolescent Fontan patients. It also highlights that given exercise performance decreases with age, as patients reach adulthood, local geometry and hemodynamics may be less relevant to exercise performance. Understanding these relationships can potentially help derive strategies to improve patient exercise performance based on their age, as well as identifying patients that are prone to exercise intolerance. Future studies will be needed with longitudinal follow-up to determine whether power loss indeed impacts the decline in exercise performance. Prospective trials with tailored TCPC designs based on pre-operative modeling will be required to determine whether a strategy of power loss minimization can impact long-term outcomes and quality of life.

5.4 Specific Aim 1(c): Effect of Stent Implantation

As demonstrated in Chapter 5.2, TCPC energy dissipation under baseline and exercise conditions was influenced by minimum vessel diameter. Therefore, it is plausible that vessel narrowing should be avoided when creating a TCPC. For patients who developed vessel stenosis after the Fontan surgery (especially patient with LT, as demonstrated by Chapter 5.2.6.1), it may be important to dilate the stenosis to minimize TCPC power loss. As noted by Mets et. al. [203], there were no standard clinical criteria for stent implantation in patients with LT stenosis; rather, a combination of hemodynamic, angiographic, and clinical considerations are usually taken into account. In this section, the hemodynamic effects of stent implantation on TCPC energy dissipation under baseline and simulated exercise conditions will be investigated in patients with LT stenosis (presented by Figure 5.17).
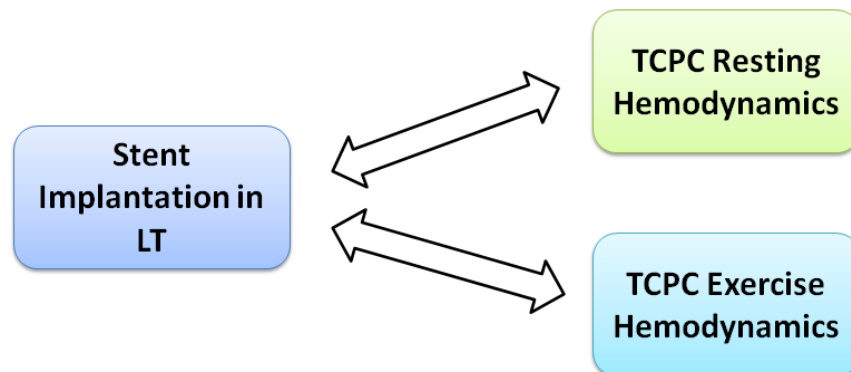
Figure 5.17 Schematic representing the objective of SA1(c)

5.4.1 Patient Cohort

A subset of patients who underwent LT Fontan palliation at Boston Children's Hospital and had post-Fontan cardiac MRI studies were retrospectively reviewed. Those with evidence of LT pathway narrowing who had both anatomic MRI and PC-MRI at the

connection vessels and the ascending aorta were selected for analysis. Six patients meeting these criteria were identified, 3 of whom (CHB024A, CHB025A, and CHB026A) underwent actual stent implantation within 4 months of MRI, and were included in the cohort reported by Mets et. al. [203]. The other 3 patients (CHB012B, CHB014B, CHB020B) did not undergo clinical stent implantation, but had computationally simulated stenting based on their MRI-derived anatomy. In all patients, MRI anatomic configurations before stent implantation in the TCPC were available. Velocity data before stent implantation were available from phase-contrast MRI at each vessel cross-section for all patients. In CHB024A, CHB025A, and CHB026A, anatomy before and after actual stent implantation were also available in the form of angiograms, along with directly measured pressures in the relevant vessels using catheterization. This analysis was approved by the IRBs of the institutions involved.

5.4.2 Virtual Stent Implantation

Patient-specific anatomies before stent implantation were obtained from MRI images. SSFP transverse MRI images were acquired from the neck to the diaphragm (16-40 slices; pixel spacing 1-1.76mm; slice thickness 5-7mm). The MRI images were interpolated and segmented to obtain the 3D surface of the geometries (Chapter 4.2.2). The reconstructed 3D patient-specific geometries for the six patients studied are shown in Figure 5.18.
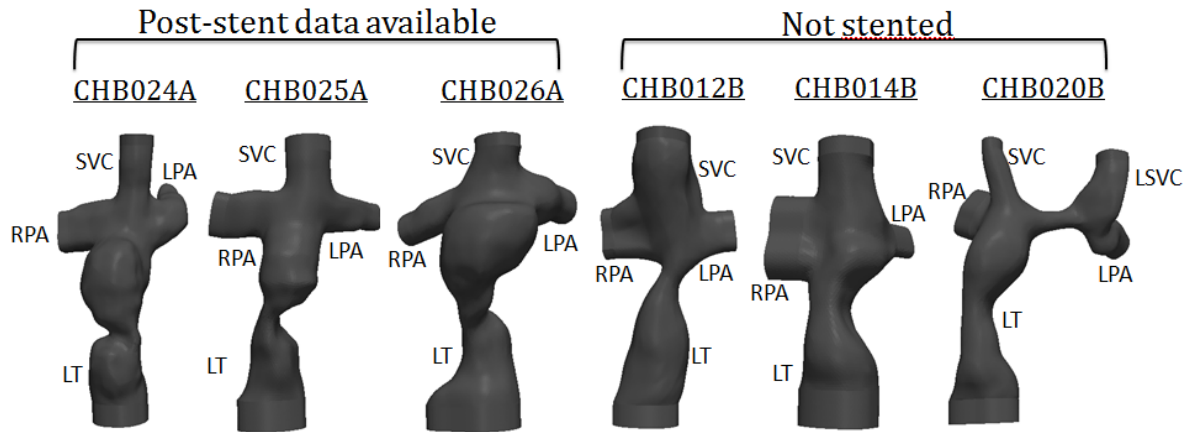
Figure 5.18 Reconstructed patient-specific geometries of the six patients included in this study

Due to the non-availability of MRI data after stent implantation, stent size had to be predicted from two 2D angiograms available in coronal and sagittal planes for patients CHB024A, CHB025A, and CHB026A (example shown in Figure 5.19). The stenotic region was dilated based on the IVC-to-stenosis diameter ratios obtained from the angiograms to create geometries after stent implantation (Appendix A.7.6.1). To investigate the effect of stent size, stent diameter of 2mm increments (which are the commercially available sizes) were created and merged with the MRI-derived geometries (LT diameters summarized in Table 5-8), keeping the stent orientation consistent in the same patient. In cases without actual stent implantation (CHB012B, CHB014B and CHB020B), stent diameter up to 20mm was simulated. Simulated stent diameter was not allowed to exceed the diameter of adjacent segments of the LT pathway.
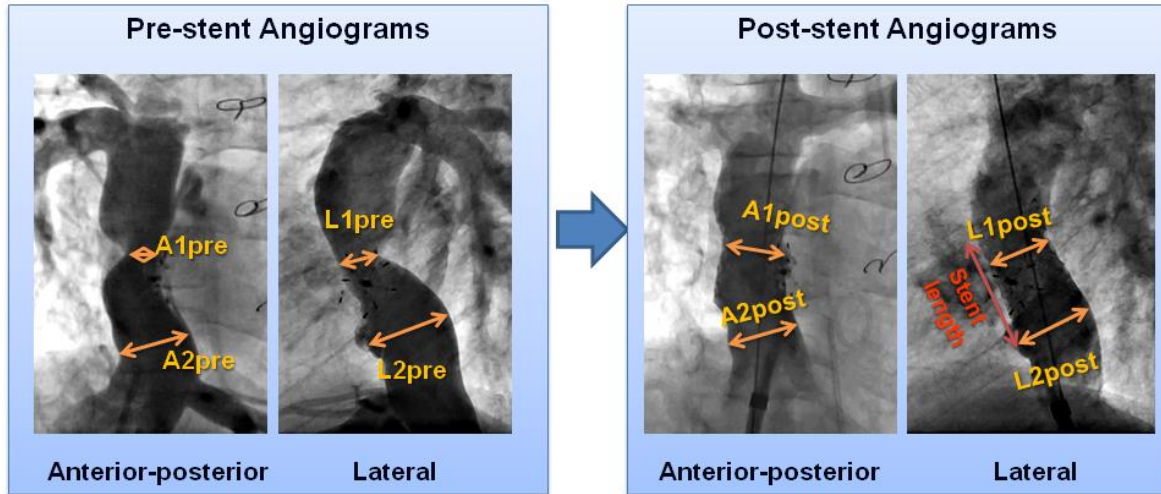
Figure 5.19 Examples of angiograms and measurements before (pre-stent)
and after (post-stent) stent implantation (CHB026A)

Table 5-8 LT diameters of the 6 patients simulated

Patient	CHB 024A	CHB 025A	CHB 026A	CHB 012B	CHB 014B	CHB 020B
Estimated stent diameter from angiogram (mm)	18	14	20	N/A	N/A	N/A
Other stent diameters simulated (mm)	20,22	10,12, 16,18	12,14, 16,18	12,14,16, 18, 20	14,16, 18, 20	14,16, 18,20

5.4.3 Metrics of Interest

5.4.3.1   Stenosis Quantification

The stenosis severity for all geometries was quantified by the normalized minimum LT
(FP) diameter, defined as follows:

$$Normalized\ minimum\ LT\ diameter\ [mm/m] = \frac{Minimum\ diameter\ along\ the\ LT\ [mm]}{\sqrt{(BSA[m^2])}}$$

(Equation 5.3)

where BSA is the patient's body surface area, which was used to account for difference in patient size.

5.4.3.2   Hemodynamics

Through-plane PC-MRI slices acquired across all vessels of interest (40 phases over each cardiac cycle) were segmented (Chapter 4.3.1), and integrated over the vessel cross-sectional areas to calculate the associated flow rates. The cycle-averaged flow rates are shown in Table 5-9. Patient-specific TCPC 3D flow dynamics were also evaluated using the in-house immersed boundary solver (Chapter 4.6) with time-averaged flow boundary connections from PC-MRI under rigid wall assumption. To simulate typical and extreme increases in cardiac output during lower-limb exercise, as documented in a recent study of Fontan patients[189], baseline patient-specific LT flow rates were doubled (2X) and tripled (3X)[2], respectively, while preserving the outlet flow ratios as in the baseline condition. Since PC-MRI data after stent implantation were not available, patient-specific flow boundary conditions before stent implantation were imposed for all geometries. TCPC resistance (Chapter 4.8) was computed to compare to literature to understand the effect of stent implantation. iPL was computed to relate to results in Chapters 5.2 and 5.3.

Table 5-9 Phase-contrast MRI segmented flow rates for baseline condition

Patient	CHB 024A	CHB 025A	CHB 026A	CHB 012B	CHB 014B	CHB 020B
Cardiac output (L/min)	5.57	3.31	4.83	5.05	3.04	4.49
Total systemic return (L/min)	3.58	2.51	3.24	4.06	2.60	4.33
LT : SVC : (LSVC) flow ratio	65:35	41:59	72:28	71:29	58:42	63:17:20
LPA : RPA flow	31:69	38:62	46:54	64:36	30:70	26:74

5.4.4 Data Analysis

Results before and after stent implantation were compared only in patients CHB024A, CHB025A and CHB026A, and CFD simulations were performed for all patients with various stent diameters. Due to small sample size, results of the actual stenting procedures were not evaluated statistically. Modeling of relationships between LT diameters and TCPC resistances was performed using non-linear regression and regression coefficients were determined. Demographic, anthropometric and LT anatomic data are summarized in Table 5-10. Available catheterization data prior to stent implantation are presented in Table 5-11. Full hemodynamic and LT diameter results were listed in Appendix A.7.6.2.

Table 5-10 Patient demographic, anthropometric and LT anatomic data

Patient	CHB 024A	CHB 025A	CHB 026A	CHB 012B	CHB 014B	CHB 020B
Age at MRI (years)	15.2	11.6	19.6	14.6*	10.7	14.7
Age at stent (years)	15.2 ⱶ	11.9	19.6	N/A	N/A	N/A
BSA (m^2)	1.57	1.11	1.80	1.43	1.05	1.47
Minimal LT diameter (pre-stent) (mm)	10	6	8	9	10	12

N/A = not available
* MRI was performed under anesthesia
ⱶ Catheterization was performed under anesthesia

Table 5-11 Pressure at the TCPC, cardiac index and vascular resistances obtained through catheterization prior to stent implantation

Patient	CHB 024A	CHB 025A	CHB 026A	CHB 012B	CHB 014B	CHB 020B
IVC (mmHg)	18	13	16	N/A	17	N/A
SVC (mmHg)	18	12	14	N/A	17	N/A
LPA (mmHg)	17	11	14	N/A	14	N/A
RPA (mmHg)	17	11	14	N/A	17	N/A
Mean PA wedge (mmHg)	12	9	11	N/A	10	N/A
Cardiac index (L/min/m^2)	2.1	3.3	3.1	3.4	3.1	3.0
Systemic vascular resistance (iWU) *	26.7	13.6	21.3	20.6	18.4	18.0
Pulmonary vascular resistance (iWU) *	4.3	1.0	1.3	1.0	1.4	1.6

*iWU = indexed Wood's units; N/A = not available

5.4.5 Numerical Results vs. Catheterization Data

The numerical simulations and the use of flow boundary conditions before stent implantation in all geometries were validated by comparison with pressures measured during catheterization. In patients CHB024A, CHB025A and CHB026A, pressure drops across the LT stenosis simulated with the numerical simulation tool were consistent with measured data (Table 5-12). Stent implantation reduced the simulated pressure drop across the stenotic region to close to 0 mmHg in all 3 patients.

Table 5-12 Comparison between simulated and measured resting pressure drop across the LT in patients A, B, and C, who underwent actual stent implantation

Baseline LT pressure drop (mmHg)	CHB024A		CHB025A		CHB026A	
	Pre -stent	Post -stent	Pre -stent	Post -stent	Pre -stent	Post -stent
Catheterization	0	0	1	0	2	0
CFD	0.5	0.1	0.8	0.1	1.6	0.1

5.4.6 Effect of Stent Implantation

Stream-traces of flow through the LT and SVC, color-coded by velocity magnitude, are presented in Figure 5.20. The flow across the stenosis consisted of a high-velocity jet followed by flow recirculation downstream of the stenosis, which corresponds to the region with highest pressure drop (Figure 5.21). During exercise conditions, the velocity across the LT increased and created a much larger pressure drop. After stent implantation, the velocity magnitude of the jet was lowered and the flow was more streamlined along the LT pathway under rest and exercise conditions.
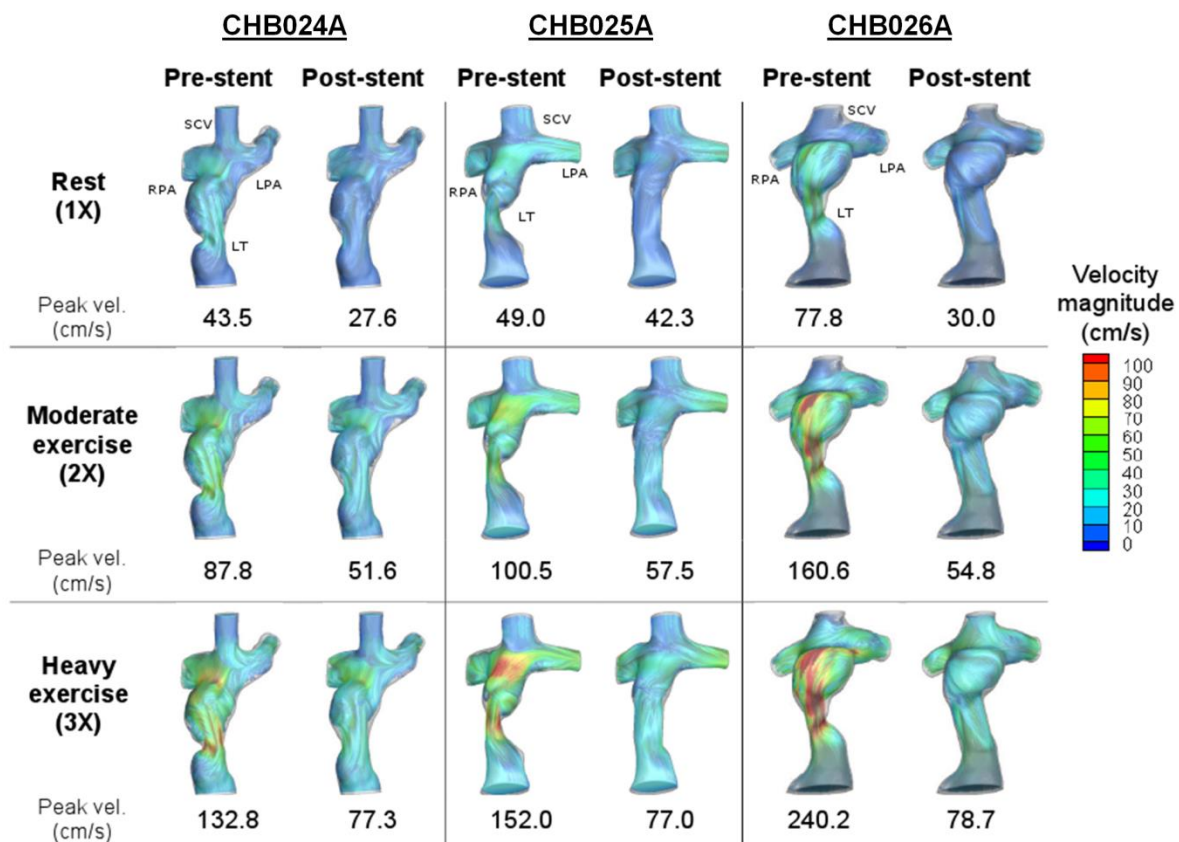
Figure 5.20 Color-coded velocity stream-traces and peak velocities in patients CHB024A, CHB025A, and CHB026A before (pre-stent) and after (post-stent) stent implantation under baseline (1X LT flow rate), moderate (2X), and heavy (3X) exercise conditions
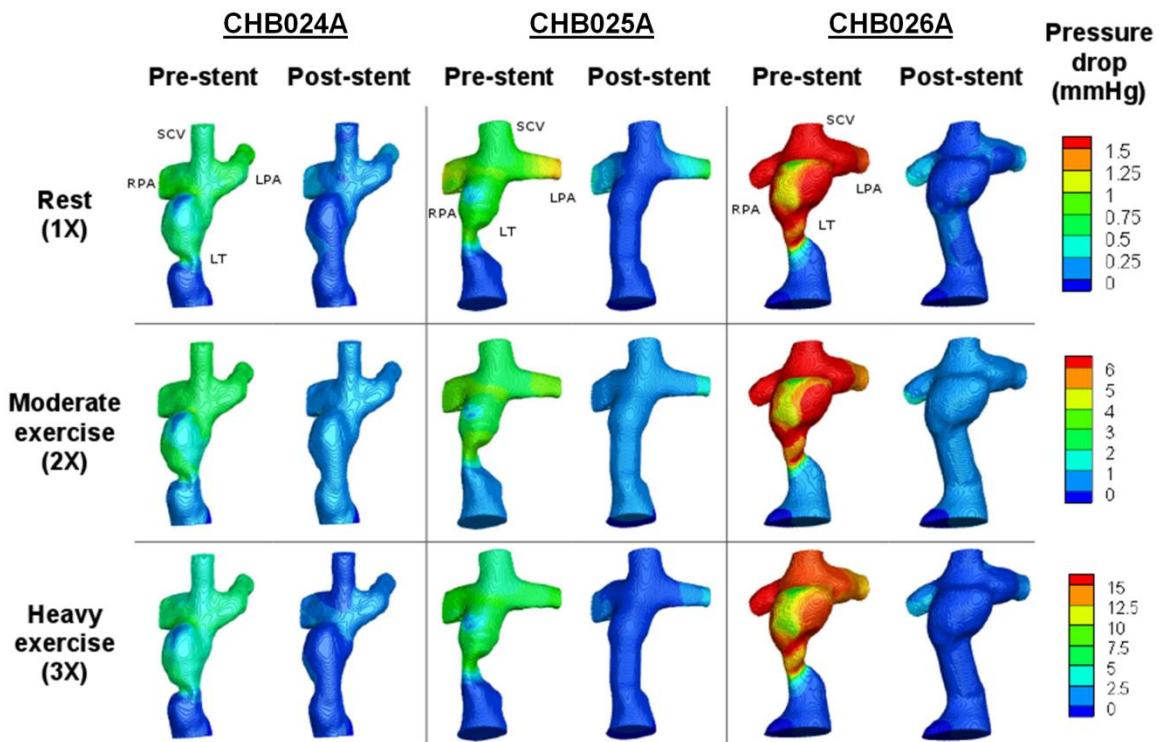
Figure 5.21 Contour plot of pressure drops relative to the LT inlet, in patients CHB024A, CHB025A, and CHB026A before (pre-stent) and after (post-stent) stent implantation under baseline (1X LT flow rate), moderate (2X), and heavy (3X) exercise conditions

TCPC resistance for patients CHB024A, CHB025A, and CHB026A were calculated under baseline and exercise conditions (Figure 5.22). In all 3 patients, a non-linear increase in TCPC resistance was observed from baseline to increasing exercise levels. After stent implantation, the overall resistance values were lower than without stent implantation, and the increases with exercise were smaller and more gradual. Stent implantation lowered the TCPC resistance in all 3 patients under all conditions, with reductions of 51-84% at rest, 70-88% at 2X, and 70-89% at 3X exercise levels from the original stenotic geometries. Among these 3 patients, the highest TCPC resistance before stent implantation was in CHB026A, which corresponded to the lowest

145

normalized minimum LT diameter. The reduction in resistance after stent implantation was also more pronounced at higher exercise levels in this patient.
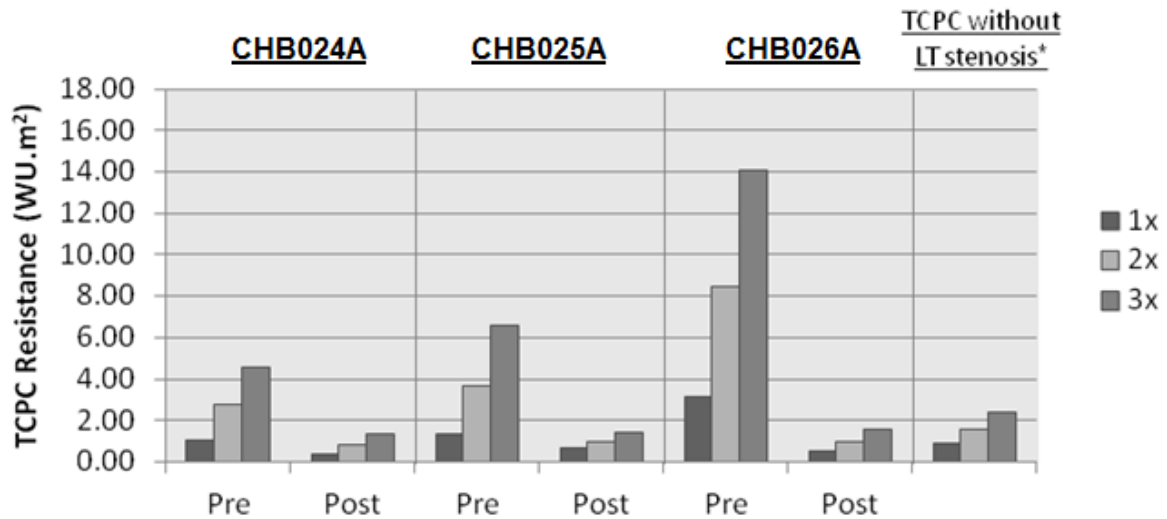
Figure 5.22 TCPC resistances of patients CHB024A, CHB025A, and CHB026A before (Pre) and after (Post) stent implantation under baseline (1X), moderate (2X), and heavy (3X) exercise conditions.
*Average TCPC resistances of patients without apparent LT stenosis reported by Sundareswaran et. al.[57]

5.4.7 Effect of Stent Size

In this study, patient specific TCPC hemodynamics before and after actual stent implantation, as well as simulated stent implantation were investigated. To understand the effect of stenosis severity at baseline and exercise hemodynamics, the results of all 6 patients and all normalized (by squared root of BSA) minimum LT diameters were compiled to look for general trends. Figure 5.23 shows the TCPC resistances of all patients under baseline and exercise conditions with various LT diameters. In all cases, the TCPC resistances and iPL were reduced by increasing the normalized minimum LT

diameter. Using a power law regression, general trends can be found for each condition.

When the normalized minimum LT diameter was smaller than 10mm/m, there was substantial reduction in TCPC resistance with a slight decrease in stenosis severity. For example, when normalized minimum LT diameter is 6 mm/m, TCPC resistance at rest is 2.68 WU.m^2 based on the regression equation. If a stent is to be implanted to increase the normalized minimum LT diameter to 8mm/m, TCPC resistance will be lowered to 1.36 WU.m^2. Increasing normalized LT diameter by 2mm/m is estimated to result in reduction in TCPC resistance of 1.32 WU.m^2.

When the normalized minimum LT diameter was greater than 10mm/m, the TCPC resistance was much lower, and the same increase in normalized minimum LT diameter resulted in smaller improvement in TCPC resistance. For example, when normalized minimum LT diameter is 18 mm/m, TCPC resistance at rest is 0.20 WU.m^2 based on the regression equation. If a stent is to be implanted to increase the normalized minimum LT diameter to 20mm/m, TCPC resistance will be lowered to 0.15 WU.m^2. Increasing normalized LT diameter by 2mm/m is estimated to result in reduction in TCPC resistance of only 0.04 WU.m^2.

Simulated exercise level	TCPC resistance	iPL
Rest (1X)	$y = 186.7x^{-2.368}$ $R^2 = 0.704$	$y = 9.2667x^{-2.476}$ $R^2 = 0.6867$
Moderate exercise (2X)	$y = 1082.7x^{-2.766}$ $R^2 = 0.7868$	$y = 35.623x^{-2.902}$ $R^2 = 0.7963$
Heavy exercise (3X)	$y = 2194.1x^{-2.857}$ $R^2 = 0.8059$	$y = 53.325x^{-3}$ $R^2 = 0.8357$
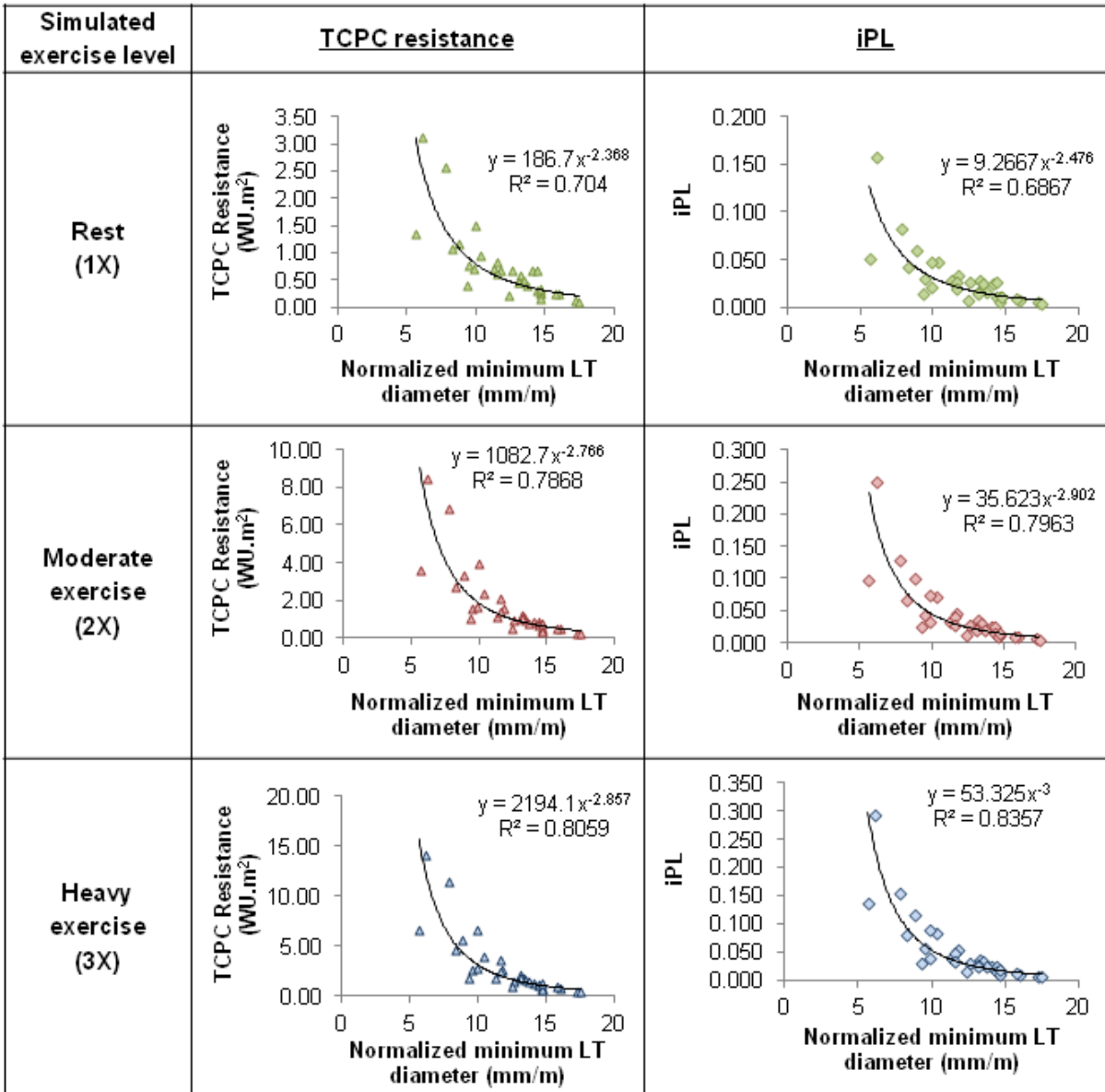
Figure 5.23 TCPC resistances and iPL of all patients at all normalized minimum LT diameters simulated, under baseline (1X), moderate (2X), heavy (3X) exercise conditions. This included all patients before and after stent implantation, as well as all simulated stent size

5.4.8 Discussion

5.4.8.1   Effect of Stent Implantation on Hemodynamics

Using the numerical simulation results, which were validated with baseline catheterization data, the baseline and exercise hemodynamics in 3 patients before and after stent implantation were investigated. In a study of 16 patients without apparent TCPC stenosis, Sundareswaran et al.[57] estimated the average TCPC resistance to be 0.87 ± 0.58 WU•m^2 at baseline, 1.56 ± 1.00 WU•m^2 at 2X exercise condition, and 2.36 ± 1.62 WU•m^2 at 3X exercise condition. Prior to stent implantation, patients CHB024A, CHB025A, and CHB026A had TCPC resistances above the average resting resistance of the patients in that series (Figure 5.22). In CHB024A, there was no measureable pressure gradient across the stenosis under baseline conditions (Table 5-12). In CHB026A, the connection resistance before stent implantation was 1.73 WU at baseline, which was similar in magnitude compared to the patient's PVR (1.3 indexed Wood's units, Table 5-11), as well as previously reported PVR values in Fontan patients (1.3-1.8 WU)[57, 204]. Thus, even though direct measurement may reveal minimal or no pressure gradient across the stenosis, TCPC resistance can still be high in these patients, especially under exercise conditions. This observation illustrates the fact that resting pressure gradients offer only limited insight into the resistance of a TCPC pathway, particularly under the artificial condition of the catheterization suite, with patients in a supine position and generally under sedation or anesthesia.

Non-linear increases in resistance were observed with increasing exercise levels both before and after stent implantation (Figure 5.22), which is consistent with previous work

[2]. However, the exercise-related increase in TCPC resistance was further exacerbated by the presence of stenosis (Figure 5.22). Previous work demonstrated the relationship between TCPC resistance and various measures of ventricular performance and work [57], and also the potential link between TCPC energy dissipation and aerobic exercise tolerance [189]. The high TCPC resistance in these patients during exercise would potentially have an adverse effect on single ventricle hemodynamics and hence contribute to limitations in exercise capacity. After stent implantation, TCPC resistance was reduced in all patients, especially during simulated exercise conditions. Notably, in patients CHB024A, CHB025A, and CHB026A, TCPC resistances after stent implantation under all conditions were below previously reported average patient values [57] (Figure 5.22).

5.4.8.2   Impact of Stenosis Severity and Stent Size on TCPC Hemodynamics

In view of the patient-specificity of both the TCPC geometry and severity of the stenosis, it is important to identify which patients are likely to benefit from intervention of the LT pathway. From the compiled TCPC resistance values of all patients with various normalized minimum LT diameters in Figure 5.23, generalized trends can be observed. When the normalized minimum LT diameter was lower than 10mm/m, TCPC resistance rose rapidly with increasing severity of stenosis (decreasing diameter) under all conditions. Stent implantation in patients with normalized minimum LT diameter of less than 10mm/m was estimated to result in significant improvement in reduction of TCPC resistance.

As shown in a previous study by Mets et. al.[203], it is possible to disrupt the baffle during stent expansion and cause a baffle leak in LT patients, highlighting the very real risk of over-dilation. Thus, it seems prudent to aim for a stent size that is sufficient to reduce the TCPC resistance as much as possible, but is not so large as to introduce the risk of pathway disruption. As shown in Figure 5.23, the improvement in TCPC resistance per unit change in stent size decreased with increasing normalized minimum LT diameter. When the normalized minimum LT diameter was larger than about 15mm/m, further increases in minimum LT diameter were estimated to yield little improvement in resistance and stent implantation would likely be of minimal benefit.

5.5   Limitations

The following sections discussed the limitations of this specific aim. Major limitations are due to the assumptions made in the computational model. However, they should not affect the conclusion of this study significantly.

5.5.1 Correlation between TCPC Geometry and Resting Hemodynamics

In Specific Aim 1(a) (Chapter 5.2), the accuracy of the reconstructed vessel sizes was limited by the CMR spatial resolution. The in-plane resolution for PC-CMR data ranged from 0.547 to 1.875 mm, considering the diameter of the right upper lobe PA ranged from 4 to 9 mm. However, in cases with PA stenosis, the sparse transverse slices could lead to inaccuracies in the PA diameter. CFD assessment was an approximation of the physiology because it applied time-averaged boundary conditions and assumed a rigid vessel wall. PC-CMR data was acquired under a breath-hold condition to reduce scan

time, which ignored the physiological variability with respiration. Effects of collateral flows and fenestrations were ignored in the simulations, which might have an influence on the hemodynamics.

5.5.2 Correlation between TCPC Geometry and Exercise Hemodynamics

For Specific Aim 1(b) (Chapter 5.3), in addition to the limitations mentioned in the previous section, there were also several limitations related to modeling exercise TCPC hemodynamics. Also, due to the motion of the TCPC during exercise, exercise flow rates at the FP and pulmonary arteries were not acquired. Patient-specific descending aorta flow rate was used as the boundary condition for the FP.

5.5.3 Stent Implantation Model

When evaluating the effect of stent implantation in Specific Aim 1 (c) (Chapter 5.4), flow boundary conditions before stent implantation were used for post-stent simulations. Also, exercise flow rates were prescribed by doubling and tripling baseline LT flow, which may not be realistic for patients with a Fontan circulation [134, 205]. Patient specific flow conditions should be applied when this data are available.

5.6   Clinical Significance

In this specific aim, the impact of TCPC geometric characteristics on TCPC baseline and exercise hemodynamics was investigated. It was found that TCPC vessel diameters are the most important geometric characteristics affecting iPL at rest and VAT. This suggested that vessel narrowing/stenosis can have important impact on patient hemodynamics. Long term post-operative follow-up is essential, and understanding the physiological outcomes after intervention by stent implantation [203] may be important, because the pathway narrowing can potentially elevate energy loss during high cardiac flow and lead to exercise intolerance in these patients [2].

This analysis was extended to patient exercise performance parameters (minute oxygen consumption and work rate at VAT) to understand the physiologic relevance of TCPC geometry and connection dissipation. The difference in the correlations of exercise performance in adolescents and adult patients (Chapter 5.3.8.3) suggested the physiologic change in the Fontan circulation as the patient reaches adulthood, which can have implications on patient exercise performance. In order to improve patient exercise capacity, optimizing local TCPC geometry and hemodynamics, and promoting vessel growth, can potentially be viable options for adolescents. However as the patient reaches adulthood, the interaction between TCPC energy dissipation and exercise performance decouples. Other strategies may have to be derived to improve exercise performance.

The analysis also shows that resting hepatic flow distribution was influenced by caval offset, FP-SVC angle and pulmonary flow distribution. This study suggests the role of connection angle to hepatic flow distribution, which is relevant to the formation of PAVMs. While caval offset has been a common control variable in optimizing hepatic flow distribution in surgical planning of TCPC, the analysis presented in this specific aim suggested the relative angle between FP and SVC should be considered for cases where caval offset is constrained and PFD is unbalanced. This can be important for future surgery planning of Fontan palliation of SV patients.

The pilot study of stent implantation in lateral tunnel stenosis patients evaluated the hemodynamic impact of LT stenosis and stent implantation under both resting and exercise conditions using a CFD simulation tool. Preliminary results highlighted the hemodynamic benefit of stent implantation in patients with severe LT stenosis, especially during exercise. Simultaneous measurement of pressure gradient across the stenosis during exercise testing in a clinical setting can be challenging. The use of numerical simulations allowed the computation of pressure gradient and connection resistance in various 'what-if' scenarios, which can be potentially useful for future interventions.

5.7   Chapter Summary

In this specific aim, the impact of TCPC geometric characteristics on TCPC baseline and exercise hemodynamics was investigated, using the largest Fontan MRI database

to date. The analysis shows that resting hepatic flow distribution was influenced by caval offset, FP-SVC angle and pulmonary flow distribution. For connection energy dissipation, minimum FP and PA diameters were inversely correlated with iPL at rest and iPL at VAT. Though it was not clear what caused the narrowing of the TCPC vessels, these correlations suggested it may be important to dilate vessel narrowing at the TCPC, or to utilize strategies to promote vessel growth, especially in intra-atrial patients.

The pilot study of stent implantation in lateral tunnel stenosis patients evaluated the hemodynamic impact of LT stenosis and stent implantation under both resting and exercise conditions using a CFD simulation tool. Preliminary results highlighted the hemodynamic benefit of stent implantation in patients with severe LT stenosis, especially during exercise. The use of numerical simulations allowed the computation of pressure gradient and connection resistance in various 'what-if' scenarios, which can be potentially useful for future interventions.

CHAPTER 6   Specific Aim 2: Investigation of the Effect of Respiration on TCPC Hemodynamics

6.1   Overview

Several clinical studies have shown that, without the presence of a sub-pulmonary ventricle, passive TCPC vessel flow is affected by respiration. Fogel et. al. showed that flow in the systemic venous pathway of Fontan patients was phasic to both cardiac and respiratory cycles: approximately 70% of flow was cardiac dependent, and the rest was respiratory [131]. Hsia et. al. reported that hepatic venous flow (measured with doppler ultrasonography) depended on respiration in Fontan subjects more than normal subjects, and was larger during inspiration than expiration [132, 133]. Hjortdal et. al. also observed increased IVC flow during inspiration in Fontan patients [134]. During inspiration, the negative intra-thoracic pressure assisted the forward flow in the SVC and the PAs, increasing venous return as compared to expiration.

While CFD models have gained popularity over the past decade to help better understand TCPC hemodynamics, respiration is a physiological influence on TCPC hemodynamics that has not been included in most CFD models. As evidenced by the clinical studies mentioned above, these effects may have important implications on TCPC hemodynamics. However, the current methods of clinically assessing TCPC flows are commonly performed at resting breath-held conditions, and respiratory information is not always available. With the patient enrollment of National Heart, Lung,

and Blood Institute Grants HL098252, Fontan patient PC-MRI data acquired with a real time sequence is available under both resting breath-held and free-breathing conditions in the Fontan pathway (FP), SVC and the aorta. These PC-MRI images were acquired over multiple respiratory cycles for the same patients, allowing for the isolation of respiratory effects from other physiologic influences that can affect TCPC hemodynamics. The objective of this specific aim is to investigate the impact of breath-holding on the evaluation of TCPC hemodynamics (TCPC flow structure, power loss and hepatic flow distribution) using CFD.

6.2   Study Protocol

6.2.1 Patient Cohort

Eleven consecutive single ventricle patients with a TCPC anatomy were selected from the Georgia Tech/Children's Hospital of Philadelphia Fontan database. With informed consent, and Institutional Review Board (IRB) approval, the patient's prospective real-time CMR data at resting breath-held and free-breathing conditions were acquired. Patients included in this study had: (i) a TCPC with no other sources of pulmonary flow, and (ii) real time CMR images acquired at all inlets of the TCPC. Patients were excluded if: (i) a pacemaker or implanted metal was present, or (ii) severe CMR image artifacts distorted the images. A total of nine patients were included in this study, after two were excluded due to severe image artifacts (Table 6-1, details listed in Appendix A.8.1.

Table 6-1 Demographic details of the 9 patients analyzed

Patient characteristics	Mean ± standard deviation
Age (years)	21.8 ± 4.2
Body surface area (m^2)	1.79 ± 0.10
Gender (M/F)	6/3
IVC connection type (IA/EC) [†]	8/1
Ventricular morphology (LV/RV/MV) [‡]	3/5/1

† IA – Intra-atrial, EC- Extra-cardiac.
‡ LV = left ventricle, RV = right ventricle, MV = mixed ventricle

6.2.2 CMR Acquisition

A 1.5 Tesla Avanto Whole Body system (Siemens Medical Solutions, Malvern, PA) was used for anatomic and real time PC-MRI acquisition. Static steady-state free precession imaging was utilized to acquire images, and 3D anatomies were reconstructed (Chapter 4.2.2) (Figure 6.1). An echoplanar (EPI) sequence utilizing shared velocity encoding was applied to acquire real time PC-MRI images [206]. Through-plane PC-MRI images across the IVC/FP (superior to the hepatic vein confluence), SVC and ascending aorta were acquired for at least 10 seconds as separate velocity maps (approximately 20 frames per second). The same imaging protocol was performed under breath-held (BH, acquired at end expiration) and free-breathing (FB) resting conditions. Conventional PC-MRI images were also acquired at the LPA and RPA during resting BH conditions. The image acquisition parameters are summarized in Table 6-2 (details listed in Appendix A.8.2).
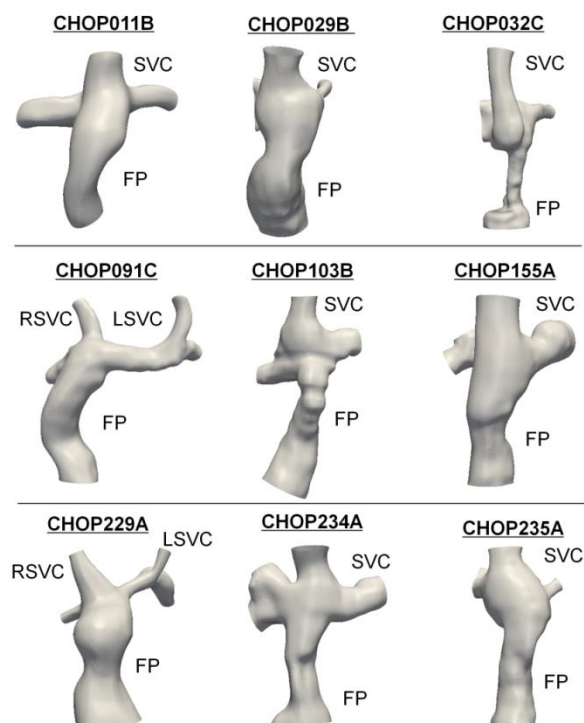
Figure 6.1 Reconstructed anatomies of the 9 patients investigated in this chapter.

Table 6-2 Summary of CMR acquisition parameters for SA2

Transverse CMR	
No. of slices	45 – 70
Matrix (pixel)	256 X168
Spatial resolution (mm)	1.17 – 1.48
Slice thickness (mm)	3 – 4
Echo time (ms)	1.21 – 1.27
Real time PC-MRI at FP and SVC	
Encoding velocity (cm/s)	60 – 150
Number of images	199 – 511
Temporal resolution (ms)	32-77
Conventional PC-MRI at LPA and RPA	
Encoding velocity (cm/s)	60 – 100
Number of images	24 – 30

6.2.3 Hemodynamic Comparison

Patient-specific flow conditions were obtained by segmenting real time PC-MRI images at the cross section of each vessel (Chapter 4.3.2), using the software Segment (Medviso, http://medviso.com/products/segment/) [150-152]. The vessel of interest was first selected on the image slice. Velocity values were then integrated over the region of interest to calculate the associated flow rate. By tracking the change in chest wall area of the same image slice, instants of inspiration and expiration were simultaneously tracked throughout the image series. By tracking the descending aorta flow waveform on the same image slice, instants of peak descending flow within a cardiac cycle were simultaneously tracked with the vessel flow to identify the frequency of the cardiac cycle (Appendix A.4). Examples of the segmented waveforms are illustrated in Figure 6.2. For each of the vessels (FP ad SVC) in all the data sets, respiratory cycles were identified by the following steps:

(i)   Respiratory cycles were identified from the chest wall area waveform in the FB condition, and a respiratory cycle was selected. The periods of the different respiratory cycles were computed. The respiratory cycle with the median period was selected.

(ii) The number of cardiac cycles within this time frame were counted.

(iii) The same duration (one respiratory cycle) of data was selected in the BH waveform, such that the selected BH cycle contains approximately the same number of cardiac cycles as the selected cycle under FB condition.

160
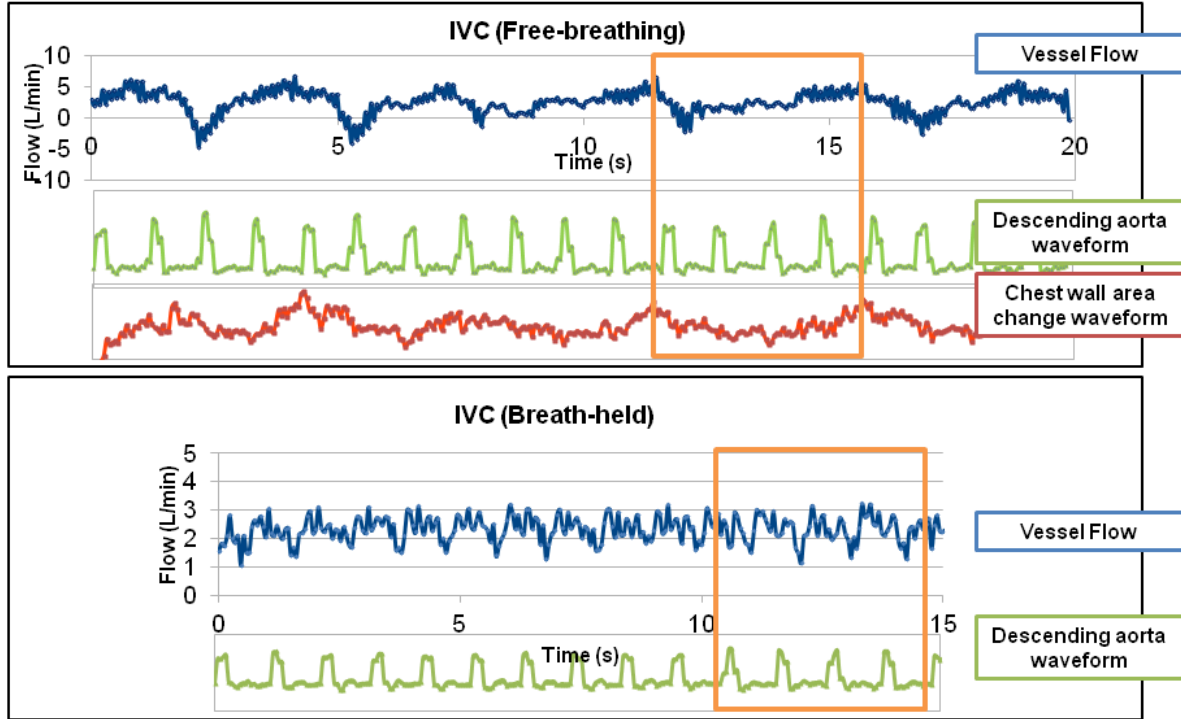
Figure 6.2 Example of segmented waveforms for vessel flow, descending aorta flow and chest wall area of CHOP011B under FB and BH conditions. The selected cycle for simulation is circled in orange.

6.2.3.1   Hemodynamics

To simulate patient specific hemodynamics under FB and BH conditions, CFD was used and patient specific boundary conditions were applied. The selected inflow waveforms (FP, SVC (and LSVC if present) under FB and BH conditions were first smoothed with a Locally Weighted Scatterplot Smoothing (LOWESS) function in Matlab (MathWorks Inc., MA, USA) to ensure numerical stability (Appendix A.4.5). The resulting waveforms were utilized as inlet boundary conditions for CFD. The flow waveforms of the outlets (LPA and RPA) with respiratory effect were not available for these patients (due to the motion of the PAs) to be used as outflow boundary conditions of CFD simulations. Therefore, resistance boundary conditions instead of flow were prescribed at the outlets, unlike the

other parts of this thesis. For this purpose, a finite element solver, LifeV (C) was used to apply a 3-element Windkessel model (Chapter 4.7.1.3) at the LPA and RPA [109].

Patient specific meshes were generated with Gmsh (Chapter 4.7.3). Tetrahedral meshes with maximum mesh edge length of 1 mm were used for all cases, based on the mesh sensitivity study reported in Mirabella et. al. [109]. For all the simulations, the blood viscosity = 3.5×10^{-6} m^2/s, and density = 1.06g/cm^3 were applied. Vessel walls were assumed to be rigid. One thousand time steps were simulated per respiratory cycle. A time step sensitivity study was performed with CHOP011B FB using pulsatile flow boundary condition. By halving the time step, time-averaged TCPC power loss only changed for 0.05%. By reducing the time step to a quarter of the original time step, time-averaged TCPC power loss changed for 0.14%. All simulations were run for at least 3 respiratory cycles to ensure periodic convergence and the results for the last cycle were analyzed.

To prescribe lung resistances at the LPA and RPA, a three-element Windkessel (resistor, capacitor, and resistor) model was employed (details described in Chapter 4.7.1.3). First, time-averaged patient specific flow rates at the LPA and RPA were obtained by segmenting conventional PC-MRI at the vessel cross section acquired under resting BH conditions (Chapter 4.3.1). The measured flow splits between the LPA and the RPA were used to estimate the ratio of the total resistances of each Windkessel model:

$$R_{LPA} = \frac{Q_{LPA} + Q_{RPA}}{Q_{LPA}} \times PVR, \qquad \text{(Equation 6.1)}$$

$$R_{RPA} = \frac{Q_{LPA}+Q_{RPA}}{Q_{RPA}} \times PVR \qquad \text{(Equation 6.2)}$$

where R_{LPA} and R_{RPA} are the total resistances of the LPA and RPA, respectively; Q_{LPA} and Q_{RPA} are the time-averaged flow rates of the LPA and RPA, respectively. The total resistance of the parallel connection of the LPA and RPA was assumed to be 1.5WU (as PVR=pulmonary vascular resistance), utilizing values from [109].
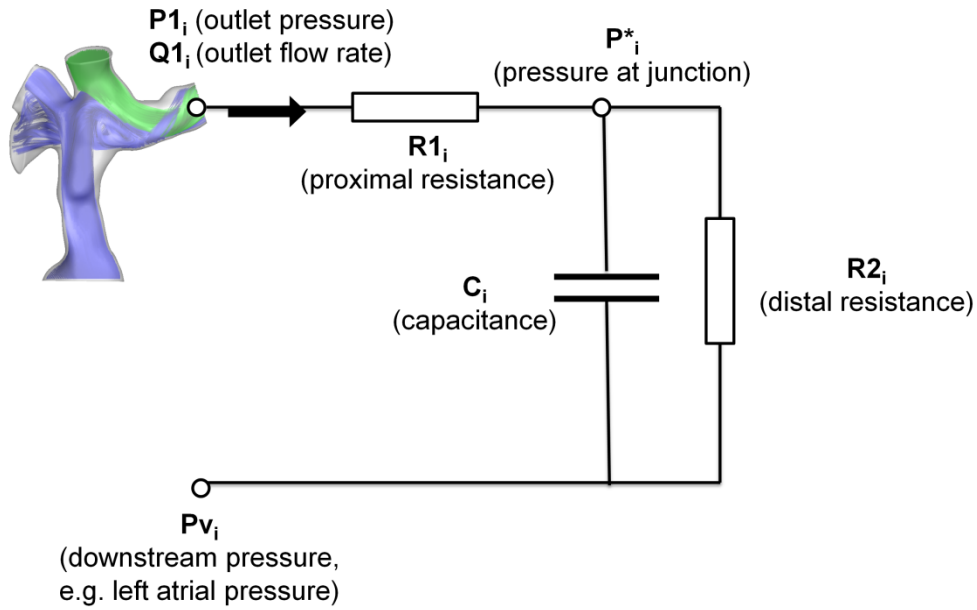
Figure 6.3 Schematic representing the 3-element Windkessel model as outlet boundary conditions of the CFD simulations of the TCPC. "i" denotes the specific outlet.

The sum of proximal resistances (R1$_i$ in Figure 6.3) was assumed to be 10% of the total resistance, according to previous studies [109, 207]. The value of proximal resistance of each outlet was assumed to be inversely proportional to the cross sectional area of the outlet:

$$R1_{LPA} + R1_{RPA} = 0.1 \times PVR \text{ (Equation 6.3)}$$

where R1$_{LPA}$ and R1$_{RPA}$ are proximal resistances of the LPA and RPA, respectively, which $R1_{LPA} \propto 1/A_{LPA}$ and $R1_{RPA} \propto 1/A_{RPA}$ (A = cross sectional area)

The value of distal resistance ($R2_i$ in Figure 6.3) was then used to account for the difference between the total resistance and the proximal resistance of each outlet.

$$R2_{LPA} = R_{LPA} - R1_{LPA} \qquad \text{(Equation 6.4)}$$

$$R2_{RPA} = R_{RPA} - R1_{RPA} \qquad \text{(Equation 6.5)}$$

where $R2_{LPA}$ and $R2_{RPA}$ are distal resistances of the LPA and RPA, respectively.

Downstream pressure (at both LPA and RPA) was assumed to be 10 mmHg [208]. Capacitance was assumed to be $1e^{-4}$ cm^5/dynes [109, 207]. Simulations were performed for each patient under pulsatile FB and BH conditions, as well as their respective time-averaged conditions (Figure 6.4 and Figure 6.5). By comparing the TCPC hemodynamics under the time-averaged FB condition and pulsatile FB condition, the influence of FB pulsatility can be understood. By comparing the TCPC hemodynamics under time-averaged FB condition and time-averaged BH condition, the influence of time-averaged flow rate will be understood. This could help differentiate how time-averaged flow rate and flow pulsatility of the free-breathing waveform affect TCPC hemodynamics. Example of flow waveforms under FB and BH conditions using the Windkessel model is illustrated in Figure 6.6.
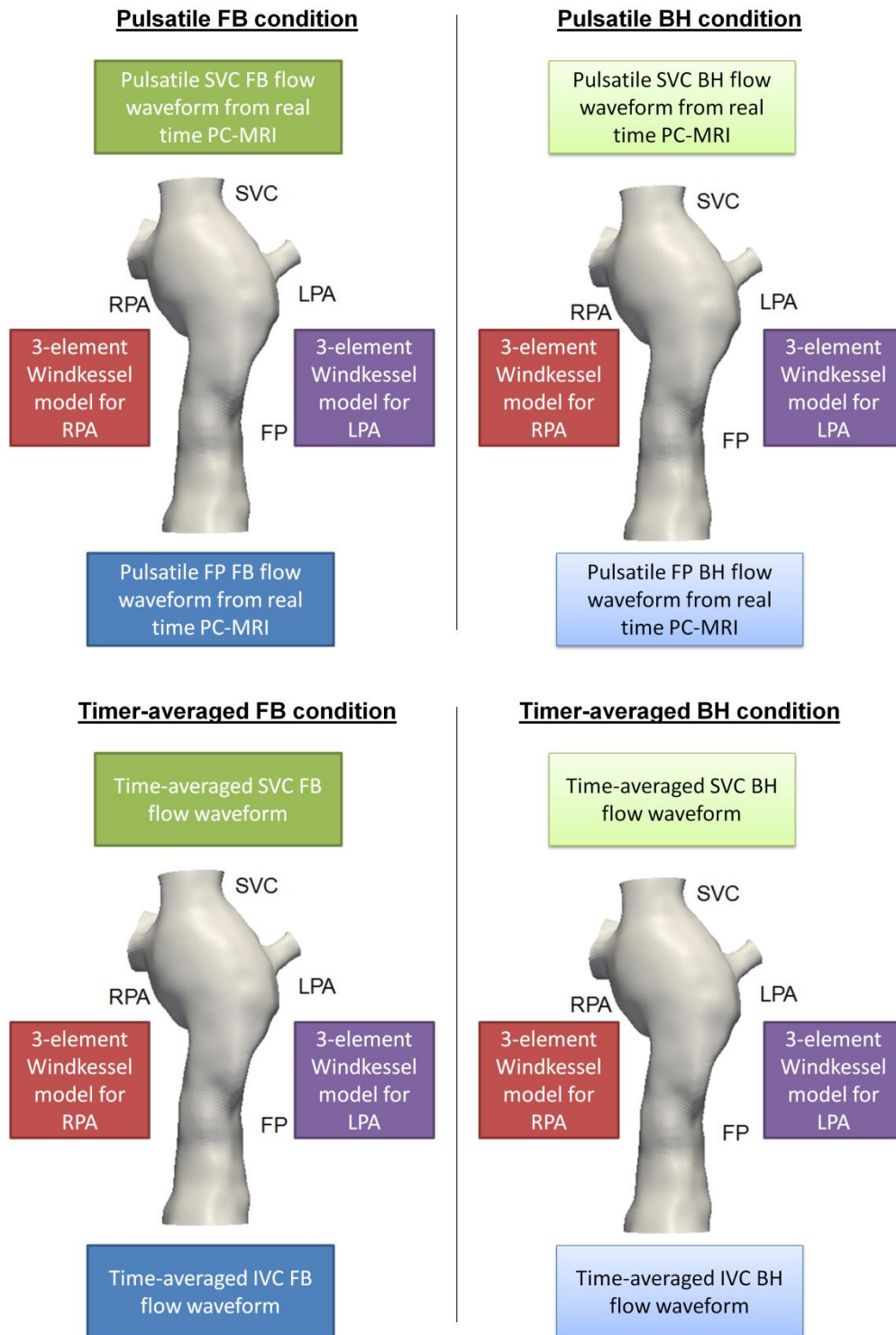
Figure 6.4 Schematic illustrating the pulsatile and time-averaged boundary conditions used in this thesis
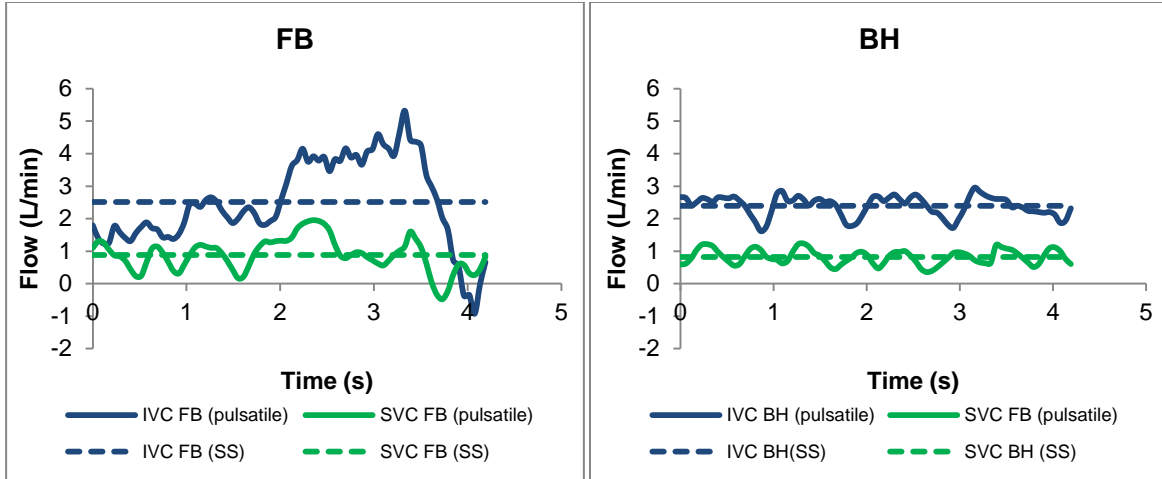
Figure 6.5 Example of flow inlet flow waveforms of the pulsatile and time-averaged boundary conditions used in this work (CHOP011B)
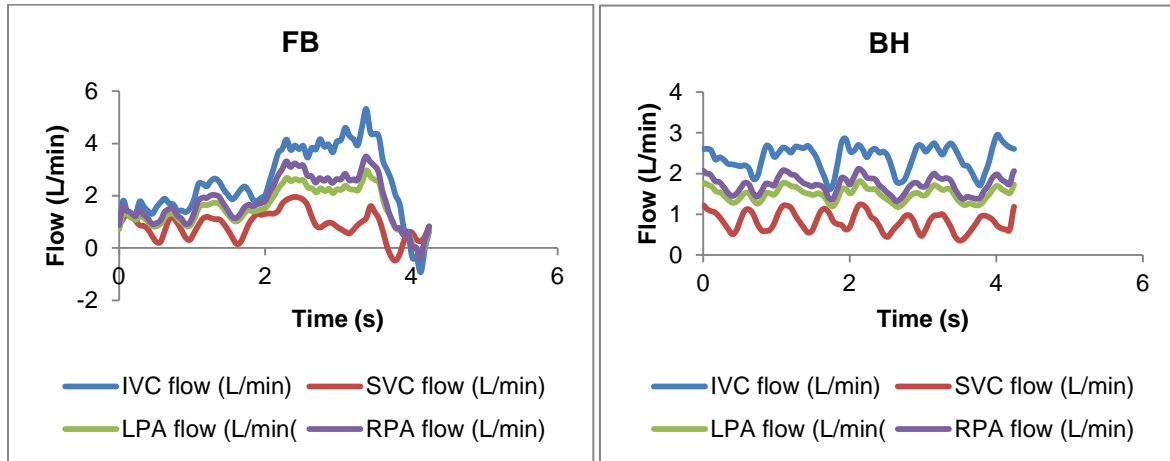
Figure 6.6 Flow waveforms of the inlets ad outlets with 3 element Windkessel model outlet boundary conditions (CHOP011B)

In order to make sure that the numerical model can simulate the possible turbulent characteristics, the average and maximum Reynolds numbers (Re) were calculated at the narrowest FP vessel location (highest velocity), and also at the locations of the PC-MRI slices:

$$Re_{FP,i} = \frac{V_i D}{v} \qquad \text{(Equation 6.6)}$$

where v is the kinematic viscosity of blood (3.5×10^{-6} m^2/s), D is the FP diameter, and V_i is the average or maximum FP velocity in time.

$$D = 2 * \sqrt{\frac{A}{\pi}} \qquad \text{(Equation 6.7)}$$

$$V_i = \frac{Q_i}{A} \qquad \text{(Equation 6.8)}$$

where A is the FP cross-sectional area, and Q_i is the maximum or average FP flow rate.

From the CFD simulations, TCPC Power loss (PL) was computed.

$$PL = \sum_{inlets} \int_A (p + \frac{1}{2}\rho v^2)v \cdot dA - \sum_{outlets} \int_A (p + \frac{1}{2}\rho v^2)v \cdot dA \qquad \text{(Equation 6.9)}$$

The difference in PL between pulsatile and time-averaged flow for each conditions (dPL) was defined as:

$$dPL = \frac{PL_{pulsatile} - PL_{non-pulsatile}}{PL_{pulsatile}} \times 100\% \qquad \text{(Equation 6.10)}$$

Indexed Power Loss (iPL), which represents the non-dimensional energy dissipation through the TCPC, was computed by normalizing time-averaged $\dot{E}_{Loss}$ by flow and patient body surface area (BSA) (iPL,$= \frac{\dot{E}_{Loss}}{\rho Qs^3/BSA^2}$) [188], where Q_s is the total systemic return and ρ is blood density = 1060 kg m^{-3}. iPL was not normalized by instantaneous Qs^3 since iPL will become extremely high when Qs is close to zero.

TCPC resistance was computed as ($\dot{E}_{Loss}/(Q_s{}^2/BSA)$), which was compared with vascular resistances. The difference in iPL (diPL) was also computed as:

$$diPL = \frac{iPL_{pulsatile} - iPL_{non-pulsatile}}{iPL_{pulsatile}} \times 100\% \qquad \text{(Equation 6.11)}$$

To visualize the flow field, particle tracking was performed with ParaView software (Kitware Inc., Clifton Park, NY, USA). Particle washout time was computed, which was defined as the number of respiratory cycles necessary for 95% of the massless particles injected into the FP during the first simulated cycle to leave the fluid domain. Hepatic flow distribution (HFD) was computed by counting the number of particles leaving through the LPA and RPA from the particle tracking results:

$$\% HFD(LPA) = \frac{n_{FP-LPA}}{n_{FP-LPA} + n_{FP-RPA}} \quad \text{(Equation 6.12)}$$

where %HFD(LPA) is the percentage of particles seeded at the FP leaving through the LPA, $n_{FP\text{-}LPA}$ and $n_{FP\text{-}RPA}$ are the total number of particles leaving from the FP to the LPA and RPA, respectively.

6.2.3.2 Flow Pulsatility

Based on the selected cycles and the smoothed waveforms, pulsatile indices (PI) of each caval vein (FP, SVC and LSVC (if present)), as well as the weighted pulsatility (wPI) of each patient was computed, based on the previously stated definition in the Methods chapter (Chapter 4.3.3).

$$wPI = \sum_{i=1\ldots n} PI_i \times c_i \quad \text{(Equation 6.13)}$$

$$c_i = \frac{Q_i}{\sum_{i=1\ldots n} Q_i} \quad \text{(Equation 6.14)}$$

PI was computed to quantify the amplitude of flow pulsations (cardiac pulsation-driven or respiratory-driven) at each vessel and wPI was used to characterize the overall vessel flow pulsatility in the TCPC.

$$PI = \frac{Q_{max} - Q_{min}}{Q_{mean}} X100\% \qquad \text{(Equation 6.15)}$$

$$wPI = \sum_{i=1}^{n} PI_i \times c_i \qquad \text{(Equation 6.16)}$$

$$c_i = \frac{average\ flow\ of\ inlet\ vessel\ i}{sum\ of\ average\ flow\ of\ all\ inlets} \qquad \text{(Equation 6.17)}$$

where Q_{mean} is the time-averaged flow rate over one respiratory or cardiac cycle, and Q_{min} and Q_{max} are the minimum and maximum instantaneous flow rates within the same cycle, n is the total number of inlet vessels and c_i is the flow split of vessel i.

6.2.4 Statistical Methods

To compare PI, wPI and %diPL between FB and BH conditions, paired-sample t-tests were performed with IBM SPSS Statistics (version 22, IBM Corporation, Armonk, New York). Wilcoxon signed-rank tests were used for non-normal data (tested by Shapiro-Wilk test). p≤0.05 was considered significant (two-tailed).

6.3   Specific Aim 2(a): *In Vivo* Characterization of FB and BH Flow

Average vessel flow and PI of the FP and SVC, as well as wPI of the TCPC, were compared between FB and BH conditions within the duration of one respiratory cycle (Table 6-3, detailed results listed in Appendix A.8.3). Average vessel flow was significantly higher at both the FP and SVC under FB condition. Vessel PI was

significantly higher at the FP under FB condition than BH condition. Although the same trend was observed for SVC PI, it was not statistically significant (Table 6-3). It is observed that wPI was significantly higher under FB condition than BH condition.

Table 6-3 Comparison of flow waveforms of the FP and SVC under FB and BH condition (N=9)

Mean ± standard deviation		Free-breathing	Breath-held	p-value
Average vessel flow within the selected cycle (L/min)	FP	3.5±1.3	2.9±1.1	0.002*
	SVC	1.5±1.1	1.1±0.9	0.011*
	LSVC (N=2)	0.5	0.3	
Pulsatility Index (%)	FP	172±64	75±26	0.002*
	SVC	221±87	168±96	0.139
	LSVC (N=2)	244	152	
Weighted Pulsatility Index (%)		186±53	97±38	0.001*

* p≤0.05

6.4 Specific Aim 2(b): Comparison of TCPC Hemodynamics under Free-breathing and Breath-held Conditions

Average and maximum Re at FB condition for each patient's FP are summarized in Table 6-4. It was observed that 6 patients (CHOP011B, 029B, 091C, 103B, 229A, 235A) had maximum FP Re < 2500. However, 3 patients (CHOP032C, 155A and 234A) had a maximum FP Re larger than 2500. Since the current mesh size and time step could not resolve the flow disturbances associated with Re larger than 2500, these cases caused numerical instability with the Navier-Stokes solver in LifeV. Direct numerical simulation should be used, but is often associated with high computational

cost since a fine spatial and temporal discretization is required to resolve the Kolmogorov scales of the flow field. For this reason, a developmental version of the LifeV solver with Large Eddy Simulation (LES) capability was applied for these cases (Chapter 4.7.1.4). This solver was validated against experimental data for fluid flow in an idealized medical device (consisting of a conical convergent, a narrow throat, and a sudden expansion, as recommended by the U.S. Food and Drug Administration) [176]. Numerical results are in good quantitative agreement with the measured axial components of the velocity and pressures for two different flow rates corresponding to turbulent regimes, even for meshes with a mesh size more than 40 times larger than the smallest turbulent scale.

Table 6-4 Average and Maximum FP Reynolds Number of each patient under FB condition

	FP area (cm^2)		FP flow (L/min)		Re at PC-MRI slice		Re at FP narrowing	
	At PC-MRI slice (averaged)	At FP narrowing	Average	Maximum	Average	Maximum	Average	Maximum
CHOP011B	3.10	1.34	2.51	5.32	772	1886	1167	2471
CHOP029B	6.48	4.62	3.69	6.29	776	1572	924	1573
CHOP032C	1.02	0.60	2.51	5.32	1251	1878	1743	3692
CHOP091C	6.48	5.08	5.45	8.75	1179	2310	1300	2087
CHOP103B	6.88	1.22	2.97	4.89	612	1210	1441	2377
CHOP155A	5.46	2.28	5.46	8.14	1252	1910	1943	2898
CHOP229A	8.45	2.64	2.66	4.58	509	1051	880	1513
CHOP234A	2.12	2.30	4.14	10.64	1505	3679	1466	3768
CHOP235A	4.21	2.46	2.04	4.79	528	1617	698	1639

6.4.1 Qualitative Comparison

Velocity fields at a cross-section within the TCPC were compared between FB and BH conditions in each patient, along with streamtraces color-coded by the vessel of origin (blue = flow originating from FP; green = flow originating from SVC). Particle tracking videos were also created to visualize the instantaneous flow fields. The following sections (Chapters 6.4.1.1-6.4.1.9) illustrate the patient specific TCPC flow fields during inspiration, end inspiration, expiration and end expiration to demonstrate the variations in TCPC flow fields within a single respiratory cycle. Note that in the flow field figures, the same velocity contour scale was used for a given patient throughout all phases of the respiratory cycle (inspiration, end inspiration, expiration and end expiration).

In general, larger variations in the TCPC flow field within the duration of a respiratory cycle were observed under FB conditions than BH conditions. In most patients, the maximum velocity magnitude in the TCPC was higher during inspiration and end inspiration under the FB conditions than during the corresponding time points under the BH conditions. During expiration, retrograde flow (as observed from the PC-MRI data and prescribed in the flow boundary conditions) in the FP and SVC was observed in some patients under FB conditions. But this was not observed under BH conditions. The flow field was the most similar between the two conditions at end expiration for most of the patients. Particle tracking was also performed to visualize the flow fields of each patient under both FB and BH conditions. The particle tracking animations for the other six patients are shown in Appendix A.8.4. The animations for the TCPC flow field for all nine patients throughout the entire respiratory cycle are shown in Appendix A.8.5.

6.4.1.1 Single SVC - CHOP011B (Intra-atrial)

The velocity field in the Fontan baffle of CHOP011B throughout different phases of the respiratory cycle is visualized in Figure 6.7. This patient case had wPI of 256% during FB condition and 70% during BH condition, which was the largest difference observed in this patient cohort. During inspiration (Figure 6.7(a)), forward flow is observed in both FB and BH conditions, while higher velocity magnitudes are observed under the FB condition. During end inspiration (Figure 6.7(b)), maximum flow and hence maximum velocity magnitudes are observed in the FP under FB condition. During expiration, retrograde flow is observed in the FP under FB condition. This resulted in different flow fields between FB and BH conditions (Figure 6.7(c)). This is also visualized in the particle tracking videos of CHOP011B (animations 6.1 (FB) and 6.2 (BH)). Finally towards end expiration, there was more similarity in velocity magnitude and direction between FB and BH conditions (Figure 6.7(d)).

(a)

(b)
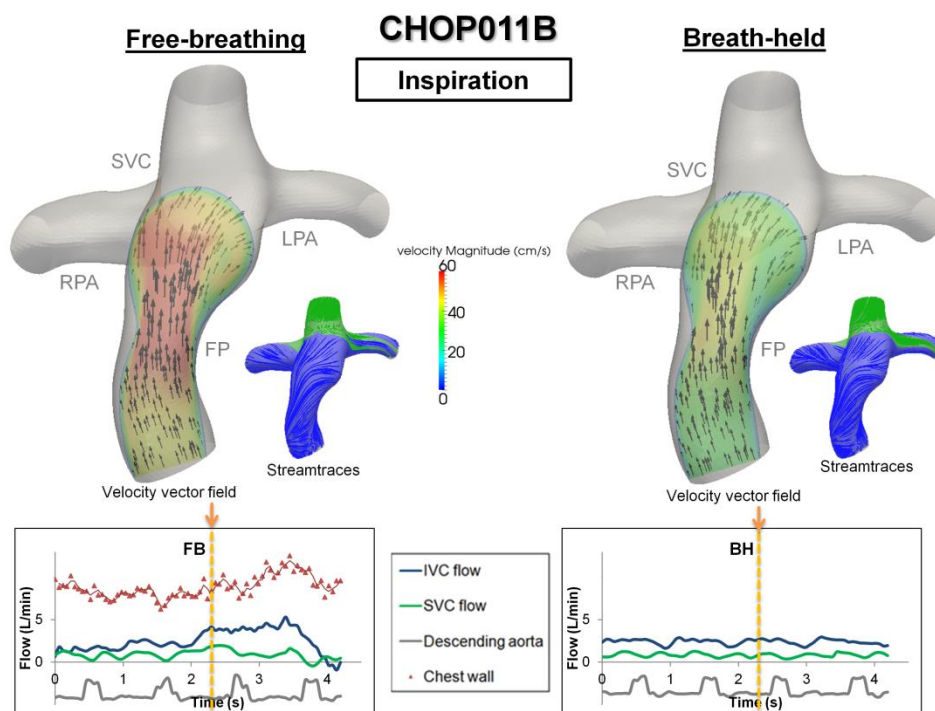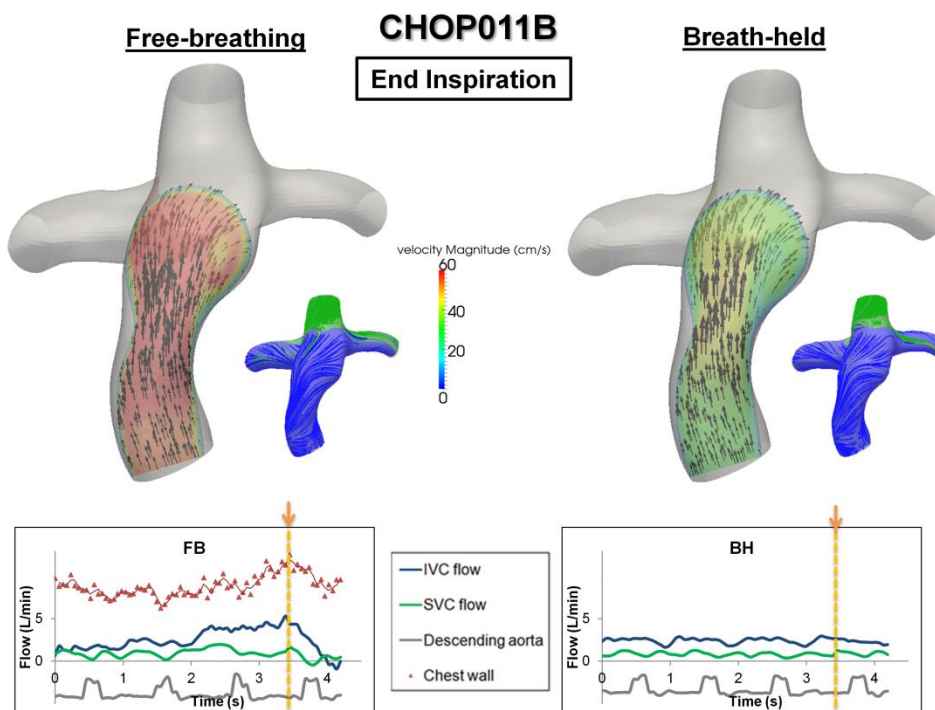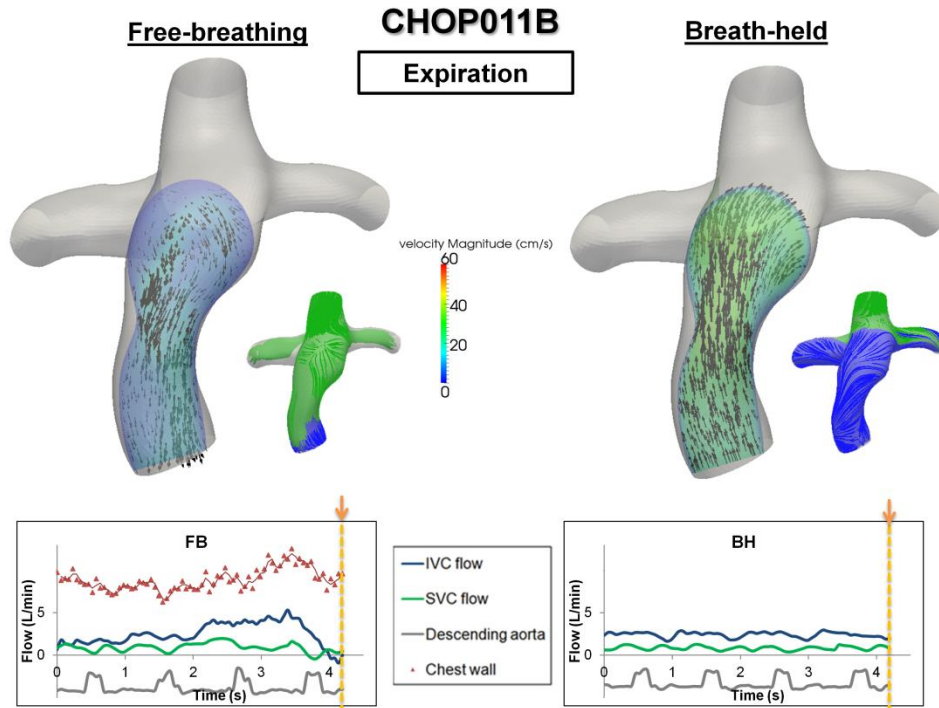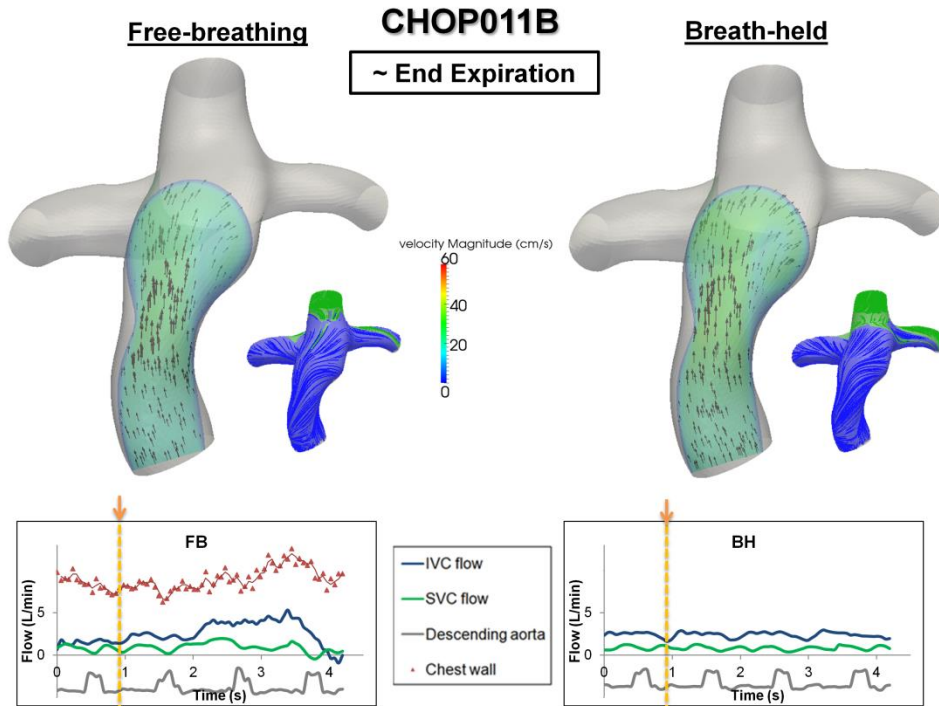
Figure 6.7 Flow fields in the Fontan pathway under free-breathing and breath-held conditions for CHOP011B, throughout different phases of the respiratory cycle: (a) inspiration, (b) end inspiration, (c) expiration, (d) end expiration. (Velocity magnitude unit: cm/s)

175

Animation 6.1 Particle tracking video of CHOP011B under FB condition. Particles were seeded at the FP and SVC for on respiratory cycle and colored by velocity magnitude (animation_6.1_CHOP011B_FB.avi, 1.77MB)

Animation 6.2 Particle tracking video of CHOP011B under BH condition. Particles were seeded at the FP and SVC for on respiratory cycle and colored by velocity magnitude (animation_6.2_CHOP011B_BH.avi, 1.64MB)

6.4.1.2   Single SVC - CHOP029B (Intra-atrial)

The velocity fields in the TCPC of CHOP029B throughout different phases of the respiration cycle are visualized in Figure 6.8. The difference in wPI between FB (wPI = 128%) and BH (wPI = 95%) was lower in this patient. As observed in Figure 6.8, the flow waveforms of the FB and BH had similar mean flow rate and flow amplitude at the FP. The velocity flow field was most different qualitatively between the two conditions during inspiration (Figure 6.8(a)). During end inspiration (Figure 6.8(b)), the velocity magnitudes were similar between the two conditions, but the direction of the velocity vectors were different. During expiration (Figure 6.8(c)) and at end expiration (Figure 6.8(d)), the velocity vectors are in similar directions and velocity magnitudes are similar between the two conditions.

(b)

Free-breathing

CHOP029B

End Inspiration

Breath-held

velocity Magnitude
45
40
30
20
10
0

FB

BH

IVC flow
SVC flow
Descending aorta
Chest wall

(c)

Free-breathing

CHOP029B

Expiration

Breath-held

velocity Magnitude
45
40
30
20
10
0

FB

BH

IVC flow
SVC flow
Descending aorta
Chest wall

178

(d)
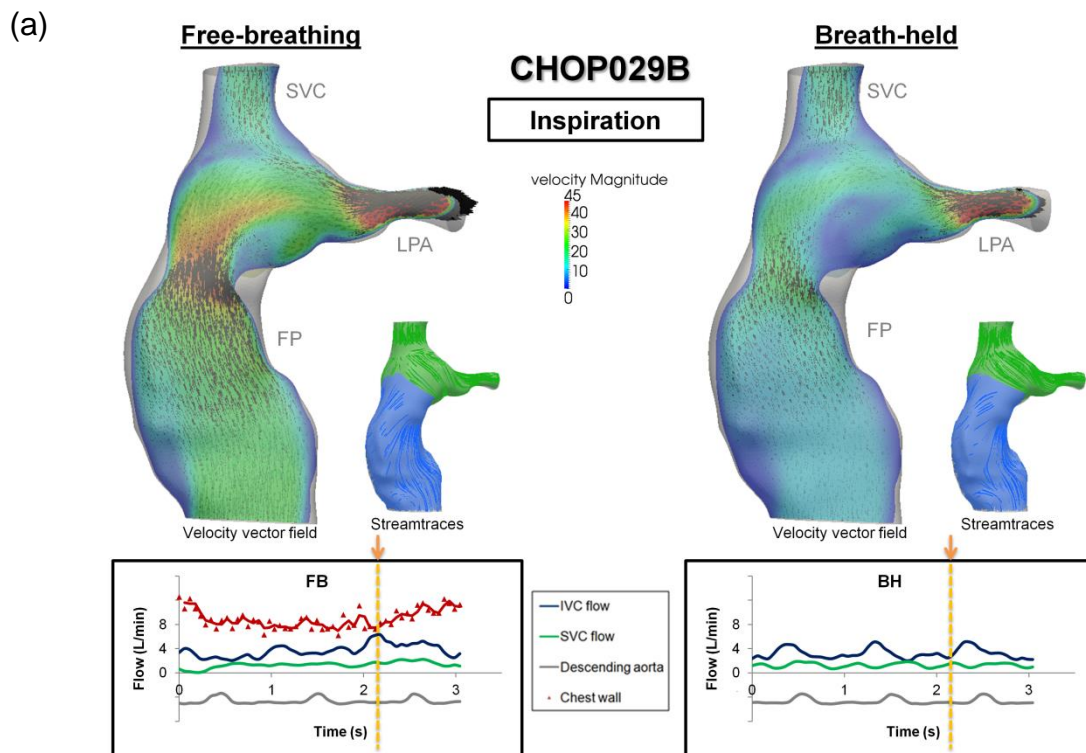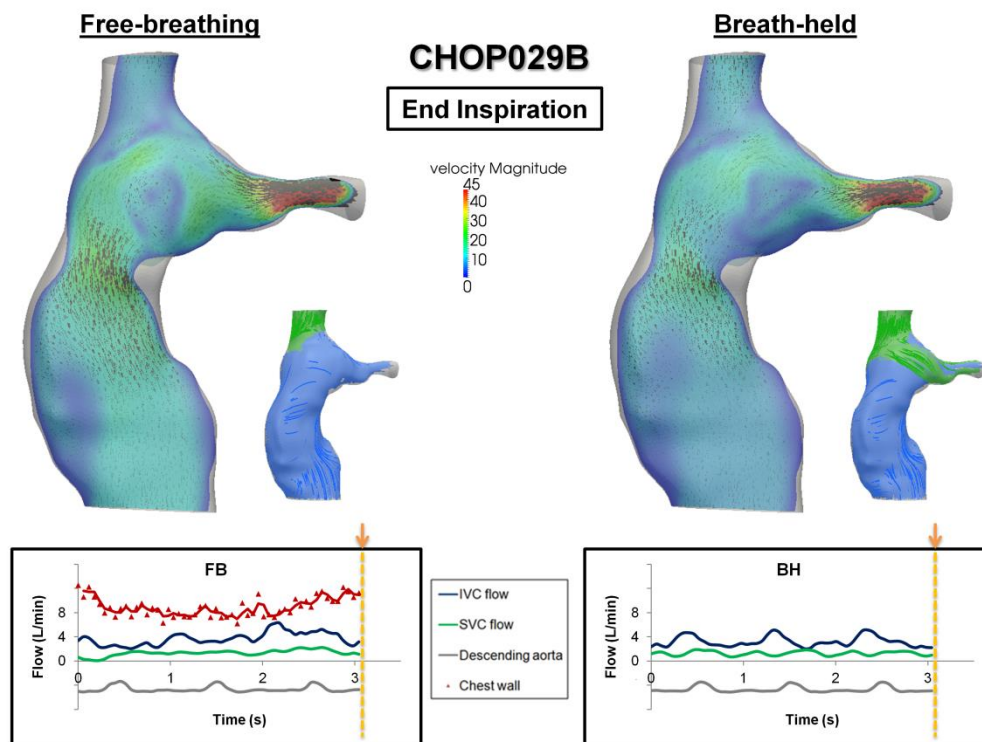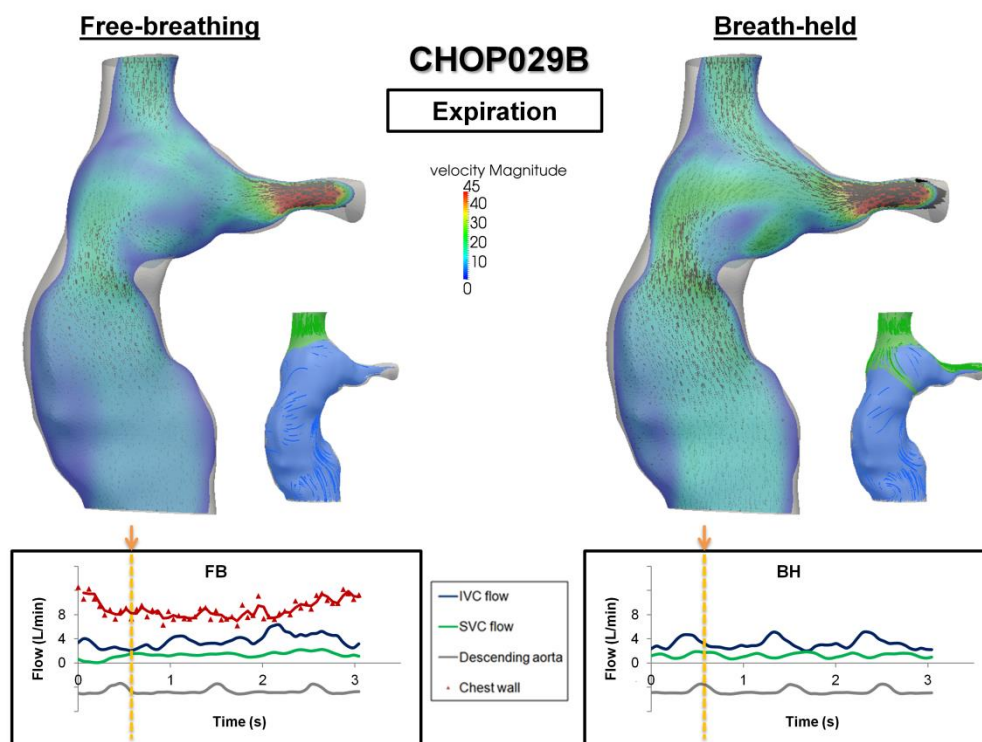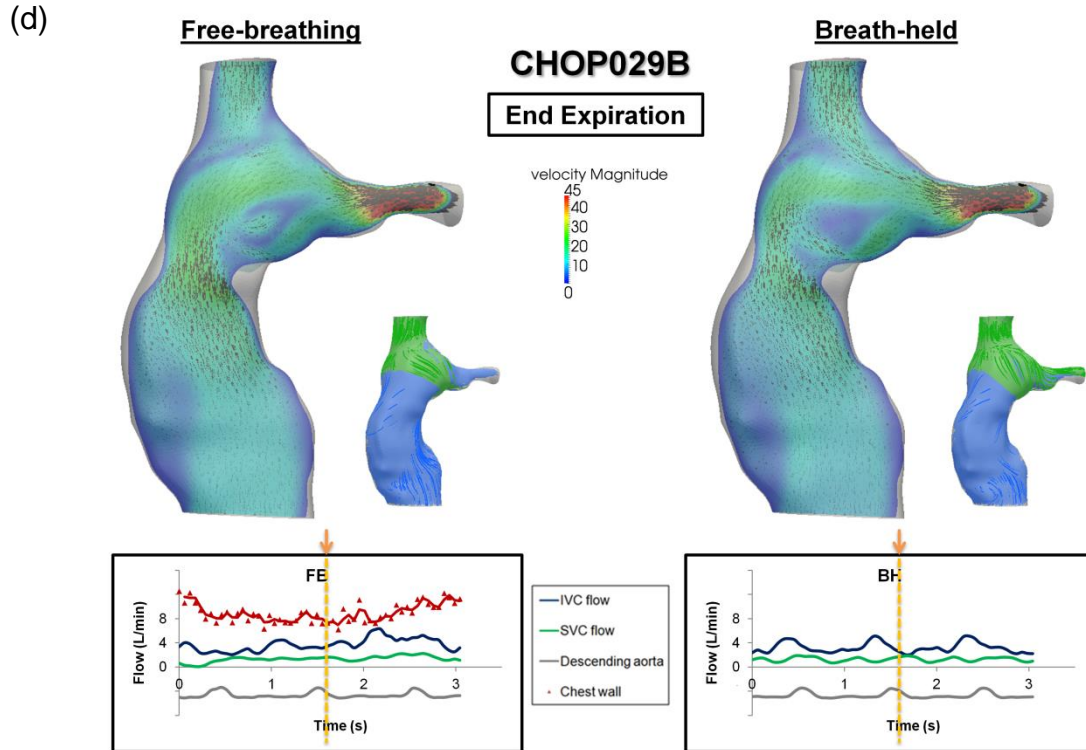
Figure 6.8 Flow fields in the TCPC under free-breathing and breath-held conditions for CHOP029B, throughout different phases of the respiratory cycle: (a) inspiration, (b) end inspiration, (c) expiration, (d) end expiration. (Velocity magnitude unit: cm/s)

6.4.1.3   Single SVC – CHOP032C (Intra-atrial)

The velocity fields in the TCPC of CHOP032C throughout different phases of the simulated cycle are visualized in Figure 6.9. The chest wall and descending aorta waveforms were not available for this patient because of the poor image quality. The simulated cycle was chosen based on the periodicity of the FP and SVC FB waveforms. Peak and low flow, acceleration and deceleration phases were compared in the two conditions. Under both FB and BH conditions, maximum velocity magnitude was observed at the narrowing of the FP. Especially during peak flow of FB condition, the maximum velocity in the narrow section of the FP was up to 149 cm/s, and the maximum pressure drop across the FP narrowing was 11.98 mmHg. As compared to

BH condition, under peak flow, the maximum velocity was 92cm/s, and the corresponding pressure drop across the FP narrowing was 7.92 mmHg. The time-averaged pressure drop over the respiratory cycle across the FP narrowing was 7.67 mmHg under FB condition and 5.83 mmHg under BH conditions. When comparing the streamtraces of flow originating from the FP and SVC during different phases, different flow patterns were observed between the two conditions. During the phase of "low flow" of FB condition, retrograde flow was observed in SVC. As observed from the streamtraces, FP flow penetrated into the SVC. This was not observed in the BH condition. For the other phases, the streamtraces were similar between the FB and BH conditions.

(b) CHOP032C — Peak flow. Free-breathing and Breath-held velocity magnitude visualizations with corresponding FB and BH flow plots (IVC flow, SVC flow).

(c) CHOP032C — Deceleration. Free-breathing and Breath-held velocity magnitude visualizations with corresponding FB and BH flow plots (IVC flow, SVC flow).

(d)
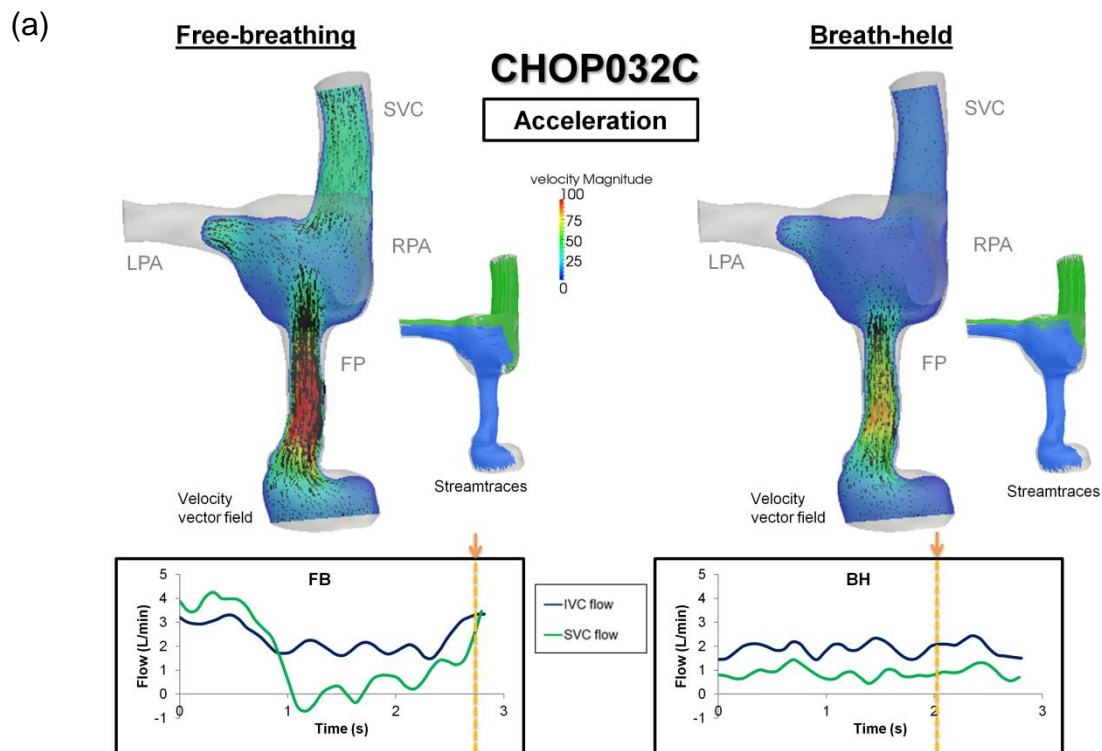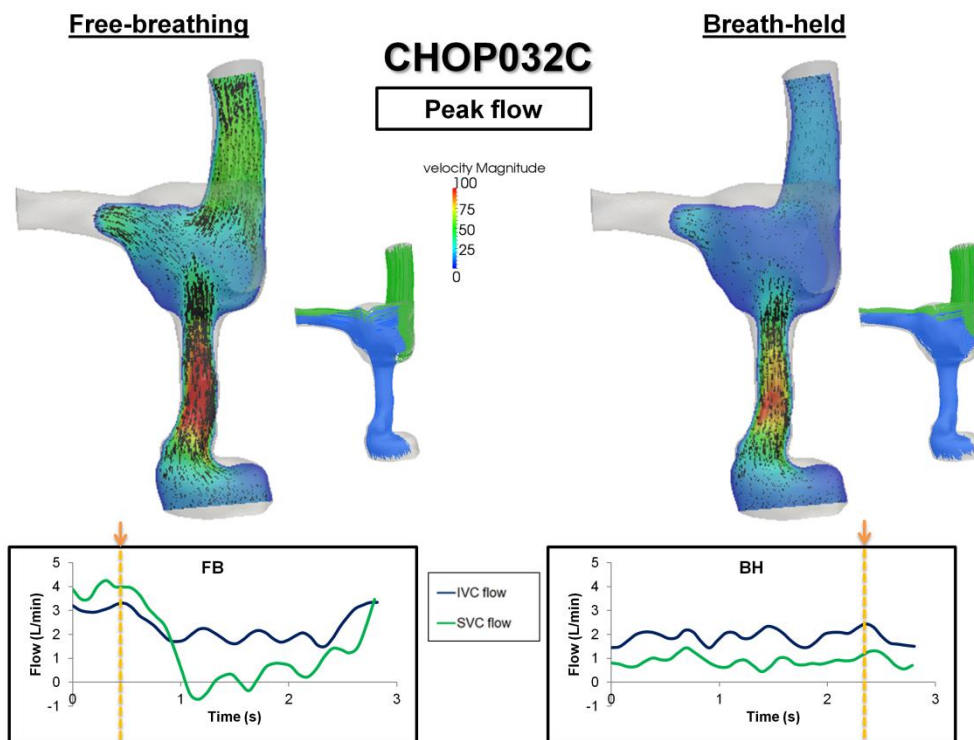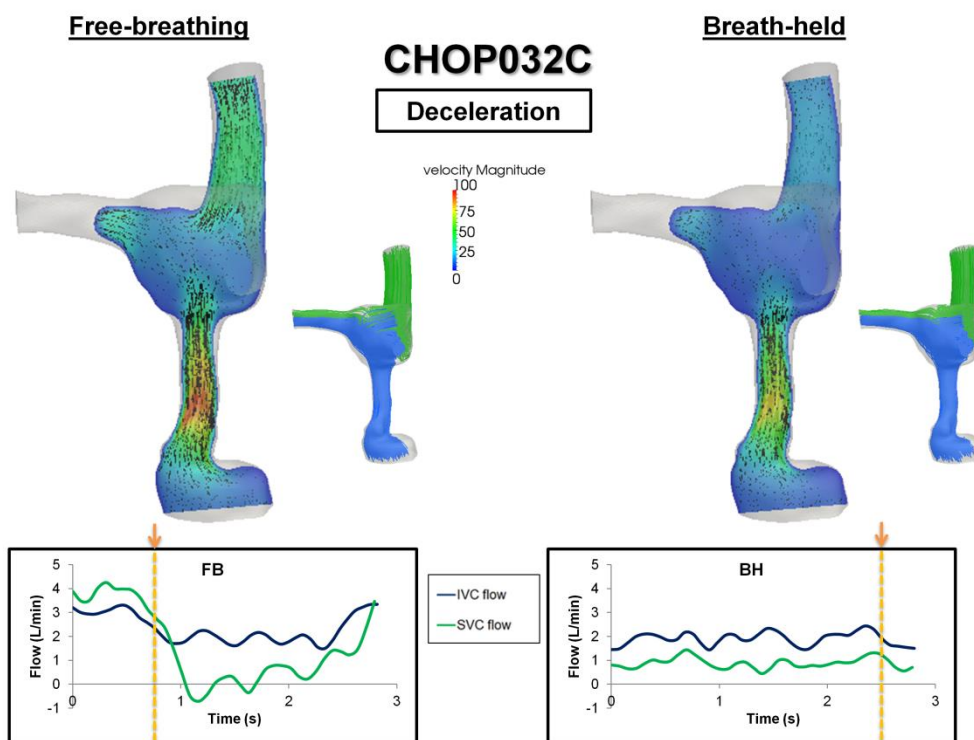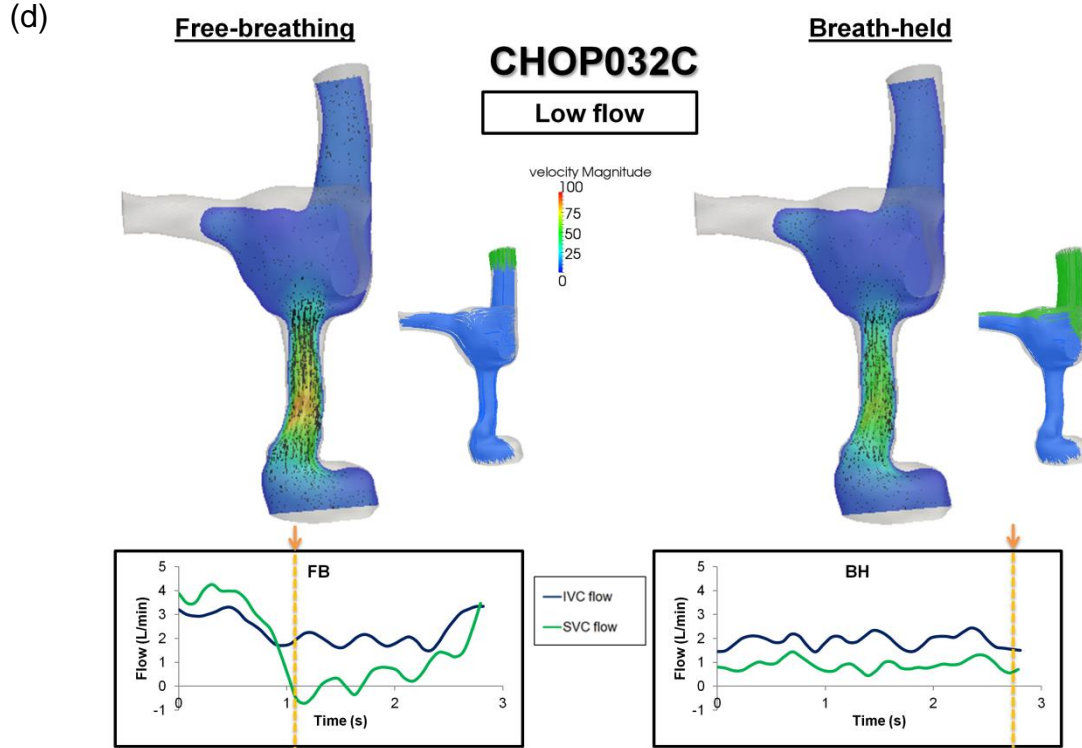
Figure 6.9 Flow fields in the TCPC under free-breathing and breath-held conditions for CHOP032C, throughout different phases of the respiratory cycle: (a) acceleration, (b) peak flow, (c) deceleration, (d) low flow. (Velocity magnitude unit: cm/s)

6.4.1.4 Single SVC – CHOP103B (Intra-atrial)

The velocity fields in the TCPC of CHOP103B are visualized in Figure 6.10. The chest wall and descending aorta waveforms were not available for this patient because of the image quality. The simulated cycle was chosen based on the periodicity of the FP and SVC FB waveforms. Peak and low flow, acceleration and deceleration phases were compared in the two conditions. The difference in wPI between FB (wPI = 206%) and BH (wPI = 179%) was also low in this patient. During acceleration and peak flow phases (Figure 6.10 (a) and (b)), the maximum velocity magnitude was higher under FB condition. During deceleration and low inflow (Figure 6.10 (c) and (d)), the velocity

magnitude was more similar between the two conditions, but the direction of velocity field was more different.
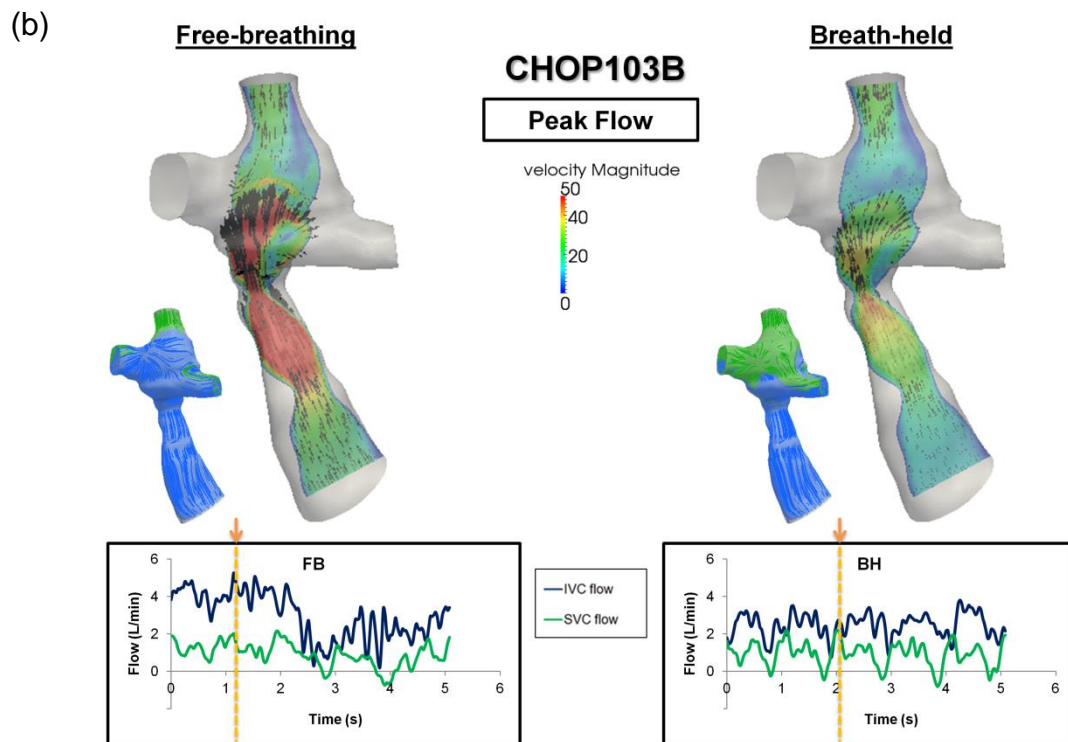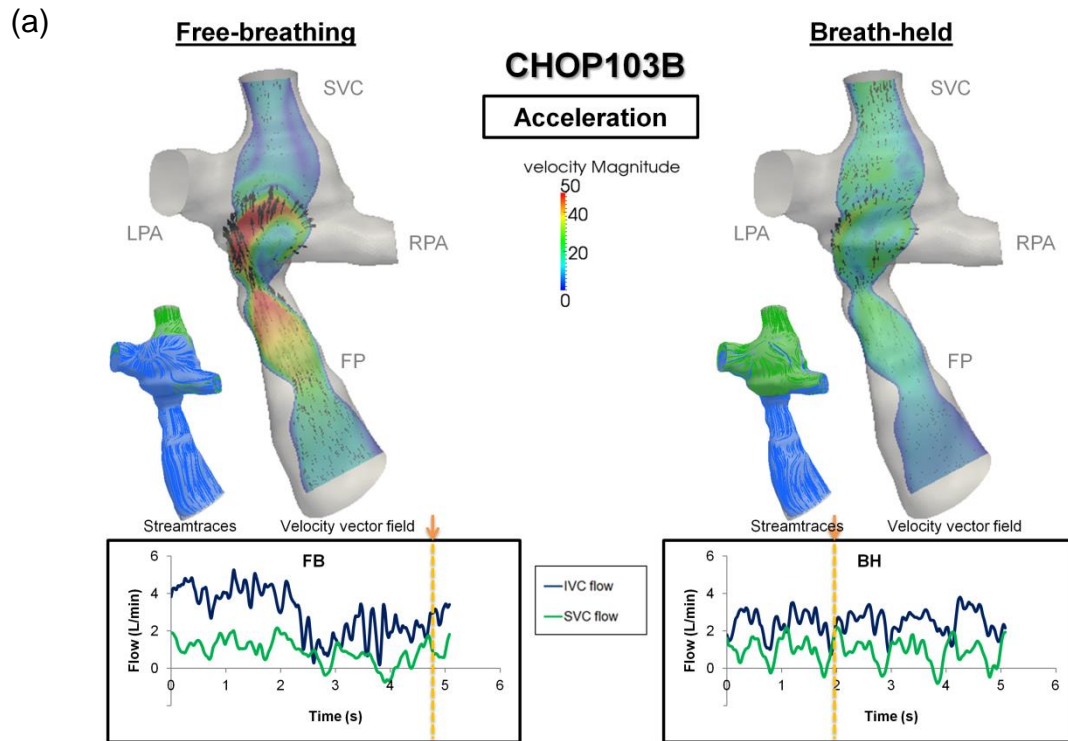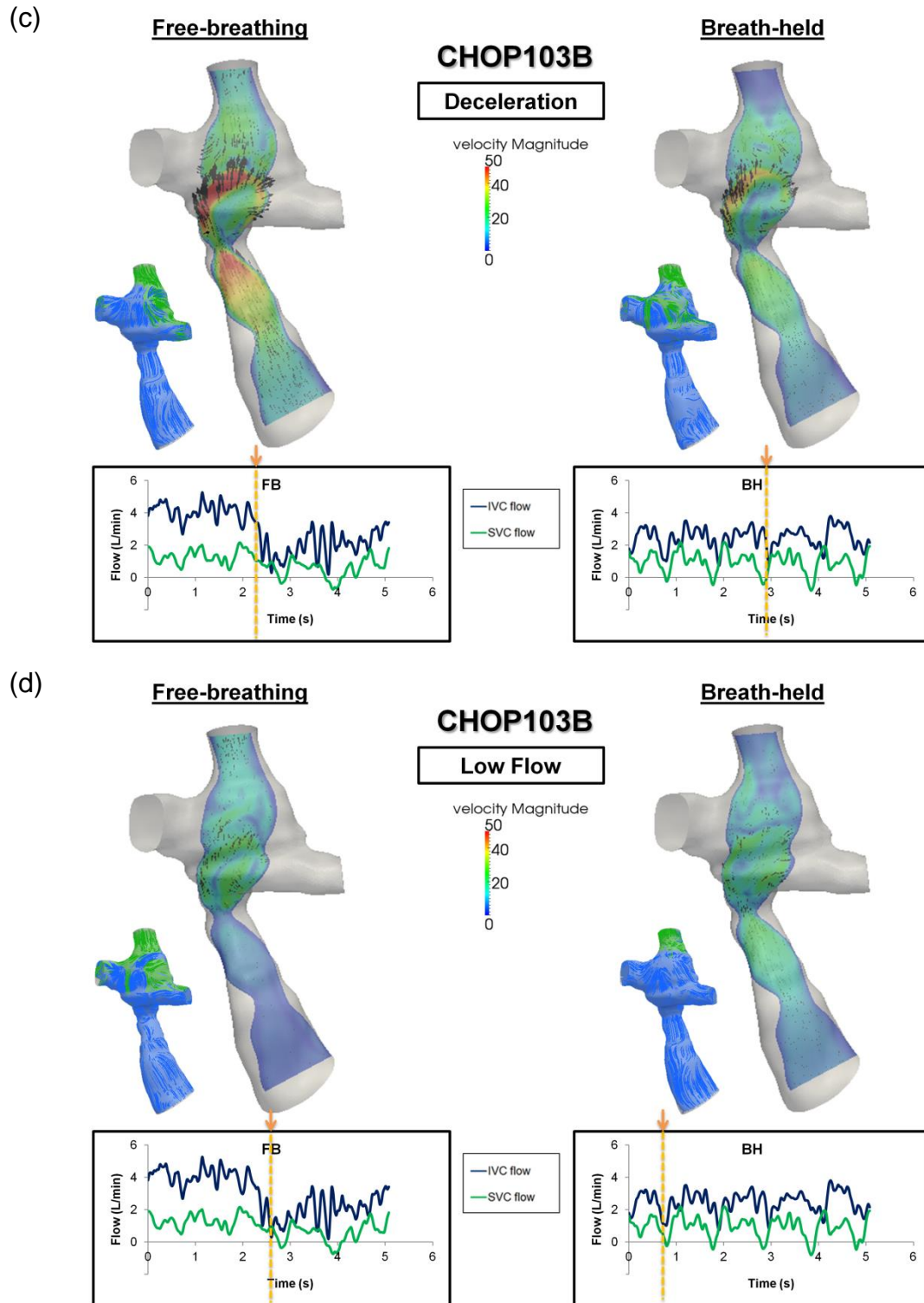
Figure 6.10 Flow fields in the TCPC under free-breathing and breath-held conditions for CHOP103B, throughout different phases of the respiratory cycle: (a) acceleration, (b) peak flow, (c) deceleration, (d) low flow. (Velocity magnitude unit: cm/s)

184

6.4.1.5   Single SVC – CHOP155A (Intra-atrial)

The velocity field in the TCPC of CHOP155A throughout different phases of the respiration cycle is visualized in Figure 6.11. There was small difference in wPI between FB (wPI = 79%) and BH (wPI = 52%) conditions in this patient. The direction of the velocity flow field was relatively consistent within the respiratory cycle, as well as between FB and BH conditions (Figure 6.11). Higher velocity magnitude was observed during end inspiration under FB condition (Figure 6.11 (b)). Smaller variation in velocity magnitude was observed within the simulated cycle under BH condition.

(b)

Free-breathing   **CHOP155A**   **Breath-held**

End Inspiration

velocity Magnitude

(c)

Free-breathing   **CHOP155A**   **Breath-held**

Expiration

velocity Magnitude
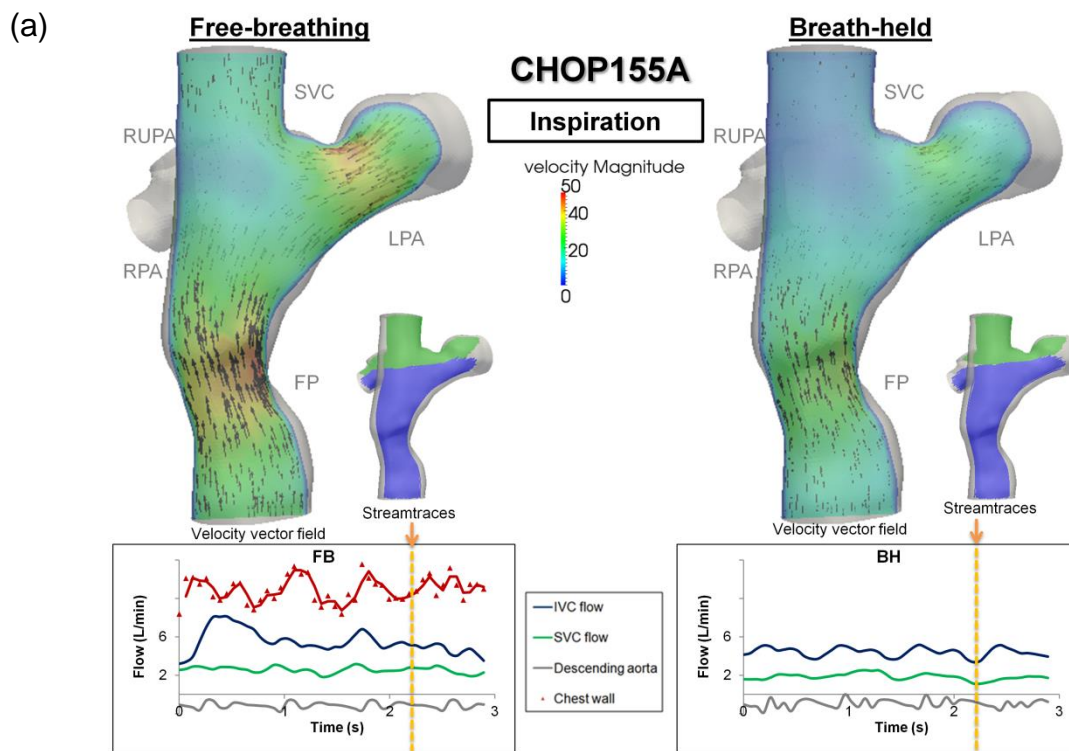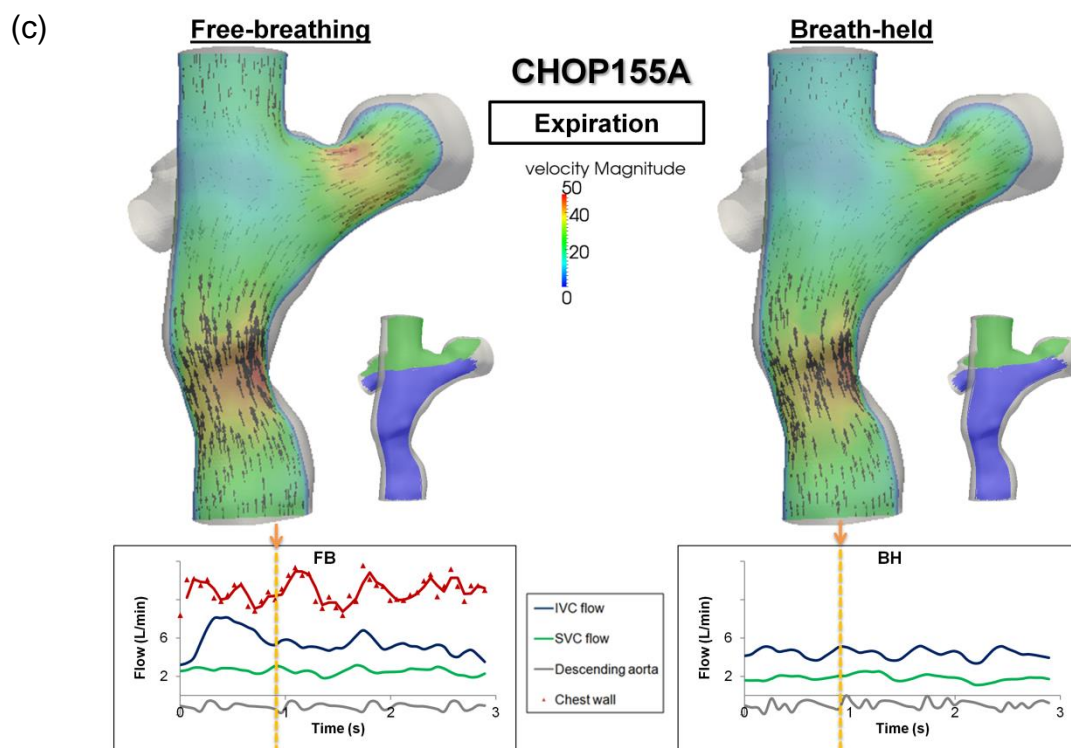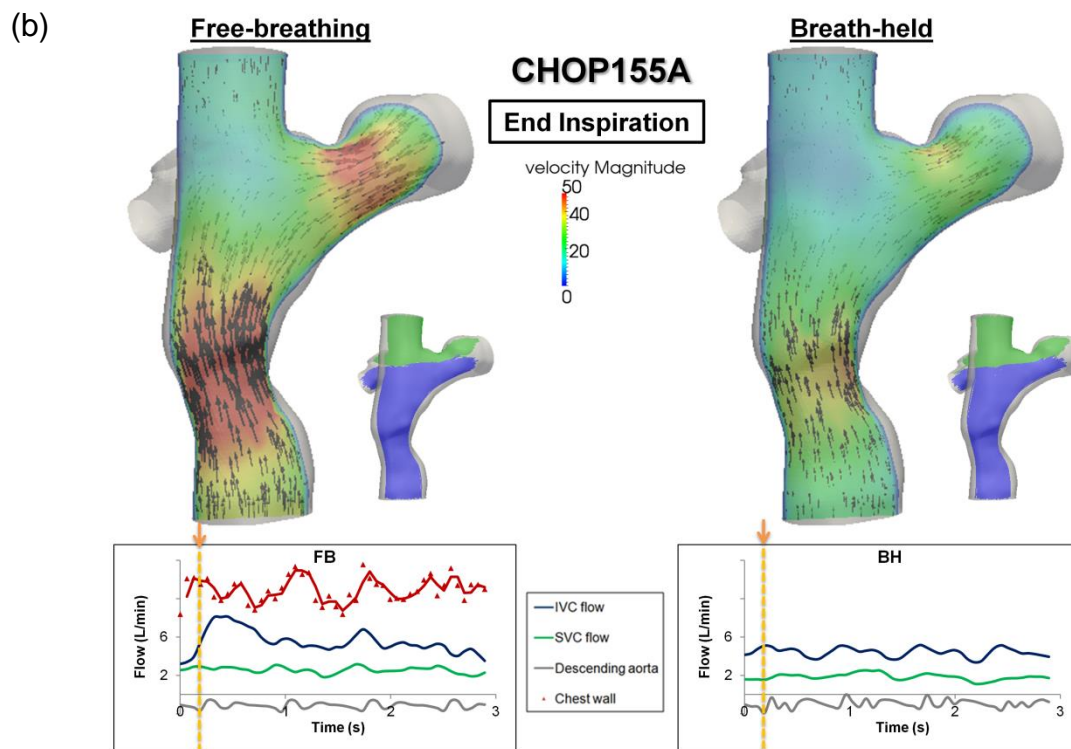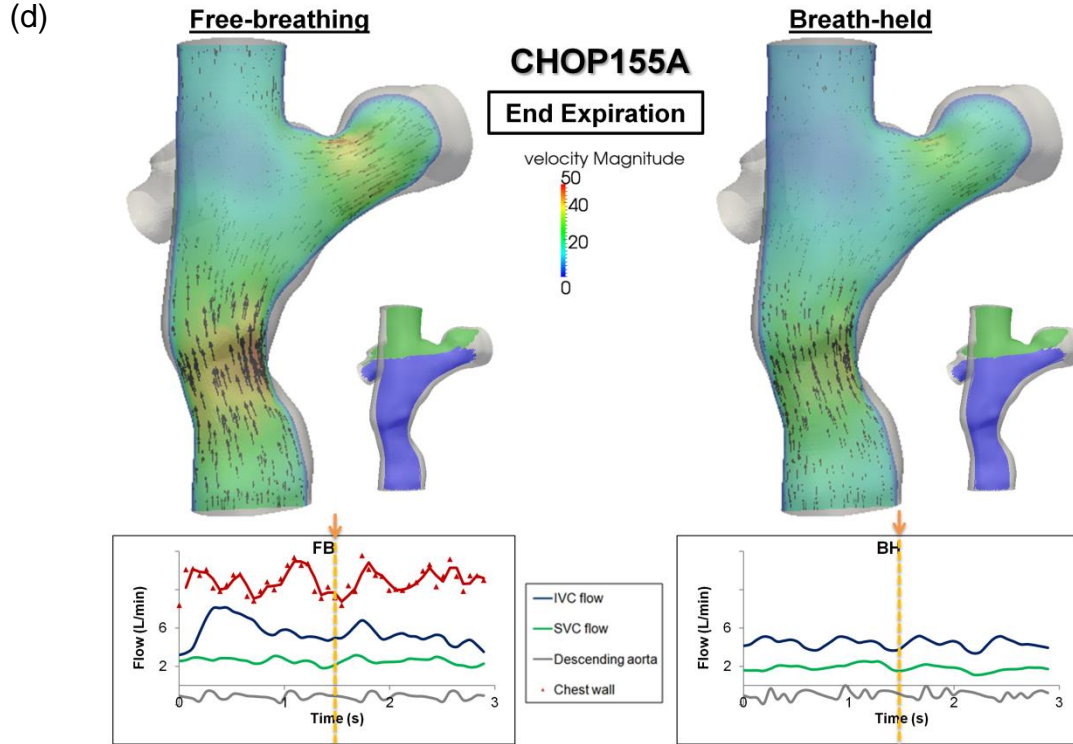
Figure 6.11 Flow fields in the TCPC under free-breathing and breath-held conditions for CHOP0155A, throughout different phases of the respiratory cycle: (a) inspiration, (b) end inspiration, (c) expiration, (d) end expiration. (Velocity magnitude unit: cm/s)

6.4.1.6   Single SVC – CHOP234A (Extracardiac)

The velocity field in the TCPC of CHOP234A throughout different phases of the respiration cycle is visualized in Figure 6.12. Similar to CHOP155A, the direction of the velocity flow field was relatively consistent within the respiratory cycle, as well as between FB and BH conditions (Figure 6.12). Higher velocity magnitude was observed during inspiration under FB condition (Figure 6.12 (a)). Smaller variation in velocity magnitude was observed within the simulated cycle under BH condition.

187

(a) **Free-breathing** CHOP234A **Breath-held**

Inspiration

(b) **Free-breathing** CHOP234A **Breath-held**
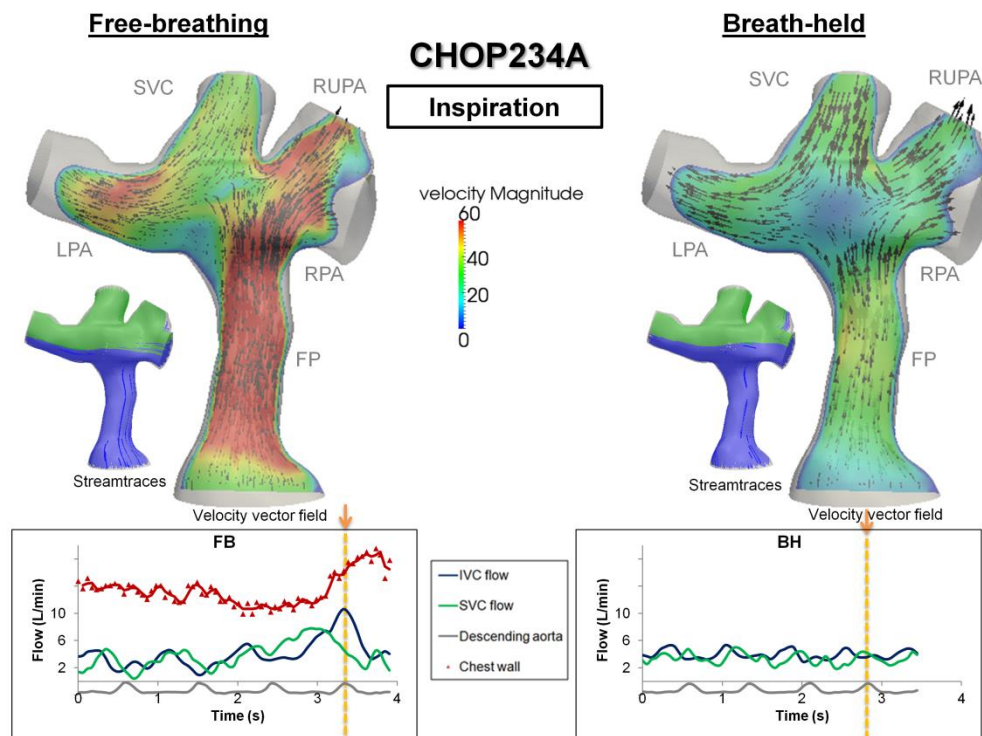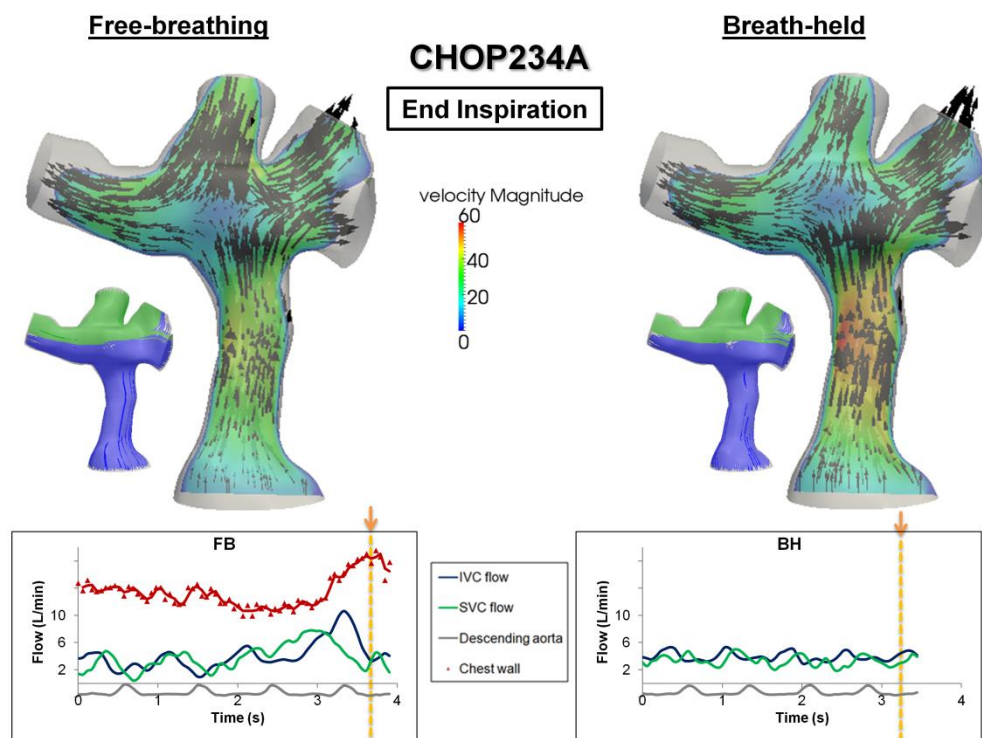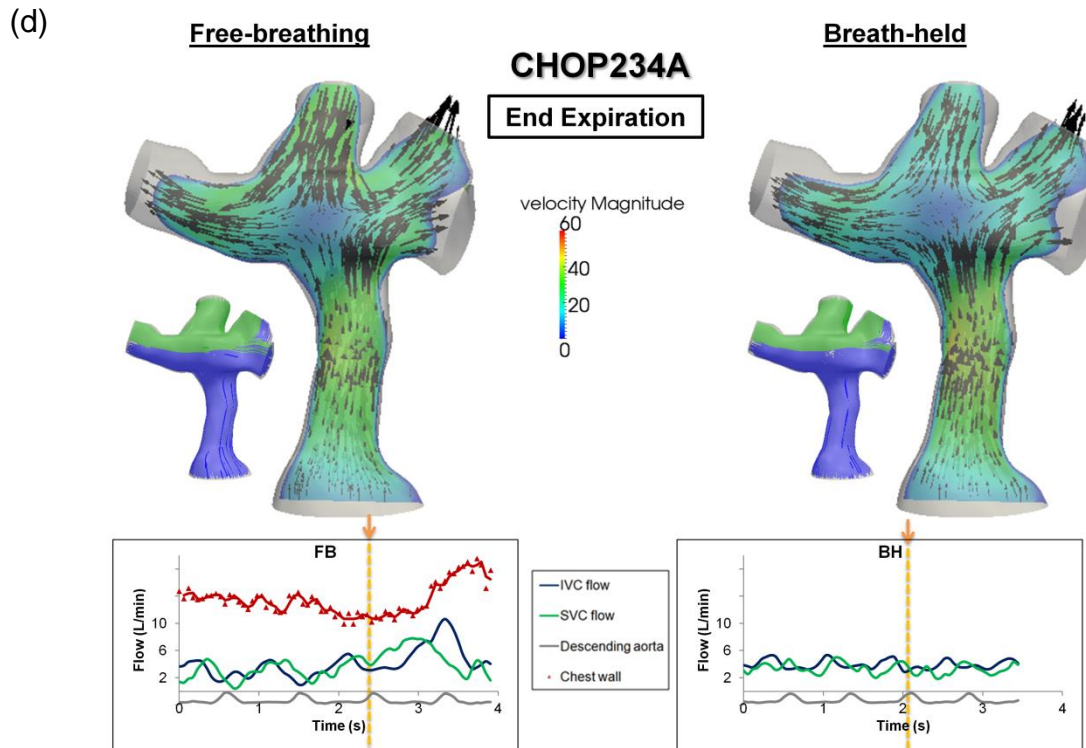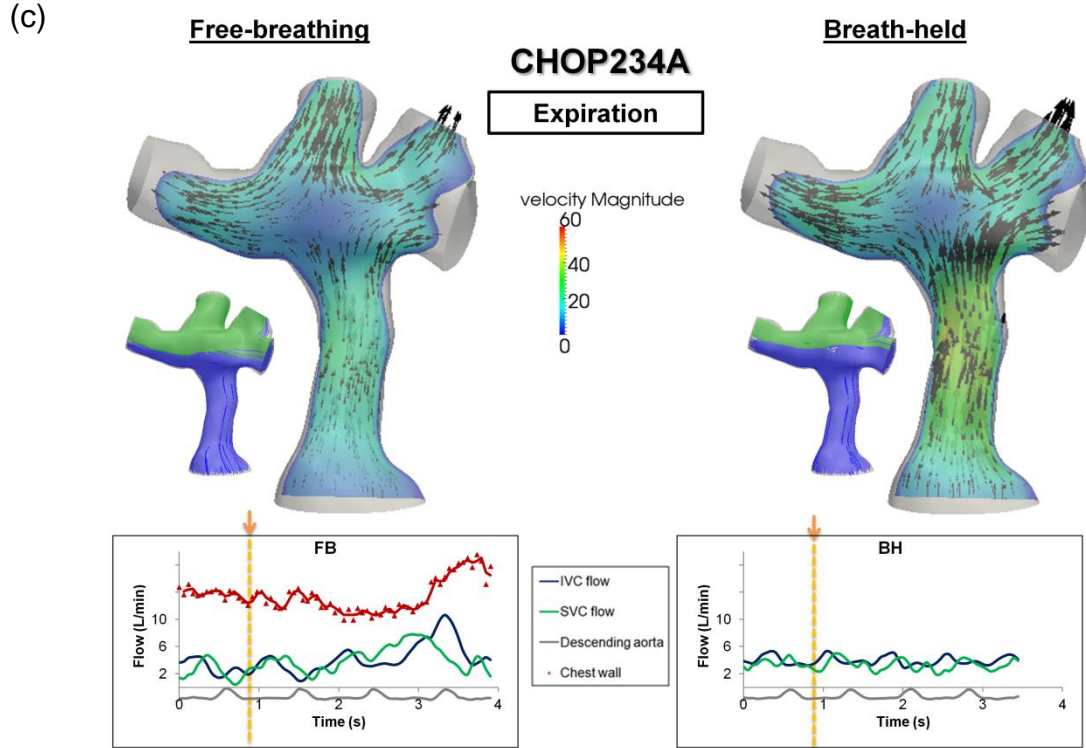
End Inspiration

Figure 6.12 Flow fields in the TCPC under free-breathing and breath-held conditions for CHOP0234A, throughout different phases of the respiratory cycle: (a) inspiration, (b) end inspiration, (c) expiration, (d) end expiration. (Velocity magnitude unit: cm/s)

6.4.1.7   Single SVC - CHOP235A (Intra-atrial)

The velocity field in the TCPC of CHOP235A throughout different phases of the respiration cycle is visualized in Figure 6.13.   Maximum velocity magnitude of FP condition under inspiration was higher than that of BH condition.   Flow mixing was observed in the center of the TCPC under FB condition during inspiration (Figure 6.13(a)).   The inflow rate of FP and SVC were similar between FB and BH conditions during end inspiration, expiration and end expiration, hence similar flow fields were observed throughout these phases (Figure 6.13(b), (c) and (d) respectively). From the particle tracking videos of CHOP235A (animation 6.3 (FB) and 6.4 (BH)), different flow recirculation patterns were observed between the two conditions. During FB condition, flow recirculation happened at the inferior part of the FP. This could be caused by SVC flow at time points which SVC flow was higher than FP flow (t = 3.84-3.97 s in Figure 6.13). As shown by screenshots (Figure 6.14) of the particle tracking videos of CHOP235A (animation 6.5 (FB) and 6.6 (BH)), with particles seeded only at the SVC, colored by the number of particle release (injection step ID)), the flow recirculation in the FP under FB condition could be caused by higher SVC flow that pushes through to the FP (corresponds to particles with injection step Id of 966-999 (purple) in Figure 6.14); on the other hand, this was not observed under BH condition. Flow circulation was observed at the center of the TCPC under BH condition (Figure 6.14).

(a) CHOP235A — Inspiration

Free-breathing / Breath-held

(b) CHOP235A — End Inspiration

Free-breathing / Breath-held

191
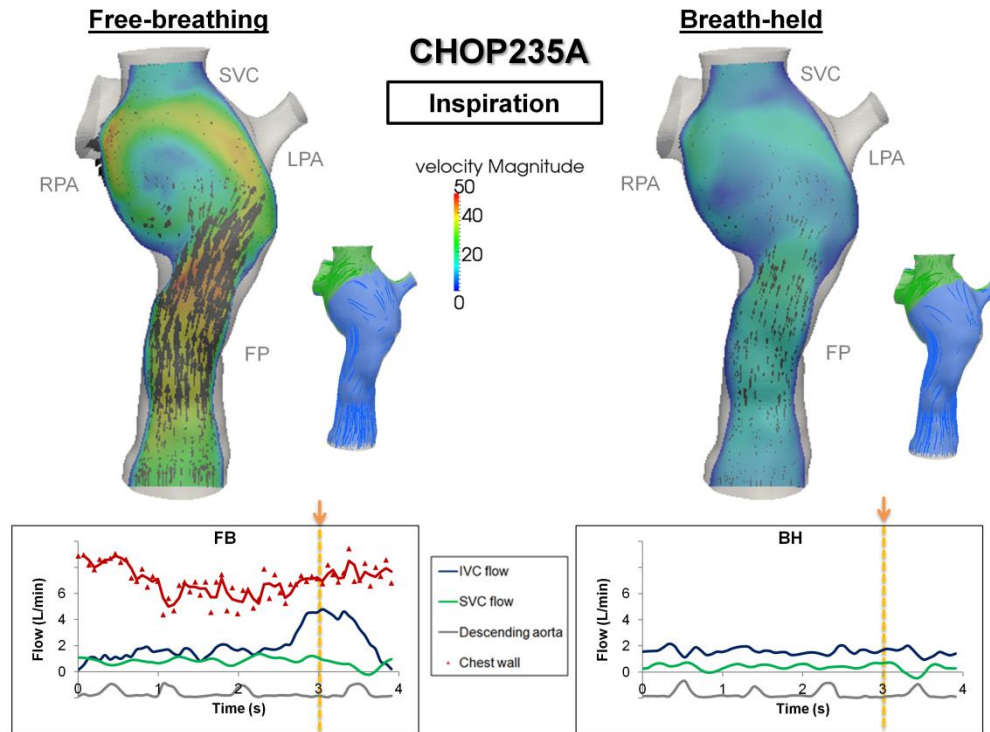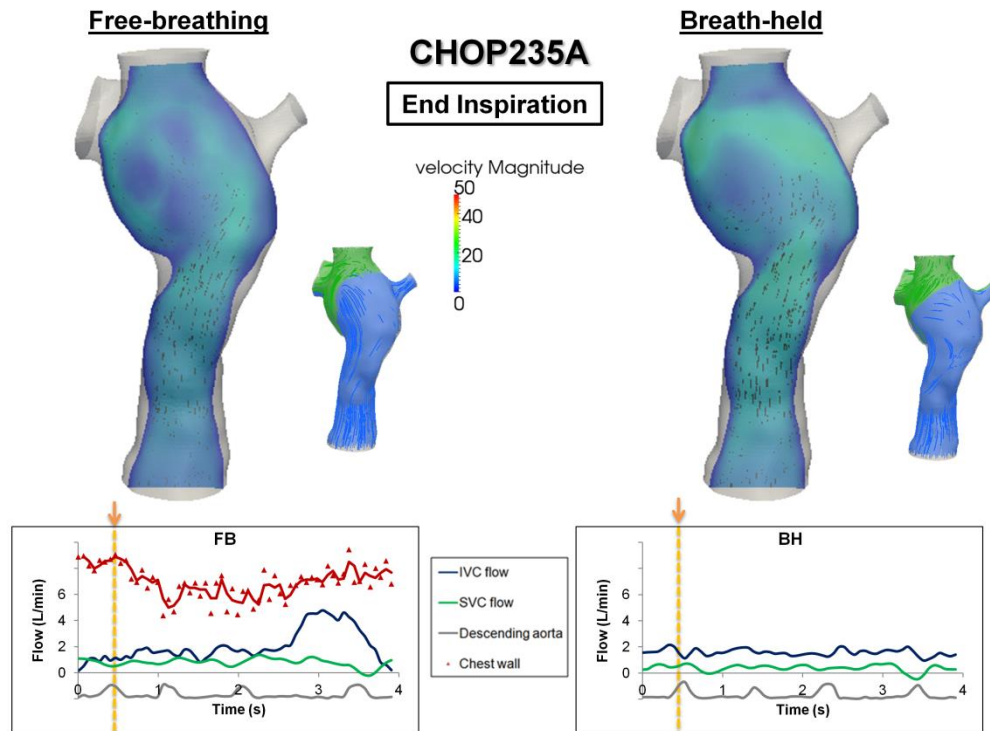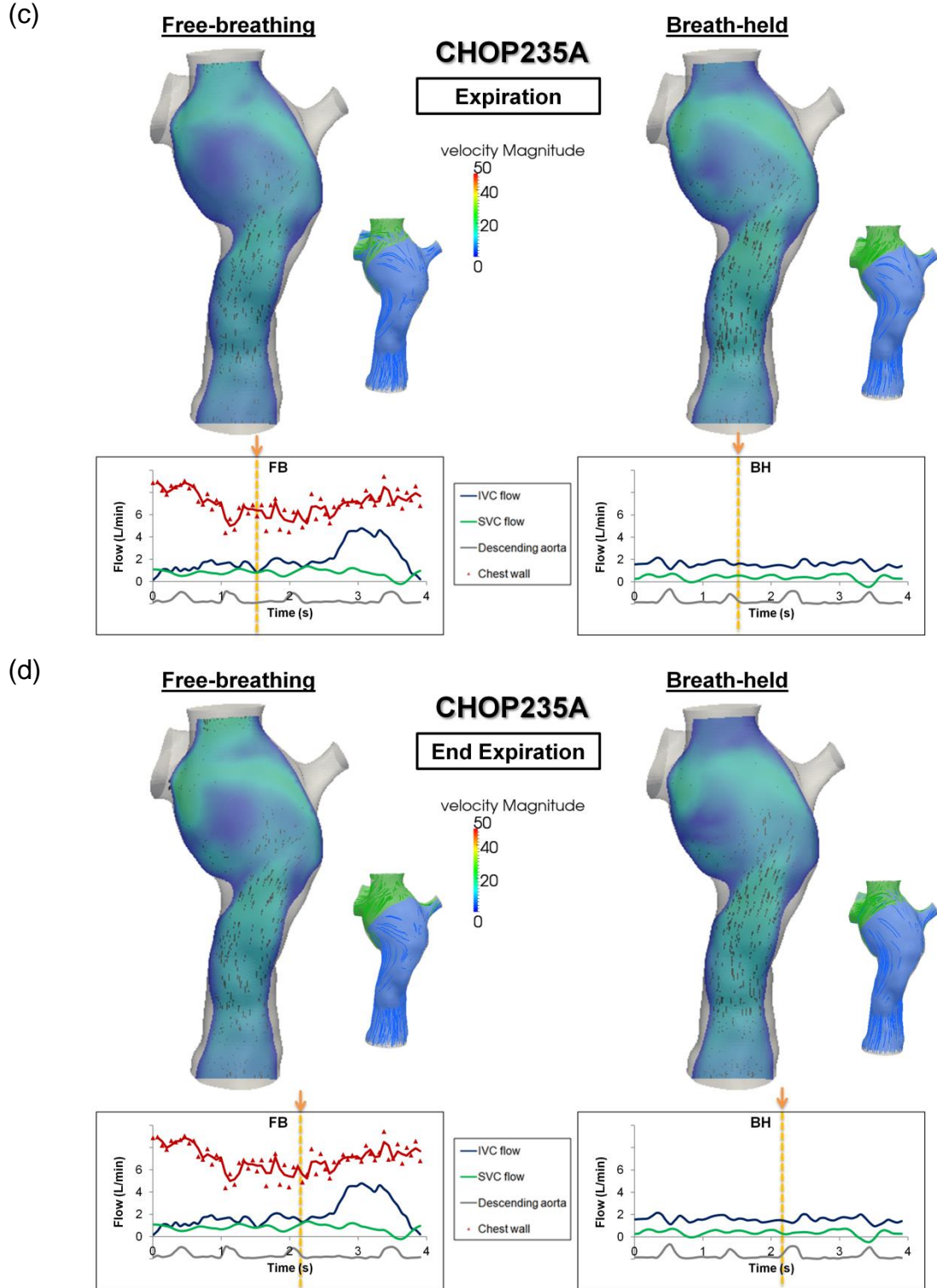
Figure 6.13 Flow fields in the TCPC under free-breathing and breath-held conditions for CHOP235A, throughout different phases of the respiratory cycle: (a) inspiration, (b) end inspiration, (c) expiration, (d) end expiration. (Velocity magnitude unit: cm/s)

Animation 6.3 Particle tracking video of CHOP235A under FB condition. Particles were seeded at the FP and SVC for on respiratory cycle and colored by velocity magnitude (animation_6.3_CHOP235A_FB_vel.avi, 3.56MB)

Animation 6.4 Particle tracking video of CHOP235A under BH condition. Particles were seeded at the FP and SVC for on respiratory cycle and colored by velocity magnitude (animation_6.4_CHOP235A_BH_vel.avi, 3.15MB)
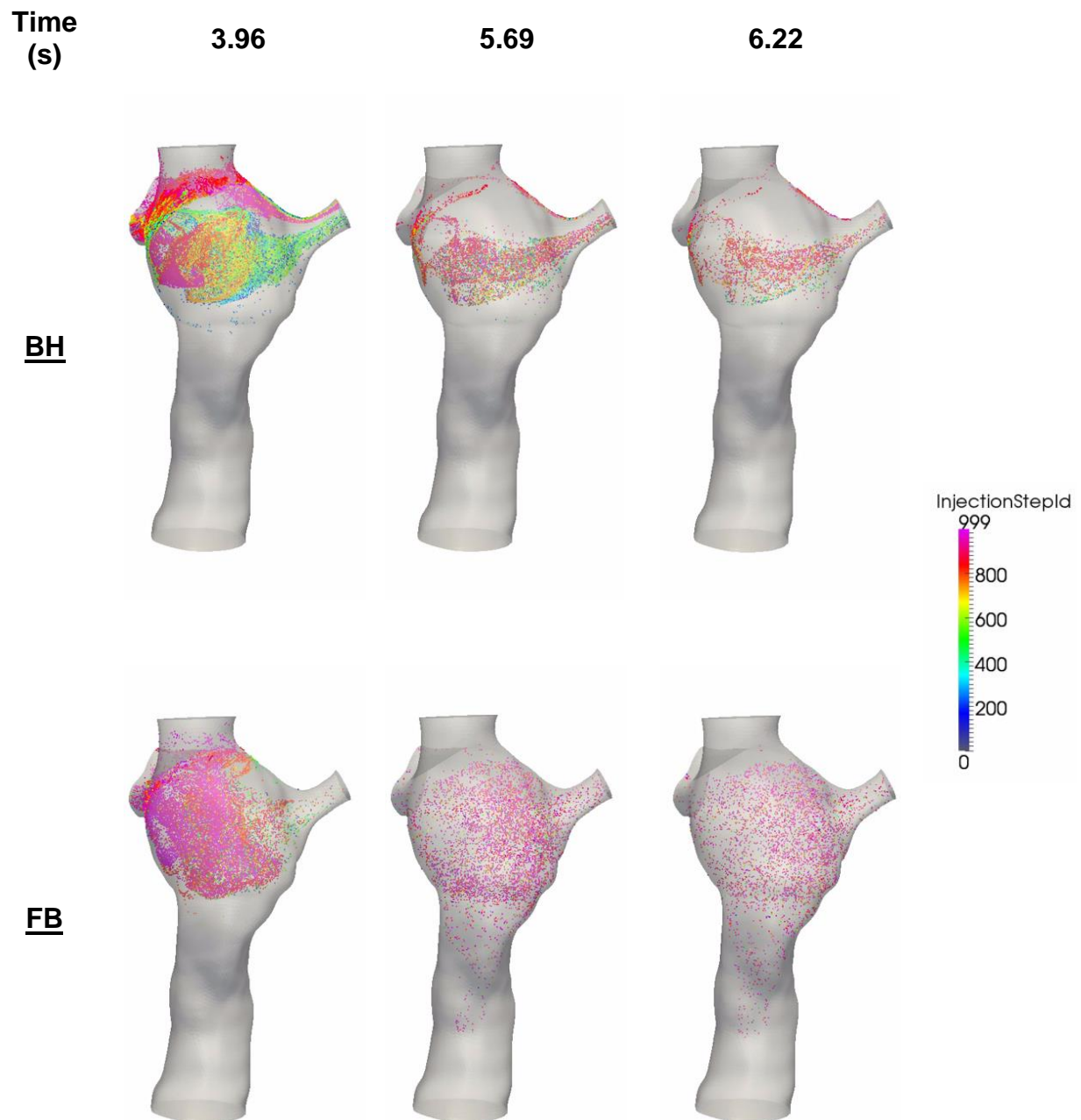
Figure 6.14 Screenshots of the particle tracking videos of CHOP235A with particles seeded at the SVC under FB and BH conditions. Higher Injection Step ID corresponds to particles released later in time.

Animation 6.5 Particle tracking video of CHOP235A under FB condition. Particles were released only at the SVC for one respiratory cycle and are colored by its release time step (animation_6.5_CHOP235A_FB_injstep.avi, 3.20MB)

Animation 6.6 Particle tracking video of CHOP235A under BH condition. Particles were released only at the SVC for one respiratory cycle and are colored by its release time step (animation_6.6_CHOP235A_BH_injstep.avi, 3.15MB)

6.4.1.8 Bilateral SVC - CHOP091C (Intra-atrial)

The velocity field in the TCPC of CHOP091C throughout different phases of the respiratory cycle is illustrated in Figure 6.15. The velocity field between inspiration, end inspiration and end expiration were very different between FP and BH conditions (Figure 6.15 (a), (b) and (d)). The velocity field during expiration was similar between the two conditions (Figure 6.15 (c)).

(c)

CHOP091C

Free-breathing **Expiration** **Breath-held**

velocity Magnitude

(d)

CHOP091C

Free-breathing **End Expiration** **Breath-held**

velocity Magnitude

197
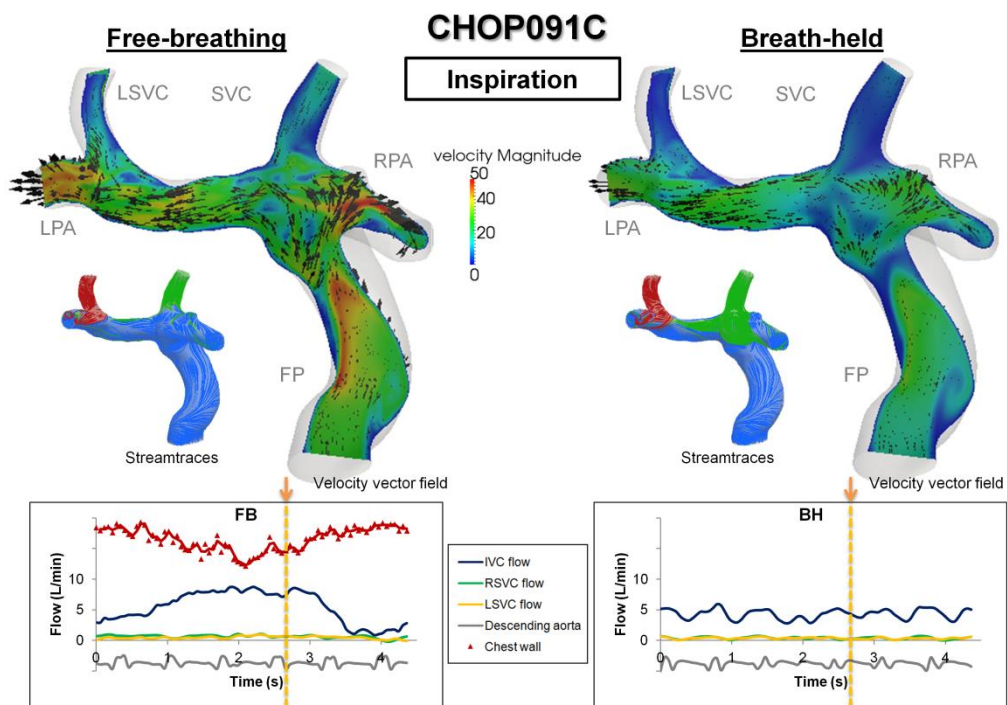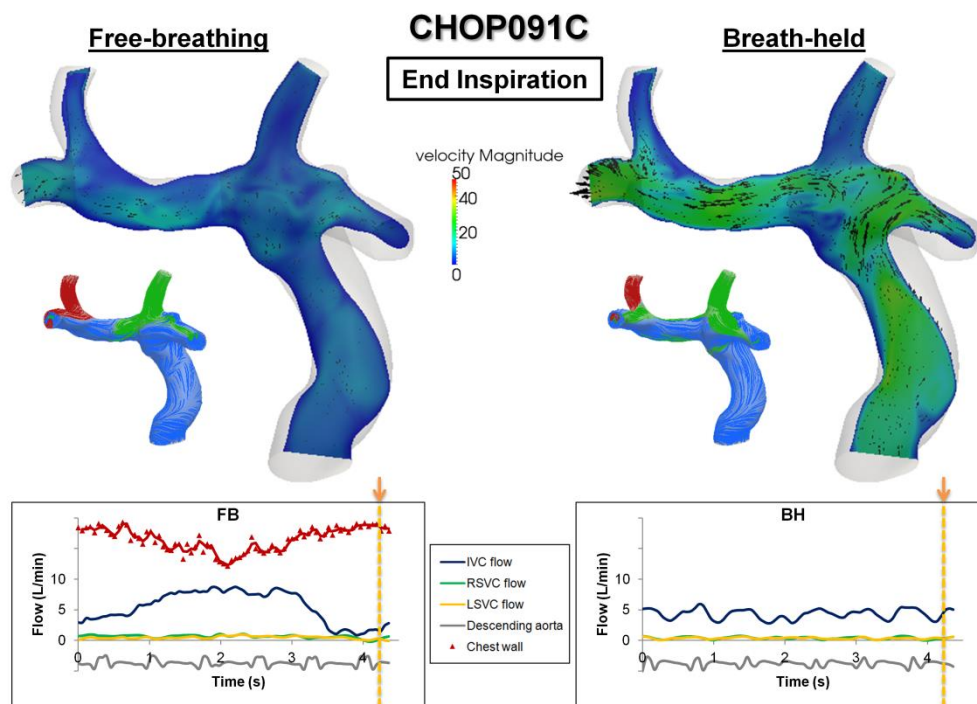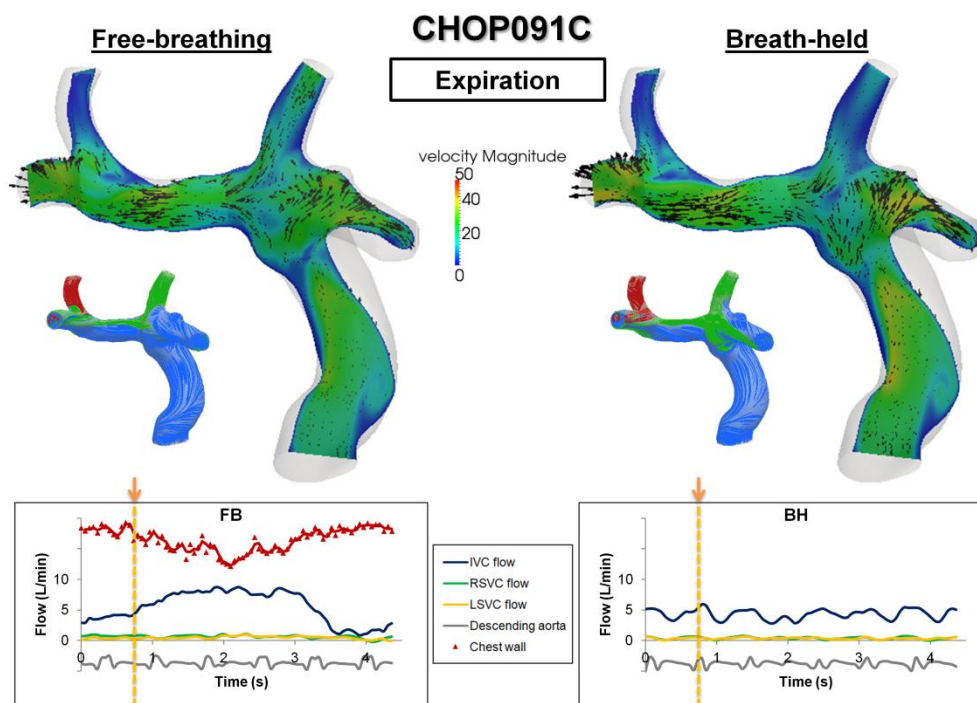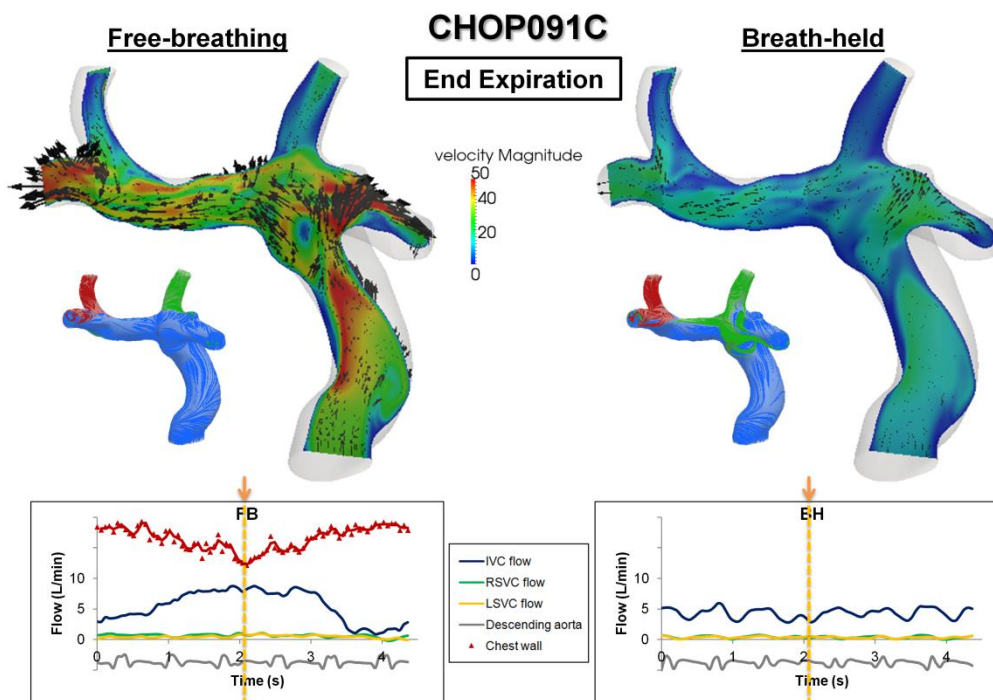
(e)
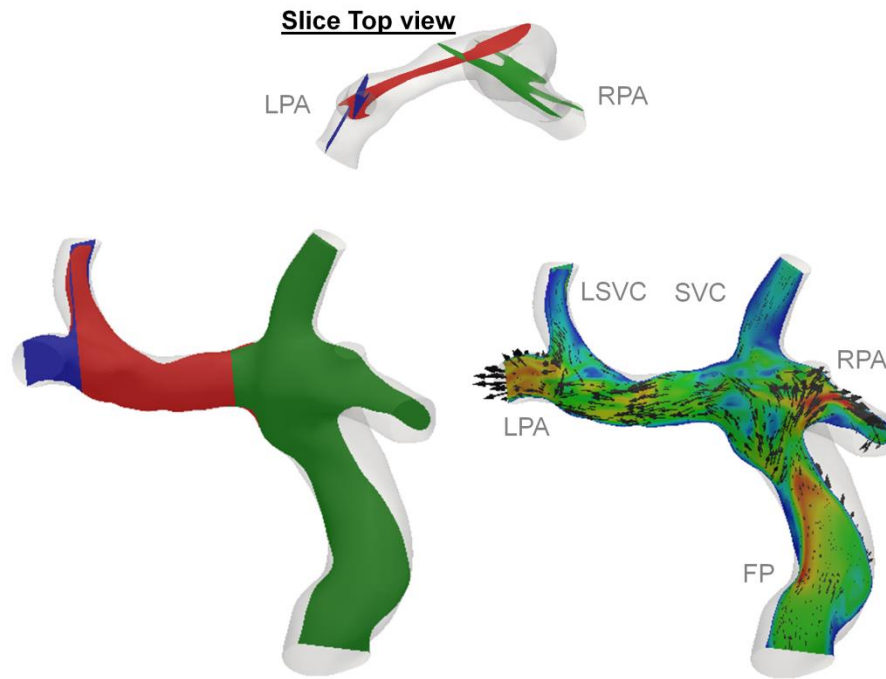
Figure 6.15 Flow fields in the TCPC under free-breathing and breath-held conditions for CHOP091C, throughout different phases of the respiratory cycle: (a) inspiration, (b) end inspiration, (c) expiration, (d) end expiration. Since it was difficult to obtain one planar surface to represent the TCPC flow field in this patient, 3 separate slices were extracted and overlaid to visualize the flow field. The slice locations are shown in (e). (Velocity magnitude unit: cm/s)

6.4.1.9   Bilateral SVC - CHOP229A (Intra-atrial)

The velocity field in the TCPC and FP of CHOP229A throughout different phases of the respiratory cycle is visualized in Figure 6.16. During inspiration, the direction of the velocity vectors was similar between FB and BH conditions but the velocity magnitude was different (Figure 6.16 (a)). The velocity field was very different between the two conditions during expiration (Figure 6.16 (c)). The velocity field was similar between FB and BH conditions during end expiration (Figure 6.16(d)). From the particle tracking videos of CHOP229A (animation 6.7 (FB) and 6.8 (BH)), retrograde flow was observed in the FP during FB condition. There was also recirculation in the upstream section of

the FP (also illustrated in Figure 6.16(c)) under FB condition. These flow features were

not observed under BH condition.
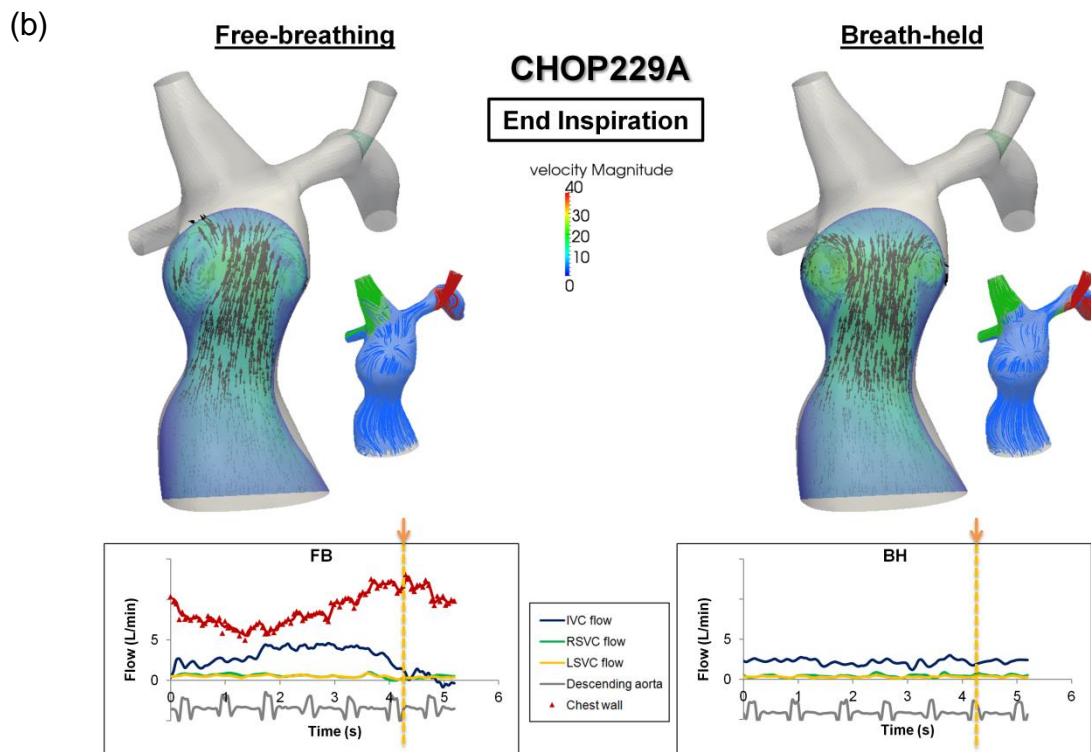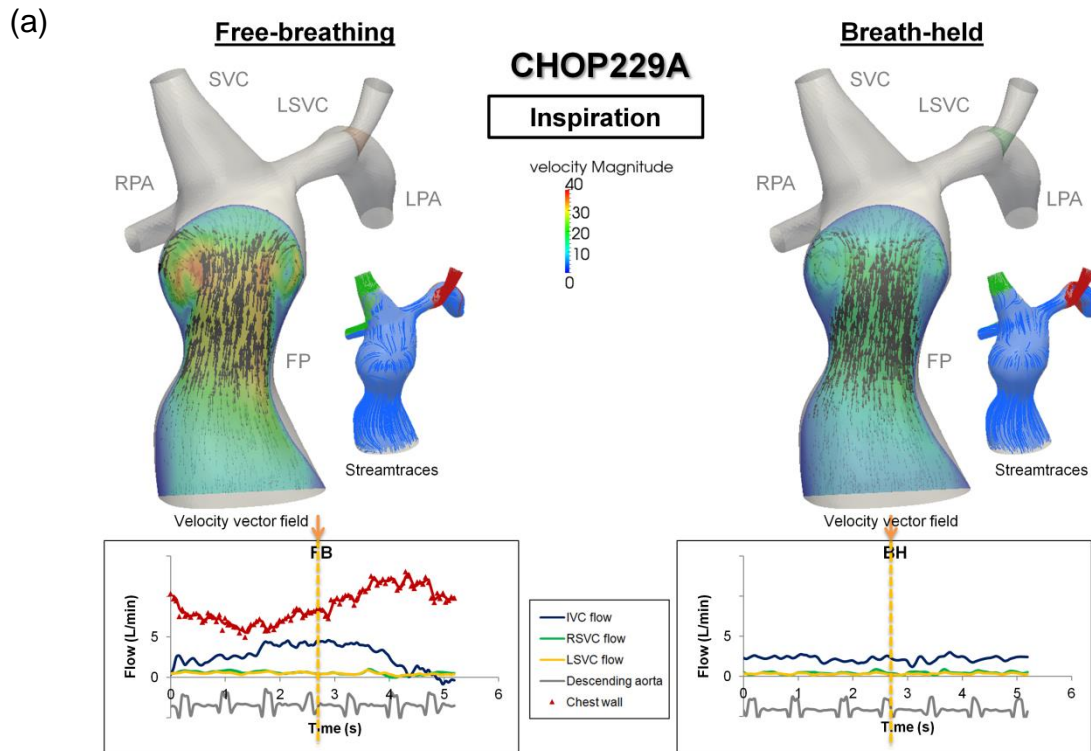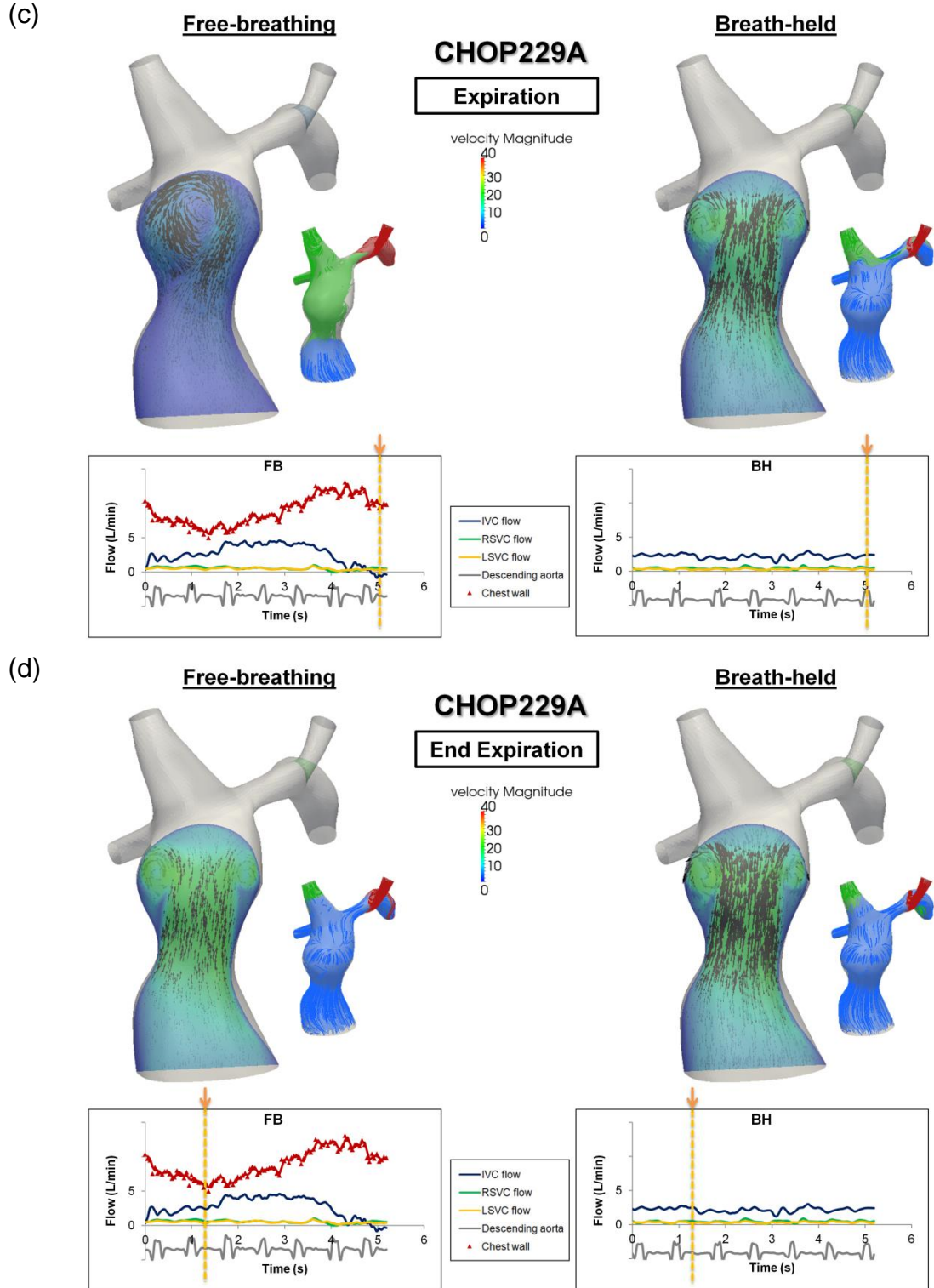
Figure 6.16 Flow fields in the TCPC under free-breathing and breath-held condition for CHOP229A, throughout different phases of the respiratory cycle: (a) inspiration, (b) end inspiration, (c) expiration, (d) end expiration. (Velocity magnitude unit: cm/s)

Animation 6.7 Particle tracking video of CHOP0229A under FB condition. Particles were seeded at the FP and SVC for on respiratory cycle and colored by velocity magnitude (animation_6.7_CHOP229A_FB.avi, 2.97MB)

Animation 6.8 Particle tracking video of CHOP0229A under BH condition. Particles were seeded at the FP and SVC for on respiratory cycle and colored by velocity magnitude (animation_6.8_CHOP229A_BH, 2.61MB)

6.4.2 Quantitative Comparison

To quantify the flow field differences between FB and BH conditions, particle washout times were computed under both FB and BH conditions with the particle tracking results. The results are summarized in Table 6-5. Also, the presence of retrograde flow in the vessels under each condition is summarized in Table 6-6. Three patients (CHOP029B, CHOP032C and CHOP103B) had higher particle washout times under BH

condition compared to FB condition. CHOP155A and CHOP234A had no difference in washout time between the two conditions. Four patients (CHOP011B, CHOP091C, CHOP229A and CHOP235A) had higher particle washout time under FB condition. CHOP229A and CHOP235A had the highest particle washout time under FB condition of all the patients investigated. As confirmed by the particle tracking videos, retrograde flow (Table 6-6) in CHOP011B (animation 6.1), CHOP229A (animation 6.7) and flow recirculation for CHOP235A (animation 6.3) under FB conditions caused the injected particles to stay in the fluid domain much longer than under BH conditions.

Table 6-5 Particle washout times computed from particle tracking results under FB and BH conditions

Particle washout time	Duration of one respiratory cycle (sec)	Number of respiratory cycles			Duration of one cardiac cycle (sec)	Number of cardiac cycles		
		Free-breathing (FB)	Breath-held (BH)	FB - BH		Free-breathing (FB)	Breath-held (BH)	FB - BH
CHOP011B	4.248	1.28	1.08	0.20	1.05	5.18	4.37	0.81
CHOP029B	3.100	1.49	1.74	-0.25	1.02	4.53	5.29	-0.76
CHOP032C	2.8866	1.08	1.29	-0.21	0.83	3.76	4.49	-0.73
CHOP091C	4.420	1.30	1.14	0.16	0.71	8.09	7.10	1.00
CHOP103B	5.100	1.08	1.16	-0.08	1.02	5.40	5.80	-0.40
CHOP155A	2.96	1.17	1.17	0	0.74	4.68	4.68	0
CHOP229A	5.24	2.37	1.10	1.27	0.67	18.54	8.60	9.93
CHOP234A	3.96 (FB) 3.5 (BH)	1.06	1.06	0	0.88 (FB) 0.76 (BH)	4.77	5.02	-0.25
CHOP235A	3.9725	3.77	1.86	1.91	0.94	15.93	7.86	8.07
Average	3.96	1.62	1.29	0.33	0.87	7.87	5.91	1.96
Standard Deviation	0.88	0.90	0.30	0.74	0.15	5.48	1.56	4.06

Table 6-6 wPI and Presence of retrograde flow in the TCPC inlets under FB and BH conditions

	Free-breathing (FB)				Breath-held (BH)				(FB wPI) - (BH wPI)
	wPI	FP	SVC	LSVC	wPI	FP	SVC	LSVC	
CHOP011B	256%	Y	Y	--	70%	N	N	--	186%
CHOP029B	129%	N	N	--	98%	N	N	--	31%
CHOP032C	174%	N	Y	--	72%	N	N	--	102%
CHOP091C	156%	N	Y	Y	89%	N	Y	N	67%
CHOP103B	206%	N	Y	--	178%	N	Y	--	28%
CHOP155A	79%	N	N	--	52%	N	N	--	27%
CHOP229A	195%	Y	Y	N	99%	N	N	N	96%
CHOP234A	215%	N	N	--	79%	N	N	--	136%
CHOP235A	221%	N	Y	--	123%	N	Y	--	98%
Average ± Standard Deviation	181± 54%				96± 37%				86±54%

Y = has retrograde flow, N = no retrograde flow

Global pulmonary flow distribution (PFD) and HFD under FB and BH conditions were computed and summarized in Table 6-7. Comparing FB and BH conditions, the maximum difference observed in HFD was 7%. The preference of hepatic flow to the left/right lungs remained unchanged with the simulated free-breathing and breath-held conditions, except for CHOP235A. For CHOP235A, under FB condition %HFD(LPA) was less than 50% (higher hepatic flow to the right lung). Under BH condition, %HFD(LPA) was greater than 50% (higher hepatic flow to the left lung).

Table 6-7 Pulmonary Flow Distribution (PFD) and Hepatic Flow Distribution (HFD) under FB and BH conditions

	%PFD(LPA)	%HFD(LPA)		
		Free-breathing (FB)	Breath-held (BH)	Difference between FB & BH
CHOP011B	46%	42%	43%	1%
CHOP029B	27%	39%	43%	4%
CHOP032C	25%	29%	26%	3%
CHOP091C	38%	32%	30%	2%
CHOP103B	53%	50%	50%	0%
CHOP155A	52%	57%	56%	1%
CHOP229A	49%	40%	43%	3%
CHOP234A	41%	28%	30%	2%
CHOP235A	31%	48%	55%	7%
Average ± Standard Deviation	40±11%	40±10%	42±11%	2±2%

The calculated wPI and the simulated TCPC power losses are summarized in Table 6-8. For each patient, power loss was the highest under FB (pulsatile) condition; then in descending order: FB (time-averaged flow), BH (pulsatile), and BH (time-averaged flow). In all patients and at all conditions, pulsatile TCPC power loss was higher than time-averaged TCPC power loss.

Table 6-8 wPI and simulated TCPC power loss under FB and BH conditions

	wPI		FB TCPC power loss (mW)		BH TCPC power loss (mW)		dPL		Difference between FB dPL & BH dPL
	FB	BH	Puls	Time-avg	Puls	Time-avg	FB	BH	
CHOP011B	256%	70%	8.43	5.31	4.75	4.62	37%	3%	34%
CHOP029B	129%	98%	13.63	11.84	9.77	9.05	13%	7%	6%
CHOP032C	174%	72%	72.61	57.75	33.37	32.38	20%	3%	17%
CHOP091C	156%	89%	10.43	6.28	3.45	3.1	40%	10%	30%
CHOP103B	206%	178%	14.01	10.58	6.99	6.02	24%	14%	10%
CHOP155A	79%	52%	102.77	100.79	61.24	60.50	2%	1%	1%
CHOP229A	195%	99%	17.75	11.42	6.8	6.29	36%	8%	28%
CHOP234A	215%	79%	81.86	63.00	62.11	60.20	23%	3%	20%
CHOP235A	221%	123%	4.25	2.9	1.39	1.33	32%	4%	28%
Average ± Standard Deviation	181 ± 54%	96 ± 37%	36.19 ± 38.15	29.99 ± 35.05	21.10 ± 24.86	20.39 ± 24.45	25 ± 12%	6 ± 4%	19 ± 12%

Puls = Pulsatile; Time-avg = Time-averaged

Table 6-9 iPL and TCPC resistances under FB and BH conditions

	FB iPL		BH iPL		diPL		FB TCPC resistance (WU.m^2)		BH TCPC resistance (WU.m^2)	
	Puls	Time-avg	Puls	Time-avg	FB	BH	Puls	Time-avg	Puls	Time-avg
CHOP011B	0.016	0.010	0.011	0.010	37%	3%	0.54	0.34	0.34	0.33
CHOP029B	0.007	0.006	0.007	0.007	13%	7%	0.42	0.37	0.37	0.35
CHOP032C	0.089	0.070	0.118	0.115	20%	3%	3.41	2.72	3.19	3.10
CHOP091C	0.002	0.001	0.002	0.001	40%	10%	0.20	0.12	0.11	0.10
CHOP103B	0.013	0.010	0.010	0.009	24%	14%	0.81	0.61	0.53	0.45
CHOP155A	0.012	0.012	0.015	0.015	2%	1%	1.31	1.29	1.30	1.28
CHOP229A	0.019	0.012	0.014	0.013	36%	8%	1.12	0.72	0.66	0.61
CHOP234A	0.01	0.008	0.01	0.01	23%	3%	1.04	0.80	0.95	0.92
CHOP235A	0.012	0.008	0.012	0.011	32%	4%	0.42	0.29	0.29	0.28
Average ± Standard Deviation	0.020 ± 0.026	0.015 ± 0.021	0.022 ± 0.036	0.021 ± 0.035	25±12%	6±4%	1.03 ± 0.97	0.81 ± 0.80	0.86 ± 0.95	0.82 ± 0.93

Puls = Pulsatile; Time-avg = Time-averaged

The computed iPL and TCPC resistances of all patients for all conditions are summarized in Table 6-9. The difference between FB iPL and BH iPL were computed ($[iPL_{FB}-iPL_{BH}]/iPL_{FB,}$), and were plotted with FB wPI. From Figure 6.17, it is observed that the difference in iPL between the two conditions was related to FB wPI. diPL was then computed under each condition to account for the slight difference in iPL between time-averaged FB and time-averaged BH conditions. In this cohort, diPL ranged from 2-40% under FB condition and 1-14% under BH condition. Comparing the two conditions, diPL was significantly higher under FB condition ($p=0.001$).
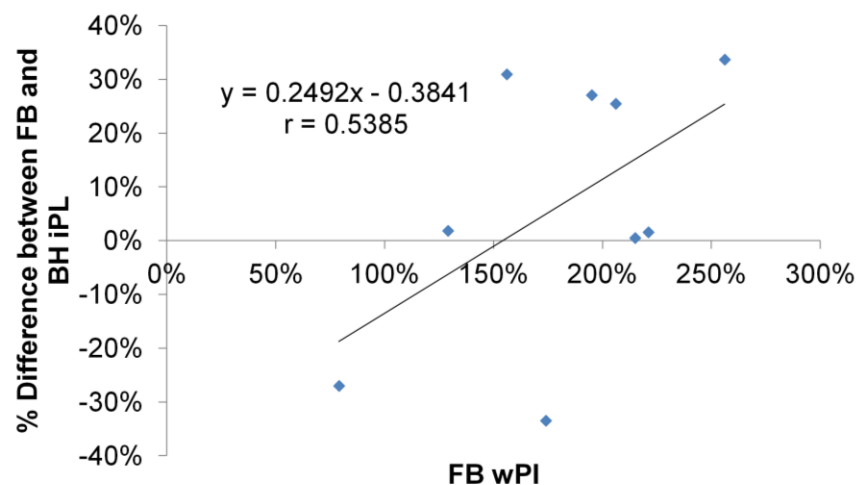
Figure 6.17 Relationship between FB wPI and the difference in iPL between FB and BH conditions

The relationship between wPI and diPL is illustrated by Figure 6.18. Combining all patients and all conditions, higher wPI was related to higher diPL. Excluding patients with bilateral SVC (CHOP091C and CHOP229A), stronger correlation between diPL and wPI is observed (Figure 6.19).
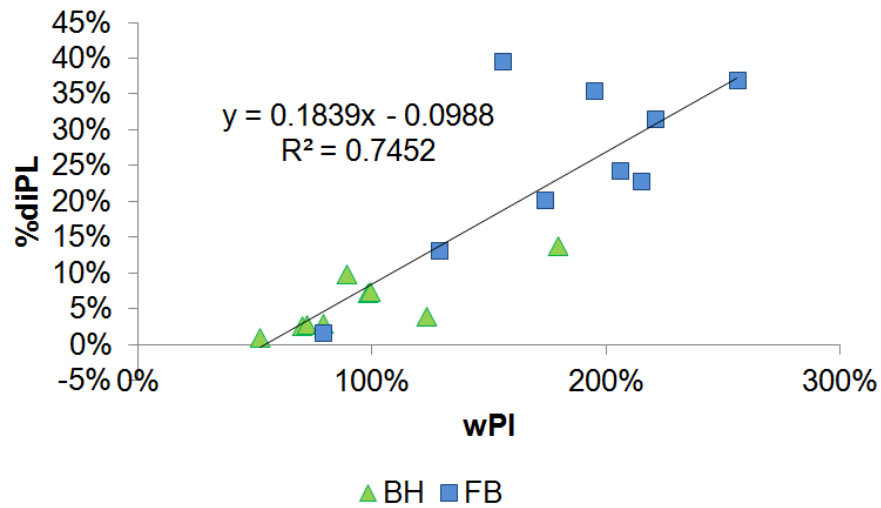
Figure 6.18 Relationship between wPI and diPL (blue data points = FB; green data points =BH)
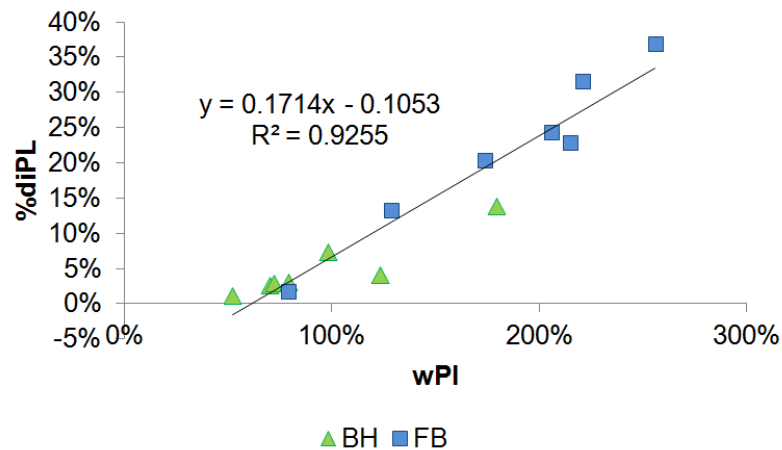
Figure 6.19 Relationship between wPI and diPL for the 7 patients with single SVC (blue data points = FB; green data points =BH)

6.5 Discussion

Clinically, when evaluating flow in the TCPC, breath-held CMR acquisitions are often routinely performed, especially in adult patients. However, recent studies have provided evidence that TCPC hemodynamics can be affected by respiration. Without the

presence of a sub-pulmonary ventricle, flow through the TCPC is thought to be passive. Change in intra-thoracic pressure during respiration can impact TCPC flow. The impact of respiration on the TCPC vessel flow waveform has been documented in literature [131-133]. However, the impact of breath-holding on TCPC flow field is not well understood, especially considering the passive nature of flow through the TCPC without the sub-pulmonary ventricle. Using patient specific flow and geometry, Marsden et. al. [91] simulated TCPC hemodynamics computationally by including respiratory influence in the IVC and SVC flow waveforms. This was done by superimposing patient specific flow waveform of a cardiac cycle with the flow waveform of a respiratory cycle from Hjortdal et. al. [134] Compared with steady flow model, the respiration model has reduced energetic efficiency. However, comparison of TCPC hemodynamics with and without respiration is still lacking to fully understand its influence. This study compared TCPC vessel flows and flow fields under BH and FB conditions, which allowed for the isolation of respiration effects from cardiac flow pulsatility.

From the *in vivo* flow waveform analysis (Chapter 6.3), it was observed that PIs of each caval vein in the TCPC as well as wPI were significantly higher under FB conditions than BH conditions. This suggests that respiratory-driven flow pulsatility can be important, as BH wPI included the effect of cardiac flow-driven pulsatility, and FB wPI included the effect of both combined respiratory and cardiac flow-driven pulsatility.

Utilizing CFD analysis, the differences in TCPC flow field under FB (respiratory-driven and cardiac-driven pulsatility) and BH (cardiac-driven pulsatility only) flow conditions were investigated. As observed in the velocity fields of the extracted slices, during

inspiration and end inspiration under FB condition, higher flow rate through the TCPC resulted in increased velocity magnitude within the TCPC. This agrees with the findings from previous studies that showed increased IVC flow during inspiration in Fontan patients [134]. During inspiration, the negative intra-thoracic pressure in the chest cavity assists the forward flow in the SVC and the PAs, increasing venous return as compared to expiration. During expiration and end expiration, the velocity magnitude and direction of velocity vectors share more similarity between the FB condition and BH condition. This is an interesting result since the BH data were acquired during end expiration, while under FB the patient was transiently passing from expiration to inhalation.

As observed in the particle tracking results, TCPC flow fields under FB and BH conditions could be very different. Particle washout time was investigated for its potential impact on flow-induced thrombus formation, also to provide quantitative information about flow stagnation [209, 210]. Particle washout time was computed for each condition for each patient. It was higher under FB conditions in 4 patients (CHOP011B, CHOP91C, CHOP229A, CHOP235A) and higher under BH conditions in the other 3 patients (CHOP029B, CHOP032C, CHOP103B).

For the four patients with higher particle washout time during the FB conditions, this could be due to the differences in wPI between the two conditions. As shown in Table 6-6, CHOP011B, CHOP091C, CHOP229A and CHOP235A had large differences in wPI between FB and BH conditions. The higher washout time under FB was also due to the presence of retrograde flow in certain caval veins under FB conditions, which was

absent under BH conditions (Table 6-6). A possible explanation for the retrograde flow seen in these patients is the increase in intra-thoracic pressure during expiration. In CHOP011B and CHOP229A, retrograde flows were observed both at the FP and SVC under FB conditions, but not under BH conditions. In CHOP091C, reverse flow was observed in the LSVC under FB condition but not under BH condition. The retrograde flow caused the seeded particles to travel backwards and hence, take longer to leave the TCPC. In CHOP235A, the SVC flow was higher than the FP flow at certain time points, causing the SVC flow to penetrate into the FP. This resulted in different flow mixing and recirculation patterns compared to the BH condition; hence it took longer for the seeded particles to leave the TCPC under FB conditions.

The particle tracking results for these patients also suggest that the sensitivity of a TCPC's flow field during breathing is a function of its specific geometry. In the two patients where particle washout time was the highest under FB conditions (CHOP229A and CHOP235A), the TCPCs had enlarged FP pathways compared to other patients. As shown in previous studies, the intra atrial FP usually has an enlarged pathway, which promotes flow recirculation and mixing within the FP [27, 194, 195], an observation that this current study confirms. As observed in the particle tracking animations (animation 6.3, 6.4 (CHOP235A) and animation 6.7, 6.8 (CHOP229A)), very different flow mixing patterns in the FP were observed between the two conditions. Also, for CHOP235A, the observed penetration of SVC flow into the FP when SVC flow was higher was due to the absence of caval offset in the TCPC [59, 61]. Future studies

should further investigate the possible confounding effect of patient specific geometry on the relationship between respiration and TCPC hemodynamics.

For two of the patients where particle washout time was higher under BH conditions (CHOP029B and CHOP103B), there was no difference in the presence/absence of retrograde flow between FB and BH conditions (Table 6-6). The wPIs between the two conditions were also similar. The lower particle washout time during the FB conditions could potentially be due to the higher time-averaged total systemic return during FB (CHOP029B FB= 5.02L/min, BH = 4.52 L/min; CHOP103B FB = 3.87L/min, BH = 3.39L/min). Since the TCPC flow carries higher velocity during FB than BH conditions, it takes less time for the seeded particles to leave the TCPC in the FB condition. For CHOP32C, even though wPI was higher under the FB condition and there was retrograde flow in the SVC (under FB condition), particle washout time was higher under the BH condition. This could be explained by the higher time-averaged total systemic return during FB (FB = 3.96L/min, BH = 2.78L/min). In addition, unlike CHOP229A and CHOP235A, these three patients had tubular SVCs and FPs, which eliminated the flow recirculation that took place in CHOP229A and CHOP235A under both FB and BH conditions.

The much higher washout time and flow recirculation in CHOP229A and CHOP235A under FB condition suggests it may be important to maintain an FP with relatively uniform diameter. The intra atrial pathway usually forms a bulge, which promotes flow recirculation and mixing within the Fontan pathway (FP) prior to entering the pulmonary arteries (PAs) [27, 194, 195]. The extracardiac conduit has more uniform cross sectional

area along the vessel which results in a more streamlined flow [196]. It has been demonstrated that such variability can in turn translate to differences in flow dynamics within the systemic venous pathway [47, 197]. By including respiration effects, this difference can potentially be exacerbated, which should be addressed in future work with increased sample size.

Hepatic flow distribution (HFD) was computed and compared between FB and BH conditions. The maximum difference in HFD between the two conditions was 7%. Even though different flow mixing patterns were observed in some cases between the two conditions, and since the left and right lung resistances were assumed to be constant under FB and BH conditions, it was not surprising that only small difference in HFD were observed.

TCPC power loss is a common metric used to quantify the energy dissipation through the TCPC, which is relevant to patient exercise performance [2, 189]. TCPC power loss is often quantified by CFD simulations using patient flow waveforms obtained from CMR or echocardiography. From this study, it is observed that TCPC power loss ranked in the following decreasing order: FB (pulsatile flow condition), FB (time-averaged flow condition), BH (pulsatile flow condition), BH (time-averaged flow condition). TCPC power loss is higher under the FB than the BH condition because:

(i) The time-averaged flow is higher under the FB condition

(ii) The flow pulsatility is higher under the FB condition

Earlier studies often assumed time-averaged flow in the CFD simulations of TCPC power loss, due to the passive nature of flow within the TCPC. Recently, there has been growing evidence that cardiac-driven flow pulsatility can be non-negligible. Khiabani et. al. [153] quantified TCPC power loss under resting breath-held conditions within a cardiac cycle, and with time-averaged flow boundary conditions using CFD simulations. The wPI of the patients in this cohort was up to ~170%. Khiabani et. al. demonstrated that cardiac-driven flow pulsatility can increase TCPC power loss.

In agreement with Khiabani et. al., pulsatile TCPC power losses (both FB and BH) quantified in the current study were higher than time-averaged power losses. The current study expands these findings by including the impact of respiratory-driven flow pulsatility in addition to cardiac-driven flow pulsatility. Comparing FB and BH conditions, diPL was higher in FB condition, since wPI was higher under the FB condition for all patients. This suggests that respiratory-driven flow pulsatility, in addition to cardiac-driven flow pulsatility, can impact TCPC flow fields and power losses.

To speculate that the effect of flow pulsatility on TCPC power loss, the following explanation is proposed. From the Navier Stokes equation, the unsteadiness term is represented by $\rho_f\left(\frac{\partial u}{\partial t}\right)$:

$$\rho_f\left(\frac{\partial u}{\partial t} + (u \cdot \nabla)u\right) - \nabla \cdot \sigma_f = g_f \quad \text{(Equation 6.18)}$$

where ρ_f represents fluid density, u is fluid velocity and g_f is body force (which is zero). σ_f is Cauchy stress tensor. Here the change in velocity in the TCPC inflow is approximated as:

$$\frac{dV}{dt} = \frac{dV_{IVC}}{dt} + \frac{dV_{SVC}}{dt} \qquad \text{(Equation 6.19)}$$

Where V_{IVC} and V_{SVC} are the average velocity (flow divided by area) at each time point:
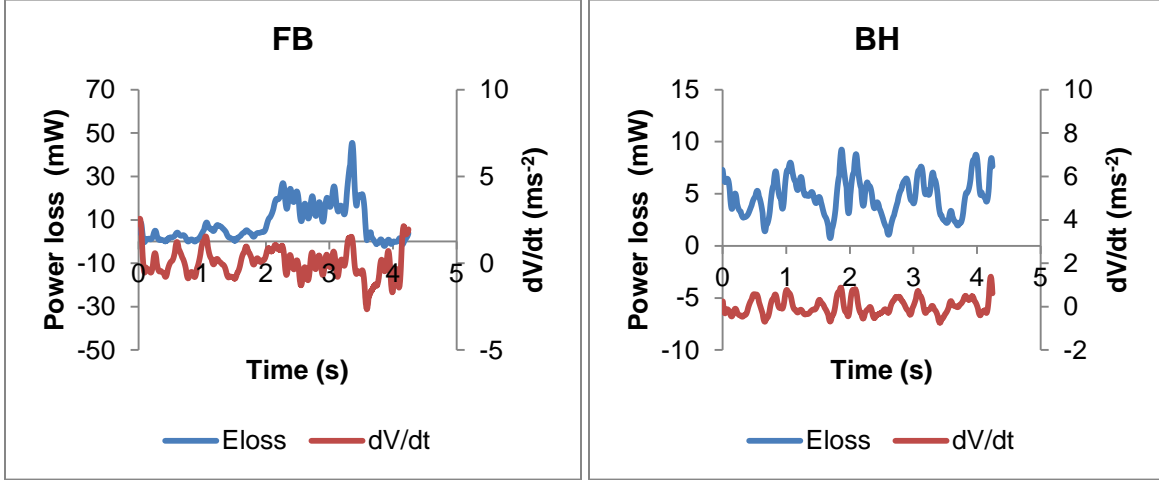
Figure 6.20 TCPC power loss and sum of rate of change of velocity at the inlets within the respiratory cycle under the FB and BH conditions

As observed in Figure 6.20, the fluctuations in dV/dt corresponded to the time points where power loss was fluctuating in time. To quantify the magnitude of dV/dt, the root mean square (RMS) value of dV/dt is computed for each condition. The RMS value of dV/dt under FB condition was 0.61 ms^{-2}, and that of BH was 0.28 ms^{-2} for this patient (CHOP011B). The magnitude of fluctuation under FB conditions was higher than BH, suggesting that the energy dissipation due to the flow unsteadiness is higher under FB condition than BH. The acceleration and deceleration (dV/dt) in flow under FB condition lead to more changes in the flow field and also contribute to more energy loss.

The higher power loss under FB pulsatile condition compared to FB time-averaged condition could be due to wall shear stress. From the Womersley solution of pulsatile flow through a cylindrical tube:

$$\frac{2}{R}\left(\frac{-\tau_{wall}}{\mu}\right) = \frac{1}{v\pi R^2}\frac{\partial Q}{\partial t} + \frac{1}{\mu}\frac{dp}{dx} \qquad \text{(Equation 6.20)}$$

where τ_{wall} is the wall shear stress, R is the radius of the tube, µ is dynamic viscosity, x is the axial direction along the cylinder

The change in flow rate under pulsatile condition contributes to a larger $\frac{\partial Q}{\partial t}$ compared to the time-averaged condition. This led to higher wall shear stress, hence causing higher TCPC power loss under the pulsatile condition.

The results from the current study also confirmed the notion that diPL increases with wPI of the TCPC (as shown in Figure 6.18), even under the influence of respiration. After excluding patients with bilateral SVC, stronger linear correlation was observed between diPL and wPI (Figure 6.19). This could be caused by the presence of a caval offset between the LSVC and FP in patients with bilateral SVCs. The results from this study suggest that wPI can be used as a metric to estimate the impact of ignoring respiratory-driven flow pulsatility and cardiac-driven flow pulsatility in the evaluation of TCPC power loss. As demonstrated in Figure 6.19, for patients with a single SVC and with a wPI of less than 100%, time-averaged flow boundary conditions can be used with relatively small error (diPL < 10%). With 100% < wPI < 200%, diPL will range from 10% to 25%. With wPI > 200%, which was seen in all free-breathing conditions, diPL can be

higher than 25%. Ignoring flow pulsatility above such wPI levels can lead to difference in diPL of more than 25%.

6.6   Limitations

In this study, rigid wall was assumed for all CFD simulations. In addition, outlet flow was estimated by the 3-element Windkessel model to mimic relative left and right lung resistances, which were obtained, for all patients, by LPA and RPA time-averaged flows from PC-MRI. In addition, respiration was only studied as an effect of vessel flow. Its interaction with changes in intra-thoracic pressures and vessel compliance warrants future investigations. Also, even though it was assumed that the only difference between breath-hold and free-breathing conditions was with or without breathing, the two conditions were still acquired as different image acquisitions. Also, the respiratory cycle in this work was identified by tracing the change in chest wall area from a transverse MRI image. Note that chest wall motion in reality is 3-dimensional. Two different CFD solvers were used in order to simulate cases with moderate Reynolds numbers. However, this should not affect the comparison between FB and BH conditions since the same solver was applied for simulations of the same patient.

6.7   Clinical Significance

The impact of acquiring TCPC vessel flow under BH conditions was investigated in this study. This study highlights that the impact of respiration on TCPC power loss and

TCPC flow fields. The findings from this specific aim suggest that evaluating TCPC hemodynamics under BH condition can affect TCPC power loss estimation.

This study also shows the importance of MRI sequence selection on evaluating TCPC hemodynamics. Provided that the relative resistances of the left and right pulmonary circulation are consistent among FB and BH conditions (assumption made in this work), breath-holding has little effect on the observed HFD. However, when quantifying TCPC power loss, utilizing breath-holding sequences for patients with high wPI may lead to error in estimation of TCPC power loss.

6.8   Chapter Summary

Instead of a free-breathing (FB) CMR acquisition, a breath-held (BH) acquisition is routinely used to evaluate patient specific TCPC hemodynamics in the clinic. However, this ignores the impact of respiration on TCPC hemodynamics, which is not yet completely understood. In this specific aim, the difference in TCPC flow fields under FB and BH flow conditions was evaluated with the use of real time PC-MRI data acquired under FB and BH conditions. By obtaining the descending aorta flow and chest wall area waveforms on the same image as the TCPC vessel flow acquisition, the duration of cardiac and respiratory cycles were tracked simultaneously with the vessel flow waveform to compare hemodynamic contributions of the two sources of pulsatility. Since the BH condition had only cardiac pulsatility, while the FB condition had both cardiac and respiratory pulsatility, the hemodynamic contributions of the two sources

towards pulsatility could be isolated. The combined flow pulsatility in the vessel was first compared between the FB and BH conditions. Using a Navier-Stokes flow solver with a 3-element Windkessel model at the outlet, patient-specific TCPC hemodynamics were simulated by applying real time PC-MRI waveforms at the inlets and prescribing relative lung resistance at the outlets. Based on this comparison, the effect of respiration on TCPC hemodynamics was isolated.

From *the in vivo* vessel flow waveform analysis, the higher weighted pulsatility index (wPI) under FB condition suggests that respiratory-driven flow pulsatility is non-negligible. Using CFD simulation, it was discovered that the TCPC flow field changed in velocity magnitude and direction within the respiratory cycle. Differences in TCPC flow fields were observed between the FB and BH conditions, especially during inspiration. Quantitative differences in particle washout time and TCPC power loss were also observed between the two conditions, which could be attributed to the magnitude of flow pulsatility, retrograde flow, relative flows between the FP and SVC, and patient specific anatomic features. Additionally, under FB conditions, elevated wPI led to higher indexed power loss differences (diPL) between pulsatile and time-averaged flow conditions. By including all patients and all conditions, positive correlation was observed between wPI and diPL.

The impact of acquiring TCPC vessel flow under BH conditions was investigated in this study. This study highlights that the impact of respiration on TCPC power loss and TCPC flow fields. The findings from this specific aim suggest that evaluating TCPC

hemodynamics under BH condition can affect TCPC power loss estimation. From an engineering standpoint, this study reinforces the importance of pulsatile boundary conditions on modeling of TCPC hemodynamics compared to time-averaged conditions. The results of this study also highlight the importance of including the impact of respiration as boundary conditions in the CFD modeling of TCPC hemodynamics. Last but not least, wPI is a good metric to quantify the effect of cardiac-driven and respiratory-driven flow pulsatility on the evaluation of TCPC power loss.

CHAPTER 7   Specific Aim 3: Investigation of the Effect of Wall Deformation on TCPC Hemodynamics

7.1   Overview

The Fontan procedure is usually completed by constructing an intra-atrial (IA) tunnel or using an extra-cardiac (EC) connection from the IVC to the pulmonary arteries. In all cases, the resulting geometries and constitutive materials can be very different. An IA TCPC is more bulgy and compliant at the IA tunnel where vena caval flows mix and re-circulate prior to entering the PAs [20, 27]. An EC TCPC is composed of a stiffer cylindrical synthetic graft (e.g. Gore-Tex and Dacron grafts) so flow is more streamlined towards the PAs [28].

CFD serves as a valuable tool to resolve the complex flows in the TCPC, and to understand the hemodynamics of the two types of the connections. CFD analysis allows for more detailed analysis of flow structures (i.e. vortices, streamlines, path lines, stagnation points, etc.), pressure distributions, and mechanical stresses (e.g. wall shear stress) than *in vitro* or *in vivo* analyses. To simplify analysis and computational cost, previous studies applied various modeling assumptions, e.g. idealized geometries, rigid wall models and steady flow boundary conditions. Recent image processing technology advancements now allow for patient specific modeling [74, 90, 91] rather than idealized geometries. These studies shifted the computational modeling paradigm to more accurately understand and simulate TCPC hemodynamics.

One limitation of these computational models is the assumption of rigid walls. It has been understood that the expansion and contraction of blood vessels contributes to blood pumping in the body. Bazilevs et al. [129], studied the hemodynamic efficiency differences of realistic extracardiac TCPC geometries between rigid and deformable walls using prescribed wall thickness, which demonstrated the difference in resting and exercise hemodynamics between rigid wall and FSI analysis. Orlando et al. [88], carried out a similar analysis using an idealized TCPC model with prescribed material properties and flow rates in the vena cavae, pulmonary arteries and suture lines, after which they found that deformable model has 10% higher power loss than the rigid model. Long et. al. also performed an FSI CFD analysis of two patient specific extracardiac TCPCs with varying wall properties [130]. The aforementioned studies established the difference between hemodynamics in rigid and deformable TCPC models, but their clinical relevance is still to be investigated as the prescribed wall properties are yet to be validated. In addition, only idealized TCPCs and extracardiac TCPCs were investigated so far. The impact of wall deformation on an intra-atrial TCPC is not well understood.

The objective of this specific aim is to characterize the degree of vessel wall deformation in TCPC vessels and to quantify the difference in TCPC hemodynamics between rigid and compliant walls. An *in vivo* analysis will first be performed to quantify the degree of vessel wall deformation of the TCPC under resting free-breathing (FB) and breath-hold (BH), as well as exercise free-breathing (EX) conditions. The

hypothesis is that TCPC vessel area change is related to both cardiac and respiratory cycles (Figure 7.1). Then, an FSI simulation will be performed on an intra-atrial patient. The wall deformation obtained from the FSI simulations will be compared with the degree of *in vivo* wall deformation. Finally, the qualitative and quantitative difference of TCPC hemodynamics between rigid wall and compliant wall conditions will be compared.
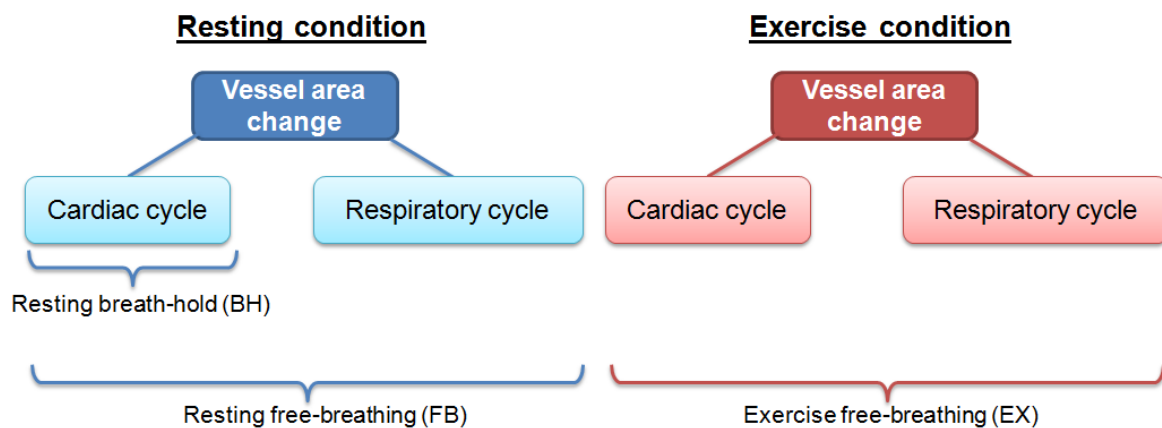
Figure 7.1 Schematic illustrating the hypothesis that vessel area change is related to both cardiac and respiratory cycles

7.2 Specific Aim 3(a): *In Vivo* Characterization of Vessel Wall Deformation

7.2.1 Patient Cohort

Eleven consecutive single ventricle patients with TCPC anatomy were selected from the Georgia Tech–Children's Hospital of Philadelphia Fontan database. Prospective real time CMR data at resting breath-held (BH), resting free-breathing (FB), and exercise (EX) free-breathing conditions were acquired in the enrolled patients. The study was

approved by the institutional review boards (IRB) of both institutions. Patient data were collected with informed consent. The inclusion criteria were: (i) minimum age of 12 years, (ii) TCPC with no other sources of pulmonary flow, (iii) patients were able to perform a metabolic exercise stress test using a stationary cycle ergometer. Exclusion criteria included: (i) a pacemaker or implanted metal, or (ii) severe CMR image artifacts. Two patient cases were excluded because of image artifacts. A total of nine patients were included in this study (Table 7-1, details listed in Appendix A.9.1).

Table 7-1 Demographic detail of the 9 patients analyzed

Patient characteristics	Mean ± standard deviation
Age (years)	21.1 ± 3.8
Body surface area (m^2)	1.77 ± 0.09
Gender (M/F)	5/4
IVC connection type (IA/EC) [†]	8/1
Ventricular morphology (LV/RV/MV) [‡]	3/5/1

† IA – Intra-atrial, EC- Extracardiac.
‡ LV = left ventricle, RV = right ventricle, MV = mixed ventricle

7.2.2 Real-time CMR Acquisition

After the metabolic stress test (as described in Chapter 4.4), the baseline and exercise CMR studies were performed. A 1.5 T Avanto Whole Body system (Siemens Medical Solutions, Malvern, PA) was used for MRI acquisition. The anatomic images acquisition was performed under baseline conditions and the protocol was the same as described in Chapter 4.2.1. An echoplanar (EPI) sequence utilizing shared velocity encoding was utilized to acquire real time PC-MR images [206]. Through-plane PC-MR images across

the IVC/FP (above the hepatic vein confluence), SVC (below the junction with the innominate vein) and the ascending aorta were acquired for at least 10 seconds as separate velocity maps (approximately 20 frames per second). The same imaging protocol was performed under breath-held (BH, acquired at end expiration) and free-breathing (FB) resting conditions. Due to the motion of the heart surrounding the LPA and RPA, PC-MRI images at the LPA and RPA were less clear than the FP and SVC. LPA and RPA images were not acquired for some of the patients hence were not included in this analysis.

After the baseline CMR acquisition, the patients were slid partially out of the bore of the MRI machine. Lower limb exercise using an MRI-compatible supine bicycle ergometer (Lode BV, Groningen, the Netherlands) was performed which allowed RPM-independent workload ranging from 10-250 Watts. The workload was set initially at 20 Watts. It was then increased at a rate of 20 Watts/min progressively to obtain HR at VAT (determined during the exercise stress test). After that, the study subject was returned to the isocenter of the magnet for imaging within 10 seconds. HR was monitored continuously. Real time PC-MRI across the SVC, ascending aorta and descending aorta (which includes the FP on the same slice) were acquired as 3 separate velocity maps. The LPA and RPA were not imaged with the real time sequence, since the motion of the heart during exercise caused a lot of movement in the LPA and RPA, making image acquisition difficult. The patients repeatedly exercised to the target heart rate (heart rate at VAT) for each acquisition. The images were acquired with free-breathing. The study lasted approximately 90 minutes with the patient

lying supine. The FP PC-MRI image sequence was not acquired. However, the FP was segmented from the descending aorta (DAO) PC-MRI images. The image acquisition parameters are summarized in Table 7-2 (details listed in Appendix A.9.2).

Table 7-2 Summary of CMR acquisition parameters for the 9 patients investigated

Real time PC-MRI	Resting	Exercise
Encoding velocity (cm/s)	60-150	60-300
Number of images	199-381	120-199
Temporal resolution (ms)	52-77	52-85

7.2.3 *In Vivo* Wall Deformation Analysis

Vessel cross-sectional area changes were obtained by segmenting real time PC-MRI images at each vessel's cross section (Chapter 4.3.2), using the software Segment [150-152]. The IVC/FP image slice was located above the hepatic vein confluence. The SVC image slice was below the junction with innominate vein. The vessel of interest was first selected on the image slice. By tracking the chest wall area change and descending aorta flow waveform on the same image slice, instants of inspiration and expiration, as well as instants of peak flow within a cardiac cycle were tracked simultaneously with the vessel area and flow (Chapter 4.3.2).

Two vessel area indices are defined here. Deformation index (DI) accounts for the overall change in vessel area, which includes the influence of both cardiac and respiratory cycles (Figure 7.2). Beat-averaged deformation index (baDI) is estimated to

225

neglect the effect of cardiac cycle by averaging the vessel area over each cardiac cycle (Figure 7.3). The use of baDI in this work will be discussed in Chapter 7.4.
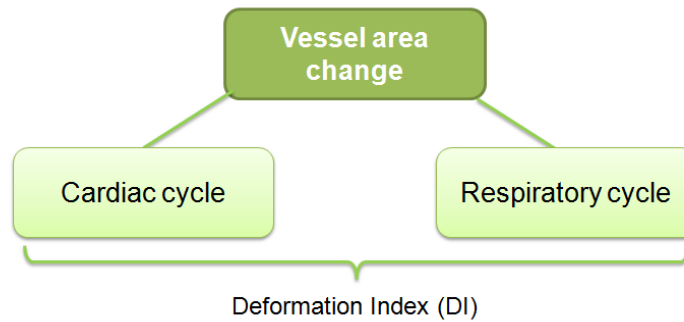
Figure 7.2 Schematic illustrating that DI is defined to include both cardiac and respiratory cycles influences
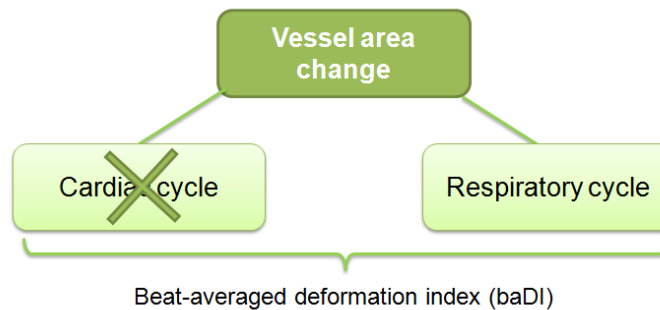
Figure 7.3 Schematic illustrating that the effect of cardiac cycle is removed in baDI

DIs of each caval vein (FP, SVC and LSVC (if present)) were computed to quantify the overall amplitude of vessel cross-sectional area change at each vessel:

$$DI = \frac{A_{max} - A_{min}}{A_{mean}} \times 100\% \qquad \text{(Equation 7.1)}$$

where A_{mean} is the time-averaged vessel area, and A_{min} and A_{max} are the minimum and maximum instantaneous vessel areas.

It is hypothesized that vessel area change is influenced by both cardiac and respiratory cycles. Beat-averaged deformation index (baDI) removed the effect of cardiac cycle by averaging vessel area over each cardiac cycle (Figure 7.3):

$$baDI = \frac{\bar{A}_{max} - \bar{A}_{min}}{\bar{A}_{mean}} X 100\% \qquad \text{(Equation 7.2)}$$

where $\bar{A}$ is the beat-averaged vessel cross sectional area (green data points in Figure 7.4) . This was computed by averaging vessel cross-sectional area at time points between two peaks (red data points in Figure 7.4) of the descending aorta (DAO) flow waveform.
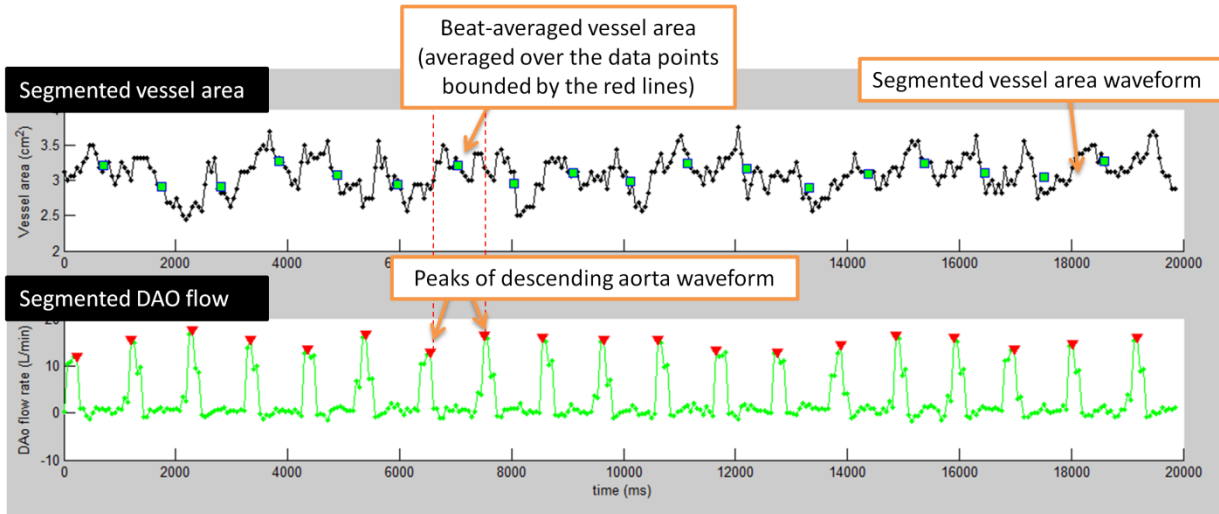
Figure 7.4 Illustration of computation of beat-averaged area: Each green square data point represents the beat-averaged area averaged over time points bounded by two red triangular data points (peak of the descending aorta flow waveform). DAO = descending aorta

To investigate the variation of vessel area over a respiratory cycle, instants of end inspiration and end expiration were identified from the chest wall area waveform for the free-breathing resting and free-breathing exercise conditions. The peaks of the chest wall area waveforms were identified as end inspiration and troughs of the chest wall area waveforms were identified as end expiration (as illustrated in Figure 7.5). The

vessel cross-sectional areas at instants of end inspiration were then averaged over the entire image series, and were compared to that of end expiration.
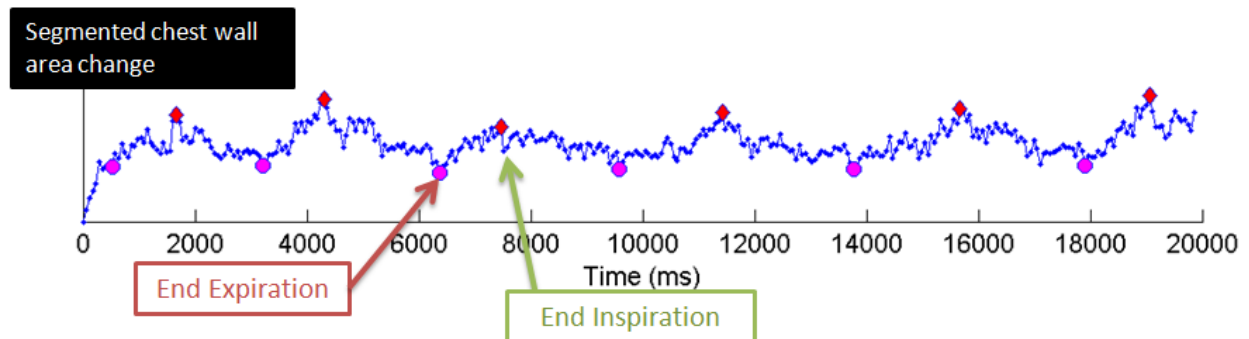
Figure 7.5 Illustration of obtaining instants of end inspiration (red data points) and end expiration (purple data points) from the chest wall area waveform

7.2.4 Statistical Methods

To compare DI and baDI between FB, BH and EX conditions, Repeated-Measures ANOVA was performed with IBM SPSS Statistics (version 22, IBM Corporation, Armonk, New York). Friedman test was used for non-normal data (tested by Shapiro-Wilk test). To compare vessel area between end inspiration and end expiration, as well as between FP and SVC, paired-samples t-test (Wilcoxon signed-rank test for non-normal data) was performed. For all statistical comparisons, p≤0.05 was considered significant (two-tailed).

7.2.5 Wall Deformation Characterization Results

DI and baDI were compared between FB, BH and EX conditions. They were also compared between FP and SVC under each condition. Instantaneous vessel areas of each vessel under FB and exercise condition were also compared at end inspiration and end expiration. Full list of results for all patients are provided in Appendix A.9.3.

7.2.5.1   Deformation Index (DI)

Deformation Indices of FB, BH and EX conditions were computed and compared for the 6 patients with data at all conditions (FB, BH and EX) available. Three patients were discarded due to poor image quality. It was found that DI was significantly different between the 3 conditions for FP ($p=0.016$) and SVC ($p=0.017$) (Figure 7.6). From Figure 7.6, comparing among the conditions, FP FB DI (0.46 ± 0.08) was significantly higher than FP BH DI (0.34 ± 0.10) ($p=0.04$). FP EX DI (0.52 ± 0.10) was significantly higher than FP BH DI ($p=0.01$). No significant difference was observed between FP FB DI and FP EX DI. SVC EX DI (0.62 ± 0.23) was significantly higher than SVC BH DI (0.39 ± 0.10) ($p=0.04$). No significant difference was observed between SVC FB DI (0.44 ± 0.16) and SVC EX DI, as well as between SVC FB DI and SVC BH DI. There was no significant difference in DI between FP and SVC under each condition.
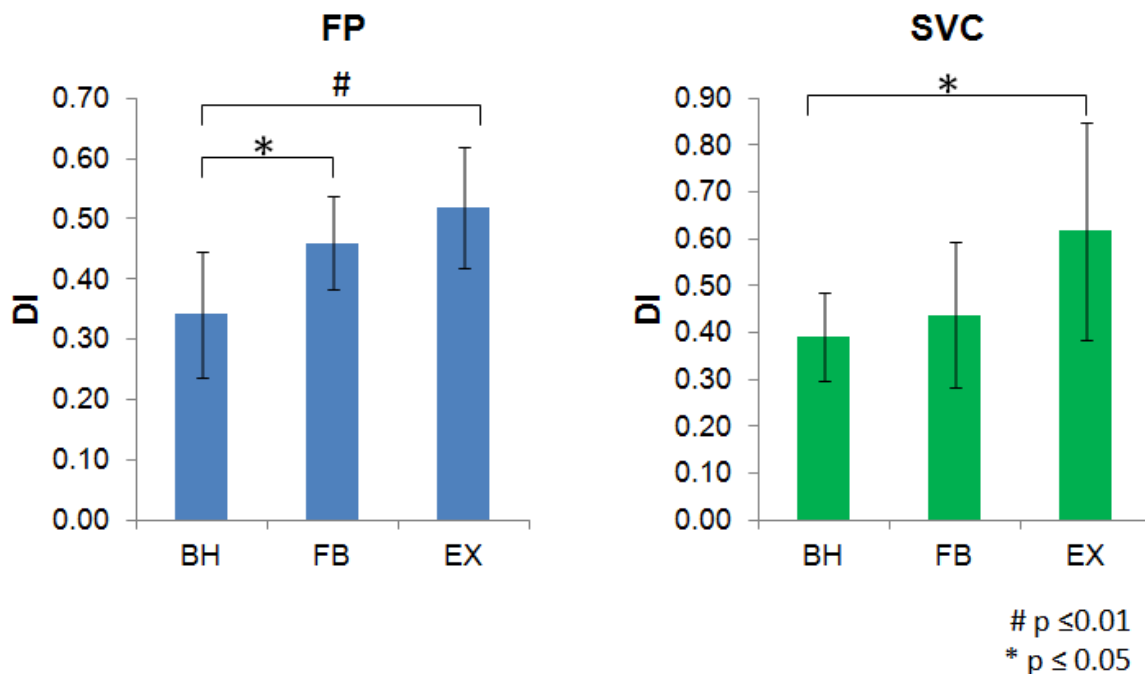
Figure 7.6 Comparison of DI under resting breath-hold (BH), resting free-breathing (FB) and free-breathing exercise (EX) conditions

7.2.5.2 Beat-averaged Deformation Index (baDI)

Beat-averaged Deformation Indices (baDI) of FB, BH and EX conditions were computed and compared for the 6 patients with data at all conditions available (Figure 7.7). Three patients were discarded due to poor image quality. It was found that baDI was significantly different between the 3 conditions for FP (p=0.02) and SVC (p=0.002). Comparing among the conditions, FP FB baDI (0.17±0.08) was significantly higher than FP BH baDI (0.07±0.03) (p=0.02). FP EX baDI (0.23±0.08) was significantly higher than FP BH baDI (p=0.02). No significant difference was observed between FP FB baDI and FP EX baDI. SVC EX baDI (0.25±0.11) was significantly higher than SVC BH baDI (0.11±0.05) (p=0.01). SVC FB baDI (0.17±0.08) was significantly higher than SVC BH baDI (p=0.01). SVC EX baDI was significantly higher than SVC FB baDI (p=0.05). There was no significant difference in baDI between FP and SVC under each condition.
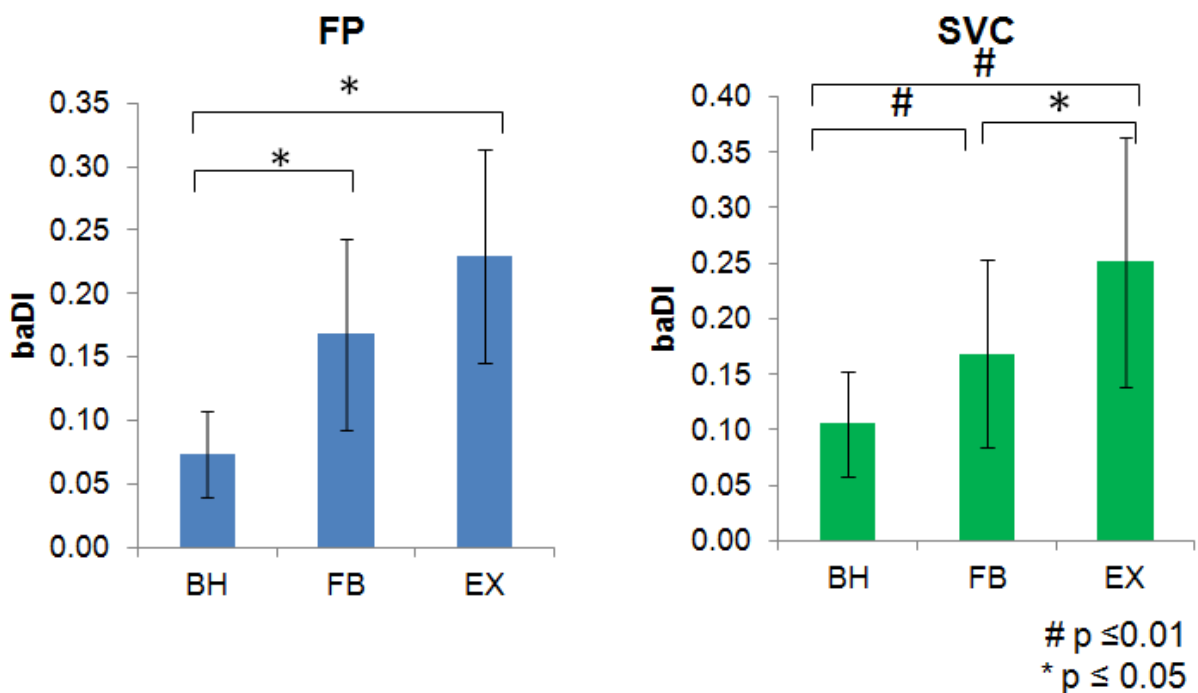
Figure 7.7 Comparison of baDI under resting breath-hold, free-breathing and exercise free-breathing conditions

7.2.5.3   *End Inspiration vs. End Expiration*

Comparing vessel area at end inspiration and end expiration, no significant differences were observed at FP FB (p=0.26), FP EX (p=0.91), SVC FP (p=0.23) and SVC EX (p=0.97) (Figure 7.8). Even though variation in vessel area was observed within a respiratory cycle, no significant differences were observed in vessel area between end inspiration and end expiration. It could be because phase differences were observed between the vessel area waveform and the chest wall area waveform (which was used to determine end inspiration and end expiration time points).
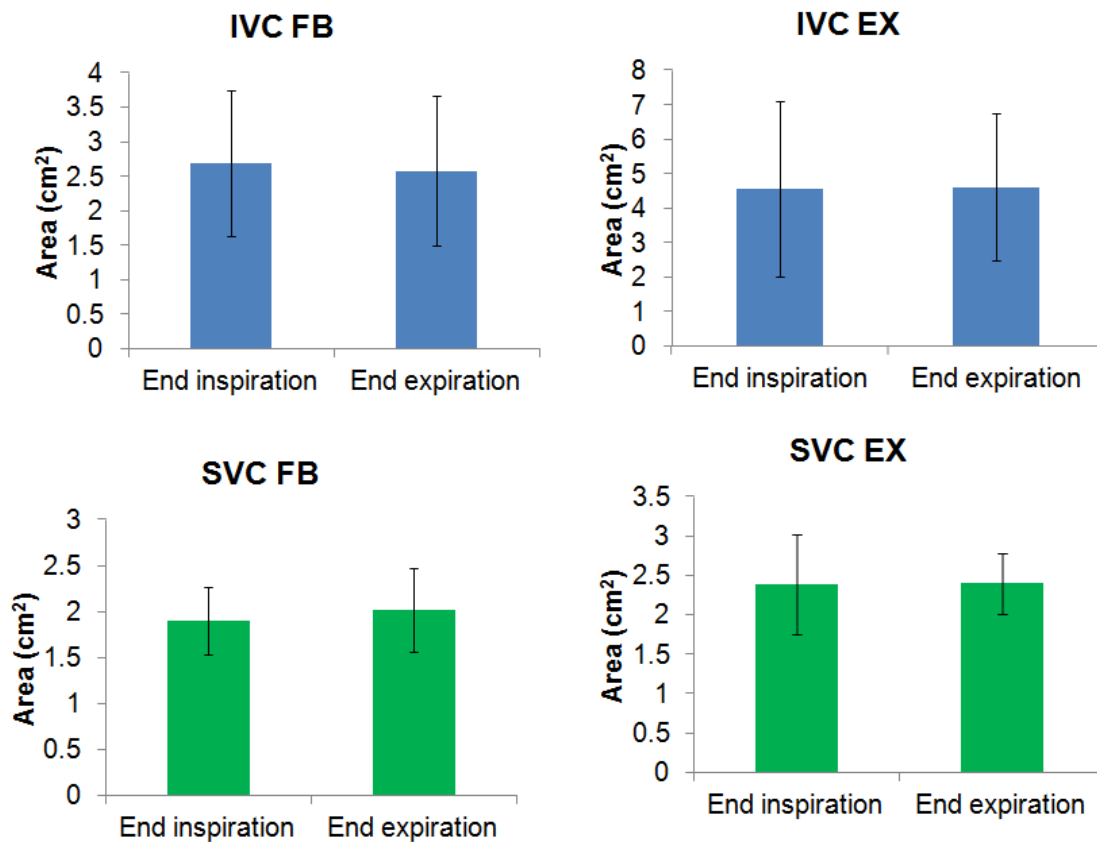
Figure 7.8 Comparison of vessel areas during end inspiration and end expiration

To quantify the phase difference between chest wall area waveform and vessel area waveform, Fourier transform was performed to decompose the area waveforms into

different frequencies. The respiratory frequencies were identified from the vessel area and chest wall area waveforms. The phase differences (example shown in Figure 7.9) between the chest wall area and vessel area waveform are summarized in Table 7-3. As shown in Table 7-3, the phase lag between chest wall area and vessel area waveforms vary between different vessels as well as different conditions.

Table 7-3 Number of respiratory cycles vessel area waveform lags behind chest wall area waveform

	FP		SVC		LSVC	
	FB	EX	FB	EX	FB	EX
CHOP011B	0.98	0.60	0.90	0.57	--	--
CHOP021C	0.16	0.48	--	1.01	--	--
CHOP029B	--	0.95	0.83	0.76	--	--
CHOP032C	0.37	0.47	0.73	--	--	--
CHOP091C	--	0.88	--	0.98	--	0.84
CHOP155A	--	0.52	0.49	--	--	--
CHOP229A	--	--	0.84	0.64	0.91	0.45
CHOP234A	0.88	--	--	--	--	--
CHOP235A	0.66	0.46	0.59	0.92	--	--
Average ± Standard deviation	0.61 ±0.34	0.62 ±0.21	0.73 ±0.16	0.81 ±0.19	0.91	0.65
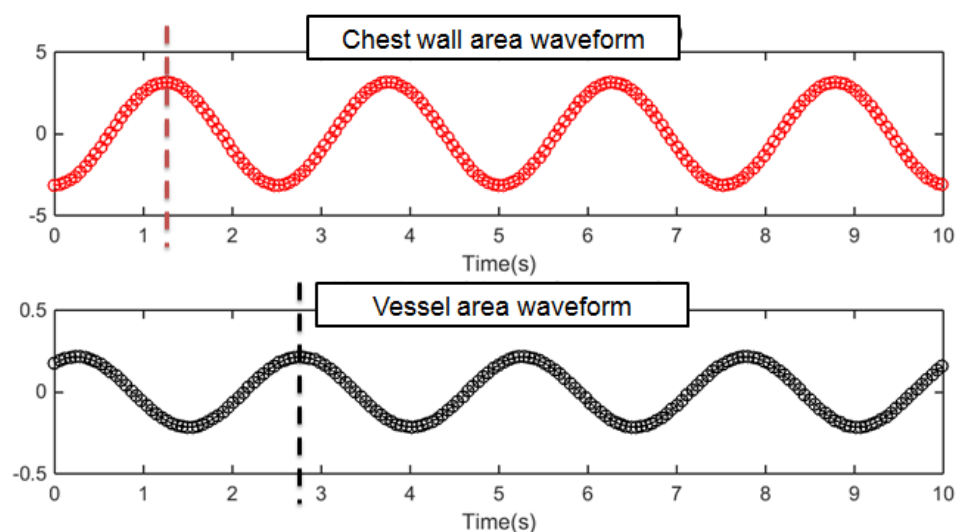
Figure 7.9 Figure illustrating the phase lag between chest wall area and vessel area waveforms

7.3 Specific Aim 3(b): Effect of Wall Deformation on TCPC Hemodynamics

7.3.1 Patient Model

A lateral tunnel patient (CHOP235A) was chosen from the cohort in Chapter 7.2, based on the following criteria: (i) Single SVC, (ii) no apparent vessel stenosis. Static steady state free precession imaging was utilized to acquire patient specific anatomic images and 3D anatomies were reconstructed (Chapter 4.2.2) (Figure 7.10(a)). PC-MRI was utilized to acquire through-plane velocity profiles across the vena cavae over a cardiac cycle under resting BH conditions. Patient-specific flow conditions were obtained by segmenting PC-MRI images at the inlet's cross section (Chapter 4.3.1.2) (Figure 7.10 (b)). The change in vessel cross-sectional area was also obtained from the segmented PC-MRI slices (Figure 7.11 (a, b)). The approximate location of the PC-MRI slice relative to the anatomy is shown in (Figure 7.11(c)). To visualize the location of the atrial wall relative to the TCPC, the heart and surrounding pulmonary veins were segmented (Figure 7.12) with Invesalius 3.0 (http://www.cti.gov.br/invesalius/).
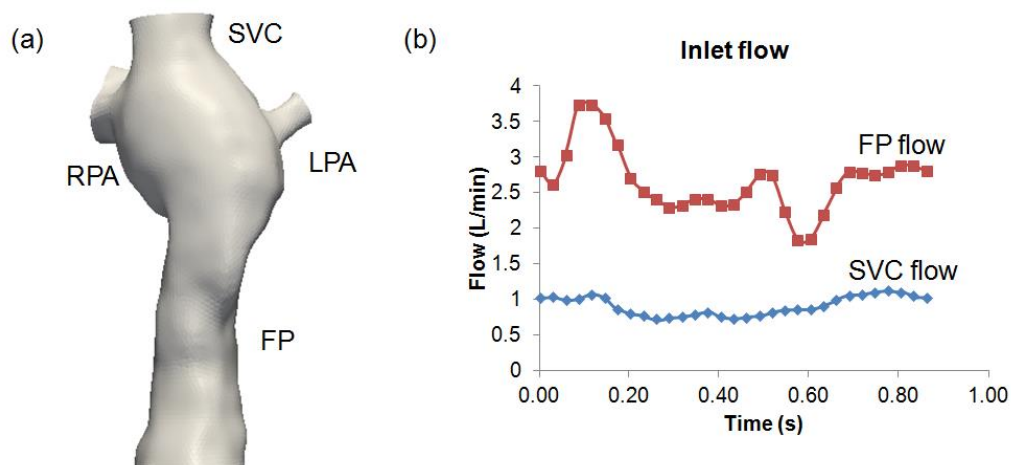
Figure 7.10 Reconstructed (a) 3D anatomy and (b) inlet flow waveforms of CHOP235A
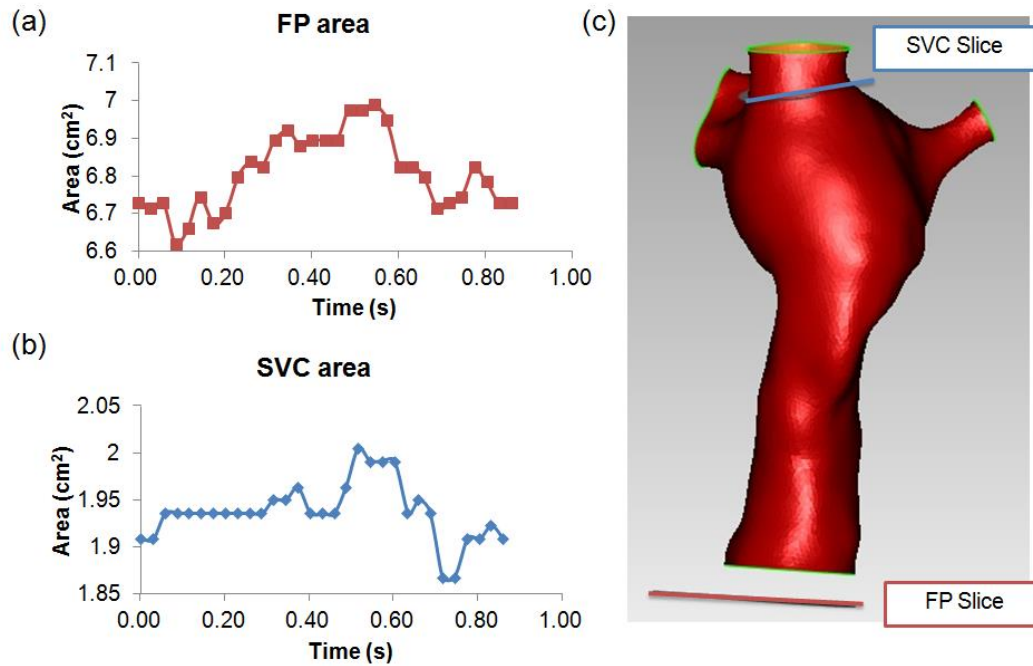
Figure 7.11 Segmented vessel area waveform of (a) FP and (b) SVC from PC-MR images. The relative orientation of the slices relative to the TCPC anatomy is shown in (c). Note the location of the FP PC-MRI slice was outside the CFD domain
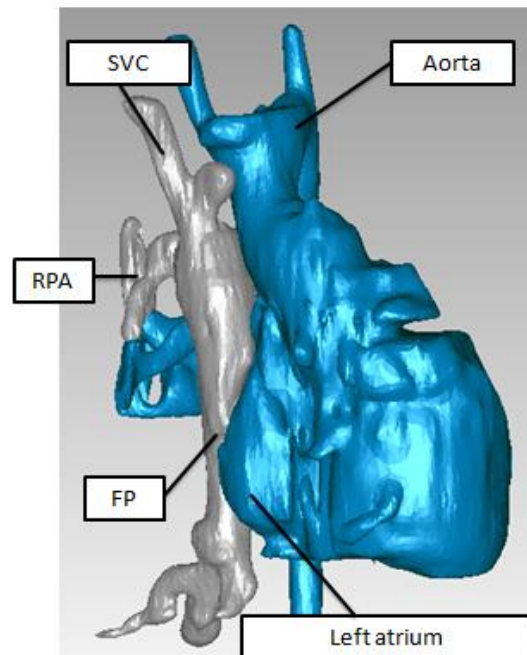
Figure 7.12 The TCPC (gray) and the surrounding heart and blood vessels (blue) of CHOP235A

7.3.2 FSI Model

The finite element method solver LifeV (www.lifev.org) was utilized in this work. The FSI solver is presented in Passerini et. al. and has been validated with experimental data of the propagation of a pressure wave in a fluid-filled elastic cylindrical tube [163]. The structural model is based on the assumption of linear elastic model. The moving fluid domain in the FSI solver is based on arbitrary Lagrangian–Eulerian (ALE) mapping.

The 3D surface of the reconstructed patient specific anatomy was prepared as described in Chapter 4.2.2. Flow extensions of 2 cm were added to each inlet and outlet for flow development. The resulting surface was loaded into GAMBIT/ANSYS Workbench (ANSYS, Inc., PA, USA) for surface meshing with unstructured triangular elements. Gmsh [187] was used to prepare volume meshes for both fluid and structure simulations based on the surface mesh. Gmsh preserves the nodes of the input surface mesh when creating a 3D volume mesh. Tetrahedral elements were created in the fluid domains while maintaining the nodes at the input surface. For the structural mesh, the input surface mesh was extruded based on the normal of each element on the surface mesh. It contains two layers of tetrahedral elements. The fluid mesh contains 97793 tetrahedrons and the structural mesh contains 82206 tetrahedrons. P2 finite elements were used for fluid and structure velocity. P1 finite elements were used for fluid pressure. The duration of one cardiac cycle was 0.86s, obtained from the MRI data. Time step of 5×10^{-4}s was utilized at least for 3 cycles for both rigid wall and FSI simulations.

For the fluid domain, the inflow waveform segmented from PC-MRI was applied as inlet flow boundary conditions. Parabolic velocity profile was assumed at both inlets. Stress-free outflow boundary conditions were used. Blood viscosity and density were assumed to be 3.5×10^{-6} m^2/s and 1.0 g/cm^3 respectively. Same inflow and outflow boundary conditions were applied for FSI and rigid wall simulations. For the structural domain, edges at all inlets and outlets were fixed. Stress-free boundary condition was applied on the outer wall of the structure. Literature values of blood vessel wall material properties were adopted from [211-215]. Young modulus of 0.07MPa, Poisson ratio of 0.3 and wall thickness of 2.0 mm were prescribed. Homogeneous material properties were assigned at the vessel wall.

7.3.3 Mesh Sensitivity Analysis

To investigate mesh sensitivity, three meshes were created and simulated with the same conditions:

(a) Very fine mesh – 1mm mesh edge length

    i. Fluid: 193974 elements

    ii. Structure: 164178 elements

(b) Fine mesh – 1.5mm mesh edge length

    i. Fluid: 97793 elements

    ii. Structure: 82206 elements

(c) Coarse mesh– 2mm mesh edge length

    i. Fluid: 27640 elements

    ii. Structure: 44406 elements

Because the very fine mesh requires much higher computational time, a time duration of 0.13s was simulated with all 3 meshes and compared. Mesh displacements at four phases (deceleration, low flow, acceleration and high flow) were extracted (Figure 7.13).
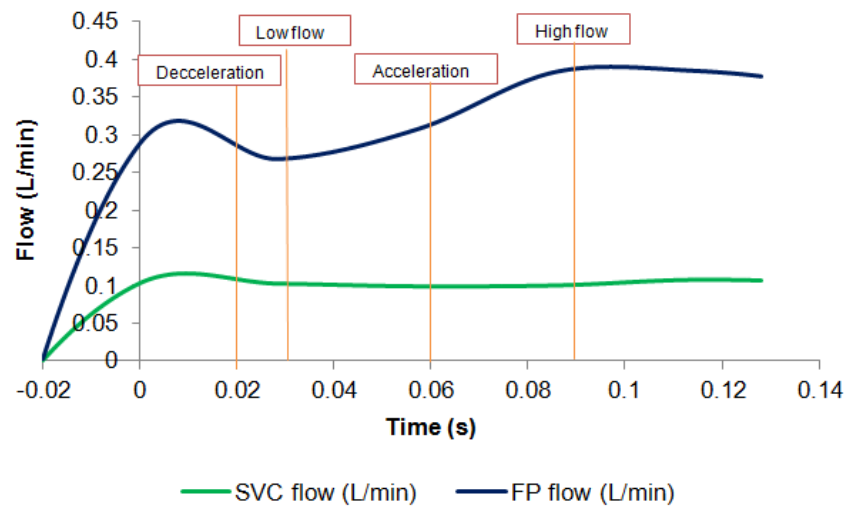
Figure 7.13 Flow waveform of the mesh sensitivity study. Maximum mesh displacement was extracted at four phases (deceleration, low flow, acceleration and high flow) and compared between the different mesh sizes

Comparing the maximum displacement between the different mesh sizes, they are all of similar magnitudes (Table 7-4). The discrepancy of maximum displacement between very fine mesh and fine mesh ranged from 0.0002 cm to 0.0031 cm. Comparing the fine mesh and the coarse mesh, the discrepancy ranged from 0.0 cm to 0.0045cm.

Table 7-4 Maximum mesh displacement with different mesh sizes

Maximum Displacement (cm)	(a) Very fine	(b) Fine	(c) coarse	Difference between	
				(a)&(b)	(b)&(c)
Deceleration (0.02s)	0.2448	0.2450	0.2457	0.0002	0.0007
Low flow (0.03s)	0.4334	0.4342	0.4342	0.0008	0
Acceleration (0.06s)	0.6955	0.6964	0.6979	0.0009	0.0015
High flow (0.09s)	0.6886	0.6917	0.6962	0.0031	0.0045

Comparing the pressure drop differences at each time step, the average (temporal) difference between the coarse and the fine mesh was 0.009 mmHg, and maximum difference was 0.015 mmHg. The average (temporal) pressure drop difference between fine and very fine mesh was 0.005 mmHg. The maximum pressure drop difference was 0.01 mmHg. Comparing time-averaged power loss over the simulated time span, there was 0.66% difference between the coarse mesh and the fine mesh, and 0.29% difference between the fine mesh and the very fine mesh (Table 7-5).

Table 7-5 Differences in pressure drop and power loss with different mesh sizes

		(a) Very fine vs (b) fine	(b) Fine vs (c) coarse
Pressure drop difference (mmHg)	**Temporal average**	0.005	0.009
	Temporal maximum	0.01	0.015
%difference in power loss		0.29%	0.66%

By refining the coarse mesh into the fine mesh, power loss estimation changed by 0.66%. By further refining the fine mesh into the very fine mesh, the power loss estimation changed by 0.29%. Simulations with the very fine mesh are computationally expensive. The hemodynamic and wall displacement predictions with the fine mesh are in close proximity to the very fine mesh prediction. Therefore, in the following sections, the **fine mesh** is used throughout this specific aim. In the following sections, t=0 s corresponds to the beginning of the cardiac cycle.

7.3.4 Results - Simulated TCPC Wall Deformation

The simulated TCPC wall displacement is shown in Figure 7.14. Wall displacement magnitude increases from t=0s to t=0.2s, expanding the TCPC volume. Maximum wall displacement of 0.21cm occurred at t=0.165s, which was 0.065s after the time point of maximum FP flow (t=0.1s). At t =0.3s, wall displacement was almost zero. At that time point, the TCPC volume (62.49ml) was almost equal to the volume of the rigid wall simulation fluid domain (62.25ml). After that time point, the wall displacement magnitudes both the FP and the center of the TCPC increased from t=0.4s to 0.5s. Wall displacement magnitude then decreased at t=0.6s. At t =0.7s, wall displacement mainly occurred at the FP. At t=0.8s, wall displacement occurred at both the FP and the center of the TCPC, expanding the TCPC volume. The simulated wall displacement is animated in Animation 7.1 and Animation 7.2.

Animation 7.1 Video of the simulated mesh displacement viewing from the anterior angle
(animation_7.1_anterior.avi, 485.KB)
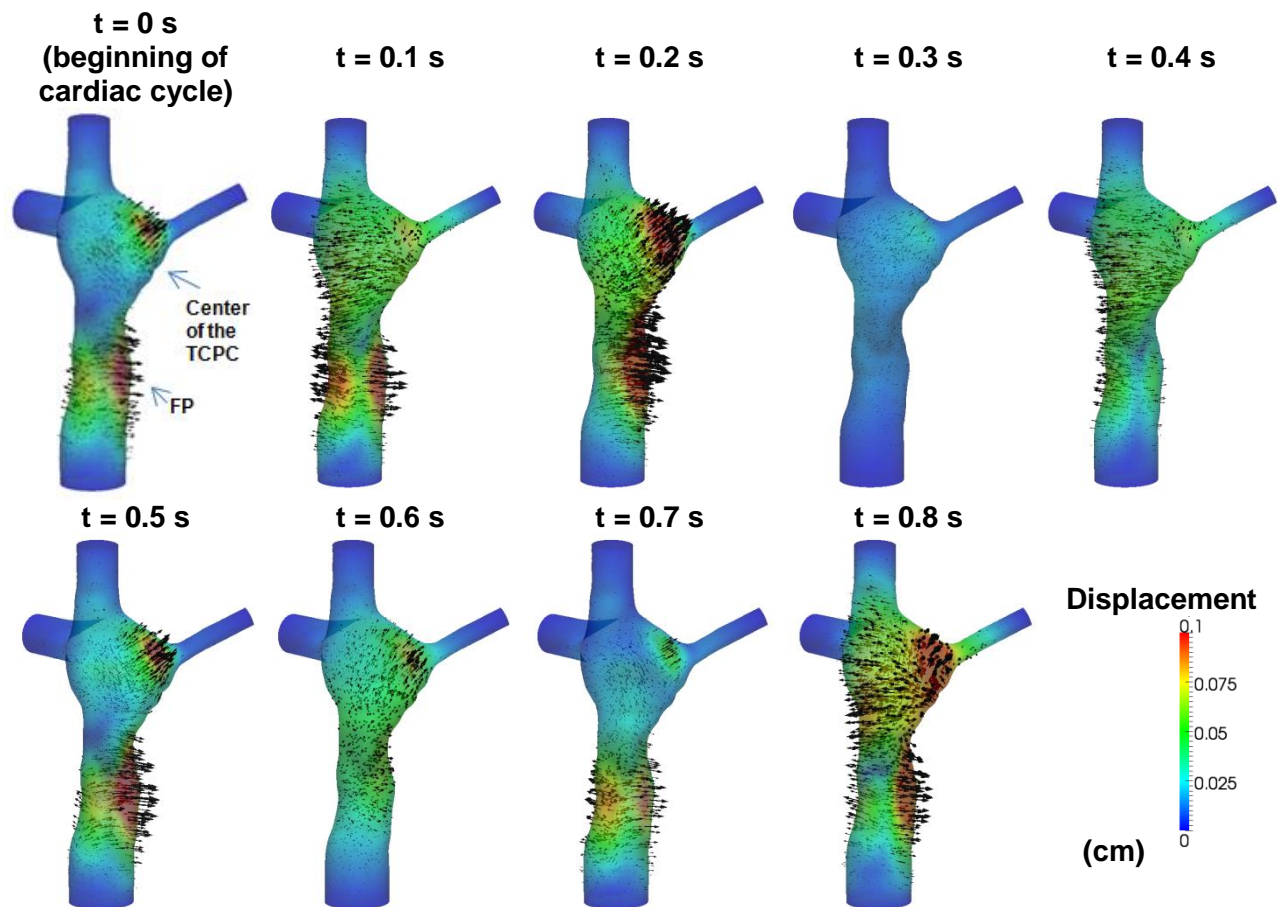
Figure 7.14 The simulated displacement fields at 9 evenly-spaced time points in the cardiac cycle. The color of the contour represents the magnitudes of the displacement and the arrows represent the direction of the displacement
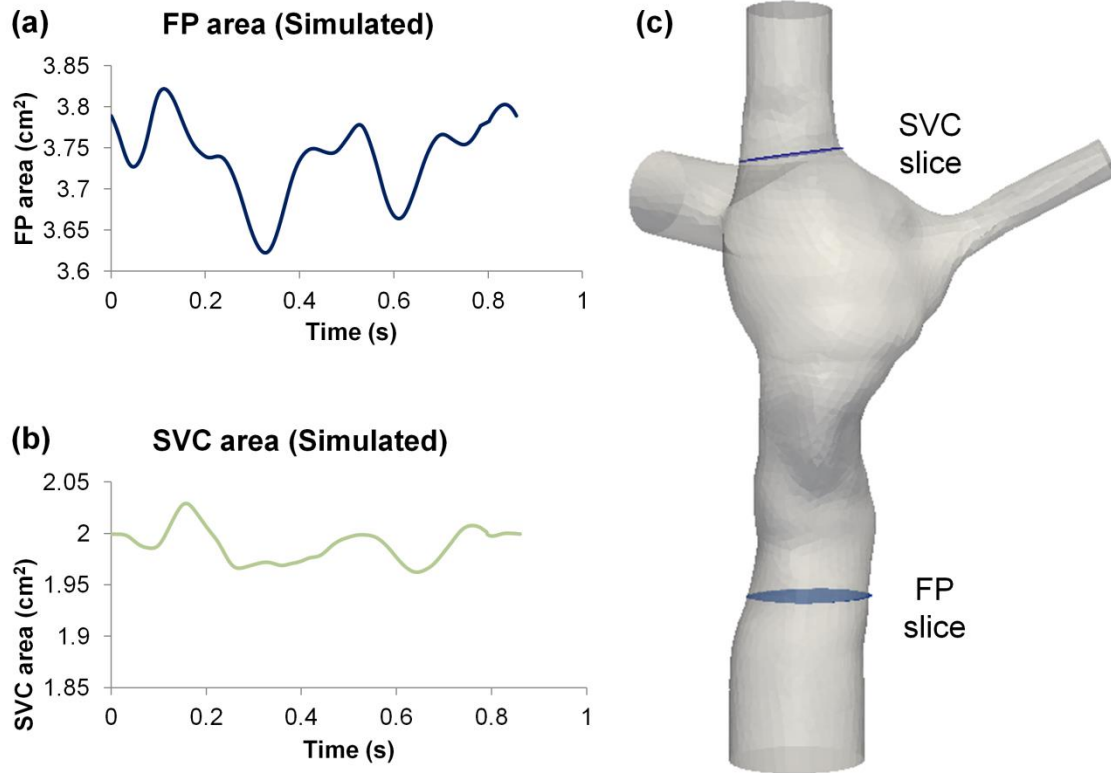
Figure 7.15 Simulated vessel area waveform of: (a) FP and (b) SVC from the FSI simulation results. The "FP slice" and "SVC slice" represent the location of where the FP and SVC area waveforms were extracted

From the FSI simulation results, the vessel cross-sectional areas of FP and SVC were extracted throughout the simulated cardiac cycle (Figure 7.15). The vessel areas were compared between FSI and PC-MRI data (Table 7-6). Since the location of the PC-MRI slice of the FP was outside the CFD domain, deformation index (DI) was compared. Simulation results showed that DI from the simulation was in close agreement with the DI of the PC-MRI data at the FP. For the SVC, even though the maximum and average areas were similar between FSI and PC-MRI, DI was underestimated in the simulation since the simulated minimum SVC area was higher.

Table 7-6 Comparison of vessel areas between FSI simulation and *in vivo* PC-MRI data

Vessel area	FSI simulation		PC-MRI data	
	FP	SVC	FP	SVC
Maximum (cm^2)	3.82	2.03	6.99	2.01
Minimum (cm^2)	3.62	1.96	6.62	1.87
Average (cm^2)	3.74	1.99	6.81	1.94
Change (cm^2)	0.20	0.07	0.37	0.14
DI	5.3%	3.4%	5.4%	7.1%

The net flow (total inflow – total outflow) through the TCPC was computed from the FSI simulations. The TCPC volume change was then computed by integrating the net flow over time using the trapezoidal rule (Figure 7.16). Throughout the simulated cardiac cycle, minimum TCPC volume was 62.49cm^3 and maximum volume 64.46 cm^3. This means the TCPC changed its volume by 1.97 mL throughout the cycle. From the FSI simulation results, the maximum pressure (relative to the PA) at the FP (averaged over the FP cross section) was 1.13 mmHg and the minimum pressure (relative to the PA, averaged over the FP cross section) was -0.07 mmHg. The change in FP pressure was therefore 1.2mmHg throughout the cycle. By dividing the maximum volume change (1.97 mL) by maximum pressure change (1.2mmHg), TCPC compliance was estimated to be 1.64 mL/mmHg.
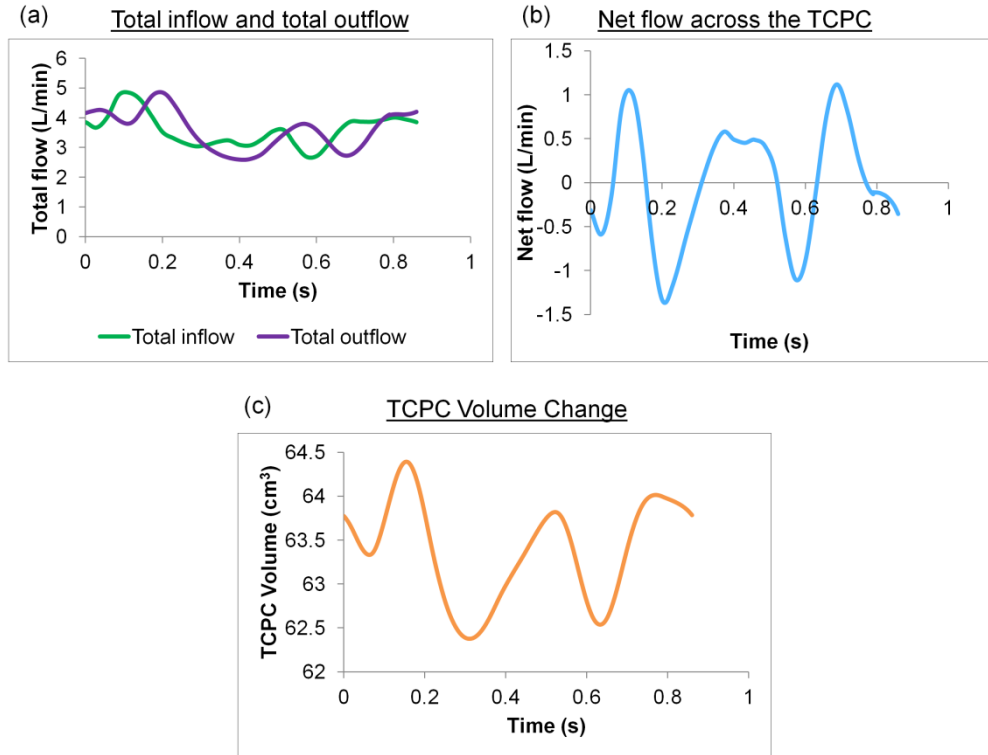
Figure 7.16 (a) Waveforms of the total inflow and outflow (b) Waveform of the net flow through the TCPC (c) Waveform of the TCPC volume throughout the cardiac cycle.

7.3.5 Results – TCPC Flow Field

The flow fields throughout 9 evenly-spaced time points of the cardiac cycle are shown in Figure 7.17. Two planes were extracted at (1) the center of the TCPC and (2) across the FP. It is interesting to note the high degree of similarity between the FSI and rigid wall simulation results. The main differences between the two flow fields are at the center of the TCPC and the FP flow jet. At t=0s, the volume of the TCPC expanded in the FSI simulation. The FP jet has higher maximum velocity in the FSI simulation than the rigid wall simulation. At t=0.1s, the FP continues to expand. However at this time point, the FP jet carried higher maximum velocity in the rigid wall than FSI simulation. At t = 0.2s, the wall deformation occurred at both the FP and the center of the TCPC. The

243

FP jet trajectory and velocity magnitude were similar between the two simulations. However, at the center of the TCPC, the velocity magnitudes and directions were different between the FSI and rigid wall simulations. At t=0.3s, the FSI and rigid wall simulations have similar total TCPC volume. However, the maximum velocity magnitude of the FP jet was lower under rigid wall condition. Also, the velocity magnitudes were different at the center of the TCPC. At t=0.4s, the TCPC continued to expand again in the FSI simulation. Maximum velocity was lower in the FSI simulation at this time point. At t=0.5s, both the FP and the center of the TCPC expanded, affecting the velocity magnitude in the FSI simulation. This also affected the velocity magnitude and direction at the center of the TCPC. From t=0.5s to t=0.8s, as the wall displacement fluctuated, the velocity magnitude and direction were different between the FSI and rigid wall simulations at the center of the TCPC.

(c)

t = 0.2 s

FSI | Rigid Wall

Velocity magnitude (cm/s)

(1) Velocity slice

(2)

Displacement (cm)

SVC flow — FP flow

(d)

t = 0.3 s

FSI | Rigid Wall

Velocity magnitude (cm/s)

(1) Velocity slice

(2)

Displacement (cm)

SVC flow — FP flow

(e)

FSI   t = 0.4 s   Rigid Wall

(f)

FSI   t = 0.5 s   Rigid Wall

(g)

FSI

t = 0.6 s

Rigid Wall

(h)

FSI

t = 0.7 s
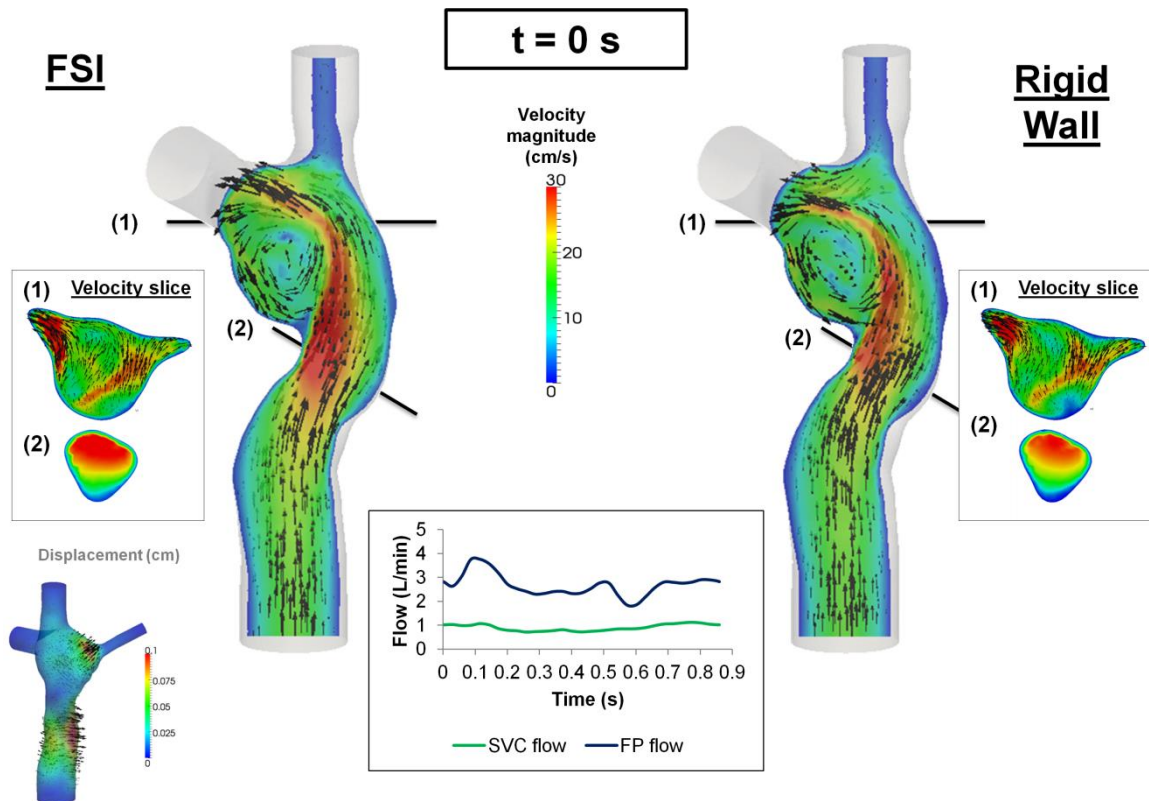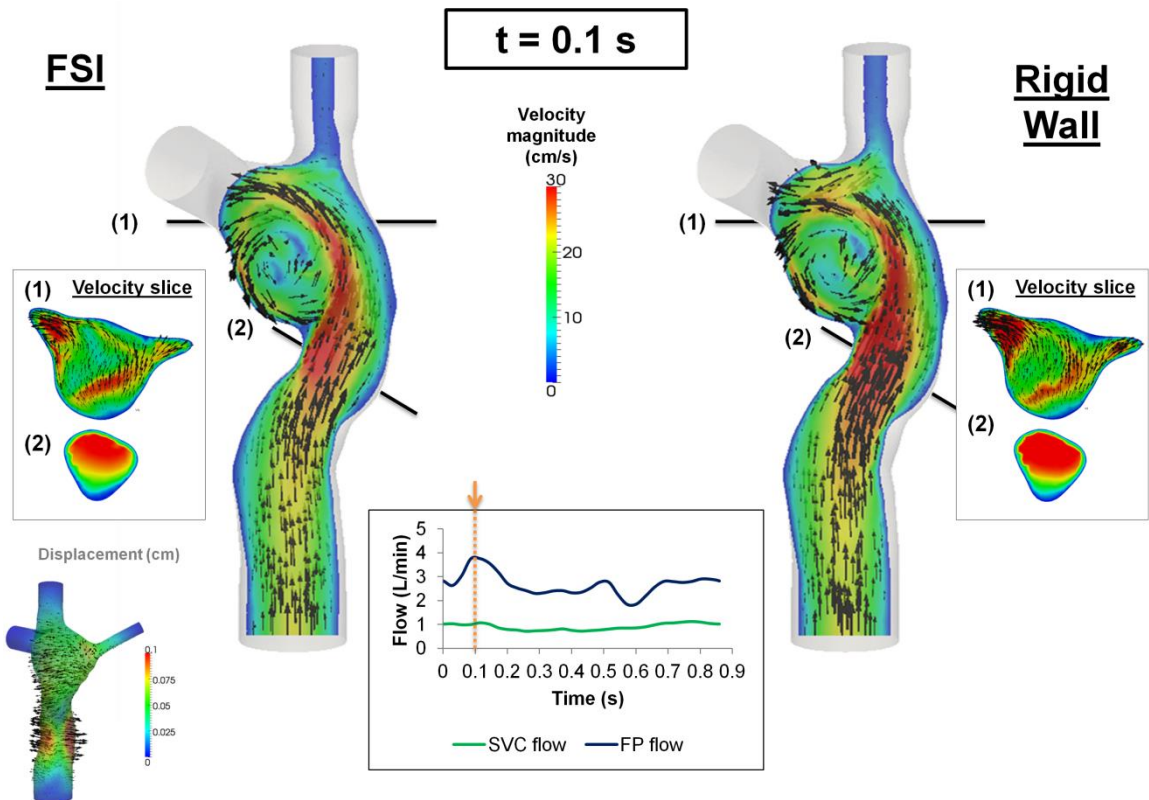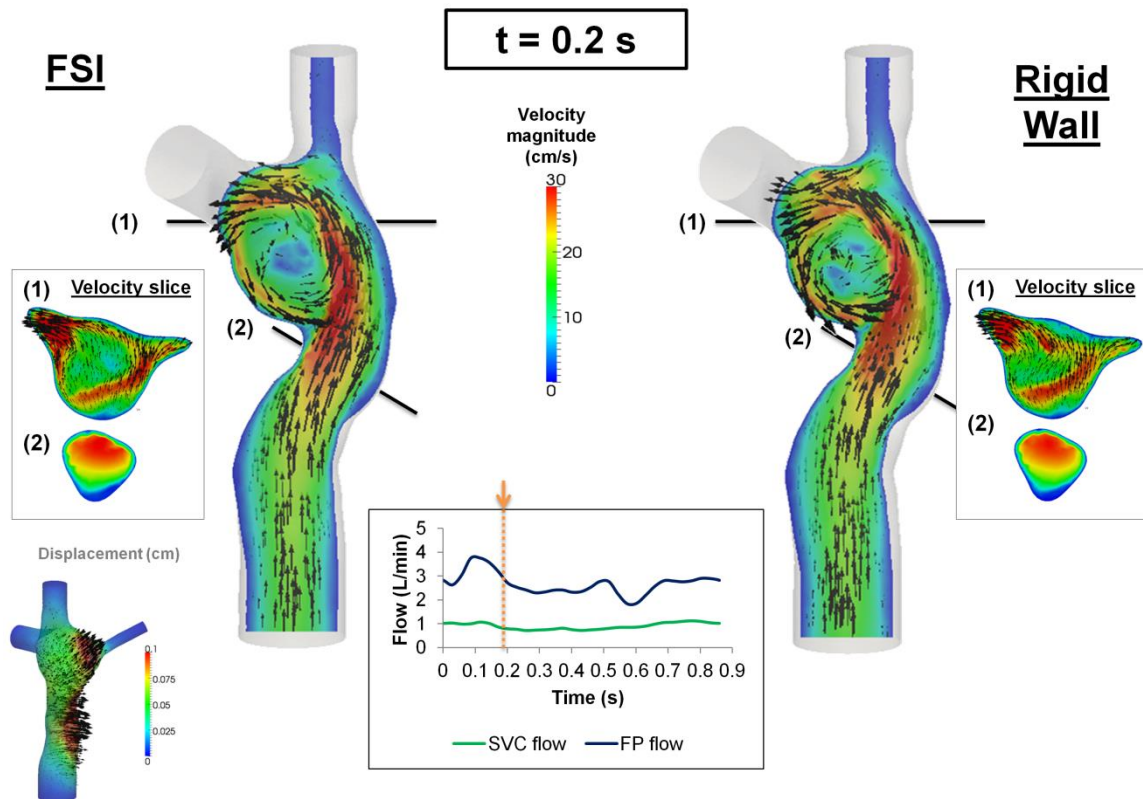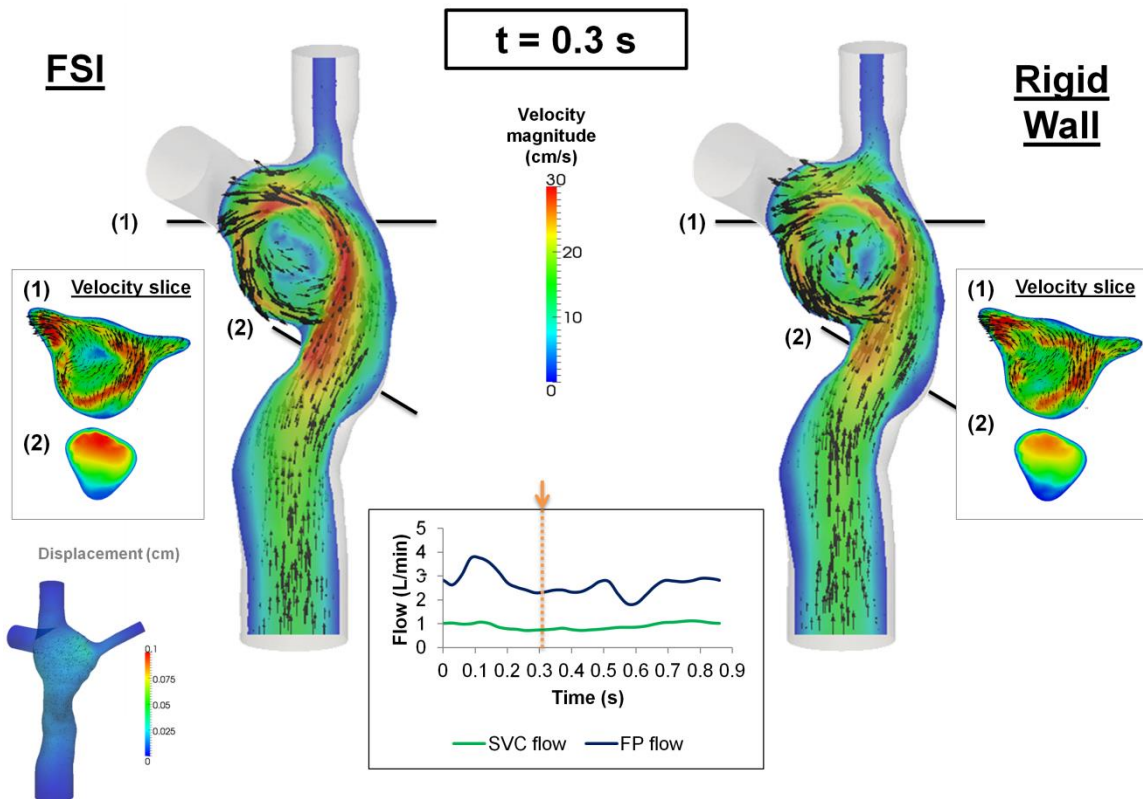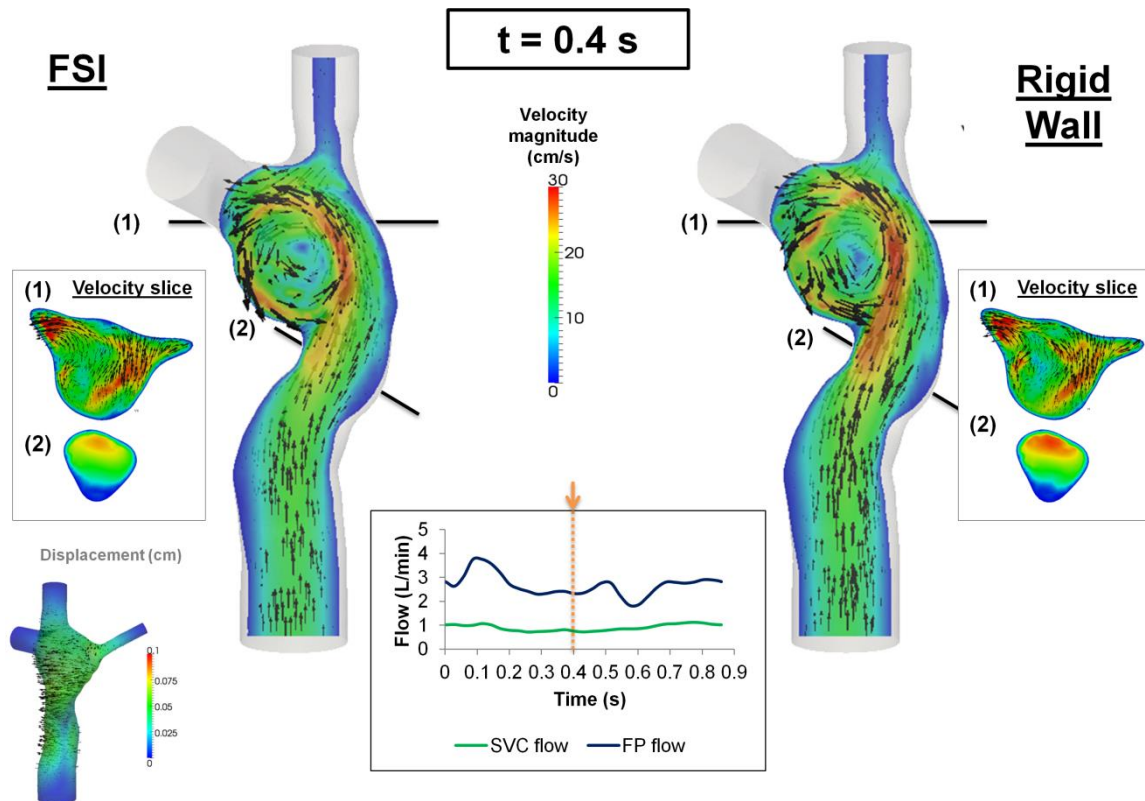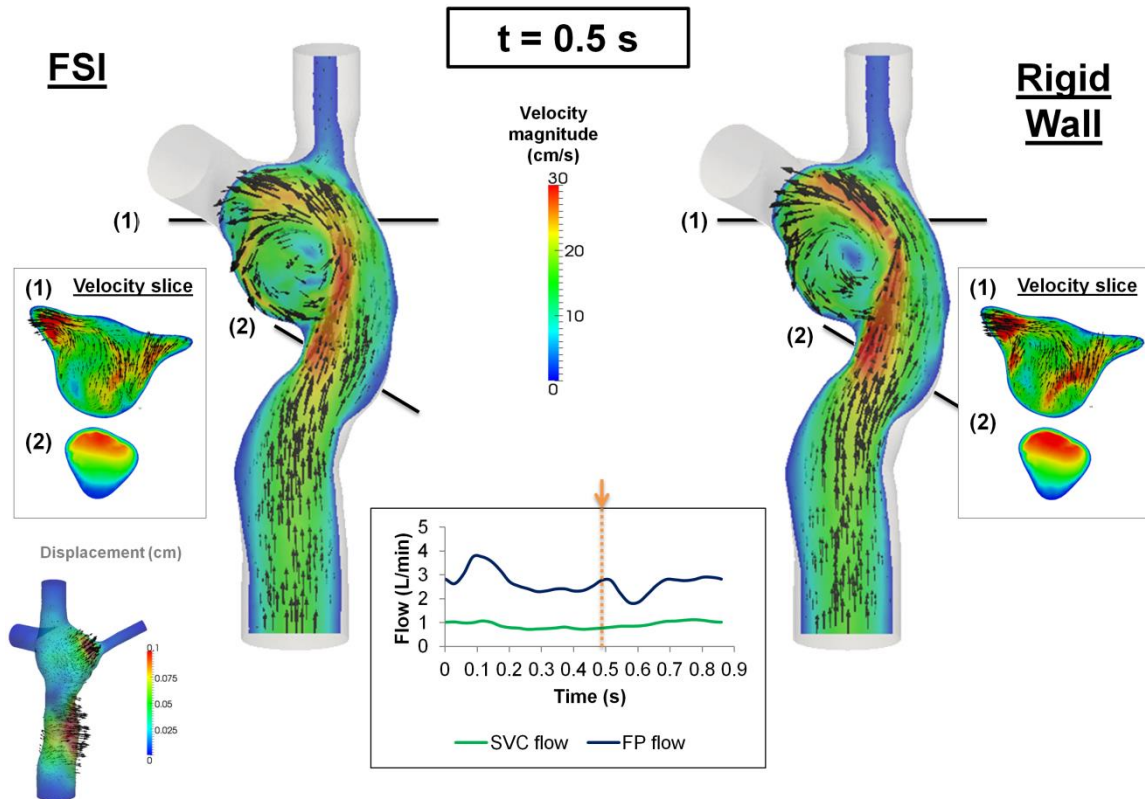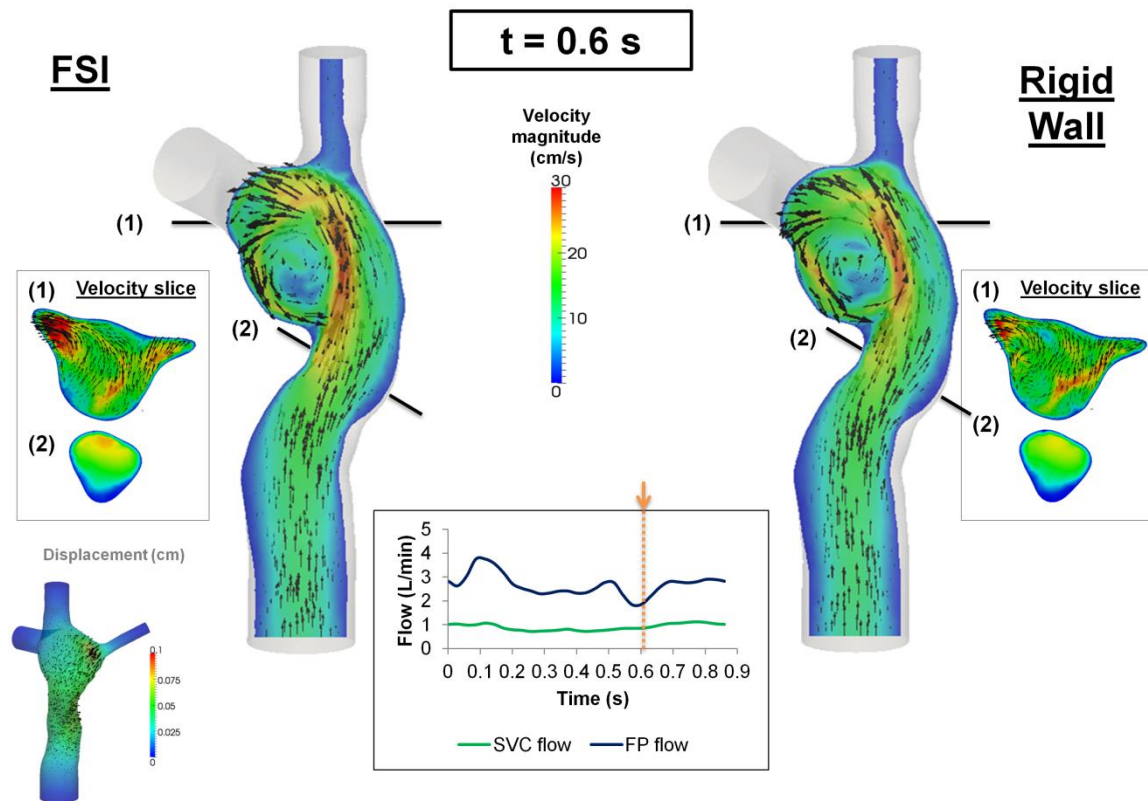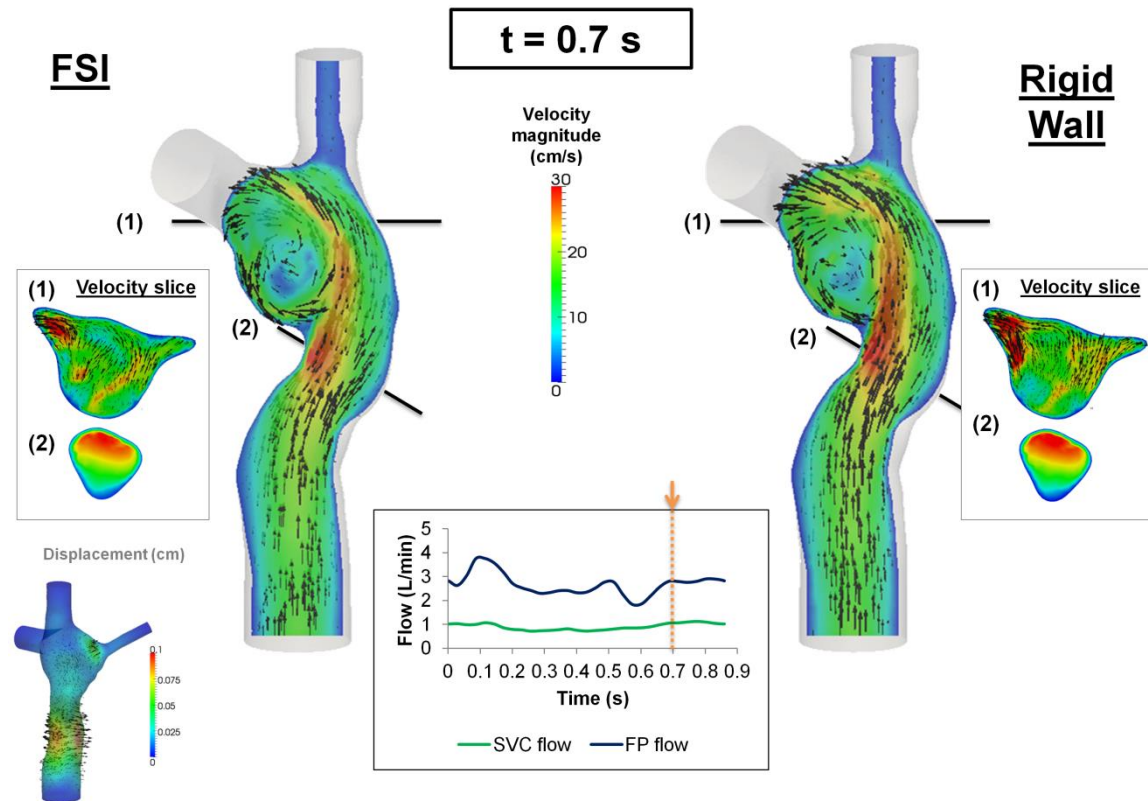
Rigid Wall

(i)
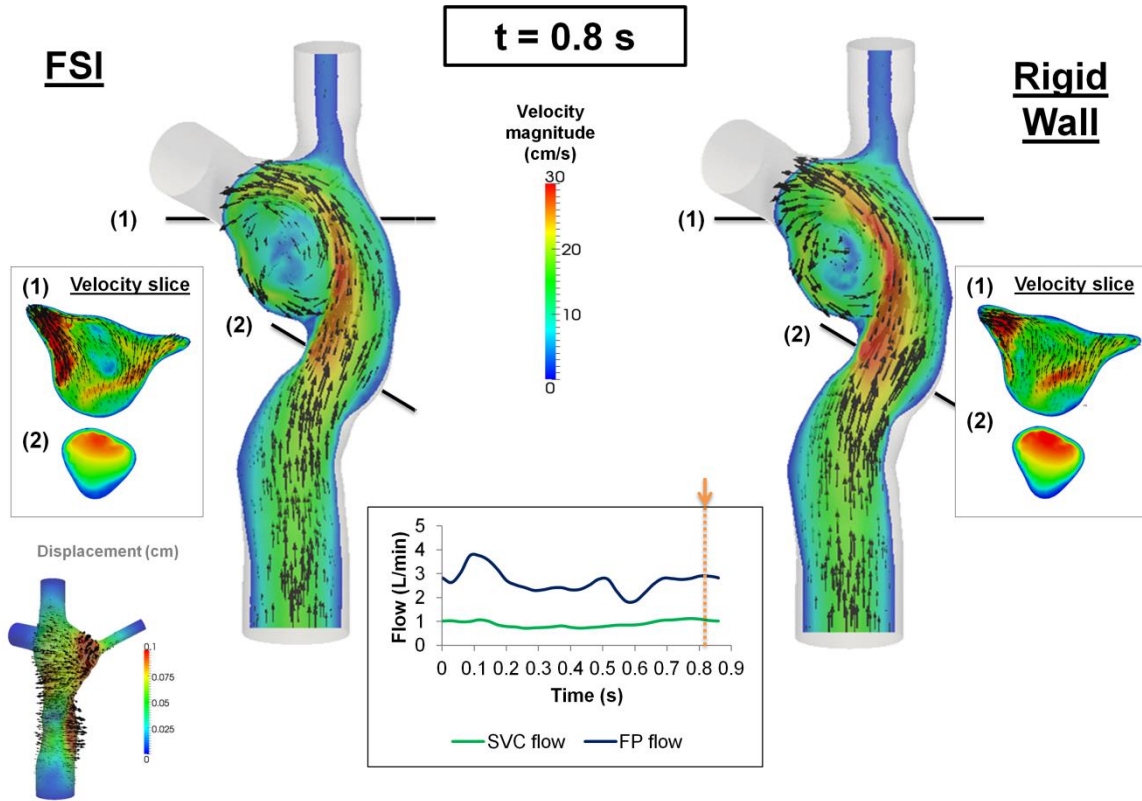
Figure 7.17 Flow field of the TCPC from the FSI and rigid wall simulations (a to i) from t=0s to t=0.8s, at a 0.1s interval. The displacement field of the FSI simulation at the corresponding time point is shown on the bottom-left corner

7.3.6 Results - Pressure Drop and TCPC Power Loss

The instantaneous pressure drop (FP – LPA pressure) and power loss across the TCPC in the cardiac cycle are shown in Figure 7.18 and Figure 7.19, respectively. The pressure drop and power loss waveforms of the rigid wall and FSI simulations shared similar shapes, while the waveforms of the FSI simulation lag behind that of the rigid wall simulation. Comparing the maximum and minimum pressure drops and power losses, the rigid wall simulation has larger fluctuations than that of the FSI simulation. The maximum pressure drop and maximum power loss were lower in the FSI

simulation, which could be due to the increase of the TCPC volume in the FSI simulation. When comparing the time-averaged pressure drop and power loss, the differences between the two simulations were small (pressure drop difference = 0.01mmHg, TCPC power loss difference = 0.1mW) (see Table 7-7).

Table 7-7 Comparison of pressure drop and TCPC power loss between rigid wall and FSI simulations over the cardiac cycle

	Pressure Drop (mmHg)			TCPC power loss (mW)		
	Minimum	Maximum	Average	Minimum	Maximum	Average
Rigid wall	-0.60	2.35	0.60	-4.46	17.33	2.89
FSI	-0.07	1.13	0.61	-0.82	9.34	2.99
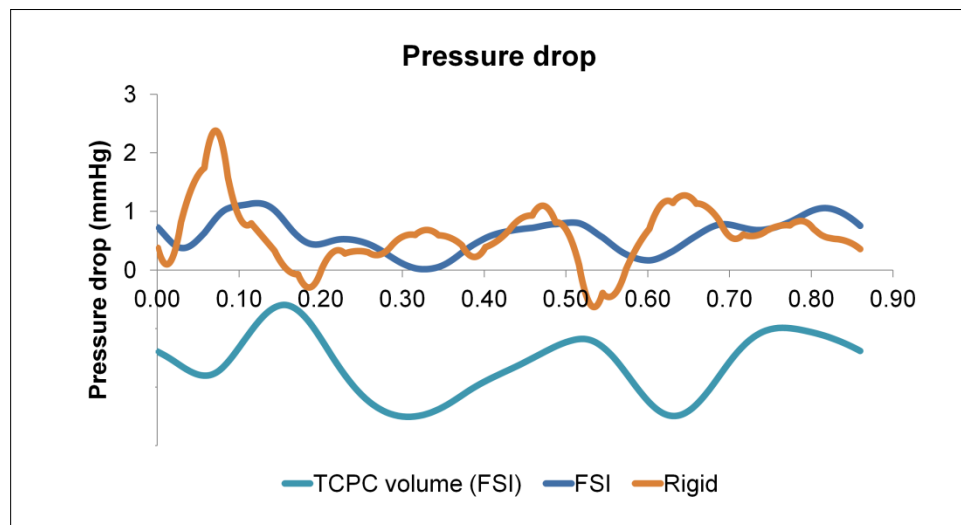
Figure 7.18 Pressure drop waveforms of rigid wall and FSI simulations within a cardiac cycle. The waveform of the TCPC volume from the FSI simulation is shown simultaneously
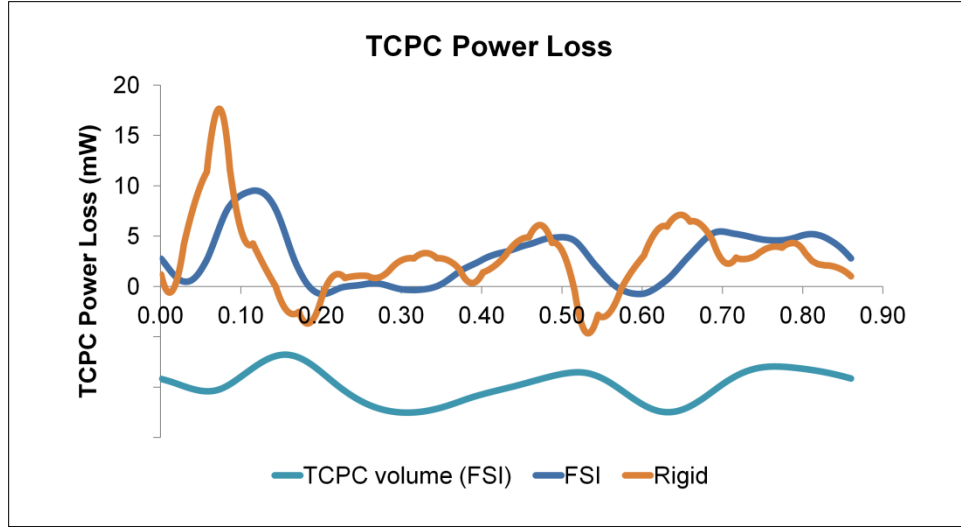
Figure 7.19 TCPC power loss waveforms of rigid wall and FSI simulations within a cardiac cycle. The waveform of the TCPC volume from the FSI simulation is shown simultaneously

7.3.7 Particle Tracking

To assess the impact of wall deformation on particle residence times and HFD, a Lagrangian particle tracking analysis was performed with ParaView (Appendix A.6.2.5.2). For each condition, approximately 700 (number of nodes at the FP cross sections) particles were seeded at the FP at every 0.001s for one cardiac cycle (0.86s) and were passively advected by the flow for five additional cardiac cycles.

The particle trajectories within the flow fields are shown in Figure 7.20 and Figure 7.21 for 8 time points and animated in Animations 7.3 (FSI) and 7.4(Rigid wall). The FP particles are color based on the time at which they were seeded, while the SVC particles are colored in black. There is no major difference in the particle trajectory at the beginning of the filling phase (t=0.3 s) between the two wall conditions. Under

251

conditions, SVC and FP flow met at the neck of the SVC-PA junction (t=0.6 s) and together they circulated at the middle of the TCPC (t=0.86 s).

After the second cycle (t>0.86 s), the particles circulate before leaving the domain under both FSI and rigid wall conditions (t=1.3 s). However, the particle washout trajectories were different in the FSI and rigid wall simulations. From t=1.5s to t=1.72s, the particles circulated at the center of the TCPC close to the PAs for the FSI simulation. For the rigid wall simulation from t=1.5s to t=1.72s, the particles circulated within the entire region of the center of the TCPC, instead of just close to the PAs. From t = 2.58s to t = 3.44s, most particles had already exited the domain in the FSI simulation. For rigid wall simulation from t = 2.58s to t = 3.44s, particles still remained in the domain. Many of these particles are found close to the walls of the TCPC.

FSI

t = 0.3s t = 0.6s t = 0.86s t = 1.3s

t = 1.5s t = 1.72s t = 2.58s t = 3.44s

InjectionStepId
860
800
600
400
200
0
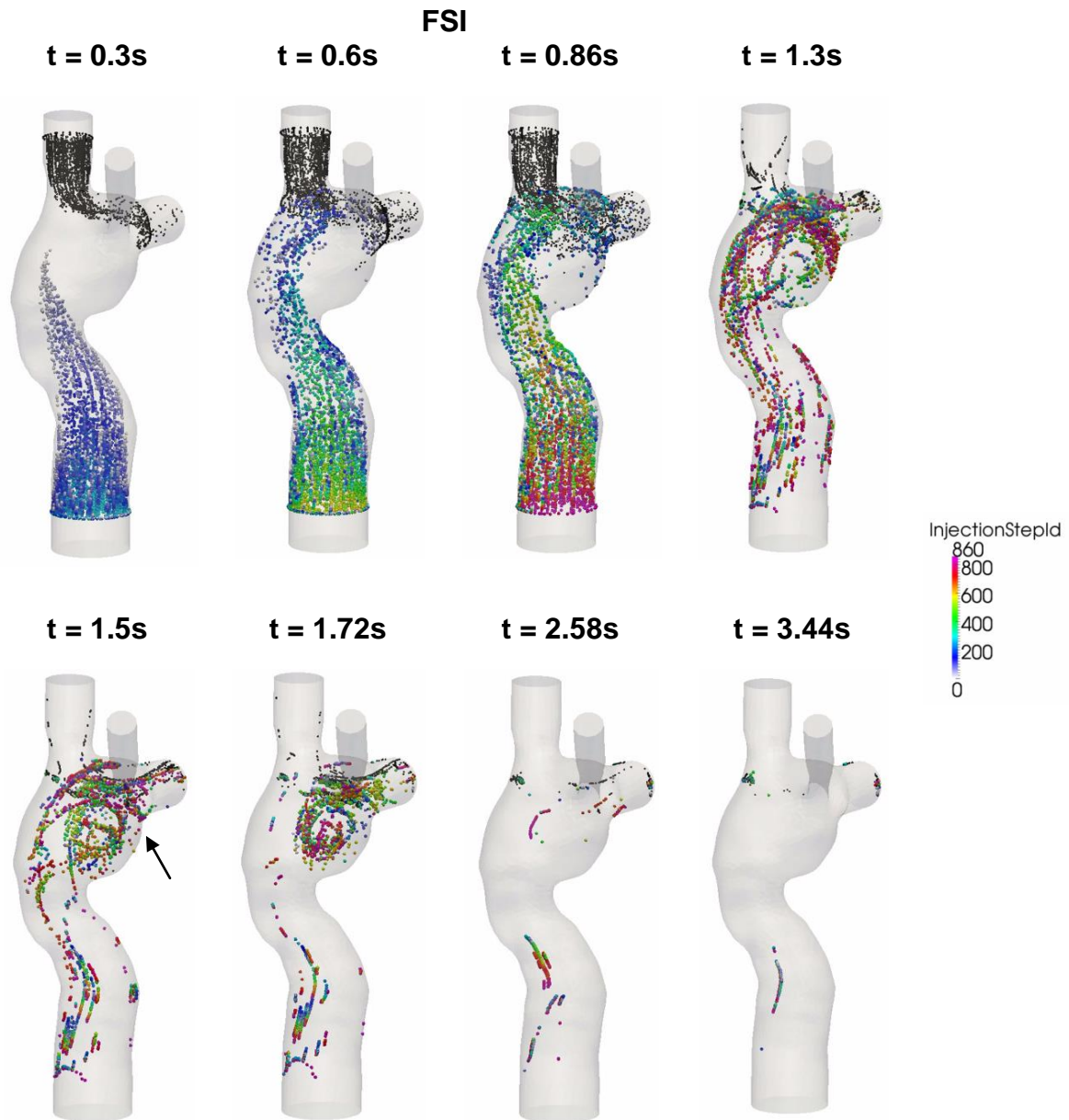
Figure 7.20 Progression of the particles seeded at the FP from the FSI simulation. The FP particles are color coded by their seeding time step. SVC particles are colored black
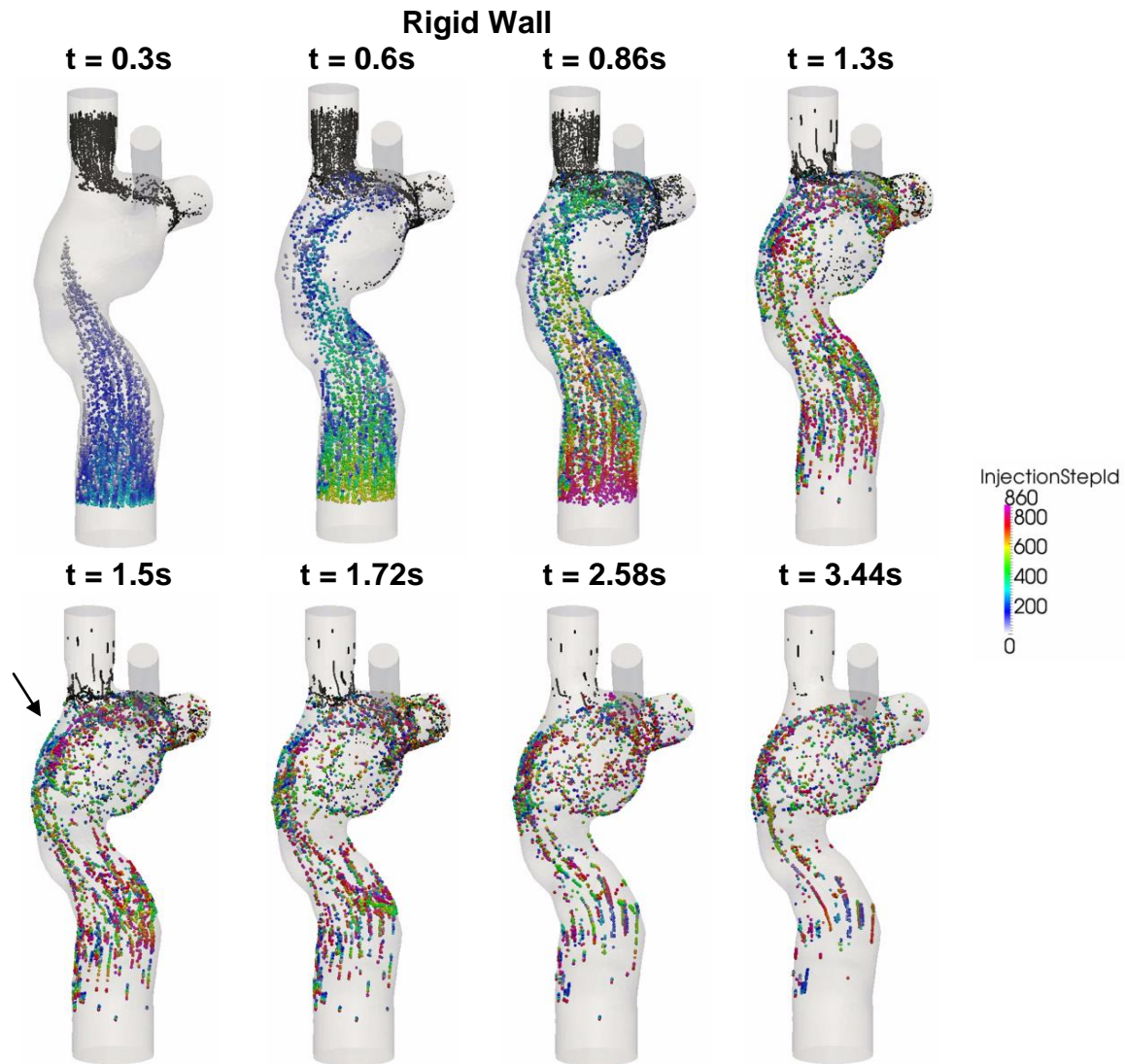
Figure 7.21 Progression of the particles seeded at the FP from the rigid wall simulation. The FP particles are color coded by their seeding time step. SVC particles are colored in black

Animation 7.3 Particle tracking video of FSI simulation. Particles are colored by its release time step (animation_7.3_FSI.avi, 2.82MB)

Animation 7.4 Particle tracking video of rigid wall simulation. Particles are colored by its release time step (animation_7.4_Rigid.avi, 2.97MB)

From Figure 7.20, it is seen that very few particles remain in the domain after one cardiac cycle (FSI simulation). It is found that with a deformable wall, most of the particles from the FP left the domain within one heart beat. The quantitative distribution of the FP particle residence times are shown in Figure 7.22 and are compared between the FSI and rigid wall simulations. The particle residence time distributions are very different. The peak of the distribution of the FSI simulation occurred at 801 ms, whereas that for the rigid wall simulations occurred at 1439 ms. Also, the peak of the rigid wall simulation is of smaller amplitude. A majority of particles seeded at the FP in the rigid wall simulation took more than one cardiac cycle to leave the TCPC. The particle washout time (time at which 95% of the FP particles left the domain) is shown in Table 7-8. It took 1.77s (~2 cardiac cycle) for 95% of the FP particles to leave the TCPC for the FSI simulation. It took much longer (3.16 s) for 95% of the FP particles to exit the domain for the rigid wall simulation.
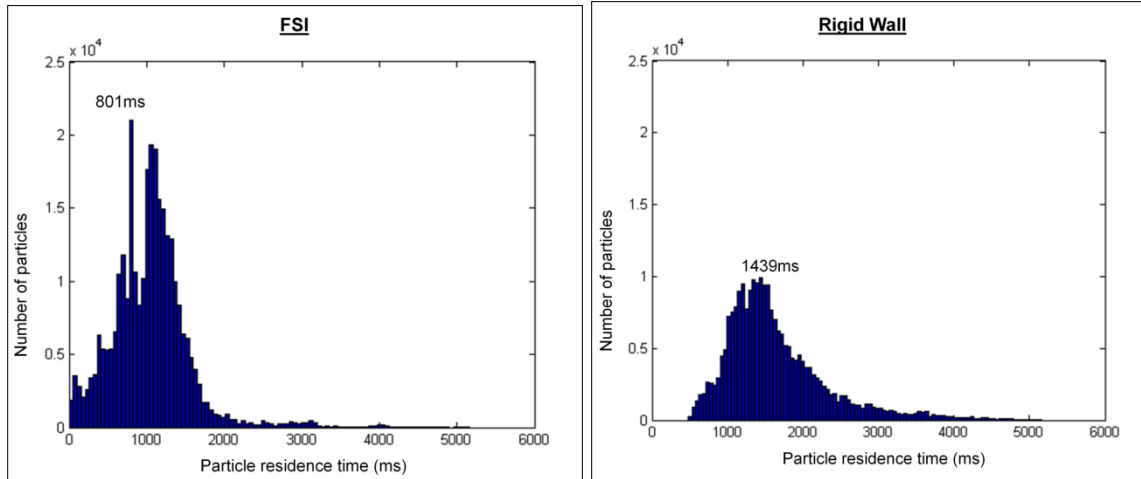
Figure 7.22 Distribution of the IVC particle residence times: (a) FSI simulation and (b) rigid wall simulation

Table 7-8 Comparison of particle washout time and time-averaged HFD between Rigid wall and FSI simulations

	Particle Washout time (s)	Particle Washout time (no. of cardiac cycle)	Time averaged %HFD(LPA)
FSI	1.77	2.06	19%
Rigid wall	3.16	3.67	19%

Particle tracking was also performed by visualizing the particles based on the vessel of origin. From Figure 7.23 and Figure 7.24. It can be observed that in both the FSI and rigid wall simulations, majority of the SVC particles exited through the RPA due to proximity. Even with the differences in velocity magnitude of the FP jet and velocity field at the center of the TCPC as observed earlier, there were little differences in the FP particle trajectory between FSI and rigid wall simulations. From the particle tracking results, HFD was also computed. Instantaneous %HFD(LPA) is shown in Figure 7.25. It is observed that %HFD to the LPA fluctuated in time more in the FSI simulation than the

256

rigid wall simulation. However, comparing the time-averaged %HFD(LPA), no difference

is found between the two conditions (Table 7-8).
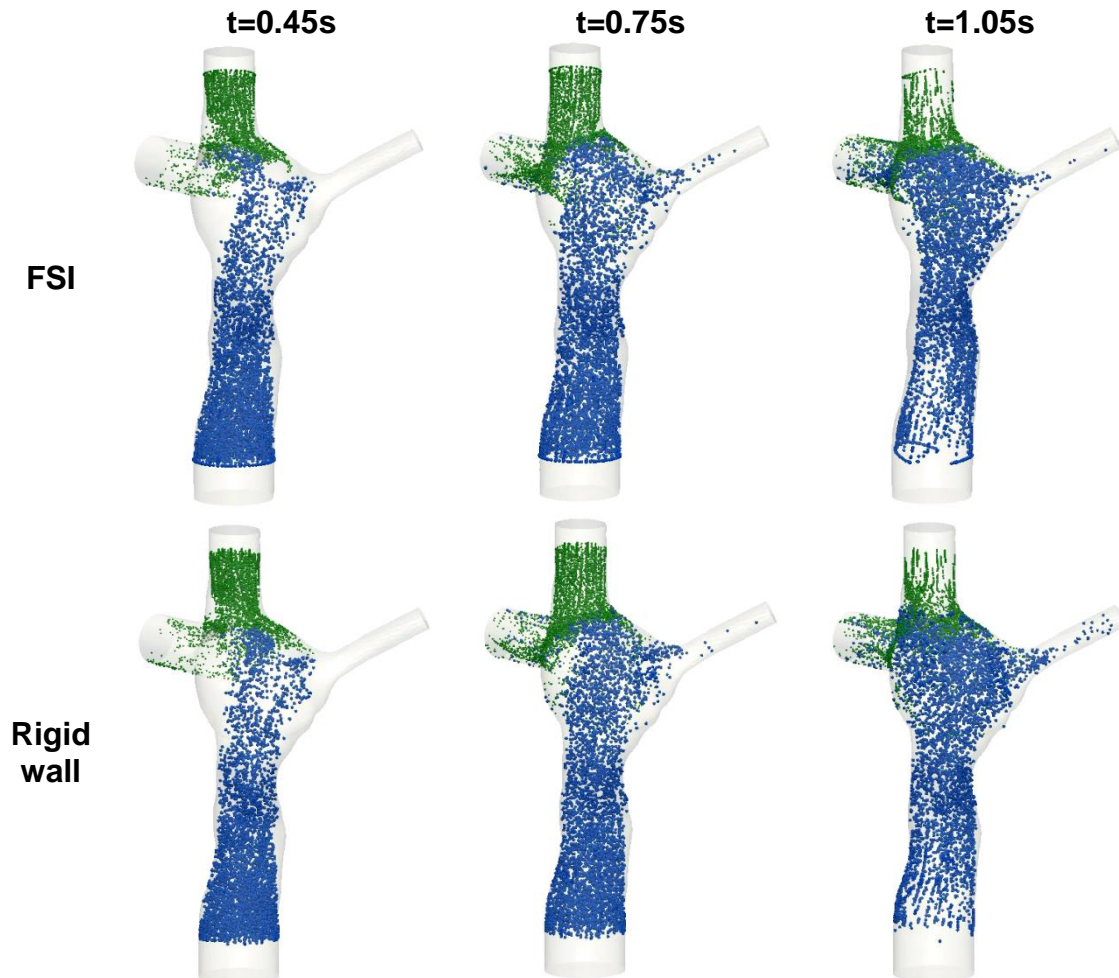
Figure 7.23 Screenshots of the particle tracking results of FSI and rigid wall simulations from t=0.45s to t=1.05s . Particles originating from the FP are colored blue and particles originating from the SVC are colored green
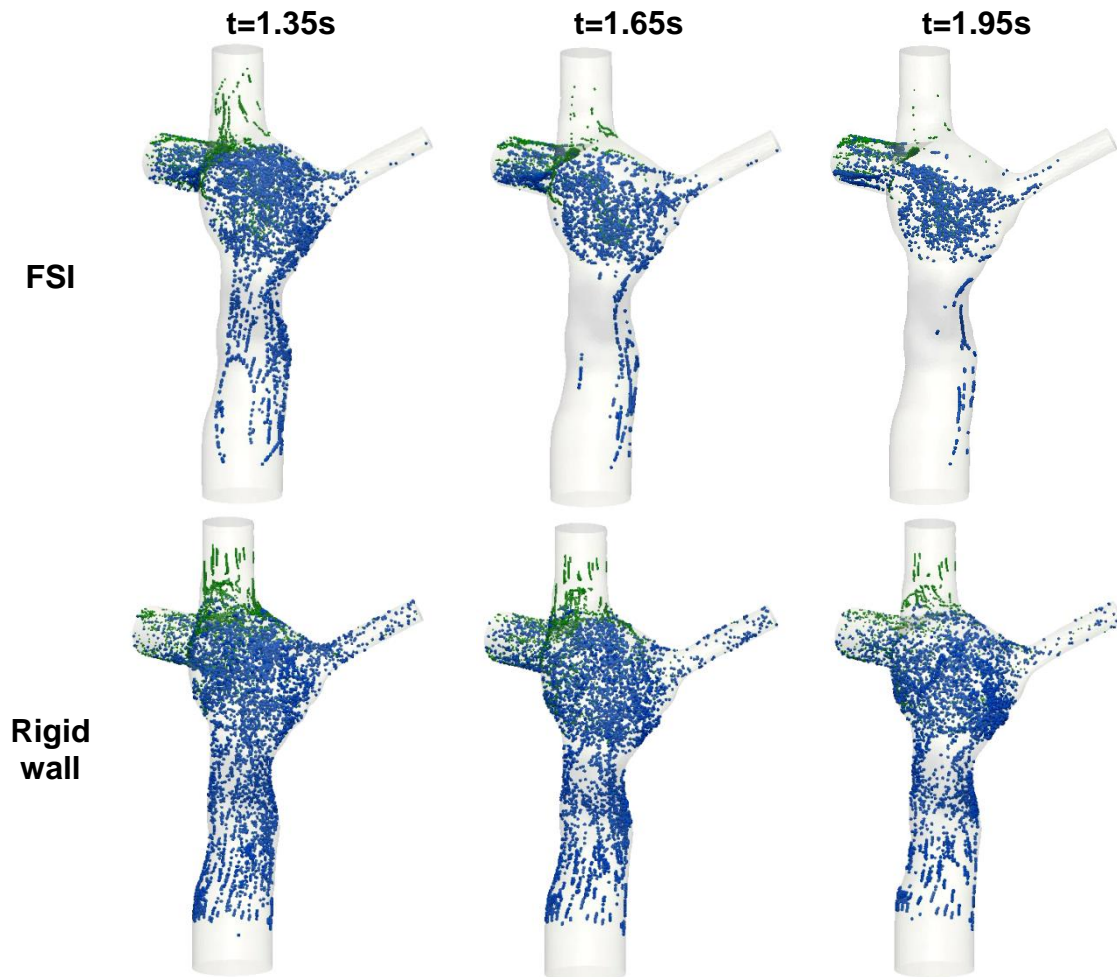
Figure 7.24 Screenshots of the particle tracking results of FSI and rigid wall simulations from t=1.35s to t=1.95s . Particles originating from the FP are colored blue and particles originating from the SVC are colored green
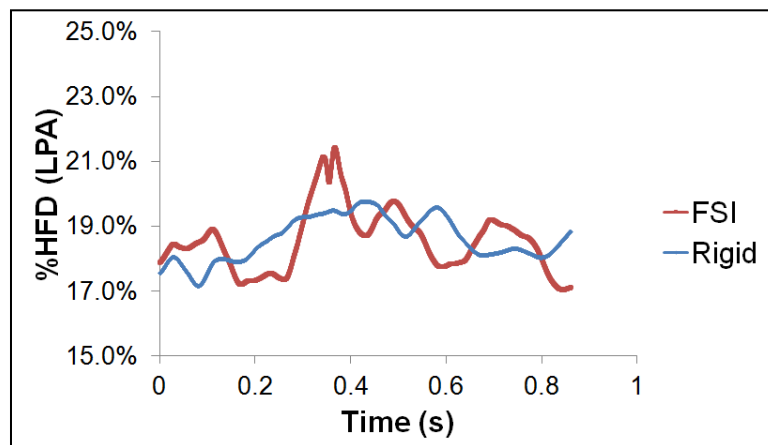
Figure 7.25 Hepatic Flow Distribution (% FP flow to the LPA) of the FSI and rigid simulations within a cardiac cycle

7.4 Discussion

In most CFD models of the TCPC, a rigid wall is often assumed for simplicity and reduced computational cost. However, in reality, the TCPC is composed of native tissues (caval veins and pulmonary arteries) which are compliant. TCPC wall deformation has been observed *in vivo*, but quantification with respect to the vessel type and flow condition is still lacking.

From the *in vivo* wall deformation characterization results (Specific Aim 3(a)), it was found that the FP and SVC deform with increasing magnitude (area change) from BH, FB to EX conditions. The results also suggest that future work should evaluate the impact of wall deformation not only with respect to the cardiac cycle, but also with respect to respiration. Because of the limited sample size, a comparison between intra-atrial and extracardiac TCPCs was not performed and should be considered in future work. Ideally, a Fourier transform should be performed on the vessel area waveform to remove the frequency of the cardiac cycle to help isolate the impact of respiration. However, the temporal resolution (about 60ms) was not sufficient to clearly identify the cardiac cycle frequency (about 1s). baDI was defined to compute change in beat-averaged vessel area. But note that it such averaging may not be completely eliminating the effect of cardiac cycle from the vessel area waveform. Descending aorta was used to estimate the duration of cardiac cycle. However, since the peak velocity of aorta is higher than the FP/SVC, which can exceed the encoding velocity of the FP/SVC image. The magnitude of descending flow is therefore subjected to error.

Knowing that TCPC vessel wall deforms *in vivo*, it is important to understand how such deformation can affect hemodynamics. Long et. al. performed FSI CFD analysis on two extracardiac TCPCs with varying wall properties [130]. The results showed that there was little effect of FSI (with both homogenous and heterogeneous vessel wall material properties) on pressure tracings, hepatic flow distribution, and time-averaged energy efficiency. However, the effect of FSI on wall shear stress, instantaneous energy efficiency, and wall deformation was significant. This study highlighted that the impact of FSI on TCPC hemodynamics is relevant to the metric of interest. However, several assumptions were made with regards to the wall material properties, which have not been validated. Also, this study was performed on extracardiac patients only. The geometry and constitutive materials of the extracardiac and intra-atrial TCPC can be very different. It is expected that the difference in flow dynamics between rigid wall and compliant wall simulations to be more profound in the intra-atrial TCPCs. Mirabella et. al. investigated the effect of wall deformability on intra-atrial TCPC hemodynamics with *in vivo* wall deformation data [109]. Using cine anatomic MRI data, the *in vivo* wall deformation was prescribed in a CFD model that includes a moving domain. The largest differences between rigid and moving wall models were observed in measures of energetic efficiency of TCPC as well as in hepatic flow distribution and transit time of seeded particles through the connection. This study highlighted the importance of wall deformation on intra-atrial TCPC hemodynamics. However, this approach is not necessarily applicable for prospective modeling, as one cannot always predict how the vessel wall will deform after the surgical connection is being altered. Therefore, the goal

of Specific Aim 3(b) was to investigate the effect of wall deformation on an intra-atrial patient using an FSI approach.

The simulated wall deformation of the FP and SVC from Specific Aim 3(b) was compared with PC-MRI data. Using a normalized metric, the deformation index, the change in vessel area at the FP and SVC were compared between the numerical simulation and PC-MRI data. It was found that FP DI was in close agreement between FSI simulation and *in vivo* data. This is important as intra-atrial FP wall deformation was the focus of this work. This suggested the assigned wall material property at the FP was a reasonable estimation of the *in vivo* wall properties. However, the SVC DI agreement between FSI simulation and PC-MRI was poor. This could be attributed to the following reasons: It was possible that the assigned homogenous material properties throughout the TCPC were different from the *in vivo* SVC wall material property. Another possible reason could be due to the PC-MRI pixel spacing (0.11719 cm). The average SVC area from the PC-MRI was 1.94 cm^2 and that of FP was 6.81 cm^2. Therefore, MRI resolution would have played a bigger role on the SVC area and contributed to more relative error than the FP. From the change in TCPC volume as well as the pressure drop across the connection, TCPC compliance was estimated to be 1.64 mL/mmHg. This is in the same order of magnitude as PA compliance in healthy subject = 2.87 mL/mmHg [216].

Qualitative differences in TCPC flow field were observed at the FP velocity jet and the center of the TCPC between rigid wall and FSI simulations. These were also the regions of which most wall displacement was observed in the FSI simulation. Particle residence

time provides a quantitative measure for the differences of particle pathways under rigid wall and compliant wall conditions. The longer residence times of the rigid wall condition were mostly associated with FP particles evolving at a low velocity close to the rigid wall (Figure 7.21). On the other hand, with deformable wall, the particles in the wall boundary layers had a higher probability to be redirected towards the bulk of the flow during contraction of the deforming wall.

TCPC pressure drop and power loss are important hemodynamic metrics, as high power loss suggests a less efficient pathway, which has been related to patient exercise intolerance [2, 217]. Pressure drop and power loss were compared between rigid wall and FSI simulations. Instantaneous pressure drop and power loss vary between FSI and rigid wall simulations. Comparing the maximum and minimum pressure drops and power loss, the rigid wall simulation has larger fluctuations than that of the FSI simulation, which is in agreement with previous similar study on carotid artery [218]. However, the differences in time-averaged pressure drops (0.01mmHg) and power losses (0.1mW) between the two simulations were small. Hepatic flow distribution was also quantified, which is a TCPC hemodynamic metric that was related to the risk of PAVMs [3, 5, 48]. As shown in Figure 7.25, the instantaneous HFD varies within the simulated cycle between rigid wall and FSI simulations. However, there was no difference in time-averaged HFD between the two conditions, which agrees with Long et. al. [130].

Previously, it was speculated that the hemodynamic differences observed in intra-atrial and extracardiac TCPCs were attributed to its geometry as well as wall properties. From this work, it was found that wall compliance has little influence on time-averaged hemodynamic quantities under resting BH condition. This also means that the compliance of the Intra-atrial TCPC did not contribute significantly to TCPC hemodynamics as one would expected.

The results in this chapter suggest that wall deformation has impact on the instantaneous hemodynamic metrics of the TCPC (instantaneous flow field, particle trajectory, pressure drop, power loss and HFD). However, FSI has little impact on time-averaged quantities (pressure drop, power loss, HFD) under resting BH condition. Considering time-averaged hemodynamic quantities are the more common surrogates of patients' hemodynamic performance of the TCPC, the results of this work suggest that a rigid wall assumption is a reasonable approximation when evaluating time-averaged quantities under resting BH condition

7.5 Limitations

A linear elastic structural model was assumed for the vessel wall. Stress-free outflow boundary conditions were also utilized. Also, the TCPC is composed in heterogeneous materials. It contains native tissue, as wells as stiffer surgical materials and suture lines. In addition, the initial condition of the FSI simulation utilized geometry from patient specific MRI images, which represents a deformed configuration stressed by the *in vivo*

conditions. In the simulation, the structure was assumed to be stress free initially. However, these limitations should not affect the conclusion of this study.

7.6   Clinical Significance

The results in this chapter suggest that wall deformation has impact on the instantaneous hemodynamic metrics of the TCPC (instantaneous flow field, particle trajectory, pressure drop, power loss and HFD). However, FSI has little impact on time-averaged quantities (pressure drop, power loss, HFD) under resting BH condition. Considering time-averaged hemodynamic quantities are the more common surrogates of patients' hemodynamic performance for surgical planning of TCPC, the results here support the notion that a rigid wall assumption is a reasonable assumption for such image-based surgical planning systems. The framework for a surgical planning system of TCPC already exists [48, 102] to prospectively model different surgical configuration. Time-averaged quantifies (mainly power loss and HFD) were compared across different surgical options, usually with resting BH flow boundary conditions. A rigid wall assumption was often applied for simplicity. It was originally expected that including vessel deformability into the system can possibly help more realistically predicting post-operative scenarios. From the results of this work, it suggests that a rigid wall assumption is a reasonable approximation when evaluating time-averaged quantities under resting BH condition. Especially when the surgery planning needs to be completed in a short time frame and FSI simulation has higher computational cost, it could be expected that the error associated with rigid wall assumption will be minimal.

7.7 Chapter Summary

In this chapter, the rigid wall assumption used in most CFD models of the TCPC was evaluated. Firstly, vessel wall area change was quantified under resting BH, FB and exercise conditions. It was found that the magnitude of wall deformation varied between these conditions. Then, a detailed comparison of TCPC hemodynamics under a rigid wall and a compliant wall condition was performed with respect to the surrogates for TCPC efficiency, namely power loss, HFD and particle washout time on an intra-atrial patient. The wall deformation in the simulated FP was in the same magnitude as that observed *in vivo.* The simulation results suggest that a rigid wall assumption appears to provide an adequate representation of the time-averaged TCPC power loss and pressure drop. Even though it was expected that HFD prediction was affected by the compliant wall in the intra-atrial TCPC, there was no difference in time-averaged HFD between rigid wall and FSI simulations. In summary, the results of this chapter support the use of a rigid wall assumption on evaluation of time-averaged TCPC hemodynamic metric under resting BH condition.

CHAPTER 8   Discussion

8.1   Overview

Currently, most CFD models of the TCPC are capable of modeling patient specific anatomy, and an increasing number of models have included the effect of cardiac-driven flow pulsatility. However, due to insufficient clinical data (e.g. lack of respiration information), and computational resources (high computational cost of FSI simulation), respiration effects and wall compliance were often neglected in previous studies. The goal of this thesis was to investigate the effect of geometry, cardiac and respiratory flow pulsatility and wall compliance on TCPC hemodynamics. Note that these effects are listed in order of increasing level of modeling difficulty and computational resource requirements.

The impact of TCPC geometric characteristics on resting (Chapter 5.2, Specific Aim 1 (a)) and exercise hemodynamics (Chapter 5.3, Specific Aim 1(b)) has been investigated. Also, the effect of stent implantation on reducing TCPC energy dissipation (Chapter 5.4, Specific Aim 1(c)) has been studied. To help understand the impact of respiration, TCPC hemodynamics under free-breathing and breath-held conditions was evaluated and compared (Chapter 6, Specific Aim 2). Finally, the degree of wall motion of the TCPC vessel was quantified and the effect of wall compliance on TCPC hemodynamics was evaluated (Chapter 7, Specific Aim 3). In this chapter, the major findings across the studies presented in this thesis will be discussed and summarized.

8.2 Impact of Geometry on TCPC Hemodynamics

8.2.1 Effect on Resting Hepatic Flow Distribution

In this thesis, the impact of TCPC geometric characteristics on TCPC hemodynamics was investigated, using the Georgia Tech Fontan MRI database. The analysis shows that resting HFD was influenced by caval offset (r=0.713), FP-SVC angle (r=-0.336) and flow split between LPA and RPA (r=0.624). This study suggests the role of connection angle to hepatic flow distribution, which is relevant to the formation of PAVMs. While caval offset has been a common control variable in optimizing HFD in surgical planning of the TCPC, the analysis presented in this specific aim suggested that the relative angle between FP and SVC should be considered in cases where caval offset is constrained and pulmonary flow distribution is unbalanced. This can be important for future Fontan surgical planning of SV patients to reduce the risk of PAVMs.

8.2.2 Effect on TCPC Power Loss

Minimum FP (r=-0.73) and PA (r=-0.50) diameters were inversely correlated with iPL at rest. Minimum FP (r=-0.66) and PA (r=-0.47) diameters were also inversely correlated with iPL at VAT. Though it was not clear what caused the narrowing of the TCPC vessels, these correlations suggest it may be important to dilate vessel narrowing at the TCPC (e.g. by stent implantation), especially in intra-atrial patients. This was confirmed also by the significant negative correlation between resting cardiac index and minimum FP diameter (r=0.36). The pilot study of stent implantation in lateral tunnel stenosis patients evaluated the hemodynamic impact of LT stenosis and stent implantation under both resting and exercise conditions using a CFD simulation tool. Preliminary results

highlighted the hemodynamic benefit of stent implantation in patients with severe LT stenosis, especially during exercise. All these results suggest that long term post-operative follow-up is essential in Fontan patients as vessel stenosis may progress over time. Understanding the physiological outcomes after intervention with stent implantation [203] may be important, because the pathway narrowing can potentially elevate energy loss during high cardiac flow and lead to exercise intolerance in these patients [2].

8.2.3 Implication on Exercise Performance

Given the close relationship between minimum TCPC diameter and iPL at VAT, it is important to investigate the clinical importance of this correlation with patients' exercise performance. In the single ventricle circulation, a low PVR is essential to achieve the increase in cardiac output required during exercise, and is therefore important for exercise performance [200]. PVR of Fontan patients was previously reported as 2.8 ± 0.9mmHg/(L/min/m^2) during peak exercise [58]. In this cohort, it was found that TCPC resistance at VAT was on average 0.57 ± 0.48mmHg/(L/min/m^2), and could be as high as 2.23mmHg/(L/min/m^2) (for the patient with the lowest TCPC diameter index, 10.8mm/m). Given that this value is comparable with PVR at peak exercise, it is clear that TCPC resistance is not negligible in all patients and could potentially impair the ability of the patient to increase pulmonary blood flow that is required for effective exercise.

This thesis for the first time explores the age-related differences in Fontan exercise performance with respect to TCPC geometry and hemodynamics. It shows the relevance of local TCPC geometry and hemodynamics to exercise performance in adolescent Fontan patients (correlation between VO_2 at VAT and iPL at VAT: r=-0.58; correlation between VO_2 at VAT and TCPC diameter index: r= 0.41). It also highlights that since exercise performance decreases with age, as patients reach adulthood, local geometry and hemodynamics may be less relevant to exercise performance (p>0.3). Understanding these relationships can potentially help derive strategies to improve patient exercise performance based on their age, as well as identifying patients that are prone to exercise intolerance.

8.3   Impact of Respiratory-Driven and Cardiac-Driven Flow Pulsatility

Breath-held MRI acquisition has been commonly used to evaluate patient specific TCPC hemodynamics. However, this ignores the impact of respiration on TCPC hemodynamics. In this thesis, the difference in TCPC flow field under FB and BH flow conditions were evaluated with the use of real time PC-MRI data acquired under FB and BH conditions. From *the in vivo* vessel flow waveform analysis, the higher wPI under FB condition suggests that respiratory-driven flow pulsatility is non-negligible. Using simulations, it was discovered that the TCPC flow field changed in velocity magnitude and direction within the respiratory cycle. Differences in the TCPC flow fields were observed between the FB and BH conditions, especially during inspiration. Quantitative differences in particle washout time and TCPC power loss were also observed between the two conditions (maximum difference = 1.91 respiratory cycles), which could be

attributed to the magnitude of flow pulsatility, retrograde flow, relative flow between FP and SVC, and patient specific anatomic features. In addition, elevated wPI led to higher power loss under FB condition. By including all patients and all conditions, a positive correlation was observed between wPI and diPL (for all patients: $R^2 = 0.7452$, for single SVC patients: $R^2 = 0.9255$).

The findings from this specific aim suggest that evaluating TCPC hemodynamics under the BH condition can affect TCPC power loss estimation. For example, for one of the patients with FP narrowing (CHOP032C, Chapter 6.4.1.3), the pressure drop across the vessel narrowing was underestimated under the BH condition when compared to the FB condition. This suggests that respiration can be important in the evaluation of hemodynamics in LT stenosis in Specific Aim 1. From an engineering standpoint, this study reinforces the importance of pulsatile boundary conditions when modeling TCPC hemodynamics instead of using time-averaged conditions. The results in this study also highlight the importance of including the impact of respiration as boundary conditions in the CFD modeling of TCPC hemodynamics. Last but not least, wPI can be a good metric to quantify the effect of cardiac-driven and respiratory-driven flow pulsatility on evaluation of TCPC power loss.

8.4   Impact of Wall Deformation on TCPC Hemodynamics

A rigid wall boundary is often assumed in most CFD models of the TCPC, including those used in Specific Aims 1 and 2 in this thesis. However, in reality, the TCPC wall motion has been observed *in vivo*, but quantification with respect to the vessel type and

flow condition is still lacking. From the *in vivo* wall motion analysis, it was found that FP and SVC deform with increasing magnitude from BH, FB to exercise conditions. Also, dependence of vessel area change with respect to respiration was observed. The results here also suggest that future work should evaluate the impact of wall deformation with respect to respiration.

Using FSI numerical simulation, the impact of wall deformation on TCPC hemodynamics was studied in an intra-atrial patient. The wall deformation of the FP and SVC from FSI simulation was compared with PC-MRI data. It was found that FP cross sectional area change was in close agreement between FSI simulation and *in vivo* data. This suggested the assigned wall property at the FP was a reasonable estimation of the *in vivo* FP wall material properties. SVC deformation was poorly matched, suggesting the need for heterogeneous material properties assignment at the wall of the TCPC.

TCPC pressure drop and power loss are important hemodynamic metrics, as high power loss suggests a less efficient pathway, which has been related to patient exercise intolerance [2, 217]. Pressure drop and power loss were compared between rigid wall and FSI simulations. Instantaneous pressure drop and power loss varied between FSI and rigid wall simulations. However, time-averaged pressure drop and power loss showed no significant differences between the two simulations. Hepatic flow distribution was also quantified, which is a TCPC hemodynamic metric that is related to the risk of PAVMs [3, 5, 48]. Instantaneous HFD varied within the simulated cycle between rigid

wall and FSI simulations. However, there was no difference in time-averaged HFD between the two conditions.

The results in this chapter suggest that wall deformation has an impact on instantaneous hemodynamic metrics of the TCPC (instantaneous flow field, particle trajectory, pressure drop, power loss and HFD). However, FSI has little impact on time-averaged quantities (pressure drop, power loss, HFD) under the resting BH condition. The results from this patient and previous studies also suggested that the rigid wall assumption used in Specific Aims 1 and 2 for the BH condition can be a reasonable assumption for time-averaged quantities.

8.5   Implications on CFD Power Loss Prediction

In this thesis, different modeling conditions were applied. The summary of modeling conditions utilized in this thesis is summarized in Table 8-1. For Specific Aim 1(a), a geometric analysis was performed across 104 patients to correlate between TCPC hemodynamics and geometric features. A subset of those patients and additional patients (49 patients in total) were studied under exercise conditions in Specific Aim 1(b). In Specific Aim 1(c), 6 patients were studied with varying LT diameters and also different simulated exercise levels. In Specific Aim 2, 9 patients were studied to understand the effect of free-breathing on TCPC hemodynamics. Four conditions were simulated (FB pulsatile, BH pulsatile and their respective time-averaged flow conditions). Finally in Specific Aim 3, the effect of wall compliance was studied under pulsatile flow condition in an intra-atrial patient.

272

Table 8-1 Summary of modeling conditions being applied in this thesis

Specific Aim		1(a)	1 (b)	1(c)	2	3
Effect Investigated		Geometry			Respiration	Wall compliance
Sample size		104	49	6	9	1
Modeling Condition	Geometry alteration	No	No	Yes	No	No
	Time-averaged Flow Rate	Rest	Exercise	Rest and exercise*	Rest	Rest
	Flow pulsatile	Steady			Steady /Pulsatile	Pulsatile
	Respiration	BH			FB/BH	BH
	Wall compliance	Rigid			Rigid	Compliant

*Simulated exercise

Since the modeling conditions were modified parametrically in each patient, the difference in time-averaged power loss within each patient may help us understand how much of the TCPC power loss is being affected by each condition. In all of the patients studied in this thesis, such power loss differences were quantified (summarized in Table 8-2). The modeling conditions being compared (geometry, time-averaged flow, flow pulsatility, respiration, wall compliance) are listed on the first column. Maximum percentage differences are compared and listed on the last column, which represent the worst case scenario of percentage error in time-averaged power loss when neglecting a certain condition.

Table 8-2 Summary of time-averaged power loss difference quantified in this thesis based on the modeling conditions

Modeling condition	Specific Aim	N	Condition being compared		% Difference between conditions *		
			Condition 1	Condition 2	Min.	Median	Max.
Geometry (diameter)	1(c)	6	Max. LT diameter (Rest)	Min. LT diameter (Rest)	99%	262%	1007%
Magnitude of time-averaged flow	1(b)	48 #	Rest	Exercise	4%	734%	3085%
	1(c)	6	Rest	Simulated Heavy Exercise	1530%	2050%	2588%
	2	9	BH (at rest, steady)	FB (at rest, steady)	5%	76%	118%
Flow pulsatility (BH)	2	9	Pulsatile (BH at rest)	Steady (BH at rest)	1%	5%	16%
Flow pulsatility (FB)			Pulsatile (FB at rest)	Steady (FB at rest)	2%	32%	66%
Respiration (rigid wall)	2	9	BH (at rest, pulsatile)	FB (at rest, pulsatile)	32%	100%	206%
Wall compliance	3	1	Rigid wall (at rest, BH, pulsatile)	Homogeneous compliant wall (at rest, BH, pulsatile)	3%		

* %Difference between conditions = $\frac{(Power\ loss\ at\ Condition2) - (Power\ loss\ at\ Condition1)}{(Power\ loss\ at\ Condition1)}$

\# Resting data was not available for one patient in Specific Aim 1(b)

As expected, patient specific geometry and magnitude of time-averaged flows are the most dominant factors affecting TCPC power loss. Out of the patients included in this thesis, the maximum changes in power loss by altering geometry and flow rate are 1007% and 3085%, respectively. This highlights the importance of accurate medical images and accurate image reconstruction techniques to capture the patient specific anatomy and time-averaged flow, since inaccurate representation of TCPC anatomy and flow will strongly influence TCPC power loss.

The next assumption related to TCPC CFD modeling is time-averaged boundary conditions. Comparing pulsatile and time-averaged flow boundary conditions under the BH condition, maximum power loss difference of 16% is observed. Under FB condition, maximum power loss difference is 66%. This suggests that the effect of flow pulsatility is secondary to geometry and flow rate. The effect of pulsatility on TCPC power loss also depends on whether FB or BH conditions are being used. Comparing TCPC power loss at FB and BH with pulsatile flow boundary conditions, the maximum power loss difference is 206%. This is higher than the effect of flow pulsatility under free-breathing (maximum power loss difference = 66%), as respiration (assuming rigid wall) also affects TCPC power loss by change in time-averaged flow (maximum power loss difference = 118%).

The final assumption assessed in this thesis is wall compliance. The effect of wall compliance on an intra-atrial patient was investigated under the BH condition. Time-averaged TCPC power loss only changed for 3% between rigid wall and compliant wall (with homogeneous wall properties) simulations. The results found here are in agreement with Long et. al. [130] on their investigation on two extracardiac patients that wall compliance has little effect on TCPC power loss under resting conditions. This suggests that under the BH condition, wall compliance has little impact on time-averaged hemodynamic quantities. Unless instantaneous hemodynamic quantities and particle washout time are of interest, the rigid wall assumption is a reasonable assumption for evaluating time-averaged power loss under the BH condition.

In summary, from the results of this thesis, it is suggested that TCPC geometry and time-averaged flow are the primary determinants on TCPC power loss. Respiratory and flow pulsatility has secondary effects. Finally, wall compliance has the smallest effect on time-averaged TCPC power loss under BH condition. Future work should include more patients to verify these findings, and also examine the effect of wall compliance under free-breathing and exercise conditions.

CHAPTER 9   Future Work and Recommendations

9.1   Overview

The goal of this thesis is to explore the impact of geometry, respiration, and wall compliance on TCPC hemodynamics. Both resting and exercise patient specific TCPC hemodynamics were studied with computational fluid dynamics simulations, employing patient specific anatomy and flow data segmented from medical images. In this chapter, the potential future directions related to this thesis work will be highlighted.

9.2   Impact of TCPC Geometry on Its Hemodynamics

The impact of the geometry of the bifurcated Fontan Y-graft [115, 219] on resting and exercise TCPC hemodynamics should be investigated in future studies.

When evaluating the effect of stent implantation in Specific Aim 1 (Chapter 5.4), flow boundary conditions before stent implantation were used for post-stent simulations. In the future, the use of a lumped parameter model for the rest of the circulation may be useful when coupled to the 3-dimensional solver [100], to help better predict flow boundary conditions after stent implantation. In addition, such lumped parameter model can help better understand the effect of TCPC hemodynamics on the global circulation (e.g. ventricular function and blood flow to the rest of the body). Also, exercise flow rates were prescribed by doubling and tripling baseline LT flow, which may not be realistic for patients with a Fontan circulation [134, 205]. Patient specific flow conditions should be applied when this data are available.

On investigating the effect of TCPC vessel stenosis, there are several potential future directions. First of all, more patients should be included to fully understand the impact of stent implantation in LT patients. In this thesis, discrete stenosis at the LT was observed. Tubular or longer segment vessel narrowing may impose different loads and should be investigated in future studies. Vessel stenosis has been observed in extracardiac FPs [196, 220-222] and pulmonary arteries [92, 198], which also warrants future investigations. When performing virtual stent implantation in Specific Aim 1(Chapter 5.4), a cylinder was created and merged with the pre-stent TCPC geometry in Geomagic Studio (Geomagic Inc., NC, USA) to mimic post-stent geometry. Through the collaboration between Drs. Yoganathan and Rossignac (GT College of Computing), the SURGEM software now offers a "stenosis mode", which provides an interface for a user to perform virtual stent implantation. This tool is highly automated, and is highly recommended for future use when modeling stent implantation at the TCPC (or any vascular anatomy).

9.3   Respiration Model

In Specific Aim 2 (Chapter 6), the effect of respiration was only studied as an effect of vessel flow. Its interaction with change in intra-thoracic pressure and vessel compliance warrants future investigations. Also, even though it was assumed that the only difference between breath-hold and free-breathing condition was with or without breathing, the two conditions were still different image acquisitions. Fourier transform

278

could be performed on the free-breathing data in the future to tease out the respiration component.

9.4   FSI Model

In Specific Aim 3 (Chapter 7), a linear elastic structural model was assumed for the vessel wall. Stress-free outflow boundary conditions were also utilized. With improvement in computational resources, future FSI simulations can be improved by utilizing a non-linear structural model. Also, a Robin boundary condition at the structure can be applied to mimic the effect of surrounding structure on TCPC hemodynamics. A robin boundary condition is a weighted combination of Dirichlet boundary conditions and Neumann boundary conditions, which allows prescription of the surrounding tissue stiffness and pressure of the thoracic cavity [223-225]. Also, the TCPC is composed in heterogeneous materials. It contains native tissue, as wells as stiffer surgical materials and suture lines. Future studies can include the material property heterogeneity. In addition, the initial condition of the FSI simulation utilized geometry from patient specific MRI images, which represents a deformed configuration stressed by the *in vivo* conditions. In the simulation, the structure was assumed to be stress free initially. Inverse analysis can be performed in the future to calculate a stress-free reference configuration as initial condition [226, 227]. For the fluid model, a Windkessel model can be applied at the outlet to control the relative flow resistance at the LPA and the RPA. All these additions will increase the computational cost, but can potentially increase the accuracy of the FSI model.

9.5   *In Vivo* Validation

For every computational model, validation is essential to ensure accurate representation of the physical and physiological phenomenon. Experimental validation was performed for the immersed boundary solver [75, 157] as well as the LifeV finite element method solver [163]. However, *in vivo* validation remains a critical challenge that should be performed in the future. The immersed boundary solver applied in this study was validated under resting conditions using *in vivo* data [228]. However, the validation of exercise CFD simulations is more difficult, since the acquisition of a patient specific time-varying 3-dimensional flow field during exercise with CMR is challenging.

9.6   Correlating Results to Patient Outcomes

In this thesis, hemodynamic metrics like iPL at rest and exercise, TCPC resistance and HFD were investigated. However, the single ventricle physiology is very complex. The clinical importance of iPL and TCPC resistance is not fully understood. Also, it is not clear how these metrics can affect a patient's long term clinical outcome. Also, TCPC hemodynamics was only investigated at the instants where the clinical data was acquired in this thesis, which is likely to evolve in time as the patients grow. These are ongoing efforts of a multi-institutional NIH R01 grant between Georgia Tech and Children's Hospital of Philadelphia. These relationships need to be investigated to translate the findings obtained in this thesis to improve patient management

CHAPTER 10 Conclusions

The hypothesis of this thesis work is that TCPC hemodynamic performance can be affected by the connection geometry, flow pulsatility, respiration and wall deformability. There are several major findings and conclusions that can be drawn from the studies performed in this thesis.

1. Impact of geometry on TCPC hemodynamics

From the geometric characterization of 108 patients, it was found that TCPC anatomy varies greatly among different patients, and that these variations affect TCPC hemodynamics . By correlating TCPC geometric features and hemodynamics, several significant relationships were found:

- Resting hepatic flow distribution was influenced by caval offset, FP-SVC angle and pulmonary flow distribution, which is important for reducing the risk of PAVMs

- Minimum FP and PA diameters were inversely correlated with iPL at rest and iPL at VAT, which suggests the potential detrimental effect of vessel stenosis on Fontan circulation

- Local TCPC geometry and iPL at VAT were significantly correlated to exercise performance in adolescents, but not adults

In view of the correlations between TCPC minimum diameter with resting and exercise power loss, a numerical frame work for evaluation of TCPC vessel stenosis and stent

implantation has been developed. Potential hemodynamic benefits of stent implantation in patients with severe LT stenosis was observed, especially during exercise.

2. <u>Impact of cardiac-driven and respiratory-driven flow pulsatility on TCPC hemodynamics</u>

The effect of respiratory-driven flow pulsatility in addition to cardiac-driven flow pulsatility on TCPC hemodynamics has been evaluated in this thesis. It was observed that vessel flow pulsatility was higher during free-breathing than breath-held conditions, suggesting respiratory-driven flow pulsatility was non-negligible. Using CFD analysis, it was observed that TCPC flow varies in time within a respiratory cycle, with differences observed during inspiration and expiration. TCPC power loss was higher during free-breathing conditions than breath-held conditions, suggesting that evaluating TCPC hemodynamics under breath-held conditions can affect power loss estimation. Finally, a pulsatile flow boundary condition including both cardiac-driven and respiratory-driven flow pulsatility can be important in TCPC hemodynamic evaluation, and wPI may be a useful metric to understand the impact of the time-averaged flow assumption.

3. <u>Impact of vessel wall deformation on TCPC hemodynamics</u>

The *in vivo* wall motion characterization resulted in a different vessel wall motion at the FP and SVC under resting free-breathing, breath-held and exercise conditions. No significant differences in wall motion patterns were observed between the FP and SVC at any one condition. An FSI simulation of a patient-specific lateral tunnel TCPC was performed under breath-held conditions. Power loss and pressure drop results

fluctuated less during the FSI simulation than during the same CFD simulation run with rigid walls. There were no observable differences in time-averaged pressure drop, TCPC power loss or HFD between the rigid wall and FSI simulations. These results suggested that employing a rigid wall is a reasonable assumption when evaluating time-averaged hemodynamic quantities of the TCPC under resting breath-held and pulsatile flow conditions.

APPENDIX

A.1. <u>Anatomic Reconstruction</u>

<u>Credit: Maria Restrepo</u>

A.1.1. List of Codes

i.   Sort and rename DICOM images (optional step): "sortimage_beta.m"

ii. ACGI interpolation: all the Matlab codes in "ACGI" folder, and the main function is "acgi_driver.m"

iii. Bouncing ball segmentation: all the Matlab codes in "Segmentation Code" folder , and the main function is "runit.m"

iv. Combining segmented binary images (optional step): "image_combine.m"

v.   Level Set Evolution: main function is"LevelSetSegmentation_3D_Phasic_v3.m", which will call "Image_To_MRI_Coord_Transform.m", "levelsetEvolution_3D.m" and "MRI_Coord_Transform_3D_axial.m"

A.1.2. Segmentation Protocol

A.1.2.1.   <u>Preparing DICOM images and Data Organization</u>

i.   Get the DICOM files for an axial sequence. <u>Do not work directly on the original raw data over the patient data server. Copy to your local drive.</u>

ii. Look for a sequence that provides the best resolution (in and out of plane) with good contrast for you to identify the TCPC structures

iii. Organize all images within the patient folder (CHOP_ID) in a folder named Raw_Images, and rename all images as 'Original_##.dcm' This step can be done manually using

software like XnView, or with the help of the Matlab code "sortimage_beta.m", which automates this process:

o "sortimage_beta.m" first obtain the user input of patient folder containing the DICOM images in folder "Raw_Images". It then sorts the dicom images based on the DICOM file name (For CHOP images, axial DICOM images are usually labeled as "<SliceLocation>_###_######.dcm"

o Then it sort the images based on slice location and rename them as 'Original_##.dcm'

o Finally, it outputs the slice thickness, pixel spacing of the DICOM files, and calculate the number of images that have to be interpolated (numims in the later ACGI interpolation), as well as the number of interpolated images the user should expect to see.

A.1.2.2. <u>ACGI Interpolation</u>

i. The folder with the ACGI codes (named "ACGI") should be one folder up from the patient folder

ii. Open the code 'acgi_driver.m'

iii. Change:

o Dataset Name: name of the patient folder

o First: number of initial file

o Last: number of Original files

o Numims = (Slice Thickness/Pixel spacing) -1 ; you can get these two from the DICOM header; Or you can just enter directly from the output of "sortimage_beta.m"

iv. Run the MATLAB code and a new folder will be created containing all interpolated images, you can check the number of interpolated images and compare with the output of "sortimage_beta.m"

A.1.2.3. <u>Bouncing Ball Segmentation</u>

i. Go to the "Segmentation Code" folder (one up of your patient folder). Type 'runit'

ii. Load the interpolated images

iii. Set a threshold (start with 90)

iv. If this threshold level does not provide a good image quality (i.e. structures other than the vessel of interest are still present) change the threshold value to include only the regions of interest

v. Make sure that the whole vessel is being displayed at that specific threshold

vi. The threshold level can be modified for every single slice

vii. Segment the vessel of interest by clicking the 'FILL' button on the interface, and then click on the vessel of interest

viii. By the algorithm of bouncing ball, the segmentation of one image can be automatically translated to its adjacent images. Therefore for most cases, you can just segment every other image, and go back to those images that weren't segmented and correct only if necessary.

- Other useful tools:
  o You can add pixels to the region of interest by clicking 'ADD' and then clicking on the screen
  o You can remove pixels the same way as the previous point, but by clicking the button 'REMOVE'

ix. Once you are done, save the segmented images in a folder within the patient

folder

o Name the new folder 'Segmentation_manual'

A.1.2.4. Combining Two Stacks of Segmented Images (Optional)

i. In some cases, a user may have missed a vessel and segmented the rest of the

TCPC. To avoid going back and re-segmenting the entire anatomy, the code

"image_combine.m" can help merging two stacks of segmented images (black

and white images in "Segmentation_manual" folder) from the bouncing ball

segmentation. It takes the white segmented region of the two image stacks and

combines them into one image stack.

In the code, specify:

o path1: folder of the 1st stack of manually segmented images (e.g. the TCPC)

o path2: folder of the 2nd stack of manually segmented images (e.g. the

missing vessel)

o path3: folder for output of the merged images

o Specify 'start_slice', 'end_slice' as the beginning and ending slices of the

images to be merged

A.1.2.5. Level Set Evolution

• Code: LevelSetSegmentation_3D_Phasic_v3.m

• Change the fields:

o FontanName

- o Numend: number of interpolated files

- o numLastUninterp: number of images before interpolation

- o numInterpolated=((Slice Thickness/Pixel spacing)-1

- Run the code

- If necessary change the contrast factor to have a better fit

- The folder 'Segmentation_Overlays' will contain the interpolated images and also red lines representing the overlays of the level set output. You can use this as a basis to see if you need to correct the segmentation.

- The output of the code is the point cloud that needs to be taken to Geomagic, stored in the "Segmentation_PointClouds" folder.

A.2. **Geometric Characterization of TCPC Using VMTK**

A.2.1. Overview

- The metrics that are obtained from this protocol are listed below, categorized according to the number of vessels present on the Fontan connection.

- For each vessel:

  o Vessel Diameter

  o Vessel Area

  o Shape factor (minimum/maximum diameter ratio)

  o Bifurcation angle

  o Tortuosity

- Across vessels (for anatomies with single SVC)

  o IVC-SVC offsets (projected on AP, LR or PA axis)

    ▪ AP: anterior-posterior direction

    ▪ LR: left-right direction

    ▪ PA: axis defined on the centerline between the two pulmonary arteries

  o VC-PA offset

    ▪ VC: vena cava, either SVC or IVC

    ▪ PA: pulmonary arteries, either LPA or RPA

  o IVC-SVC angle

  o LPA-RPA angle

  o Angle between adjacent vessels (each VC to each PA)

- Across vessels (for anatomies with bilateral SVC)

  o IVC-LSVC, IVC-SVC, LSVC-SVC offsets (projected on AP, LR or PA axis)

- o VC-PA offset

- o Angle between adjacent vessels (each VC to each PA)

- o IVC-LSVC, IVC-SVC angle, LPA-RPA angle

- With Azygos Vein (AZY)

  - o IVC-AZY, AZY-SVC, AZY-LSVC offsets (projected on AP, LR or PA axis)

  - o AZY- PA offset

  - o Angle between AZY and other vessels

- The parameters are computed as follows:

  - o Vessel diameter = Maximum Inscribed Radius (r) X 2

  - o Cross section area = πr^2

  - o Shape factor = dmin/dmax

  - o Bifurcation angle = $\cos^{-1}(\frac{b2.b3}{|b2||b3|})$, where b2 and b3 are two vectors coming out from the main branch, and |b2|,|b3| are their respective magnitudes, and b2.b3 is the dot product of the two vectors

  - o Angle across vessel = angle between specified vectors

  - o Tortuosity (Curvature) = Length of vessel / (Shortest distance between starting point to ending point of the vessel)

  - o IVC-SVC offset = distance between IVC and SVC vectors projected on the anterior-posterior (AP) / left-right (LR) / pulmonary artery (PA) axis

  - o VC-PA offset = closet distance between points on PA line and points on VC line

  - o AZY-PA offset = closet distance between points on PA line and points on AZY-VCs line

290

A.2.2. Geometric Characterization Protocol

A.2.2.1.   <u>Mesh Preparation</u>

- Take the same mesh that you prepared for the CFD simulations with immersed boundary method solver (surface mesh) and add the following extensions:

  o IVC: 10mm

  o SVC, LPA, RPA: 5mm (If RPA is much bigger than LPA, use 8mm for RPA). If later in VMTK you see a "Segmentation fault" error, you should consider increasing the length of the extension.

  o (If present) LSVC, AZY, RUPA: 5m

  o (The flow extension is necessary as VMTK centerline starts at certain length (~ radius of that vessel) from the edge of the vessel. Mesh only the extended TCPC wall, the flow extensions but not the end caps, (Triangular mesh, ".FDNEUT" format), mesh size is same as how you prepare the mesh for IB code preprocessing.

A.2.2.2.   <u>Running The VMTK Code</u>

a. To run the VMTK code you first need to use a computer that has VMTK installed. It can also be downloaded into MAC and PC computers (www.vmtk.org). The process is the same as long as you used the command-prompt code (using a terminal).

b. Create a new folder for each patient case, copy the following text files:

i.   Single SVC: "1TCPC_resamp_geo_bv.txt" and "2VCPAline.txt"

    ii.   Bilateral SVC: "1BLSVC_resamp_geo_bv.txt" and "2BLSVC_VCPAline.txt"

    iii.   And also the .FDNEUT mesh file inside the folder created

c. Open   the   first   text   file   ("1TCPC_resamp_geo_bv.txt"   or

    "1BLSVC_resamp_geo_bv.txt"), rename the file in the first line.

    vmtkmeshtosurface -ifile **MESHNAME**.FDNEUT -ofile surface.stl \

    And save the text file.

d. Run the first part of code by typing in the command line

    i.   "**vmtk --file 1TCPC_resamp_geo_bv.txt**" (Single SVC)

    ii.   "**vmtk --file 1BLSVC_resamp_geo_bv.txt**" (Bilateral SVC)
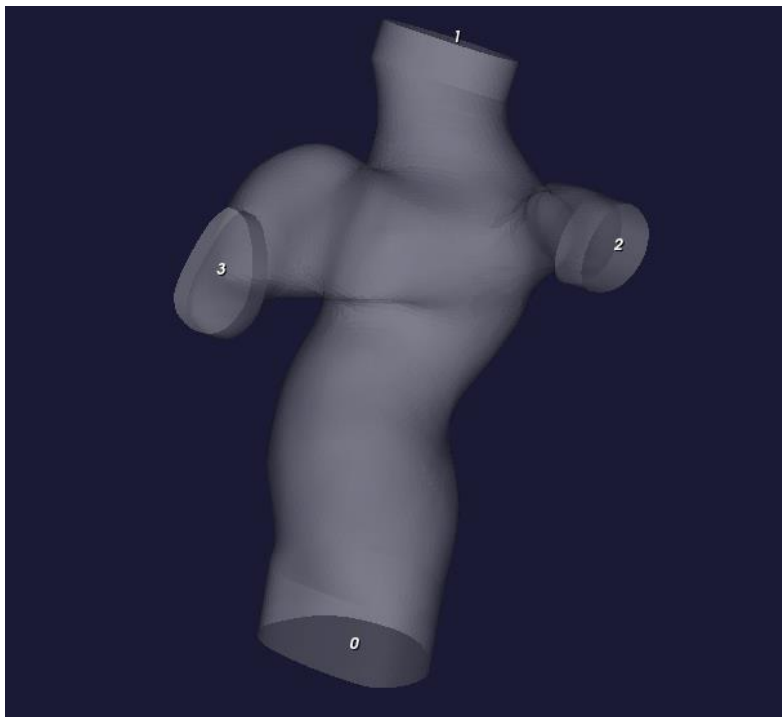
Figure A. 1 Screenshot of the VMTK tool

e. Plotting centerlines for IVC

    i.   A window with the model will pop up, showing the translucent mesh with numbers denoted on the inlets/outlets. Rotate the model view using left

mouse click, zoom in/out using right/middle mouse click, until you can see all

vessels and numbers, then press "q" in the new window.

ii. Go back to the command window, enter the vessel number for inlet (0 for IVC

in this case)

iii. Enter the vessel numbers for outlets: '2 [space] 3' for LPA and RPA in this

case.

f. Repeat step d for other vessels according to this:

Single SVC			**Bilateral SVC**	
Inlet	Outlet		Inlet	Outlet
IVC	LPA RPA		IVC	LPA RPA
SVC	LPA RPA		LSVC	LPA RPA
LPA	SVC IVC		SVC	LPA RPA
RPA	SVC IVC		LPA	LSVC IVC
			RPA	SVC IVC

Sequence of plotting points for the outlets does not matter, but the sequence of

specifying the inlets does matter. The program first saves the IVC centerline first,

then SVC, LPA and RPA. So it is important to follow that order to save the

centerline with the right name. (You can change the sequence in the text file to

accommodate your own preference).

g. Run the second part of code by typing "vmtk --file 2VCPAline.txt" (Single SVC) or

"vmtk --file 2BLSVC_VCPAline" (Bilateral SVC) in the command line

i. A window with the model will pop up, showing the translucent mesh with

numbers denoted on the inlets/outlets. Rotate the model view using left

mouse click, zoom in/out using right/middle mouse click, until you can see all

vessels and numbers, then press "q" in the new window.

ii.   Enter inlets and outlets according to the following:

Single SVC			**Bilateral SVC**	
Inlet	Outlet		Inlet	Outlet
IVC	SVC		IVC	LSVC
LPA	RPA		IVC	SVC
			LPA	RPA

h. Now the folder should be full of .vtk and .vtp files for each vessel:

- XXXbv.vtk

- XXXcl.vtp

- XXXclat.vtp

- XXXclgeo.vtk

- XXXcloff.vtk

- XXXclresample.vtp

Where XXX denotes the vessels

And   also   IVC_SVCline.vtk   (and   IVC_LSVCline.vtk,   Azy_VCline.vtk),

LPA_RPAline.vtk for the centerline from LPA to RPA.

A.2.2.3.   Azygos Vein Characterziation

a. Start with previous parts of VMTK code to compute parameters of the other

vessels first.

b. Copy "3Azy.txt" to the folder, run the code by typing "vmtk --file 3Azy.txt" in the

command line.

c. Compute centerlines based on the following:

Inlet	Outlet
AZ	LPA RPA
AZ	IVC SVC (LSVC)

A.2.2.4. <u>RUPA (Right Upper Pulmonary Artery) Characterization</u>

a. Start with previous parts of VMTK code to compute parameters of the other vessels first (including azygos vein if present).

b. Copy and run the code by typing "**vmtk --file 4RUPA.txt**" in the command line.

c. Compute centerlines based on the following:

Inlet	Outlet
RUPA	LPA RPA

A.2.2.5. <u>MATLAB Code</u>

a. To run the MATLAB code for data processing, you will need the "XXXclgeo.vtk" and "XXXbv.vtk" for each vessel, and also the "IVC_SVCline.vtk", "LPA_RPAline.vtk" (And "IVC_LSVCline.vtk" and/or "Azy_VCline.vtk") to reference your offset to the LPA-RPA centerline.

b. Copy the "**TCPCgeo5.m**", "**compute_vessel3.m**", "**PAVC_offset.m**", "**searchPApt_beta.m**" and "**comAngle.m**" MATLAB files to the folder one level above the folder you created.

c. In Matlab command, type

TCPCgeo5 ('foldername', has LSVC?, has AZY?, has_RUPA? export txt? Export excel? IVC extension length, SVC ext length, LPA ext length, RPA ext length, RUPA ext length, LSVC ext length, AZY ext length)

 i. Single SVC, no AZY, no RUPA:

  TCPCgeo5 ('CHOP057A',0,0,0,1,1,10,5,5,5,0,0,0)

 ii. Bilateral SVC, no AZY, no RUPA:

  TCPCgeo5 ('CHOP057A,1,0,0,1,1,10,5,5,5,0,5,0)

 iii. Single SVC, has AZY, no RUPA:

  TCPCgeo5 ('CHOP057A,0,1,0,1,1,10,5,5,5,0,0,5)

 iv. BilateralSVC, has AZY, no RUPA:

 TCPCgeo5 ('CHOP057A,1,1,0,1,1,10,5,5,5,0,5,5)

d. As it finishes running, enter the folder, you will see a '.csv' file that summarizes all the output:

Output for VMTK analysis - CHOP013A - 2012823 - 23:39:13

has LSVC	1	has AZY	0	has_RUPA	0

IVC diameter (mm)			SVC diameter (mm)			LPA diameter (mm)			RPA diameter (mm)			LSVC diameter (mm)		
Min	Mean	Max	Min	Mean	Max	Min	Mean	Max	Min	Mean	Max	Min	Mean	Max
13.9396	24.1546	34.5051	9.0187	11.0804	21.0327	11.0889	17.2189	23.9782	9.7622	13.2271	24.0885	8.1113	27.3951	51.0892

Shape factor (mm/mm)							Bifurcation angle(degree)				
IVC	SVC	LPA	RPA	LSVC			IVC	SVC	LPA	RPA	LSVC
0.40399	0.42879	0.46246	0.40526	0.15877			106.1704	154.2964	124.1792	146.916	106.1786

Tortuosity (mm/mm)							Length (mm)				
IVC	SVC	LPA	RPA	LSVC			IVC	SVC	LPA	RPA	LSVC
1.09	1.0268	1.0495	1.0343	2.9092			79.4943	61.01	42.8518	23.8087	256.7973

Offsets(mm)									
IVC-SVC			IVC-LSVC			LSVC-SVC			
PA	AP	LR	PA	AP	LR	PA	AP	LR	
1.0769	0.364	1	0	0	0	1.0769	0.364	1	

VC-PA (SVC)	VC-PA (LSVC)
5.9988	-21.6799

Angle between (degree)									
IVC-LPA	IVC-RPA	SVC-LPA	SVC-RPA	IVC-SVC	LPA-RPA	LSVC-LPA	LSVC-RPA	LSVC-SVC	IVC-LSVC
116.778	96.5651	97.093	90.147	129.274	127.5314	116.7773	96.5674	129.2722	0.002855

Figure A. 2 Screenshot of the spreadsheet output

e. You can open the geometry (.stl / .vtk) and centerlines files in ParaView in case you have any doubts.

Velocity Segmentation for Conventional PC-MRI

Credit: Dr Alan Wei, Dr Maria Restrepo

A.3.1. List of Codes

i.   Rename DICOM images: "z_rename_vel_data.m"

ii.   Velocity segmentation: main function "flow_chop_nonGUI_beta_phase.m", which

      calls   "Cartesan_Mesh_Generator.m",   "Determine_Correlation_Energy",

      "Final_Snakes.m",   "Image_To_MRI_Coord_Transform.m"   and

      "Level_Set_Evolution_2D.m"

A.3.2. Segmentation Protocol

A.3.2.1.   <u>Preparing DICOM Images and Data Organization</u>

- The velocity data provided includes two sets of images per vessel to be

  segmented: one that contains the magnitude images and another one that

  contains the phase images. <u>Do not work directly on the original raw data over the</u>

  <u>patient data server. Copy to your local drive.</u> The magnitude files are usually

  under the folder name after the vessel's name and the phase files are under *_P

  folder. For example,

  /yogi2/grant/Raw_data/MRI/FromRavi/CHOP240A/0036_ivc

  /yogi2/grant/Raw_data/MRI/FromRavi/CHOP240A/0037_ivc_P

i.   Copy the stacks of images of vessels you want to work on, and put them in a

      patient folder e.g. "CHOP240A" on your local drive.

ii. For each vessel folder, delete those numbers (i.e. "0036_", "0037_") in the folder name, and change the "_P" to lowercase "_p".

iii. Run the Matlab code named "z_rename_vel_data.m". In this step, you can put all vessel's information to the patient folder, i.e. ivc, svc, etc. The code can handle them together.

Few things are important for the output.

o Number of files: Check if the data is continuous, starting from 0 to 29; the last number may change depending on how many phases were present in the data

o Naming the files: Record the "SequenceName" of *_P, i.e.

```
SequenceName of  ivc_P  is   *fl2d1_v100in
```

o VENC number: The 'v100in' indicates that the encoding velocity (VENC) is 100, which will be used later. The sequence name can also be obtained from the DICOM header using the 'dicominfo' MATLAB function: go to the phase images folder (i.e. ivc_p) and get the info from one of these files. The VENC can be found in the 'SequenceName' field

o RR: this information is also obtained from the DICOM header. The field of interest is 'ImageComments':

```
ImageComments: 'RR 896 +/- 26; 63 heartbeats'
```

This indicates that the respiratory rate (RR) is 896 +/- 26 ms averaged over 63 heartbeats.

A.3.2.2.   Segmentation

- Few lines in the "flow_chop_nonGUI_beta_phase" are variables based on the case:

  o edataset = patient folder name, i.e. "CHOP240A" ;

  o evessel = the name of the segmenting vessel, i.e. 'ivc';

  o evenc = encoding velocity, i.e. 100;

  o efirstphase = 0 and elastphase = 29, since the phase files are named from 0 ~ 29.

- The Matlab script produces the images and requires a few steps here:

  i. Draw a box enclosing the segmenting vessel to limit the auto detection of the MATLAB code, see the figure below. Then, double-click inside the box to proceed.
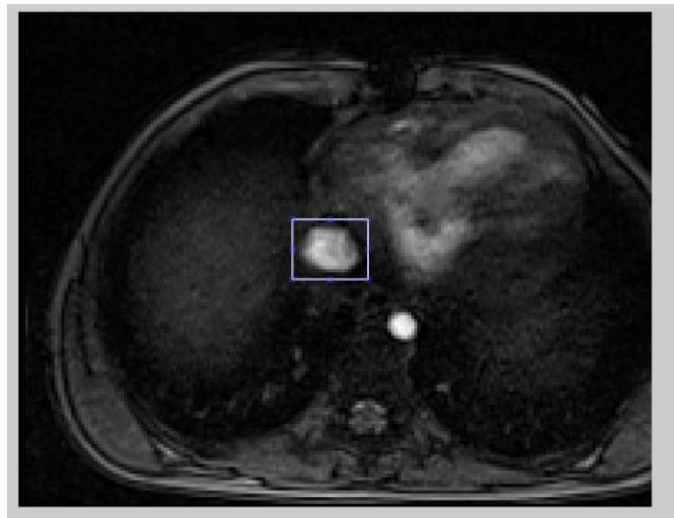
Figure A. 3 Selecting the region of interest

  ii. Now, left-click the mouse until it ends. It will scan through all images and you can see if the vessel would ever go out of the limiting box.

iii. Left-click to draw a circle. All points of the circle should be approximately two pixels inside the observable vessel boundaries. Double-click inside the circle to proceed. Tips:

   o At the end of drawing, roughly click the beginning point would complete the drawing process;

   o Hold the left-button of the mouse to drag/move the existing points.
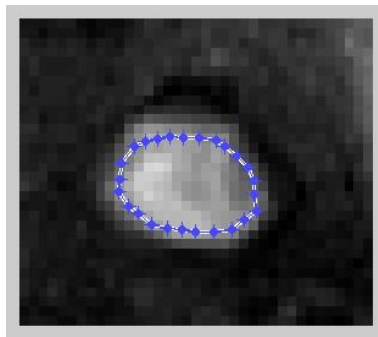
Figure A. 4 Create the initialization contour

iv. Go back to check the MATLAB console to answer the following questions:

   o Phase number to correct wrap around (type number followed by enter): skip it by pressing "Enter"

   o Please enter the radius of the structuring element: 2

v. The program will automatically detect the vessel and propagates through all images. After it is done, it will remind you:

If the Segmentation Results were acceptable, click a mouse button.If NOT acceptable, press a key on the keyboard.

vi. The code will output data if a mouse button is clicked. Otherwise, it will go back to modify the segmentation:

   o Do you want to manually segment phases one by one? y/n :

   a) "No" will start over the program;

b) "Yes" will let you manually segment the vessel. You can pick up any image to manually segment the vessel.

- Which slice to segment manually (Enter 1 to 30 followed by enter; Press just enter to check results)? the ordering is shown here
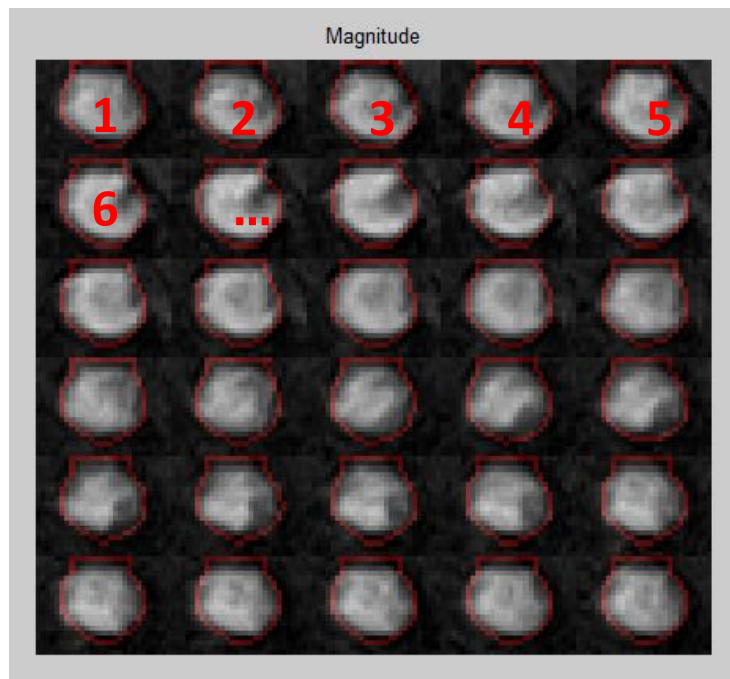
Figure A. 5 Segmented contour propagated through all the phases

- Manual segmentation does not involve auto detection:

a. Double-click anywhere inside the console to proceed;

b. Check console if you need to manual segment additional images. If NO, press "Enter".

- Manual segmentation cannot propagate to other images.

vii. All figures will be outputted into /_matlab_processed_datasets_ under the working directory.

viii. Important output files:

- o ivc_numcomp_*: values for all quantities of each phase;

- o overview_ivc_numcomp_*: mean values for all quantities;

- o Inside the patient folder, you will see ".dat" and ".vtx" files of the vessel you just segmented. Those are the data files related to the plane of the velocity slices. They were computed by registering the segmented region of interest with the PC-MRI slice location (read from the DICOM tags). You can use this file to see approximately where the PC-MRI slice was acquired relative to the reconstructed 3D patient specific geometry. Note that it may not always be accurate because the anatomic MRI and PC-MRI obtained from different image acquisitions. You can import the ".vtx" file in Geomagic and wrap the point cloud to get a surface.
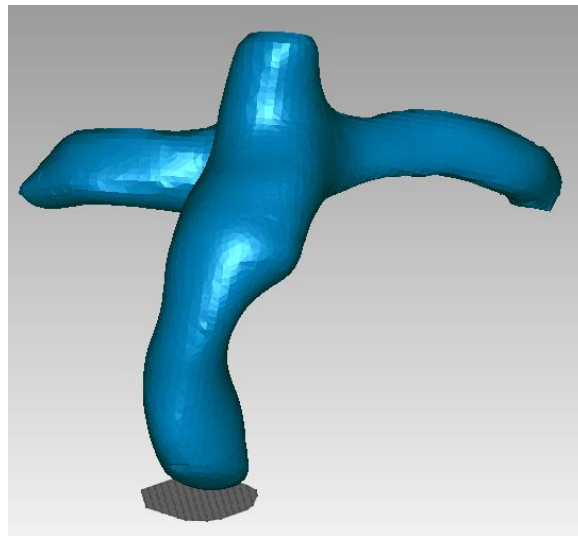
Figure A. 6 The reconstructed 3D patient geometry (blue) and the approximate location and orientation of PC-MRI slice of IVC (gray)

A.4. <u>Velocity Segmentation for Real Time PC-MRI</u>

<u>Credit: Dr Alan Wei, Dr Reza Khiabani</u>

A.4.1. Segment Software

- An external package, Medviso Segment, is used, which can be downloaded from its website (http://medviso.com/products/segment/)

A.4.2. Segmentation Protocol – Vessel Flow

- The conventions for real-time data are: *_RT_*, *_R_*, or *_Real_Time_*, i.e. /CHOP021C/ 0193_ivc_rest_RT_mag_SVE. Find both the magnitude and phase files and copy them to the patient folder under your working directory.

- Run the Matlab code "segment.m" to open Mediviso Segment. Note that Matlab also has a built-in function called "segment", so make sure you actually launch the Medviso Segment code instead of calling the Matlab built-in function.

- After the Segment GUI is launched→File → Open image files → Load Selected Files(s) or Folders(s). Two things you need to make sure:
  - Load both image/magnitude and velocity/phase files.
  - ROI size = Full Image.
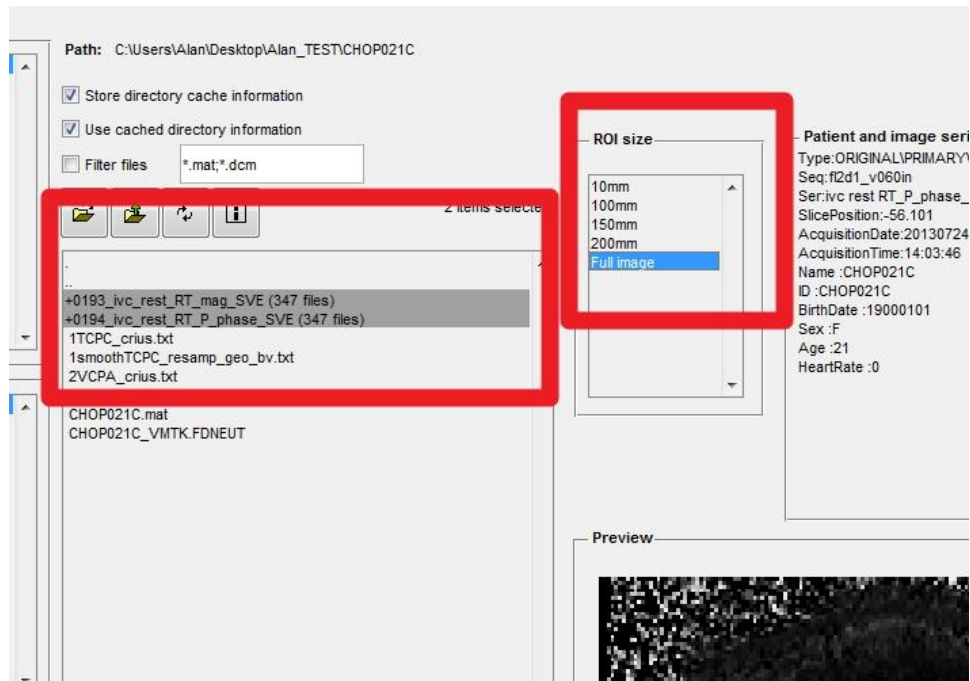
Figure A. 7 Loading DICOM files In Segment

- If an error message comes up, ignore it by clicking "OK".
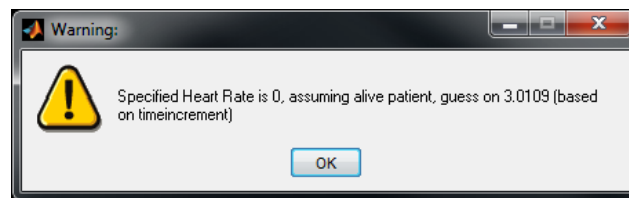
- There are some control panels on the right-bottom corner. The ROI stands for Region Of Interest.

- If 'select slices tool' is enabled, as see below, hold the middle mouse and move it on the image can change the contrast. Also, move the cross sign on the image to the center of the vessel.
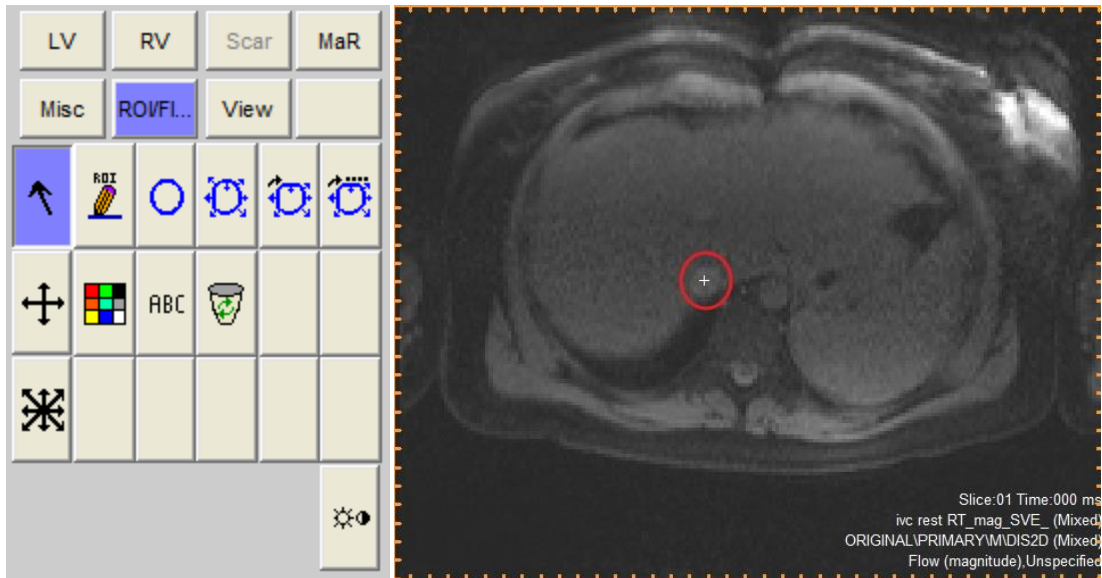
Figure A. 8 Selecting ROI in Segment

- Alternative way to "auto" change the contrast is also available, see below. (Reset the contrast is next to it)

Figure A. 9 Adjusting contrast of the images

- Select the "manual draw/adjust ROI" and draw a circle by holding the left mouse button. "Refine ROI" will automatic detect the real boundary.
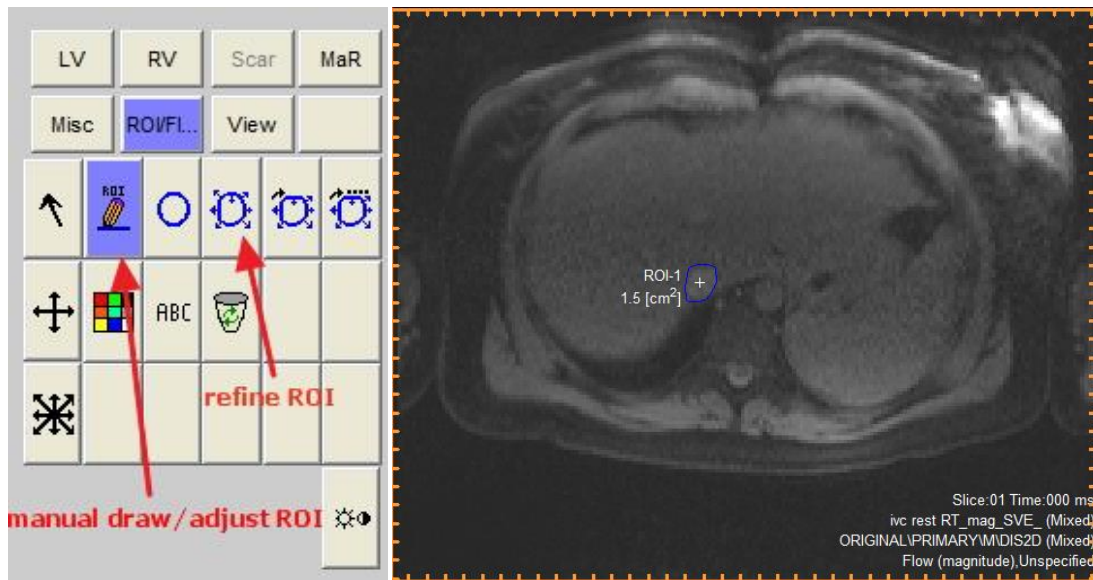
Figure A. 10 Refine ROI in Segment

- Then, you can "propagate and refine ROI forward" to propagate the ROI of one image by one image forward, or "track a vessel in all timeframe" to propagate the ROI for all images.
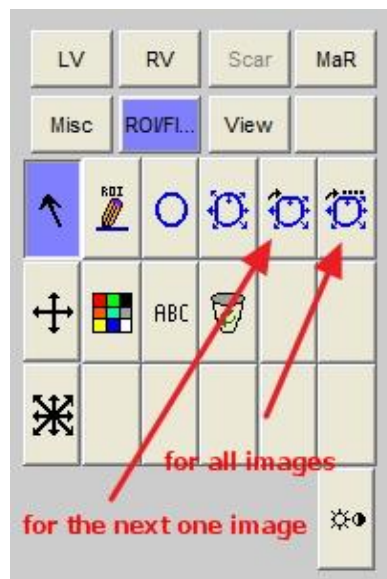
Figure A. 11 Propagate ROI in Segment

- You can "play" to see if the auto-segmentation is good. If they're not, you can stop at any image, delete the ROI, and redo it. The "track a vessel in all timeframe" is able to accomplish the auto propagation of the ROI for the rest of images.

Figure A. 12 Play forward or backward of the image series

- Save both image stacks and segmentation for future use.
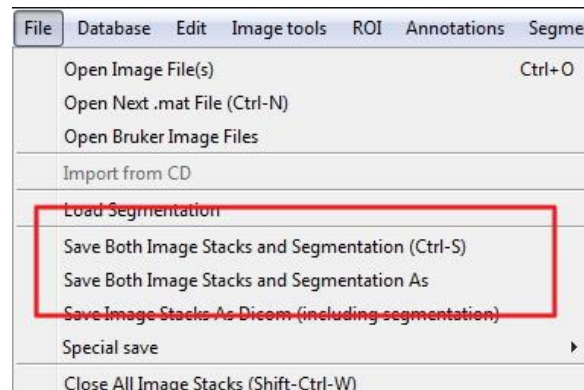
Figure A. 13 Saving segmentation results in Segment

- Output data with:
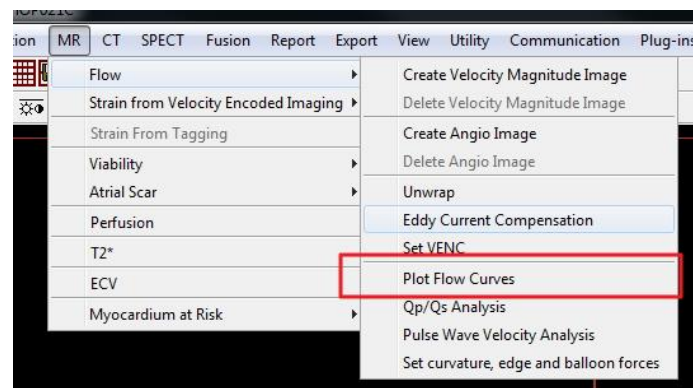
Figure A. 14 Plot Flow Curve of ROI

- After you click "export", all data are copied to the clipboard and you need to paste them into Excel/notepad.
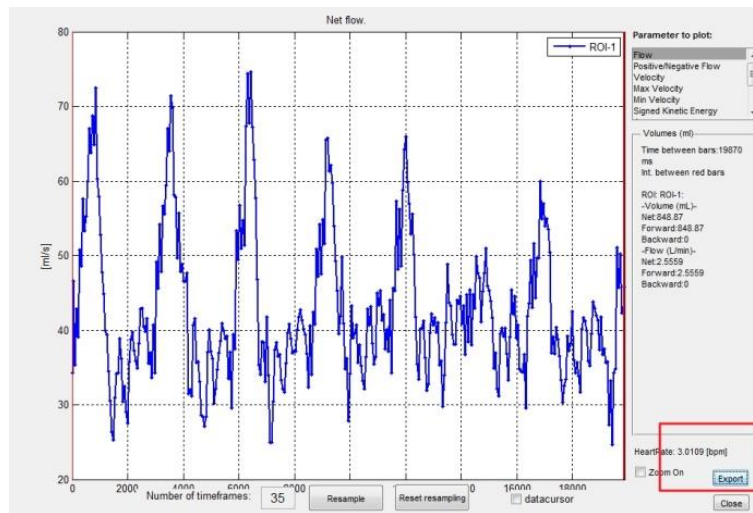
Figure A. 15 Flow curve plotted in Segment

- Notice that the "Total Flow" may be negative for some vessels, i.e. svc, since the sign only indicate the direction of the blood flow. You need to multiply the negative values by "-1". **CAUTION**, do NOT use the absolute value, which would disregard all reverse flow information. Also convert the unit of flow if necessary.

A.4.3. Segmentation Protocol – Chest Wall Area

- This is similar to segmenting a vessel for flow. Follow the previous steps given, but instead your ROI contains the entire chest activity. The ROI fit is extremely important considering you're measuring chest wall activities and an accurate area is essential.

- If data is unclear at a certain portion of the mage and you make an assumption when generating the ROI, make sure to be consistent throughout all images. Also

you can skip the unclear portion of the image at the beginning by loading smaller ROI of the image (when loading the images, instead of "Full Image", choose a smaller ROI, e.g. "200mm")

- Segmentation Tips:

  o There is a cropping tool under the "Misc" tab in the bottom right (next to "ROI"). Find the image with maximum chest area, and crop all dark space as well as any limbs that might appear in the MRI. The ROI cannot go beyond this border so it ensures a constant fit along the sides and back of the patient, and won't jump to static seen outside of the body.

  o If having issues with ROI jumping try and create the ROI when the chest area is at a minimum. The program seems to have an easier time expanding an ROI, and when contracting can revert to that initial ROI at the chest area minimum.

- Similar to vessel flow, obtain the chest wall area waveform by clicking "Plot Flow Curves" under "ROI". Export the data and look under the column "area". To obtain the chest wall area change, you can minus all the data points by the minimum data point.

A.4.4. Segmenting Aorta on The Same Image Slice of IVC/SVC

- Note that this is for qualitative purpose (e.g. to identify time points of systole and diastole from the IVC/SVC slices), since the ascending/descending aorta flow obtained from the IVC/SVC images may not be very accurate.

- This is similar to segmenting a vessel for flow. Follow the previous steps given, but instead your ROI contains the descending aorta or ascending aorta (for SVC slices).

- Segmentation Tips:
  - Sometimes on the SVC slices, instead of separate vessels of ascending and descending aorta, sometimes the slices may be acquired close to the aortic arch, and separating the ascending and descending aorta may be cumbersome. One trick is to use a fixed ROI throughout the entire image series (instead of letting the ROI to propagate in time). This can be done by drawing the ROI in the first image and plot the flow curve immediately afterwards (and do not refine nor propagate the ROI). When drawing the ROI this way, make sure this ROI is a close approximation of ROI for the entire image series.

- Similar to vessel flow, obtain the aorta waveform by clicking "Plot Flow Curves" under "ROI". Export the data. Remember for descending aorta flow waveform you might need to reverse the sign of the flow rate.

A.4.5. Smoothing Waveforms
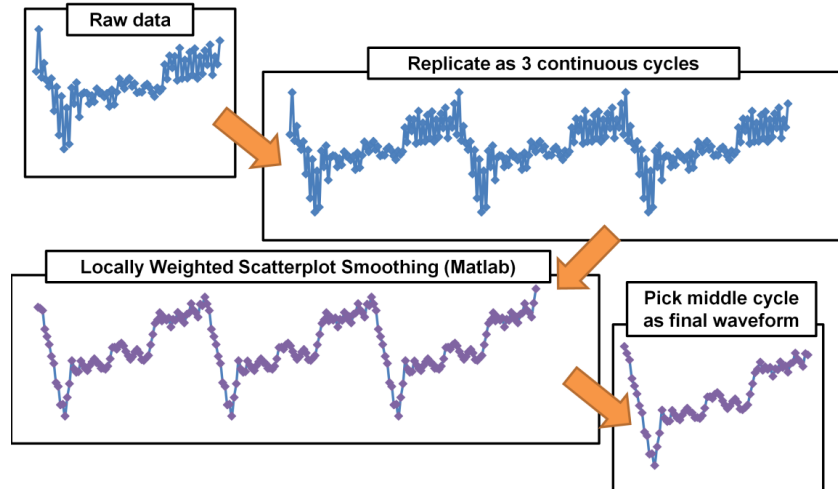
- To ensure numerical stability for CFD simulations, the segmented vessel flow waveform is smoothed with MATLAB function LOWESS.

- First, the selected cycle (stored in variable "raw_flow"), is duplicated for 3 times:

  o flow = [raw_flow raw_flow raw_flow];

- Then the "flow" variable is smoothed with LOWESS

  o lowess_fl = smooth(flow,'lowess');

- Then, the middle cycle of the smoothed cycle is selected as waveform for CFD simulation

  o lowess_fl=lowess_fl(size(raw_flow,2)+1:size(raw_flow,2)*2);
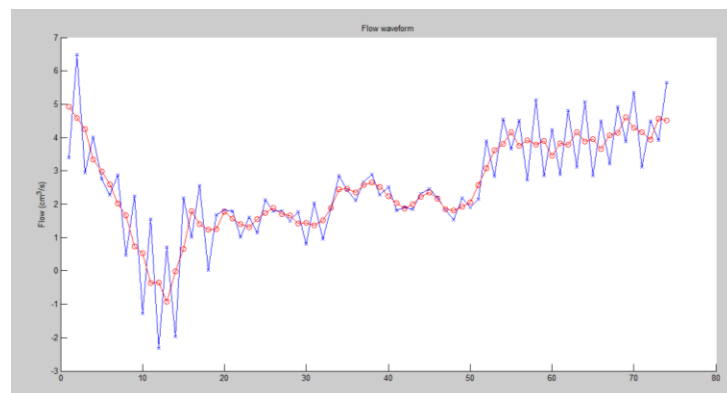
Blue line: original waveform, red line: smoothed waveform with LOWESS

A.5.   Immersed Boundary Methods CFD Solver

Credits: Dr. Diane de Zélicourt, Dr. Lucia Mirabella, Dr. Alan Wei and Dr Maria Restrepo

A.5.1. Overview

Step [1]: Surface mesh generation

    a. 3D surface preparation with Geomagic Studio

    b. Surface mesh generation with GAMBIT or ANSYS toolbox

Step [2]: Volume mesh generation

    a. Description of the source codes

    b. Setting up the meshing parameters

    c. Running the code to generate the volume mesh

Step [3]: Setting up the CFD Simulation

    a. Imposing boundary conditions

        i.   Non-pulsatile boundary conditions

       ii.   Pulsatile boundary conditions

    b. Setting up the simulations

Step [4]: Running the CFD Simulation

    a. Description of the source codes

    b. Code compilation

    c. Running a simulation in parallel and in serial

    d. Description of convergence criteria

    e. Restarting a simulation

Step [5]: Post-processing

    a. Initial post-processing

    b. Flow field visualization

    c. Computing power loss: for steady and pulsatile simulations

    d. Computing hepatic flow distribution for steady and pulsatile simulations
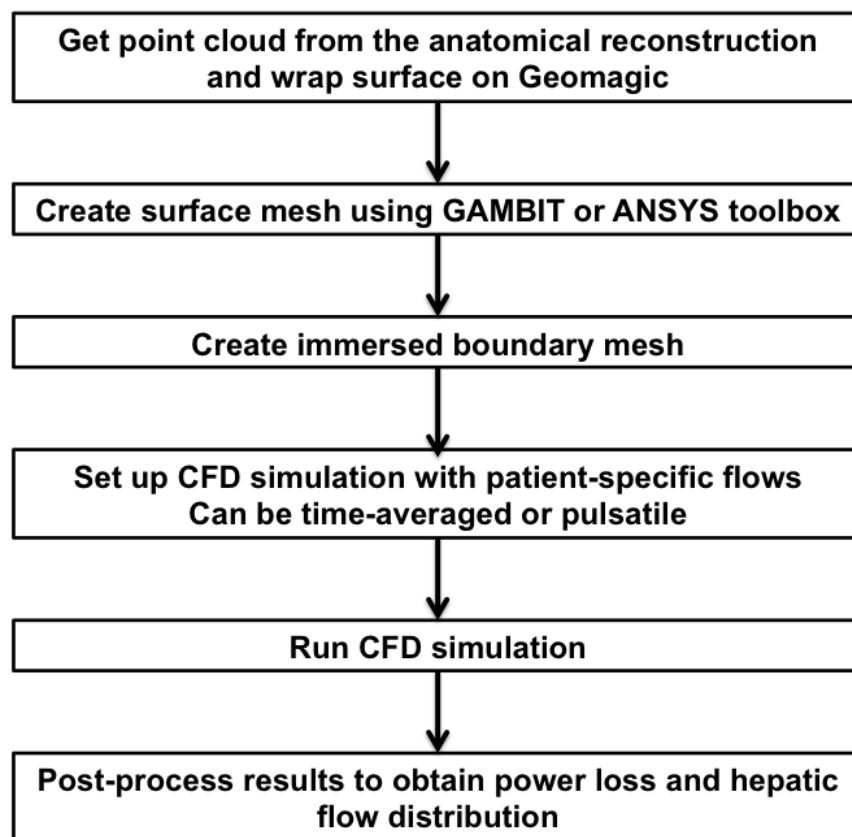
Figure A. 16 Overview of running a CFD simulation with the immersed boundary solver

A.5.2. CFD Protocol for Immersed Boundary Solver

A.5.2.1. <u>Step [1] Surface Mesh Generation</u>

A.5.2.1.1.   Step [1a] 3D Surface Preparation with Geomagic Studio

1. Import the point cloud data obtained from the MRI segmentation and 3D reconstruction (Go to File/Import)

2. Fit surface:

   a. Surface Wrap: Go to Points/Wrap, the default settings should work.

   b. Fill the holes left after the surface wrapping (Go to Polygons/Fill holes or select). Use the default settings first.

      i) If filling some of the holes leads to the formation of artificial bumps, change the "Fill type" from "Curvature" to "Flat"

      ii) Another option might be to create a bridge () across the center of the hole and then fill the smaller holes independently

3. Remove the local surface irregularities:

   a. If the geometry is very irregular the first step might be to apply smoothing to the entire geometry (Polygons/Smooth/Relax or Polygons/Smooth/ Reduce Noise). Be careful using this tool since this may impact the vessel diameter, especially at the pulmonary arteries.

   b. One possible trick is to refine the mesh first, so the triangle size will be smaller before smoothing and hence smoothing will result in less abrupt change in the geometry (Polygons/Remesh/Refine).

   c. If the irregularities are more limited in space, then the two best performing options are either:

i) To apply a local smoothing with Polygons/Smooth/Sandpaper

ii) To delete the local irregularity and fill back the hole using the curvature-based filling

d. Attention should be paid to delete all inverted surface elements and fill back the corresponding holes. It is important to fix these inverted triangles, because these will become a problem when generating the volume mesh.

i) The inverted surface elements can easily be visualized, as they will appear in yellow, whereas the rest of the surface should appear in blue.

ii) Rotating the anatomy helps detect the inverted elements as the surface rendering used by Geomagic Studio will lead these yellow triangles to show up more easily.
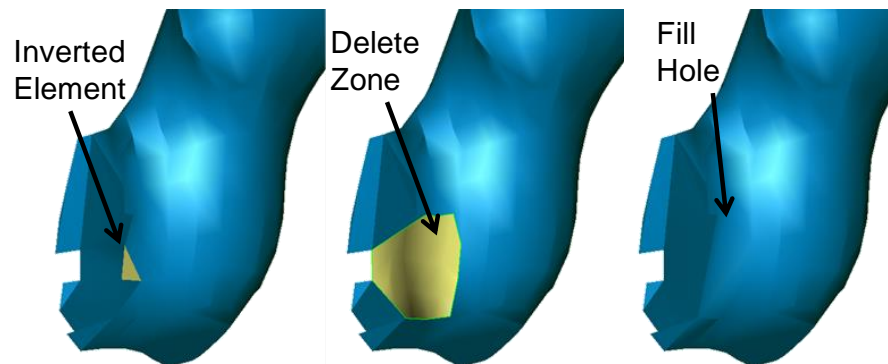
Figure A. 17 Detection and removal of an inverted surface element in Geomagic Studio.

4. Create the inlet/outlet cross-sections.

a. Select the vessel to be cut

i) Right click on the mouse and choose "Select Through" (Or Keyboard: Ctrl+G). In the same menu, go to "Selection Tools" and pick the method of choice. "Lasso" typically is the easiest to use. Ctrl+C to deselect everything if needed.

b. Cut the vessel

i) Go to Polygons/Trim/Trim with Plane or select the icon

ii) There are two relative easy method to define the plane, either of them will work:

- Change the plane orientation method from "System Plane" to "Three Points" and select three points on the vessel surface such that the plane is visually perpendicular to the vessel axis. Click "Align" to align the plane with the selected points.

- Change the plane orientation method from "System Plane" to "Line" and click to draw a line on the plane the user want to cut on the surface. The plane will be automatically aligned one the line that was just drawn.

iii) "select three Intersect Plane"

iv) "Delete Selection". The section that will be deleted is the section highlighted in red after the plane intersection. If this section is not the one that should be removed first select "Reverse Selection" and then "Delete Selection"

v) "Close Intersection" to create a water-tight geometry

vi) "OK" to accept the thus created vessel cross-section

c. Repeat the operation for each inlet and outlet

5. Convert the surface from its triangular structure to a format that can easily be imported into other computer aided design (CAD) or meshing software by creating a limited number of B-spline patches rather than the large number of surface triangles.

   a. Switch from the polygon to the shape phase: Go to Edit/Phase/Shape Phase

   b. Create Patches: Go to Patches/Construct Patches. Use "Auto-estimate" for the number of patches required. The default options work for most geometries

   c. If the defaults fail to adequately describe the geometry

      i) Go to Contours/Detect Curvature

      ii) Go to Contours/Shuffle Curvature Lines. Modify the main curvature lines (in orange) so as to provide proper guidelines for the patch generation. As a general rule, two curvature lines should run along the sides of each vessel, diametrically opposite to one another. Another curvature line should run all along the base of each vessel when two vessels merge together.

      iii) Go to Contours/Construct Patches. The patches will be defined using the curvature lines defined above.

   d. Go to Patches/Repair Patches and check the quality of the patch layout. The most important point is to avoid patch overlap. The easiest option to use is to edit patches (⊠) and move the patch corners until no patches overlap any longer.

6. Construct the grid (Grids/Construct Grids). The defaults should work.

318

a. If they fail, the faulty patches will be highlighted in red and the user should cancel the operation and correct these patches accordingly

7. Fit surface

a. Go to Grids/Specify Planar Region. Select all the patches on a given inlet or outlet and click "Next". Repeat until the operation is completed. At this step, make sure ' Select Visible' instead of 'Select Through' is being used (Keyboard: Ctrl+V).

b. Go to NURBS/Fit Surface. A baseline tension of 0.7 should provide a smooth geometry. The user may adjust that value until a satisfying rendering is achieved

8. Export as an .igs file format

A.5.2.1.2.   Step [1b] Surface Mesh Generation with GAMBIT or ANSYS toolbox

A.5.2.1.2.1.   Mesh Generation Using GAMBIT (ANSYS Inc., PA, USA)

1. Import the .igs file exported from Geomagic Studio (File/Import/IGES)

a. The default import settings should be fine

b. If the import operation takes longer than normal, the most likely cause is a faulty surface generation in Geomagic Studio and the user should go back to the previous step and check the quality of the surface.

2. Merge patches: after the surface preparation in Geomagic Studio, the TCPC surface is typically discretized with hundreds of patches. The patches should

thus be merged into larger surfaces by boundary type for definition of boundary conditions.

a. Under "Operation", select the Geometry mode ( )

b. Under "Geometry", select the faces ( )

c. Under the "Face" options, select "Merge Surfaces" ( )

d. Select all the patches that belong to the same boundary (e.g. all IVC surfaces), and apply

e. Repeat the previous step for all boundaries (e.g. SVC, LPA, RPA, other vessels if present, and TCPC surface)
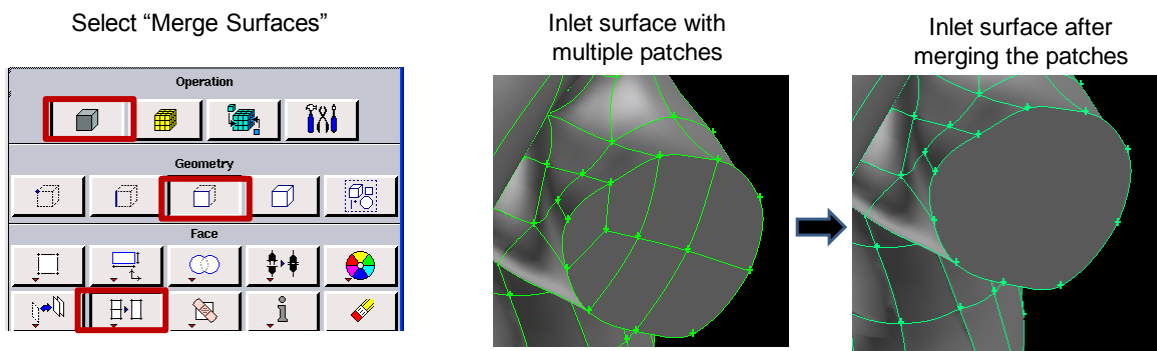
Figure A. 18 Merge the patches belonging to the same boundary type

3. Extend the inlet/outlet entrance lengths

a. In the geometry/vertex menu, select "create vertex on edge" and create N number of points such that each edge has at least 3 distinct points (Figure A. 19). Shift click on the edge to define a vertex.
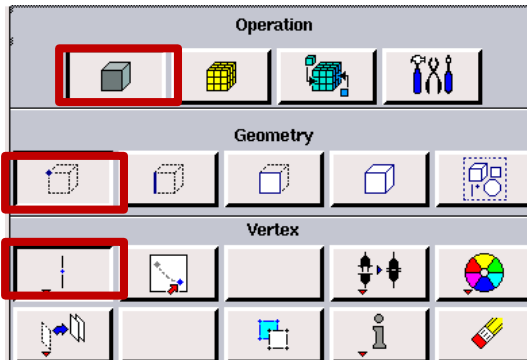
"Create Vertex on Edge"   Create 2 new vertices on each inlet/outlet boundary
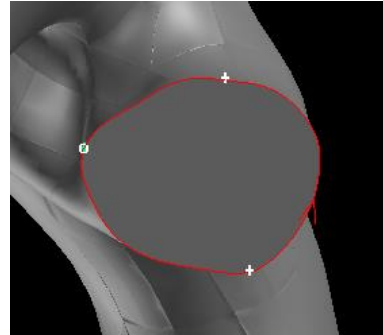
Figure A. 19 Create N independent points on each inlet/outlet boundary to ensure that each one of them has at least three distinct, unaligned points.

b. Under Operation, choose the "Toolbox" menu (🛠), select "Axis" (⤢) and then "Create Coordinate System" (✎). Check the box "Vertices" to define the coordinate system using the vertices created in the previous step. Select three distinct vertices on a given edge, and accept.
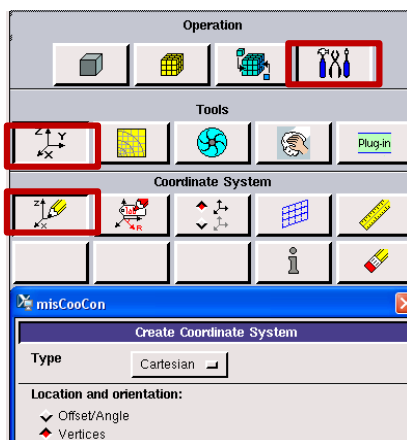
"Create Coordinate System"   Define a coordinate system for each inlet/outlet using three independent vertices
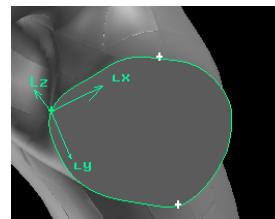
Figure A. 20 Create a new coordinate system for each inlet/outlet

c. Extend the inlet and outlet vessel lengths in the direction normal to the cross-sectional plane.

    i) Go to the "Geometry/Volume" menu and select "Sweep surface"

    ii) Select the cross-section of the inlet/outlet to be extended

    iii) For the "Path" option, check the "Vector" box and then click "Define" to define the extension direction

    iv) Select the coordinates axis defined on the inlet/outlet to be extended. The z-axis will be oriented normally to the surface. If the z-axis is pointing towards the inside of the TCPC choose the "negative" direction, otherwise "positive".

    v) Set the extension length and accept

For the cases studied in this thesis, the inlet vessels were typically extended by 10mm, while the outlets were typically extended by 50mm.
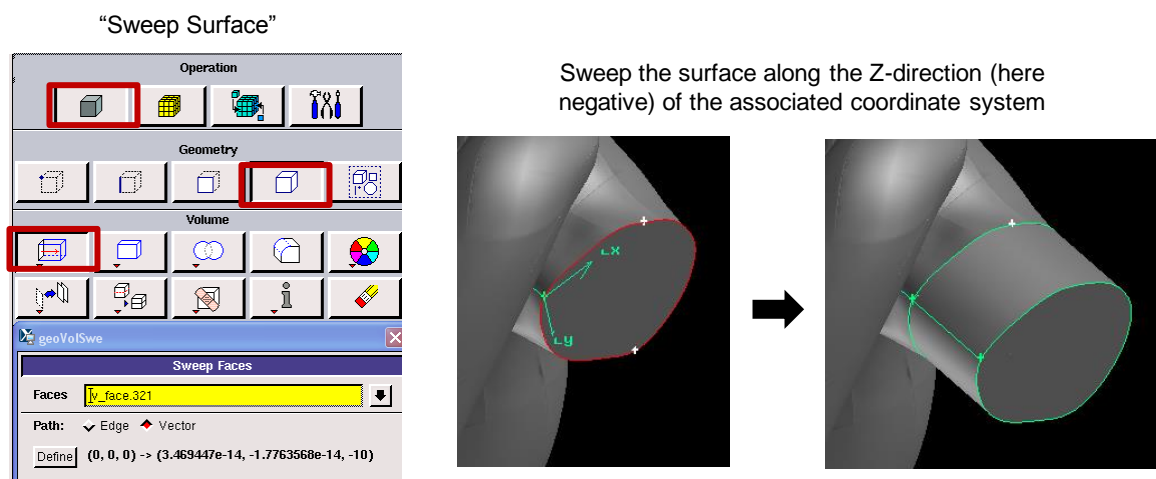
Figure A. 21 Inlet/outlet extension

4. Unstructured Surface Mesh Generation

322

a. Mesh all edges. Using the edges to define the mesh resolution allows for an easy control over the surface mesh spacing. If a finer resolution is needed, for example along one the pulmonary arteries then this can be ensured by simply defining a finer mesh spacing along the corresponding edges.

   i) Go to the mesh/edges menu

   ii) Select all edges and set your mesh spacing (typically 1 or 1.5mm).

   iii) In cases where one vessel is significantly smaller than the others, the corresponding edge may be meshed independently with a finer setting.
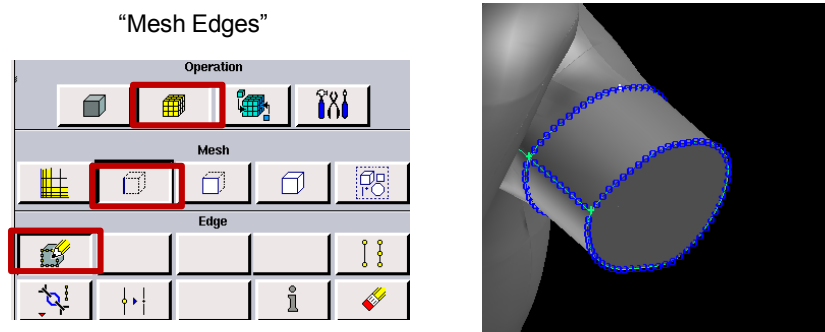
Figure A. 22 Edge mesh generation. Meshing the edges first allows for a detailed control over the surface mesh resolution, allowing for finer resolutions in regions where it is needed.

b. Mesh surfaces

   i) Select the TCPC wall, the extension walls and the outer inlet/outlet cross-sections (do not select the cross-section lying at the interface between the TCPC and the extensions)

   ii) Change the mesh type to "Tri", uncheck "Spacing" and "Apply"

"Mesh Surfaces"
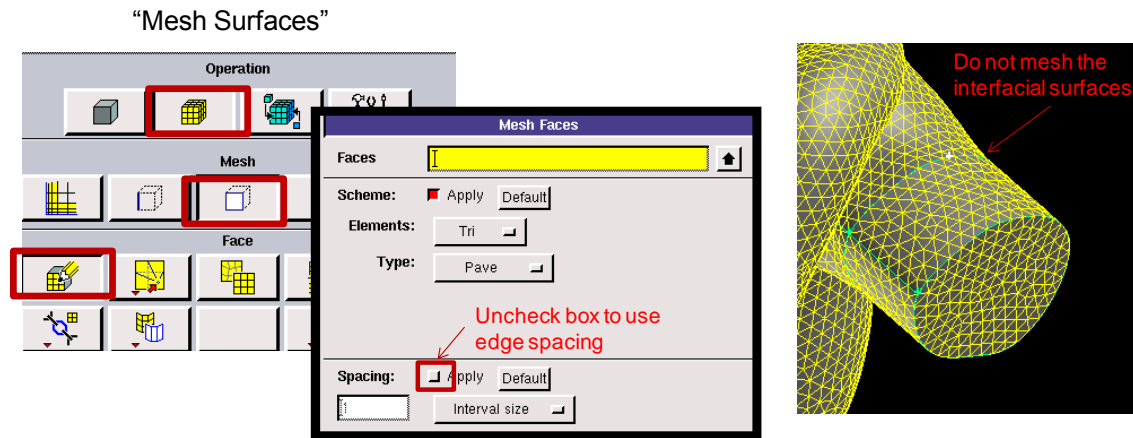
Figure A. 23 Surface mesh generation

5. Label the inlet/outlet cross-sections

   This operation will ease the prescription of the inlet and outlet boundary conditions with the in-house code.

   a. Change solver type to FIDAP

   b. In operation select "Zones" ( ), and then select "Specify Continuum Type" ( )

   c. The default setting for the continuum types to be select is "Volume", change to "Faces"

   d. Select one inlet or outlet, name it (e.g. IVC or LPA) and apply

   e. Repeat the operation for all inlets and outlets

   The advantage of labeling the inlets and outlets is that Gambit will export the mesh surfaces in the order in which they are labeled. Controlling the order in which the surfaces are labeled allows for an easier prescription of the boundary conditions.

6. Export the mesh (File/Export/Mesh) "mesh_name.FDNEUT"

324

Specify Boundary Name

Define as LPA
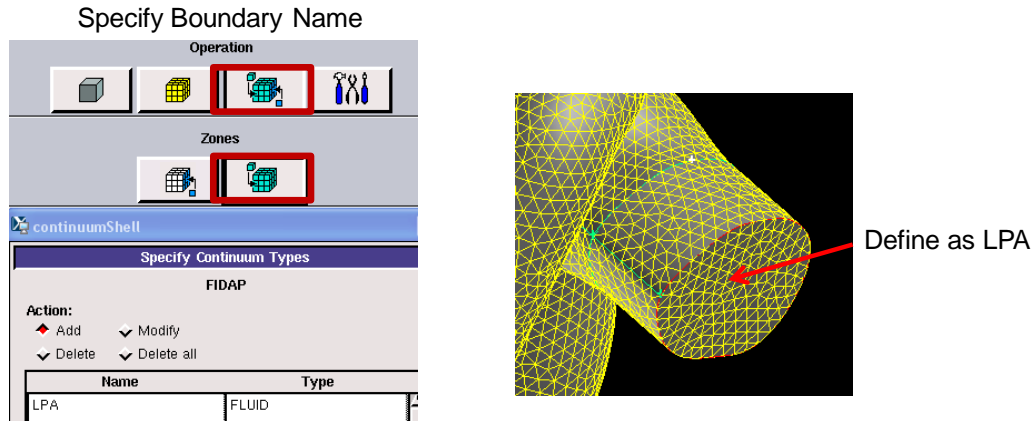
Figure A. 24 Label each inlet and outlet, in the same order as the one that will be used for the boundary condition prescription in the in-house code.

A.5.2.1.2.2. Mesh Generation Using ANSYS Workbench (ANSYS Inc., PA, USA)

In this tutorial, the major modules that will be used in ANSYS Workbench are:

1. ANSYS Design Module -- Geometry;

2. ANSYS Meshing Module -- Mesh;

3. ICEM CFD – Output (as .FDNEUT).

Some Tips:

- You can skip using the ANSYS Meshing Module and directly do meshing with ICEM CFD. However, that would be a little more complicated, especially for the mesh quality required in our cases.

- Anytime you see the lighting mark on any module in ANSYS Workbench, you may want to right-click to "Update" or "Generate" for the sake of proceeding.

1. ANSYS Design Module – Geometry

a. First, open the ANSYS Workbench under the ANSYS folder (Figure A. 25)
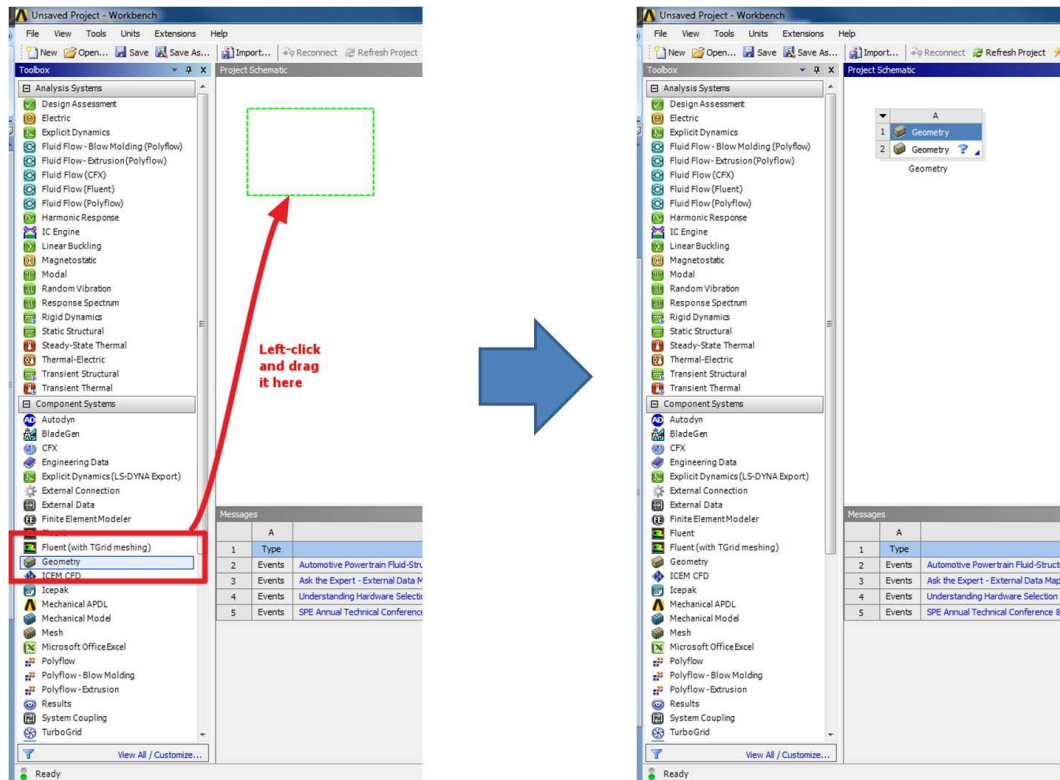
Figure A. 25 Workbench panel

b. Drag "Geometry" to the empty space. Double-click the question mark next to the "Geometry" to open the ANSYS Design Module.

c. Under "File" button of the menu bar, select "import external geometry file". It will ask about the metric unit; choose 'millimeter'. Make sure change the "Operation" to "Add Material", and then "Generate" the geometry. The geometry will show on the screen, as shown in Figure A. 26.
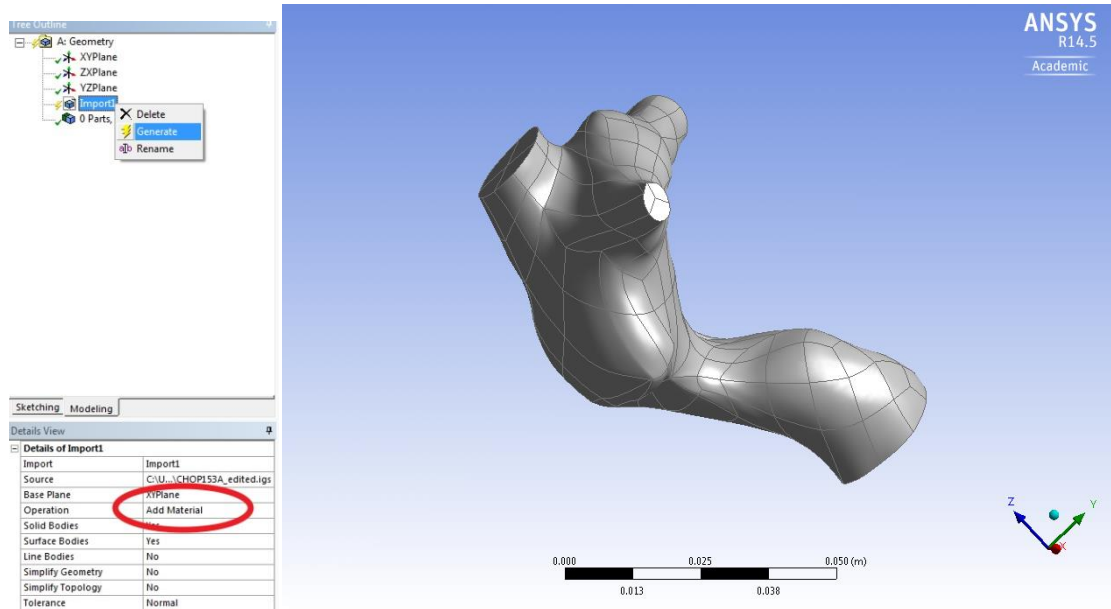
Figure A. 26 Screenshot of ANSYS workbench

d. On the screen shown in (right of Figure A. 26) (which will be referred as 'working screen' in the following context), you can use your mouse to adjust the perspective of view.

e. If you had any trouble and need to reset the view, the following buttons in the tool bar may help. (In the software, you can see the tips by moving your mouse on top of the button and keeping it still.)

f. Now, you need to identify surfaces. Go to the "Concept" button on the menu bar (Figure A. 27), click "Surfaces From Faces".
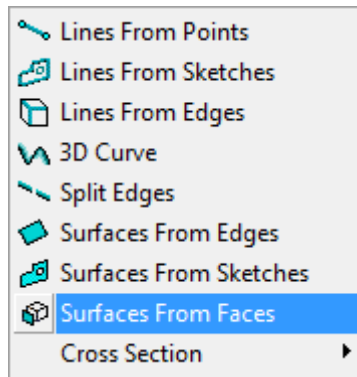
Figure A. 27 Concept button

a. It is better to identify the body surface first, which you need to use the "Box select". By default, it should be just the row under the menu bar and located in the nearly middle of your screen)

b. Now, you can hold the left button and draw a box on the working screen to include everything. And then switch to the "Single Select" to de-select boundaries that are not belonging to the body surface. The way to deselect is hold "Ctrl".
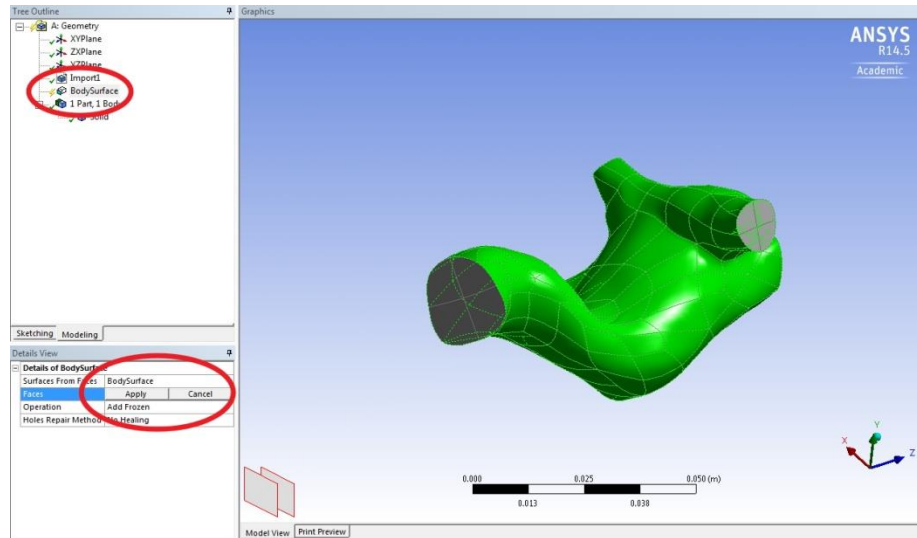
Figure A. 28 Screenshot of ANSYS workbench

c. On Figure A. 28 you need to:

   i)   Make sure the operation is "Add Frozen";

   ii) Change the name of the surface;

   iii) Click "Apply" after you make sure all desired faces are included, which are usually marked as green before you click "Apply" and turn teal afterwards;

   iv) Do not forget to right-click the lighting mark and click the "Generate" to complete this step.

   v)   **You need to make the surface for all boundaries/surfaces, no matter if you need to mesh it or not.**

d. Now, you need to create the extension for all vessels. Get into "Create" and find "Extrude", make sure:

   i)   Your "Selection Filter: Faces" on the tool bar is enabled:

Details of IVC_Extension	
Extrude	IVC_Extension
Geometry	8 Edges
Operation	Add Material
Direction Vector	Face Normal
Direction	Normal
Extent Type	Fixed
☐ FD1, Depth (>0)	0.01 m
As Thin/Surface?	No
Merge Topology?	Yes
Geometry Selection: 8	
Edges	8

Figure A. 29 ANSYS workbench parameters

ii) Change the name in the Figure A. 29

iii) "Operation" = "Add Material";

iv) "Direction Vector" is chosen properly, as shown in Figure A. 30. When you click the "Direction Vector", the software will automatically reset the "Selection Filter", you may want to manually correct it.
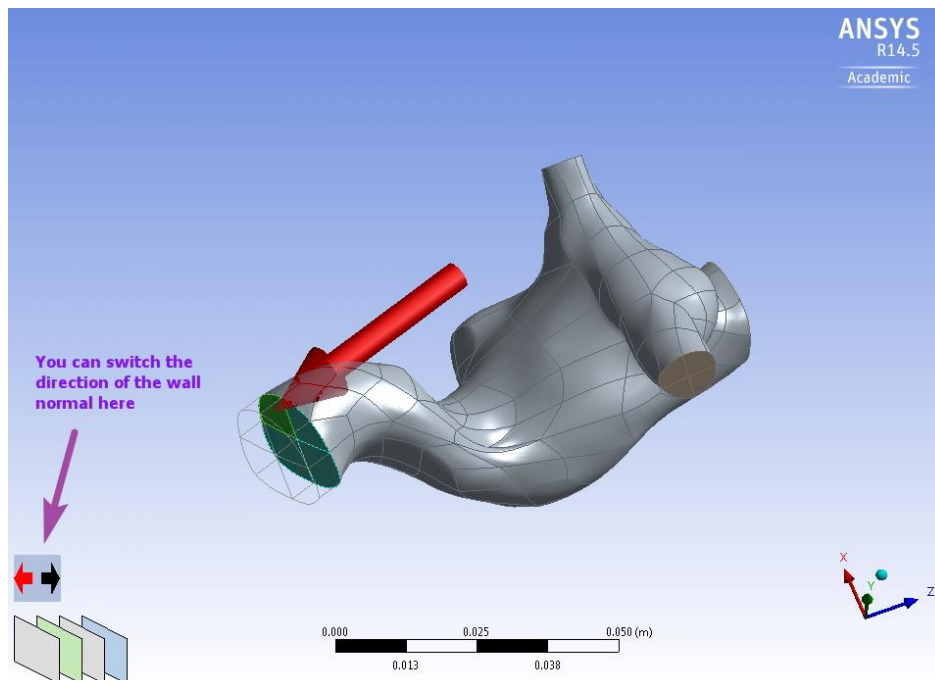
Figure A. 30 Normal vector direction

v) "Depth" are:

➢ No extension:

• Mesh all surfaces.

➢ CFD:

• IVC, SVC: 0.01 m; (10mm)

• LPA, RPA: 0.05 m; (50mm)

• Do NOT mesh the interface between the vessel ends and the corresponding extensions. (i.e. marked as green in Figure A. 30)

• Mesh the end of the extensions.

➢ VMTK:

• IVC: 0.01 m; (10mm)

• Others: 0.005 m; (5mm)

• NO MESH for the end of the vessels as well as the interface between the extension and vessel end.

➢ Notice:

• The meshing details will be further demonstrated later.

• Once you generate a set of extensions, you can modify their length arbitrarily. Also, you can right-click and suppress them if you do not need them, i.e. to create mesh without the extensions.

e. After extensions are created, you can distinguish them from the original body by the color difference. (Tips: if you really cannot tell the difference, you can

331

change the "Operation = Add Frozen" in the step 3. It won't be a matter in our

cases)
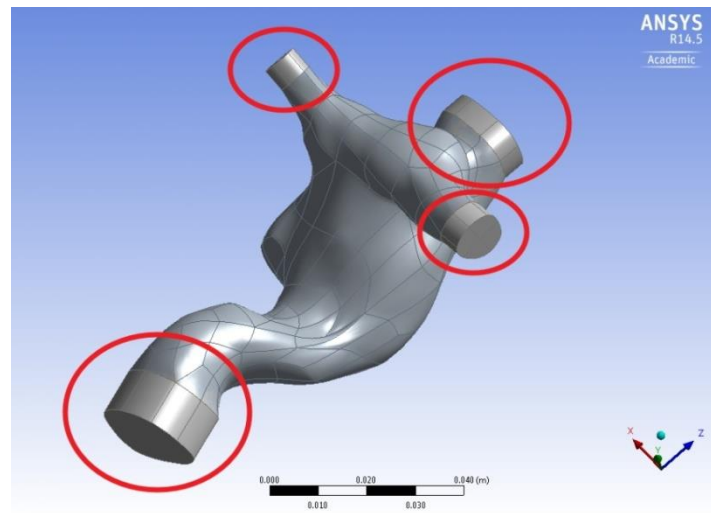
Figure A. 31 Mesh extensions

f. Then, make the surface for the extension sidewalls and the extension ends, as shown in Figure A. 31. Remember, keep the "Operation = Add Frozen" here.

g. After you made all surfaces, you can right-click the "Solid" and "Suppress Body" (Figure A. 32). By doing this, you exclude the body-volume from your geometry, which left only the surfaces; therefore, no volume/body mesh will be generated later.
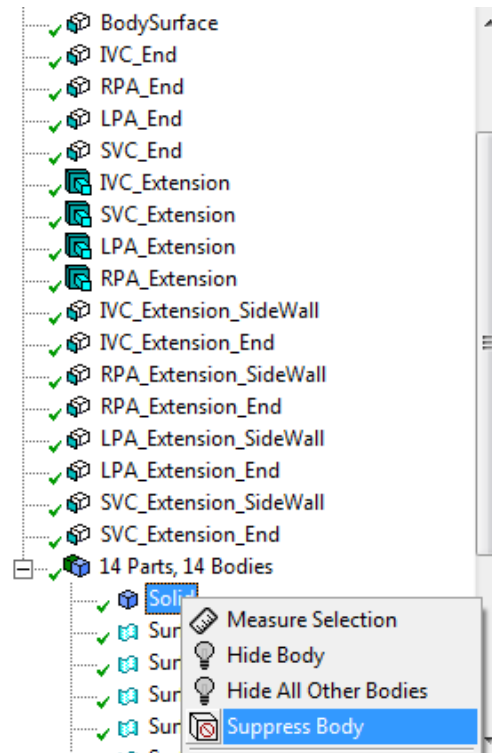
Figure A. 32 Suppress Body

h. Similar "Suppress" operations you be used for those "Surface Body" for original vessel ends since, with the extensions, original vessel ends becomes interior. Notice, you need to find the "Surface Body", as shown in Figure A. 33, rather than those surface names you made before. It is "Surface Body" that will be inputted into ANSYS meshing module in the next step. After suppressed the "Solid", original vessel ends should be easily found.
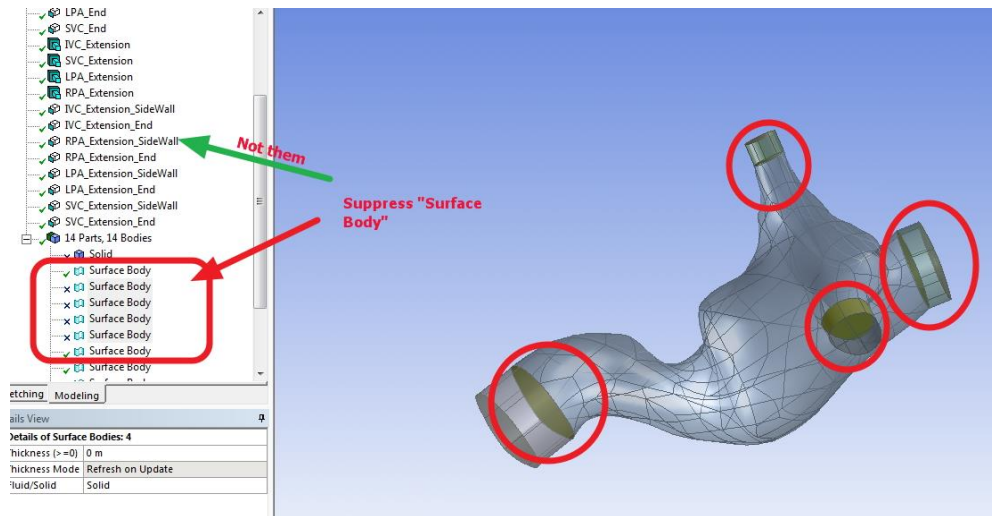
Figure A. 33 Surface Body

i. In addition, you can use "Boolean" under "Create" menu bar to unite the "WholeBody" surface (Figure A. 34), which consist the original body surfaces and side walls of the extensions. This is an option. (Before you do this, you need "suppress" the "solid" volume under the "parts" outline. Otherwise, the "Boolean" will only take volume bodies rather than surface bodies)
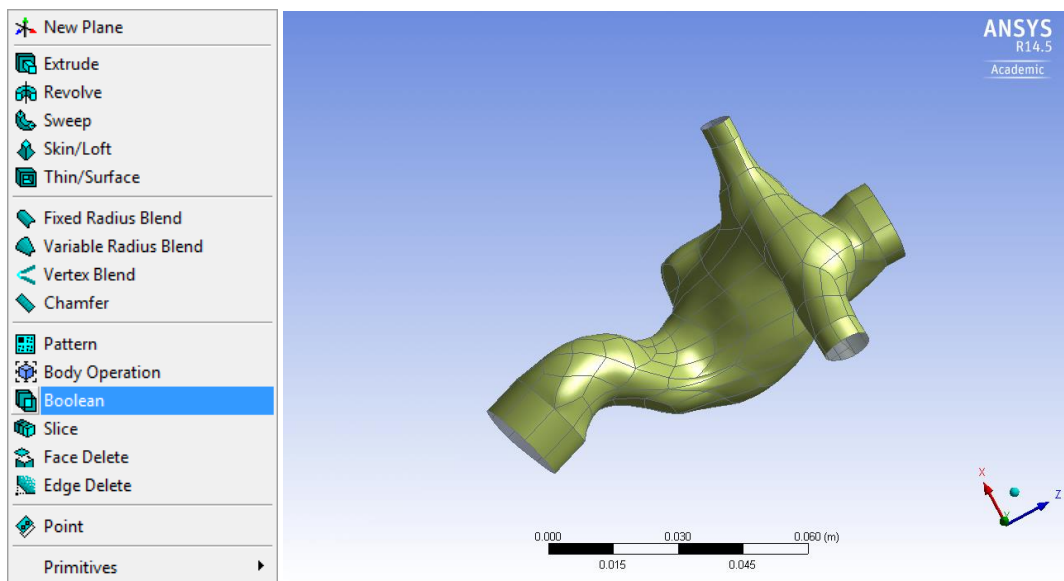
Figure A. 34 Boolean operation

j. After all these, you can save the project and close the ANSYS Design Module.

2. ANSYS Meshing Module - Mesh

   a. Go back to the ANSYS Workbench panel and add a "Mesh" into the working flow. Follow Figure A. 35 to connect the existing geometry to the meshing module.

   b. Then, double-click to launch the software.
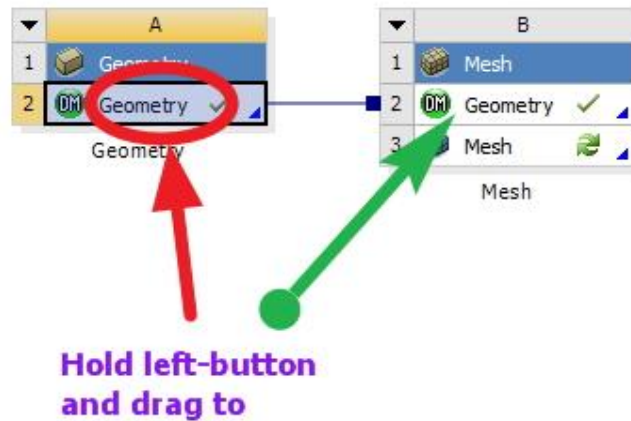
Figure A. 35 Connecting the existing geometry to the meshing module

   c. Click the "Mesh" in the outline and make sure "Physical Preference = CFD", as shown in Figure A. 36
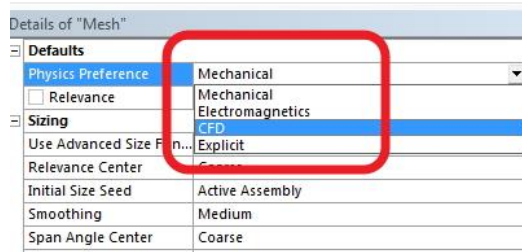
Figure A. 36 Physics reference: CFD

d. Right-click the "Mesh" and "Insert" the "Mapped Face Meshing". Use "Box Select" to involve all faces and change the "Method = Triangles: Best Split", as shown in Figure A. 37

Figure A. 37 Method: triangles best split

e. The other way that will also work:

- Under "Mesh", right click → "Insert" → "Method". Select the body of interest. For Method, choose "Triangles"

- To control the size of the element, you can right-click the "Mesh" and "Insert" → "Sizing". Enter the Element size you want to use (e.g. 1mm). Select "Hard" as "Behaviour" to allow uniform element size.

f. Then, right-click the "Mesh" and "Generate" (or "Update").

3. ICEM CFD - Output

a. Again, go back to the ANSYS Workbench panel and launch the "ICEM CFD" module. Link the mesh from the ANSYS Meshing Module to the ICEM CFD, as shown in Figure A. 38. (Left-click and drag)
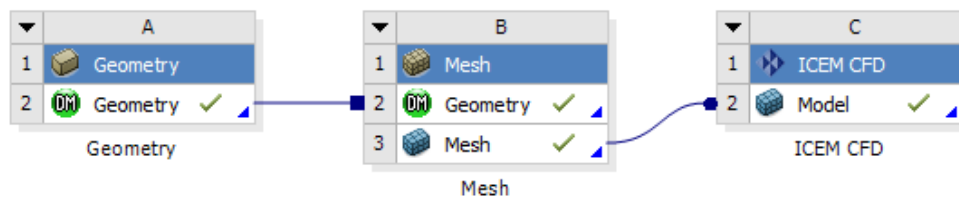
Figure A. 38 ICEM CFD

b. Double-click and open ICEM CFD. On the navigation bar, find "Output

→Select Solver"

c. On the left-bottom corner of the screen, change "Output Solver → Fidap" (Figure A. 39)
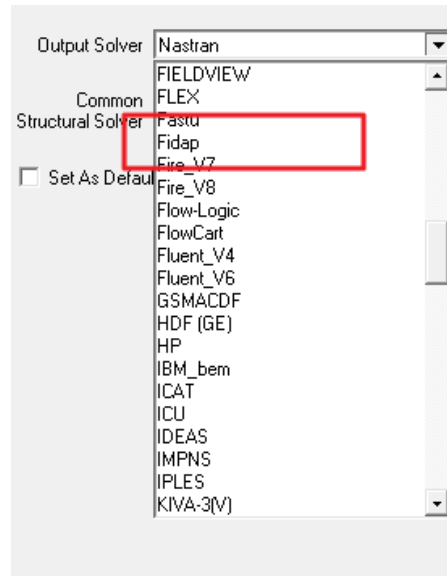
Figure A. 39 Change output to FIDAP

d. Then, "Write Input" under the "Output" of the navigation bar:
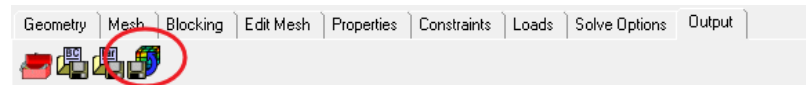
e. It will require you to save the project; then a dialog pop-up, as shown in Figure A. 40.
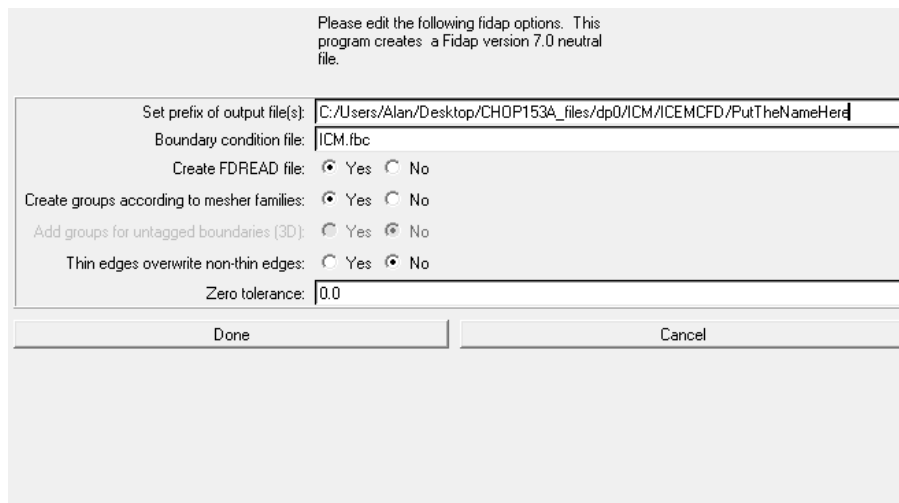
Figure A. 40 Dialog pop-up to save the project

A.5.2.2.   <u>Step [2] Volume Mesh Generation</u>

A.5.2.2.1.   Step [2a] Description of the Source Codes

The unstructured Cartesian grid for the immersed boundary solver is generated with an in-house mesh preprocessing code. The necessary files are:

1. The code source files. Since the code is written in Fortran 90, these are the files with an .F90 extension

   a. main.F90: which contains the main program section, containing all calls to subroutines

   b. global.F90: which contains the variable declarations for all global variables

   c. alloc.F90: where all dynamic array allocations are performed

   d. The core of the code (i.e. sorting the nodes between those that are fluid, IB or wall nodes) which is performed by the following subroutines:

      i) ibm_init.F90 & grid.F90: read the unstructured surface mesh generate the background structured Cartesian grid

      ii) ibm_init_nds_fn.F90: sort the nodes between fluid (NVERT=0), IB (NVERT>0) or wall (NVERT=-3)

      iii) ibm.F90 : for all IB nodes detect the closest fluid and wall elements and set the parameters for the quadratic interpolation

      iv) CG_ibm_correction.F90: final check to make sure that all nodes are set-up properly

      v) sort_grid.F90: re-order the nodes from their structured Cartesian indexing to the unstructured indexing system

vi) lnm1.F90: function that establishes a correspondence between the 1D index L and the 3D coordinates of a point (i,j,k)

e. Code input/outputs

    i) plot_picture.F90: output all the tecplot compatible outputs

    ii) rest_dmp.F90: which reads and writes the binary restart files for geometry (Rest_GeomXXXX). The default output format is Rest_Geom0000

f. init_restart.F90: which is used if the code is called with a geometric restart file (Rest_GeomXXXX)

2. The file with all the compiling options: Makefile

a. To compile the code, go to the folder with the source files, and type "*make*" in the command line.

ifort -c -r8 -mp -xW -ipo global.F90 -o global.o

....

This should output an executable file named IBUns_Li_MPI_PreProcess

b. Changing the compilation options: modifying F90FLAGS in Makefile:

    i) For faster performance, compile the code with optimization options.

F90FLAGS   = -r8 -mp -xW –ipo

The compilation output with these options should read as:

ifort -c -r8 -mp -xW -ipo global.F90 -o global.o

....

    ii) When debugging, it might be helpful to change the compilation options to the debugging options. Open the Makefile, and change F90FLAGS to:

F90FLAGS   = -r8 -g -C -traceback –fpe0

The compilation output should now read as:

ifort -c -r8 -g -C -traceback –fpe0 global.F90 -o global.o

…

3. The code input file (Input_MPI.txt), which contains all the user information required for the executable to run. The exact parameters to be set-up in that file are discussed in more details in the following section.

A.5.2.2.2.   Step [2b] Setting Up the Meshing Parameters (input_MPI.txt)

All settings for the volume mesh generation are controlled from the text file input_MPI.txt. This file includes parameters that pertain both to the flow solver and to the pre-processor. We will only present the parameters associated with the mesh generation. The input_MPI.txt file is divided into sections with specific instructions, which are here listed, with examples of parameter settings.

1. General information

   a. NAME_PROBLEM: This can be any word or short sentence that helps the user remember characteristics of the simulation, e.g. the patient ID. NAME_PROBLEM will appear on the top of the screen output.

   b. REST_Q_UH and REST_GEOM: these are the numbers associated with the geometric and flow restart files.

      i. For the pre-processor REST_Q_UH does not come into play.

      ii. Setting REST_GEOM = 0 means that the pre-processing should be started from scratch

iii. Setting REST_GEOM > 0 means that the pre-processing has already been done, but that the user wants to associate the volume mesh with a finer surface mesh for example.

2. Parameters to read the immersed boundary

   a. F_FDNEUT: The name of the .FDNEUT file with the unstructured triangular surface mesh

   b. (N)PT_TO_REMOVE, (N)NC_TO_REMOVE, (N)NC_TO_ADD, NC_TO_ADD, and are options allowing the user to correct selected surface elements (point and cell) if there are a few defects after the Gambit mesh generation steps. If there are too many holes or inverted elements, then it is simpler to go back to Gambit or Geomagic.

      i. If there are no defects in the surface mesh, all these parameters should be set to 0

   c. NINVERT_NORMAL allows the user to invert the normal directions over an entire boundary so as to ensure that all normals are pointing into the fluid.

      i. In most cases Gambit exports the mesh with all normals pointing outward from the fluid domain. In these cases, set NINVERT_NORMAL to any value larger than the number of boundaries in your surface mesh (e.g. 100).

      ii. If some but not all boundaries have inverted normals, you should set NINVERT_NORMAL to the number of boundaries that should be flipped. For example, set NINVERT_NORMAL=2, and then, assuming that the two zones in your surface mesh that have inverted normals are zones number

7 and 11, you should list the corresponding zone numbers as GROUPS_TO_INVERT(1:2)=7,11. Here we will also discuss how to check for these vectors and how to fix them.

3. Scaling of the physical dimensions

The in-house code is written using the non-dimensional form of the Navier-Stokes equations. A first step is thus to normalize the geometry by a characteristic length.

a. IJK_BODY_LENGTH offers a number of pre-set options, including the maximum x, y, or z dimensions (IJK_BODY_LENGTH = 1 to 3) or using the equivalent hydraulic diameter of a given inlet or outlet (IJK_BODY_LENGTH > 100)

b. For all other characteristic lengths set IJK_BODY_LENGTH = 0 and type in the normalization parameter to use as L_REF.

4. Spatial resolution of the Cartesian volume mesh

Two options are offered to define the spatial resolution:

a. If GRID_OPTION = 1, then the user fixes the number of grid cells in each direction (IMG, JMG, KMG) and the code adjusts the mesh resolution to cover the entire geometry

b. If GRID_OPTION = 2, then the user fixes the mesh spacing (GRID_DX) after non-dimensionalization and the code adjusts the number of grid cells in each directions to cover the entire geometry.

In this thesis the geometries were discretized using option 2, and the mesh spacing was typically set to be isotropic and equal to 0.02 non-dimensional units (i.e. $h = 0.02 \, D_{IVC}$)

5. IB-node detection parameter

   a. In order to sort the Cartesian grid nodes between those that fall inside or outside of the fluid domain, a preliminary search is performed that only takes into consideration the Cartesian cell centers that fall within a certain search radius of the immersed boundary nodes (see Figure A. 41). This search radius is defined as R = COEFF_DSMAX · Δx

   b. COEFF_DSMAX should be set to a large enough value such that none of the IB cell centers are overlooked, but kept small enough to minimize computation time. The typical setting used in this thesis was COEFF_DSMAX = 9.0.

   c. EPS_VEC is the tolerance for points to be considered as being within the fluid domain versus outside of it. This parameter was typically set to EPS_VEC=0.001.

With all these parameters in place, the preprocessing code will automatically generate the desired unstructured Cartesian grid. All geometric information will be written into the geometric restart file Rest_Geom0000. It is advisable to change the restart file name to any number other than the default value of 0000 afterwards.
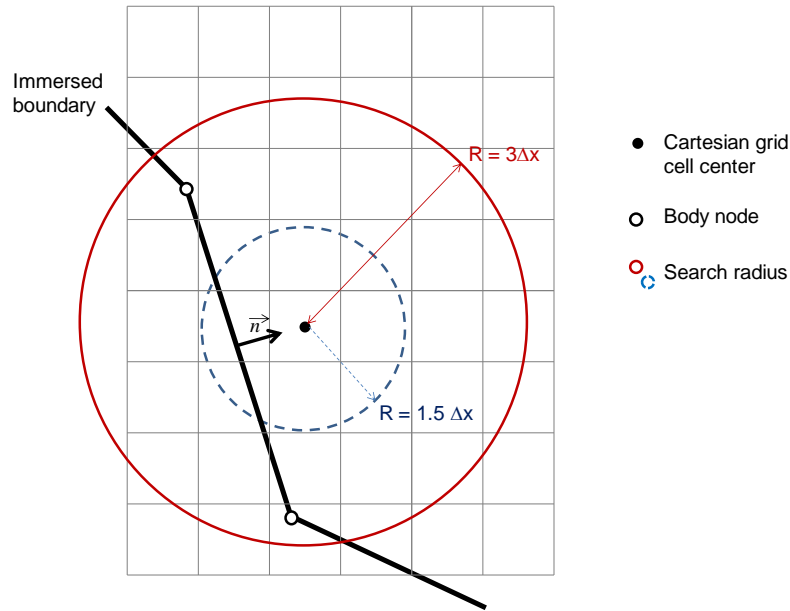
Figure A. 41 IB-detection. In the preliminary search, only the Cartesian grid cell centers that fall within a certain distance R of the immersed boundary node are differentiated between those that fall inside or outside of the fluid domain. If R is too small (e.g. R= 1.5□x), then some IB cell centers may be overlooked.

A.5.2.2.3. *Step [2c] Setting Up the Meshing Parameters (input_MPI.txt)*

To run the code, create a folder to store your results and make sure the following files are in there:

1. The code executable: IBUns_Li_MPI_PreProcess

2. The input file: input_MPI.txt

3. The unstructured surface mesh: Mesh_name.FDNEUT

4. (Optional) A geometric restart file: Rest_GeomXXXX

After setting up the input file, the code may then be run in interactive mode with the following command:

    ./IBUns_Li_MPI_PreProcess

or in batch mode (which allows the user to close his active windows without stopping the pre-processing) with the following command:

345

nohup ./IBUns_Li_MPI_PreProcess >screen_output &

screen_output contains all the information that would otherwise be outputted to the screen.

To check for any inverted normals, load the following files in Tecplot 360 (Initial Plot Type: 3D Cartesian):

　　Tec_BC01.dat, Tec_BC02.dat….

Check the "Vector" box to visualize the direction of the normals in Tecplot. Use relative length of 0.02 Grid Units/Magntitude (Plot →Vector→Length) to better visualize the vectors. You can also load TecBody.dat to show the original surface simultaneously.

A.5.2.3. 　　　<u>Step [3] Setting Up the CFD Simulation</u>

To run CFD simulation with the immersed boundary solver, you will need the following files: (examples are in
/yogi6/Pediatric_PatientData/grant/Analysis_output/CFD_results/0000-Examples)

1. EXCEL template file for preparation of

    a. CFD template, i.e. CHOP069C.xlsx

    b. BC template, i.e. CHOP069C_BC.xlsx

2. *.FDNEUT file in the working directory

3. Executable files, input files and source codes:

    a. IBUns_Li_MPI_PreProcess is the executable preprocessing code;

    b. ACNP_MPI_Solver is the executable IB code;

    c. "input_MPI.txt" is for preprocessing and input for IB code;

d. pulseBC_forCode.F90 can generates the pulsatile input BCs;

e. Please change modes for all executable files. For example, "chmod 777 ACNP_MPI_Solver".

4. Optional PBS files for cluster:

a. Alan-Prepocessing.pbs;

b. parallel.pbs (usually) and ParallelSim.pbs;

5. MATLAB files:

a. BCinput.m

A.5.2.3.1.   Step [3a] Imposing boundary conditions

In input_MPI.txt

▪ REN: Reynolds Number (calculated with time-averaged flow, equivalent hydraulic diameter of the IVC inlet cross-section, (normalization length))

▪ BC_STEADY = T or F: If this value is set to T (true) then the code will use the constant (steady) boundary conditions and boundary types prescribed below, otherwise it will look for a time-varying input prescribed in BC.txt

▪ To help prepare these files, two kinds of template files are used:

o CFD template, i.e. CHOP069C.xlsx

o BC template, i.e. CHOP069C_BC.xlsx

(i) Non-Pulsatile boundary conditions

Many of the options here are also applicable for pulsatile boundary conditions. In input_MPI.txt

- BC_NUM: number of boundaries for which the boundary conditions will be specified. This number should be at least equal to the number of inlets and outlets.
  - In usual cases, BC_NUM = Total number of vessels X 2 (end caps and extensions) + 1 (TCPC surface), (i.e. if only having IVC, SVC, LPA and RPA, the real number of vessel is 4; therefore, fill 9 here)
- BC_NGROUP: index of the BC_NUM boundaries for which the boundary conditions will be specified
  - E.g. BC_NGROUP = 1, 2, 3, 4, 5, 6, 7, 8, 9 (if only having IVC, SVC, LPA and RPA)
- BC_TYPE(1:BC_NUM): type of boundary condition to use
  - BC_TYPE(N) > 0: inlet. 1=flat velocity profile, 2=parabolic velocity profile based on the inlet equivalent diameter, 3=prescribed velocity profile to be specified in text files stored in a folder named BC_N_profiles
  - BC_TYPE(N) = -3: outlet
  - BC_TYPE(N) ≤ -100: wall. -100: IB velocity set to 0, -101: no slip wall with the IB velocity reconstructed using a bi-quadratic interpolation, -102: slip wall
  - E.g. BC_TYPE = 1, 1, -3, -3, -101, -101, -101, -101, -101 (if only having IVC, SVC, LPA and RPA)
- BC_SPLIT: portion of the flow coming or exiting through a given boundary. This value should be 0 for walls, >0 for an inlet and <0 for an outlet. The sum

of the inlet ratios should be 1 and the sum of the outlet ratios should be -1 (be careful not to create any rounding error)

- o Note: If nothing is specified for a given boundary, the default setting will be BC_SPLIT = 0 (i.e. no flow) and BC_TYPE = -101 (i.e. no slip wall).

- The total flow rate or cardiac output coming in and out of the geometry may be set in one of two ways:

  - o If the Reynolds number was computed using the mean velocity through inlet N as a characteristic velocity then, set NORM_VEL = N. The total flow rate, DVOL_0, will be computed as the ratio of the cross-sectional area of inlet N and BC_SPLIT(N). This will ensure a mean non-dimensional velocity of 1 through the inlet taken as a reference.

  - o Otherwise, set NORM_VEL =0 and DVOL_0 to the desired value. Ensure that DVOL_0 is consistent with the characteristic distances and velocities chosen to compute the Reynolds number REN.

(ii) Pulsatile boundary conditions

For pulsatile simulations, the two following parameters should be set in input_MPI.txt: REN and BC_STEADY=F. Settings mentioned for BC_NUM, BC_NGROUP, BC_TYPE, BC_SPLIT, etc. in the previous section are still applicable here. The time-dependent cardiac output, flow splits and boundary types should be specified in BC.txt:

- NT_UNSTBC_MAX: number of time-points for which the boundary conditions are specified

- List of the non-dimensional time-points

349

- List of the total non-dimension flow rate for each time point

- For each boundary (indexed by NBC= N), the lists of

  o BC_TYPE for each time-point

  o BC_SPLIT for each time point

Example of a BC.txt file with 4 time-steps and three different types of inlet/outlet boundary

conditions

```
NT_UNSTBC_MAX= 4
Non-dimensional time
0.00  0.25  0.50 0.75

Total Non-Dimensional Flow Rate
1.23  1.45  1.01  0.60

NBC= 1
 1  1  -3  -3
0.01  0.1 -0.01 -0.1

NBC= 2
1 1 1 1
0.99 0.9 1.0 1.0

NBC= 3
-3 -3 -3 -3
-1.00 -1.00 -0.99 -0.90
```

Any boundary not listed in BC.txt will be considered as a no-slip wall for all time-steps (i.e. BC_TYPE = -101 and BC_SPLIT = 0). Similarly to the non-pulsatile settings the sum of the inflow splits should be equal to 1 at every time-step, while the sum of the outflow splits should be equal to -1. If the temporal resolution used in the simulations is finer than that used in BC.txt, the intermediate velocity and flow split values are reconstructed by quadratic interpolation.

Attention should be paid to ensure that the time-varying non-dimensional total flow rate is consistent with the characteristic distance and velocity retained to compute the Reynolds number. For the simulations conducted in this thesis, the characteristic distance was chosen to be the equivalent hydraulic diameter of the IVC inlet cross-section, D_{IVC}, and the characteristic velocity to be the mean IVC velocity averaged both over the cardiac cycle and the inlet cross-section, $\overline{U}_{IVC}$. With this notation the time-varying non-dimensional flow rate, CO^*, is given by:

$$CO^*\left(t^*\right) = \frac{CO(t)}{\overline{U}_{IVC} \cdot D_{IVC}^{\,2}}$$

where CO is the measured time-varying flow rate, t is the physical time, and t^* is the corresponding non-dimensional time-instant given by $t^* = t \cdot \overline{U}_{IVC}/D_{IVC}$.

NOTE: for steady simulations you do not need to create these files; you just need the mean values that are inputted in the input_MPI.txt file

1. Find values under "IVC Reynolds Number Calculation" in CFD template spreadsheet and fill them into BC template:

    a. "VIVC (m/s)" → "vel_ivc (m/s)";

    b. "IVC diameter (m)" → "d_ivc (m)";

2. Find the dimensional time interval for one cardiac cycle by:

    a. Find one DICOM file in:

    /yogi6/Pediatric_PatientData/grant/Analysis_output

    /Anatomy_and_Velocity/Velocity_Segmentations/;

351

b. Open MATLAB. You could use "matlab –nodesktop –nosplash" to launch the non-GUI MATLAB on the server (optional);

c. Find the DICOM, i.e. /ao/ao_0.dcm, and type the following commands:

    i. t = dicominfo('ao_0.dcm')

    ii. t.ImageComments

    iii. An example of output is: RR 593 +/- 0; 80 heartbeats. It means that the time for one cardiac cycle is 593 +/- 0 (ms) which is averaged over 90 heartbeats;

    iv. You need to convert the cardiac cycle time to second and fill it into "period (s)" in BC template;

3. Find the pulsatile velocity waveforms in /yogi6/Pediatric_PatientData/grant/Analysis_output/Anatomy_and_Velocity/Velocity_Segmentations/_matlab_processed_datasets_/ and fill them to BC template. A good example for the velocity waveform is "ivc_numcomp_1_*.txt";

a. **You need to make sure that the inlet flows are all positive and outlets are negative!!**

4. Now, use MATLAB to run "BCinput.m".

a. Record "NonDimPeriod" to BC template;

b. The output file "BCinput.txt" is necessary input for the next step;

5. Open "pulseBC_forCode.F90 " by "vi":

a. Change "TPERIOD" by "NonDimPeriod";

b. Compile "pulseBC_forCode.F90" with "ifort";

c. Run "./a.out"

d. You can view the output in Tecplot 360.

A.5.2.3.2.   Step [3b] Setting up the simulations

First change, the file name "Rest_Geom0000" to "Rest_Geom9999".

This is applicable regardless of the type of boundary conditions used. In input_MPI.txt

1. REST_Q_UH = 0000 if starting from the beginning or filling in the number of iteration you want to restart (but you need to make sure the restart file exists).

2. REST_GEOM = 9999

   DELTI is the timestep size, which usually is "NonDIMPeriod"/2000

3. NT2 is the total time step, which usually is 2000*6 (means running 6 cycles)

4. ERR_TOL = 1E-15 (you may want to try 1E-6 if 1E-15 is too small)

5. Frequency at which the flow fields should be outputted

   o NWOUT: instantaneous pressure and velocity fields in Tecplot format

   o NWAVE: running-average (velocity and pressure) in Tecplot format

   o NWDUMP: flow restart file in binary format (REST_Q_UH)

   o DUMP_OVERWRITE: if this is set to F (false) then each output will be written to a new file, indexed by the time-step number. If it is set to T (true) the restart files will be overwritten, in order to save space. For pulsatile simulations this value is automatically switched to F within the code itself. Usually, it is "T" for steady simulations and "F" for pulsatile ones

6. Monitoring the simulations and convergence: The user can specify a series of points for which he or she wants the time-history of the pressure and velocity components. For each one of these points the code will output a Tecplot-

compatible file containing the time-series of the instantaneous pressure and velocity components (P,U,V,W) and the corresponding running averages (PM,UM,VM,WM)

o MONITOR_FILE: file header

o MONITOR_NUM_POINTS: number of points to track

o MONITOR_XYZ(N,1:3) = X,Y,Z: coordinates of the Nth point monitor

   a. Open "TechFl0000.dat" with "Tecplot Data Loader"

   b. "Data" → "Extract" → "Slice from Plane". Play with "Constant Z" (red-box) to adjust the plane intersecting with the connection between SVC, LPA and RPA (Figure A. 42)

   c. "Zone Style": disable "Zone Show" for "Zone 001" (right-click) and change the "Shade color" for the new plane to a visible color

   d. "Extract" → "Points from Polyline". Draw a polyline with three points (Figure A. 43). Click to select the start and end points.

   e. By clicking "Extract", save coordinates of these three points to a file

   f. Update MONITOR_XYZ(1,1:3) with the coordinate of the middle points.

7. Checks for debugging: Unless the user wants to debug a specific problem, these checks should be set to F (false) as they will result in a large number of outputs that will drastically slow down the simulations. Check information will be outputted to the files MPIYYY_output_ZZZ.dat where YYY is the number of processors and ZZZ is the processor identification number.

   o CHECK and CHECK_P = T or F: general information for the momentum and pressure projection step, respectively

○ CHECK2_INPUT = F or T: track the computation at a specific grid cell of

index L_TO_PRN_INPUT. This cell index is the global cell index, the code will

then identify which processor it is associated with and its local index.
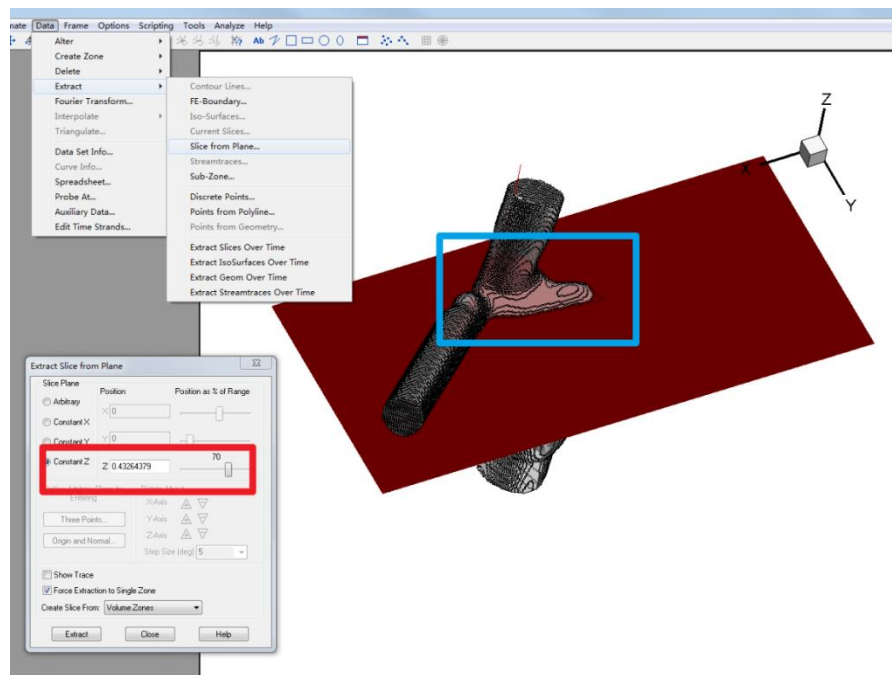
Figure A. 42 Screenshot from TECPLOT: how to get a cross sectional slice
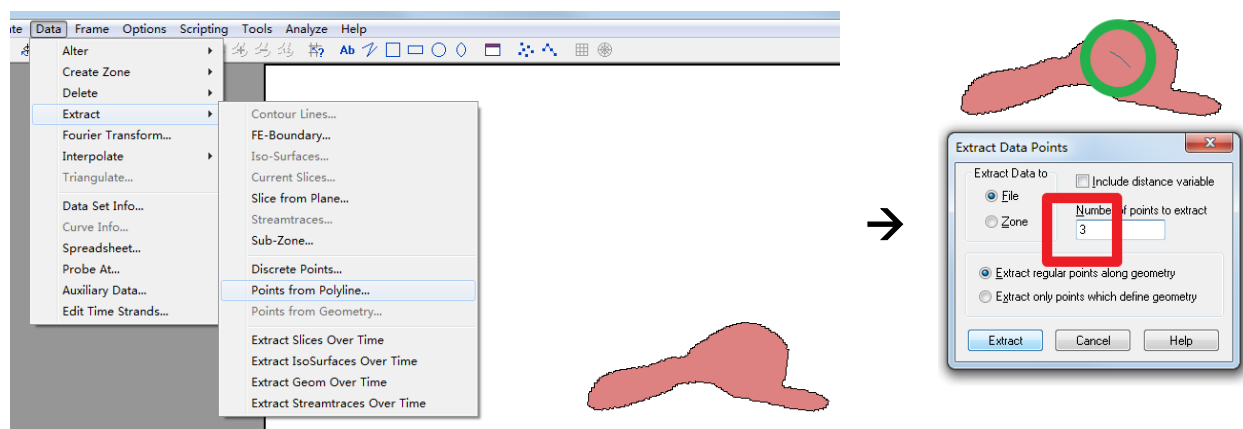
Figure A. 43 Screenshot from TECPLOT: how to extract the monitor points

A.5.2.4.   <u>Step [4] Running the CFD Simulation</u>

A.5.2.4.1.   *Step [4a] Description of the Source Codes*

The flow solver contains two different options: an artificial compressibility formulation and a fractional step formulation. The necessary files include:

1. The code source files. Since the code is written in Fortran 90, these are the files with an .F90 extension

   a. main.F90: main program, controls the time iteration loop and calls all other subroutines

   b. global.F90: all global variables

   c. communicate.F90: communication subroutines for parallel simulations using MPI

   d. initialization of the simulations

      i)   alloc.F90: allocate all dynamic arrays

      ii) mg_initial.F90

      iii) init_restart.F90

      iv) split_domain.F90: create the local processor domains for parallel simulations using MPI

   e. artificial compressibility subroutines

      i)   ac_implicit_rk4.F90

      ii) rk4_solver.F90: a number of these subroutines are also shared by the fractional step method

   f. fractional step method

      i)   poisson_solver.F90

ii) mg_modules.F90

iii) mg_fs_implicit_RK4.F90

g. boundary treatment:

i)   interp_q.F90

ii) ibm_interpol.F90

iii) interp_u_h.F90

iv) bcond.F90

h. Code inputs/outputs

i)   new_resid.F90: compute residual

ii) output_time_history.F90: outputs the time series at the desired points and computes the running average

iii) plot_picture.F90: all flow field outputs in Tecplot format

iv) rest_dmp.F90: read/write binary restart files

2. The file with all the compiling options: Makefile & MAKE-ALL (see later section for details)

3. The code input files (input_MPI.txt and control.txt), which contain all the user information required for the executable to run. The exact parameters to be set-up in that file are discussed in more details in the following section.

A.5.2.4.2.   Step [4b] Code Compilation

In Makefile & MAKE-ALL

a. For simplicity the compilation commands are stored in different files within the MAKE-ALL folder. These files are called from Makefile

b. To use the artificial compressibility option, compile with the DAC_RK4 option. The corresponding make command is:

    i) make ACNP: to have the optimization options ➔ ACNP_MPI_Solver

    ii) make AC_DBG: to have the debug options ➔ ACNP_MPI_Solver_dbg

c. To use the fractional step method compile with:

    i) Make FS: with the optimization options ➔ FS_MPI_Solver

    ii) Make FS_DBG: with the debug options ➔ FS_MPI_Solver_dbg

    iii) The fractional step command requires PetSc. Make sure that these libraries are properly installed before proceeding.

The IB code has been compiled on PACE cluster by Lucia Mirabella and Elaine Tang in a common folder for all CFM users (/gpfs/pace1/project/pcfm1/cfm-shared/IBcode). Here are the instructions to compile on PACE cluster:

1. Necessary modules in pace to compile the codes:

d. ssh onto PACE

e. Create or modify the file .pacemodules in your home directory, to make it contain the following lines

> *module load use.own*
> *module load hwloc/1.5*
> *module load intel/13.2.146*
> *module load mvapich2/1.9*
> *module load acml/4.4.0/gfortran*
> *module load matlab/r2012b*
> *module load ansys/14.5*
> *module load cmake/2.8.7*

In case you need different modules for other applications I suggest you make a back up of your previous .pacemodules and use this one to run IB code, at least for now.

f. Log off and log on again onto PACE (so that .pacemodules is automatically loaded.

g. You will need to do step (1a,b,c) only the first time

h. Check that the modules loaded are the ones in .pacemodules file, using the command

   module list

2. Compiling the petsc library

Here, we use the name PETSC_SRC to refer to the path to the folder that contains petsc source code. Remember to change it in ALL the commands.

a. De-compress the petsc library file; you will end up with a folder call petsc-2.3.3-p8, and the absolute path of that folder will be PETSC_SRC

   tar –xvf petsc-2.3.3-p8.tar.gz

b. Replace files in PETSC: Copy files from */alicia4/yogi-lab/IBcode_pace/petsc_modification* to replace files in *PETSC_SRC/include/finclude*

c. Compile PETSC library by running the following commands.

   cd PETSC_SRC

   export PETSC_DIR=PETSC_SRC

> *./config/configure.py   PETSC_ARCH=linux-gnu   --with-mpi-*
>
> *dir=/usr/local/packages/mvapich2/1.9/intel-13.2.146/   --download-f-blas-*
>
> *lapack=1 --with-debugging=1 --with-shared=0 --with-batc*
>
> *make*

    d. make test will probably not work as it is, because of pace's queue system, but if you manually run a test it should work

3. Compiling the IB code

    a. Create a new folder for the IBcode, let's call it IBSOLVER here

> *mkdir IBSOLVER*
>
> *cd IBSOLVER*

    b. Copy and de-compress the IBcode file in the IBSOLVER folder

> *tar -xvf ACFS_MPI_Solver_2010_09_16_1658.tar.gz*

    c. Now we have to compile IB code

> *make clean*

    d. Open file IBSOLVER/MAKE-ALL/Makefile.FS and replace the PETSC line with:

> *export PETSC_DIR=PETSC_SRC*

    e. Compile IB code now:

> *make FS*

4. Changes to be made to input_MPI.txt if running on PACE

    1. Comment out the "PREVIOUS_VERSION = 0" by inserting a "!" in front of it;

A.5.2.4.3.   Step [4c] Running a Simulation in Serial or Parallel

(i) Running Serial Simulation

- After setting up the input file(s), the code may then be run in interactive mode

  with the following command:

    ./ACNP_MPI_Solver or ./FS_MPI_Solver

  or in batch mode (which allows the user to close his or her active windows

  without stopping the pre-processing) with the following command:

    nohup ./FS_MPI_Solver > screen_output &

- screen_output contains all the information that would otherwise be outputted to

  the screen.

(ii) Running Parallel simulation

- Utilize the pbs system on PACE cluster

- Change "-N", "-M", and "export PBS_O_WORKDIR = working directory".

    qsub parallel.pbs (or ParallelSim.pbs)

A.5.2.4.4.   Step [4d] Description of Convergence Criteria

In the input_MPI.txt

- DIV_MAX convergence criterion is set to 0.05. Thus, the code will only move to

  the next iteration when either that number is met, or when it has reached the

  number of sub iterations you specified.

- You must check the screen file to see if your simulation is converging. Figure A.

  44 shows an example where the sub iteration limit was met (200 sub iterations)

but the convergence criterion was not met (DIM_MAX = 0.0507). Therefore, the simulation moved to the next time step without reaching convergence.

- You can fix this increasing the number of sub iterations, or determining which convergence criterion is appropriate for your simulations. This must be manually checked for both pulsatile and steady simulations.

```
NT=   13837  IT=     199  G_DIVMAX=-0.51426E-01  G_LMD=       369331  G_ERMAX= 0.36703E-01
NT=   13837  IT=     200  G_DIVMAX=-0.50740E-01  G_LMD=       389619  G_ERMAX= 0.36678E-01
NT=   13837  # of pseudo_iter is increased to ITM=     400 ABS(G_DIVMAX)=  0.05074050 >DIV_MAX=  0.05000000
NT=   13837  TIME= 0.83728E+01  DVOL_0= 0.11758E+01
      IT=     200   G_DIV2= 0.19276E+02  G_ERMAX=-0.39854E+00
      G_DIVMAX=-0.50740E-01    LMD  389619
NT=   13838  IT=       1  G_DIVMAX=-0.19486E+00  G_LMD=       236750  G_ERMAX= 0.00000E+00
NT=   13838  IT=       2  G_DIVMAX=-0.12775E+00  G_LMD=       290542  G_ERMAX= 0.36027E-01
NT=   13838  IT=       3  G_DIVMAX=-0.13071E+00  G_LMD=       290542  G_ERMAX= 0.38918E-01
```

Figure A. 44 Screenshot of the CFD output screen

A.5.2.4.5. Step [4e] Restarting a simulation

(i) Non-Pulsatile boundary conditions

When the simulation finished the total no. of iteration and you still want to run more iteration, you can simply increase the no. of total time step "NT2" in input_MPI.txt. then you can execute the solver again. Note that the previous monitor points, output files will be overwritten.

(ii) Pulsatile boundary conditions

For pulsatile simulations, here are the following things to consider changing when restarting:

- NT2: Increase the number to more number of cycle(s),

  e.g. NT2 = <original NT2> + 2000*<no. of additional cycles>

- Change "REST_Q_Uh" from "0000" to the latest "REST_Q_Uh" file number

  you have

362

- NWDUMP: You may want to decrease this value to increase the frequency of REST_Q_Uh output as the solution gets close to convergence.

  o The rule of thumb is, start with a large no. of NWDUMP (e.g. 500) to save computational time and space, then slower decreases to smaller NWDUMP (e.g. 20) to output REST_Q_Uh for more time points.

  a. For example, for the initial run:

    ▪ NT2 = 2000*3 = 6000 (running 3 cycles each with 2000 time steps)

    ▪ REST_Q_Uh = 0000

    ▪ NWDUMP = 500

    This will result in REST_Q_Uh0001, REST_Q_Uh0002 … REST_Q_Uh0012 at the end of this run (last file number = 6000/50 = 12)

  b. Then, you want to run 2 more cycles and also output more files to check convergence. So to restart the simulation, set the following in input_MPI.txt

    ▪ NT2 = 6000+2*2000 = 10000

    ▪ REST_Q_Uh = 0012 (largest file no. of REST_Q_Uh file available)

    ▪ NWDUMP = 200

    This will result in REST_Q_Uh0031….0050. The REST_Q_Uh no. started with 31, since based on NWDUMP, the code assumes you already have 6000/200 = 30 files before already.

c. When the solution is converged, you want to run 1 more cycle with most frequent output of the REST_Q_Uh file:

- NT2 = 10000+2000 = 12000

- REST_Q_Uh = 0050

- NWDUMP = 20

This will result in REST_Q_Uh0501….0600. The REST_Q_Uh no. started with 501, since based on NWDUMP, the code assumes you already have 10000/20 files before already.

o This explains why it is always a good idea to start with larger NWDUMP then decrease later, but not the other way round. If you start with small NWDUMP (e.g.1) in (a), e.g. REST_Q_Uh0001…6000 will be created. In (b) NWDUMP is increased to 200, the REST_Q_Uh0031….0050 created will overwrite the previous files. This will also create confusion in the numbering of the files.

A.5.2.5.   Step [5] Post-processing

A.5.2.5.1.   Step [5a] Initial Post-processing

Before studying the flow field, the output needs to be dimensionalized and also be converted into ASCII format.

- To run this step you need the following files:

  o Getflowfield (executable)

  o Getflowfield_input.txt

  o Getflofield.pbs (if running on PACE)

- In the input file (Getflowfield_input.txt) you need to change:

  - NFLOW_START: if steady simulations just put the number of the REST_Q_Uh file. If pulsatile, put the first number of the last cycle

  - NFLOW_END: for steady doesn't matter; for pulsatile put the id of the last REST_Q_Uh of the cycle

  - NFLOW_SKIP = N: determine the interval of no. of files that skips post-processing. Usually N=1. Unless you output a large number of REST_Q_Uh files during the simulation and now you only want to post-process every other N files.

  - FLOW_FIELD: 2 for steady, 10 for pulsatile

  - FDNEUT_SM: this is the name of the smaller mesh (without extensions)

  - NUM_IO_SM: number of boundary conditions

  - L_NORM: get this from the pre-processing; it is the normalization length

  - L0: L_NORM*0.01

  - REN: get this from the CFD template spreadsheet

- To run on Poseidon or Crius just type on the terminal

  nohup ./Getflowfield >screen_output &

- To run on PACE use the PBS script

A.5.2.5.2.   Step [5b] Flow Field Visualization

Tecplot macros were created to automatically create figures of streamtraces from CFD results of the solver:

- extract_streamtraces_ribbon.f90 (created by Dr. Diane de Zélicourt)

- Tecplot macros (created by Elaine Tang)

  o IVCSVC_ribbon_compute_no_extravessel.mcr

  o IVCSVC_ribbon_compute_AZ.mcr

  o IVCSVC_ribbon_compute_LSVC.mcr

  o IVCSVC_ribbon_compute_LSVC_AZ.mcr

1. For each inlet, get IVC.dat/RSVC.dat/LSVC.dat/AZ.dat from TecPlot

   o Load the re-dimensionalized geometry from the post-processed CFD results, then extract a slice in the IVC/RSVC/LSVC/AZ perpendicular to the vessel's centerline in Tecplot. Save as ASCII, '*.dat' and save the 'X', 'Y', 'Z' coordinates of the extracted slice

   o E.g. For TCPC with only IVC and SVC as inlets, IVC.dat and SVC.dat should be created

2. Obtain tecplot macro for each inlet

   o For each inlet, open 'extract_streamtraces_ribbon.f90' in text editor. Based on the inlet, change 'NN'

     ▪ NN=1 for IVC

     ▪ NN=2 for AZ

     ▪ NN=3 for RSVC

     ▪ NN=4 for LSVC

   o Execute by:

        $ifort 01_extract_streamtraces.90

        $./a.out

366

- o Based on the vessel, a new macro called 'XXX_ribbon.mcr' should be generated

3. Run macro to generate streamtraces and figures

   - o Run macro based on the number of inlet

      - ▪ Only IVC and SVC: IVCSVC_ribbon_compute_no_extravessel.mcr

      - ▪ With IVC, SVC and AZ: IVCSVC_ribbon_compute_AZ.mcr

      - ▪ With IVC, RSVC and LSVC: IVCSVC_ribbon_compute_LSVC.mcr

      - ▪ With IVC, RSVC, LSVC and AZ: IVCSVC_ribbon_compute_LSVC_AZ.mcr

   - o This macro will call the 'XXX_ribbon.mcr' macros generated in the previous step automatically

   - o This macro can also be called in batch mode (no GUI window will pop up) through command line

      ```
      $ tec360 -b -p <macro name>.mcr
      ```

A.5.2.5.3.   Step [5c] Computing Power Loss

- • Steady: Add the non-dimensional pressure values to the spreadsheet and it should automatically compute the power loss

- • Pulsatile: Use the code developed by Phillip Trusty (he developed several options depending on the number of vessels): Powerloss.m

   - o You will have to input the normalization length, BSA and sum of inlets. It computes power loss and TCPC resistance

367

A.5.2.5.4.   Step [5d] Computing Hepatic Flow Distribution

(i) Steady simulation HFD

The necessary codes to do so can be found on:

/yogi6/Pediatric_PatientData/grant/Analysis_output/CFD_results/Elaine_HFD_postproce

ssing/

1. Get IVC.dat from TecPlot: load the re-dimensionalized geometry, then extract a slice in the IVC perpendicular to the vessel's centerline

2. Extract the 'threshold' z-direction slice, points and normals of the PAs from TecPlot and enter them to 03_compute_IVC_split_beta.90

3. Run ./00_HFD_shell_script on a terminal

4. The output is a TecPlot layout with the streamtraces going to each PA

(ii) Pulsatile: Particle Tracking

In the pulsatile results folder create a subfolder called 'PT'

1. Files needed in this folder:

   - all_data.f

   - main.f

   - Makefile

2. These are the steps to run the Particle Tracking code:

   a. Load non-dimensional file to Tecplot 'TecFl_02_####.dat'

   b. Get slice at the IVC. Save slice as ASCII (IVC.dat)

   c. Open file, remove all headers and write at the top:

      Nodes

      ####

X, Y, Z

    d. Save as 'IVC.txt'

3. all_data.f

- Check that the directories match where you have the Rest files; If you created the PT folder within the results, the directories should be the same:

      '../Rest_Q_Uh_'

      '../Rest_Geom'

- BC_NUM_MAX=11 - this is BC plus extension walls (check the output of the IB preprocessing)

- NF_PERIOD=100 - number of Rest_Qh per cycle

- PART_RELEASE_TIME=   100 - time duration of rest files with particle release

- NFPART=20 - particle release frequency; dictates number of releases

- NFILES=100 - number of files to treat

- NFILES_START=501 - when the last cycle starts

- NJUMP=1 - Interval between 2 files

- DT_FILES= 0.00664 =DELTI*NWDUMP (from input.txt)

- NF_OUT=250 - Frequency of writing particle .dat files

  o IF YOU ARE MAKING A MOVIE CHANGE IT TO 20

  o Select 5 for creating movies: it creates a lot of files and takes longer

- XFC_LPA, YFC_LPA, ...,NFZ_RPA - get these values from Tecplot similar to what you did for steady HFD

- Change the ID of your LPA/RPA:

INTEGER, PARAMETER :: NV_LPA = 4,

.   NV_RPA = 5,

.   NV_WALL= -200

- o If you have a 4 vessel TCPC, the ID's are:

  LPA=3

  RPA=4

- o If you have a 5 vessel TCPC, the ID's are:

  LPA=4

  RPA=5

4. main.f

- BC_TYPE(1:6) = [1,1,1,-3,-3,-101]

  - o Make sure to have the same number of BC

- BC_SPLIT(1:6) = [0.6,0.2,0.2,-0.5,-0.5,0]

  - o Make sure to have the same number of BC

- ~line 1773

  - o IF(XPAR(NP,3).LT.5.63 .AND. XPAR(NP,3).GT.4.43)

  - o In tecplot select a slice below the PAs (GT (greater than) value) and one above it (LT (less than) value) to determine the region where the particles will be counted for HFD

- In the command line enter the following to compile the particle tracking executable:

  make

- Then run PT.pbs file

5. MATLAB CODE 'PARTICLEHFD.m'

- First open tecplot and load one of the TecFl_02_####.dat files (The last one should be OK). Take a slice in the IVC and Write the file (ASCII, point) saving the variables: X,Y,Z,U,V,W

- Open the file and delete all the headers, and just write at the top:

  'Nodes

  ####'

- And leave all the node information

- Save the file as 'IVC_vel.txt'

- In the Matlab code make sure to change the ID of the LPA and RPA: lines 40 and 43

  o if you have a 4 vessel TCPC, the ID's are:

      LPA=3

      RPA=4

  o if you have a 5 vessel TCPC, the ID's are:

      LPA=4

      RPA=5

  o Change the number of particles (line 16)

  o Read this from Particles_T_00000500.dat

  o N=#####

- Run the Matlab code and get the HFD (prints out a txt file with results)

A.6.   LifeV Finite Element Solver

A.6.1. Overview

Step [1]: Surface mesh generation

    a. 3D surface preparation with Geomagic Studio

    b. Surface mesh generation

Step [2]: Volume mesh generation

    a. Description of the Gmsh scripts

    b. Preprocess the volume mesh

Step [3]: Setting up the CFD Simulation

    a. Imposing inflow boundary conditions

    b. Computing parameters for Windkessel model

    c. Setting up the simulations

Step [4]: Running the CFD Simulation

    a. Description of the source codes

        i.   Windkessel model - LifeV 2011

        ii. FSI solver – LifeV 2013

    b. Code compilation

    c. Running a simulation

Step [5]: Post-processing

    a. Computing power loss

    b. Particle tracking

Important: Note that cgs unit system is used in this thesis. It does not matter what units are used in LifeV, as long as it's consistent.

A.6.2. CFD Protocol for LifeV Solver

A.6.2.1.　　　Step [1] Surface Mesh Generation

A.6.2.1.1.　　Step [1a] 3D Surface Preparation with Geomagic Studio

The surface preparation protocol from transverse MRI slices is the same as Step [1a] for the immersed boundary solver.

A.6.2.1.2.　　Step [1b] Surface Mesh Generation

The input needed to generate volume mesh for LifeV is a 3D surface mesh. In this thesis, triangular surface elements were used and were exported as STL format. To generate surface mesh in STL format, ANSYS Workbench can be utilized to prepare the surface mesh as in Step [1b] for the immersed boundary solver. One difference is that the inlet and outlet faces should not be meshed (still, create the surface entity). The other difference is that for the last step, export the mesh as STL in ICEM CFD.
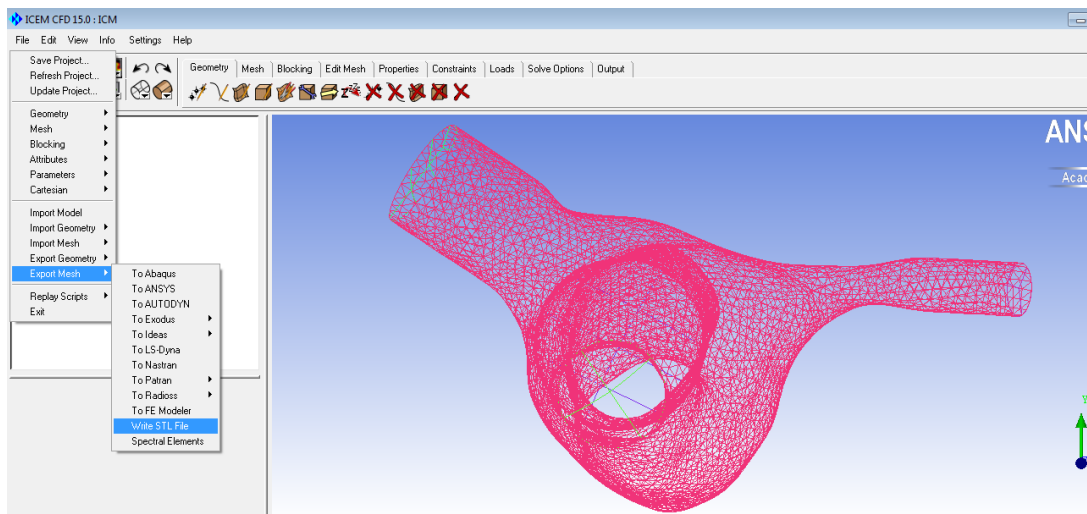
Figure A. 45 Exporting surface mesh as STL file in ICEM CFD

Another alternative is to create the surface mesh in Geomagic without going through ANSYS. This is more straightforward, but in general meshing in ANSYS provides better mesh quality.

- To export the surface mesh in Geomagic, perform surface wrapping and trim planes at the inlet and outlet faces just as in Step [1a] (but without doing "Exact Surfaces"). Since we don't want the inlet and outlet to have closed caps, we can either (i) don't press "close intersection" when trimming the plane, or (ii) delete the end cap surface.

  o Go the tab "Select", press "Select By Angle"

  o Make sure "Selection Mode' is "Select Visible Only"

  o Click on the end cap and press "delete" on keyboard

  o Repeat for all inlets and outlets
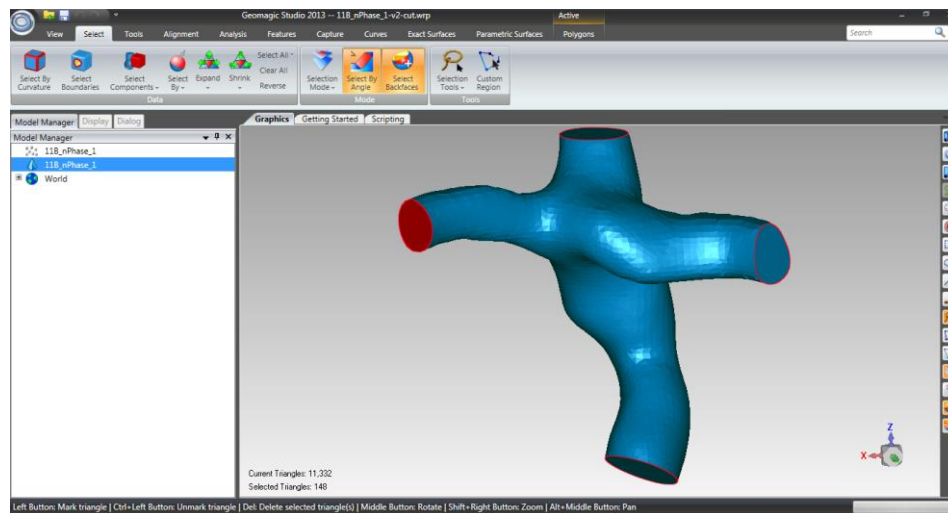
Figure A. 46 Selecting end cap to delete by "Select By Angle"

- To better visualize the surface mesh, turn on "Edges" under "Display".

374
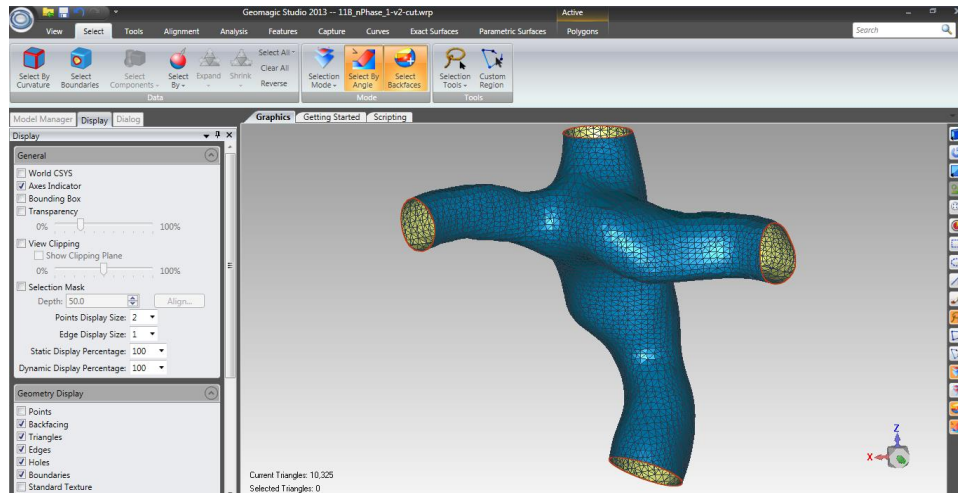
Figure A. 47 Visualizing surface mesh in Geomagic

- To re-mesh the surface, go to "Polygon" → "Remesh"

    o Enter the target edge length. Click "Apply" to check mesh quality

    o If it looks good, click "OK"
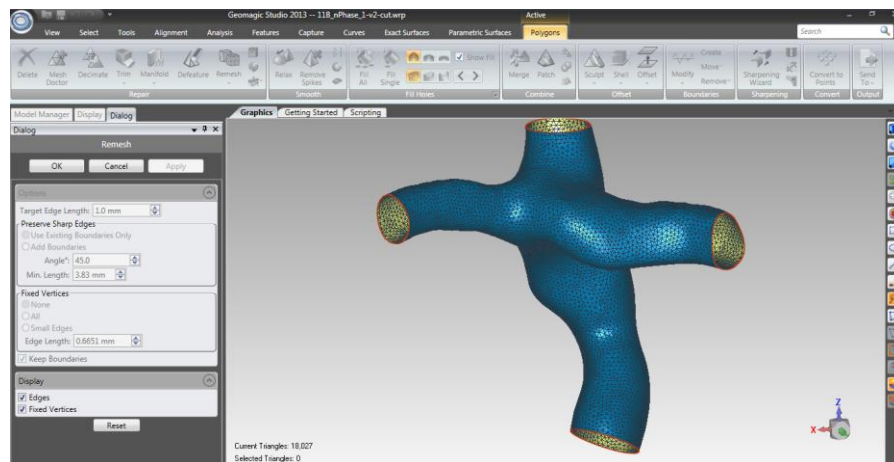
Figure A. 48 Re-meshing surface in Geomagic

    o Make sure the triangle quality is good, especially at the edges. If the triangles at the edges are skewed, very likely the vertices at the edges were not evenly distributed.

    o To fix that, go to "Polygon", under "Boundaries", select "Modify". Click on the edge and click Apply.

375

- o Remesh the entire surface again if necessary.

- o Use Geomagic Mesh Doctor to check mesh quality

- o Save as STL (ASCII)
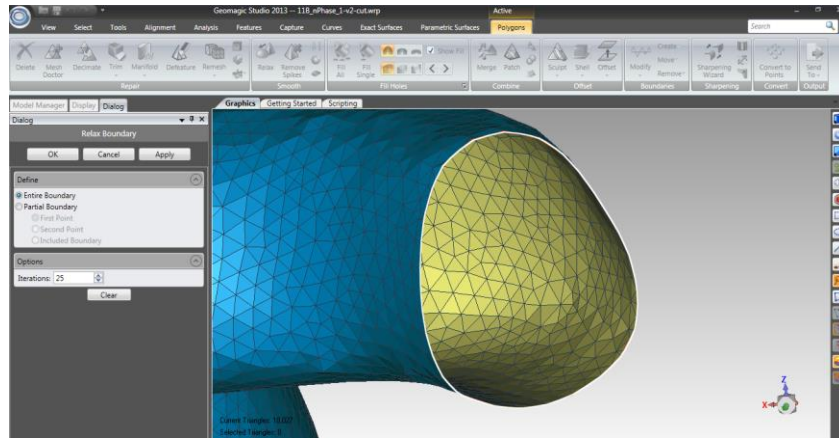
Figure A. 49 Relax Boundary

A.6.2.2. Step [2] Volume Mesh Generation

Note that cgs unit system is being used. Therefore, unit conversation may be necessary before creating the volume mesh to convert the mesh to cm. This can be achieved with Geomagic Studio:

- First, make sure you load the STL file in the correct unit in Geomagic:
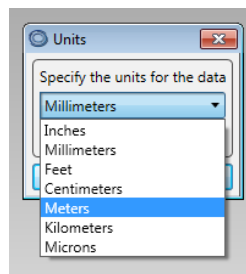
Figure A. 50 Select unit
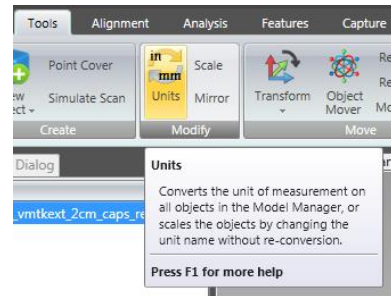
- Go to the tab 'Tools', click on the button 'Unit'

- Select 'Change Display', and select "Centimeters" for unit, and click OK.
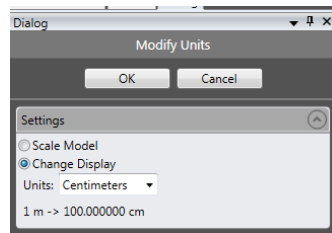
Figure A. 51 Modify Units

- To confirm the unit is correct, you can measure the distance on the mesh to confirm the units. Go to "Analysis" tab → Distance → Measure Distance. And click on two points the in surface (e.g. two ends of the vessel). TCPC vessel diameter usually is in the order of magnitude of 1cm.
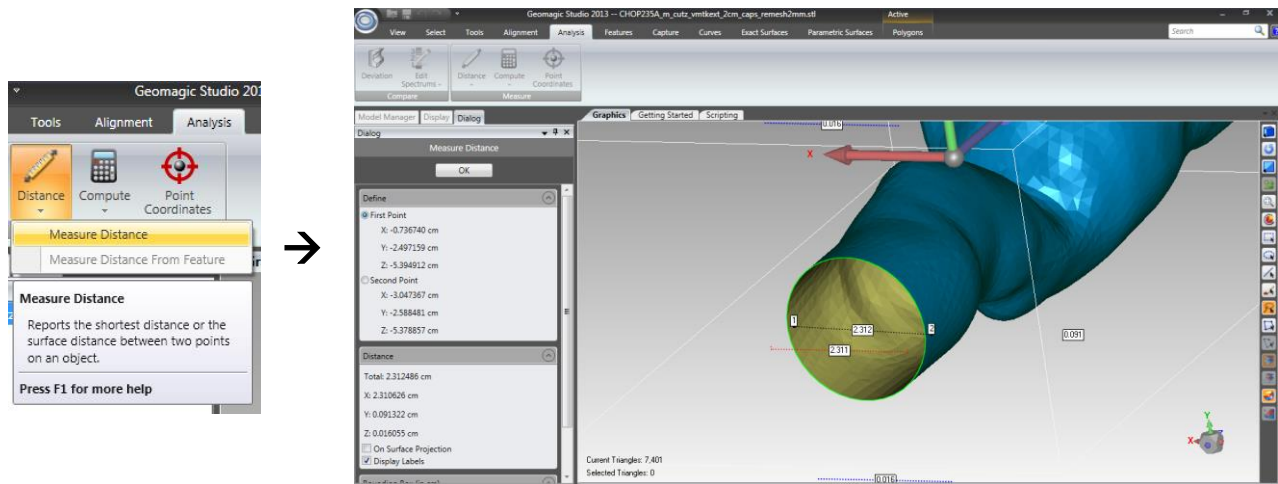
Figure A. 52 Verifying unit conversion

To generate volume mesh for LifeV, the STL surface from Step [1] is used as input. LifeV supports multiple mesh format, and in this thesis, INRIA Medit (*.mesh) is being used. The following sections describe how to generate fluid and structure meshes for LifeV.

A.6.2.2.1. Step [2a] Description of Gmsh scripts

- To generate INRIA Medit mesh for LifeV, the following files are required:
  - o STL mesh prepared as in Step [1]
  - o boundaryLayer.geo
  - o TCPCWithBL_Fluidnew.geo
  - o TCPCWithBL_Structurenew.geo
- Open 'boundaryLayer.geo' with a text editor
  - o At the line: Merge "<……>.stl", enter the name of the STL file

378

- o At the section: out[] = Extrude{Surface{1}; Layers{<num_lay>, <thickness>};};

  - ▪ Non-FSI: Comment out this section with '//' if you don't need structural mesh

  - ▪ FSI: This part extrudes the structural mesh based on the elements in the STL. Enter the number of layer of structural element at <num_lay>, and the thickness at <thickness (in cm)>. Also comment out the line "Geometry.ExtrudeReturnLateralEntities = 1;"

- Open 'boundaryLayer.geo' with GMSH

  - o Make sure the surface layer is extruded for FSI cases
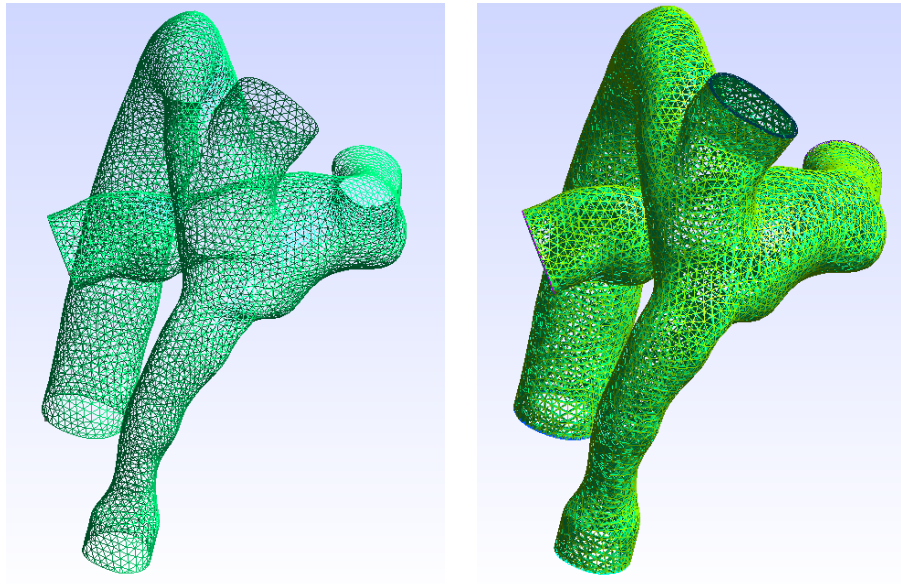
Figure A. 53 boundaryLayer.geo without extrusion (left) and with extrusion (right)

  - o Save the mesh as boundaryLayer.msh (File → Save Mesh)

o   If a structural mesh is needed for FSI, it is important to check the direction of the layer extrusion. In addition to saving as boundaryLayer.msh, also save an STL for the extrude layer (File → Save as → boundaryLayer.stl (ASCII))

- In Software like ParaView, you can visualize the original STL surface and boundaryLayer.stl. Make sure the original STL is on the inside of the extruded shell

- You can change the color of the STL in ParaView to better distinguish the meshes
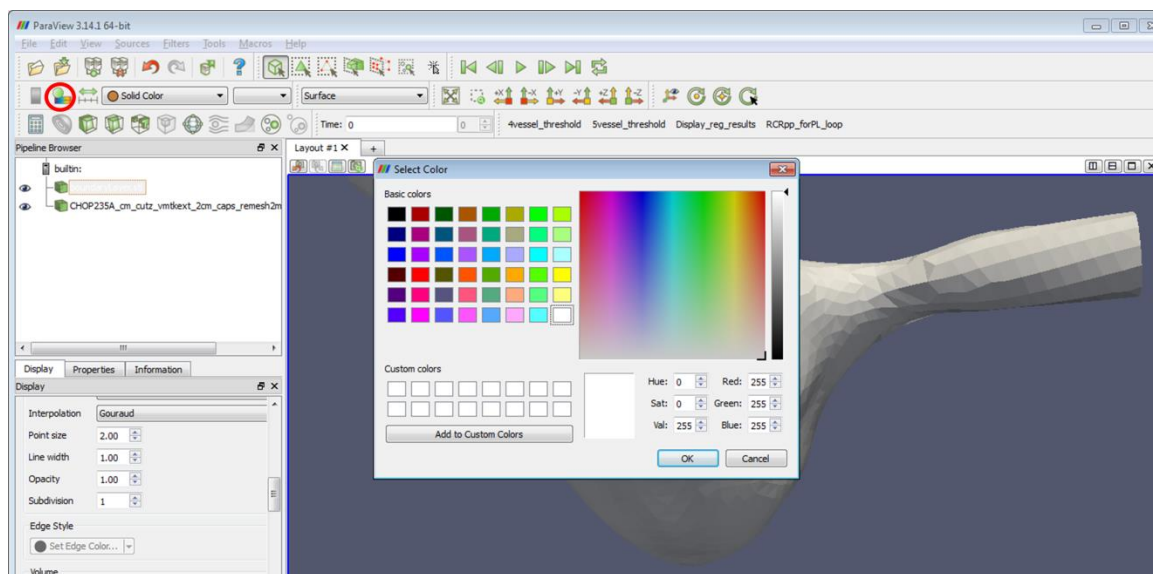
Figure A. 54 Select color in ParaView

- To better visualize the meshes, you can also change the opacity of the meshes in ParaView

380
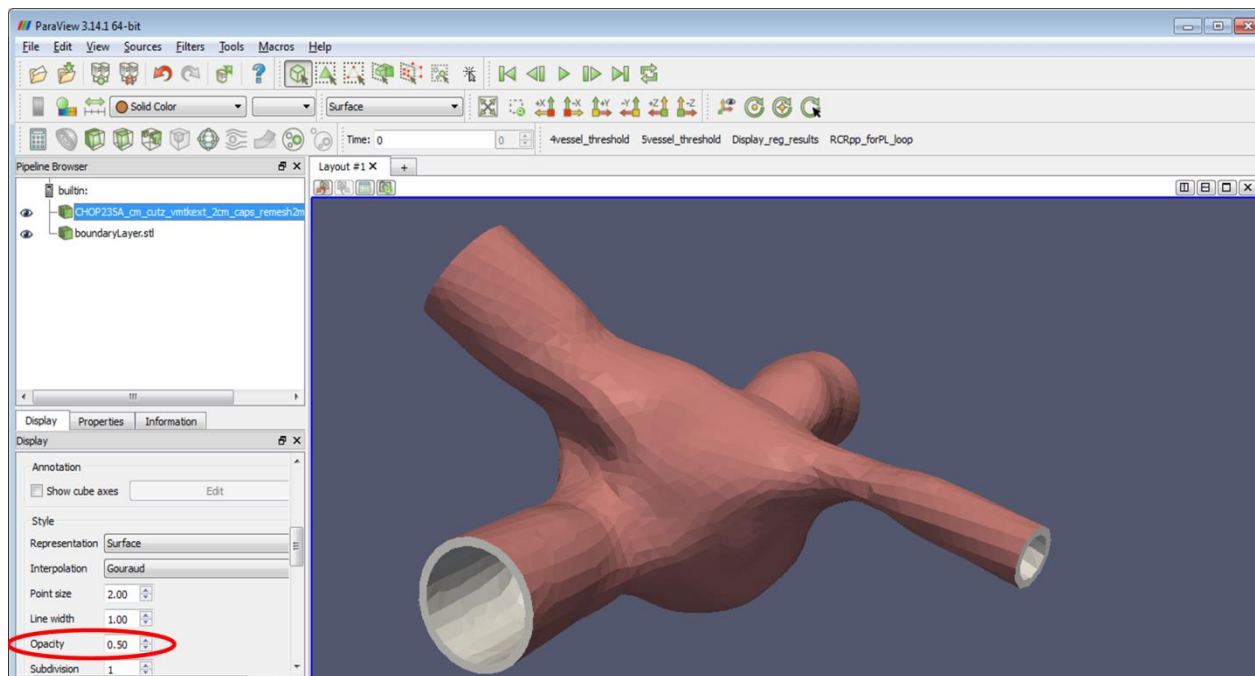
Figure A. 55 Changing opacity in ParaView

- As shown in the above figure, the extruded layer is pointing inwards (white) and the original STL surface (red) is the outer surface of the structural mesh, which is not correct.

- To correct this, go back to boundaryLayer.geo in the text editor,

  - At the section: out[] = Extrude{Surface{1}; Layers{<num_lay>, <thickness>};};

  - Change Surface{1} to Surface{-1} (or vice versa) to invert the direction of the extrusion. And save boundaryLayer.msh again
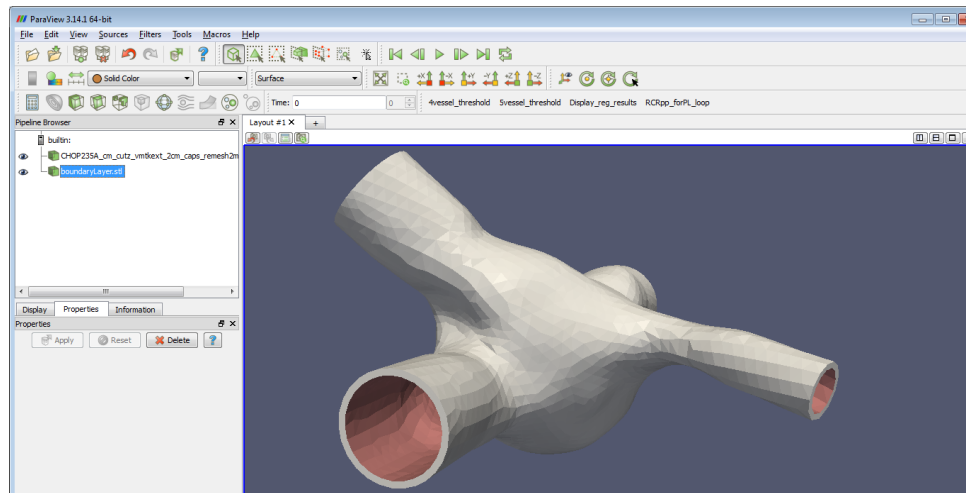
Figure A. 56 Checking extrusion in ParaView

- Now the extrusion is in the correct direction.

Preparing fluid mesh (For non-FSI and FSI simulations)

- Open 'TCPCWithBL_Fluidnew.geo' with a text editor

  - Input 1: Setup mesh engine

    - Mesh.CharacteristicLengthMax determines the maximum edge length of the mesh. You can change this number based on the edge length of the STL mesh, e.g. 0.1 (cm).

    - You can change the rest of the meshing parameters according to the GMSH user manual if necessary.

  - Input 2: Indicate presence of extra vessels

    - Change 'hasRUPA' to 1 if the TCPC has RUPA

    - Change 'hasLSVC' to 1 if the TCPC has LSVC

    - Change 'hasAZ' to 1 if the TCPC has azygos vein

    - Otherwise, keep these variables as zero

- o Input 3: Add additional vessels

  - ▪ For the line 'Surface Loop(1000)={1,10,20,30,40};', 1 is the TCPC surface, 10 to 40 represents IVC, (R)SVC, LPA and RPA.

  - ▪ Therefore, if there are any additional vessels, add '50', '60' in the bracket and so on.

  - ▪ For example, if the TCPC in total has 6 vessels, change that line to:

    - • Surface Loop(1000)={1,10,20,30,40,50,60};

- o Input 4: Assign labels to vessels

  - ▪ Assign labels, '10', '20', etc., to IVC, SVC, LPA, RPA, etc. These are surface labels corresponding to "Elementary Entities" in Gmsh

  - ▪ Since this is the first trial, the ordering of the vessel can only be guessed.

  - ▪ E.g. for patients with an azygos vein

    ```
    IVC = 10;
    RSVC = 20;
    LPA = 30;
    RPA = 40;
    AZ = 50;
    //RUPA =;
    //LSVC =;
    ```

  - ▪ Make sure the other vessels remained commented

- o Save

- • Inspect vessel labeling by opening 'TCPCWithBL_Fluidnew.geo' with GMSH

  - o Inspect the vessel labeling by 'Tools' →'Visibility' → Select Physical Group

383
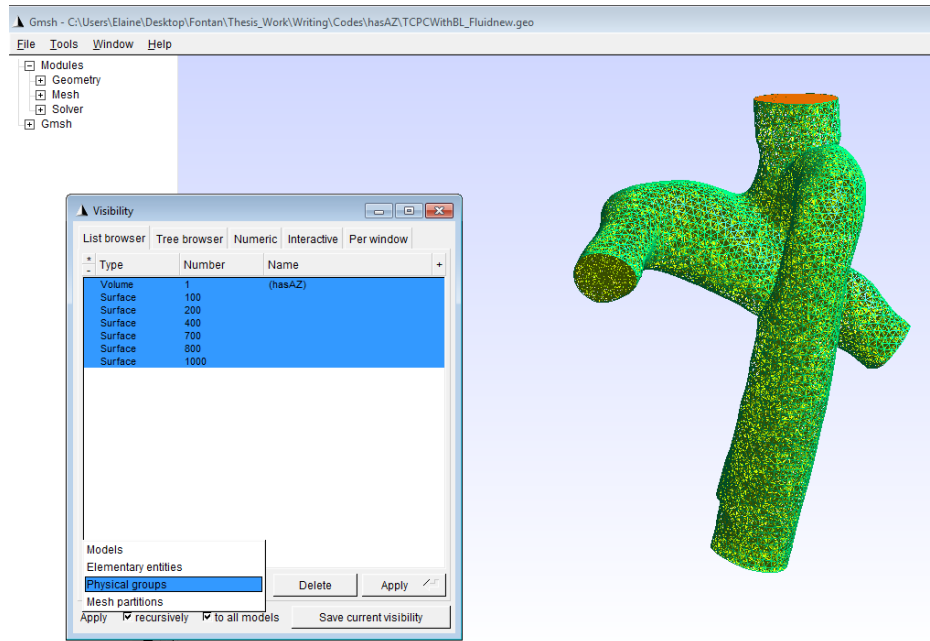
Figure A. 57 Inspecting mesh labeling

- To inspect the labeling, click on each surface and click "Apply"
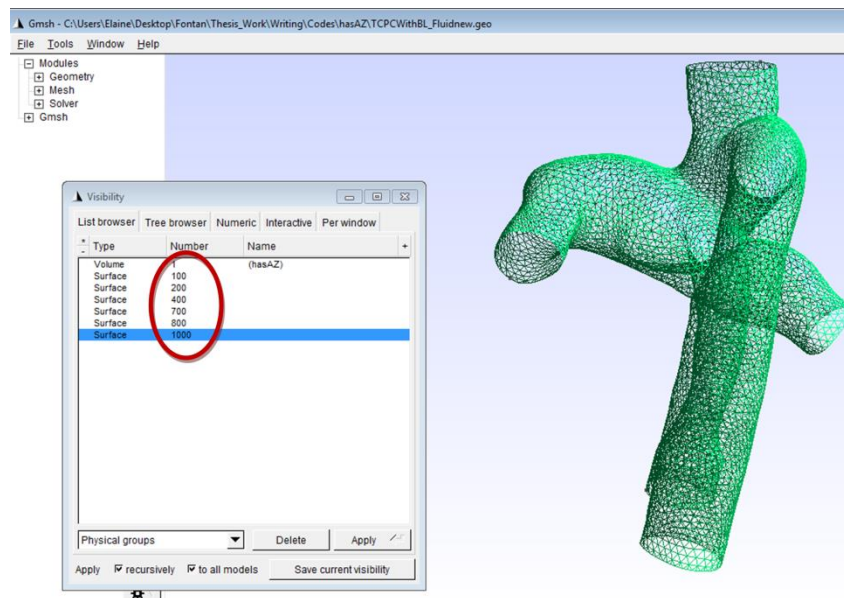
Figure A. 58 Visualize selected entity

- Inspect each vessel and see if the Surface label follows the following convection:

    IVC: 100
    RSVC: 200
    LSVC: 300
    AZ: 400
    LPA: 700
    RPA: 800
    RUPA: 900

- If the labeling is wrong, open 'TCPCWithBL_Fluidnew.geo' in text editor and rearrange the label under Input 4 section.

- For example, for this case with IVC,SVC,LPA,RPA and AZ, the initial labels in 'TCPCWithBL_Fluidnew.geo'

    IVC = 10;
    RSVC = 20;
    LPA = 30;
    RPA = 40;
    AZ = 50;

Surface 100 is LPA

Surface 200 is RPA

Surface 400 is AZ

Surface 700 is IVC

Surface 800 is SVC
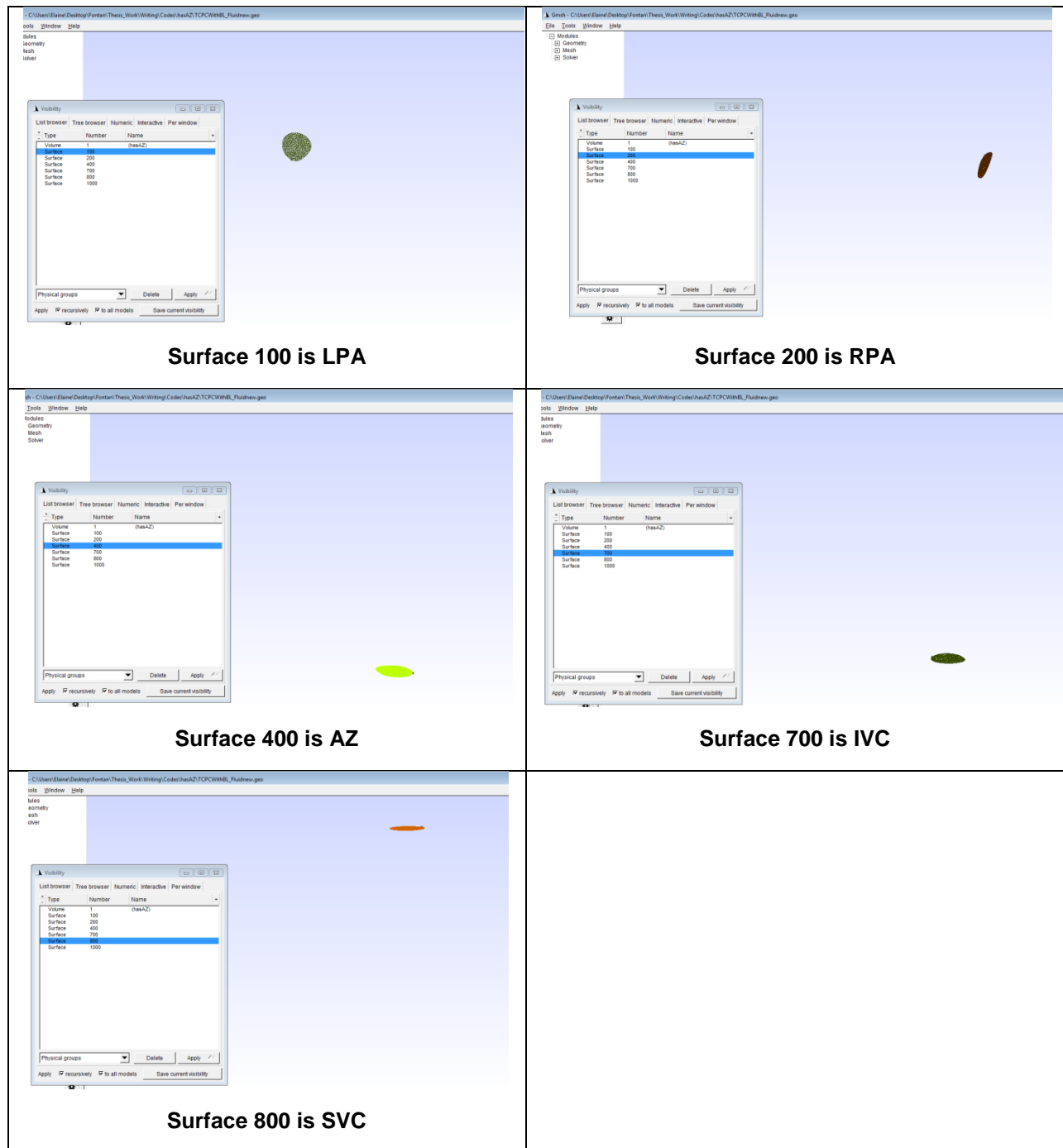
Figure A. 59 Check mesh labeling

o Therefore, the labels should be rearranged in 'TCPCWithBL_Fluidnew.geo' as follows:

IVC = 30;

RSVC = 40;
LPA = 10;
RPA = 20;
AZ = 50;

Save .geo file

- o Open 'TCPCWithBL_Fluidnew.geo' in GMSH again to verify the labels

- o After making sure the labels are correct, in GMSH, 'File' → 'Save as', enter the file name you want to save the fluid mesh as. Make sure to include the extension '.mesh' when entering the file name. When the window 'MESH options' show up, choose 'Physical entity', so that all physical groups will be saved.

Preparing structure mesh (For FSI simulations)

Preparing structure mesh with GMSH is very similar to preparing fluid mesh. But please be sure to use GMSH 2.5 for the structure mesh (not GMSH 2.8.5). Also, the labeling will be slightly trickier:

- Open 'TCPCWithBL_Structurenew.geo' with a text editor

  - o Input 1: Setup mesh engine

    - You can change the meshing parameters according to the GMSH user manual if necessary. If not, just keep the default settings

  - o Input 2: Indicate presence of extra vessels

    - Change 'hasRUPA' to 1 if the TCPC has RUPA

    - Change 'hasLSVC' to 1 if the TCPC has LSVC

    - Change 'hasAZ' to 1 if the TCPC has azygos vein

- Otherwise, keep these variables as zero
  - Then, comment the part of the script starting from Input 3 till the end of the code by /* ....*/

```
// Input 1: set up the mesher engine
Mesh.CharacteristicLengthFactor=1.;
Mesh.Algorithm3D=4;
Mesh.Optimize=1;
Mesh.OptimizeNetgen=1;


// load the boundary layer (3D) mesh
Merge "boundaryLayer.msh";


//Input 2: Change 0 to 1 if has extra vessel
hasRUPA = 0;
hasLSVC = 0;
hasAZ = 1;



noVessel = 4; // IVC, SVC, LPA, RPA only
If ( hasRUPA > 0)
  noVessel = noVessel+1;
EndIf
If ( hasLSVC > 0)
  noVessel = noVessel+1;
EndIf
If ( hasAZ> 0)
  noVessel = noVessel+1;
EndIf



// extract the geometry components of the boundary layer volume
```

```
CreateTopology;


// define new geometry entities
For n In {1:noVessel}
  Line Loop(n)={n};
  Plane Surface(10*n)={n};
EndFor




// Comment the following for the first step
/*
//Input 3: Enter labels of Inlet/Outlet faces
IVC = ;
RSVC = ;
LPA = ;
RPA = ;


//RUPA =;
//LSVC = ;
//AZ =;



// Inlet/Outlet faces (Solid) IVC, SVC, LPA, RPA,
Physical Surface(10) = {IVC}; //IVC
Physical Surface(20) = {RSVC}; //SVC
Physical Surface(70) = {LPA}; //LPA
Physical Surface(80) = {RPA}; //RPA


If ( hasLSVC > 0)
Physical Surface(30) = {LSVC}; // LSVC
EndIf
```

```
If ( hasAZ > 0)

Physical Surface(40) = {AZ}; // AZ

EndIf

If ( hasRUPA > 0)

Physical Surface(90) = {RUPA}; // RUPA

EndIf


// Inner FSI wall

Physical Surface(1000) = {1};

// Outer FSI wall

Physical Surface(9999) = {26};


Physical Volume(1) = {1};


Hide "*";

Show {

Volume{1};

Surface{1000};

Surface{9999};

Surface{IVC};

Surface{RSVC};

Surface{LPA};

Surface{RPA};

}


If ( hasLSVC > 0)

Show {

Surface {LSVC};

}

EndIf

If ( hasAZ > 0)

Show {
```

```
Surface {AZ};

}

EndIf

If ( hasRUPA > 0)

Show {

Surface {RUPA};

}

EndIf

*/
```

- - This is because the label numbering with more vessels are not straight forward

- Open 'TCPCWithBL_Structurenew.geo' with a GMSH 2.5

  - Go to 'Tools' → 'Visibility', and view 'Elementary entities' instead

  - Inspect the surfaces with number that are 1-99
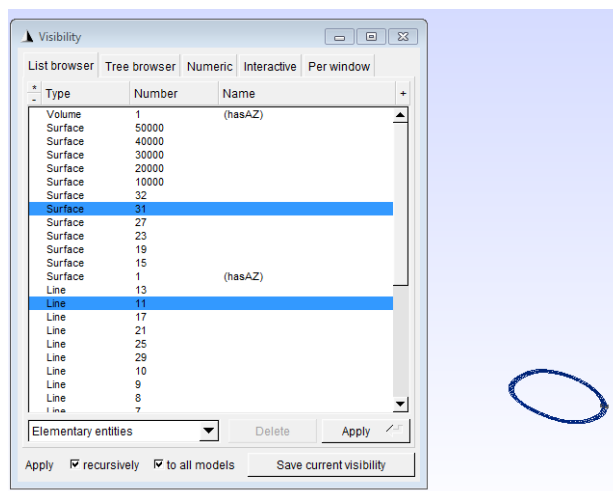
Figure A. 60 Visualizing elementary entities

  - Assign those labels to IVCring, SVCring, LPAring, RPAring, (AZring), (RUPAring), (LSVCring), InnerWall and OuterWall

Surface 1 is inner wall	Surface 15 is LPA ring
Surface 19 is RPA ring	Surface 23 is IVC ring
Surface 27 is SVC ring	Surface 31 is AZ ring
Surface 32 is outer wall	
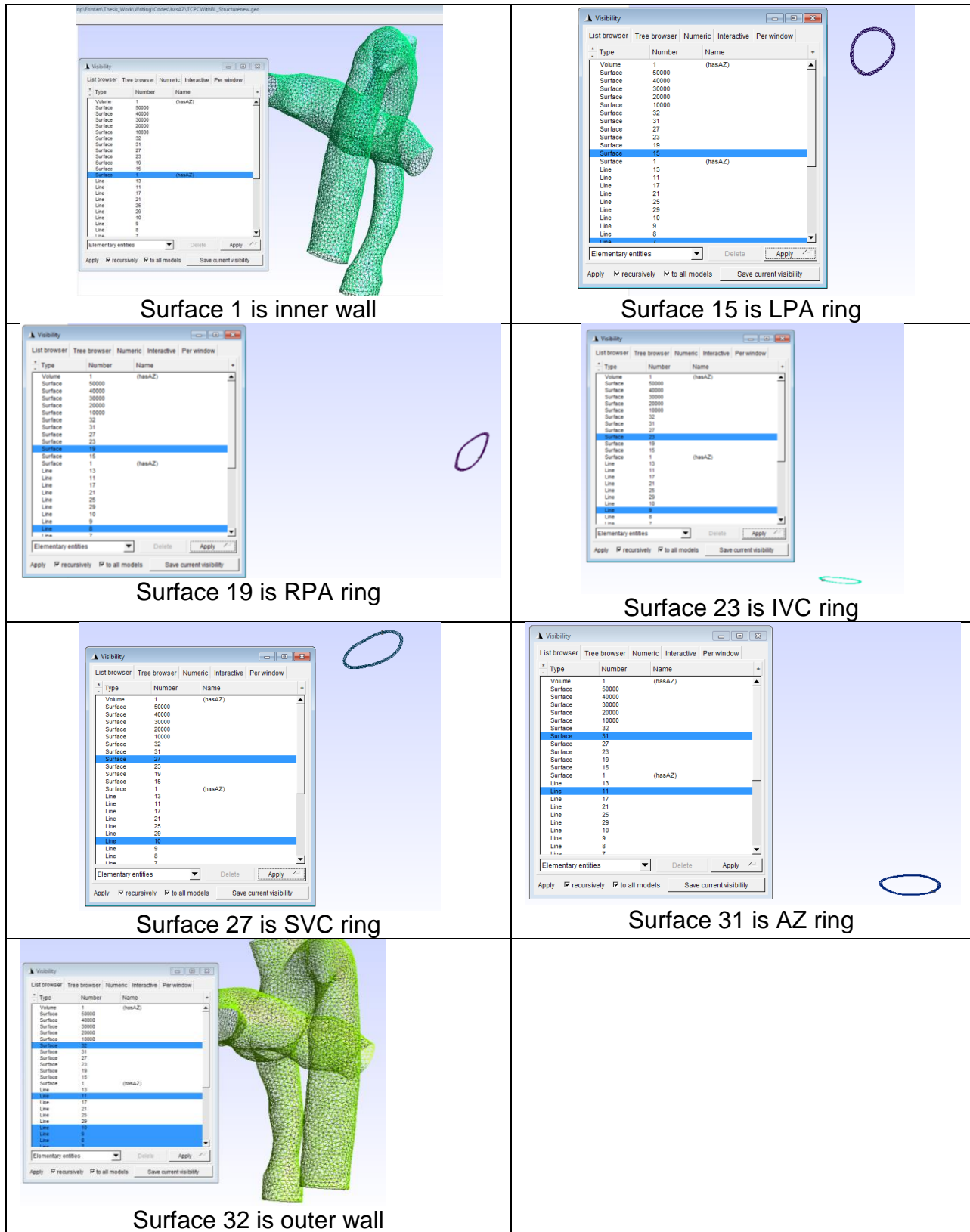
Figure A. 61 Checking mesh labeling

- ○ Open 'TCPCWithBL_Structurenew.geo' in text editor. For this case with Azygos vein, Input 3 in 'TCPCWithBL_Structurenew.geo' will then become:

  ```
  IVCring = 23;
  RSVCring = 27;
  LPAring = 15;
  RPAring = 19;
  AZring = 31;
  InnerWall = 1;
  OuterWall = 32;
  //RUPAring = ;
  //LSVCring = ;
  ```

- ○ Now the code from Input 3 till the end can be uncommented after the labels are entered. Save the .geo script

- Open 'TCPCWithBL_Structurenew.geo' with a GMSH 2.5

  - ○ Now inspect the labels through 'Physical group' in 'Visibility'

  - ○ Inspect each vessel and see if the Surface label follows the following convection:

    ```
    IVC ring: 10
    RSVC ring: 20
    LSVC ring: 30
    AZ ring: 40
    LPA ring: 70
    RPA ring: 80
    RUPA ring: 90
    Inner wall: 1000   ← Make sure the lab of the structure mesh
    inner wall is the same as the label of the wall of the fluid mesh
    for FSI simulations
    Outer wall: 9999
    ```

  - ○ After making sure the labels are correct, in GMSH, 'File' → 'Save as', enter the file name you want to save the structure mesh as. Make sure to include the extension '.mesh' when entering the file name. When the

window 'MESH options' show up, choose 'Physical entity', so that all physical groups will be saved.

A.6.2.2.2.   *Step [2b] Preprocess the volume mesh*

This step is to correct the labeling of the meshes before running simulations in LifeV. This involves the rewriteMeshGeneralVolume2.cpp, which after compilation will produce executable 'preprocess_mesh'.

- In terminal put "./preprocess_mesh <fluidmesh>.mesh"

- This will generate a new mesh. Rename the new mesh.

- Preprocess the structure mesh and rename the new mesh if you are running FSI simulations.

A.6.2.3.   Step [3] Setting up the CFD Simulation

A.6.2.3.1.   *Step [3a] Imposing Inflow Boundary conditions*

- Smoothing: After selecting the flow waveform of interest, you may want to apply smoothing to the waveform for the high frequency noises. In this thesis, the 'lowess' function in Matlab (MathWorks, Inc., Natick, MA, USA) was utilized (Try_smoothing.m).

- Unit conversion: Since cgs unit system was being used, all flow rate should be converted to cm^3/s.

- Input file: For each inlet, prepare a '.dat' file as follows. Make sure there are at least 5 data points for flow rates. Note that all numbers here should be **positive**, unless you have reveres flow. If the flow rate data points are too coarse, LifeV has built-in function to interpolate the flow waveform.

Template	Example
\<number of flow rate data points\>	**6**
\<flow rate at t1\>	**20**
\<flow rate at t2\>	**10**
\<flow rate at t3\>	**-5**
\<flow rate at t4\>	**15**
\<flow rate at t5\>	**30**
….	**20**

A.6.2.3.2.   Step [3b] Computing Parameters for Windkessel Model

- Matlab script (Credit: Dr Lucia Mirabella) was used to compute relative resistances for 3-element Windkessel outlet boundary conditions. There are two versions:

  - computeRCR_template_noRUPA.m (without RUPA)

  - computeRCR_template_withRUPA.m (with RUPA)

- The usage of the Matlab script is the same regardless of the presence of RUPA

- Enter the LPA, RPA, RUPA (L/min) waveforms from the segmented PC-MRI data at

  ```
  lpa_flow_lm=[1  0.5  1.4  3.1  1.8  0.5];
  rpa_flow_lm=[-1  -1.5  -2.4  -4.1  -2.8  -1.5];
  ```

```
urpa_flow_lm=[-0.5 -0.2 -0.18 -0.17 -0.20];
```

- The following two lines take care of the opposite signs of RPA and RUPA flows. Comment them out if you don't need them:

```
rpa_flow_lm=-rpa_flow_lm;
urpa_flow_lm=-urpa_flow_lm;
```

- Enter the cross-sectional area (in cm^2) of the outlets:

```
lpa_area=;
rpa_area=;
urpa_area=;
```

- Enter the pulmonary vascular resistance (in Wood Units). For TCPC, PVR is ~1.5 Wood Units

```
Rtotpulm_w=1.5;
```

- Run the script in Matlab, which will give the proximal (R1) and distal (R2) resistances of each outlet. For example:

```
R1lpa_new =   32.5771
R1rpa_new =  112.9064
R1urpa_new =  148.2199
R2lpa_new =  188.5857
R2rpa_new =  311.3998
R2urpa_new =  539.0709
```

- Note down those numbers as they will be used in the following step.

A.6.2.3.3.   *Step [3c] Computing Parameters for Windkessel Model*

- To run simulations with LifeV, the following files are needed:

  - 'data' file

  - solversOptions.xml

  - Mesh file(s)

  - Boundary conditions data file

  - Solver executable

- 'data' file

  o This file controls the majority of the simulation settings. The simulation

    parameters are arranged in a hierarchy, just like folders ad subfolders:

For runTCPC code with LifeV 2011 (with Windkessel outlet boundary condition)

Data file	Description

# Data file for Navier-Stokes 	
 	
[prescribed_motion]
  moving = 0
  ANN_tolerance = 1e-7
  ANN_nearest = 1
  scale_factor = 10
  frame_step = 0.0031
  writePointsFile = 0
  numVarFromFile = 1
    [./var0]
      varName = position   file_prefix = ./ph_pts_RS_interp1000_
      file_postfix = .txt   [../var1]
      varName = velocity   file_prefix = ./ph_vel_RS_interp1000_
      file_postfix = .txt
	This section is for when running simulation with prescribed wall motion. If rigid wall simulation is ran, make sure 'moving' = 0

[fluid]
  [./problem]
    period = 3.9725
    preloadT = 0.07945
    interpolateBoundaryData = true
	'period' = period of one cycle
	'preloadT' = time to start the simulation before time point zero. When starting a simulation, all initial velocities are zero. When prescribing a boundary condition, you want to allow sufficient time for the flow to increase to zero, as a sudden increase in flow will cause instability.

```
wallList = '1000'
inflowList = '100,200'
RCRList = '700,800'


[./inflow0]
  rescale = 1.0
  correction = 1.0
  smoothRatio = 0.8
  profileShape = flat
  input_file = CHOP235A_FB_inflow_ivc_shift.dat
[../]
[./inflow1]
  rescale = 1.0
  correction = 1.0
  smoothRatio = 0.8
  profileShape = flat
  input_file = CHOP235A_FB_inflow_svc_shift.dat
[../]
   [./outflow0]
  R1        = 94.5555
  R2        = 433.1982
  C         = 1e-4
  # RT       = 1.e4
  venous_pressure = 13332.0
[../]
[./outflow1]
  R1        = 4.4413
  R2        = 150.8742
  C         = 1e-4
  # RT       = 1.e4
  venous_pressure = 13332.0
[../]


[fluid/physics]
  density      = 1.06  # g/cm^3
```

'wallList' = mesh label of TCPC surface

'inflowList' = mesh labels that are inlets and flow waveforms will be prescribed. Based on previous convention, 100=IVC, 200=RSVC,300=LSVC,400=AZ

'RCRList' = mesh labels that are outlets and 3-element Windkessel model will be prescribed. Based on previous convention, 700=LPA, 800=RPA, 900=RUPA

[inflow0], [inflow1],… Corresponds to the order other label you specified in 'inflowList'. Specify here the .dat file(s) you created for flow boundary condition in step [3a]

[outflow0], [outflow1],… Corresponds to the outlets specified in 'RCRList'. Under each outlet, specify parameters of Windkessel model, again, in cgs units:

'R1' = proximal resistance

'R2' = distal resistance

'C' = compliance

'RT' = not used

'venous_pressure' = pressure at the end of the Windkessel model

```
    viscosity      = 0.035 #  g/(cm*s)


  [fluid/space_discretization]                              'density' = density of fluid  (g/cm³)
    mesh_dir      = ./                                      ' viscosity' = viscosity of fluid
    mesh_type     = .mesh
    mesh_file                                     =
CHOP235A_noext_nocap_cm_new_processed.mesh                 'mesh_type' = extension of mesh file
    mesh_faces    = all                                    'mesh_dir' = location of the mesh file. This can be
    mesh_edges    = all                                    absolute or relative path
    velocity_fespace = P1Bubble                            'mesh_file' = mesh file name (with extension)
    pressure_fespace = P1
    mass_lumping    = true                                 '…..feSpace'                                    =
    stiff_strain    = true                                 P2Bubble/P2/P1Bubble/P1/P0/Q2/Q,          etc.
    matrix_pattern  = true                                 determines the time of finite element for spatial
                                                           discretization. Make sure fluid velocity order is
    [./stabilization]                                      higher than pressure
      betaSD       = 0.
      divBetaUV    = false
      stabilizeBackflows = 0.
      stiffstrainUseNumViscosity = true                    This section describes parameter for stabilization.
                                                           If  you  need  to  stabilize  backflow  change
                                                           'stabilizeBackflows' to > 0. With this, an numerical
                                                           viscosity will be added to the outflow to stabilize
                                                           back flow.
                                                           'stiffstrainUseNumViscosity' is a new parameter I
                                                           added to the lifeV code:
                                                           If you want a constant numerical viscosity (0.035)
                                                           to         be         added,          set
                                                           'stiffstrainUseNumViscosity'=false.
                                                           If you want the magnitude of numerical viscosity
                                                           to  be  proportional  to  the  backflow  velocity
  [fluid/time_discretization]                              magnitude, set 'stiffstrainUseNumViscosity'=true
    initialtime   = -0.07945
    endtime       = 19.8625
    timestep      = 0.0039725
```

verbose = 0	
BDF_order = 2	'initialtime' = initial time of simulation. If preload is being used, use the negative value of preload to be initial time.
order_yosida = 1	
	'endtime' = end time of simulation
[exporter]	'timestep' = time step of simulation
type = Ensight	'BDF_order' = order of fluid temporal discretization with backward difference formula
post_dir = ./results/	
multimesh = false	
save = 10	
exportMode = 2	
floatPrecision = 1	
time_id_width = 5	
	'post_dir' = path of output of simulation results
	'save' = 10 means save results of every 1o time step

For Benchmark FSI code with LifeV 2013

Data file	Description
# -*- getpot -*- (GetPot mode activation for emacs) # Data file for Greenshields&Weller test problem = 1 # 0: Turek, 1: Aorta, 2: Greenshields&Weller	'problem': this determines the type of boundary conditions to be used for FSI, which details are defined in BCManager.cpp of the benchmark FSI source code. 0=Turek → Averaged velocity is prescribed 1=Aorta → Inflow will be read from a data file 2=Greenshields&Weller→ Pressure is prescribed
#[importer] # type = Ensight # fluidPrefix = fluid # structurePrefix = structure # post_dir = ./results_stdy1/ # should be the path to previous results # multimesh = false # save = 1 # numImportProc = 8 # depends on how many processors you used last time	Uncomment this 'Importer' section (by removing '#') if you are restarting a simulation. Specify 'post_dir' as path of the results of your previous run of simulation. Specify also the number of processor previously used at 'numImportProc'. Change 'save' if the results of previous simulation was not saved for every 1 time step

[fluid]
  [./mesh]
    mesh_type = .mesh
    mesh_dir   = Mesh/
    mesh_file   = CHOP235A_vmtkext_2cm_caps_remesh1mm_fluid_processed.mesh
    mesh_edges = all
    mesh_faces = all
    inflowList = '100, 200'   # 100--> IVC; 200-->SVC
    outflowList = '700, 800'   # 700-- LPA; 800--RPA
    interfaceList = '1000'
	'mesh_type' = extension of mesh file
	'mesh_dir' = location of the mesh file. This can be absolute or relative path
	'mesh_file' = mesh file name (with extension)
	
	'inflowList' = mesh labels that are inlets and flow waveforms will be prescribed. Based on previous convention, 100=IVC, 200=RSVC,300=LSVC,400=AZ
	'outflowList' = mesh labels that are outlets and stress-free boundary condition will be prescribed. Based on

```
[../physics]
   density  = 1.   # g/cm3
   viscosity = 0.035    # g/(cm.s)


 [../problem]
   preloadT = 0.02
   period = 0.86


   [./inflow0]
    input_file = 'CHOP235A_cBH_ivc.dat'   # IVC
   [../inflow1]
    input_file = 'CHOP235A_cBH_svc.dat'   # SVC













[structure]
  [./mesh]
    mesh_type  = .mesh
    mesh_dir   = Mesh/
    mesh_file                           =
CHOP235A_vmtkext_2cm_caps_remesh1mm_structure_2la
y_processed.mesh
    mesh_edges = all
    mesh_faces = all
    interfaceList = '1000'          dirichletList = '10, 20, 70,
80'    # Essential BC --> zero velocity
    neumannList = '9999'
```

previous convention, 700=LPA, 800=RPA, 900=RUPA

'interfaceList' = mesh label of the fluid structure interface (surface of the TCPC of the fluid mesh and inner wall of the structural mesh)

'density' = density of fluid (g/cm^3)

' viscosity' = viscosity of fluid

'preloadT' = time to start the simulation before time point zero. When starting a simulation, all initial velocities are zero. When prescribing a boundary condition, you want to allow sufficient time for the flow to increase to zero, as a sudden increase in flow will cause instability.

'period' = period of one cycle

[inflow0], [inflow1],…. Corresponds to the order other label you specified in 'inflowList'. Specify here the .dat file(s) you created for flow boundary condition in step [3a]

If you used other outflow boundary conditions, you can specify the parameters using [outflow0], [outflow1], etc. as well

The structure part is needed for FSI

Specify structure mesh the way similar to fluid mesh

[../physics]
 	
  density   = 1.
 	
  thickness   = 0.1
 	
  youngModulus = 7.e5
 	
  poissonRatio = 0.3
 	
  rayleighAlpha = 0.08
 	
  rayleighBeta = 0.001
 	
  nonLinearStressTensor = false
	'diricheltList' = specify the labels of the vessel rings that you want to fix (zero velocity)
	
	'neumannList' = specify the label of the structure mesh that you want to apply stress free boundary condition (e.g. the structure outer wall here)

	'density' = density of structure 'thickness' = thickness of structural wall (cm

[../problem]
 	
  [./essentialBC0]
 	
   fix_x = true
 	
   fix_y = true
 	
   fix_z = true
 	
  [../essentialBC1]
 	
   fix_x = true
 	
   fix_y = true
 	
   fix_z = true
 	
  [../essentialBC2]
 	
   fix_x = true
 	
   fix_y = true
 	
   fix_z = true
 	
  [../essentialBC3]
 	
   fix_x = true
 	
   fix_y = true
 	
   fix_z = true
	'youngModulus' = Young's modulus of structure. Make sure the unit matches:
	
	Pressure(mmHg) = Pressure(cgs)*0.1/133.332
	
	Pressure (Pascal) = Pressure(cgs)*0.1
	
	'poissonRatio' = Poisson ratio
	
	'rayleighAlpha' and 'rayleighBeta' are the Rayleigh damping coefficients
	
	'fix_x', 'fix_y', 'fix_z' = true/false → whether you want to fix the structure in x, y and/or z direction. These are parameters I added to the original benchmark FSI code. Set all to 'true' if you want to fix in all directions

[interface]
 	
  matchingTolerance = 1.e-9
 	
[time_discretization]
 	
  restart   = false
 	
   #restart_timeIndex =
 	
  spectralRadius = 0.
 	
  timestep   = 1.e-4
	'matchingTolerance' = This is the tolerance setting when matching the fluid nodes with the structural nodes at the fluid structure interfaces

endtime = 8.6 initialtime = -0.02 fluidConvectiveTermStrategy = 0 # 0: Semi-implicit, 1: Explicit, 2: KIO91, 3: None maxPicardIter = 3 PicardTolerance = 1.e-4 fluidVelocityBDFOrder = 2 fluidPressureBDFOrder = 1 [space_discretization] structureVelocityFeSpace = P2 fluidVelocityFeSpace = P2 fluidPressureFeSpace = P1 fluidMass_lumping = false structureMass_lumping = false stabilizeFluidBackflows = 0 smoothExtensionType = 0 #moveMesh = false [exporter] type = Ensight post_dir = ./results/ save = 1 multimesh = false	'restart' = Change this to 'true' when restarting a simulation ' restart_timeIndex' = time index of the file you want to restart from. This is a parameter I added to the original benchmark FSI code. Uncomment this when restarting a simulation → restart_timeIndex = (initialtime+preload)/timestep 'timestep' = time step of simulation 'endtime' = end time of simulation 'initialtime' = initial time of simulation. If preload is being used, use the negative value of preload to be initial time. When restarting simulation, set this as the time you want to restart simulation from. Should be referring to the time of the file specified in 'restart_timeIndex' 'maxPicardIter' = maximum number if Picard simulation. Within each time step, when convergence criteria is not met (determined by 'PicardTolerance'), additional Picard iterations will be solved, until maxPicardIter is met or PicardTolerance is met 'fluidVelocityBDFOrder' and 'fluidPressureBDFOrder' = order of fluid temporal discretization with backward difference formula '…..FeSpace' = P2Bubble/P2/P1Bubble/P1/P0/Q2/Q, etc. determines the time of finite element for spatial discretization. Make sure the order is the same for structure velocity and fluid velocity, and fluid velocity order is higher than pressure 'post_dir' = path of output of simulation results 'save' = 1 means save results of every 1 time step

404

For Leray application code with LifeV 2015 (For Large Eddy Simulations)

```
#-------------------------------------------#
#      Data file for the TCPC     Case 1      #
#-------------------------------------------#


[miscellanea]
  show_data                  = true      # if true, show all the data structures
  oseen_manager_verbose         = false      # if true, the oseen manager will print stuff
  solver_verbose              = true      # if true, the solver will print stuff
  chrono_log_file             = ChronoLog.txt # file where the log of all the timings will be written
  timings_file              = chrono.txt   # file where the timings are written as matrix (easy to load)
  print_residuals               = false       # if true, prints the real residuals at the end of the time iteration
(meaningless if filter is on!)
  check_status                 = true       # if true, checks methods are called in the right order (initialize,
assembly, build operator, solve, ..)


[fluid]
  period = 3.96    # Period of one cycle
  preloadT = 0.0792   # Time to simulate before t=0
  oseen_manager_type           = 'HOY'       # options: LSC (Least Squares Commutator), HOY (High order
Yosida)
  solvers_options_file         = solversOptions.xml


  [./filter]
    use_filter               = true       # if true, enables the deconvolution-based non-linear filter
    delta_type               = h_min       # 'given', 'h_min' or 'h_avg'
    delta_factor              = 1.0         # scaling factor for delta in case delta_type is 'h_min' or 'h_avg'
    delta                = 0.01         # used only if delta_type=given
    dynamic_chi              = true        # if true, the relaxation parameter is scaled by |a| (norm of indicator)
    kolmogorov_length            = 2.6371e-3     # the kolmogorov length (i.e., the size of a mesh that would
resolve all the scales)
    adaptive_filter              = false        # if true, computes the current kolmogorov length (based on Re),
otherwise uses the regime one
    solvers_options_file         = solversOptionsFilter.xml
    deconvolution_order         = 1
```

```
    decoupling_strategy        = evolve_filter_relax # filter_evolve or evolve_filter_relax
    indicator_norm            = two          # one, two, two_squared or infinity
    normalize_indicator       = true
    compute_sensitivities     = false
  [../]


  [./problem] # In NetGen codes are 100,70,80,90,10,20 <---> In GMsh codes are 1000, 700, 800, 900, 100, 200
    wall_markers             = '1000'        # homogeneous Dirichlet BCs
    outflow_markers          = '700,800,900'       # homogeneous Neumann BCs
    inflow_markers           = '100,200'         # data-based Dirichlet BCs


    [./inflow_100] # IVC
       functor_type          = normal       # the type of the functor (function for boundary conditions)
       scalar_functor_type   = transient    # the scalar part s of the functor F=s*n
       bc_name              = inflowIVC    # arbitrary name for the bc (need not be unique)
       bc_type              = essential    # type of bc (essential or natural)
       transient_type        = cosine       # type of the transient (linear, cosine)
       transient_length      = 0.0792      # the length of the transient = preload
       regime_initial_time   = 0.0          # when the transient ends and the regime is established


       [./regime_functor]
          functor_type           = data_fitting  # type of the functor (data_fitting, transient, shaped_profile,
constant, windkessel)
          data_type          = flux        # flux or average
          data_file          = ./CHOP234A_FB_inflow_ivc.dat # file where the data are stored
          initial_time       = 0          # only used if the data_file stores only the values, not the time stamps
          period             = 3.96        # only used if the data_file stores only the values, not the time stamps
          rescale = 1.0
          correction = 1.0
          smoothRatio = 0.8


          [./profile_functor] # data_fitting functor requires a subsection for the functor taking care of the
spatial profile
             profile_shape  = flat
          [../]
```

```
      [../]
    [../]


  [./inflow_200] # SVC
    functor_type          = normal       # the type of the functor
    scalar_functor_type   = transient     # the scalar part s of the functor F=s*n
    bc_name              = inflowSVC    # arbitrary name for the bc (need not be unique)
    bc_type              = essential    # type of bc (essential or natural)
    transient_type        = cosine       # type of the transient (linear, cosine)
    transient_length      = 0.0792       # the length of the transient
    regime_initial_time   = 0.0          # when the transient ends and the regime is established


    [./regime_functor]
        functor_type             = data_fitting  # type of the functor (data_fitting, transient, shaped_profile,
constant, windkessel)
        data_type           = flux        # flux or average
        data_file           = ./CHOP234A_FB_inflow_svc.dat # file where the data are stored
        initial_time        = 0           # only used if the data_file stores only the values, not the time stamps
        period              = 3.96         # only used if the data_file stores only the values, not the time stamps
        rescale = 1.0
        correction = 1.0
        smoothRatio = 0.8


        [./profile_functor] # data_fitting functor requires a subsection for the functor taking care of the
spatial profile
            profile_shape   = flat
        [../]
      [../]
    [../]


  [./wall_1000]
    functor_type          = constant
    bc_name             = wall
    bc_type             = essential
    values              = '0,0,0'
```

```
[../]


[./outflow_700] #lpa
   functor_type        = windkessel
   bc_name             = outflowLPA
   bc_type             = natural
   Rp            = 49.0982    #Proximal resistance
   Rd            = 236.2143    #Distal resistance
   C             = 1e-4
   venous_pressure        = 13332
   pressure_units        = dyn/cm^2
timestep           = 0.00396
[../]


[./outflow_800] #rpa
   functor_type         = windkessel
   bc_name             = outflowRPA
   bc_type            = natural
   Rp            = 68.1308
   Rd            = 314.2123
   C             = 1e-4
   venous_pressure        = 13332
   pressure_units        = dyn/cm^2
timestep           = 0.00396
[../]


[./outflow_900] #rupa
   functor_type         = windkessel
   bc_name             = outflowRUPA
   bc_type            = natural
   Rp            = 90.2582
   Rd            = 361.6267
   C             = 1e-4
   venous_pressure        = 13332
   pressure_units         = dyn/cm^2
```

```
        timestep          = 0.00396
    [../]



  [../physics]
    density             = 1.06      # density g/cm^3
    viscosity           = 0.035      # viscosity g/(cm*s)


  [../space_discretization]
    mesh_dir             = ./  # directory where the mesh file is
    mesh_file            = CHOP234A_noext_nocap_cm_new_L1mm_processed.mesh
    mesh_type            = .mesh      # .vol -> Netgen reader, .mesh -> INRIA reader


    velocity_order        = P1Bubble        # FE space order for the velocity
    pressure_order        = P1        # FE space order for the pressure
    mass_lumping         = true      # mass lumping accelerate convergence, reduce accuracy
    stiff_strain         = true      # if true we discretize \int (grad(u) + grad(u)^T)*(grad(v) + grad(v)^T)
    matrix_pattern        = true       # improves efficiency and reduces memory footprint


    [./stabilization]
      betaSD            = 0.5        # scalar parameter of SD stabilization
      divBetaUV          = false       # add \int div(w)u*v stabilization
      stabilizeBackflows     = 0.02            # add numerical viscosity proportional to the magnitude of
"backflow" velocity
    [../]


  [../time_discretization]
    initialtime          = -0.0792         # initial time of the simulation
    endtime             = 19.8         # final time of the simulation
    timestep            = 0.00396    # 0.00198       # timestep
    BDF_order           = 2        # order of the bdf
    restart_simulation      = false       # if true, restarts a previous simulation from the last saved timestep


    [./restart]
      restart_time        =       # the time where we should restart
```

```
        initial_time          = -0.0792          # the initial time in the simulation tha generated the restart solution
                               # WARNING: if that simulation was done with restart, you must put the restart
time!
        timestep              = 0.00396     # the time step in the simulation tha generated the restart solution
        import_history          = false         # if true, we import all the saved solution, not just the one for the
restart


        [./importer]
          type              = ensight      # hdf5, ensight or VTK
          post_dir           = ./initial_data_restart/    # where to look for the previously exported files
          multimesh          = false       # saved also the geometry (may be useful if time-dependent)
          verbose            = false
          save              = 100         # was written on file every 'save' time steps
          numImportProc     = 2
          exportMode         = 2          # only for VTK export (1: ascii, 2: binary)
          floatPrecision     = 1          # only for VTK export (1: single precision, 2: double precision)
          time_id_width      = 3          # how many digits reserved for the time index in the file name
      [../]
    [../]


[exporter_fluid]
  type                      = ensight      # hdf5, ensight or VTK
  post_dir                  = ./results/    # where to write the results. BEWARE: if the folder is not existent,
nothing will be written on disk.
  export_variables              = 'velocity,pressure' # list of variables to export (velocity, pressure indicator,
half_step_velocity, half_step_pressure)
  multimesh                = false       # save also the geometry (may be useful if time-dependent)
  verbose                  = false
  save                     = 10         # will write on file every 'save' time steps
  exportMode               = 1          # only for VTK export (1: ascii, 2: binary)
  floatPrecision           = 1          # only for VTK export (1: single precision, 2: double precision)
  time_id_width            = 5          # how many digits reserved for the time index in the file name
```

- solverOptions.xml

    o This file mainly controls the settings of the Trilinos solver for the 'ApplyInverse' command in LifeV. This file is different for non-FSI and FSI simulations. It describes the type of linear solver and type of preconditioner to be used by the CFD/FSI simulations.

    o The parameters of interest include:

        ▪ <Parameter name="max_iter" type="int" value="1500"/>

            - This determines the maximum number of iterations to be ran for each time when "ApplyInverse" in the LifeV code is being called

        ▪ <Parameter name="output" type="string" value="summary"/>

            - This determines the amount of output produced by the Trilinos solver. Change "summary" to "all_res" if you want to observe the residual of each iteration.

        ▪ <Parameter name="tol" type="double" value="1e-05"/>

            - This determines the tolerance of the Trilinos solver

    o For more details of these parameters you can refer to the LifeV website (www.lifev.org) and Trilinos Project website (https://trilinos.org)

A.6.2.4.   Step [4] Running the CFD Simulation

A.6.2.4.1.   *Step [4a] Description of Source Code*

In this thesis, the LifeV applications used are runTCPC with LifeV 2011 and benchmarkFSI with LifeV 2013.

- runTCPC (Navier stokes solver): This originally the moving wall code (CFD with prescribed mesh motion) developed by Dr Lucia Mirabella. This was utilized to use the Navier Stokes with Windkessel model while mesh motion is turned off in this thesis. This has been compiled at multiple locations:
    - Crius:/yogi6/home/etang/Programs/lifev_parallel2011/lifev-ecm2-parallel-2011_newRCR_stabilizebf_v3/lifev-ecm2-parallel-build/playground/lucia/tcpc/ runTCPC_stabilizebf_v3
    - Isabella (my home folder): /gpfs/pace1/project/pcfm1/ttang9/data/lifev-ecm2-parallel-2011-stabilizebf_v3/lifev-ecm2-parallel-build/playground/lucia/tcpc/ runTCPC_stabilizebf_v3
- benchmarkFSI solver: This was developed by Dr Tiziano Passerini. This code has been compiled in different locations:
    - Crius: /yogi6/home/etang/lifev/lifev_solver_v2/benchmarkFSI_component_restart/benchmarkFSI.exe
    - Poseidon: /opt/casa/LifeV_Elaine/benchmarkFSI_component_restart/benchmarkFSI.exe
    - Isabella (my home folder): /gpfs/pace1/project/pcfm1/ttang9/data/lifev_emoryexperimental2013_v2/benchmarkFSI_component_restart/ benchmarkFSI.exe

A.6.2.4.2.   Step [4b] Code Compilation

LifeV utilizes several other libraries. And the compilation of those libraries and LifeV code is highly dependent on each individual system. You can refer the LifeV website for detailed documentation on LifeV code compilation. For other libraries, read the "readme" or "install" text files along with the package. If there are any errors, internet search related to those libraries are very useful since many of them have been used in applications not limited to LifeV. Here are some tips based on my experience in compiling this code on Crius, Poseidon and PACE.

1. Cmake: Version at least 2.8 or higher. This is for compilation of other libraries and LifeV. On most machines and cluster, this is usually already installed

2. Boost library: I used Boost 1.45.0

    - $./bootstrap.sh –prefix=/installation folder/

    - Added 'using mpi ;' in project_config.jam   (but I don't think this is necessary, I did it just in case)

    - ./b2 install

3. UMFPACK and AMD libraries

    - You will need LAPACK and BLAS libraries

    - Choice 1: Install UMFPACK and AMD as individual libraries

        o   I used AMD-2.3.1, UMFPACK-5.6.1 and Suitesparse config

        o   In suitesparse_config.mk, change the following lines with the correct path:
            - BLAS = -L/usr/lib64/-lblas –L/usr/lib/gcc/x86_64-redhat-linux/3.4.5 –lg2c –lgfortran
            - LAPACK = -L/usr/lib64 –llapack
            - Also in suitesparse_config.mk, UMFPACK_CONFIG = -DNCHOLMOD

413

- o I tried using atlas's blas and lapack for some reason it wasn't very successful. So I used lapack and blas outside of atlas when compiling on Crius

  - o Later when compiling Trilinos, if there is an error saying AMD or UMFPACK cannot look for suitesparse_config.h, create link in the "include" folder of AMD and UMFPACK for suitesparse_config.h

- Choice 2: Install the entire Suitesparse package. This is what I used when I compiled the code on Poseidon.

  - o Change settings in UFconfig/UFconfig.mk

  - o Specify install_lib and install_include paths, create 'lib' and 'include ' directories if necessary

    INSTALL_LIB = /opt/casa/LifeV_Elaine/Programs/SuiteSparse/SuiteSparse_install/lib
    INSTALL_INCLUDE   =
    /opt/casa/LifeV_Elaine/Programs/SuiteSparse/SuiteSparse_install/include

  - o For metis path, you can just use ParMetis-3.1, Make necessary links in Parmetis to direct the paths

    METIS_PATH = /yogi7/home/mrestrepo3/Desktop/LifeV_Elaine/Programs/ParMetis-3.1/
    METIS = /opt/casa/LifeV_Elaine/Programs/ParMetis-3.1/libmetis.a

  - o On Poseidon, I used BLAS and LAPACK from ATLAS.

    BLAS = -L/usr/lib64/atlas -lf77blas –lcblas -latlas -lg2c
    LAPACK = -L/usr/lib64/atlas -llapack

  - o Make sure to install lg2c (libg2c)

    - ▪ To look for package that contains –lg2c, with root privilege at command line, type:

      $ yum provides */libg2c*

- if it build successfully, it will be outputting results of a bunch of demos

- If the Suitesparse package is used, make sure to include extra libraries, e.g. libcholmod.a, when compiling trilinos in later steps

4. HDF5: I used hdf5-1.8.5-patch1

   - Make sure to use the necessary compilation tags, e.g.

     ./configure cc=/usr/local/mpichxxxx/bin/mpicc   --enable-parallel –with-default-api-version = v16 –prefix =/installation_folder/

5. ParMetis-3.1

   - In Makefile.in , make sure to specify CC path and also INCDIR (folder that contains mpi.h and mpio.h)

6. Trilinos: I used trilinos-10.6.4

   - Make sure to specify MPI path in configuration script if cluster has multiple versions

   - Refer to Pace/Crius/Poseidon installed Trilinos for examples of compilation scripts

7. ANN: I used ann_1.1.2

8. LifeV: Make sure to specify MPI path if the cluster has multiple versions

   - LifeV 2011 and runTCPC code

     o To compile program for debug mode, change the compile tag "--enable-opt3" to "--enable-debug" (for both lifev-parallel-2011 and lifev-ecm2-parallel-2011)

     o (instead of build, compile in debug mode) → now it is going to output anything in the code with "Debug() << "

     o You will need to install:

415

- lifev-parallel-2011: Contains core libraries in LifeV

- lifev-ecm2-parallel-2011: Contains the applications

1. Build and install lifev-parallel-2011

   a. Create a <mark>source code</mark> folder (to store source code), a build folder, and an <mark>install</mark> folder

   b. In build folder, run in command line (Correct paths if necessary)

```
../lifev-parallel-src/configure --prefix=/yogi6/home/etang/Programs/lifev_parallel2011/lifev-parallel-2011/lifev-parallel-build-install/ --enable-opt3 --with-parmetis-lib=/yogi6/home/etang/Programs/ParMetis-3.1/ --with-parmetis-include=/yogi6/home/etang/Programs/ParMetis-3.1/ --with-mpi-include=/usr/lib/gcc/x86_64-redhat-linux/3.4.6/include/ --with-mpi-lib=/usr/lib/gcc/x86_64-redhat-linux/3.4.6/ --with-trilinos=/yogi6/home/etang/Programs/trilinos/trilinos-install/ --with-boost=/usr/ --with-acml=/yogi6/home/etang/Programs/acml/gfortran64/ --with-hdf5=/usr/local/ F77=gfortran CXX=mpicxx --with-umfpack-lib=/yogi6/home/etang/Programs/SuiteSparse_3.6.0/Suitesparse_install/lib/ --with-umfpack-include=/yogi6/home/etang/Programs/SuiteSparse_3.6.0/Suitesparse_install/include/ --with-amd-lib=/yogi6/home/etang/Programs/SuiteSparse_3.6.0/SuiiteSparse_build/AMD/Lib/ --with-amd-include=/yogi6/home/etang/Programs/SuiteSparse_3.6.0/SuiiteSparse_build/AMD/Include/ LDFLAGS=-L/usr/lib/gcc/x86_64-redhat-linux/3.4.6/;/yogi6/home/etang/Programs/acml/gfortran64/lib/;/yogi6/home/etang/Programs/acml/gfortran64_mp/lib/ CC=gcc --no-create --no-recursion
```

   c. After configuration, type 'make' in command line. To compile in parallel, use 'make –j <number of processors>'

   d. Then type 'make install'

2. Link necessary files in parmetis

   a. Parmetis folder create symbolic link for parMETISLib folder as Lib

b. ParMETISLib: create symbolic link for parmetis.h

3. Install new relevant libraries (For lifev-ecm2-parallel-2011):

    a. acml 4.4.0 gfortran

    b. Suitesparse 3.6.0

4. Build lifev-ecm2-parallel-2011

    a. Create a source code folder (to store source code) and a build folder. Link to the install folder of lifev-parallel-2011

    b. In build folder, run command line (with correct paths)

```
../lifev-ecm2-parallel-src/configure --with-life=/yogi6/home/etang/Programs/lifev_parallel2011/lifev-parallel-2011/lifev-parallel-build-install/ --enable-opt3 --with-parmetis=/yogi6/home/etang/Programs/ParMetis-3.1/ --with-parmetis-lib=/yogi6/home/etang/Programs/ParMetis-3.1/ --with-parmetis-include=/yogi6/home/etang/Programs/ParMetis-3.1/ --with-mpi-include=/usr/lib/gcc/x86_64-redhat-linux/3.4.6/include/ --with-mpi-lib=/usr/lib/gcc/x86_64-redhat-linux/3.4.6/ --with-trilinos=/yogi6/home/etang/Programs/trilinos/trilinos-install/ --with-boost=/usr/ --with-acml=/yogi6/home/etang/Programs/acml/gfortran64/ --with-hdf5=/usr/local/ F77=gfortran CXX=mpicxx --with-umfpack-lib=/yogi6/home/etang/Programs/SuiteSparse_3.6.0/Suitesparse_install/lib/ --with-umfpack-include=/yogi6/home/etang/Programs/SuiteSparse_3.6.0/Suitesparse_install/include/ --with-amd-lib=/yogi6/home/etang/Programs/SuiteSparse_3.6.0/SuiiteSparse_build/AMD/Lib/ --with-amd-include=/yogi6/home/etang/Programs/SuiteSparse_3.6.0/SuiiteSparse_build/AMD/Include/ --with-ann=/yogi6/home/etang/Programs/ann_1.1.2/ --with-umfpack-extra-libs='-lcholmod -lcolamd -lccolamd -lcamd' LDFLAGS=-L/usr/lib/gcc/x86_64-redhat-linux/3.4.6 --with-extra-ldflags=-L/yogi6/home/etang/Programs/acml/gfortran64/lib/ --with-extra-ldflags=-L/yogi6/home/etang/Programs/acml/gfortran64_mp/lib/ --with-extra-ldflags=-L/usr/local/lib/ CC=gcc
```

    c. After configuration, type 'make' in command line. Then type 'make install'

    d. cd to <build_folder>/playground/lucia/tcpc

    e. Enter at command line: make runTCPC

- LifeV 2013 and benchmarkFSI code

    1. Build and install lifev-parallel-2013

        a. Create a source code folder (to store source code), a build folder, and an install folder

        b. In build folder, run in command line the configure script (correct paths in configure script if necessary), e.g. $ ./do-configure

        c. After configuration, type 'make' in command line. To compile in parallel, use 'make –j <number of processors>'

        d. Then type 'make install'

    2. Build benchmarkFSI

        a. Create a source code folder (to store source code)

        b. cd into the source code folder, open do-cmake-opt3 in text editor to change path to the install folder of LifeV 2013

        c. run in command line

            ./ do-cmake-opt3

        e. After configuration, type 'make' in command line.

<u>Tips for troubleshooting</u>

- 'SEEK' error

    - If see this error in Trilinos or Lifev compilation:

        /opt/mpich2-gcc/include/mpicxx.h:26:2: #error "SEEK_SET is #defined but must not be for the C++ binding of MPI"

        /opt/mpich2-gcc/include/mpicxx.h:30:2: #error "SEEK_CUR is #defined but must not be for the C++ binding of MPI"

        /opt/mpich2-gcc/include/mpicxx.h:35:2: #error "SEEK_END is #defined but must not be for the C++ binding of MPI"

    - Add export CXXFLAGS="-DMPICH_IGNORE_CXX_SEEK" in .bashrc

    - Or $ make 'CXXFLAGS=-DMPICH_IGNORE_CXX_SEEK'

    - Reference: https://trilinos.org/faq.html#building_10

- PMPI_send error

    - On Isabella, use Parmetis 3.1, not 3.1.1, otherwise get MPI (PMPI_send) error

- When in doubt, check configuration scripts in my previous installations (Crius/Poseidon/Isabella)

A.6.2.4.3.   *Step [4c] Running a Simulation*

- As previously mentioned, to run simulations with LifeV, the following files are needed:

    - 'data' file

    - solversOptions.xml

- o Mesh file(s)

- o Boundary conditions data file

- o Solver executable

- Command to run the solver is specific to your system:

  - o Crius:

    - ▪ $ nohup mpirun -np [no. of processors] [runTCPC or benchmarkFSI executable] > screen.out &

  - o Poseidon:

    - ▪ $ mpd &

    - ▪ $ /opt/mpich2/bin/mpiexec -n 24 ./benchmarkFSI.exe >screen.out &

  - o PACE:

    - ▪ Use PBS script, or in interactive mode:

      - • mpiexec ./FSI_CHOP235A_component &> screen_FSI.out

- Restarting the simulation

  - o In data file, specify

    - ▪ 'Importer' parameters

    - ▪ restart =true

    - ▪ restart_timeIndex (for benchmarkFSI code)

    - ▪ initialtime

  - o Refer to Step [3c] for detail

- Make sure at least run 3- 5 time steps ahead, in case during the restart, the first few time steps are not stabilized yet

- Monitoring the simulation

  - From FluxesAndPressure.dat file, check

    - Mass conservation at inlets and outlets

    - Inlet flow rate (Note that **inlet fluxes** are **negative**)

    - Outlet flow splits

    - Pressures

A.6.2.5. Step [5] Post-processing

A.6.2.5.1. *Step [5a] Computing Power Loss*

Fluxes and pressures can be read from FluxesAndPressure.dat, from which power loss can be computed.

A.6.2.5.2. *Step [5b] Particle Tracking*

EnsightImport

To perform visualization and particle tracking in ParaView using LifeV results, the partitioned simulation results should be exported as one partition. For this, the executable 'EnsightImport' should be used:

- Compile:

  - cd to: /yogi6/home/etang/Programs/lifev_parallel2011/lifev-parallel-2011/lifev-parallel-build/testsuite/lifefilters/exporterEnsight

  - make ensightImport

- Run EnsightImport

  a. Create new folder (results_ensight_export)

  b. Copy ensightImport executable short cut and data file

  c. In data file:

    - Update all the paths, mesh name etc.

    - Initial time = time of end of 2nd cycle

    - Endtime = time of end of 3rd cycle

    - Timestep = CFD timestep * 10 (for save=10 during CFD)

    - Start = 200 (for 2 cycles)

    - Save = 1

    - Set number of processors

  d. Run nohup ./ensightImport >screen_ensight.out &

  e. Check if the correct file is imported and exported

  f. Go to results_ensight_export

    - Duplicated first timestep and add it to the end.

      - E.g. fluidReduced_pressure.00000.000scl → copy as: fluidReduced_pressure.00100.000scl

      - fluidReduced_velocity.00000.000scl → copy as: fluidReduced_velocity.00100.000scl

    - make a copy of file fluidReduced.000.case

  g. Open fluidReduced.000.case

    - Change number of steps to 101

- Shift time values so that it starts with zero, and have 101 datapoints
- Make sure you time values have enough decimal points. If not, time interval (delta t) will be slightly different at each time step and ParaView particle tracking will give you segmentation fault and crash

Particle Tracer in ParaView

1) Launch ParaView 3.14

2) Change background of ParaView to white

3) Make sure case file that:
   o result only contain 1 cycle (number of steps, filename start number)
   o time values starts with zero, ends with period length
   o Change the fluid and pressure results file so that the first datapoint is the same as the last data point (e.g. For CHOP011B, 0s and 4.248s contain the same data)

4) Load case file

5) Warp be vector → Displacement (If wall is moving, e.g. for FSI simulation)

6) Filter → temporal interpolator if you want finer time step for particle tracking

7) Filter → temporal shift scale – Maximum number of periods = 3 (or 5), periodic, periodic end correction
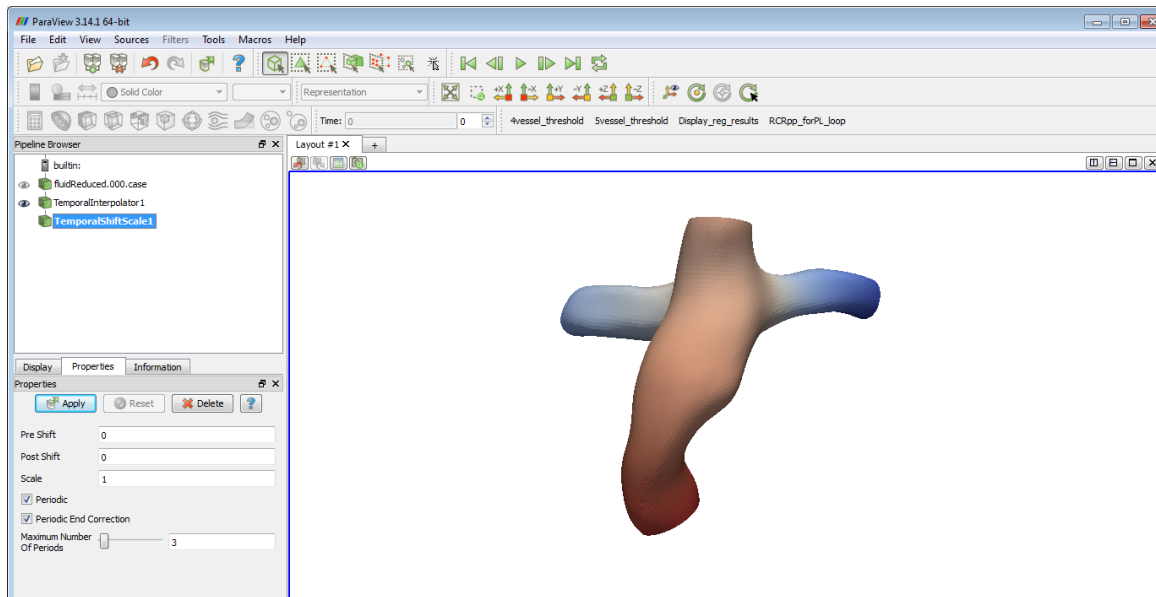
Figure A. 62 Temporal shift scale in ParaView

8) Filter → temporal cache → used 2

9) Select temporal interpolator , take SVC and IVC slice; rename slice accordingly

   o Take slice further from the caps if there are reversal flow

   o Save slice coordinates for reference
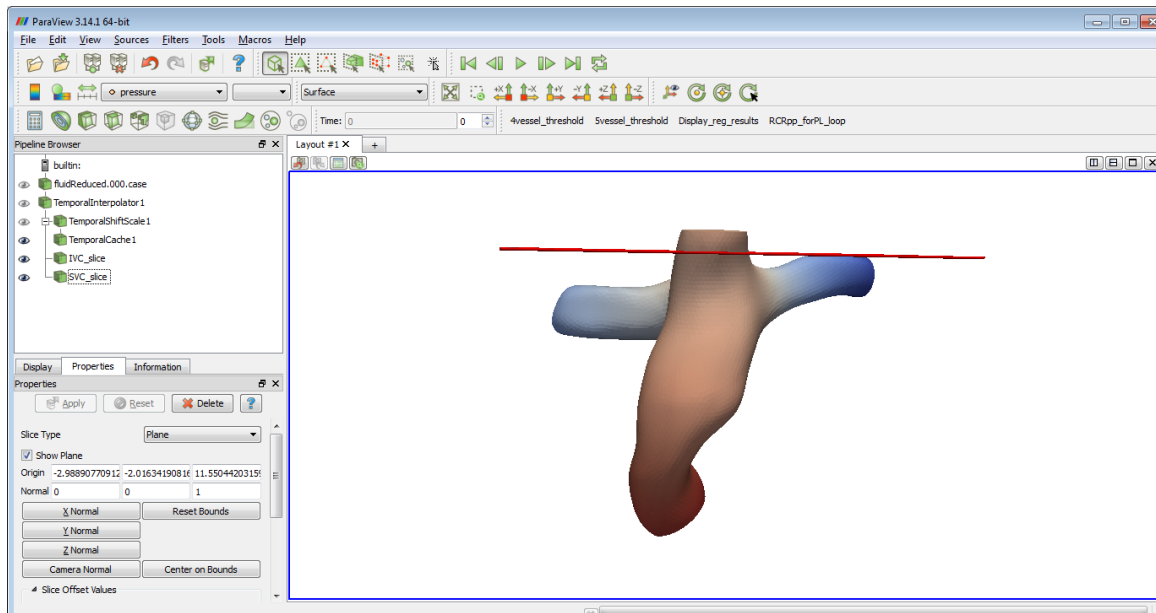
Figure A. 63 Take slice on Temporal Interpolator

10) Change the color of the visible geometry (right now it's the Temporal Cache) as white and change opacity as 0.5

11) Save state now, so that you can load this for other conditions directly

12) To start here for other condition(s), just change the path of the results when you the load state

13) Select temporal cache, Particle tracer, input = temporal cache, source = IVC/SVC slice. **Don't click Apply yet**

14) Repeat (12) for the other slice

15) For each particle tracer, set:

   o Force injection Every Nsteps = 1 (or increase if needed)

   o Term Speed = 1e-2 (particles will disappear when the velocity drops below this value)
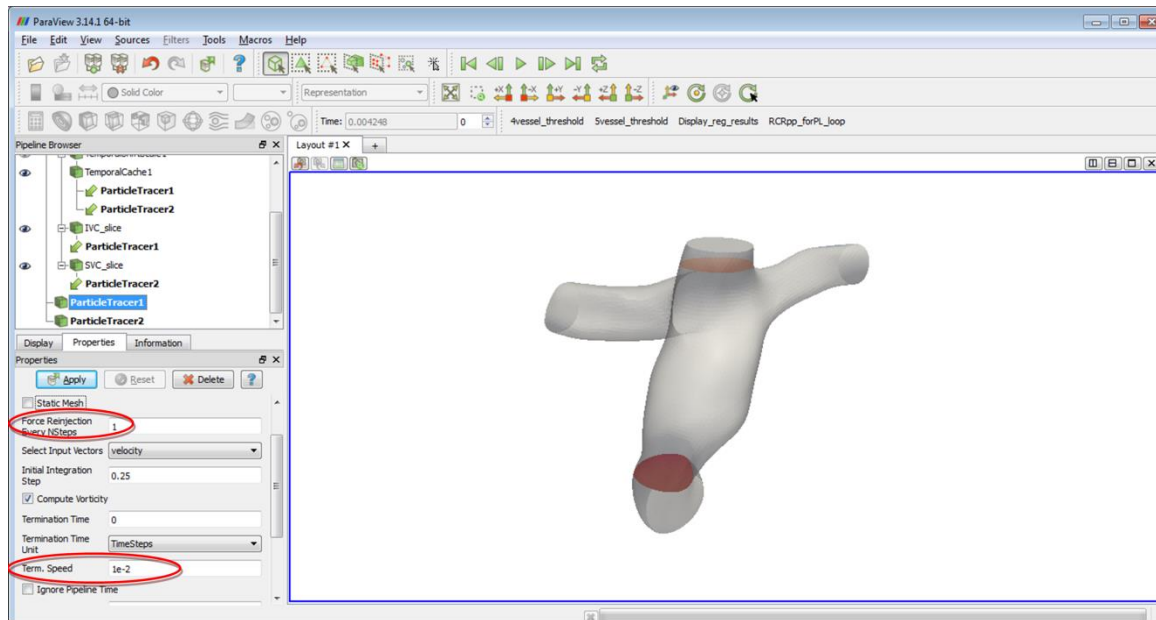
Figure A. 64 Changing particle tracking parameters

16) (After you click apply here, ParaView will crash easily when you change the time step. So make sure you did all the manipulations you want before clicking 'Apply' for this tstep) Apply for each particle tracer

17) Apply threshold on both particle tracers

- InjectionstepId → range 0 to 999 (if there are 1000 time step in one cycle and you only want to seed for one cycle)
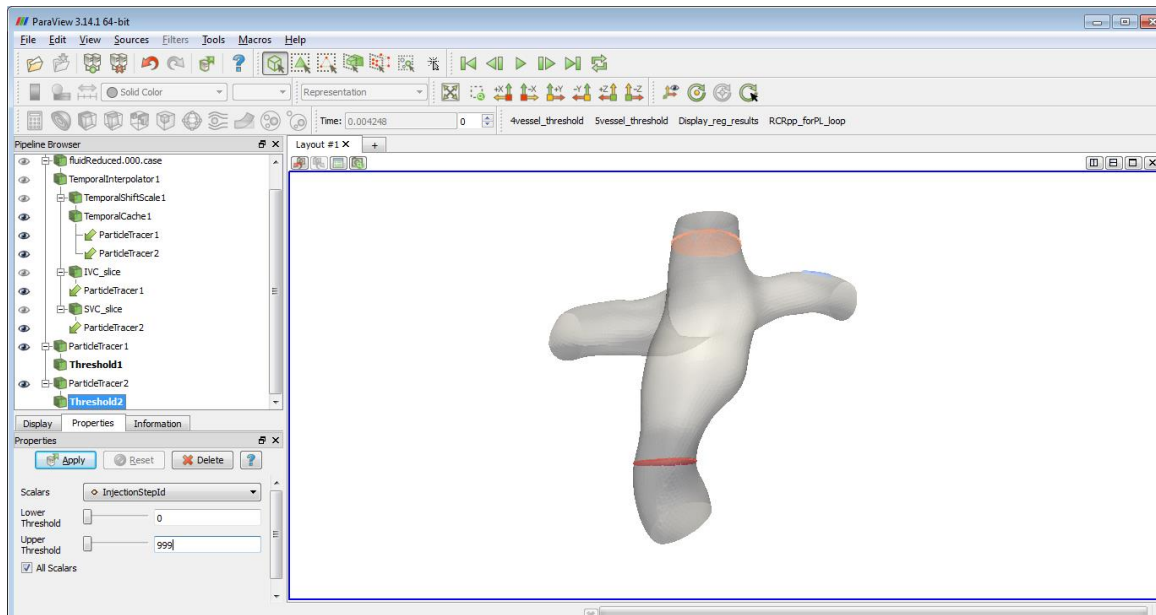
Figure A. 65 Adding threshold so that only first cycle's particle will be visualized

18) Change color and presentation for each particle tracer/threshold

- (HFD) e.g. IVC = blue, SVC = green

- (velocity) use velocity, change preset, set range
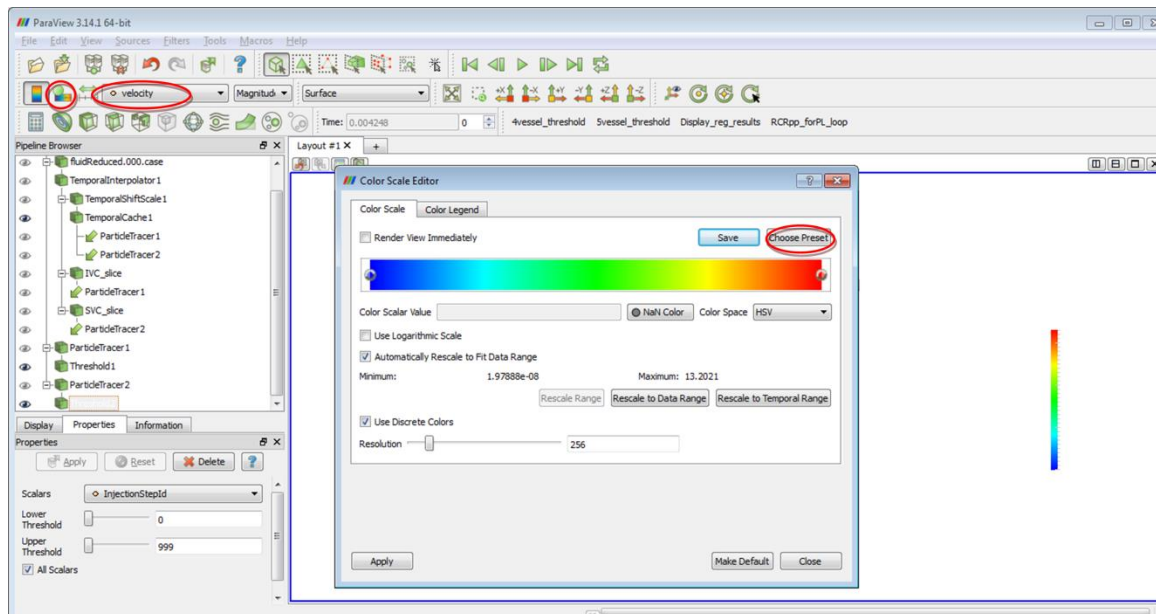
Figure A. 66 Changing contour color for velocity
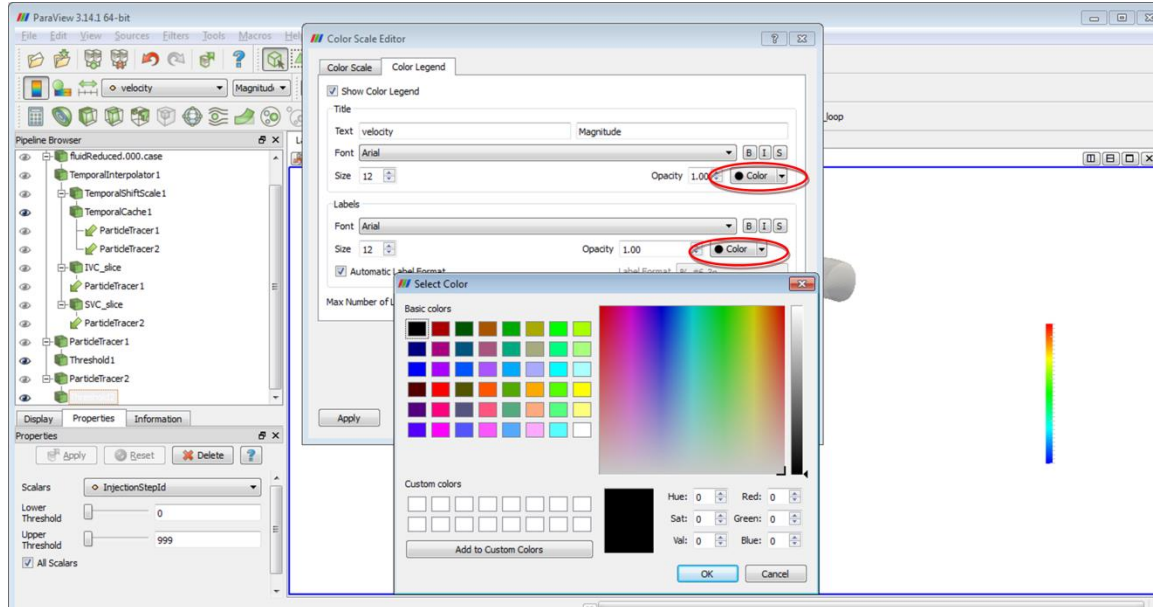
Figure A. 67 Changing text color of legend

- o If you want to use sphere to represent the particles, click on the particle tracer/threshold → Filter → Glyph → Properties

    - Glyph type: Sphere

    - Radius: Specify radius e.g. 0.05 (cm)

    - Theta resolution: 8 (default)

    - Start theta: 0

    - End theta:360

    - Phi resolution: 8 (default)

    - Start phi: 0

    - End phi: 180

    - Scale mode: Off (otherwise sphere radius will be scaled based on the vector specified)

428

19) Annotate time filter so show time on screen
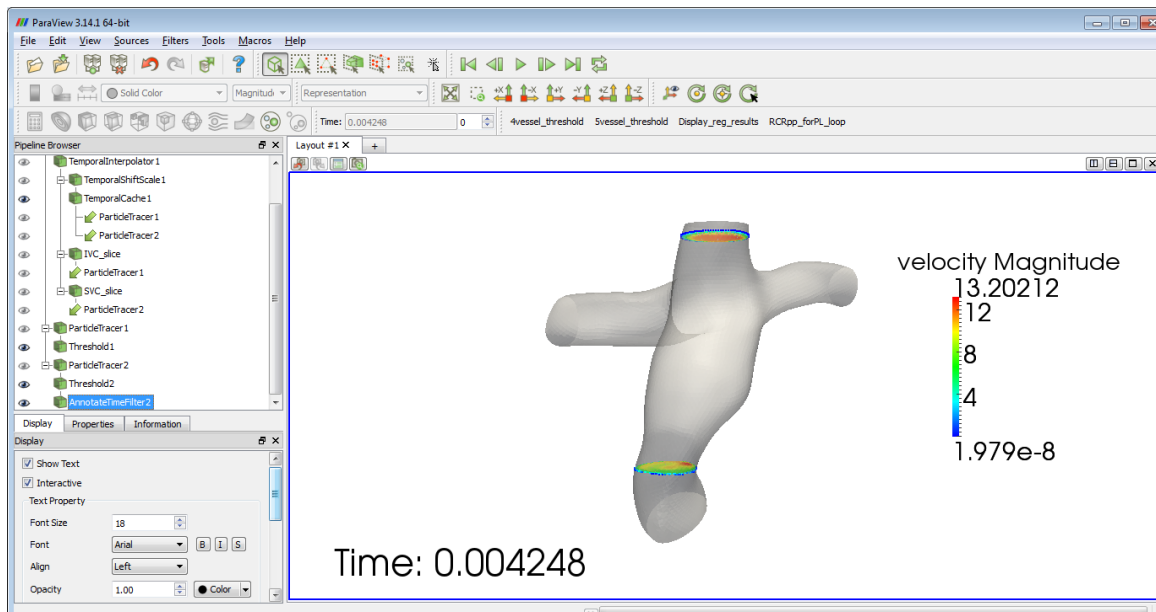
Figure A. 68 Annotate time filter

20) Don't play yet! Make sure orientation and color of the view is good enough

21) Ready? File → Save Animation

  o   Frame rate = 1 fps

  o   No of frame/timestep =1

22) Don't click on ParaView now. Let it run.

Computing residence time and HFD from Particle Tracking

To compute particle residence time and HFD, particle tracking needs to first be performed in ParaView first. Then, MATLAB scripts were used to compute particle washout time and HFD.

[I] Getting partricle tracking data in ParaView

Similar to particle tracking setup,

1) Load case file

2) Warp vector by displacement (for moving wall)

3) Temporal interpolator (optional). For my cases, I have 1000 time step in one cycle

4) Add slice at IVC

5) Select temporal interpolator, Temporal shift scale, periodic, periodic end correction, 6 cycles

6) Temporal cache

7) Particle Tracer: Input: Temporal Cache, Source: slice;

   o Reinject every 10 steps

   o Terminal speed = 1e-2

8) Don't have to set threshold in this case because the MATLAB code will only include particles under certain injectionstepID

9) Don't run the PT or advance in time step (stay at first time step)

10) Select Particle Tracer → File → Save Data → Write all time steps (points)

11) Now let ParaView run. On the background it will export the position, velocity of the particles present at each time step as a separate .csv file.

[II] Computing Particle Washout Time

1) Run MATLAB code "PRTfromParticles.m"

- This code will go through the .csv files exported from ParaView in the earlier step and select particles released in the first cycle to see how many are alive

- Alive particles → go into each text file, check if injectionstepID < max. injectionstepID of 1 cycle

- Dead particles → (particles seed * no. of release in 1 cycle) – alive particles in 1 cycle

- Dropped at T = number of newly died particles at each time steps

2) Run MATLAB code "post_process_PRT.m"

- This code will compute particle washout time based on threshold set. Note that the output is in terms of file numbers. So have to divide this number by number of files per cycle to get particle washout time in terms of number of cycles

[III] Computing Hepatic Flow Distribution

1) Getting HFD from these .csv spreadsheets: "HFDfromParticles.m"

- This code will go through the .csv files exported from ParaView in the earlier step and count how many particles have exit through the LPA and RPA.

- Set time and number of files, number of release time, path, prefix

- Check the column number of the .csv files. Make sure ParticleXCol, ParticleYCol, ParticleZCol are the last 3 columns of the exported csv files. Also check the column number for particleIdCol (column that

stores particle ID), injectionStepCol (column that stores Injection Step ID), and particleAgeCol (column that stores Particle Age).

- o Define LPA, RPA planes

  - In ParaView, extract a slice across which particles can be counted as exiting through the LPA. Make sure the arrow points towards the outlet.

    - xCenterLPA, yCenterLPA, zCenterLPA = origin of the slice

    - nxLPA, nyLPA, nzLPA = normal of the slice

  - Do the same for the RPA
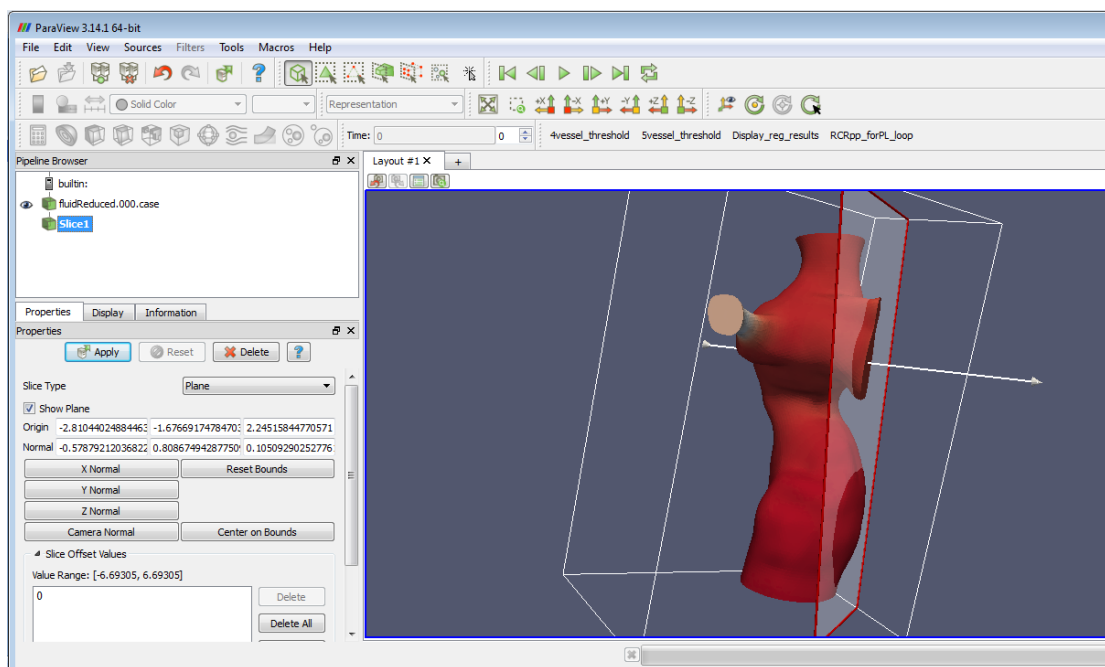
Figure A. 69 Extracting plane in ParaView (CHOP029B as example)

- o Define LPA, RPA thresholds

  - Sometimes the plane that was defined at the LPA or RPA will intersect through the FP/SVC (e.g. Figure A.69). To avoid

432

counting the particles in the FP/SVC, thresholds should be defined.

- xminLPA, xmaxLPA = threshold in x-direction

- yminLPA, ymaxLPA = threshold in y-direction

- zminLPA, zmaxLPA = threshold in z-direction

- If no threshold is needed, you can keep all the default values (e.g. xminLPA=-100, xmaxLPA = 100, same for y and z directions)

- Do the same for RPA

- For example for Figure A.69, threshold of zminRPA=0.45 should be set. For the rest (xminRPA, xmaxRPA, yminRPA, ymaxRPA, zmaxRPA), the default values of the threshold can be kept (-100 or 100).

o Run at let the code count particles

A.7. Detailed Results for Specific Aim 1

A.7.1. Raw Data and Detailed Results for Specific Aim 1(a)

A.7.1.1. Complete List of Computed Geometric and Resting Hemodynamic Parameters in Specific Aim 1(a) (N=108)

A.7.1.1.1. Patient Demographic Information

Table A. 1 Patient Demographic Information of the 108 patients included

Patient ID	Gender (M=male, F = female)	IVC connection type (IA = intra-atrial, EC = extra-cardiac)	Hypoplastic Left Heart Syndrome?	Age (yrs)	BSA (m^2)
CHOP001B	F	IA	Y	16	1.23
CHOP004B	F	IA	N	17	1.49
CHOP005B	F	IA	N	19	1.51
CHOP007B	M	IA	N	18	2.01
CHOP008A	M	IA	Y	15	1.94
CHOP014A	M	EC	N	9	1.04
CHOP016A	M	EC	Y	6	0.83
CHOP017B	F	EC	N	15	1.64
CHOP018A	M	IA	N	7	0.68
CHOP019A	M	IA	Y	14	1.68
CHOP021A	F	IA	Y	11	1.23
CHOP022A	M	EC	Y	7	0.91
CHOP023A	M	IA	N	12	1.22
CHOP024A	F	IA	N	7	0.74
CHOP025A	F	EC	N	9	1.01
CHOP026A	F	IA	Y	6	0.83
CHOP028A	M	IA	Y	18	1.92
CHOP029A	M	IA	Y	9	1.08
CHOP031A	M	IA	N	7	0.89
CHOP032A	F	IA	N	18	1.64
CHOP033A	M	IA	N	10	1.32
CHOP034A	M	IA	N	14	1.89
CHOP035A	F	EC	N	8	0.69
CHOP036A	M	IA	N	11	1.19
CHOP037A	M	IA	Y	10	1
CHOP039A	F	IA	Y	10	1.02
CHOP040A	F	IA	N	19	2.05
CHOP041A	F	IA	Y	14	1.51
CHOP042B	F	EC	N	3	0.62
CHOP046B	M	IA	Y	13	1.36
CHOP051B	M	EC	N	4	0.63
CHOP052B	M	EC	N	10	1.06
CHOP053B	F	EC	Y	3	0.59
CHOP054A	F	IA	Y	4	0.46
CHOP057A	F	EC	N	21	1.6

CHOP061A	M	IA	Y	10	1.13
CHOP062A	F	IA	N	12	1.11
CHOP063A	F	EC	N	9	1.06
CHOP064A	F	IA	Y	6	0.94
CHOP065A	M	IA	Y	16	1.36
CHOP068B	F	IA	Y	4	0.61
CHOP069B	M	IA	Y	11	1.11
CHOP072A	M	IA	N	14	1.65
CHOP073A	F	IA	N	20	1.54
CHOP074A	M	IA	Y	12	1.24
CHOP080A	F	IA	N	17	1.91
CHOP081A	F	EC	N	3	0.54
CHOP082A	M	EC	N	7	0.87
CHOP083A	F	EC	N	8	1.15
CHOP084A	M	EC	N	8	0.99
CHOP085A	M	IA	Y	2	0.5
CHOP086A	F	EC	N	6	0.81
CHOP087A	M	IA	N	5	0.81
CHOP088A	F	EC	N	8	1.25
CHOP089A	M	IA	N	10	0.93
CHOP091A	M	IA	N	18	2.08
CHOP094A	M	IA	N	13	1.2
CHOP097A	F	IA	Y	5	0.67
CHOP100A	M	IA	N	19	1.66
CHOP102A	F	IA	N	25	1.6
CHOP103A	M	IA	N	22	1.86
CHOP105A	M	IA	Y	8	0.95
CHOP108A	M	IA	Y	8	0.93
CHOP109B	F	EC	N	4	0.65
CHOP114A	M	IA	Y	15	1.75
CHOP118A	M	EC	N	5	0.77
CHOP119A	F	IA	N	4	0.76
CHOP121A	M	EC	N	5	0.75
CHOP122A	M	IA	Y	15	1.51
CHOP128A	F	IA	N	10	0.93
CHOP134A	F	EC	N	4	0.63
CHOP135A	M	EC	N	6	0.77
CHOP139A	M	IA	N	9	1.18
CHOP144C	F	EC	N	4	0.75
CHOP145A	F	IA	N	19	1.51
CHOP148A	M	IA	N	4	0.73
CHOP152A	M	IA	N	17	1.89
CHOP155A	M	IA	N	16	1.95
CHOP159A	F	IA	N	24	1.9
CHOP161A	F	EC	N	14	1.65
CHOP166A	M	IA	Y	15	1.41
CHOP181A	M	IA	Y	25	1.72
CHOP187A	F	IA	N	42	1.64
CHOP188A	M	IA	N	17	1.51
CHOP191A	F	EC	N	16	1.25
CHOP203A	M	IA	N	16	1.93

CHOP204A	F	IA	N	17	1.51
CHOP_M11	F	IA	Y	10	1.03
CHOP_M12	M	EC	N	2	0.46
CHOP_M7	M	EC	N	11	1.16
CHOP_M8	M	EC	N	6	0.89
CBF010	M	EC	Y	2	0.56
CBF033	M	EC	Y	4	0.81
CBF040	M	IA	Y	3	0.62
CBF043	M	EC	N	4	0.69
CBF051	M	EC	N	3	0.64
CBF057	M	IA	Y	3	0.61
CBF058	M	EC	Y	3	0.59
CBF059	M	EC	N	4	0.75
CBF063	F	EC	Y	2	0.65
CBF069	M	EC	Y	6	0.75
CBF070	M	EC	Y	3	0.51
CBF071	F	IA	N	3	0.69
CBF075	F	IA	Y	2	0.58
CBF083	M	EC	N	3	0.62
CBF093	M	EC	N	3	0.71
CBF100	F	IA	N	3	0.69
CBF112	M	EC	Y	3	0.63
Average				10.2	1.12
Standard deviation				6.8	0.45

CBF =cerebral blood flow cohort from CHOP

A.7.1.1.2. Computed Geometric Parameters

A.7.1.1.2.1. Vessel Diameter

Table A. 2 Absolute Vessel Diameter for FP, SVC, LPA and RPA (mm)

	FP diameter			SVC diameter			LPA diameter			RPA diameter		
Patient ID	**Min**	**Mean**	**Max**	**Min**	**Mean**	**Max**	**Min**	**Mean**	**Max**	**Min**	**Mean**	**Max**
CHOP001B	17.3	21.9	24.9	11.3	14.8	19.9	7.2	9.6	17.1	10.8	12.6	16.7
CHOP004B	14.9	19.4	24.5	11.5	13.4	17.0	11.5	14.1	17.8	6.9	9.2	14.4
CHOP005B	18.7	25.9	32.4	9.9	12.4	14.3	8.3	12.0	16.7	13.3	14.0	15.6
CHOP007B	18.8	22.9	26.7	10.0	12.9	19.7	8.9	10.9	13.1	13.1	14.8	16.8
CHOP008A	20.5	24.9	32.4	16.0	19.8	26.8	7.2	12.8	24.1	13.1	16.9	22.5
CHOP014A	16.5	19.0	22.4	13.1	14.8	20.9	8.8	12.6	19.8	11.8	14.0	19.4
CHOP016A	12.8	15.7	18.8	13.5	14.2	14.7	4.5	7.1	13.9	10.8	11.6	12.9
CHOP017B	14.7	17.8	24.5	14.4	15.6	16.5	5.5	9.6	14.9	14.8	15.9	18.2
CHOP018A	16.7	17.7	19.1	11.7	12.3	13.7	8.7	11.6	18.6	8.6	10.1	13.4
CHOP019A	15.9	20.7	24.8	11.7	15.3	20.9	7.6	11.4	20.6	11.7	17.4	23.4
CHOP021A	13.8	16.8	20.2	10.5	11.5	13.6	5.2	10.3	19.8	9.3	10.3	13.0
CHOP022A	14.4	15.3	16.6	10.7	12.7	16.9	7.6	8.0	8.1	9.6	11.0	14.5
CHOP023A	7.9	13.0	23.1	13.7	16.2	19.6	10.2	15.0	20.5	7.6	12.9	23.2
CHOP024A	14.9	16.9	20.1	13.1	15.0	16.5	5.8	10.7	18.7	8.8	13.1	19.7
CHOP025A	9.5	10.7	13.3	7.9	8.6	10.5	7.0	9.5	15.1	10.5	11.9	12.5
CHOP026A	18.7	20.0	21.3	11.8	13.8	14.3	4.5	9.4	19.5	7.8	9.2	15.6
CHOP028A	16.0	20.2	25.3	13.4	15.3	19.6	6.7	9.1	17.2	13.9	16.5	19.3
CHOP029A	16.2	20.6	24.1	14.9	16.4	18.4	7.0	11.3	21.7	8.2	11.9	20.8
CHOP031A	17.5	19.1	22.3	12.1	12.7	13.7	11.6	15.1	19.3	10.2	11.0	12.5
CHOP032A	10.7	14.5	24.6	13.8	15.8	19.7	7.3	10.9	19.9	11.0	13.9	19.4
CHOP033A	16.1	17.5	20.8	11.9	14.5	19.2	11.8	14.4	17.1	12.1	14.9	19.4
CHOP034A	13.9	18.9	23.4	16.5	19.1	22.9	7.9	12.6	22.2	10.1	15.1	23.8
CHOP035A	11.6	14.8	19.1	12.1	12.9	14.2	10.5	11.2	11.9	12.5	13.5	14.5
CHOP036A	15.3	19.6	25.7	12.5	13.9	16.8	12.1	13.8	16.9	9.8	13.1	17.0
CHOP037A	11.8	15.1	21.4	11.6	13.6	17.8	4.2	9.5	20.0	8.4	11.3	18.4
CHOP039A	17.3	20.3	22.4	14.4	16.6	19.5	7.9	12.6	17.8	6.7	10.1	16.1
CHOP040A	16.4	21.5	28.8	15.9	17.1	21.6	8.6	12.6	21.8	11.4	14.1	22.5
CHOP041A	18.0	21.1	26.6	12.5	13.5	14.3	6.4	9.1	16.9	11.2	13.8	21.7
CHOP042B	11.0	11.4	12.4	5.8	6.2	6.3	6.0	9.8	15.0	4.3	4.4	4.5
CHOP046B	18.0	19.6	21.6	11.7	13.0	16.4	7.0	10.9	18.4	13.7	15.6	17.1
CHOP051B	15.5	17.0	18.0	7.4	8.3	11.4	8.0	9.2	10.1	7.0	8.3	11.9
CHOP052B	14.0	15.1	16.5	13.8	13.9	14.1	8.9	12.1	15.3	6.6	7.7	10.1
CHOP053B	13.6	15.4	16.3	8.1	9.2	12.4	6.6	8.7	12.1	6.8	9.0	13.2
CHOP054A	18.7	21.2	23.1	13.5	15.9	17.8	8.6	12.2	19.0	10.1	13.7	17.1
CHOP057A	12.4	16.5	19.5	15.7	16.5	17.2	9.0	10.5	11.8	14.0	15.3	16.4
CHOP061A	21.9	25.3	27.7	15.5	17.8	22.9	6.8	12.8	25.0	12.6	15.7	22.2
CHOP062A	14.5	16.6	19.3	12.8	14.1	16.3	8.1	11.2	17.6	15.3	15.5	15.7
CHOP063A	12.4	14.0	19.5	13.2	15.9	18.0	9.4	12.4	17.2	9.4	10.6	13.0
CHOP064A	15.2	17.6	19.7	11.1	13.2	15.3	6.4	10.3	15.9	8.3	10.1	15.7
CHOP065A	17.2	21.1	28.2	16.1	18.3	23.2	14.2	18.4	23.9	12.3	13.3	16.0

CHOP068B	15.8	18.1	21.1	13.1	15.8	19.2	5.7	10.8	18.7	7.5	11.2	18.8
CHOP069B	19.4	24.0	28.8	12.2	17.3	24.0	6.8	14.7	25.9	10.3	14.6	24.7
CHOP072A	11.5	16.5	24.6	12.8	16.6	19.6	8.4	12.9	22.4	8.0	11.3	20.0
CHOP073A	16.3	21.3	28.1	17.0	18.3	18.9	12.3	15.3	19.5	14.7	16.0	17.6
CHOP074A	13.0	16.7	21.6	10.4	14.0	17.9	8.9	12.6	19.4	7.7	12.6	19.7
CHOP080A	10.4	16.6	25.2	17.6	22.5	27.0	9.2	10.2	11.7	10.4	17.6	26.9
CHOP081A	18.0	20.0	21.1	14.1	15.1	16.3	6.4	8.9	14.1	10.6	12.7	16.5
CHOP082A	17.3	18.4	19.7	13.7	14.7	16.0	8.6	12.6	18.3	11.1	11.7	13.1
CHOP083A	17.1	17.5	18.6	16.0	16.4	16.9	10.3	12.8	15.9	13.7	14.8	16.5
CHOP084A	15.6	19.0	22.3	15.5	15.6	15.7	10.4	13.5	18.0	8.8	10.8	12.9
CHOP085A	13.9	16.6	18.3	11.7	13.0	14.9	4.1	7.1	14.8	7.4	7.9	9.3
CHOP086A	15.3	16.8	18.7	7.1	8.6	11.9	6.5	7.7	9.6	10.4	11.3	12.5
CHOP087A	20.4	22.2	23.6	18.3	19.7	20.8	5.9	10.4	21.9	12.6	15.3	20.5
CHOP088A	15.4	17.2	18.9	13.2	14.2	15.4	9.0	11.6	15.3	7.5	8.5	11.0
CHOP089A	15.5	17.7	19.7	12.5	14.6	17.5	10.4	12.9	17.9	10.5	14.6	19.8
CHOP091A	17.3	20.8	24.1	9.4	12.3	16.7	13.0	13.5	14.0	11.4	14.1	18.6
CHOP094A	15.0	17.1	20.5	14.8	15.4	16.1	6.4	10.0	16.2	14.1	15.3	17.8
CHOP097A	17.2	18.6	20.2	13.6	14.8	16.1	3.8	8.4	16.3	10.3	12.4	15.8
CHOP100A	18.2	23.3	29.2	21.1	22.8	24.1	13.7	16.3	24.2	12.9	15.3	19.4
CHOP102A	15.2	17.6	24.8	11.2	14.2	23.3	13.0	13.2	13.4	15.1	18.1	24.1
CHOP103A	10.6	16.7	25.1	13.6	16.5	22.3	9.0	12.1	20.2	11.5	16.0	21.8
CHOP105A	17.6	19.1	21.1	12.7	15.4	19.7	6.9	12.5	22.2	9.4	12.5	17.1
CHOP108A	17.3	18.7	21.0	13.0	14.8	16.3	5.2	9.4	16.0	9.6	11.8	17.0
CHOP109B	14.1	17.2	18.9	11.5	11.8	12.5	7.2	9.5	13.1	6.5	9.0	13.0
CHOP114A	13.2	17.5	24.9	12.7	16.0	22.1	8.9	14.4	20.8	15.0	15.4	16.1
CHOP118A	15.0	16.1	18.1	10.8	11.7	13.5	5.9	9.0	14.8	8.4	10.6	14.0
CHOP119A	12.3	17.5	19.7	12.1	12.4	12.6	7.0	8.8	10.7	9.3	10.7	11.6
CHOP121A	12.2	14.1	15.4	12.0	12.3	13.0	6.3	8.0	12.5	10.0	11.2	12.9
CHOP122A	18.1	20.6	22.5	14.3	16.3	19.6	6.4	7.3	7.9	10.7	12.7	19.6
CHOP128A	17.4	18.9	20.6	13.2	14.3	17.0	13.3	15.7	17.7	12.8	14.4	17.3
CHOP134A	13.4	16.1	17.6	9.4	10.7	12.6	6.0	9.6	13.7	8.4	9.4	12.4
CHOP135A	15.2	16.6	17.0	9.9	10.7	13.1	5.9	6.5	8.2	6.7	9.0	12.8
CHOP139A	18.3	21.2	25.5	13.4	15.1	18.8	8.1	12.3	19.0	13.9	15.9	19.0
CHOP144C	9.4	12.3	14.3	8.4	9.6	10.7	11.2	11.5	12.1	6.1	7.3	9.9
CHOP145A	14.9	19.2	27.0	16.9	18.2	19.0	12.7	17.3	25.2	14.1	15.7	18.7
CHOP148A	14.4	17.5	19.7	12.7	13.2	13.5	6.1	7.8	11.8	6.1	7.8	10.8
CHOP152A	21.7	29.9	41.8	15.9	25.9	31.6	9.4	10.8	14.3	12.2	14.6	17.4
CHOP155A	15.9	19.5	23.9	18.5	19.7	21.9	14.7	17.2	22.9	11.0	13.2	18.5
CHOP159A	17.7	26.1	38.7	14.8	18.6	26.0	9.3	14.1	27.2	10.8	16.2	27.6
CHOP161A	13.1	14.5	21.1	17.8	18.4	18.8	11.7	12.4	13.2	8.7	11.9	15.7
CHOP166A	19.7	23.1	26.6	11.4	15.0	22.4	5.2	10.8	20.5	13.4	16.4	19.5
CHOP181A	21.6	24.3	27.6	13.7	15.7	18.9	8.3	14.2	22.7	9.5	12.9	19.1
CHOP187A	29.7	36.5	43.1	16.9	19.5	22.6	9.2	14.1	27.2	17.3	18.7	21.9
CHOP188A	22.0	25.4	30.8	15.0	16.6	19.8	10.6	15.1	18.4	10.5	11.6	12.0
CHOP191A	18.2	19.1	20.6	11.2	12.5	15.0	9.7	11.2	13.5	13.4	13.8	14.4
CHOP203A	21.5	24.0	30.1	17.3	19.8	21.6	16.2	19.1	24.7	18.3	19.3	22.4
CHOP204A	13.4	16.4	22.7	13.8	15.3	19.2	12.9	15.4	20.7	16.4	17.2	18.0

Table A.2 (Continued)

CHOP_M11	15.7	20.6	23.8	12.7	13.9	14.7	4.1	8.4	14.2	8.7	10.5	13.8
CHOP_M12	15.6	17.1	18.1	7.0	7.7	9.5	8.4	9.4	10.1	6.5	9.5	13.9
CHOP_M7	11.8	14.6	17.0	11.2	12.9	16.8	11.9	12.5	14.2	10.4	12.4	14.6
CHOP_M8	12.5	13.2	15.2	7.9	8.4	8.7	10.8	11.7	14.2	10.0	10.3	10.6
CBF010	15.4	17.2	18.4	10.5	11.2	12.5	8.5	9.9	13.1	8.1	9.6	12.9
CBF033	15.3	17.9	19.1	11.9	13.5	15.0	5.5	8.5	14.8	9.1	10.2	11.4
CBF040	12.2	14.9	17.5	10.6	11.4	13.0	5.9	9.2	14.4	7.4	9.4	11.6
CBF043	15.3	16.7	18.0	10.4	11.5	12.9	7.6	10.2	14.0	8.8	9.2	10.1
CBF051	12.7	14.1	15.3	11.2	12.2	13.0	5.7	7.5	12.7	9.7	10.5	11.4
CBF057	13.6	15.4	19.0	11.5	13.7	17.0	9.1	12.4	19.8	7.2	10.0	15.0
CBF058	14.7	17.2	19.7	11.4	12.5	14.3	5.9	8.7	13.7	9.6	10.6	12.5
CBF059	13.5	14.4	17.2	13.0	13.9	14.6	6.9	9.0	11.9	7.2	8.3	10.9
CBF063	12.2	14.5	17.4	10.8	11.4	11.8	6.7	7.6	10.4	7.0	7.5	7.9
CBF069	14.8	16.5	16.8	10.0	11.3	12.1	6.4	8.1	11.8	8.2	8.3	8.8
CBF070	16.3	17.8	19.1	12.1	13.0	13.5	5.3	6.9	10.2	7.2	9.1	13.1
CBF071	13.2	15.7	18.9	11.3	13.4	17.6	5.7	10.7	17.1	10.0	13.0	17.7
CBF075	13.7	16.9	20.3	8.8	11.2	13.2	5.6	8.1	12.4	9.5	10.8	13.8
CBF083	15.8	17.6	21.0	10.4	11.4	12.3	6.4	8.2	12.0	8.4	8.7	8.8
CBF093	13.0	16.1	18.3	11.2	12.7	15.3	9.0	10.9	15.1	8.8	9.0	9.1
CBF100	13.9	16.8	19.6	9.0	12.2	15.0	4.8	9.6	18.1	7.6	9.8	14.5
CBF112	15.3	16.3	17.5	13.3	14.0	14.8	7.4	9.3	14.3	8.1	10.2	14.5
Average	15.5	18.4	22.1	12.6	14.4	17.0	8.2	11.2	16.8	10.2	12.3	16.0
Standard deviation	3.2	3.8	5.2	2.7	3.2	4.2	2.6	2.6	4.4	2.7	2.9	4.3

CBF =cerebral blood flow cohort from CHOP

Table A. 3 Absolute Vessel Diameter for RUPA. LSVC and AZ (mm)

Patient ID	RUPA diameter			LSVC diameter			AZ diameter			Only have 4 typical TCPC vessels (Y/N)
	Min	Mean	Max	Min	Mean	Max	Min	Mean	Max	
CHOP001B										Y
CHOP004B										Y
CHOP005B	8.9	10.6	13.3							Y
CHOP007B				10.1	11.0	13.3				N
CHOP008A										Y
CHOP014A	9.0	13.9	19.3							Y
CHOP016A										Y
CHOP017B										Y
CHOP018A										Y
CHOP019A	8.4	9.0	11.3							Y
CHOP021A	8.0	9.2	10.3							Y
CHOP022A	5.4	5.6	6.2	7.9	9.1	9.8				N
CHOP023A							8.5	9.6	16.5	N
CHOP024A										Y
CHOP025A				8.1	11.5	14.6				N
CHOP026A										Y
CHOP028A	6.8	7.5	8.9							Y
CHOP029A	8.8	9.0	9.5							Y
CHOP031A										Y
CHOP032A	8.9	11.9	17.5							Y
CHOP033A	4.1	7.0	12.9							Y
CHOP034A										Y
CHOP035A										Y
CHOP036A										Y
CHOP037A	5.9	6.7	9.1							Y
CHOP039A										Y
CHOP040A										Y
CHOP041A	7.1	7.8	8.9							Y
CHOP042B				13.4	14.8	16.5	5.6	6.5	10.6	N
CHOP046B										Y
CHOP051B				8.6	10.0	10.4				N
CHOP052B	6.1	6.3	6.4							Y
CHOP053B										Y
CHOP054A										Y
CHOP057A										Y
CHOP061A										Y
CHOP062A										Y
CHOP063A										Y
CHOP064A										Y
CHOP065A										Y
CHOP068B										Y
CHOP069B										Y
CHOP072A										Y
CHOP073A										Y
CHOP074A										Y

Table A.3 (Continued)

CHOP080A				10.0	12.7	15.5				N
CHOP081A										Y
CHOP082A										Y
CHOP083A										Y
CHOP084A										Y
CHOP085A	5.0	8.2	12.9							Y
CHOP086A				11.5	12.0	12.1				N
CHOP087A										Y
CHOP088A										Y
CHOP089A										Y
CHOP091A	4.6	5.5	8.0	9.5	10.7	12.6				N
CHOP094A										Y
CHOP097A	4.9	8.5	14.6							Y
CHOP100A										Y
CHOP102A				10.7	11.6	12.8				N
CHOP103A										Y
CHOP105A										Y
CHOP108A										Y
CHOP109B										Y
CHOP114A										Y
CHOP118A	6.9	7.3	7.6							Y
CHOP119A	5.1	6.5	7.9							Y
CHOP121A										Y
CHOP122A	6.9	7.1	7.3	6.0	7.7	9.3				N
CHOP128A										Y
CHOP134A										Y
CHOP135A	4.9	5.8	8.0	8.1	9.0	9.6				N
CHOP139A	6.2	7.8	10.3							Y
CHOP144C				9.4	11.5	14.8	8.7	11.3	13.7	N
CHOP145A										Y
CHOP148A	5.9	6.1	6.4							Y
CHOP152A	5.8	8.5	12.3							Y
CHOP155A	8.8	12.4	19.2							Y
CHOP159A										Y
CHOP161A										Y
CHOP166A										Y
CHOP181A										Y
CHOP187A										Y
CHOP188A	6.0	11.2	16.0							Y
CHOP191A										Y
CHOP203A										Y
CHOP204A	6.9	7.8	10.9							Y
CHOP_M11	6.0	8.9	13.5							Y
CHOP_M12				5.7	6.0	6.5				N
CHOP_M7				7.1	8.3	14.3	11.0	13.0	15.3	N
CHOP_M8				7.8	11.2	15.0	8.5	10.5	11.7	N
CBF010	5.2	6.0	6.7							Y

CBF033	4.9	5.7	7.0							Y
CBF040	4.5	4.7	5.0							Y
CBF043										Y
CBF051	4.5	5.5	6.9							Y
CBF057	5.4	6.1	6.9							Y
CBF058	7.8	8.5	9.1							Y
CBF059										Y
CBF063										Y
CBF069										Y
CBF070	6.0	6.4	7.0							Y
CBF071										Y
CBF075										Y
CBF083	6.5	6.9	7.2							Y
CBF093	5.2	5.4	5.5							Y
CBF100	5.1	5.3	5.4							Y
CBF112										Y
Average	6.3	7.7	9.9	8.9	10.5	12.5	8.5	10.2	13.6	
Standard deviation	1.5	2.2	3.9	2.1	2.2	2.8	1.9	2.4	2.4	

CBF =cerebral blood flow cohort from CHOP

Normalized vessel diameter = absolute vessel diameter divided by square root of patient's BSA

Table A. 4 Normalized Vessel Diameter for FP, SVC, LPA and RPA (mm/m)

Patient ID	FP diameter			SVC diameter			LPA diameter			RPA diameter		
	Min	Mean	Max	Min	Mean	Max	Min	Mean	Max	Min	Mean	Max
CHOP001B	15.6	19.8	22.4	10.2	13.3	18.0	6.5	8.7	15.4	9.7	11.4	15.1
CHOP004B	12.2	15.9	20.1	9.4	11.0	13.9	9.4	11.5	14.6	5.7	7.5	11.8
CHOP005B	15.2	21.1	26.4	8.1	10.1	11.7	6.8	9.7	13.6	10.8	11.4	12.7
CHOP007B	13.3	16.1	18.9	7.1	9.1	13.9	6.3	7.7	9.2	9.2	10.4	11.9
CHOP008A	14.7	17.9	23.3	11.5	14.2	19.2	5.2	9.2	17.3	9.4	12.1	16.2
CHOP014A	16.1	18.6	22.0	12.9	14.5	20.5	8.6	12.4	19.4	11.5	13.7	19.1
CHOP016A	14.1	17.3	20.7	14.8	15.5	16.1	5.0	7.8	15.2	11.9	12.7	14.1
CHOP017B	11.5	13.9	19.1	11.2	12.2	12.9	4.3	7.5	11.6	11.5	12.4	14.2
CHOP018A	20.3	21.5	23.2	14.1	14.9	16.6	10.6	14.1	22.6	10.4	12.2	16.3
CHOP019A	12.2	16.0	19.1	9.0	11.8	16.2	5.9	8.8	15.9	9.0	13.4	18.1
CHOP021A	12.4	15.1	18.2	9.4	10.3	12.3	4.7	9.3	17.8	8.4	9.3	11.8
CHOP022A	15.1	16.0	17.4	11.2	13.3	17.7	8.0	8.4	8.5	10.0	11.5	15.2
CHOP023A	7.1	11.8	20.9	12.4	14.7	17.8	9.2	13.6	18.6	6.9	11.6	21.0
CHOP024A	17.4	19.6	23.4	15.2	17.4	19.2	6.7	12.5	21.8	10.3	15.2	22.9
CHOP025A	9.4	10.7	13.3	7.8	8.6	10.4	7.0	9.5	15.0	10.5	11.8	12.5
CHOP026A	20.6	21.9	23.4	12.9	15.1	15.7	4.9	10.3	21.4	8.5	10.1	17.2
CHOP028A	11.6	14.6	18.3	9.7	11.1	14.2	4.8	6.6	12.4	10.0	11.9	14.0
CHOP029A	15.6	19.8	23.2	14.3	15.8	17.7	6.8	10.9	20.9	7.8	11.4	20.0
CHOP031A	18.6	20.2	23.6	12.8	13.5	14.5	12.3	16.0	20.5	10.8	11.7	13.3
CHOP032A	8.3	11.4	19.2	10.8	12.4	15.4	5.7	8.6	15.5	8.6	10.8	15.1
CHOP033A	14.1	15.2	18.1	10.4	12.7	16.7	10.3	12.6	14.9	10.5	13.0	16.8
CHOP034A	10.1	13.8	17.0	12.0	13.9	16.7	5.7	9.2	16.1	7.4	11.0	17.3
CHOP035A	14.0	17.8	23.0	14.6	15.5	17.0	12.7	13.5	14.3	15.1	16.2	17.4
CHOP036A	14.0	18.0	23.6	11.4	12.7	15.4	11.1	12.6	15.5	9.0	12.0	15.6
CHOP037A	11.8	15.1	21.4	11.6	13.6	17.8	4.2	9.5	20.0	8.4	11.3	18.4
CHOP039A	17.1	20.1	22.2	14.2	16.4	19.3	7.8	12.5	17.6	6.6	10.0	15.9
CHOP040A	11.5	15.0	20.1	11.1	11.9	15.1	6.0	8.8	15.2	7.9	9.8	15.7
CHOP041A	14.6	17.1	21.6	10.1	11.0	11.7	5.2	7.4	13.7	9.1	11.2	17.6
CHOP042B	14.0	14.5	15.8	7.4	7.8	8.0	7.6	12.5	19.0	5.4	5.5	5.7
CHOP046B	15.5	16.8	18.5	10.1	11.2	14.1	6.0	9.3	15.7	11.8	13.4	14.7
CHOP051B	19.5	21.4	22.7	9.3	10.4	14.3	10.1	11.6	12.7	8.8	10.5	14.9
CHOP052B	13.6	14.7	16.0	13.4	13.5	13.7	8.7	11.8	14.8	6.4	7.5	9.8
CHOP053B	17.8	20.0	21.2	10.5	12.0	16.1	8.6	11.3	15.8	8.8	11.8	17.2
CHOP054A	27.6	31.2	34.0	19.9	23.5	26.2	12.6	18.0	28.0	14.8	20.1	25.2
CHOP057A	9.8	13.1	15.4	12.4	13.1	13.6	7.1	8.3	9.3	11.1	12.1	12.9
CHOP061A	20.6	23.8	26.1	14.6	16.7	21.5	6.4	12.1	23.5	11.8	14.8	20.9
CHOP062A	13.7	15.7	18.3	12.2	13.4	15.5	7.7	10.6	16.7	14.5	14.7	14.9
CHOP063A	12.0	13.6	18.9	12.8	15.4	17.5	9.1	12.1	16.7	9.1	10.3	12.7
CHOP064A	15.7	18.1	20.3	11.5	13.6	15.8	6.6	10.7	16.4	8.6	10.4	16.2
CHOP065A	14.8	18.1	24.2	13.8	15.7	19.9	12.1	15.8	20.5	10.6	11.4	13.7
CHOP068B	20.2	23.2	27.0	16.8	20.2	24.6	7.3	13.9	23.9	9.6	14.3	24.1
CHOP069B	18.4	22.7	27.3	11.6	16.4	22.8	6.5	13.9	24.6	9.8	13.8	23.4
CHOP072A	8.9	12.9	19.2	10.0	12.9	15.3	6.5	10.1	17.4	6.2	8.8	15.6
CHOP073A	13.2	17.2	22.7	13.7	14.8	15.3	9.9	12.3	15.7	11.8	12.9	14.2

CHOP074A	11.7	15.0	19.4	9.4	12.5	16.1	8.0	11.3	17.4	6.9	11.3	17.7
CHOP080A	7.5	12.0	18.2	12.7	16.3	19.5	6.7	7.4	8.5	7.5	12.7	19.4
CHOP081A	24.5	27.3	28.7	19.1	20.5	22.2	8.8	12.1	19.1	14.4	17.3	22.5
CHOP082A	18.6	19.7	21.2	14.7	15.8	17.1	9.3	13.5	19.6	11.9	12.6	14.1
CHOP083A	16.0	16.3	17.4	15.0	15.3	15.8	9.6	12.0	14.8	12.8	13.8	15.4
CHOP084A	15.7	19.1	22.5	15.6	15.7	15.8	10.4	13.6	18.1	8.8	10.8	12.9
CHOP085A	19.7	23.5	25.8	16.6	18.3	21.1	5.7	10.0	20.9	10.4	11.2	13.2
CHOP086A	17.0	18.7	20.8	7.9	9.6	13.3	7.2	8.5	10.6	11.5	12.5	13.9
CHOP087A	22.7	24.7	26.2	20.4	21.9	23.2	6.6	11.5	24.4	14.0	16.9	22.8
CHOP088A	13.8	15.4	16.9	11.8	12.7	13.8	8.0	10.4	13.7	6.7	7.6	9.8
CHOP089A	16.1	18.3	20.4	13.0	15.1	18.1	10.8	13.3	18.5	10.9	15.1	20.5
CHOP091A	12.0	14.4	16.7	6.5	8.5	11.6	9.0	9.4	9.7	7.9	9.8	12.9
CHOP094A	13.7	15.6	18.7	13.5	14.1	14.7	5.8	9.1	14.8	12.9	14.0	16.2
CHOP097A	21.0	22.7	24.6	16.6	18.1	19.6	4.6	10.3	19.9	12.6	15.1	19.3
CHOP100A	14.1	18.0	22.6	16.4	17.7	18.7	10.6	12.6	18.8	10.0	11.8	15.0
CHOP102A	12.0	13.9	19.6	8.8	11.2	18.4	10.3	10.5	10.6	12.0	14.3	19.0
CHOP103A	7.8	12.2	18.4	9.9	12.1	16.3	6.6	8.9	14.8	8.5	11.7	16.0
CHOP105A	18.1	19.6	21.7	13.0	15.8	20.2	7.0	12.9	22.8	9.6	12.8	17.6
CHOP108A	18.0	19.4	21.7	13.5	15.3	16.9	5.4	9.7	16.6	10.0	12.2	17.6
CHOP109B	17.4	21.4	23.5	14.3	14.7	15.4	8.9	11.7	16.3	8.0	11.2	16.2
CHOP114A	10.0	13.3	18.8	9.6	12.1	16.7	6.7	10.9	15.7	11.3	11.7	12.2
CHOP118A	17.1	18.4	20.7	12.4	13.4	15.4	6.8	10.3	16.9	9.6	12.1	16.0
CHOP119A	14.1	20.1	22.6	13.9	14.2	14.5	8.1	10.1	12.2	10.7	12.3	13.3
CHOP121A	14.1	16.2	17.8	13.9	14.2	15.1	7.3	9.3	14.4	11.5	12.9	14.9
CHOP122A	14.7	16.8	18.3	11.6	13.3	15.9	5.2	5.9	6.4	8.7	10.3	16.0
CHOP128A	18.1	19.6	21.4	13.7	14.9	17.6	13.7	16.2	18.4	13.3	14.9	18.0
CHOP134A	16.9	20.2	22.2	11.9	13.5	15.9	7.6	12.1	17.2	10.6	11.9	15.6
CHOP135A	17.3	18.9	19.4	11.3	12.2	14.9	6.8	7.4	9.4	7.6	10.3	14.6
CHOP139A	16.8	19.6	23.5	12.4	13.9	17.3	7.4	11.3	17.4	12.8	14.6	17.5
CHOP144C	10.8	14.2	16.5	9.7	11.1	12.4	12.9	13.3	14.0	7.1	8.4	11.5
CHOP145A	12.1	15.7	22.0	13.7	14.8	15.5	10.3	14.1	20.5	11.5	12.8	15.2
CHOP148A	16.9	20.5	23.1	14.9	15.5	15.8	7.2	9.1	13.8	7.2	9.1	12.6
CHOP152A	15.8	21.7	30.4	11.5	18.8	23.0	6.8	7.9	10.4	8.9	10.6	12.7
CHOP155A	11.4	14.0	17.1	13.3	14.1	15.7	10.5	12.3	16.4	7.9	9.4	13.3
CHOP159A	12.9	18.9	28.1	10.7	13.5	18.9	6.8	10.2	19.7	7.8	11.7	20.0
CHOP161A	10.2	11.3	16.4	13.8	14.3	14.6	9.1	9.7	10.3	6.8	9.3	12.2
CHOP166A	16.6	19.5	22.4	9.6	12.6	18.9	4.4	9.1	17.3	11.3	13.8	16.4
CHOP181A	16.5	18.5	21.1	10.5	12.0	14.4	6.3	10.8	17.3	7.3	9.8	14.5
CHOP187A	23.2	28.5	33.6	13.2	15.2	17.6	7.2	11.0	21.2	13.5	14.6	17.1
CHOP188A	17.9	20.7	25.1	12.2	13.5	16.1	8.6	12.3	15.0	8.5	9.4	9.8
CHOP191A	16.3	17.1	18.5	10.0	11.2	13.5	8.7	10.1	12.0	12.0	12.4	12.9
CHOP203A	15.5	17.3	21.7	12.5	14.3	15.5	11.7	13.8	17.8	13.1	13.9	16.1
CHOP204A	10.9	13.3	18.5	11.2	12.5	15.7	10.5	12.5	16.8	13.3	14.0	14.6
CHOP_M11	15.5	20.3	23.4	12.5	13.7	14.5	4.0	8.2	14.0	8.5	10.4	13.6
CHOP_M12	23.0	25.2	26.8	10.4	11.3	14.0	12.3	13.8	14.9	9.5	14.0	20.5
CHOP_M7	11.0	13.6	15.8	10.4	12.0	15.6	11.0	11.6	13.2	9.7	11.5	13.6
CHOP_M8	13.2	14.0	16.1	8.4	8.9	9.2	11.4	12.4	15.1	10.6	10.9	11.2
CBF010	20.6	23.0	24.5	14.0	15.0	16.8	11.4	13.3	17.5	10.8	12.8	17.2

CBF033	17.0	19.9	21.2	13.2	15.0	16.7	6.1	9.4	16.4	10.1	11.3	12.7
CBF040	15.5	18.9	22.2	13.5	14.5	16.5	7.4	11.7	18.3	9.4	12.0	14.7
CBF043	18.4	20.1	21.7	12.5	13.8	15.5	9.2	12.3	16.8	10.6	11.1	12.1
CBF051	15.8	17.6	19.2	14.0	15.3	16.3	7.2	9.4	15.8	12.1	13.1	14.3
CBF057	17.4	19.7	24.3	14.7	17.6	21.8	11.7	15.9	25.3	9.2	12.8	19.2
CBF058	19.1	22.4	25.6	14.8	16.2	18.7	7.7	11.3	17.8	12.5	13.8	16.3
CBF059	15.6	16.6	19.9	15.0	16.1	16.8	8.0	10.4	13.7	8.3	9.5	12.5
CBF063	15.1	18.0	21.6	13.4	14.1	14.6	8.4	9.4	12.9	8.6	9.3	9.8
CBF069	17.1	19.0	19.5	11.5	13.0	14.0	7.4	9.4	13.6	9.5	9.6	10.2
CBF070	22.8	24.9	26.7	16.9	18.2	18.9	7.4	9.7	14.3	10.1	12.8	18.3
CBF071	15.9	18.9	22.7	13.6	16.1	21.2	6.8	12.9	20.6	12.1	15.7	21.3
CBF075	18.0	22.3	26.6	11.6	14.8	17.4	7.3	10.6	16.3	12.4	14.2	18.1
CBF083	20.1	22.3	26.7	13.2	14.5	15.7	8.1	10.4	15.3	10.6	11.0	11.2
CBF093	15.5	19.1	21.7	13.3	15.0	18.2	10.7	12.9	17.9	10.5	10.7	10.8
CBF100	16.7	20.3	23.6	10.8	14.7	18.0	5.7	11.6	21.8	9.2	11.8	17.4
CBF112	19.2	20.5	22.1	16.8	17.6	18.7	9.3	11.7	18.0	10.2	12.9	18.2
Average	15.5	18.2	21.5	12.4	14.1	16.5	8.0	11.0	16.4	10.0	12.0	15.6
Standard deviation	3.8	3.8	3.7	2.6	2.7	3.0	2.2	2.2	3.9	2.1	2.2	3.4

CBF =cerebral blood flow cohort from CHOP

Normalized vessel diameter = absolute vessel diameter divided by square root of patient's BSA

Table A. 5 Normalized Vessel Diameter for RUPA. LSVC and AZ (mm/m) and relative LPA area

Patient ID	RUPA diameter			LSVC diameter			AZ diameter			Relative LPA area
	Min	Mean	Max	Min	Mean	Max	Min	Mean	Max	
CHOP001B										0.31
CHOP004B										0.73
CHOP005B	7.3	8.6	10.8							0.28
CHOP007B				7.1	7.8	9.4				0.32
CHOP008A										0.23
CHOP014A	8.9	13.6	18.9							0.36
CHOP016A										0.15
CHOP017B										0.12
CHOP018A										0.51
CHOP019A	6.5	6.9	8.7							0.30
CHOP021A	7.2	8.3	9.3							0.24
CHOP022A	5.7	5.9	6.5	8.3	9.6	10.3				0.39
CHOP023A							7.7	8.7	15.0	0.64
CHOP024A										0.30
CHOP025A				8.0	11.4	14.6				0.31
CHOP026A										0.25
CHOP028A	4.9	5.4	6.4							0.19
CHOP029A	8.4	8.6	9.2							0.43
CHOP031A										0.56
CHOP032A	6.9	9.3	13.7							0.31
CHOP033A	3.6	6.1	11.2							0.49
CHOP034A										0.38
CHOP035A										0.41
CHOP036A										0.60
CHOP037A	5.9	6.7	9.1							0.20
CHOP039A										0.58
CHOP040A										0.36
CHOP041A	5.8	6.4	7.3							0.24
CHOP042B				17.0	18.8	21.0	7.1	8.3	13.5	0.66
CHOP046B										0.21
CHOP051B				10.8	12.6	13.1				0.57
CHOP052B	6.0	6.2	6.3							0.65
CHOP053B										0.49
CHOP054A										0.42
CHOP057A										0.29
CHOP061A										0.23
CHOP062A										0.22
CHOP063A										0.50
CHOP064A										0.37
CHOP065A										0.57
CHOP068B										0.37
CHOP069B										0.30
CHOP072A										0.53
CHOP073A										0.41
CHOP074A										0.57
CHOP080A				7.3	9.2	11.2				0.44

CHOP081A										0.27
CHOP082A										0.38
CHOP083A										0.36
CHOP084A										0.58
CHOP085A	7.1	11.6	18.3							0.23
CHOP086A				12.8	13.3	13.5				0.28
CHOP087A										0.18
CHOP088A										0.59
CHOP089A										0.50
CHOP091A	3.2	3.8	5.5	6.6	7.4	8.7				0.56
CHOP094A										0.17
CHOP097A	6.0	10.3	17.9							0.12
CHOP100A										0.53
CHOP102A				8.5	9.2	10.1				0.42
CHOP103A										0.38
CHOP105A										0.35
CHOP108A										0.23
CHOP109B										0.55
CHOP114A										0.26
CHOP118A	7.9	8.3	8.7							0.33
CHOP119A	5.9	7.5	9.1							0.36
CHOP121A										0.28
CHOP122A	5.6	5.8	6.0	4.9	6.3	7.5				0.27
CHOP128A										0.52
CHOP134A										0.34
CHOP135A	5.6	6.6	9.2	9.3	10.2	10.9				0.44
CHOP139A	5.7	7.1	9.5							0.25
CHOP144C				10.8	13.3	17.1	10.0	13.0	15.8	0.77
CHOP145A										0.45
CHOP148A	6.9	7.1	7.5							0.50
CHOP152A	4.2	6.2	8.9							0.37
CHOP155A	6.3	8.9	13.8							0.64
CHOP159A										0.43
CHOP161A										0.65
CHOP166A										0.13
CHOP181A										0.43
CHOP187A										0.22
CHOP188A	4.9	9.1	13.0							0.50
CHOP191A										0.34
CHOP203A										0.44
CHOP204A	5.6	6.4	8.8							0.38
CHOP_M11	5.9	8.8	13.3							0.18
CHOP_M12				8.4	8.9	9.6				0.63
CHOP_M7				6.6	7.7	13.3	10.2	12.1	14.2	0.57
CHOP_M8				8.3	11.9	15.9	9.0	11.2	12.5	0.54
CBF010	7.0	8.0	9.0							0.52
CBF033	5.4	6.4	7.8							0.27
CBF040	5.8	6.0	6.4							0.38
CBF043										0.43
CBF051	5.6	6.8	8.6							0.26
CBF057	6.9	7.8	8.9							0.62

CBF058	10.1	11.1	11.9							0.27
CBF059										0.48
CBF063										0.48
CBF069										0.38
CBF070	8.4	9.0	9.8							0.35
CBF071										0.24
CBF075										0.26
CBF083	8.3	8.8	9.1							0.37
CBF093	6.1	6.4	6.6							0.51
CBF100	6.2	6.3	6.4							0.28
CBF112										0.45
Average	6.3	7.7	9.8	9.0	10.5	12.4	8.8	10.7	14.2	0.39
Standard deviation	1.4	1.9	3.4	3.0	3.2	3.6	1.4	2.1	1.3	0.15

CBF =cerebral blood flow cohort from CHOP

Minimum/maximum diameter ratio = (minimum diameter) / (maximum diameter)

Table A. 6 Minimum/Maximum Diameter Ratio (mm/mm)

Patient ID	FP	SVC	LPA	RPA	RUPA	LSVC	AZ
CHOP001B	0.70	0.57	0.42	0.65			
CHOP004B	0.61	0.68	0.64	0.48			
CHOP005B	0.58	0.69	0.50	0.85	0.67		
CHOP007B	0.70	0.51	0.68	0.78		0.76	
CHOP008A	0.63	0.60	0.30	0.58			
CHOP014A	0.73	0.63	0.44	0.61	0.47		
CHOP016A	0.68	0.92	0.33	0.84			
CHOP017B	0.60	0.87	0.37	0.81			
CHOP018A	0.87	0.85	0.47	0.64			
CHOP019A	0.64	0.56	0.37	0.50	0.74		
CHOP021A	0.68	0.77	0.26	0.71	0.78		
CHOP022A	0.87	0.63	0.94	0.66	0.87	0.81	
CHOP023A	0.34	0.70	0.50	0.33			0.51
CHOP024A	0.74	0.79	0.31	0.45			
CHOP025A	0.71	0.75	0.47	0.84		0.55	
CHOP026A	0.88	0.82	0.23	0.50			
CHOP028A	0.63	0.68	0.39	0.72	0.77		
CHOP029A	0.67	0.81	0.32	0.39	0.92		
CHOP031A	0.78	0.88	0.60	0.82			
CHOP032A	0.43	0.70	0.37	0.57	0.51		
CHOP033A	0.78	0.62	0.69	0.62	0.32		
CHOP034A	0.59	0.72	0.36	0.42			
CHOP035A	0.61	0.86	0.88	0.86			
CHOP036A	0.59	0.74	0.72	0.58			
CHOP037A	0.55	0.66	0.21	0.46	0.64		
CHOP039A	0.77	0.74	0.44	0.42			
CHOP040A	0.57	0.73	0.39	0.51			
CHOP041A	0.68	0.87	0.38	0.52	0.80		
CHOP042B	0.89	0.92	0.40	0.96		0.81	0.52
CHOP046B	0.84	0.72	0.38	0.80			
CHOP051B	0.86	0.65	0.79	0.59		0.82	
CHOP052B	0.85	0.98	0.58	0.65	0.95		
CHOP053B	0.84	0.65	0.54	0.51			
CHOP054A	0.81	0.76	0.45	0.59			
CHOP057A	0.64	0.92	0.76	0.86			
CHOP061A	0.79	0.68	0.27	0.57			
CHOP062A	0.75	0.79	0.46	0.98			
CHOP063A	0.63	0.73	0.55	0.72			
CHOP064A	0.77	0.73	0.40	0.53			
CHOP065A	0.61	0.69	0.59	0.77			
CHOP068B	0.75	0.69	0.31	0.40			
CHOP069B	0.68	0.51	0.26	0.42			
CHOP072A	0.47	0.66	0.38	0.40			
CHOP073A	0.58	0.90	0.63	0.83			
CHOP074A	0.60	0.58	0.46	0.39			
CHOP080A	0.41	0.65	0.79	0.39		0.65	
CHOP081A	0.85	0.86	0.46	0.64			

CHOP082A	0.88	0.86	0.47	0.85			
CHOP083A	0.92	0.95	0.65	0.83			
CHOP084A	0.70	0.99	0.58	0.68			
CHOP085A	0.76	0.79	0.27	0.79	0.39		
CHOP086A	0.82	0.60	0.68	0.83		0.95	
CHOP087A	0.86	0.88	0.27	0.61			
CHOP088A	0.82	0.86	0.59	0.69			
CHOP089A	0.79	0.72	0.58	0.53			
CHOP091A	0.72	0.56	0.93	0.61	0.57	0.76	
CHOP094A	0.73	0.92	0.39	0.79			
CHOP097A	0.85	0.84	0.23	0.65	0.33		
CHOP100A	0.62	0.88	0.57	0.67			
CHOP102A	0.61	0.48	0.97	0.63		0.84	
CHOP103A	0.42	0.61	0.44	0.53			
CHOP105A	0.83	0.65	0.31	0.55			
CHOP108A	0.83	0.80	0.32	0.57			
CHOP109B	0.74	0.93	0.55	0.50			
CHOP114A	0.53	0.57	0.43	0.93			
CHOP118A	0.83	0.80	0.40	0.60	0.91		
CHOP119A	0.62	0.96	0.66	0.80	0.65		
CHOP121A	0.79	0.92	0.50	0.78			
CHOP122A	0.81	0.73	0.82	0.54	0.93	0.65	
CHOP128A	0.84	0.78	0.75	0.74			
CHOP134A	0.76	0.75	0.44	0.68			
CHOP135A	0.89	0.76	0.72	0.52	0.61	0.85	
CHOP139A	0.72	0.71	0.43	0.73	0.60		
CHOP144C	0.65	0.78	0.92	0.62		0.63	0.64
CHOP145A	0.55	0.89	0.50	0.75			
CHOP148A	0.73	0.94	0.52	0.57	0.92		
CHOP152A	0.52	0.50	0.66	0.70	0.47		
CHOP155A	0.67	0.84	0.64	0.59	0.46		
CHOP159A	0.46	0.57	0.34	0.39			
CHOP161A	0.62	0.95	0.89	0.55			
CHOP166A	0.74	0.51	0.25	0.69			
CHOP181A	0.78	0.73	0.36	0.50			
CHOP187A	0.69	0.75	0.34	0.79			
CHOP188A	0.71	0.76	0.57	0.87	0.38		
CHOP191A	0.88	0.74	0.72	0.93			
CHOP203A	0.71	0.80	0.66	0.81			
CHOP204A	0.59	0.72	0.62	0.91	0.63		
CHOP_M11	0.66	0.86	0.29	0.63	0.44		
CHOP_M12	0.86	0.74	0.83	0.47		0.87	
CHOP_M7	0.69	0.66	0.84	0.71		0.50	0.72
CHOP_M8	0.82	0.91	0.76	0.94		0.52	0.72
CBF010	0.84	0.83	0.65	0.63	0.78		
CBF033	0.80	0.79	0.37	0.80	0.70		
CBF040	0.70	0.81	0.41	0.64	0.90		
CBF043	0.85	0.81	0.55	0.87			
CBF051	0.83	0.86	0.45	0.85	0.65		
CBF057	0.71	0.67	0.46	0.48	0.77		
CBF058	0.74	0.79	0.43	0.77	0.86		

CBF059	0.79	0.89	0.58	0.66			
CBF063	0.70	0.91	0.65	0.88			
CBF069	0.88	0.82	0.54	0.93			
CBF070	0.86	0.89	0.52	0.55	0.85		
CBF071	0.70	0.64	0.33	0.57			
CBF075	0.68	0.67	0.45	0.69			
CBF083	0.75	0.85	0.53	0.95	0.91		
CBF093	0.71	0.73	0.60	0.97	0.93		
CBF100	0.71	0.60	0.26	0.53	0.96		
CBF112	0.87	0.90	0.51	0.56			
Average	0.72	0.76	0.51	0.66	0.70	0.73	0.62
Standard deviation	0.12	0.12	0.18	0.16	0.20	0.14	0.10

CBF =cerebral blood flow cohort from CHOP

A.7.1.1.2.2. Connection Angle

Table A. 7 Connection Angle

Patient ID	Angles between (degree)					
	FP-LPA	FP-RPA	SVC-LPA	SVC_RPA	FP-SVC	LPA-RPA
CHOP001B	111	71	84	102	165	121
CHOP004B	121	95	96	93	116	132
CHOP005B	100	86	82	105	136	164
CHOP007B	101	106	122	77	122	54
CHOP008A	115	64	128	96	114	119
CHOP014A	110	84	104	120	121	117
CHOP016A	102	87	109	85	143	135
CHOP017B	95	103	87	83	129	162
CHOP018A	127	78	106	100	123	115
CHOP019A	122	108	102	110	111	102
CHOP021A	123	61	94	104	143	119
CHOP022A	85	92	129	74	145	106
CHOP023A	105	90	93	101	161	73
CHOP024A	121	110	117	127	105	76
CHOP025A	146	118	131	105	83	64
CHOP026A	125	88	104	108	131	82
CHOP028A	128	119	107	114	93	95
CHOP029A	114	92	106	115	134	84
CHOP031A	133	80	84	105	140	108
CHOP032A	111	91	98	101	128	131
CHOP033A	123	97	80	91	147	119
CHOP034A	115	89	108	92	135	104
CHOP035A	91	90	93	97	172	96
CHOP036A	111	76	81	98	114	173
CHOP037A	114	98	108	114	112	111
CHOP039A	117	80	106	88	137	111
CHOP040A	113	109	130	117	97	90
CHOP041A	104	77	97	111	156	99
CHOP042B	89	57	120	66	110	82
CHOP046B	128	108	126	114	105	60
CHOP051B	51	77	128	90	167	75
CHOP052B	101	104	92	72	162	138
CHOP053B	114	93	114	90	126	115
CHOP054A	94	75	102	93	162	100
CHOP057A	82	92	92	92	173	107
CHOP061A	128	78	94	101	135	112
CHOP062A	115	111	102	116	91	119
CHOP063A	97	82	116	99	127	134
CHOP064A	123	95	116	104	121	73
CHOP065A	113	82	116	101	126	111
CHOP068B	115	82	95	104	151	77
CHOP069B	117	99	111	109	115	105
CHOP072A	119	55	82	107	154	103
CHOP073A	109	90	109	105	116	127
CHOP074A	114	96	112	121	125	80
CHOP080A	116	117	130	101	112	44

CHOP081A	96	91	112	81	149	132
CHOP082A	119	70	84	97	155	145
CHOP083A	76	96	113	88	144	155
CHOP084A	121	61	105	90	133	141
CHOP085A	101	75	114	108	143	102
CHOP086A	74	79	120	88	157	71
CHOP087A	108	91	99	121	137	93
CHOP088A	104	82	115	89	138	126
CHOP089A	119	101	83	108	132	113
CHOP091A	105	86	97	78	152	87
CHOP094A	125	129	110	111	104	75
CHOP097A	114	81	109	123	131	90
CHOP100A	111	90	111	94	123	127
CHOP102A	71	81	131	97	146	48
CHOP103A	104	92	84	114	130	139
CHOP105A	104	83	109	93	146	107
CHOP108A	117	88	88	97	155	92
CHOP109B	107	96	116	77	137	100
CHOP114A	83	68	93	130	159	122
CHOP118A	121	71	97	115	131	124
CHOP119A	90	75	105	105	148	143
CHOP121A	118	117	119	65	121	99
CHOP122A	121	73	114	99	118	76
CHOP128A	128	103	115	91	115	92
CHOP134A	105	85	116	94	132	121
CHOP135A	105	89	121	90	120	52
CHOP139A	106	105	122	114	103	105
CHOP144C	100	104	148	107	111	56
CHOP145A	126	89	103	120	125	88
CHOP148A	98	101	110	93	132	127
CHOP152A	92	57	132	90	135	133
CHOP155A	124	74	88	98	141	136
CHOP159A	106	90	101	97	144	117
CHOP161A	62	91	109	116	131	134
CHOP166A	99	107	125	101	107	117
CHOP181A	137	93	85	104	134	89
CHOP187A	108	72	91	92	161	138
CHOP188A	116	58	76	141	150	123
CHOP191A	116	73	69	121	158	131
CHOP203A	145	91	94	104	120	91
CHOP204A	126	88	94	98	108	138
CHOP_M11	122	93	96	106	140	82
CHOP_M12	123	98	99	58	126	75
CHOP_M7	90	112	111	119	118	101
CHOP_M8	110	89	124	61	113	86
CBF010	110	71	103	101	143	128
CBF033	106	78	114	96	135	124
CBF040	125	88	98	111	132	95
CBF043	107	87	100	77	150	147
CBF051	104	71	110	97	143	130

CBF057	111	75	116	102	131	108
CBF058	107	84	92	91	148	152
CBF059	111	56	89	106	160	149
CBF063	80	73	119	102	157	125
CBF069	101	82	99	93	160	102
CBF070	99	75	116	100	138	125
CBF071	112	107	103	98	135	92
CBF075	109	88	110	119	138	75
CBF083	101	57	107	100	151	141
CBF093	91	71	109	112	149	124
CBF100	111	87	129	114	110	96
CBF112	104	92	119	90	130	119
Average	109	87	106	100	133	108
Standard deviation	16	15	15	15	19	27

CBF =cerebral blood flow cohort from CHOP

Table A. 8 Connection Angle (Cont')

Patient ID	LSVC-LPA	LSVC-RPA	LSVC-SVC	LSVC-FP	AZ-FP	AZ-SVC	AZ-LPA	AZ-RPA	AZ-LSVC
	Angles between (degree)								
CHOP001B									
CHOP004B									
CHOP005B									
CHOP007B	90	125	98	121					
CHOP008A									
CHOP014A									
CHOP016A									
CHOP017B									
CHOP018A									
CHOP019A									
CHOP021A									
CHOP022A	113	117	43	137					
CHOP023A					133	47	99	59	
CHOP024A									
CHOP025A	91	136	65	103					
CHOP026A									
CHOP028A									
CHOP029A									
CHOP031A									
CHOP032A									
CHOP033A									
CHOP034A									
CHOP035A									
CHOP036A									
CHOP037A									
CHOP039A									
CHOP040A									
CHOP041A									
CHOP042B	129	128	63	141	96	78	43	53	118
CHOP046B									
CHOP051B	117	111	27	164					
CHOP052B									
CHOP053B									
CHOP054A									
CHOP057A									
CHOP061A									
CHOP062A									
CHOP063A									
CHOP064A									
CHOP065A									
CHOP068B									
CHOP069B									

CHOP072A								
CHOP073A								
CHOP074A								
CHOP080A	93	124	79	115				
CHOP081A								
CHOP082A								
CHOP083A								
CHOP084A								
CHOP085A								
CHOP086A	91	131	62	140				
CHOP087A								
CHOP088A								
CHOP089A								
CHOP091A	101	109	30	151				
CHOP094A								
CHOP097A								
CHOP100A								
CHOP102A	101	113	59	152				
CHOP103A								
CHOP105A								
CHOP108A								
CHOP109B								
CHOP114A								
CHOP118A								
CHOP119A								
CHOP121A								
CHOP122A	102	163	67	121				
CHOP128A								
CHOP134A								
CHOP135A	90	131	86	134				
CHOP139A								
CHOP144C	133	141	41	110	115	104	54	12	132
CHOP145A								
CHOP148A								
CHOP152A								
CHOP155A								
CHOP159A								
CHOP161A								
CHOP166A								
CHOP181A								
CHOP187A								
CHOP188A								
CHOP191A								
CHOP203A								

CHOP204A									
CHOP_M11									
CHOP_M12	76	110	66	151					
CHOP_M7	80	141	34	107	153	86	70	57	88
CHOP_M8	134	94	33	116	106	99	35	52	125
CBF010									
CBF033									
CBF040									
CBF043									
CBF051									
CBF057									
CBF058									
CBF059									
CBF063									
CBF069									
CBF070									
CBF071									
CBF075									
CBF083									
CBF093									
CBF100									
CBF112									
Average	103	125	57	131	121	83	60	47	116
Standard deviation	19	17	22	19	23	22	26	20	20

CBF =cerebral blood flow cohort from CHOP

A.7.1.1.2.3. Caval Offset

Normalized caval offset was computed by dividing caval offset by mean FP diameter

Table A. 9 Caval Offset

Patient ID	Absolute caval offset (mm)			with LSVC	Normalized caval offset (mm/mm)			with LSVC
	with SVC				with SVC			
	Offset	Magnitude	VC-PA	Magnitude	Offset	Magnitude	VC-PA	Magnitude
CHOP001B	5.7	5.7	0.2		0.26	0.26	0.01	
CHOP004B	2.8	2.8	7.2		0.15	0.15	0.37	
CHOP005B	6.5	6.5	0.0		0.25	0.25	0.00	
CHOP007B	3.8	3.8	7.4	37.6	0.16	0.16	0.32	1.64
CHOP008A	0.0	0.0	7.1		0.00	0.00	0.29	
CHOP014A	0.3	0.3	7.9		0.02	0.02	0.42	
CHOP016A	-3.2	3.2	0.8		-0.20	0.20	0.05	
CHOP017B	-6.1	6.1	0.3		-0.34	0.34	0.01	
CHOP018A	5.4	5.4	3.8		0.30	0.30	0.21	
CHOP019A	2.0	2.0	8.9		0.09	0.09	0.43	
CHOP021A	4.5	4.5	9.6		0.27	0.27	0.57	
CHOP022A	-2.5	2.5	1.2	36.6	-0.16	0.16	0.08	2.39
CHOP023A	0.0	0.0	7.3		0.00	0.00	0.56	
CHOP024A	5.9	5.9	10.1		0.35	0.35	0.60	
CHOP025A	17.7	17.7	0.0	4.6	1.65	1.65	0.00	0.43
CHOP026A	5.9	5.9	7.0		0.30	0.30	0.35	
CHOP028A	2.4	2.4	11.7		0.12	0.12	0.58	
CHOP029A	2.8	2.8	6.0		0.14	0.14	0.29	
CHOP031A	8.1	8.1	8.1		0.42	0.42	0.42	
CHOP032A	0.9	0.9	9.9		0.06	0.06	0.68	
CHOP033A	3.2	3.2	6.0		0.18	0.18	0.34	
CHOP034A	0.5	0.5	3.0		0.02	0.02	0.16	
CHOP035A	-32.6	32.6	0.0		-2.21	2.21	0.00	
CHOP036A	4.2	4.2	3.4		0.22	0.22	0.17	
CHOP037A	0.0	0.0	8.9		0.00	0.00	0.59	
CHOP039A	0.0	0.0	4.8		0.00	0.00	0.24	
CHOP040A	-0.5	0.5	17.2		-0.03	0.03	0.80	
CHOP041A	4.1	4.1	2.2		0.20	0.20	0.10	
CHOP042B	8.9	8.9	0.0	27.3	0.78	0.78	0.00	2.39
CHOP046B	0.2	0.2	10.5		0.01	0.01	0.53	
CHOP051B	-2.2	2.2	0.1	30.4	-0.13	0.13	0.01	1.79
CHOP052B	-7.9	7.9	0.0		-0.52	0.52	0.00	
CHOP053B	0.5	0.5	3.2		0.03	0.03	0.21	
CHOP054A	-0.6	0.6	6.9		-0.03	0.03	0.33	
CHOP057A	29.1	29.1	0.0		1.76	1.76	0.00	
CHOP061A	1.7	1.7	5.2		0.07	0.07	0.21	
CHOP062A	0.8	0.8	9.5		0.05	0.05	0.57	
CHOP063A	-1.3	1.3	2.4		-0.09	0.09	0.17	
CHOP064A	1.8	1.8	8.6		0.10	0.10	0.49	
CHOP065A	-2.1	2.1	10.3		-0.10	0.10	0.49	

CHOP068B	1.1	1.1	7.6		0.06	0.06	0.42	
CHOP069B	2.8	2.8	4.0		0.12	0.12	0.17	
CHOP072A	7.0	7.0	14.0		0.42	0.42	0.85	
CHOP073A	6.6	6.6	6.4		0.31	0.31	0.30	
CHOP074A	2.4	2.4	4.5		0.14	0.14	0.27	
CHOP080A	5.3	5.3	13.5	31.6	0.32	0.32	0.81	1.91
CHOP081A	-6.0	6.0	0.0		-0.30	0.30	0.00	
CHOP082A	3.8	3.8	5.2		0.20	0.20	0.29	
CHOP083A	-8.4	8.4	0.1		-0.48	0.48	0.00	
CHOP084A	3.2	3.2	0.1		0.17	0.17	0.00	
CHOP085A	0.0	0.0	5.5		0.00	0.00	0.33	
CHOP086A	3.7	3.7	0.0	21.4	0.22	0.22	0.00	1.27
CHOP087A	2.4	2.4	6.8		0.11	0.11	0.31	
CHOP088A	-7.2	7.2	0.0		-0.42	0.42	0.00	
CHOP089A	4.2	4.2	10.1		0.24	0.24	0.57	
CHOP091A	0.0	0.0	0.0	47.8	0.00	0.00	0.00	2.30
CHOP094A	-0.6	0.6	10.4		-0.04	0.04	0.61	
CHOP097A	3.9	3.9	6.0		0.21	0.21	0.32	
CHOP100A	-4.7	4.7	13.3		-0.20	0.20	0.57	
CHOP102A	4.5	4.5	7.5	41.2	0.26	0.26	0.43	2.34
CHOP103A	0.4	0.4	1.5		0.03	0.03	0.09	
CHOP105A	2.0	2.0	6.6		0.11	0.11	0.35	
CHOP108A	3.9	3.9	5.3		0.21	0.21	0.28	
CHOP109B	-2.8	2.8	5.4		-0.16	0.16	0.31	
CHOP114A	3.9	3.9	6.3		0.22	0.22	0.36	
CHOP118A	4.1	4.1	1.6		0.26	0.26	0.10	
CHOP119A	-5.4	5.4	0.0		-0.31	0.31	0.00	
CHOP121A	-3.4	3.4	2.6		-0.24	0.24	0.19	
CHOP122A	1.9	1.9	10.1	40.7	0.09	0.09	0.49	1.98
CHOP128A	1.3	1.3	7.1		0.07	0.07	0.38	
CHOP134A	-1.9	1.9	1.1		-0.12	0.12	0.07	
CHOP135A	0.0	0.0	4.6	30.9	0.00	0.00	0.28	1.87
CHOP139A	2.3	2.3	10.9		0.11	0.11	0.51	
CHOP144C	-0.7	0.7	5.1	38.8	-0.06	0.06	0.42	3.16
CHOP145A	7.1	7.1	9.4		0.37	0.37	0.49	
CHOP148A	-4.6	4.6	0.1		-0.26	0.26	0.00	
CHOP152A	10.5	10.5	0.0		0.35	0.35	0.00	
CHOP155A	4.9	4.9	7.7		0.25	0.25	0.39	
CHOP159A	-0.5	0.5	6.7		-0.02	0.02	0.26	
CHOP161A	5.5	5.5	3.9		0.38	0.38	0.27	
CHOP166A	0.5	0.5	11.6		0.02	0.02	0.50	
CHOP181A	4.2	4.2	11.9		0.17	0.17	0.49	
CHOP187A	5.4	5.4	0.1		0.15	0.15	0.00	
CHOP188A	-0.8	0.8	0.7		-0.03	0.03	0.03	
CHOP191A	10.2	10.2	0.1		0.53	0.53	0.00	
CHOP203A	5.0	5.0	13.0		0.21	0.21	0.54	
CHOP204A	1.8	1.8	5.9		0.11	0.11	0.36	
CHOP_M11	1.9	1.9	7.7		0.09	0.09	0.37	

CHOP_M12	-6.7	6.7	0.2	25.3	-0.39	0.39	0.01	1.48
CHOP_M7	30.2	30.2	0.0	0.5	2.07	2.07	0.00	0.03
CHOP_M8	1.9	1.9	1.8	38.4	0.14	0.14	0.14	2.91
CBF010	0.2	0.2	0.4		0.01	0.01	0.03	
CBF033	-3.5	3.5	3.2		-0.19	0.19	0.18	
CBF040	2.6	2.6	5.3		0.17	0.17	0.36	
CBF043	2.0	2.0	2.5		0.12	0.12	0.15	
CBF051	-0.5	0.5	0.0		-0.03	0.03	0.00	
CBF057	1.1	1.1	5.8		0.07	0.07	0.38	
CBF058	-1.4	1.4	0.0		-0.08	0.08	0.00	
CBF059	4.9	4.9	0.1		0.34	0.34	0.00	
CBF063	-8.5	8.5	0.0		-0.58	0.58	0.00	
CBF069	-0.8	0.8	0.2		-0.05	0.05	0.01	
CBF070	-2.3	2.3	1.3		-0.13	0.13	0.07	
CBF071	0.0	0.0	6.3		0.00	0.00	0.40	
CBF075	2.1	2.1	3.3		0.13	0.13	0.20	
CBF083	-7.3	7.3	0.1		-0.41	0.41	0.00	
CBF093	-3.7	3.7	0.3		-0.23	0.23	0.02	
CBF100	0.0	0.0	0.0		0.00	0.00	0.00	
CBF112	-2.4	2.4	2.1		-0.15	0.15	0.13	
Average	1.5	4.1	4.7	30.2	0.08	0.24	0.25	1.86
Standard deviation	6.6	5.3	4.2	13.2	0.43	0.36	0.22	0.83

CBF =cerebral blood flow cohort from CHOP

A.7.1.1.3. Computed Hemodynamic Parameters

$$iPL, = \frac{\dot{E}_{Loss}}{\rho Qs^3 / BSA^2}$$

Table A. 10 Hemodynamic Results under baseline condition

Patient ID	Cardiac Output (L/min)	Cardiac Index (L/min/m²)	Total systemic return (L/min)	%PFD(LPA)	%HFD(LPA)	Power Loss (mw)	iPL
CHOP001B	2.0	1.6	2.2	39	48	0.35	0.010
CHOP004B	5.6	3.8	4.1	56	71	6.69	0.044
CHOP005B	4.5	3.0	4.6	56	68	17.88	0.087
CHOP007B	8.4	4.2	6.9	28	17	9.63	0.024
CHOP008A	3.2	1.6	3.2	46	53	1.33	0.032
CHOP014A	3.8	3.6	2.2	59.	33.	0.77	0.016
CHOP016A	3.3	3.9	3.3	25.	3.	10.50	0.042
CHOP017B	5.1	3.1	3.7	16.	0.	3.38	0.035
CHOP018A	3.1	4.5	2.6	42.	67.	1.41	0.007
CHOP019A	5.5	3.3	5.0	41.	52.	7.43	0.035
CHOP021A	3.7	3.0	3.1	41	49	10.56	0.109
CHOP022A	3.4	3.7	2.6	49	33	1.70	0.016
CHOP023A	3.0	2.4	3.0	42	53	10.40	0.121
CHOP024A	2.7	3.6	2.6	43	58	3.06	0.021
CHOP025A	3.2	3.2	2.9	58	50	5.78	0.047
CHOP026A	3.1	3.7	2.1	40	79	4.66	0.072
CHOP028A	3.5	1.8	3.7	36	40	3.62	0.052
CHOP029A	4.0	3.7	3.6	22	40	3.58	0.019
CHOP031A	3.3	3.7	2.7	40	78	1.58	0.013
CHOP032A	5.8	3.5	4.7	42	43	22.20	0.120
CHOP033A	3.4	2.6	3.8	52	63	2.47	0.016
CHOP034A	8.2	4.3	5.0	43	41	18.15	0.103
CHOP035A	5.1	7.4	3.5	62	21	5.08	0.011
CHOP036A	4.2	3.5	5.2	55	71	7.57	0.015
CHOP037A	3.8	3.8	2.4	35	46	4.04	0.057
CHOP039A	3.9	3.9	4.4	48	52	7.75	0.019
CHOP040A	5.8	2.8	6.9	37	50	16.40	0.043
CHOP041A	4.0	2.7	2.8	37	21	1.17	0.025
CHOP042B	2.2	3.5	1.5	77	43	1.78	0.042
CHOP046B	4.4	3.2	3.9	31	44	3.76	0.024
CHOP051B	1.9	3.0	1.5	78	58	2.00	0.051
CHOP052B	5.8	5.5	3.3	44	21	3.35	0.022
CHOP053B	2.4	4.0	1.8	54	38	1.33	0.015
CHOP054A	2.1	4.5	2.0	21	17	0.66	0.003
CHOP057A	4.2	2.7	3.7	40	48	3.21	0.033
CHOP061A	5.0	4.4	4.4	59	52	9.56	0.028
CHOP062A	2.8	2.6	2.3	30	43	0.85	0.018
CHOP063A	3.7	3.5	3.5	50	71	5.76	0.032
CHOP064A	1.6	1.7	1.3	55	82	0.37	0.033
CHOP065A	3.3	2.5	2.4	35	39	0.47	0.013
CHOP068B	2.3	3.8	2.1	43	41	4.57	0.035
CHOP069B	3.2	2.9	3.1	46	65	2.24	0.020
CHOP072A	4.6	2.8	4.6	52	44	18.06	0.101

CHOP073A	3.9	2.5	3.6	46	60	1.39	0.015
CHOP074A	2.2	1.8	2.2	37	60	1.31	0.038
CHOP080A	5.6	2.9	4.4	53	29	11.80	0.106
CHOP081A	3.9	7.2	1.5	38	3	0.58	0.011
CHOP082A	2.7	3.1	2.6	40	57	1.38	0.013
CHOP083A	3.8	3.3	3.4	70	48	5.70	0.038
CHOP084A	3.0	3.0	3.3	52	72	1.41	0.008
CHOP085A	1.6	3.2	1.2	49	35	1.66	0.048
CHOP086A	2.9	3.6	3.7	36	4	7.63	0.020
CHOP087A	2.7	3.3	1.9	35	39	2.19	0.041
CHOP088A	3.4	2.7	2.7	52	27	4.20	0.070
CHOP089A	2.9	3.1	3.2	46	61	1.94	0.010
CHOP091A	5.0	2.4	5.3	46	33	5.25	0.032
CHOP094A	5.5	4.6	4.5	36	45	9.09	0.030
CHOP097A	2.3	3.4	2.3	22	30	2.63	0.020
CHOP100A	3.5	2.1	3.2	43	13	0.95	0.016
CHOP102A	4.7	2.9	4.6	42	31	6.32	0.034
CHOP103A	4.9	2.7	4.6	52	76	18.18	0.134
CHOP105A	3.9	4.1	3.0	33	44	2.56	0.018
CHOP108A	2.9	3.2	2.5	39	42	3.70	0.041
CHOP109B	2.6	4.1	2.7	51	5	3.20	0.015
CHOP114A	5.5	3.2	5.6	44	49	11.62	0.042
CHOP118A	3.3	4.2	2.2	27	44	1.26	0.014
CHOP119A	2.8	3.7	2.8	36	1	3.14	0.017
CHOP121A	2.2	2.9	1.9	53	38	2.09	0.034
CHOP122A	5.0	3.3	3.2	40	30	3.88	0.053
CHOP128A	3.7	4.0	3.7	37	60	1.44	0.005
CHOP134A	2.3	3.7	2.1	38	28	1.84	0.016
CHOP135A	3.2	4.1	2.4	39	30	4.32	0.037
CHOP139A	4.5	3.8	3.9	29	49	3.06	0.015
CHOP144C	1.8	2.4	1.8	59	0	1.88	0.037
CHOP145A	3.7	2.5	3.1	40	61	3.37	0.051
CHOP148A	2.5	3.4	1.8	42	39	1.25	0.024
CHOP152A	7.7	4.1	5.6	24	36	8.81	0.036
CHOP155A	7.5	3.9	7.0	54	56	30.00	0.067
CHOP159A	4.1	2.2	3.7	48	57	5.17	0.074
CHOP161A	7.6	4.6	5.4	54	66	11.28	0.039
CHOP166A	5.3	3.7	4.7	26	13	6.12	0.023
CHOP181A	7.0	4.1	4.9	36	54	8.95	0.045
CHOP187A	4.2	2.5	3.5	34	41	1.55	0.020
CHOP188A	5.3	3.5	3.3	58	50	0.82	0.010
CHOP191A	3.9	3.1	2.4	45	65	0.45	0.011
CHOP203A	6.7	3.4	5.2	47	46	1.91	0.010
CHOP204A	5.5	3.6	4.5	37	47	6.73	0.035
CHOP_M11	3.9	3.8	2.6	27	26	5.90	0.076
CHOP_M12	1.8	3.9	1.2	62	54	0.72	0.019
CHOP_M7	4.3	3.7	4.0	65	100	5.59	0.025
CHOP_M8	3.6	4.0	3.3	55	0	5.06	0.023
CBF010	2.2	3.9	2.7	55	40	0.76	0.002
CBF033	2.7	3.4	3.6	45	29	3.82	0.011
CBF040	2.0	3.3	2.7	28	60	0.48	0.002

CBF043	2.4	3.5	3.1	69	94	2.98	0.010
CBF051	2.9	4.6	3.6	31	21	1.08	0.002
CBF057	2.1	3.5	2.7	44	66	0.52	0.002
CBF058	3.2	5.4	3.8	35	12	2.18	0.003
CBF059	3.5	4.6	4.2	38	55	1.37	0.002
CBF063	2.5	3.8	3.1	24	0	1.13	0.003
CBF069	4.6	6.2	5.4	31	10	14.23	0.011
CBF070	1.9	3.7	2.4	40	18	3.50	0.014
CBF071	2.4	3.5	3.1	32	8	0.67	0.002
CBF075	2.7	4.6	3.3	58	79	2.85	0.006
CBF083	4.4	7.1	5.0	31	0	1.68	0.001
CBF093	3.8	5.3	4.5	44	0	4.01	0.004
CBF100	2.7	3.9	3.4	41	55	4.98	0.012
CBF112	3.3	5.2	3.9	55	24	3.81	0.005
Average	3.8	3.6	3.4	43	42	4.89	0.031
Standard deviation	1.5	1.0	1.2	12	22	5.17	0.028

CBF =cerebral blood flow cohort from CHOP

A.7.2. Detailed Results of Statistical Analysis in Specific Aim 1(a)

A.7.2.1. Resting iPL vs TCPC Geometry

Table A. 11 Significant correlations between iPL and independent variables

Independent variables correlated with iPL	Bivariate analysis		Multiple regression		
	Regression coefficient (r)	p	Standardized coefficient	Partial correlation (r)	p
(Normalized minimum diameter of FP) $^{-2.274}$	0.745	< 0.001	0.657	0.730	<0.001
(Normalized mean diameter of FP) $^{-2.474}$	0.619	<0.001			
(Normalized maximum diameter of FP) $^{-2.175}$	0.307	0.002			
(Normalized minimum diameter of SVC) $^{-1.808}$	0.253	0.01			
(Normalized mean diameter of SVC) $^{-1.792}$	0.221	0.024			
(Normalized minimum diameter of LPA) $^{-1.492}$	0.377	<0.001	0.324	0.496	<0.001
(Normalized mean diameter of LPA) $^{-1.989}$	0.339	<0.001			
(Normalized minimum diameter of RPA) $^{-1.893}$	0.422	<0.001	0.161	0.254	0.01
(Normalized mean diameter of RPA) $^{-1.581}$	0.251	0.01			
FP Minimum/maximum diameter ratio	-0.577	<0.001			
RPA Minimum/maximum diameter ratio	-0.331	0.001			
Normalized VC-PA offset	0.272	0.005			
			R^2 adjusted (Multiple regression)		**0.670**
			No. of observations*		**104**

* 4 outlier were excluded (CHOP_M7, CHOP025A, CHOP035A, CHOP057A)

A.7.2.2. Resting Cardiac Index vs TCPC Geometry

Table A. 12   Significant correlations between cardiac index and independent variables

Independent variables correlated with cardiac index	Bivariate analysis		Multiple regression		
	Regression coefficient (r)	p	Standardized coefficient	Partial correlation (r)	p
Normalized minimum diameter of FP	0.388	< 0.001	0.347	0.355	< 0.001
Normalized mean diameter of FP	0.313	0.001			
Normalized minimum diameter of SVC	0.321	0.001			
Normalized mean diameter of SVC	0.251	0.01			
FP Minimum/maximum diameter ratio	0.371	< 0.001			
SVC Minimum/maximum diameter ratio	0.280	0.004	0.215	0.229	0.02
Normalized caval offset with SVC	-0.253	0.009			
Normalized VC-PA offset	-0.293	0.003			
Angle between FP and SVC	0.198	0.044			
			R^2 adjusted (Multiple regression)		**0.195**
			No. of observations*		**104**

* 4 outlier were excluded (CHOP_M7, CHOP025A, CHOP035A, CHOP057A)

A.7.2.3.　Resting %PFD(LPA) vs TCPC Geometry

Table A. 13　Significant correlations between %PFD(LPA) and independent variables

Independent variables correlated with %PFD(LPA)	Bivariate analysis		Multiple regression		
	Regression coefficient (r)	p	Standardized coefficient	Partial correlation (r)	p
Normalized minimum diameter of LPA	0.356	< 0.001			
Normalized mean diameter of LPA	0.226	0.021			
Normalized minimum diameter of RPA	-0.285	0.003			
Normalized mean diameter of RPA	-0.288	0.003			
LPA Minimum/maximum diameter ratio	0.345	< 0.001			
Relative LPA area (%)	0.519	< 0.001	0.519	0.519	<0.001
Angle between SVC and RPA	-0.223	0.023			
No. of observations					**104***

* 4 outlier were excluded (CHOP_M7, CHOP025A, CHOP035A, CHOP057A)

A.7.2.4. Resting HFD vs TCPC Geometry

Table A. 14 Significant correlations between %HFD(LPA) and independent variables

Independent variables correlated with %HFD(LPA)	Bivariate analysis		Multiple regression		
	Regression coefficient (r)	p	Standardized coefficient	Partial correlation (r)	p
%PFD(LPA)	0.490	<0.001	0.466	0.624	<0.001
Normalized mean LPA diameter	0.240	0.023			
RPA Minimum/maximum diameter ratio	-0.222	0.035			
Normalized caval offset with SVC	0.639	<0.001	0.595	0.713	<0.001
Normalized VC-PA offset	0.242	0.022			
FP & LPA angle	0.405	<0.001			
SVC & LPA angle	-0.220	0.037			
SVC & RPA angle	0.267	0.011			
FP & SVC angle	-0.247	0.019	-0.209	-0.336	0.001
	R^2 adjusted (Multiple regression)				**0.649**
	No. of observations				**90***

* Excluded patients with LSVC and AZ

A.7.3. Raw Data and Detailed Statistical Results for Specific Aim 1(b)

A.7.3.1.　　　Complete List of Computed Geometry, Hemodynamic and Exercise Stress

Test Parameters (N=49)

A.7.3.1.1.　Patient Demographic Information

Table A. 15　Patient Demographic Information of the 49 patients included

Patient ID	Gender (M=male, F = female)	IVC connection type (IA/EC)	Left(LV)/ Right(RV)/ Mixed(MV) ventricle	Age (yrs)	Age group*	BSA (m^2)	Weight (kg)
CHOP004D	F	IA	LV	25.2	2	1.58	53.8
CHOP011B	F	IA	RV	21	2	1.64	62.9
CHOP014B	M	EC	RV	17	1	1.91	70.3
CHOP015B	M	EC	MV	22.3	2	1.85	63.6
CHOP017C	F	EC	LV	22	2	1.89	79.2
CHOP018C	M	IA	LV	15.8	1	1.25	34.1
CHOP019B	M	IA	RV	21	2	1.86	71.3
CHOP021C	F	IA	RV	21	2	1.75	69.8
CHOP023B	M	IA	LV	22	2	1.59	53.5
CHOP024B	F	IA	RV	15.3	1	1.36	44.1
CHOP025B	F	EC	LV	19	2	1.63	58.0
CHOP029B	M	IA	RV	19	2	1.74	64.3
CHOP030C	F	IA	RV	25.4	2	1.5	55.7
CHOP032B	F	IA	RV	26	2	1.53	49.3
CHOP039C	F	IA	RV	19	2	1.35	
CHOP046B	M	IA	RV	12.7	1	1.36	43.0
CHOP052E	M	EC	LV	15.1	1	1.62	54.1
CHOP061B	M	IA	RV	15	1	1.8	65.8
CHOP063B	F	EC	LV	14	1	1.52	52.1
CHOP069C	M	IA	RV	15.7	1	1.34	41.8
CHOP073B	F	IA	LV	26.7	2	1.6	61.1
CHOP082B	M	EC	LV	12	1	1.32	40.8
CHOP084B	M	EC	LV	14	1	1.63	56.2
CHOP088B	F	EC	RV	13.1	1	1.7	65.8
CHOP091B	M	IA	LV	23	2	1.8	103.6
CHOP100B	M	IA	LV	25.1	2	1.69	59.1
CHOP122B	M	IA	RV	21	2	1.69	59.5
CHOP128B	F	IA	RV	15.2	1	1.48	52.3
CHOP152A	M	IA	RV	18.9	1	1.89	74.3
CHOP155A	M	IA	LV	17.2	1	1.83	69.1
CHOP157A	M	IA	RV	15	1	1.72	64.5
CHOP159A	F	IA	MV	25.6	2	1.88	78.7
CHOP161A	F	EC	RV	16.1	1	1.66	59.3
CHOP166A	M	IA	RV	14.6	1	1.65	53.9
CHOP169C	M	IA	MV	19	2	1.81	63.8

CHOP173A	F	EC	MV	13.1	1	1.98	93.2
CHOP181A	M	IA	RV	25.6	2	1.76	61.9
CHOP185A	M	IA	LV	32.7	2	2.2	105.7
CHOP187A	F	IA	RV	42.2	2	1.64	59.4
CHOP188A	M	IA	LV	17.4	1	1.52	52.8
CHOP191A	F	EC	LV	16.3	1	1.25	36.7
CHOP197A	M	IA	RV	17	1	1.67	57.2
CHOP203A	M	IA	MV	16.2	1	1.93	73.3
CHOP204A	F	EC	LV	17.3	1	1.49	51.7
CHOP218A	F	IA	RV	12	1	1.22	34.7
CHOP224A	F	IA	RV	17	1	1.8	72.3
CHOP229A	M	IA	MV	22	2	1.92	84.6
CHOP234A	F	EC	LV	17	1	1.8	71.6
CHOP235A	M	IA	RV	19	2	1.77	63.0
Average				19.2		1.66	61.8
Standard deviation				5.6		0.21	15.4

*(1=Adolescents, 2= adults)

A.7.3.1.2.   Computed Geometric Parameters

A.7.3.1.2.1. Vessel Diameter

Table A. 16   Absolute Vessel Diameter for FP, SVC, LPA and RPA (mm)

Patient ID	FP diameter			SVC diameter			LPA diameter			RPA diameter		
	Min	Mean	Max	Min	Mean	Max	Min	Mean	Max	Min	Mean	Max
CHOP004D	14.3	19.8	24.5	12.7	14.1	16.7	13.9	14.7	15.5	8.4	10.6	16.6
CHOP011B	11.8	15.2	18.5	13.3	15.5	16.8	7.3	9.9	16.9	10.3	12.5	17.1
CHOP014B	18.8	23.0	29.8	13.8	16.0	23.8	8.5	12.5	22.4	15.3	18.2	22.4
CHOP015B	8.9	12.3	21.0	11.1	16.2	19.7	13.2	18.1	22.8	11.1	12.9	19.3
CHOP017C	13.3	16.6	24.3	15.3	16.1	16.6	5.3	9.1	16.2	17.6	19.1	20.7
CHOP018C	21.3	25.8	31.6	14.7	16.2	17.9	9.5	13.9	21.7	11.0	13.7	19.2
CHOP019B	19.5	23.2	26.5	16.1	18.3	22.7	11.3	17.1	24.3	16.4	18.4	22.2
CHOP021C	15.4	19.4	25.3	14.5	16.2	18.6	6.0	11.5	20.7	11.3	15.8	20.7
CHOP023B	13.6	17.0	24.0	14.8	17.1	20.9	11.9	15.3	21.0	11.3	14.0	23.4
CHOP024B	16.3	20.0	24.4	14.1	19.4	22.7	5.5	12.2	23.3	9.3	16.8	22.9
CHOP025B	8.5	10.4	15.0	10.0	11.3	14.1	8.4	11.2	19.2	8.8	11.4	15.6
CHOP029B	19.3	25.4	29.8	14.8	18.7	25.6	5.9	12.4	28.0	13.1	19.5	27.7
CHOP030C	18.3	21.3	24.2	10.6	12.3	13.8	7.2	8.9	12.3	15.8	17.2	18.8
CHOP032B	8.7	13.9	22.3	13.2	14.6	20.1	8.5	12.3	18.6	8.4	12.6	18.6
CHOP039C	18.1	22.0	27.6	12.9	14.4	17.2	10.3	13.5	18.8	8.5	11.1	17.5
CHOP046B	18.0	19.6	21.6	11.7	13.0	16.4	7.0	10.9	18.4	13.7	15.6	17.1
CHOP052E	15.0	15.3	15.8	13.1	13.4	14.5	9.0	12.8	16.0	8.8	10.0	11.9
CHOP061B	22.6	26.9	31.7	15.0	17.3	21.4	9.1	16.0	23.7	11.5	15.2	22.2
CHOP063B	11.6	13.3	20.0	13.3	18.0	22.3	13.6	14.0	14.2	9.2	12.5	18.8
CHOP069C	19.8	25.9	33.2	13.7	18.0	26.6	8.8	15.6	29.4	10.3	16.0	28.6
CHOP073B	12.3	19.7	26.9	10.9	16.3	18.9	13.4	14.6	18.1	13.5	14.5	15.1
CHOP082B	13.3	15.9	18.9	14.9	15.8	16.4	8.8	13.1	18.7	9.8	10.4	12.4
CHOP084B	13.9	16.5	21.7	12.1	12.8	15.2	12.7	15.2	16.1	9.0	10.4	13.7
CHOP088B	16.5	17.9	19.1	14.2	15.5	16.8	11.1	13.3	17.4	10.9	12.1	14.7
CHOP091B	20.5	24.5	28.0	11.6	13.9	17.5	13.9	14.3	14.6	13.8	16.6	20.6
CHOP100B	16.1	20.9	27.2	18.9	21.2	24.0	13.4	16.3	23.2	15.0	15.3	15.4
CHOP122B	18.3	20.0	22.2	14.8	15.6	16.6	5.2	6.0	7.4	9.7	11.9	21.9
CHOP128B	17.3	19.8	22.6	15.6	17.8	21.6	10.3	16.0	23.2	13.1	16.5	21.2
CHOP152A	21.7	29.9	41.8	15.9	25.9	31.6	9.4	10.8	14.3	12.2	14.6	17.4
CHOP155A	15.9	19.5	23.9	18.5	19.7	21.9	14.7	17.2	22.9	11.0	13.2	18.5
CHOP157A	21.6	25.2	29.6	19.8	24.0	27.0	12.6	14.9	25.2	14.1	17.5	27.2
CHOP159A	17.7	26.1	38.7	14.8	18.6	26.0	9.3	14.1	27.2	10.8	16.2	27.6
CHOP161A	13.1	14.5	21.1	17.8	18.4	18.8	11.7	12.4	13.2	8.7	11.9	15.7
CHOP166A	19.7	23.1	26.6	11.4	15.0	22.4	5.2	10.8	20.5	13.4	16.4	19.5
CHOP169C	12.2	16.9	22.4	9.3	15.2	20.9	14.9	16.7	19.3	10.3	12.7	22.3
CHOP173A	17.4	20.1	25.9	7.4	9.9	11.7	9.5	11.2	13.5	9.4	10.3	11.5

CHOP181A	21.6	24.3	27.6	13.7	15.7	18.9	8.3	14.2	22.7	9.5	12.9	19.1
CHOP185A	27.9	32.1	40.4	22.1	28.3	32.4	11.4	21.0	39.4	13.2	18.4	28.8
CHOP187A	29.7	36.5	43.1	16.9	19.5	22.6	9.2	14.1	27.2	17.3	18.7	21.9
CHOP188A	22.0	25.4	30.8	15.0	16.6	19.8	10.6	15.1	18.4	10.5	11.6	12.0
CHOP191A	18.2	19.1	20.6	11.2	12.5	15.0	9.7	11.2	13.5	13.4	13.8	14.4
CHOP197A	19.8	22.6	27.5	13.0	15.9	21.4	8.9	13.7	20.1	13.0	15.7	18.5
CHOP203A	21.5	24.0	30.1	17.3	19.8	21.6	16.2	19.1	24.7	18.3	19.3	22.4
CHOP204A	13.4	16.4	22.7	13.8	15.3	19.2	12.9	15.4	20.7	16.4	17.2	18.0
CHOP218A	12.0	13.7	17.5	10.0	10.7	12.5	10.9	11.5	12.4	7.5	9.7	14.0
CHOP224A	14.5	16.4	17.3	13.9	14.6	15.3	8.1	11.5	17.4	13.0	14.1	15.7
CHOP229A	18.0	24.2	32.2	10.8	14.1	19.6	11.2	13.5	15.6	11.5	13.2	18.5
CHOP234A	12.3	16.0	23.6	16.5	17.5	20.0	15.0	17.1	20.5	13.4	16.1	20.6
CHOP235A	15.3	19.4	28.8	8.1	14.9	25.3	5.3	12.2	25.7	12.4	18.0	26.2
Average	16.9	20.5	25.9	13.9	16.5	20.0	10.1	13.6	19.9	11.9	14.5	19.3
Standard deviation	4.5	5.2	6.3	2.9	3.5	4.5	2.9	2.8	5.5	2.7	2.8	4.4

Table A. 17   Absolute Vessel Diameter for RUPA. LSVC and AZ (mm)

Patient ID	RUPA diameter			LSVC diameter			AZ diameter		
	Min	Mean	Max	Min	Mean	Max	Min	Mean	Max
CHOP004D									
CHOP011B									
CHOP014B									
CHOP015B							15.1	16.4	19.9
CHOP017C									
CHOP018C									
CHOP019B									
CHOP021C									
CHOP023B									
CHOP024B									
CHOP025B	5.7	8.0	12.7	10.6	20.1	29.5	6.2	10.4	29.6
CHOP029B									
CHOP030C									
CHOP032B									
CHOP039C									
CHOP046B									
CHOP052E	4.7	6.5	10.6						
CHOP061B	8.3	8.6	9.1						
CHOP063B	6.4	6.7	7.0	7.5	8.7	12.9			
CHOP069C									
CHOP073B									
CHOP082B	7.6	8.1	8.2						
CHOP084B									
CHOP088B									
CHOP091B	10.2	10.8	11.4	10.1	11.1	12.7			
CHOP100B									
CHOP122B				7.2	9.2	11.0			
CHOP128B									
CHOP152A	5.8	8.5	12.3						
CHOP155A	8.8	12.4	19.2						
CHOP157A									
CHOP159A									
CHOP161A									
CHOP166A									
CHOP169C				7.1	10.3	19.7	15.5	17.6	22.0
CHOP173A				9.5	10.4	13.9			
CHOP181A									
CHOP185A	9.0	9.4	9.5						
CHOP187A									
CHOP188A	6.0	11.2	16.0						
CHOP191A									
CHOP197A									
CHOP203A									
CHOP204A	6.9	7.8	10.9						
CHOP218A				8.4	8.9	11.0			
CHOP224A									
CHOP229A				9.6	11.5	12.8			
CHOP234A	11.8	12.5	13.1						
CHOP235A									

Table A.17 (Continued)

Average	7.6	9.2	11.7	8.8	11.3	15.4	12.3	14.8	23.8
Standard deviation	2.1	2.1	3.4	1.4	3.7	6.3	5.2	3.9	5.1

Normalized vessel diameter = absolute vessel diameter divided by square root of patient's BSA

Table A. 18   Normalized Vessel Diameter for FP, SVC, LPA and RPA (mm/m)

Patient ID	FP diameter			SVC diameter			LPA diameter			RPA diameter		
	Min	Mean	Max	Min	Mean	Max	Min	Mean	Max	Min	Mean	Max
CHOP004D	11.4	15.7	19.5	10.1	11.2	13.3	11.1	11.7	12.4	6.6	8.4	13.2
CHOP011B	9.2	11.9	14.4	10.4	12.1	13.1	5.7	7.7	13.2	8.0	9.7	13.3
CHOP014B	13.6	16.6	21.6	10.0	11.6	17.3	6.2	9.0	16.2	11.1	13.1	16.2
CHOP015B	6.5	9.0	15.5	8.2	11.9	14.5	9.7	13.3	16.8	8.2	9.5	14.2
CHOP017C	9.6	12.1	17.6	11.1	11.7	12.1	3.8	6.6	11.8	12.8	13.9	15.1
CHOP018C	19.1	23.1	28.2	13.2	14.5	16.0	8.5	12.5	19.4	9.9	12.3	17.2
CHOP019B	14.3	17.0	19.4	11.8	13.4	16.7	8.3	12.5	17.8	12.0	13.5	16.3
CHOP021C	11.6	14.6	19.1	11.0	12.3	14.1	4.5	8.7	15.6	8.6	11.9	15.6
CHOP023B	10.7	13.5	19.1	11.8	13.6	16.6	9.4	12.1	16.7	9.0	11.1	18.5
CHOP024B	14.0	17.1	20.9	12.1	16.7	19.4	4.7	10.4	19.9	8.0	14.4	19.6
CHOP025B	6.7	8.2	11.8	7.8	8.9	11.1	6.6	8.7	15.0	6.9	8.9	12.2
CHOP029B	14.6	19.3	22.6	11.2	14.2	19.4	4.5	9.4	21.2	10.0	14.8	21.0
CHOP030C	14.9	17.4	19.7	8.7	10.0	11.3	5.9	7.3	10.0	12.9	14.1	15.4
CHOP032B	7.0	11.2	18.1	10.7	11.8	16.3	6.8	10.0	15.0	6.8	10.2	15.0
CHOP039C	15.6	18.9	23.7	11.1	12.4	14.8	8.9	11.6	16.2	7.3	9.5	15.0
CHOP046B	15.5	16.8	18.5	10.1	11.2	14.1	6.0	9.3	15.7	11.8	13.4	14.7
CHOP052E	11.8	12.0	12.4	10.3	10.6	11.4	7.1	10.0	12.6	6.9	7.9	9.3
CHOP061B	16.8	20.0	23.6	11.2	12.9	15.9	6.8	11.9	17.7	8.6	11.3	16.6
CHOP063B	9.4	10.8	16.2	10.8	14.6	18.1	11.0	11.3	11.5	7.5	10.1	15.2
CHOP069C	17.1	22.3	28.7	11.8	15.5	23.0	7.6	13.5	25.4	8.9	13.8	24.7
CHOP073B	9.7	15.6	21.2	8.6	12.9	14.9	10.6	11.5	14.3	10.7	11.4	12.0
CHOP082B	11.6	13.9	16.5	13.0	13.8	14.3	7.6	11.4	16.3	8.5	9.1	10.8
CHOP084B	10.9	13.0	17.0	9.5	10.0	11.9	9.9	11.9	12.6	7.1	8.1	10.7
CHOP088B	12.6	13.7	14.7	10.9	11.9	12.9	8.5	10.2	13.3	8.3	9.3	11.3
CHOP091B	15.3	18.2	20.9	8.6	10.3	13.0	10.4	10.7	10.9	10.3	12.4	15.3
CHOP100B	12.4	16.1	20.9	14.5	16.3	18.5	10.3	12.6	17.8	11.5	11.7	11.9
CHOP122B	14.1	15.4	17.1	11.4	12.0	12.8	4.0	4.6	5.7	7.5	9.2	16.8
CHOP128B	14.2	16.3	18.6	12.9	14.6	17.8	8.5	13.1	19.1	10.8	13.5	17.4
CHOP152A	15.8	21.7	30.4	11.5	18.8	23.0	6.8	7.9	10.4	8.9	10.6	12.7
CHOP155A	11.8	14.4	17.7	13.7	14.6	16.2	10.9	12.7	16.9	8.1	9.7	13.7
CHOP157A	16.5	19.2	22.6	15.1	18.3	20.6	9.6	11.4	19.2	10.7	13.4	20.7
CHOP159A	12.9	19.0	28.2	10.8	13.6	19.0	6.8	10.3	19.8	7.9	11.8	20.1
CHOP161A	10.2	11.2	16.4	13.8	14.3	14.6	9.1	9.7	10.2	6.7	9.2	12.2
CHOP166A	15.4	18.0	20.7	8.9	11.7	17.4	4.0	8.4	16.0	10.4	12.8	15.2
CHOP169C	9.1	12.5	16.7	6.9	11.3	15.5	11.1	12.4	14.3	7.7	9.4	16.6
CHOP173A	12.3	14.3	18.4	5.3	7.0	8.3	6.7	8.0	9.6	6.7	7.3	8.2
CHOP181A	16.3	18.3	20.8	10.4	11.8	14.2	6.2	10.7	17.1	7.2	9.7	14.4
CHOP185A	18.8	21.7	27.2	14.9	19.1	21.8	7.7	14.1	26.6	8.9	12.4	19.4
CHOP187A	23.2	28.5	33.6	13.2	15.2	17.6	7.2	11.0	21.2	13.5	14.6	17.1
CHOP188A	17.8	20.6	25.0	12.2	13.4	16.1	8.6	12.3	14.9	8.5	9.4	9.7
CHOP191A	16.3	17.1	18.5	10.0	11.2	13.5	8.7	10.1	12.0	12.0	12.4	12.9
CHOP197A	15.3	17.5	21.3	10.0	12.3	16.6	6.9	10.6	15.5	10.1	12.2	14.3

CHOP203A	15.5	17.3	21.7	12.5	14.3	15.5	11.7	13.8	17.8	13.1	13.9	16.1
CHOP204A	11.0	13.4	18.6	11.3	12.6	15.8	10.6	12.6	16.9	13.4	14.1	14.7
CHOP218A	10.8	12.4	15.9	9.0	9.7	11.4	9.8	10.4	11.3	6.8	8.8	12.7
CHOP224A	10.8	12.2	12.9	10.4	10.9	11.4	6.1	8.6	13.0	9.7	10.5	11.7
CHOP229A	13.0	17.5	23.2	7.8	10.2	14.2	8.1	9.7	11.2	8.3	9.5	13.4
CHOP234A	9.2	11.9	17.6	12.3	13.0	14.9	11.2	12.8	15.3	10.0	12.0	15.4
CHOP235A	11.5	14.6	21.7	6.1	11.2	19.0	4.0	9.2	19.3	9.3	13.6	19.7
Average	13.1	16.0	20.1	10.8	12.8	15.5	7.9	10.6	15.5	9.3	11.3	15.0
Standard deviation	3.4	3.9	4.6	2.1	2.4	3.2	2.2	2.0	4.0	2.0	2.1	3.3

Normalized vessel diameter = absolute vessel diameter divided by square root of patient's BSA

$$TCPC\ diameter\ index = \frac{\sum_{i=1}^{n}(Minimum\ vessel\ diameter)}{n \cdot \sqrt{BSA}}$$

where n = number of vessels present at the TCPC, BSA = body surface area (m^2)

Table A. 19   Normalized Vessel Diameter for RUPA. LSVC, AZ and TCPC diameter index (mm/m)

Patient ID	RUPA diameter			LSVC diameter			AZ diameter			TCPC diameter Index
	Min	Mean	Max	Min	Mean	Max	Min	Mean	Max	
CHOP004D										9.8
CHOP011B										8.3
CHOP014B										10.2
CHOP015B							11.1	12.1	14.6	8.7
CHOP017C										9.4
CHOP018C										12.6
CHOP019B										11.6
CHOP021C										8.9
CHOP023B										10.2
CHOP024B										9.7
CHOP025B	4.5	6.3	9.9	8.3	15.7	23.1	4.9	8.1	23.2	6.5
CHOP029B										10.1
CHOP030C										10.6
CHOP032B										7.8
CHOP039C										10.7
CHOP046B										10.8
CHOP052E	3.7	5.1	8.3							8.0
CHOP061B	6.2	6.4	6.8							9.9
CHOP063B	5.2	5.4	5.7	6.1	7.1	10.5				8.3
CHOP069C										11.4
CHOP073B										9.9
CHOP082B	6.6	7.0	7.1							9.5
CHOP084B										9.3
CHOP088B										10.1
CHOP091B	7.6	8.0	8.5	7.5	8.2	9.5				10.0
CHOP100B										12.2
CHOP122B				5.5	7.1	8.5				8.5
CHOP128B										11.6
CHOP152A	4.2	6.2	8.9							9.5
CHOP155A	6.5	9.1	14.2							10.2
CHOP157A										13.0
CHOP159A										9.6
CHOP161A										10.0
CHOP166A										9.7
CHOP169C				5.3	7.7	14.7	11.5	13.1	16.4	8.6
CHOP173A				6.8	7.4	9.9				7.6
CHOP181A										10.0
CHOP185A	6.1	6.3	6.4							11.3
CHOP187A										14.3

CHOP188A	4.9	9.1	12.9							10.4
CHOP191A										11.7
CHOP197A										10.6
CHOP203A										13.2
CHOP204A	5.6	6.4	8.9							10.4
CHOP218A				7.6	8.0	10.0				8.8
CHOP224A										9.2
CHOP229A				6.9	8.3	9.2				8.8
CHOP234A	8.8	9.3	9.8							10.3
CHOP235A										7.7
Average	5.8	7.1	9.0	6.8	8.7	11.9	9.2	11.1	18.0	10.0
Standard deviation	1.4	1.5	2.5	1.1	2.9	4.9	3.7	2.6	4.5	1.5

Minimum/maximum diameter ratio = (minimum diameter) / (maximum diameter)

Table A. 20   Minimum/Maximum Diameter Ratio (mm/mm)

Patient ID	FP	SVC	LPA	RPA	RUPA	LSVC	AZ
CHOP004D	0.58	0.76	0.89	0.50			
CHOP011B	0.64	0.79	0.43	0.60			
CHOP014B	0.63	0.58	0.38	0.68			
CHOP015B	0.42	0.56	0.58	0.58			0.76
CHOP017C	0.55	0.92	0.33	0.85			
CHOP018C	0.68	0.82	0.44	0.57			
CHOP019B	0.74	0.71	0.46	0.74			
CHOP021C	0.61	0.78	0.29	0.55			
CHOP023B	0.56	0.71	0.57	0.49			
CHOP024B	0.67	0.62	0.23	0.41			
CHOP025B	0.57	0.71	0.44	0.56	0.45	0.36	0.21
CHOP029B	0.65	0.58	0.21	0.48			
CHOP030C	0.76	0.77	0.59	0.84			
CHOP032B	0.39	0.66	0.45	0.45			
CHOP039C	0.66	0.75	0.55	0.49			
CHOP046B	0.84	0.72	0.38	0.80			
CHOP052E	0.95	0.91	0.56	0.74	0.45		
CHOP061B	0.71	0.70	0.38	0.52	0.91		
CHOP063B	0.58	0.60	0.95	0.49	0.91	0.58	
CHOP069C	0.60	0.51	0.30	0.36			
CHOP073B	0.46	0.58	0.74	0.90			
CHOP082B	0.70	0.91	0.47	0.79	0.93		
CHOP084B	0.64	0.80	0.79	0.66			
CHOP088B	0.86	0.84	0.64	0.74			
CHOP091B	0.73	0.66	0.95	0.67	0.89	0.80	
CHOP100B	0.59	0.79	0.58	0.97			
CHOP122B	0.82	0.90	0.71	0.45		0.65	
CHOP128B	0.77	0.72	0.44	0.62			
CHOP152A	0.52	0.50	0.66	0.70	0.47		
CHOP155A	0.67	0.84	0.64	0.59	0.46		
CHOP157A	0.73	0.73	0.50	0.52			
CHOP159A	0.46	0.57	0.34	0.39			
CHOP161A	0.62	0.95	0.89	0.55			
CHOP166A	0.74	0.51	0.25	0.69			
CHOP169C	0.54	0.45	0.77	0.46		0.36	0.70
CHOP173A	0.67	0.63	0.70	0.81		0.69	
CHOP181A	0.78	0.73	0.36	0.50			
CHOP185A	0.69	0.68	0.29	0.46	0.94		
CHOP187A	0.69	0.75	0.34	0.79			
CHOP188A	0.71	0.76	0.57	0.87	0.38		

CHOP191A	0.88	0.74	0.72	0.93			
CHOP197A	0.72	0.61	0.45	0.70			
CHOP203A	0.71	0.80	0.66	0.81			
CHOP204A	0.59	0.72	0.62	0.91	0.63		
CHOP218A	0.68	0.79	0.88	0.54		0.76	
CHOP224A	0.83	0.91	0.47	0.83			
CHOP229A	0.56	0.55	0.72	0.62		0.75	
CHOP234A	0.52	0.83	0.73	0.65	0.90		
CHOP235A	0.53	0.32	0.21	0.47			
Average	0.66	0.71	0.54	0.64	0.69	0.62	0.56
Standard deviation	0.12	0.14	0.20	0.16	0.24	0.17	0.30

A.7.3.1.2.2. Connection Angle

Table A. 21   Connection Angle

Patient ID	Angles between (degree)					
	FP-LPA	FP-RPA	SVC-LPA	SVC_RPA	FP-SVC	LPA-RPA
CHOP004D	122	105	97	90	119	120
CHOP011B	130	108	118	115	104	79
CHOP014B	109	88	111	114	116	116
CHOP015B	152	88	88	112	116	96
CHOP017C	89	113	113	65	129	155
CHOP018C	126	91	97	100	130	106
CHOP019B	141	121	105	99	104	80
CHOP021C	117	98	112	109	131	66
CHOP023B	109	87	94	93	157	82
CHOP024B	113	91	91	111	146	96
CHOP025B	140	109	129	117	91	54
CHOP029B	120	97	110	115	124	82
CHOP030C	112	90	99	80	149	102
CHOP032B	110	83	98	103	108	150
CHOP039C	129	79	99	117	125	103
CHOP046B	128	108	126	114	105	60
CHOP052E	101	102	97	71	158	140
CHOP061B	123	95	93	100	143	80
CHOP063B	135	87	101	114	122	86
CHOP069C	111	101	108	104	127	101
CHOP073B	128	77	103	110	106	130
CHOP082B	121	78	85	94	136	154
CHOP084B	126	64	92	93	141	141
CHOP088B	100	78	114	88	144	129
CHOP091B	103	82	97	87	153	71
CHOP100B	97	121	115	75	134	117
CHOP122B	132	103	104	91	119	52
CHOP128B	124	97	104	107	129	81
CHOP152A	92	57	132	90	135	133
CHOP155A	124	74	88	98	141	136
CHOP157A	111	120	108	102	122	91
CHOP159A	106	90	101	97	144	117
CHOP161A	62	91	109	116	131	134
CHOP166A	99	107	125	101	107	117
CHOP169C	107	144	146	126	59	46
CHOP173A	95	92	124	102	141	59

CHOP181A	137	93	85	104	134	89
CHOP185A	121	94	104	117	130	78
CHOP187A	108	72	91	92	161	138
CHOP188A	116	58	76	141	150	123
CHOP191A	116	73	69	121	158	131
CHOP197A	119	72	102	98	124	144
CHOP203A	145	91	94	104	120	91
CHOP204A	126	88	94	98	108	138
CHOP218A	95	95	82	71	166	72
CHOP224A	147	133	141	125	65	60
CHOP229A	101	90	140	90	120	85
CHOP234A	87	91	112	84	156	138
CHOP235A	112	129	111	102	108	94
Average	116	94	105	101	127	103
Standard deviation	17	18	16	15	22	30

Table A. 22 Connection Angle (Cont')

Patient ID	Angles between (degree)								
	LSVC-LPA	LSVC-RPA	LSVC-SVC	LSVC-FP	AZ-FP	AZ-SVC	AZ-LPA	AZ-RPA	AZ-LSVC
CHOP004D									
CHOP011B									
CHOP014B									
CHOP015B					118	14	89	98	
CHOP017C									
CHOP018C									
CHOP019B									
CHOP021C									
CHOP023B									
CHOP024B									
CHOP025B	105	125	33	112	127	47	89	116	16
CHOP029B									
CHOP030C									
CHOP032B									
CHOP039C									
CHOP046B									
CHOP052E									
CHOP061B									
CHOP063B	91	175	62	98					
CHOP069C									
CHOP073B									
CHOP082B									
CHOP084B									
CHOP088B									
CHOP091B	108	115	29	149					
CHOP100B									
CHOP122B	95	117	41	132					
CHOP128B									
CHOP152A									
CHOP155A									
CHOP157A									
CHOP159A									
CHOP161A									
CHOP166A									
CHOP169C	141	99	64	112	93	45	114	82	67
CHOP173A	97	142	66	121					
CHOP181A									
CHOP185A									
CHOP187A									

CHOP188A									
CHOP191A									
CHOP197A									
CHOP203A									
CHOP204A									
CHOP218A	92	124	54	140					
CHOP224A									
CHOP229A	100	131	54	135					
CHOP234A									
CHOP235A									
Average	104	129	50	125	113	35	97	99	41
Standard deviation	16	22	14	17	18	18	14	17	36

A.7.3.1.2.3. Caval Offset

Normalized caval offset was computed by dividing caval offset by mean FP diameter

Table A. 23 Caval Offset

Patient ID	Absolute caval offset (mm)				Normalized caval offset (mm/mm)			
	with SVC			with LSVC	with SVC			with LSVC
	Offset	Magnitude	VC-PA	Magnitude	Offset	Magnitude	VC-PA	Magnitude
CHOP004D	4.36	4.36	6.45		0.22	0.22	0.33	
CHOP011B	1.05	1.05	10.31		0.07	0.07	0.68	
CHOP014B	1.81	1.81	10.35		0.08	0.08	0.45	
CHOP015B	11.99	11.99	13.11		0.97	0.97	1.07	
CHOP017C	-10.85	10.85	0.06		-0.65	0.65	0.00	
CHOP018C	7.19	7.19	5.66		0.28	0.28	0.22	
CHOP019B	2.42	2.42	13.14		0.10	0.10	0.57	
CHOP021C	0.00	0.00	13.65		0.00	0.00	0.70	
CHOP023B	-0.89	0.89	7.36		-0.05	0.05	0.43	
CHOP024B	6.02	6.02	8.00		0.30	0.30	0.40	
CHOP025B	21.77	21.77	0.00	13.89	2.09	2.09	0.00	1.33
CHOP029B	1.55	1.55	7.87		0.06	0.06	0.31	
CHOP030C	-8.23	8.23	0.02		-0.39	0.39	0.00	
CHOP032B	3.96	3.96	10.67		0.28	0.28	0.77	
CHOP039C	3.44	3.44	6.67		0.16	0.16	0.30	
CHOP046B	0.21	0.21	10.49		0.01	0.01	0.53	
CHOP052E	-8.67	8.67	0.02		-0.57	0.57	0.00	
CHOP061B	-1.91	1.91	11.76		-0.07	0.07	0.44	
CHOP063B	0.77	0.77	2.68	31.86	0.06	0.06	0.20	2.39
CHOP069C	1.88	1.88	5.62		0.07	0.07	0.22	
CHOP073B	8.98	8.98	7.70		0.46	0.46	0.39	
CHOP082B	4.55	4.55	8.59		0.29	0.29	0.54	
CHOP084B	6.08	6.08	0.14		0.37	0.37	0.01	
CHOP088B	-6.48	6.48	0.02		-0.36	0.36	0.00	
CHOP091B	0.59	0.59	0.17	53.77	0.02	0.02	0.01	2.20
CHOP100B	-6.07	6.07	13.59		-0.29	0.29	0.65	
CHOP122B	0.74	0.74	15.45	39.67	0.04	0.04	0.77	1.99
CHOP128B	1.35	1.35	8.87		0.07	0.07	0.45	
CHOP152A	10.52	10.52	0.02		0.35	0.35	0.00	
CHOP155A	4.88	4.88	7.68		0.25	0.25	0.39	
CHOP157A	0.00	0.00	8.91		0.00	0.00	0.35	
CHOP159A	-0.54	0.54	6.70		-0.02	0.02	0.26	
CHOP161A	5.55	5.55	3.86		0.38	0.38	0.27	
CHOP166A	0.51	0.51	11.63		0.02	0.02	0.50	
CHOP169C	2.43	2.43	16.42	49.18	0.14	0.14	0.97	2.91
CHOP173A	19.45	19.45	0.00	5.38	0.97	0.97	0.00	0.27
CHOP181A	4.17	4.17	11.89		0.17	0.17	0.49	
CHOP185A	6.43	6.43	17.91		0.20	0.20	0.56	
CHOP187A	5.37	5.37	0.12		0.15	0.15	0.00	
CHOP188A	-0.79	0.79	0.73		-0.03	0.03	0.03	
CHOP191A	10.20	10.20	0.09		0.53	0.53	0.00	
CHOP197A	0.22	0.22	7.75		0.01	0.01	0.34	

CHOP203A	4.98	4.98	13.04		0.21	0.21	0.54	
CHOP204A	1.79	1.79	5.85		0.11	0.11	0.36	
CHOP218A	1.11	1.11	9.05	32.23	0.08	0.08	0.66	2.36
CHOP224A	-0.53	0.53	15.46		-0.03	0.03	0.94	
CHOP229A	0.34	0.34	4.58	28.71	0.01	0.01	0.19	1.19
CHOP234A	-5.43	5.43	1.07		-0.34	0.34	0.07	
CHOP235A	0.00	0.00	6.14		0.00	0.00	0.32	
Average	2.41	4.47	7.09	31.84	0.14	0.25	0.36	1.83
Standard deviation	6.07	4.74	5.26	16.37	0.41	0.35	0.29	0.85

A.7.3.1.3.   Hemodynamic Results under Exercise Condition

Qs at VAT= total systemic return at VAT

iQs at VAT= indexed Qs at VAT = (Qs at VAT) / BSA

%Qs at VAT from FP = (FP flow at VAT) / (Qs at VAT)

TCPC resistance at VAT $= \dfrac{\dot{E}_{Loss}}{\frac{(Qs\ at\ VAT)^2}{BSA}}$

iPL at VAT $=\dfrac{\dot{E}_{Loss}\ at\ VAT}{\rho(Qs\ at\ VAT)^3/BSA^2}$

Table A. 24 Hemodynamic Results under exercise condition

Patient ID	Qs at VAT (L/min)	iQs at VAT (L/min/m^2)	% Qs at VAT from FP	Power loss at VAT(mw)	TCPC resistance at VAT (WU.m^2)	iPL at VAT
CHOP004D	6.10	3.86	70%	17.3	0.33	0.039
CHOP011B	9.05	5.52	79%	88.7	0.80	0.066
CHOP014B	7.96	4.17	80%	11.1	0.15	0.016
CHOP015B	8.70	4.70	13%	34.6	0.38	0.037
CHOP017C	8.80	4.66	88%	70.4	0.77	0.075
CHOP018C	7.39	5.91	78%	11.3	0.12	0.009
CHOP019B	10.16	5.46	71%	43.9	0.36	0.030
CHOP021C	9.09	5.19	82%	84.6	0.81	0.070
CHOP023B	5.86	3.68	80%	17.0	0.36	0.044
CHOP024B	9.10	6.69	51%	166.4	1.23	0.083
CHOP025B	9.78	6.00	74%	288.3	2.21	0.167
CHOP029B	12.63	7.26	84%	247.3	1.21	0.076
CHOP030C	5.40	3.60	83%	6.7	0.15	0.019
CHOP032B	6.42	4.20	80%	133.6	2.23	0.241
CHOP039C	6.76	5.01	71%	25.0	0.33	0.030
CHOP046B	5.30	3.90	80%	9.2	0.20	0.023
CHOP052E	7.60	4.69	79%	42.4	0.54	0.052
CHOP061B	7.16	3.98	73%	15.4	0.24	0.028
CHOP063B	6.10	4.01	73%	36.5	0.67	0.076
CHOP069C	5.29	3.95	69%	3.1	0.07	0.008
CHOP073B	6.87	4.29	81%	38.5	0.59	0.062
CHOP082B	8.19	6.21	58%	39.5	0.35	0.026
CHOP084B	5.50	3.37	71%	17.2	0.42	0.056
CHOP088B	10.01	5.89	82%	52.1	0.40	0.031
CHOP091B	8.75	4.86	81%	19.0	0.20	0.019
CHOP100B	8.63	5.11	80%	23.3	0.24	0.021
CHOP122B	7.85	4.64	52%	119.1	1.47	0.143

CHOP128B	12.00	8.11	76%	68.7	0.32	0.018
CHOP152A	9.00	4.76	83%	34.7	0.36	0.035
CHOP155A	10.75	5.87	77%	77.2	0.55	0.042
CHOP157A	9.40	5.47	64%	26.3	0.23	0.019
CHOP159A	8.00	4.26	86%	56.4	0.75	0.079
CHOP161A	12.10	7.29	71%	123.0	0.63	0.039
CHOP166A	6.86	4.16	69%	30.0	0.47	0.052
CHOP169C	12.90	7.13	28%	292.3	1.43	0.091
CHOP173A	8.80	4.44	68%	86.8	1.00	0.102
CHOP181A	8.00	4.55	80%	38.3	0.47	0.047
CHOP185A	11.77	5.35	80%	38.4	0.27	0.023
CHOP187A	5.03	3.07	78%	4.5	0.13	0.019
CHOP188A	7.30	4.80	62%	8.8	0.11	0.011
CHOP191A	4.90	3.92	82%	3.9	0.09	0.011
CHOP197A	6.22	3.73	84%	9.1	0.18	0.021
CHOP203A	10.05	5.21	68%	16.0	0.14	0.012
CHOP204A	9.60	6.44	80%	89.0	0.65	0.046
CHOP218A	6.48	5.31	69%	41.1	0.54	0.046
CHOP224A	10.20	5.66	78%	97.7	0.76	0.061
CHOP229A	9.59	5.00	74%	64.0	0.60	0.054
CHOP234A	12.63	7.02	75%	139.0	0.71	0.046
CHOP235A	7.55	4.27	83%	43.9	0.61	0.065
Average	8.36	5.03	73%	62.3	0.57	0.051
Standard deviation	2.15	1.15	14%	68.0	0.48	0.043

A.7.3.1.4. Exercise Stress Test Results

Table A. 25 Exercise Stress Test Results (N=47)*

Patient ID	VO$_2$ at rest (mL/kg/min)	VO$_2$ at VAT (mL/kg/min)	HR at rest (bpm)	HR at VAT (bpm)	Work at VAT (W)	Work at VAT/weight (W/kg)
CHOP004D	3.5	16	72	110	40	0.74
CHOP011B	4.3	16	59	105	69	1.10
CHOP014B	4.2	27	67	102	93	1.32
CHOP015B	4.8	17	44	89	66	1.04
CHOP017C	3.2	12	82	104	36	0.45
CHOP018C	4.5	25	44	115	47	1.38
CHOP019B	4.2	16	83	114	75	1.05
CHOP021C	5.1	16	60	138	53	0.76
CHOP024B	3.4	15	63	101	27	0.61
CHOP025B	4.5	15	64	95	52	0.90
CHOP029B	4.6	23	55	98	88	1.37
CHOP030C	4.9	17	85	136	44	0.79
CHOP032B	5.8	16	64	102	53	1.08
CHOP046B	4.7	25	58	122	54	1.26
CHOP052E	5.4	18	110	129	53	0.98
CHOP061B	5.2	16	83	103	69	1.05
CHOP063B	5.6	17	91	136	41	0.79
CHOP069C	5.2	22	75	155	53	1.27
CHOP073B	3.7	11	76	100	36	0.59
CHOP082B	4.0	24	49	92	47	1.15
CHOP084B	4.0	18	80	126	35	0.62
CHOP088B	5.7	17	90	135	54	0.82
CHOP091B	3.6	13	86	105	80	0.77
CHOP100B		16	71	94	46	0.78
CHOP122B	5.4	16	76	135	41	0.69
CHOP128B	4.7	26	48	144	89	1.70
CHOP152A	5.1	19	64	99	88	1.18
CHOP155A	6.2	21	84	148	102	1.48
CHOP157A	4.0	18	71	110	63	0.98
CHOP159A	4.4	11	71	103	34	0.43
CHOP161A	4.7	16	86	160	49	0.83
CHOP166A	6.1	16	95	139	40	0.74
CHOP169C	4.2	20	78	98	77	1.21
CHOP173A	4.2	12	82	114	44	0.47
CHOP181A	3.8	19	63	98	45	0.73
CHOP185A	4.0	13	65	106	58	0.55
CHOP187A	5.7	13	78	128	51	0.86
CHOP188A	4.9	20	55	105	37	0.70
CHOP191A	3.9	17	69	120	24	0.65
CHOP197A	4.4	11	52	72	37	0.65
CHOP203A	4.7	20	42	107	90	1.23
CHOP204A	5.4	17	68	126	47	0.91
CHOP218A	6.0	17	72	98	35	1.01

Table A.25 (Continued)

CHOP224A	4.0	14	51	93	43	0.59
CHOP229A	4.9	16	98	153	61	0.72
CHOP234A	4.5	17	106	147	92	1.28
CHOP235A	4.6	18	74	109	54	0.86
Average	4.6	17	71	115	56	0.92
Standard deviation	0.8	4	16	20	20	0.29

* Exercise stress test was not completed by CHOP023B and CHOP039C

489

A.7.4. Statistical Comparison Results for Specific Aim 1(b)

Table A. 26 Comparison of exercise stress test results, iPL at VAT, TCPC diameter index and iQs at VAT between the adolescents and adult group

Mean ± Standard Deviation	Adolescents (age 12-18, N=26)	Adults (age > 18, N=21)	p-value
VO$_2$ at VAT (mL/kg/min)	19 ± 4	16 ± 3	0.009*
Work at VAT/weight (W/kg)	0.99 ± 0.32	0.83 ± 0.24	0.071
iPL at VAT	0.037 ± 0.024	0.069 ± 0.055	0.016*
TCPC diameter index (mm/m)	10.2 ± 1.4	9.6 ±1.7	0.212
iQs at VAT (L/min/m^2)	5.19 ± 1.25	4.90 ± 1.02	0.401

* Significant difference between groups (p≤0.05)

Two of the 49 patients (CHOP023B and CHOP039C) did not complete the entire metabolic stress test protocol

A.7.5. Detailed Statistical Correlation Results for Specific Aim 1(b)

Table A. 27 Bivariate correlations between patient age, exercise stress test results, iPL at VAT, TCPC diameter index and iQs at VAT for the adolescent and adult group

Correlations between		Adolescents (age 12-18, N=26)		Adults (age > 18, N=21)		Difference in correlation coefficient between 2 groups (p-value)
		Correlation coefficient (r)	p-value	Correlation coefficient (r)	p-value	
VO$_2$ at VAT	iPL at VAT	-0.5799	0.002*	0.0849	0.71	0.02*
Work at VAT /weight	iPL at VAT	-0.5316	0.005*	0.2022	0.38	0.01*
VO$_2$ at VAT	TCPC diameter index	0.4127	0.036*	-0.2012	0.38	0.04*
Work at VAT /weight	TCPC diameter index	0.4399	0.025*	-0.1404	0.54	0.05*
iQs at VAT	Patient Age	0.1619	0.43	-0.6555†	0.001*	0.003*
VO$_2$ at VAT	Patient Age	-0.1334	0.52	-0.4671†	0.03*	0.24
Work at VAT /weight	Patient Age	0.056	0.79	-0.3237†	0.15	0.21
VO$_2$ at VAT	iQs at VAT	0.1487	0.47	0.5335	0.013*	0.16
Work at VAT /weight	iQs at VAT	0.3489	0.08	0.5548	0.009*	0.41

* $p \leq 0.05$
† Nonlinear correlations
Two of the 49 patients (CHOP023B and CHOP039C) did not complete the entire metabolic stress test protocol

A.7.6. Stent Size Estimation Protocol and Raw Data for Specific Aim 1(c)

A.7.6.1.   <u>Estimation of Stent Sizes from Angiogram</u>
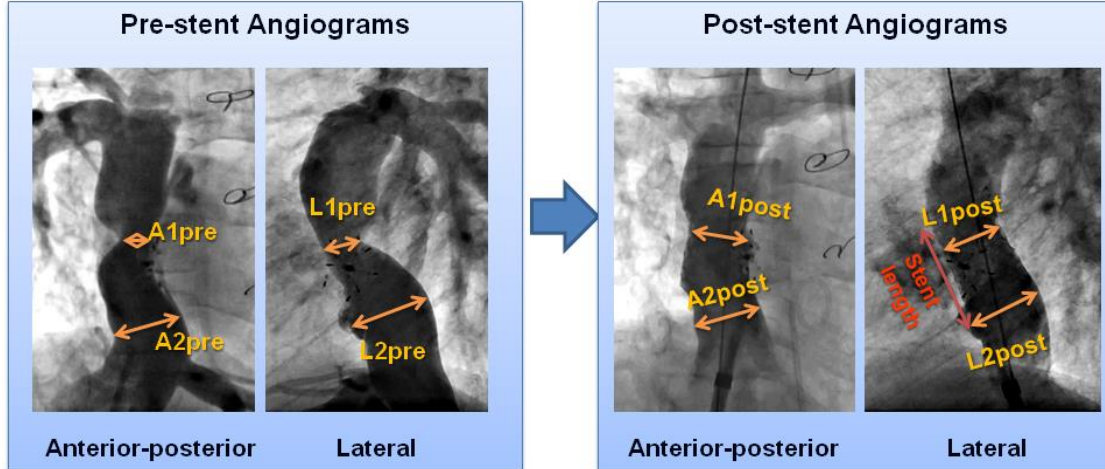
To estimate the stent size implemented, the minimum lateral tunnel diameter and diameter at a reference location (directly downstream of the hepatic venous confluence, or the point with maximum lateral tunnel diameter, depending on the angiograms available) were measured both before and after stent implantation. Shape factors (SF) were estimated from both angiograms to estimate the relative minimum (cross-sectional) area of the lateral tunnel:

$$SF_i = \frac{(\text{Minimum area})_i}{(\text{Reference area})_i}$$

$$(\text{Minimum area})_i = \frac{1}{4}\pi(A1_i)(L1_i)$$

$$(\text{Reference area})_i = \frac{1}{4}\pi(A2_i)(L2_i)$$

Where i = before or after stent implantation, A1 and L1 are the minimum diameters of the lateral tunnel, and A2 and L2 are the lateral tunnel diameters at the reference

location; "A" denotes diameter measured from the anterior-posterior view angiogram and "L" denotes diameter measured from the lateral view angiogram.

The dilation ratio (stent cross-sectional area / stenosis cross-sectional area) from the angiogram was calculated as:

$$\text{Dilation ratio} = \frac{\text{SF}_{\text{post}-\text{stent}}}{\text{SF}_{\text{pre}-\text{stent}}}$$

Stent length was also estimated from the angiograms by scaling the lateral tunnel diameters. Virtual stents, created as perfect cylinders with diameter based on the dilation ratio, were placed according to the orientation in the angiograms and merged with the reconstructed 3-dimensional stenotic geometry in Geomagic Studio (Geomagic Inc., NC, USA).

A.7.6.2.   Patient Angiograms

A.7.6.2.1.   *CHB024A (Patient 3 in CHB LT stenosis cohort)*
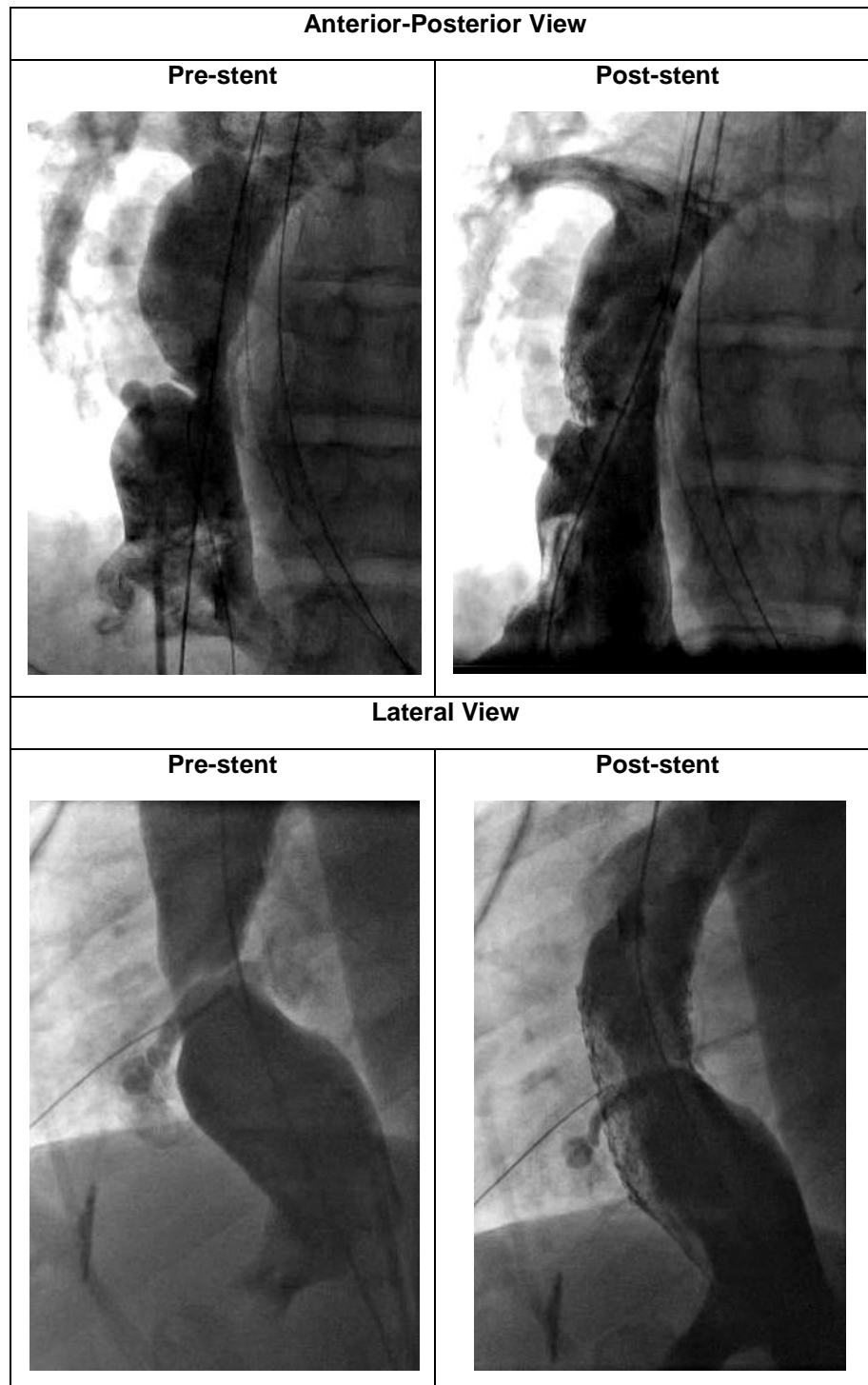
Anterior-Posterior View	
Pre-stent	**Post-stent**
Lateral View	
Pre-stent	**Post-stent**

A.7.6.2.2.   CHB025A (Patient 4 in CHB LT stenosis cohort)

Anterior-Posterior View	
Pre-stent	**Post-stent**
Lateral View	
Pre-stent	**Post-stent**

A.7.6.2.3.   CHB026A (Patient 8 in CHB LT stenosis cohort)
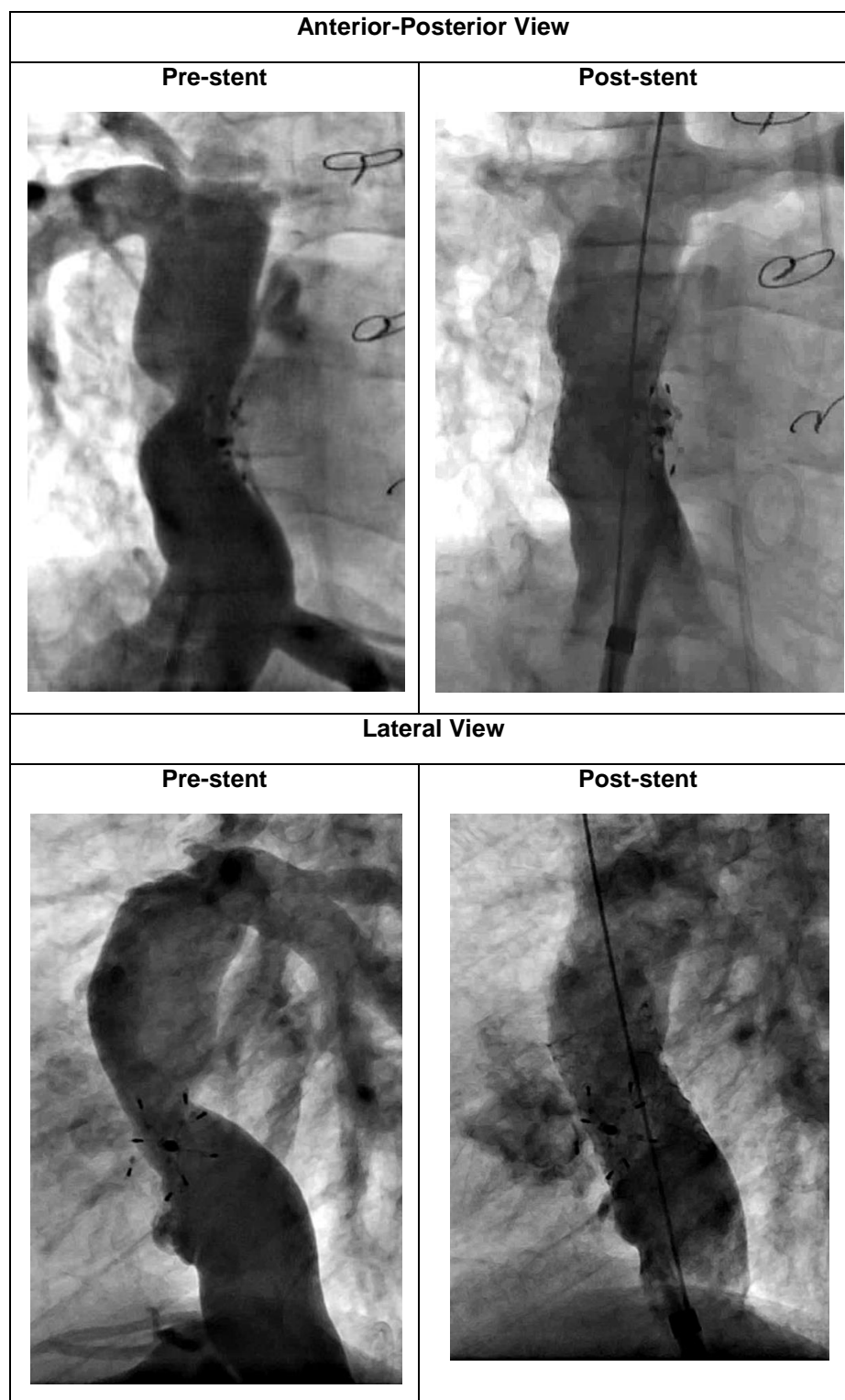
Anterior-Posterior View	
Pre-stent	Post-stent
Lateral View	
Pre-stent	Post-stent
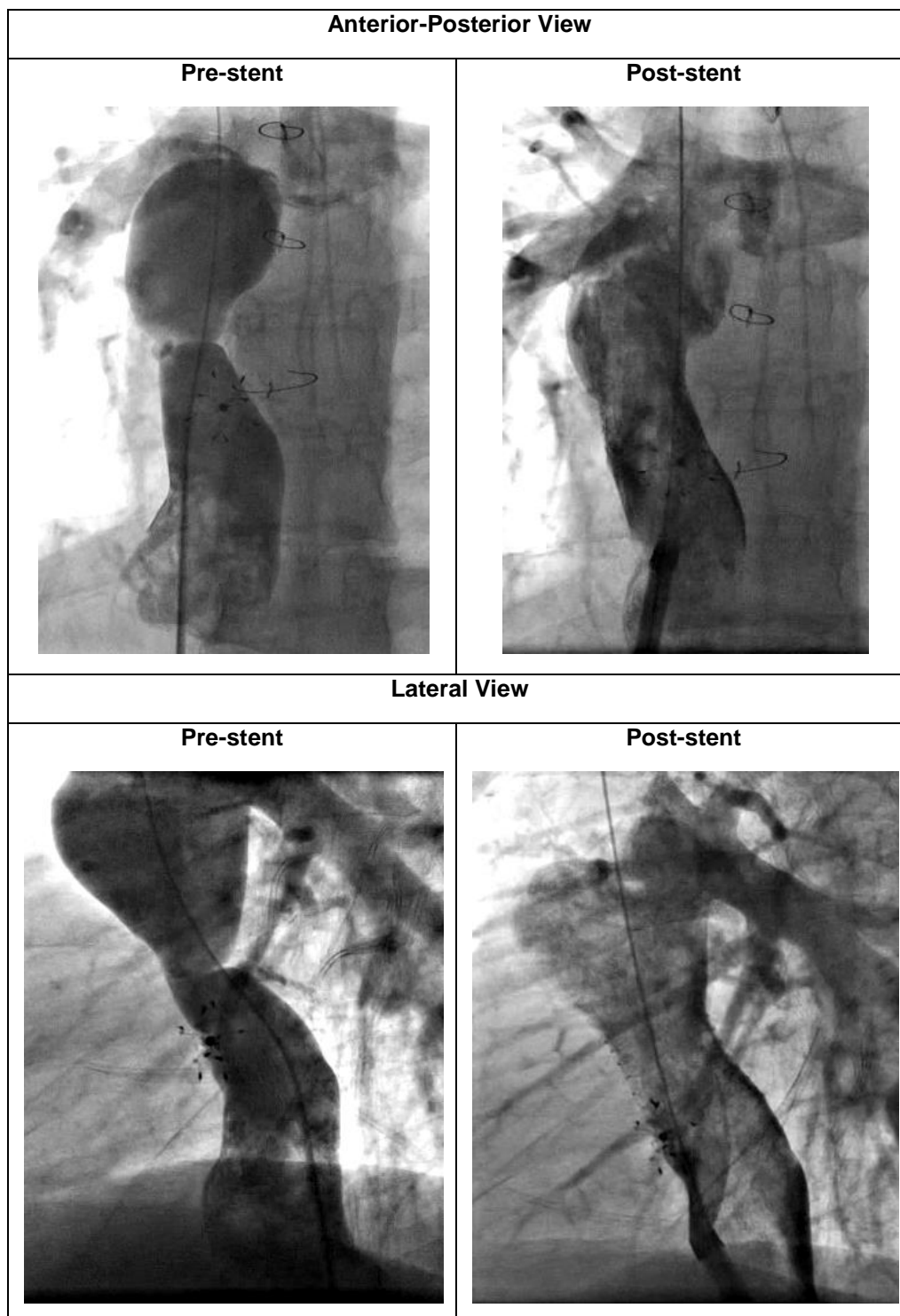
A.7.6.3. Complete List of Computed Geometric and Hemodynamic Results in Specific Aim 1(c)

$$Normalized\ minimum\ LT\ diameter\ [mm/m] = \frac{Minimum\ diameter\ along\ the\ LT\ [mm]}{\sqrt{(BSA[m^2])}}$$

A.7.6.3.1. CHB024A (Patient 3 in CHB LT stenosis cohort)

Table A. 28 Hemodynamics and geometric results of CHB024A (BSA = 1.57m^2)

Pre/post-stent	Stent size (mm)	Power Loss (mW)			TCPC resistance (WU.m^2)			iPL			Min. LT diameter (mm)	Normalized min. LT diameter (mm/m)
		1X	2X	3X	1X	2X	3X	1X	2X	3X		
Pre-stent	N/A	3.90	27.26	88.41	1.07	2.73	4.56	0.043	0.066	0.079	10.4	8.3
Actual Post-stent	18	1.44	8.24	26.47	0.40	0.82	1.36	0.016	0.020	0.024	17.2	13.7
Simulated post-stent	20	1.03	5.16	16.02	0.29	0.51	0.82	0.011	0.012	0.014	18.4	14.6
Simulated post-stent	22	0.98	4.68	14.26	0.27	0.47	0.73	0.011	0.011	0.013	18.4	14.7
iQs (L/min/m^2)	2.28	3.77	5.25									

A.7.6.3.2. CHB025A (Patient 4 in CHB LT stenosis cohort)

Table A. 29 Hemodynamics and geometric results of CHB025A (BSA = 1.11m^2)

Pre/post-stent	Stent size (mm)	Power Loss (mW)			TCPC resistance (WU.m^2)			iPL			Min. LT diameter (mm)	Normalized min. LT diameter (mm/m)
		1X	2X	3X	1X	2X	3X	1X	2X	3X		
Pre-stent	N/A	3.25	17.47	52.97	1.36	3.64	6.60	0.052	0.098	0.138	6.0	5.6
Simulated post-stent	10	1.88	7.77	21.27	0.78	1.62	2.64	0.030	0.044	0.055	10.0	9.5
Simulated post-stent	12	1.73	5.65	14.56	0.71	1.18	1.82	0.028	0.032	0.038	11.9	11.3
Actual Post-stent	14	1.62	4.73	11.18	0.67	0.98	1.40	0.026	0.026	0.029	13.3	12.6
Simulated post-stent	16	1.60	4.43	9.62	0.67	0.91	1.20	0.025	0.025	0.025	14.9	14.1
Simulated post-stent	18	1.63	4.29	9.33	0.67	0.89	1.16	0.026	0.024	0.024	15.2	14.4
iQs (L/min/m^2)	2.26	3.20	4.13									

A.7.6.3.3. CHB026A (Patient 8 in CHB LT stenosis cohort)

Table A. 30 Hemodynamics and geometric results of CHB026A (BSA = 1.8m^2)

Pre/post-stent	Stent size (mm)	Power Loss (mW)			TCPC resistance (WU.m^2)			iPL			Min. LT diameter (mm)	Normalized min. LT diameter (mm/m)
		1X	2X	3X	1X	2X	3X	1X	2X	3X		
Pre-stent	N/A	8.12	64.96	218.30	3.11	8.44	14.09	0.158	0.249	0.292	8.3	6.2
Simulated post-stent	12	3.04	25.80	87.70	1.18	3.36	5.67	0.059	0.099	0.117	11.9	8.8
Simulated post-stent	14	2.49	18.49	61.38	0.96	2.40	3.96	0.048	0.071	0.082	13.9	10.4
Simulated post-stent	16	1.77	12.17	39.26	0.69	1.58	2.53	0.034	0.047	0.053	15.8	11.8
Simulated post-stent	18	1.49	8.96	27.64	0.58	1.16	1.78	0.029	0.034	0.037	17.8	13.3
Actual Post-stent	20	1.30	7.77	24.40	0.49	1.00	1.58	0.025	0.030	0.033	18.1	13.5
iQs (L/min/m^2)		1.80	3.09	4.39								

A.7.6.3.4. CHB012B

Table A. 31 Hemodynamics and geometric results of CHB012B (BSA = 1.43m^2)

Pre/post-stent	Stent size (mm)	Power Loss (mW)			TCPC resistance (WU.m^2)			iPL			Min. LT diameter (mm)	Normalized min. LT diameter (mm/m)
		1X	2X	3X	1X	2X	3X	1X	2X	3X		
Pre-stent	N/A	13.39	103.60	348.38	2.58	6.84	11.49	0.083	0.129	0.154	9.3	7.8
Simulated post-stent	12	7.78	59.49	200.99	1.51	3.93	6.64	0.048	0.074	0.089	11.9	9.9
Simulated post-stent	14	4.24	31.84	106.76	0.82	2.11	3.53	0.026	0.040	0.047	13.9	11.6
Simulated post-stent	16	2.47	18.38	61.59	0.47	1.22	2.02	0.015	0.023	0.027	15.7	13.1
Simulated post-stent	18	1.66	10.78	34.74	0.31	0.71	1.16	0.010	0.013	0.015	17.2	14.4
Simulated post-stent	20	1.21	7.63	24.14	0.24	0.51	0.80	0.008	0.010	0.011	19.1	16.0
iQs (L/min/m^2)		2.84	4.85	6.86								

No actual stent implantation was performed for this patient.

A.7.6.3.5. CHB014B

Table A. 32 Hemodynamics and geometric results of CHB014B (BSA = 1.05m^2)

Pre/post-stent	Stent size (mm)	Power Loss (mW)			TCPC resistance (WU.m^2)			iPL			Min. LT diameter (mm)	Normalized min. LT diameter (mm/m)
		1X	2X	3X	1X	2X	3X	1X	2X	3X		
Pre-stent	N/A	1.14	7.32	23.03	0.40	1.02	1.71	0.015	0.024	0.030	9.6	9.3
Simulated post-stent	14	0.64	3.86	12.10	0.22	0.53	0.91	0.008	0.013	0.016	12.7	12.4
Simulated post-stent	16	0.48	2.62	8.22	0.16	0.36	0.62	0.006	0.009	0.011	15.0	14.6
Simulated post-stent	18	0.41	2.08	6.38	0.13	0.29	0.47	0.005	0.007	0.008	17.7	17.3
Simulated post-stent	20	0.35	1.62	4.82	0.11	0.22	0.36	0.004	0.005	0.006	17.9	17.5
iQs (L/min/m^2)		2.48	3.91	5.33								

No actual stent implantation was performed for this patient.

A.7.6.3.6. CHB020B

Table A. 33 Hemodynamics and geometric results of CHB020B (BSA = 1.47m^2)

Pre/post-stent	Stent size (mm)	Power Loss (mW)			TCPC resistance (WU.m^2)			iPL			Min. LT diameter (mm)	Normalized min. LT diameter (mm/m)
		1X	2X	3X	1X	2X	3X	1X	2X	3X		
Pre-stent	N/A	4.07	26.09	82.78	0.71	1.71	2.84	0.022	0.033	0.039	12.0	9.9
Simulated post-stent	14	3.53	22.02	70.82	0.62	1.44	2.42	0.019	0.028	0.034	14.1	11.6
Simulated post-stent	16	2.73	16.34	53.28	0.47	1.07	1.82	0.015	0.021	0.025	15.9	13.1
Simulated post-stent	18	2.02	11.80	38.27	0.36	0.78	1.31	0.011	0.015	0.018	17.8	14.7
Simulated post-stent	20	1.59	8.20	28.07	0.27	0.53	0.96	0.009	0.010	0.013	19.1	15.8
iQs (L/min/m^2)		2.95	4.79	6.64								

No actual stent implantation was performed for this patient.

A.8. Detailed Results for Specific Aim 2

Two patients of the 11 patients were excluded due to severe image artifacts

A.8.1. Patient Demographic Information

Table A. 34 Patient Demographic Information of the 9 patients included

Patient ID	Gender (M=male, F = female)	IVC connection type (IA = intra-atrial, EC = extra-cardiac)	Ventricular Morphology (LV = left ventricle, RV = right ventricle, MV = mixed ventricle)	Age (yrs)	BSA (m^2)
CHOP011B	F	IA	RV	21	1.64
CHOP029B	M	IA	RV	19	1.74
CHOP032C	F	IA	RV	28	1.64
CHOP091C	M	IA	LV	26	1.82
CHOP103B	M	IA	RV	27	1.92
CHOP155A	M	IA	LV	17.2	1.83
CHOP229A	M	IA	MV	22	1.92
CHOP234A	F	EC	LV	17	1.8
CHOP235A	M	IA	RV	19	1.77
Average				21.8	1.79
Standard deviation				4.2	0.10

A.8.2. CMR Acquisition Parameters

Table A. 35 Details of CMR parameters for anatomy acquisition

Patient ID	No. of slices	Matrix (pixel)	Pixel spacing (mm)	Slice thickness (mm)	Echo time (ms)
CHOP011B	50	256 X168	1.36719	3	1.23
CHOP029B	65	256 X168	1.25	3	1.24
CHOP032C	65	256 X168	1.17188	3	1.27
CHOP091C	60	256 X168	1.48438	3	1.23
CHOP103B	70	256 X168	1.4844	3	1.23
CHOP155A	65	256 X168	1.25	3	1.24
CHOP229A	45	256 X168	1.32813	4	1.21
CHOP234A	70	256 X168	1.28906	3	1.23
CHOP235A	65	256 X168	1.2891	3	1.23
Average	62		1.3238	3.1	1.23
Standard deviation	9		0.1060	0.3	0.02

Table A. 36 Details of CMR parameters for real-time PC-MRI acquisition (free-breathing)

Patient ID	IVC/FP			SVC		
	Encoding velocity (cm/s)	No. of images	Temporal resolution (ms)	Encoding velocity (cm/s)	No. of images	Temporal resolution (ms)
CHOP011B	150	347	57.406069	121	347	57.406069
CHOP029B	150	347	57.413295	121	347	57.413295
CHOP032C	150	347	66.137695	121	347	67.568027
CHOP091C	80	353	56.62642	80	353	56.62642
CHOP103B	150	511	31.72549	150	511	31.72549
CHOP155A	60	199	64.255051	60	199	64.255051
CHOP229A	60	381	52.407895	60	381	52.407895
CHOP234A	150	263	57.40458	60	263	57.232824
CHOP235A	150	347	66.208333	150	347	66.208333
Average	122	344	57	103	344	57
Standard deviation	42	84	10	38	84	11

Table A. 37 Details of CMR parameters for real-time PC-MRI acquisition (breath-held)

Patient ID	IVC/FP			SVC		
	Encoding velocity (cm/s)	No. of images	Temporal resolution (ms)	Encoding velocity (cm/s)	No. of images	Temporal resolution (ms)
CHOP011B	150	263	57.40458	121	263	57.414122
CHOP029B	150	263	57.40458	121	263	57.414122
CHOP032C	150	261	75.774112	150	261	77.34456
CHOP091C	80	263	56.622137	80	263	56.622137
CHOP103B	150	511	31.72549	150	511	31.72549
CHOP155A	60	199	64.255051	60	199	64.255051
CHOP229A	60	263	52.414122	60	285	52.403169
CHOP234A	150	263	57.414122	60	263	57.232824
CHOP235A	150	261	68.150685	150	261	66.928251
Average	122	283	58	106	285	58
Standard deviation	42	88	12	41	88	12

Table A. 38 Details of CMR parameters for conventional PC-MRI acquisition of LPA/RPA

| Patient ID | Encoding velocity (cm/s) | | No. of phases |
	LPA	RPA	
CHOP011B	60	60	30
CHOP029B	60	60	30
CHOP032C	100	60	30
CHOP091C	60	60	24
CHOP103B	60	60	28
CHOP155A	80	80	30
CHOP229A	70	70	30
CHOP234A	80	60	28
CHOP235A	60	60	30
Average	70	63	29
Standard deviation	14	7	2

A.8.3. Raw Data Specific Aim 2

Table A. 39 Time-averaged vessel flow obtained from the selected cycle

| Vessel flow (L/min) | Free-breathing | | | Breath-held | | |
Patient ID	FP	SVC	LSVC	FP	SVC	LSVC
CHOP011B	2.513	0.883		2.395	0.822	
CHOP029B	3.695	1.323		3.240	1.279	
CHOP032C	2.351	1.611		1.899	0.877	
CHOP091C	5.452	0.622	0.471	4.350	0.398	0.372
CHOP103B	2.967	0.907		2.463	0.926	
CHOP155A	5.461	2.561		4.405	1.830	
CHOP229A	2.664	0.542	0.500	2.209	0.470	0.311
CHOP234A	4.139	3.839		3.956	3.334	
CHOP235A	2.045	0.769		1.579	0.385	
Average	3.476	1.451	0.485	2.944	1.147	0.341
Standard deviation	1.299	1.094	0.021	1.075	0.942	0.043

Table A. 40 Pulsatility index of vessel flow obtained from the selected cycle

Pulsatility index	Free-breathing			Breath-held		
Patient ID	FP	SVC	LSVC	FP	SVC	LSVC
CHOP011B	249%	275%		56%	107%	
CHOP029B	115%	162%		96%	95%	
CHOP032C	78%	308%		53%	114%	
CHOP091C	183%	297%	337%	92%	245%	191%
CHOP103B	170%	318%		124%	322%	
CHOP155A	91%	52%		40%	76%	
CHOP229A	205%	179%	151%	82%	163%	113%
CHOP234A	233%	193%		61%	91%	
CHOP235A	227%	206%		76%	302%	
Average	172%	221%	244%	75%	168%	152%
Standard deviation	64%	87%	131%	26%	96%	56%

A.8.4. Particle Tracking Videos for Specific Aim 2

Animation A. 1 Particle tracking video of CHOP029B FB simulation
(animation_A1_CHOP029B_FB.avi, 1.83MB)

Animation A. 2 Particle tracking video of CHOP029B BH simulation
(animation_A2_CHOP029B_BH.avi, 1.86MB)

Animation A. 3 Particle tracking video of CHOP032C FB simulation
(animation_A3_CHOP032C_FB.avi, 2.59MB)

Animation A. 4 Particle tracking video of CHOP032C BH simulation
(animation_A4_CHOP032C_BH.avi, 2.89MB)

Animation A. 5 Particle tracking video of CHOP091C FB simulation
(animation_A5_CHOP091C_FB.avi, 2.95MB)

Animation A. 6 Particle tracking video of CHOP091C BH simulation
(animation_A6_CHOP091C_BH.avi, 2.72MB)

Animation A. 7 Particle tracking video of CHOP103B FB simulation
(animation_A7_CHOP103B_FB.avi, 2.96MB)

Animation A. 8 Particle tracking video of CHOP103B BH simulation
(animation_A8_CHOP103B_BH.avi, 3.05MB)

Animation A. 9 Particle tracking video of CHOP155A FB simulation
(animation_A9_CHOP155A_FB.avi, 2.84MB)

Animation A. 10 Particle tracking video of CHOP155A BH simulation
(animation_A10_CHOP155A_BH.avi, 2.70MB)

Animation A. 11 Particle tracking video of CHOP234A FB simulation
(animation_A11_CHOP234A_FB.avi, 2.61MB)

Animation A. 12 Particle tracking video of CHOP234A BH simulation
(animation_A12_CHOP234A_BH.avi, 2.71MB)

A.8.5. Flow Field Videos for Specific Aim 2

Animation A. 13 Particle tracking video of CHOP011B FB simulation
(animation_A13_CHOP011B_FB_flowfield.avi, 5.63MB)

Animation A. 14 Particle tracking video of CHOP011B BH simulation
(animation_A14_CHOP011B_BH_flowfield.avi, 6.20MB)

Animation A. 15 Particle tracking video of CHOP029B FB simulation
(animation_A15_CHOP029B_FB_flowfield.avi, 6.10MB)

Animation A. 16 Particle tracking video of CHOP029B BH simulation
(animation_A16_CHOP029B_BH_flowfield.avi, 5.75MB)

Animation A. 17 Particle tracking video of CHOP032C FB simulation
(animation_A17_CHOP032C_FB_flowfield.avi, 6.75MB)

Animation A. 18 Particle tracking video of CHOP032C BH simulation
(animation_A18_CHOP032C_BH_flowfield.avi, 6.07MB)

Animation A. 19 Particle tracking video of CHOP091C FB simulation
(animation_A19_CHOP091C_FB_flowfield.avi, 8.32MB)

Animation A. 20 Particle tracking video of CHOP091C BH simulation
(animation_A20_CHOP091C_BH_flowfield.avi, 7.80MB)

Animation A. 21 Particle tracking video of CHOP103B FB simulation
(animation_A21_CHOP103B_FB_flowfield.avi, 5.57MB)

Animation A. 22 Particle tracking video of CHOP103B BH simulation
(animation_A22_CHOP103B_BH_flowfield.avi, 5.58MB)

Animation A. 23 Particle tracking video of CHOP155A FB simulation
(animation_A23_CHOP155A_FB_flowfield.avi, 7.94MB)

Animation A. 24 Particle tracking video of CHOP155A BH simulation
(animation_A24_CHOP155A_BH_flowfield.avi, 7.36MB)

Animation A. 25 Particle tracking video of CHOP229A FB simulation
(animation_A25_CHOP229A_FB_flowfield.avi, 7.33MB)

Animation A. 26 Particle tracking video of CHOP229A BH simulation
(animation_A26_CHOP229A_BH_flowfield.avi, 7.73MB)

Animation A. 27 Particle tracking video of CHOP234A FB simulation
(animation_A27_CHOP234A_FB_flowfield.avi, 7.88MB)

Animation A. 28 Particle tracking video of CHOP234A BH simulation
(animation_A28_CHOP234A_BH_flowfield.avi, 7.66MB)

Animation A. 29 Particle tracking video of CHOP235A FB simulation
(animation_A29_CHOP235A_FB_flowfield.avi, 5.86MB)

Animation A. 30 Particle tracking video of CHOP235A BH simulation
(animation_A30_CHOP235A_BH_flowfield.avi, 5.42MB)

A.9. Detailed Results for Specific Aim 3

Two patients of the 11 patients were excluded due to severe image artifacts

A.9.1. Patient Demographic Information

Table A. 41 Patient Demographic Information of the 9 patients included

Patient ID	Gender (M=male, F = female)	IVC connection type (IA = intra-atrial, EC = extra-cardiac)	Ventricular Morphology (LV = left ventricle, RV = right ventricle, MV = mixed ventricle)	Age (yrs)	BSA (m²)
CHOP011B	F	IA	RV	21	1.64
CHOP021C	F	IA	RV	21	1.75
CHOP029B	M	IA	RV	19	1.74
CHOP032C	F	IA	RV	28	1.64
CHOP091C	M	IA	LV	26	1.82
CHOP155A	M	IA	LV	17.2	1.83
CHOP229A	M	IA	MV	22	1.92
CHOP234A	F	EC	LV	17	1.8
CHOP235A	M	IA	RV	19	1.77
Average				21.1	1.77
Standard deviation				3.8	0.09

A.9.2. CMR Acquisition Parameters

Table A. 42 Details of CMR parameters for real-time PC-MRI acquisition (free-breathing)

Patient ID	IVC/FP			SVC		
	Encoding velocity (cm/s)	No. of images	Temporal resolution (ms)	Encoding velocity (cm/s)	No. of images	Temporal resolution (ms)
CHOP011B	150	347	57.406069	121	347	57.406069
CHOP021C	60	347	57.427746	60	347	57.427746
CHOP029B	150	347	57.413295	121	347	57.413295
CHOP032C	150	347	66.137695	121	347	67.568027
CHOP091C	80	353	56.62642	80	353	56.62642
CHOP155A	60	199	64.255051	60	199	64.255051
CHOP229A	60	381	52.407895	60	381	52.407895
CHOP234A	150	263	57.40458	60	263	57.232824
CHOP235A	150	347	66.208333	150	347	66.208333
Average	112	326	59	93	326	60
Standard deviation	45	57	5	36	57	5

Table A. 43 Details of CMR parameters for real-time PC-MRI acquisition (breath-held)

Patient ID	IVC/FP			SVC		
	Encoding velocity (cm/s)	No. of images	Temporal resolution (ms)	Encoding velocity (cm/s)	No. of images	Temporal resolution (ms)
CHOP011B	150	263	57.40458	121	263	57.414122
CHOP021C	60	263	57.423664	60	263	57.433206
CHOP029B	150	263	57.40458	121	263	57.414122
CHOP032C	150	261	75.774112	150	261	77.34456
CHOP091C	80	263	56.622137	80	263	56.622137
CHOP155A	60	199	64.255051	60	199	64.255051
CHOP229A	60	263	52.414122	60	285	52.403169
CHOP234A	150	263	57.414122	60	263	57.232824
CHOP235A	150	261	68.150685	150	261	66.928251
Average	112	255	61	96	258	61
Standard deviation	45	21	7	40	23	8

Table A. 44 Details of CMR parameters for real-time PC-MRI acquisition (exercise)

Patient ID	IVC/FP			SVC		
	Encoding velocity (cm/s)	No. of images	Temporal resolution (ms)	Encoding velocity (cm/s)	No. of images	Temporal resolution (ms)
CHOP011B	250	175	57.399425	150	175	57.413793
CHOP021C	300	175	56.221264	120	175	56.221264
CHOP029B	250	175	57.413793	150	175	57.399425
CHOP032C	275	175	78.661417	121	175	77.597656
CHOP091C	300	175	56.637931	100	175	56.623563
CHOP155A	250	189	52.406915	120	189	52.406915
CHOP229A	250	175	56.810345	133	175	57.413793
CHOP234A	250	120	83.94958	121	130	84.661017
CHOP235A	250	175	57.399425	150	175	57.413793
Average	264	173	63	119	174	63
Standard deviation	22	22	11	27	19	11

A.9.3. Deformation Indices, Beat-averaged Deformation Indices and Vessel Area at End Inspiration and End Expiration

$$DI = \frac{A_{max} - A_{min}}{A_{mean}} \times 100\%$$

where A_{mean} is the time-averaged vessel area, and A_{min} and A_{max} are the minimum and maximum instantaneous vessel areas.

Table A. 45 Deformation Indices

Patient ID	FP			SVC			LSVC		
	BH	FB	EX	BH	FB	EX	BH	FB	EX
CHOP011B	0.23	0.42	0.57	0.35	0.46	0.46	--	--	--
CHOP021C	0.29	0.55	0.35	0.40	--	0.52	--	--	--
CHOP029B	0.36	0.51	0.49	0.37	0.25	0.35	--	--	--
CHOP032C	0.46	0.43	0.66	0.26	0.36	0.70	--	--	--
CHOP091C	0.30	--	0.58	0.41	0.56	0.53	0.47	0.49	0.62
CHOP155A	0.25	0.34	0.50	0.35	0.74	--	--	--	--
CHOP229A	0.32	--	--	0.55	0.67	1.01	0.62	0.54	1.27
CHOP234A	0.31	0.46	--	--	--	--	--	--	--
CHOP235A	0.46	0.51	0.54	0.40	0.33	0.66	--	--	--
N	9	7	7	8	7	7	2	2	2
Average	0.33	0.46	0.53	0.39	0.48	0.60	0.54	0.51	0.94
Standard deviation	0.08	0.07	0.09	0.08	0.18	0.22	0.11	0.04	0.46

FP = Fontan pathway, SVC = Superior vena cava; LSVC = left SVC; BH = breath-held; FB = free-breathing; EX = exercise

$$baDI = \frac{\bar{A}_{max} - \bar{A}_{min}}{\bar{A}_{mean}} X 100\%$$

where $\bar{A}$ is the beat-averaged vessel cross sectional area

Table A. 46 Beat-averaged Deformation Indices

Patient ID	FP			SVC			LSVC		
	BH	FB	EX	BH	FB	EX	BH	FB	EX
CHOP011B	0.04	0.12	0.29	0.05	0.10	0.25	--	--	--
CHOP021C	0.06	0.26	0.13	0.05	--	0.29	--	--	--
CHOP029B	0.09	0.23	0.28	0.07	0.09	0.10	--	--	--
CHOP032C	0.10	0.10	0.22	0.08	0.13	0.32	--	--	--
CHOP091C	0.06	--	0.21	0.14	0.21	0.24	0.11	0.17	0.35
CHOP155A	0.04	0.09	0.32	0.09	0.21	--	--	--	--
CHOP229A	0.13	--	--	0.18	0.32	0.43	0.13	0.16	0.96
CHOP234A	0.10	0.29	--	--	--	--	--	--	--
CHOP235A	0.12	0.22	0.13	0.11	0.16	0.17	--	--	--
N	9	7	7	8	7	7	2	2	2
Average	0.08	0.19	0.23	0.10	0.17	0.26	0.12	0.16	0.65
Standard deviation	0.03	0.08	0.08	0.04	0.08	0.10	0.01	0.01	0.43

Table A. 47 Instantaneous vessel area at end inspiration and end expiration

Patient ID	FP FB		FP EX		SVC FB		SVC EX		LSVC FB		LSVC EX	
	End insp	End exp	End insp	End exp	End insp	End exp	End insp	End exp	End insp	End exp	End insp	End exp
CHOP011B	3.17	3.08	3.14	3.99	1.51	1.59	1.78	2.45	--	--	--	--
CHOP021C	2.96	2.83	5.99	6.68	--	--	2.54	2.03	--	--	--	--
CHOP029B	--	--	7.54	6.27	2.49	2.51	2.41	2.32	--	--	--	--
CHOP032C	1.03	1.06	0.98	0.94	1.54	1.61	--	--	--	--	--	--
CHOP091C	--	--	7.67	6.62	--	--	2.31	1.98	--	--	1.56	1.27
CHOP155A	--	--	3.69	4.78	2.07	2.55	--	--	--	--	--	--
CHOP229A	--	--	--	--	1.81	1.65	1.77	2.55	1.67	1.52	1.11	2.59
CHOP234A	2.40	1.99	--	--	--	--	--	--	--	--	--	--
CHOP235A	3.88	3.93	2.96	3.00	1.94	2.17	3.50	3.04	--	--	--	--
N	5	5	7	7	6	6	6	6	1	1	2	2
Average	2.69	2.58	4.57	4.61	1.89	2.01	2.39	2.40	1.67	1.52	1.33	1.93
Standard deviation	1.07	1.09	2.54	2.14	0.37	0.46	0.63	0.39			0.32	0.93

End insp = end inspiration; End exp = end expiration

REFERENCES

[1] Jayakumar, K. A., Addonizio, L. J., Kichuk-Chrisant, M. R., Galantowicz, M. E., Lamour, J. M., Quaegebeur, J. M., and Hsu, D. T., 2004, "Cardiac Transplantation after the Fontan or Glenn Procedure," J Am Coll Cardiol, 44(10), pp. 2065-72.

[2] Whitehead, K. K., Pekkan, K., Kitajima, H. D., Paridon, S. M., Yoganathan, A. P., and Fogel, M. A., 2007, "Nonlinear Power Loss During Exercise in Single-Ventricle Patients after the Fontan: Insights from Computational Fluid Dynamics," Circulation, 116(11 Suppl), pp. I165-71.

[3] Pike, N. A., Vricella, L. A., Feinstein, J. A., Black, M. D., and Reitz, B. A., 2004, "Regression of Severe Pulmonary Arteriovenous Malformations after Fontan Revision and "Hepatic Factor" Rerouting," Ann Thorac Surg, 78(2), pp. 697-9.

[4] Duncan, B., and Desai, S., 2003, "Pulmonary Arteriovenous Malformations after Cavopulmonary Anastomosis," Ann Thorac Surg, 76(pp. 1759-1766.

[5] Srivastava, D., Preminger, T., Lock, J. E., Mandell, V., Keane, J. F., Mayer, J. E., Jr., Kozakewich, H., and Spevak, P. J., 1995, "Hepatic Venous Blood and the Development of Pulmonary Arteriovenous Malformations in Congenital Heart Disease," Circulation, 92(5), pp. 1217-22.

[6] April 2015, World Health Organization Fact Sheet N°370 - Congenital Anomalies, 5/18/2015, http://www.who.int/mediacentre/factsheets/fs370/en/

[7] Go As, M. D., Roger Vl, Benjamin Ej, Berry Jd, Borden Wb, Bravata Dm, Dai S, Ford Es, Fox Cs, Franco S, Fullerton Hj, Gillespie C, Hailpern Sm, Heit Ja, Howard Vj, Huffman Md, Kissela Bm, Kittner Sj, Lackland Dt, Lichtman Jh, Lisabeth Ld, Magid D, Marcus Gm, Marelli a, Matchar Db, Mcguire Dk, Mohler Er, Moy Cs, Mussolino Me, Nichol G, Paynter Np, Schreiner Pj, Sorlie Pd, Stein J, Turan Tn, Virani Ss, Wong Nd, Woo D, Turner Mb; on Behalf of the American Heart Association Statistics Committee and Stroke Statistics Subcommittee., 2013, "Heart Disease and Stroke Statistics—2013 Update: A Report from the American Heart Association," Circulation, 127(pp. e6-e245.

[8] Van Der Linde, D., Konings, E., Slager, M., Witsenburg, M., Helbing, W., Takkenberg, J., and Roos-Hesselink, J., 2011, "Birth Prevalence of Congenital Heart Disease Worldwide: A Systematic Review and Meta-Analysis," J Am Coll Cardiol., 58(21), pp. 2241-2247.

[9] Hoffman, J., and Kaplan, S., 2002, "The Incidence of Congenital Heart Disease," J Am Coll Cardiol, 39(12), pp. 1890-1900.

[10] Norwood, W., Kirklin, J., and Sanders, S., 1980, "Hypoplastic Left Heart Syndrome: Experience with Palliative Surgery," Am J Cardiol, 45(1), pp. 87-91.

[11] Fontan, F., and Baudet, E., 1971, "Surgical Repair of Tricuspid Atresia," Thorax, 26(3), pp. 240-8.

[12] Mahle, W. T., Rychik, J., and Rome, J. J., 2000, "Clinical Significance of Pulmonary Arteriovenous Malformations after Staging Bidirectional Cavopulmonary Anastomosis," Am J Cardiol, 86(2), pp. 239-41.

[13] Duncan, B. W., and Desai, S., 2003, "Pulmonary Arteriovenous Malformations after Cavopulmonary Anastomosis," Ann Thorac Surg, 76(5), pp. 1759-66.

[14] Kreutzer, G., Galíndez, E., Bono, H., De Palma, C., and Laura, J., 1973, "An Operation for the Correction of Tricuspid Atresia," J Thorac Cardiovasc Surg, 66(4), pp. 613-621.

[15] Dobell, A., Trusler, G., Smallhorn, J., and Williams, W., 1986, "Atrial Thrombi after the Fontan Operation," Ann Thorac Surg, 42(6), pp. 664-667.

[16] Driscoll, D., Offord, K., Feldt, R., Schaff, H., Puga, F., and Danielson, G., 1992, "Five- to Fifteen-Year Follow-up after Fontan Operation," Circulation, 85(2), pp. 469-496.

[17] Fontan, F., Kirklin, J., Fernandez, G., Costa, F., Naftel, D., Tritto, F., and Blackstone, E., 1990, "Outcome after a "Perfect" Fontan Operation," Circulation, 81(5), pp. 1520-1536.

[18] Mair, D., Puga, F., and Danielson, G., 1992, "Late Functional Status of Survivors of the Fontan Procedure Performed During the 1970s," Circulation, 86(5 Suppl), pp. II106-9.

[19] Lardo, A., Del Nido, P., Webber, S., Friehs, I., and Cape, E., 1997, "Hemodynamic Effect of Progressive Right Atrial Dilatation in Atriopulmonary Connections," J Thorac Cardiovasc Surg, 114(1), pp. 2-8.

[20] De Leval, M., Kilner, O., Gewillig, M., and Bull, C., 1988, "Total Cavopulmonary Connection: A Logical Alternative to Atriopulmonary Connection for Complex Fontan Operations. Experimental Studies and Early Clinical Experience " J Thorac Cardiovasc Surg, 96(pp. 682-695.

[21] Alphonso N, B. M., Sundar P, Tulloh R, Austin C, Anderson D, 2005, "Intermediate-Term Outcome Following the Fontan Operation: A Survival, Functional, and Risk-Factor Analysis," European Journal of Cardio-Thoracic Surgery, 28(pp. 529-535.

[22] Mair Dd, Puga Fj, and Gk, D., 2001, "The Fontan Procedure for Tricuspid Atresia: Early and Late Results of a 25-Year Experience with 216 Patients," J Am Coll Cardiol., 37(3), pp. 933-939.

[23] Gaynor Jw, Bridges Nd, Cohen Mi, Mahle Wt, Decampli Wm, Steven Jm, Nicolson Sc, and Tl, S., 2002, "Predictors of Outcome after the Fontan Operation: Is Hypoplastic Left Heart Syndrome Still a Risk Factor?," J Thorac Cardiovasc Surg., 123(2), pp. 237-245.

[24] Marcelletti, C., Hanley, F., Mavroudis, C., Mcelhinney, D., Abella, R., Marianeschi, S., Seddio, F., Reddy, V., Petrossian, E., De La Torre, T., Colagrande, L., Backer, C., Cipriani, A., Iorio, F., and Fontan, F., 2000, "Revision of Previous Fontan Connections to Total Extracardiac Cavopulmonary Anastomosis: A Multicenter Experience," J Thorac Cardiovasc Surg, 119(2), pp. 340-346.

[25] Podzolkov, V., Zaets, S., Chiaureli, M., Alekyan, B., Zotova, L., and Chernikh, I., 1997, "Comparative Assessment of Fontan Operation in Modifications of Atriopulmonary and Total Cavopulmonary Anastomoses," Eur J Cardiothorac Surg, 11(3), pp. 458-465.

[26] Pearl, J., Laks, H., Stein, D., Drinkwater, D., George, B., and Williams, R., 1991, "Total Cavopulmonary Anastomosis Versus Conventional Modified Fontan Procedure," Ann Thorac Surg, 52(2), pp. 189-196.

[27] De Zelicourt, D., Pekkan, K., Wills, L., Kanter, K., Forbess, J., Sharma, S., Fogel, M., and Yoganathan, A. P., 2005, "In Vitro Flow Analysis of a Patient-Specific Intraatrial Total Cavopulmonary Connection," Ann Thorac Surg, 79(6), pp. 2094-102.

[28] Amodeo, A., Galletti, L., Marianeschi, S., Picardo, S., Giannico, S., Renzi, P. D., and Marcelletti, C., 1997, "Extracardiac Fontan Operation for Complex Cardiac Anomalies: Seven Years' Experience," J Thorac Cardiovasc Surg 114(pp. 1020-1031.

[29] Nakano, T., Kado, H., Ishikawa, S., Shiokawa, Y., Ushinohama, H., Sagawa, K., Fusazaki, N., Nishimura, Y., Tanoue, Y., Nakamura, T., and Ueda, Y., 2004, "Midterm Surgical Results of Total Cavopulmonary Connection: Clinical Advantages of the Extracardiac Conduit Method," J Thorac Cardiovasc Surg, 127(pp. 730-737.

[30] Haas, G. S., Hess, H., Black, M., Onnasch, J., Mohr, F. W., and Son, J. a. M. V., 2000, "Extracardiac Conduit Fontan Procedure: Early and Intermediate Results," European Journal of Cardio-thoracic Surgery 17(pp. 648-654.

[31] Petrossian, E., Reddy, V. M., Mcelhinney, D. B., Akkersdijk, G. P., Moore, P., Parry, A. J., Thompson, L. D., and Hanley, F. L., 1999, "Early Results of the Extracardiac Conduit Fontan Operation," J Thorac Cardiovasc Surg, 117(pp. 688-696

[32] Tam, V. K. H., Miller, B. E., and Murphy, K., 1999, "Modified Fontan without Use of Cardiopulmonary Bypass," Ann Thorac Surg 68(5), pp. 1698-703.

[33] Khairy P, Fernandes Sm, John E. Mayer J, Triedman Jk, Walsh Ep, Lock Je, and Mj, L., 2008, "Long-Term Survival, Modes of Death, and Predictors of Martality in Patients with Fontan Surgery," Circulation, 117(pp. 85-92.

[34] Jayakumar, K. A., Addonizio, L. J., Kichuk-Chrisant, M. R., Galantowicz, M. E., Lamour, J. M., Quaegebeur, J. M., and Hsu, D. T., 2004, "Cardiac Transplantation after the Fontan or Glenn Procedure," Journal of the American College of Cardiology, 44(10), pp. 2065-72.

[35] Senzaki, H., Masutani, S., Ishido, H., Taketazu, M., Kobayashi, T., Sasaki, N., Asano, H., Katogi, T., Kyo, S., and Yokote, Y., 2006, "Cardiac Rest and Reserve Function in Patients with Fontan Circulation," J Am Coll Cardiol, 47(12), pp. 2528-35.

[36] Szabo, G., Buhmann, V., Graf, A., Melnitschuk, S., Bahrle, S., Vahl, C. F., and Hagl, S., 2003, "Ventricular Energetics after the Fontan Operation: Contractility-Afterload Mismatch," J Thorac Cardiovasc Surg, 125(5), pp. 1061-9.

[37] Sundareswaran, K. S., Kanter, K. R., Kitajima, H. D., Krishnankutty, R., Sabatier, J. F., Parks, W. J., Sharma, S., Yoganathan, A. P., and Fogel, M., 2006, "Impaired Power Output and Cardiac Index with Hypoplastic Left Heart Syndrome: A Magnetic Resonance Imaging Study," Ann Thorac Surg, 82(4), pp. 1267-75; discussion 1275-7.

[38] Kirklin, J. K., Blackstone, E. H., Kirklin, J. W., Pacifico, A. D., and Bargeron, L. M., Jr., 1986, "The Fontan Operation. Ventricular Hypertrophy, Age, and Date of Operation as Risk Factors," J Thorac Cardiovasc Surg, 92(6), pp. 1049-64.

[39] Eicken, A., Fratz, S., Gutfried, C., Balling, G., Schwaiger, M., Lange, R., Busch, R., Hess, J., and Stern, H., 2003, "Hearts Late after Fontan Operation Have Normal Mass, Normal Volume, and Reduced Systolic Function: A Magnetic Resonance Imaging Study," J Am Coll Cardiol, 42(6), pp. 1061-5.

[40] Fogel, M. A., Weinberg, P. M., Chin, A. J., Fellows, K. E., and Hoffman, E. A., 1996, "Late Ventricular Geometry and Performance Changes of Functional Single Ventricle Throughout Staged Fontan Reconstruction Assessed by Magnetic Resonance Imaging," J Am Coll Cardiol, 28(1), pp. 212-21.

[41] Wu, F., Ukomadu, C., Odze, R., Valente, A., Mayer, J. J., and Earing, M., 2011, "Liver Disease in the Patient with Fontan Circulation," Congenit Heart Dis, 6(3), pp. 190-201.

[42] Rychik, J., Veldtman, G., Rand, E., Russo, P., Rome, J. J., Krok, K., Goldberg, D. J., Cahill, A. M., and Wells, R. G., 2012, "The Precarious State of the Liver after a Fontan Operation: Summary of a Multidisciplinary Symposium," Pediatr Cardiol, 33(7), pp. 1001-12.

[43] Elder, R. W., Mccabe, N. M., Hebson, C., Veledar, E., Romero, R., Ford, R. M., Mahle, W. T., Kogon, B. E., Sahu, A., Jokhadar, M., Mcconnell, M. E., and Book, W. M., 2013, "Features of Portal Hypertension Are Associated with Major Adverse Events in Fontan Patients: The Vast Study," Int J Cardiol, 168(4), pp. 3764-9.

[44] Bryant, T., Ahmad, Z., Millward-Sadler, H., Burney, K., Stedman, B., Kendall, T., Vettukattil, J., Haw, M., Salmon, A. P., Cope, R., Hacking, N., Breen, D., Sheron, N., and Veldtman, G. R., 2011, "Arterialised Hepatic Nodules in the Fontan Circulation: Hepatico-Cardiac Interactions," Int J Cardiol, 151(3), pp. 268-72.

[45] Sherlock, S., 1951, "The Liver in Heart Failure; Relation of Anatomical, Functional, and Circulatory Changes," Br Heart J, 13(3), pp. 273-93.

[46] Kiesewetter, C. H., Sheron, N., Vettukattill, J. J., Hacking, N., Stedman, B., Millward-Sadler, H., Haw, M., Cope, R., Salmon, A. P., Sivaprakasam, M. C., Kendall, T., Keeton, B. R., Iredale, J. P., and Veldtman, G. R., 2007, "Hepatic Changes in the Failing Fontan Circulation," Heart, 93(5), pp. 579-84.

[47] Dasi, L. P., Whitehead, K., Pekkan, K., Zelicourt, D. D., Sundareswaran, K., Kanter, K., Fogel, M. A., and Yoganathan, A. P., 2011, "Pulmonary Hepatic Flow Distribution in Total Cavopulmonary Connections: Extracardiac Versus Intracardiac," J Thorac Cardiovasc Surg, 141(pp. 207-14.

[48] Sundareswaran, K. S., De Zelicourt, D., Sharma, S., Kanter, K. R., Spray, T. L., Rossignac, J., Sotiropoulos, F., Fogel, M. A., and Yoganathan, A. P., 2009, "Correction of Pulmonary Arteriovenous Malformation Using Image-Based Surgical Planning," JACC Cardiovasc Imaging, 2(8), pp. 1024-30.

[49] Marsden, A. L., Bernstein, A. J., Reddy, V. M., Shadden, S. C., Spilker, R. L., Chan, F. P., Taylor, C. A., and Feinstein, J. A., 2009, "Evaluation of a Novel Y-Shaped Extracardiac Fontan Baffle Using Computational Fluid Dynamics," Journal of Thoracic and Cardiovascular Surgery, 137(pp. 394-403.

[50] P.G., S., and J.H., M., 1984, "The Role of Maximal Oxygen Uptake in Exercise Performance," Clin Chest Med, 5(1), pp. 51-62.

[51] Reybrouck, T., Weymans, M., Stijns, H., Knops, J., and Van Der Hauwaert, L., 1985, "Ventilatory Anaerobic Threshold in Healthy Children. Age and Sex Differences," Eur J Appl Physiol Occup Physiol, 54(3), pp. 278-84.

[52] Wasserman K, H. J., Sue Dy, Casaburi R, Whipp Bj., 1999,

[53] Paridon, S. M., Mitchell, P. D., Colan, S. D., Williams, R. V., Blaufox, A., Li, J. S., Margossian, R., Mital, S., Russell, J., and Rhodes, J., 2008, "A Cross-Sectional Study of Exercise Performance During the First 2 Decades of Life after the Fontan Operation," J Am Coll Cardiol, 52(2), pp. 99-107.

[54] Takken, T., Tacken, M. H., Blank, A. C., Hulzebos, E. H., Strengers, J. L., and Helders, P. J., 2007, "Exercise Limitation in Patients with Fontan Circulation: A Review," J Cardiovasc Med (Hagerstown), 8(10), pp. 775-81.

[55] O'donnell, C. P., and Landzberg, M. J., 2002, "The 'Failing' Fontan Circulation," Prog Pediatr Cardiol, 16(1), pp. 105-114.

[56] Kung, E., Perry, J., Davis, C., Migliavacca, F., Pennati, G., Giardini, A., Hsia, T., and Marsden, A., 2014, "Computational Modeling of Pathophysiologic Responses to Exercise in Fontan Patients," Ann Biomed Eng, 43(6), pp. 1335-47.

[57] Sundareswaran, K. S., Pekkan, K., Dasi, L. P., Whitehead, K., Sharma, S., Kanter, K. R., Fogel, M. A., and Yoganathan, A. P., 2008, "The Total Cavopulmonary Connection Resistance: A Significant Impact on Single Ventricle Hemodynamics at Rest and Exercise," Am J Physiol Heart Circ Physiol, 295(pp. H2427-H2435.

[58] Goldstein, B. H., Connor, C. E., Gooding, L., and Rocchini, A. P., 2010, "Relation of Systemic Venous Return, Pulmonary Vascular Resistance, and Diastolic Dysfunction to Exercise Capacity in Patients with Single Ventricle Receiving Fontan Palliation," Am J Cardiol. , 105(8), pp. 1169–1175.

[59] Ensley, A. E., Lynch, P., Chatzimavroudis, G. P., Lucas, C., Sharma, S., and Yoganathan, A. P., 1999, "Toward Designing the Optimal Total Cavopulmonary Connection: An in Vitro Study," Ann Thorac Surg, 68(4), pp. 1384-90.

[60] Krishnankuttyrema, R., Dasi, L. P., Pekkan, K., Sundareswaran, K., Fogel, M. A., Sharma, S., Kanter, K., Spray, T., and Yoganathan, A. P., 2008, "Quantitative Analysis of Extracardiac Versus Intraatrial Fontan Anatomic Geometries," Ann Thorac Surg, 85(pp. 810-7.

[61] Sharma, S., Goudy, S., Walker, P., Panchal, S., Ensley, A., Kanter, K., Tam, V., Fyfe, D., and Yoganathan, A., 1996, "In Vitro Flow Experiments for Determination of Optimal Geometry of Total Cavopulmonary Connection for Surgical Repair of Children with Functional Single Ventricle," J Am Coll Cardiol, 27(5), pp. 1264-9.

[62] De Zelicourt, D. A., Pekkan, K., Wills, L., Kanter, K., Forbess, J., Sharma, S., Fogel, M., and Yoganathan, A. P., 2005, "In Vitro Flow Analysis of a Patient-Specific Intraatrial Total Cavopulmonary Connection," Ann Thorac Surg, 79(6), pp. 2094-102.

[63] Degroff, C. G., Carlton, J. D., Weinberg, C. E., Ellison, M. C., Shandas, R., and Valdes-Cruz, L., 2002, "Effect of Vessel Size on the Flow Efficiency of the Total Cavopulmonary Connection: In Vitro Studies," Pediatr Cardiol, 23(2), pp. 171-7.

[64] Ensley, A. E., Ramuzat, A., Healy, T. M., Chatzimavroudis, G. P., Lucas, C., Sharma, S., Pettigrew, R., and Yoganathan, A. P., 2000, "Fluid Mechanic Assessment of the Total Cavopulmonary Connection Using Magnetic Resonance Phase Velocity Mapping and Digital Particle Image Velocimetry," Ann Biomed Eng, 28(10), pp. 1172-83.

[65] Gerdes, A., Hanke, T., Ahrens, V., Pfister, G., and Sievers, H. H., 2002, "Does Caval Aplanarity Influence Power Losses across in Vitro Cavopulmonary Connections?," Pediatr Cardiol, 23(4), pp. 388-93.

[66] Gerdes, A., Kunze, J., Pfister, G., and Sievers, H. H., 1999, "Addition of a Small Curvature Reduces Power Losses across Total Cavopulmonary Connections," Ann Thorac Surg, 67(6), pp. 1760-4.

[67] Khunatorn, Y., Shandas, R., Degroff, C., and Mahalingam, S., 2003, "Comparison of in Vitro Velocity Measurements in a Scaled Total Cavopulmonary Connection with Computational Predictions," Ann Biomed Eng, 31(7), pp. 810-22.

[68] Kim, S. H., Park, Y. H., and Cho, B. K., 1997, "Hemodynamics of the Total Cavopulmonary Connection: An in Vitro Study," Yonsei Med J, 38(1), pp. 33-9.

[69] Ryu, K., Healy, T. M., Ensley, A. E., Sharma, S., Lucas, C., and Yoganathan, A. P., 2001, "Importance of Accurate Geometry in the Study of the Total Cavopulmonary Connection: Computational Simulations and in Vitro Experiments," Ann Biomed Eng, 29(10), pp. 844-853.

[70] Sievers, H. H., Gerdes, A., Kunze, J., and Pfister, G., 1998, "Superior Hydrodynamics of a Modified Cavopulmonary Connection for the Norwood Operation," Ann Thorac Surg, 65(6), pp. 1741-5.

[71] Walker, P. G., Howe, T. T., Davies, R. L., Fisher, J., and Watterson, K. G., 2000, "Distribution of Hepatic Venous Blood in the Total Cavo-Pulmonary Connection: An in Vitro Study," Eur J Cardiothorac Surg, 17(6), pp. 658-65.

[72] Grigioni, M., Amodeo, A., Daniele, C., D' Avenio, G., Formigari, R., and Di Donato, R. M., 2000, "Particle Image Velocimetry Analysis of the Flow Field in the Total Cavopulmonary Connection," Artificial Organs, 24(12), pp. 946-952.

529

[73] Kitajima, H., Sundareswaran, K., Teisseyre, T., Astary, G., Parks, W., Skrinjar, O., Oshinski, J., and Yoganathan, A., 2008, "Comparison of Particle Image Velocimetry and Phase Contrast Mri in a Patient-Specific Extracardiac Total Cavopulmonary Connection," J Biomech Eng, 130(4), pp. 041004.

[74] Pekkan, K., De Zelicourt, D., Ge, L., Sotiropoulos, F., Frakes, D., Fogel, M. A., and Yoganathan, A. P., 2005, "Physics-Driven Cfd Modeling of Complex Anatomical Cardiovascular Flows-a Tcpc Case Study," Ann Biomed Eng, 33(3), pp. 284-300.

[75] Tang, E., Haggerty, C. M., Khiabani, R. H., De Zélicourt, D. A., Kanter, J., Sotiropoulos, F., Fogel, M., and Yoganathan, A. P., 2013, "Numerical and Experimental Investigation of Pulsatile Hemodynamics in the Total Cavopulmonary Connection," J Biomech, 46(2), pp. 373–82.

[76] Haggerty, C., Fynn-Thompson, F., Mcelhinney, D., Valente, A., Saikrishnan, N., Del Nido, P., and Yoganathan, A., 2012, "Experimental and Numeric Investigation of Impella Pumps as Cavopulmonary Assistance for a Failing Fontan," J Thorac Cardiovasc Surg, 144(3), pp. 563-569.

[77] Throckmorton, A., Ballman, K., Myers, C., Litwak, K., Frankel, S., and Rodefeld, M., 2007, "Mechanical Cavopulmonary Assist for the Univentricular Fontan Circulation Using a Novel Folding Propeller Blood Pump," ASAIO J, 53(6), pp. 734-741.

[78] Santhanakrishnan, A., Maher, K. O., Tang, E., Khiabani, R. H., Johnson, J., and Yoganathan, A. P., 2013, "Hemodynamic Effects of Implanting a Unidirectional Valve in the Inferior Vena Cava of the Fontan Circulation Pathway: An in Vitro Investigation," Am J Physiol Heart Circ Physiol, 305(10), pp. H1538-H1547.

[79] Migliavacca, F., De Leval, M. R., Dubini, G., Pietrabissa, R., and Fumero, R., 1999, "Computational Fluid Dynamic Simulations of Cavopulmonary Connections with an Extracardiac Lateral Conduit," Med Eng Phys, 21(3), pp. 187-93.

[80] Pekkan, K., Kitajima, H. D., De Zelicourt, D., Forbess, J. M., Parks, W. J., Fogel, M. A., Sharma, S., Kanter, K. R., Frakes, D., and Yoganathan, A. P., 2005, "Total Cavopulmonary Connection Flow with Functional Left Pulmonary Artery Stenosis: Angioplasty and Fenestration in Vitro," Circulation, 112(21), pp. 3264-71.

[81] Migliavacca, F., and Dubini, G., 2005, "Computational Modeling of Vascular Anastomoses," Biomech Model Mechanobiol, 3(4), pp. 235-50.

[82] Degroff, C., Birnbaum, B., Shandas, R., Orlando, W., and Hertzberg, J., 2005, "Computational Simulations of the Total Cavo-Pulmonary Connection: Insights in Optimizing Numerical Solutions," Med Eng Phys., 27(2), pp. 135-46.

[83] Degroff, C., and Shandas, R., 2002, "Designing the Optimal Total Cavopulmonary Connection: Pulsatile Versus Steady Flow Experiments," Med Sci Monit. , 8(3), pp. MT41-5.

[84] Dubini, G., De Leval, M. R., Pietrabissa, R., Montevecchi, F. M., and Fumero, R., 1996, "A Numerical Fluid Mechanical Study of Repaired Congenital Heart Defects. Application to the Total Cavopulmonary Connection," J Biomech, 29(1), pp. 111-21.

[85] Grigioni, M., D'avenio, G., Del Gaudio, C., and Morbiducci, U., 2005, "Critical Issues in Studies of Flow through the Fontan Circuit after 10 Years of Investigation," Cardiol Young, 15(Suppl 3), pp. 68-73.

[86] Khunatorn, Y., Mahalingam, S., Degroff, C. G., and Shandas, R., 2002, "Influence of Connection Geometry and Svc-Ivc Flow Rate Ratio on Flow Structures within the Total Cavopulmonary Connection: A Numerical Study," J Biomech Eng, 124(4), pp. 364-77.

[87] Masters, J. C., Ketner, M., Bleiweis, M. S., Mill, M., Yoganathan, A., and Lucas, C. L., 2004, "The Effect of Incorporating Vessel Compliance in a Computational Model of Blood Flow in a Total Cavopulmonary Connection (Tcpc) with Caval Centerline Offset," J Biomech Eng, 126(6), pp. 709-13.

[88] Orlando, W., Shandas, R., and Degroff, C., 2006, "Efficiency Differences in Computational Simulations of the Total Cavo-Pulmonary Circulation with and without Compliant Vessel Walls," Comput Methods Programs Biomed, 81(3), pp. 220-7.

[89] Van Haesdonck, J. M., Mertens, L., Sizaire, R., Montas, G., Purnode, B., Daenen, W., Crochet, M., and Gewillig, M., 1995, "Comparison by Computerized Numeric Modeling of Energy Losses in Different Fontan Connections," Circulation, 92(9 Suppl), pp. II322-6.

[90] Migliavacca, F., Dubini, G., Bove, E. L., and De Leval, M. R., 2003, "Computational Fluid Dynamics Simulations in Realistic 3-D Geometries of the Total Cavopulmonary Anastomosis: The Influence of the Inferior Caval Anastomosis," J Biomech Eng, 125(6), pp. 805-13.

[91] Marsden, A. L., Vignon-Clementel, I. E., Chan, F. P., Feinstein, J. A., and Taylor, C. A., 2007, "Effects of Exercise and Respiration on Hemodynamic Efficiency in Cfd Simulations of the Total Cavopulmonary Connection," Ann Biomed Eng, 35(2), pp. 250-63.

[92] Dasi, L. P., Whitehead, K., Pekkan, K., De Zelicourt, D., Sundareswaran, K., Kanter, K., Fogel, M. A., and Yoganathan, A. P., 2011, "Pulmonary Hepatic Flow Distribution in Total Cavopulmonary Connections: Extracardiac Versus Intracardiac," J Thorac Cardiovasc Surg, 141(1), pp. 207-214.

[93] Haggerty, C. M., Restrepo, M., Tang, E., De Zelicourt, D. A., Sundareswaran, K. S., Mirabella, L., Bethel, J., Whitehead, K. K., Fogel, M. A., and Yoganathan, A. P., 2013, "Fontan Hemodynamics from 100 Patient-Specific Cardiac Magnetic Resonance Studies: A Computational Fluid Dynamics Analysis," J Thorac Cardiovasc Surg, pp.

[94] Peskin, C. S., and Tu, C., 1986, "Hemodynamics in Congenital Heart Disease," Comput Biol Med, 16(5), pp. 331-59.

[95] Migliavacca, F., Pennati, G., Dubini, G., Fumero, R., Pietrabissa, R., Urcelay, G., Bove, E. L., Hsia, T. Y., and De Leval, M. R., 2001, "Modeling of the Norwood Circulation: Effects of Shunt Size, Vascular Resistances, and Heart Rate," Am J Physiol Heart Circ Physiol, 280(5), pp. H2076-86.

[96] Pennati, G., Migliavacca, F., Dubini, G., Pietrabissa, R., and De Leval, M. R., 1997, "A Mathematical Model of Circulation in the Presence of the Bidirectional Cavopulmonary Anastomosis in Children with a Univentricular Heart," Med Eng Phys, 19(3), pp. 223-34.

[97] Tu, C., and Peskin, C. S., 1989, "Hemodynamics in Transposition of the Great Arteries with Comparison to Ventricular Septal Defect," Comput Biol Med, 19(2), pp. 95-128.

[98] Pekkan, K., Frakes, D., De Zelicourt, D., Lucas, C. W., Parks, W. J., and Yoganathan, A. P., 2005, "Coupling Pediatric Ventricle Assist Devices to the Fontan Circulation: Simulations with a Lumped-Parameter Model," ASAIO Journal, 51(5), pp. 618-628.

[99] Migliavacca, F., Balossino, R., Pennati, G., Dubini, G., Hsia, T., De Leval, M., and Bove, E., 2006, "Multiscale Modelling in Biofluidynamics: Application to Reconstructive Paediatric Cardiac Surgery," J Biomech, 39(6), pp. 1010-1020.

[100] Pennati, G., Corsini, C., Cosentino, D., Hsia, T., Luisi, V., Dubini, G., and Migliavacca, F., 2011, "Boundary Conditions of Patient-Specific Fluid Dynamics Modelling of Cavopulmonary Connections: Possible Adaptation of Pulmonary Resistances Results in a Critical Issue for a Virtual Surgical Planning," Interface Focus, 1(3), pp. 297-307.

[101] Baretta, A., Corsini, C., Yang, W., Vignon-Clementel, I., Marsden, A., Feinstein, J., Hsia, T., Dubini, G., Migliavacca, F., Pennati, G., and Investigators, M. O. C. H. a. M., 2011, "Virtual Surgeries in Patients with Congenital Heart Disease: A Multi-Scale Modelling Test Case," Philos Trans A Math Phys Eng Sci, 369(1954), pp. 4316-4330.

[102] Pekkan, K., Whited, B., Kanter, K., Sharma, S., De Zelicourt, D., Sundareswaran, K., Frakes, D., Rossignac, J., and Yoganathan, A. P., 2008, "Patient-Specific Surgical Planning and Hemodynamic Computational Fluid Dynamics Optimization through Free-Form Haptic Anatomy Editing Tool (Surgem)," Med Biol Eng Comput, 46(11), pp. 1139-52.

[103] Vignon-Clementel, I. E., Marsden, A. L., and Feinstein, J. A., 2010, "A Primer on Computational Simulation in Congenital Heart Disease for the Clinician," Prog Pediatr Cardiol, 30(1-2), pp. 3-13.

[104] Kung, E., Baretta, A., Baker, C., Arbia, G., Biglino, G., Corsini, C., Schievano, S., Vignon-Clementel, I., Dubini, G., Pennati, G., Taylor, A., Dorfman, A., Hlavacek, A., Marsden, A., Hsia, T., Migliavacca, F., and Investigators, M., 2013, "Predictive Modeling of the Virtual Hemi-Fontan Operation for Second Stage Single Ventricle Palliation: Two Patient-Specific Cases," J Biomech, 46(2), pp. 423-429.

[105] Corsini, C., Baker, C., Kung, E., Schievano, S., Arbia, G., Baretta, A., Biglino, G., Migliavacca, F., Dubini, G., Pennati, G., Marsden, A., Vignon-Clementel, I., Taylor, A., Hsia, T., Dorfman, A., and Investigators., M., 2014, "An Integrated Approach to Patient-Specific Predictive Modeling for Single Ventricle Heart Palliation," Comput Methods Biomech Biomed Engin, 17(14), pp. 1572-1589.

[106] Yang, W., Feinstein, J., Shadden, S., Vignon-Clementel, I., and Marsden, A., 2013, "Optimization of a Y-Graft Design for Improved Hepatic Flow Distribution in the Fontan Circulation," J Biomech Eng, 135(1), pp. 011002.

[107] Quail, M., and Taylor, A., 2013, "Computer Modeling to Tailor Therapy for Congenital Heart Disease," Curr Cardiol Rep, 15(9), pp. 395.

[108] De Zelicourt, D., Haggerty, C. M., Sundareswaran, K. S., Whited, B., Rossignac, J., Kanter, K., Gaynor, J. W., Spray, T. L., Sotiropoulos, F., Fogel, M. A., and Yoganathan, A. P., 2011, "Individualized Computer-Based Surgical Planning to Address Pulmonary Ateriovenous Malformations in Patients with a Single Ventricle with an Interrupted Inferior Vena Cava and Azygous Continuation," Journal of Thoracic and Cardiovascular Surgery, 141(5), pp. 1170-1177.

[109] Mirabella, L., Haggerty, C. M., Passerini, T., Piccinelli, M., Powell, A. J., Nido, P. J. D., Veneziani, A., and Yoganathan, A. P., 2012, "Treatment Planning for a Tcpc Test Case: A Numerical Investigation under Rigid and Moving Wall Assumptions," Int J Numer Method Biomed Eng, 29(2), pp. 197-216.

[110] Haggerty, C., Yoganathan, A., and Fogel, M., 2013, "Magnetic Resonance Imaging-Guided Surgical Design: Can We Optimise the Fontan Operation?," Cardiol Young, 23(6), pp. 818-823.

[111] Haggerty, C., De Zélicourt, D., Restrepo, M., Rossignac, J., Spray, T., Kanter, K., Fogel, M., and Yoganathan, A., 2012, "Comparing Pre- and Post-Operative Fontan Hemodynamic Simulations: Implications for the Reliability of Surgical Planning," Ann Biomed Eng, 40(12), pp. 2639-2651.

[112] Soerensen, D. D., Pekkan, K., De Zélicourt, D., Sharma, S., Kanter, K., Fogel, M., and Yoganathan, A. P., 2007, "Introduction of a New Optimized Total Cavopulmonary Connection," Ann Thorac Surg, 83(6), pp. 2182–2190.

[113] Kanter, K. R., Haggerty, C. M., Restrepo, M., De Zelicourt, D. A., Rossignac, J., Parks, W. J., and Yoganathan, A. P., 2012, "Preliminary Clinical Experience with a Bifurcated Y-Graft Fontan Procedure-a Feasibility Study," J Thorac Cardiovasc Surg, pp.

[114] Kanter, K. R., Haggerty, C. M., Restrepo, M., De Zelicourt, D., Rossignac, J., Parks, W. J., and Yoganathan, A. P., 2011, "Preliminary Clinical Experience with a Bifurcated Y-Graft Fontan Procedure (Abstract)," Western Thoracic Surgical Association 37th Annual Meeting, pp.

[115] Haggerty, C. M., Kanter, K. R., Restrepo, M., De Zelicourt, D., Parks, W. J., Rossignac, J., Fogel, M. A., and Yoganathan, A. P., 2013, "Simulating Hemodynamics of the Fontan Y-Graft Based on Patient-Specific in Vivo Connections," J Thorac Cardiovasc Surg, 145(3), pp. 663-70.

[116] Yang, W., Feinstein, J. A., Shadden, S. C., Vignon-Clementel, I. E., and Marsden, A. L., 2013, "Optimization of a Y-Graft Design for Improved Hepatic Flow Distribution in the Fontan Circulation," J Biomech Eng, 135(1), pp. 011002.

[117] Formaggia, L., Quarteroni, A., and Veneziani, A., 2009, "Multiscale Models of the Vascular System," Cardiovascular Mathematics: Modeling and Simulation of the Circulatory System, 1(11), pp. 395-446.

[118] Kim, H. J., Vignon-Clementel, I. E., Figueroa, C. A., Ladisa, J. F., Jansen, K. E., Feinstein, J. A., and Taylor, C. A., 2009, "On Coupling a Lumped Parameter Heart Model and a Three-Dimensional Finite Element Aorta Model," Ann Biomed Eng, 37(11), pp. 2153-69.

[119] Laganà, K., Dubini, G., Migliavacca, F., Pietrabissa, R., Pennati, G., Veneziani, A., and Quarteroni, A., 2002, "Multiscale Modelling as a Tool to Prescribe Realistic Boundary Conditions for the Study of Surgical Procedures," Biorheology, 39(3), pp. 359–364.

[120] Migliavacca, F., Balossino, R., Pennati, G., Dubini, G., Hsia, T. Y., De Leval, M. R., and Bove, E. L., 2006, "Multiscale Modelling in Biofluidynamics: Application to Reconstructive Paediatric Cardiac Surgery," J Biomech, 39(6), pp. 1010-20.

[121] Baretta, A., Corsini, C., Yang, W., Vignon-Clementel, I. E., Marsden, A. L., Feinstein, J. A., Hsia, T. Y., Dubini, G., Migliavacca, F., Pennati, G., and Modeling of Congenital Hearts Alliance, I., 2011, "Virtual Surgeries in Patients with Congenital Heart Disease: A Multi-Scale Modelling Test Case," Philos Trans A Math Phys Eng Sci, 369(1954), pp. 4316-30.

[122] Corsini, C., Cosentino, D., Pennati, G., Dubini, G., Hsia, T. Y., and Migliavacca, F., 2011, "Multiscale Models of the Hybrid Palliation for Hypoplastic Left Heart Syndrome," J Biomech, 44(4), pp. 767-70.

[123] Minich, L., Tani, L., Olson, A., Orsmond, G., and Shaddy, R., 1996, "Reversal of Flow in the Left Pulmonary Artery after Cavopulmonary Connection," J Am Soc Echocardiogr, 9(2), pp. 202-205.

[124] Penny, D., and Redington, A., 1991, "Doppler Echocardiographic Evaluation of Pulmonary Blood Flow after the Fontan Operation: The Role of the Lungs," Br Heart J, 66(5), pp. 372-374.

[125] Degroff, C. G., and Shandas, R., 2002, "Designing the Optimal Total Cavopulmonary Connection: Pulsatile Versus Steady Flow Experiments," Med Sci Monit, 8(3), pp. MT41-MT45.

[126] De Zelicourt, D., 2010, "Pulsatile Fontan Hemodynamics and Patient-Specific Surgical Planning: A Numerical Investigation," Department of Biomedical Engineering, Georgia Institute of Technology and Emory University, pp.

[127] De Zélicourt, D., Ge, L., Wang, C., Sotiropoulos, F., A., G., and Yoganathan, A., 2009, "Flow Simulations in Arbitrarily Complex Cardiovascular Anatomies - an Unstructured Cartesian Grid Approach," Computers & Fluids, 38(9), pp. 1749-1762.

[128] Khiabani, R. H., Restrepo, M., Tang, E., De Zelicourt, D., Sotiropoulos, F., Fogel, M., and Yoganathan, A. P., 2012, "Effect of Flow Pulsatility on Modeling the Hemodynamics in the Total Cavopulmonary Connection," J Biomech, 45(14), pp. 2376-81.

[129] Bazilevs, Y., Hsu, M. C., Benson, D. J., Sankaran, S., and Marsden, A. L., 2009, "Computational Fluid–Structure Interaction: Methods and Application to a Total Cavopulmonary Connection," Comput Mech, 45(pp. 77-89.

[130] Long, C., Hsu, M., Bazilevs, Y., Feinstein, J., and Marsden, A., 2012, "Fluid–Structure Interaction Simulations of the Fontan Procedure Using Variable Wall Properties," Int J Numer Method Biomed Eng, 28(pp. 513-527.

[131] Fogel, M. A., Weinberg, P. M., Hoydu, A., Hubbard, A., Rychik, J., Jacobs, M., Fellows, K. E., and Haselgrove, J., 1997, "The Nature of Flow in the Systemc Venous Pathway Measured by Magnetic Resonance Blood Tagging in Patients Having the Fontan Operation," J Thorac Cardiovasc Surg, 114(pp. 1032-1041.

[132] Hsia, T. Y., Khambadkone, S., Deanfield, J. E., Taylor, J. F., Migliavacca, F., and De Leval, M. R., 2001, "Subdiaphragmatic Venous Hemodynamics in the Fontan Circulation," J Thorac Cardiovasc Surg, 121(3), pp. 436-47.

[133] Hsia, T. Y., Khambadkone, S., Redington, A. N., Migliavacca, F., Deanfield, J. E., and Leval, M. R. D., 2000, "Effects of Respiration and Gravity on Infradiaphragmatic Venous Flow in Normal and Fontan Patients," Circulation, 102(suppl III), pp. 148-153.

[134] Hjortdal, V. E., Emmertsen, K., Stenbog, E., Frund, T., Schmidt, M. R., Kromann, O., Sorensen, K., and Pedersen, E. M., 2003, "Effects of Exercise and Respiration on Blood Flow in Total Cavopulmonary Connection: A Real-Time Magnetic Resonance Flow Study," Circulation, 108(10), pp. 1227-31.

[135] Formaggia, L., Quarteroni, A., and Veneziani, A., 2009, "Multiscale Models of the Vascular System," Cardiovascular Mathematics: Modeling and Simulation of the Circulatory System, 1(pp. 395-446.

[136] Petrossian, E., Reddy, V. M., Collins, K. K., Culbertson, C. B., Macdonald, M. J., Lamberti, J. J., Reinhartz, O., Mainwaring, R. D., Francis, P. D., Malhotra, S. P., Gremmels, D. B., Suleman, S., and Hanley, F. L., 2006, "The Extracardiac Conduit Fontan Operation Using Minimal Approach Extracorporeal Circulation: Early and Midterm Outcomes," J Thorac Cardiovasc Surg, 132(5), pp. 1054-63.

[137] Fujii, Y., Kotani, Y., Takagaki, M., Arai, S., Kasahara, S., Otsuki, S., and Sano, S., 2010, "Growth of the Lateral Tunnel in Patients Who Underwent a Total Cavopulmonary Connection at Less Than 5 Years of Age," Eur J Cardiothorac Surg, 38(1), pp. 66-70.

[138] Stamm, C., Friehs, I., Mayer, J. E., Zurakowski, D., Triedman, J. K., Moran, A. M., Walsh, E. P., Lock, J. E., Jonas, R. A., and Del Nido, P. J., 2001, "Long-Term Results of the Lateral Tunnel Fontan Operation," Journal of Thoracic and Cardiovascular Surgery, 121(1), pp. 28-41.

[139] Restrepo, M., Mirabella, L., Tang, E., Haggerty, C., Khiabani, R., Fynn-Thompson, F., Valente, A., Mcelhinney, D., Fogel, M., and Yoganathan, A., 2014, "Fontan Pathway Growth: A Quantitative Evaluation of Lateral Tunnel and Extracardiac Cavopulmonary Connections Using Serial Cardiac Magnetic Resonance," Ann Thorac Surg, 97(3), pp. 916-22.

[140] Restrepo, M., Tang, E., Haggerty, C. M., Khiabani, R. H., Mirabella, L., Bethel, J., Valente, A. M., Whitehead, K. K., Mcelhinney, D. B., Fogel, M. A., and Yoganathan, A. P., 2014, "Energetic Implications of Vessel Growth and Flow Changes over Time in Fontan Patients," Ann Biomed Eng, In press(pp.

[141] Frakes, D. H., Conrad, C. P., Healy, T. M., Monaco, J. W., Fogel, M., Sharma, S., Smith, M. J., and Yoganathan, A. P., 2003, "Application of an Adaptive Control Grid Interpolation Technique to Morphological Vascular Reconstruction," IEEE Trans Biomed Eng, 50(2), pp. 197-206.

[142] Frakes, D. H., Smith, M. J., Parks, J., Sharma, S., Fogel, M., and Yoganathan, A. P., 2005, "New Techniques for the Reconstruction of Complex Vascular Anatomies from Mri Images," J Cardiovasc Magn Reson, 7(2), pp. 425-32.

[143] Antiga, L., Piccinelli, M., Botti, L., Ene-Iordache, B., Remuzzi, A., and Steinman, D. A., 2008, "An Image-Based Modeling Framework for Patient-Specific Computational Hemodynamics," Med Biol Eng Comput, 46(pp. 1097–1112.

[144] Passerini, T., Sangalli, L. M., Vantini, S., Piccinelli, M., Bacigaluppi, S., Antiga, L., Boccardi, E., Secchi, P., and Veneziani, A., 2011, "An Integrated Statistical Investigation of Internal Carotid Arteries of Patients Affected by Cerebral Aneurysms," CVET, 3(1), pp. 26-40.

[145] Piccinelli, M., Veneziani, A., Steinman, D. A., Remuzzi, A., and Antiga, L., 2009, "A Framework for Geometric Analysis of Vascular Structures: Application to Cerebral Aneurysms," IEEE Trans. Med. Imag., 28(8), pp. 1141-1155.

[146] Khunatorn, Y., Shandas, R., Degroff, C., and Mahalingam, S., 2003, "Comparison of in Vitro Velocity Measurements in a Scaled Total Cavopulmonary Connection with Computational Predictions," Ann Biomed Eng, 31(7), pp. 810-822.

[147] Frakes, D., Smith, M., De Zelicourt, D., Pekkan, K., and Yoganathan, A., 2004, "Three-Dimensional Velocity Field Reconstruction," J Biomech Eng, 126(6), pp. 727-35.

[148] Sundareswaran, K. S., Frakes, D. H., Fogel, M. A., Soerensen, D. D., Oshinski, J. N., and Yoganathan, A. P., 2009, "Optimum Fuzzy Filters for Phase-Contrast Magnetic Resonance Imaging Segmentation," J Magn Reson Imaging, 29(1), pp. 155-65.

[149] Lin, H., Bender, J., Ding, Y., Chung, Y., Hinton, A., Pennell, M., Whitehead, K., Raman, S., and Simonetti, O., 2012, "Shared Velocity Encoding: A Method to Improve the Temporal Resolution of Phase-Contrast Velocity Measurements," Magn Reson Med, 68(3), pp. 703-710.

[150] Heiberg, E., Sjögren, J., Ugander, M., Carlsson, M., Engblom, H., and Arheden, H., 2010, "Design and Validation of Segment - Freely Available Software for Cardiovascular Image Analysis," BMC Med Imaging, 10(1), pp.

[151] Carlsson, M., Töger, J., Kanski, M., Bloch, K. M., Ståhlberg, F., Heiberg, E., and Arheden, H., 2011, "Quantification and Visualization of Cardiovascular 4d Velocity Mapping Accelerated with Parallel Imaging or K-T Blast: Head to Head

Comparison and Validation at 1.5 T and 3 T," J Cardiovasc Magn Reson, 13(55), pp.

[152] Bernstein, M. A., Zhou, X. J., Polzin, J. A., King, K. F., Ganin, A., Pelc, N. J., and Glover, G. H., 1998, "Concomitant Gradient Terms in Phase Contrast Mr: Analysis and Correction," MAGNET RESON MED, 39(2), pp. 300-308.

[153] Khiabani, R., Restrepo, M. R., Tang, E., De Zelicourt, D., Sotiropoulos, F., Fogel, M. A., and Yoganathan, A. P., 2012, "Effect of Flow Pulsatility on Modeling the Hemodynamics in the Total Cavopulmonary Connection," J Biomech, 45(14), pp. 2376-81.

[154] Myers, J., Buchanan, N., Walsh, D., Kraemer, M., Mcauley, P., Hamilton-Wessler, M., and Froelicher, V. F., 1991, "Comparison of the Ramp Versus Standard Exercise Protocols," J Am Coll Cardiol, 17(6), pp. 1334-1342.

[155] 1995, "Standardization of Spirometry, 1994 Update. American Thoracic Society.," Am J Respir Crit Care Med. , 152(3), pp. 1107-36.

[156] Beaver, W. L., Wasserman, K., and Whipp, B. J., 1986, "A New Method for Detecting Anaerobic Threshold by Gas Exchange," J APPL PHYSIOL, 60(6), pp. 2020-2027.

[157] De Zelicourt, D., 2010, "Pulsatile Fontan Hemodynamics and Patient-Specific Surgical Planning: A Numerical Investigation," PhD thesis, Department of Biomedical Engineering, Georgia Institute of Technology and Emory University, pp.

[158] De Zélicourt, D., Ge, L., Wang, C., Sotiropoulos, F., Gilmanov, A., and Yoganathan, A., 2009, "Flow Simulations in Arbitrarily Complex Cardiovascular Anatomies - an Unstructured Cartesian Grid Approach," Comput Fluids, 38(9), pp. 1749-1762.

[159] Gilmanov, A., and Sotiropoulos, F., 2005, "A Hybrid Cartesian/Immersed Boundary Method for Simulating Flows with 3d, Geometrically Complex, Moving Bodies," J COMPUT PHYS, 207(2), pp. 457-492.

[160] Harlow, F. H., and Welch., J. E., 1965, "Numerical Calculation of Time-Dependent Viscous Incompressible Flow of Fluid with Free Surface," Physics of fluids, 8(12), pp. 2182.

[161] Ge, L., and Sotiropoulos, F., 2007, "A Numerical Method for Solving the 3d Unsteady Incompressible Navier-Stokes Equations in Curvilinear Domains with Complex Immersed Boundaries.," Journal of Computational Physics, 225(2), pp. 1782-1809.

[162] Zélicourt, D. D., Ge, L., Wang, C., Sotiropoulos, F., Gilmanov, A., and Yoganathan, A., 2009, "Flow Simulations in Arbitrarily Complex Cardiovascular Anatomies – an Unstructured Cartesian Grid Approach," Computers & Fluids, 38(9), pp. 1749-1762.

[163] Passerini, T., Quaini, A., Villa, U., Veneziani, A., and Canic, S., 2013, "Validation of an Open Source Framework for the Simulation of Blood Flow in Rigid and Deformable Vessels," Int. J. Numer. Meth. Biomed. Engng., Special Issue(pp.

[164] Quarteroni, A., Sacco, R., and F., S., 2007, "Numerical Mathematics," Springer Verlag: Heidelberg, pp.

[165] Quarteroni, A., and Valli, A., 1994, "Numerical Approximation of Partial Differential Equations," Springer-Verlag: Berlin Heidelberg, pp.

[166] Quarteroni, A., Saleri, F., and Veneziani, A., 1999, "Analysis of the Yosida Method for the Incompressible Navier–Stokes Equations," Journal de Mathèmatiques Pures et Appliquèes, 78(pp. 473–503.

[167] Quarteroni, A., Saleri, F., and Veneziani, A., 2000, "Factorization Methods for the Numerical Approximation of Navier–Stokes Equations " Comp Meth Appl Mech Eng, 188(pp. 505–526.

[168] Gervasio, P., Saleri, F., and Veneziani, A., 2006, "Algebraic Fractional-Step Schemes with Spectral Methods for the Incompressible Navier–Stokes Equations," J Comp Phys, 214(1), pp. 347–365.

[169] Villa, U., 2012, "Scalable Efficient Methods for Incompressible Fluid-Dynamics in Engineering Problems.," Ph.D. Thesis, Emory University, pp.

[170] Gauthier, A., and Saleri, F. V., A., 2004, "A Fast Preconditioner for the Incompressible Navier Stokes Equations," Comput Vis Sci., 6(2), pp. 105-112.

[171] Saleri, F., and Veneziani, A., 2006, "Pressure Correction Algebraic Splitting Methods for the Incompressible Navier–Stokes Equations," SIAM J Num An, 43(1), pp. 174–194.

[172] Laganà, K., Balossino, R., Migliavacca, F., Pennati, G., Bove, E. L., De Leval, M. R., and Dubini, G., 2005, "Multiscale Modeling of the Cardiovascular System: Application to the Study of Pulmonary and Coronary Perfusions in the Univentricular Circulation," J Biomech, 38(5), pp. 1129-41.

[173] Formaggia, L., Nobile, F., Quarteroni, A., and Veneziani, A., 1999, "Multiscale Modelling of the Circulatory System: A Preliminary Analysis," Comput Vis Sci., 2(2), pp. 75-83.

[174] Kind, T., Faes, T. J., Lankhaar, J. W., Vonk-Noordegraaf, A., and Verhaegen, M., 2010, "Estimation of Three- and Four-Element Windkessel Parameters Using Subspace Model Identification," IEEE Trans Biomed Eng, 57(7), pp. 1531-1538.

[175] Layton, W. J., and Rebholz, L. G., 2012, "Approximate Deconvolution Models of Turbulence: Analysis, Phenomenology and Numerical Analysis," Springer Science & Business Media, pp.

[176] Bertagna, L., Quaini, A., and Veneziani, A., 2015, "Deconvolution-Based Nonlinear Filtering for Incompressible Flows at Moderately Large Reynolds Numbers," to appear in Int J Num Methd Fluids, pp.

[177] Bertagna, L., Quaini, A., Bonilla-Alicea, R. J., Tang, E., Taylor, W. R., Yoganathan, A. P., and Veneziani, A., 2015, "Numerical Modeling of Blood Flow at Moderate Reynolds Numbers: A Les Approach and Its Applicatiosn to Vascular Surgery (Abstract)," 4th International Conference on Computational and Mathematical Biomedical Engineering - CMBE2015, 29 June-1 July 2015, France, pp.

[178] Rebholz, W. J. L. L. G., and Trenchea, C., 2012, "Modular Nonlinear Filter Stabilization of Methods for Higher Reynolds Numbers Flow," J. Math. Fluid Mech, 14(pp. 325–354.

[179] Taylor, C. A., and Figueroa, C. A., 2009, "Patient-Specific Modeling of Cardiovascular Mechanics," Annual Review of Biomedical Engineering, 11(pp. 109-34.

[180] Crosetto, P., Deparis, S., Fourestey, G., and Quarteroni, A., 2011, "Parallel Algorithms for Fluid-Structure Interaction Problems in Haemodynamics," SIAM J. SCI. COMPUT., 33(4), pp. 1598-1622.

[181] Perktold, K., and Rappitsch, G., 1995, "Computer Simulation of Local Blood Flow and Vessel Mechanics in a Compliant Carotid Artery Bifurcation Model," Journal of Biomechanics, 28(7), pp. 845-856

[182] Razzaq, M., Hron, J., and Turek, S., 2010, "Numerical Simulation of Laminar Incompressible Fluid-Structure Interaction for Elastic Material with Point Constraints " Advances in Mathematical Fluid Mechanics, pp.

[183] Erlicher, S., Bonaventura, L., and Bursi, O. S., 2002, "The Analysis of the Generalized-Alpha$_\varsigma$ Method for Non-Linear Dynamic Problems," COMPUT MECH, 20(pp. 83–104.

[184] Wood, W. L., Bossak, M., and Zienkiewicz, O. C., 1981, "An Alpha Modification of Newmarks Method," INT J NUMER METH ENG, 15(pp. 1562–1566.

[185] Quaini, A., and Quarteroni, A., 2007, "A Semi-Implicit Approach for Fluid–Structure Interaction Based on an Algebraic Fractional Step Method," MATH MOD METH APPL S, 17(6), pp. 957–983.

[186] Badia, S., Quaini, A., and Quarteroni, A., 2008, "Splitting Methods Based on Algebraic Factorization for Fluid–Structure Interaction," SIAM J SCI COMPUT, 30(4), pp. 1778–1805.

[187] Geuzaine, C., and Remacle, J., 2009, "Gmsh: A Three-Dimensional Finite Element Mesh Generator with Built-in Pre-and Postprocessing Facilities," INT J NUMER METH ENG, 79(pp. 1309–1331.

[188] Dasi, L. P., Pekkan, K., De Zelicourt, D., Sundareswaran, K. S., Krishnankuttyrema, R., Del Nido, P., and Yoganathan, A. P., 2009, "Hemodynamic Energy Dissipation in the Cardiovascular System: Generalized Theoretical Analysis on Disease States," Ann Biomed Eng, 37(4), pp. 661-673.

[189] Khiabani, R. H., Whitehead, K. K., Han, D., Restrepo, M., Tang, E., Bethel, J., Paridon, S. M., Fogel, M. A., and Yoganathan, A. P., 2015, "Exercise Capacity in

Single-Ventricle Patients after Fontan Correlates with Haemodynamic Energy Loss in Tcpc," Heart, 101(2), pp. 139-43.

[190] Dasi, L. P., Krishnankuttyrema, R., Kitajima, H. D., Pekkan, K., Sundareswaran, K., Fogel, M., Sharma, S., Whitehead, K., Kanter, K., and Yoganathan, A. P., 2009, "Fontan Hemodynamics: Importance of Pulmonary Artery Diameter," J Thorac Cardiovasc Surg, 137(3), pp. 560-564.

[191] Sundareswaran, K., De Zélicourt, D., Sharma, S., Kanter, K., Spray, T., Rossignac, J. R., Sotiropoulos, F., Fogel, M., and Yoganathan, A. P., 2009, "Correction of Pulmonary Arteriovenous Malformation Using Image Based Surgical Planning," JACC Imaging, 2(8), pp. 1024-1030.

[192] Ensley, A., Lynch, P., Chatzimavroudis, G. P., Lucas, C. L., Sharma, S., and Yoganathan, A. P., 1999, "Toward Designing the Optimal Total Cavopulmonary Connection: An in Vitro Study," Ann Thorac Surg, 68(pp. 1384-1390.

[193] Itatani, K., Miyaji, K., Tomoyasu, T., Nakahata, Y., Ohara, K., Takamoto, S., and Ishii, M., 2009, "Optimal Conduit Size of the Extracardiac Fontan Operation Based on Energy Loss and Flow Stagnation," Ann Thorac Surg, 88(2), pp. 565-572.

[194] De Leval, M., Kilner, O., Gewillig, M., and Bull, C., 1988, "Total Cavopulmonary Connection: A Logical Alternative to Atriopulmonary Connection for Complex Fontan Operations. Experimental Studies and Early Clinical Experience ." J Thorac Cardiovasc Surg, 96(pp. 682-695.

[195] Sundareswaran, K. S., Haggerty, C. M., De Zelicourt, D., Dasi, L. P., Pekkan, K., Frakes, D., Powell, A. J., Kanter, K. R., Fogel, M. A., and Yoganathan, A. P., 2012, "Visualization of Flow Structures in Fontan Patients Using Three-Dimensional Phase Contrast Magnetic Resonance Imaging," J Thorac Cardiovasc Surg, 143(pp. 1108-1116.

[196] Amodeo, A., Galletti, L., Marianeschi, S., Picardo, S., Giannico, S., Renzi, P. D., and Marcelletti, C., 1997, "Extracardiac Fontan Operation for Complex Cardiac Anomalies: Seven Years' Experience," J Thorac Cardiovasc Surg 114(6), pp. 1020-1031.

[197] Lardo, A. C., Webber, S., Friehs, I., Del Nido, P., and Cape, E. G., 1999, "Fluid Dynamic Comparison of Intra-Atrial and Extracardiac Total Cavopulmonary Connections," J Thorac Cardiovasc Surg, 117(pp. 697-704.

[198] Tang, E., Restrepo, M., Haggerty, C., Mirabella, L., Bethel, J., Whitehead, K., Fogel, M., and Yoganathan, A., 2014, "Geometric Characterization of Patient Specific Total Cavopulmonary Connections and Its Relationship to Hemodynamics," JACC Cardiovasc Imaging, 7(3), pp. 215-224.

[199] Giannico, S., Hammad, F., Amodeo, A., Michielon, G., Drago, F., Turchetta, A., Di Donato, R., and Sanders, S., 2006, "Clinical Outcome of 193 Extracardiac Fontan Patients: The First 15 Years," J Am Coll Cardiol, 47(10), pp. 2065-2073.

[200] Gewillig, M., Brown, S. C., Eyskens, B., Heying, R., Ganame, J., Budts, W., Gerche, A. L., and Gorenflo, M., 2009, "The Fontan Circulation: Who Controls Cardiac Output?," Interact Cardiovasc Thorac Surg, 10(3), pp. 428-433.

[201] Giardini, A., Hager, A., Napoleone, C. P., and Picchio, F. M., 2008, "Natural History of Exercise Capacity after the Fontan Operation: A Longitudinal Study," Ann Thorac Surg, 85(3), pp. 818-22.

[202] Diller, G. P., Giardini, A., Dimopoulos, K., Gargiulo, G., Müller, J., Derrick, G., Giannakoulas, G., Khambadkone, S., Lammers, A. E., Picchio, F. M., Gatzoulis, M. A., and Hager, A., 2010, "Predictors of Morbidity and Mortality in Contemporary Fontan Patients: Results from a Multicenter Study Including Cardiopulmonary Exercise Testing in 321 Patients," Eur Heart J, 31(24), pp. 3073-83.

[203] Mets, J. M., Bergersen, L., Mayer, J. E. J., Marshall, A. C., and Mcelhinney, D. B., 2013, "Outcomes of Stent Implantation for Obstruction of Intracardiac Lateral Tunnel Fontan Pathways," Circ Cardiovasc Interv, 6(1), pp. 92-100.

[204] Khairy, P., Fernandes, S. M., Mayer, J. E. J., Triedman, J. K., Walsh, E. P., Lock, J. E., and Landzberg, M. J., 2008, "Long-Term Survival, Modes of Death, and Predictors of Mortality in Patients with Fontan Surgery," Circulation, 117(1), pp. 85-92.

[205] Cordina, R. L., O'meagher, S., Karmali, A., Rae, C. L., Liess, C., Kemp, G. J., Puranik, R., Singh, N., and Celermajer, D. S., 2013, "Resistance Training Improves Cardiac Output, Exercise Capacity and Tolerance to Positive Airway Pressure in Fontan Physiology," Int J Cardiol, 168(2), pp. 780-8.

[206] Lin, H. Y., Bender, J. A., Ding, Y., Chung, Y. C., Hinton, A. M., Pennell, M. L., Whitehead, K. K., Raman, S. V., and Simonetti, O. P., 2012, "Shared Velocity Encoding: A Method to Improve the Temporal Resolution of Phase-Contrast Velocity Measurements," Magn Reson Med, 68(3), pp. 703–710.

[207] Kim, H., Vignon-Clementel, I., Figueroa, C., Ladisa, J., Jansen, K., Feinstein, J., and Taylor, C., 2009, "On Coupling a Lumped Parameter Heart Model and a Three-Dimensional Finite Element Aorta Model," Ann Biomed Eng., 37(11), pp. 2153-69.

[208] Estafanous, F. G., Barash, P. G., and Reves, J. G., 2001 "Cardiac Anesthesia: Principles and Clinical Practice, 2nd Edition," pp. 526.

[209] Wootton, D., and Ku, D., 1999, " Fluid Mechanics of Vascular Systems, Diseases, and Thrombosis," Annu Rev Biomed Eng. , 1(pp. 299-329.

[210] Rayz, V., Boussel, L., Ge, L., Leach, J., Martin, A., Lawton, M., Mcculloch, C., and Saloner, D., 2010, "Flow Residence Time and Regions of Intraluminal Thrombus Deposition in Intracranial Aneurysms," Ann Biomed Eng, 38(10), pp. 3058-69.

[211] Bhatia, S. K., 2010, *Biomaterials for Clinical Applications*, Springer,

[212] Caro, C. G., Pedley, T. J., Schroter, R. C., Seed, W. A., and Parker, K. H., 2011, *The Mechanics of the Circulation, 2nd Ed.*, Cambridge University Press,

[213] Pedley, T. J., 2008, *The Fluid Mechanics of Large Blood Vessels Cambridge Monographs on Mechanics*, Cambridge University Press,

[214] Ganong, W. F., 2003, *Review of Medical Physiology*, *Lange Basic Science*, McGraw-Hill/Appleton & Lange,

[215] Ling, L. H., Oh, J. K., Tei, C., Click, R. L., Breen, J. F., Seward, J. B., and Tajik, A. J., 1997, "Pericardial Thickness Measured with Transesophageal Echocardiography: Feasibility and Potential Clinical Usefulness," Journal of the American College of Cardiology, 29(6), pp. 1317-1323

[216] Reuben, S., 1971, "Compliance of the Human Pulmonary Arterial System in Disease," Circ Res, 29 (pp. 40-50.

[217] Khiabani, R. H., Whitehead, K. K., Han, D., Restrepo, M., Tang, E., Bethel, J., Paridon, S. M., Fogel, M. A., and Yoganathan, A. P., 2013, "Correlation between Power Loss of the Total Cavopulmonary Connection and Exercise Oxygen Consumption in Fontan Patients (Abstract)," American Heart Association Scientific Sessions, November 16-20, 2013, pp.

[218] Toma, M., Krdey, A., Takagi, S., and Oshima, M., 2011, "Strongly Coupled Fluid-Structure Interaction Cardiovascular Analysis with the Effect of Peripheral Network," SEISAN KENKYU, 63(3), pp. 339-344.

[219] Kanter, K. R., Haggerty, C. M., Restrepo, M., De Zelicourt, D. A., Rossignac, J., Parks, W. J., and Yoganathan, A. P., 2012, "Preliminary Clinical Experience with a Bifurcated Y-Graft Fontan Procedure—a Feasibility Study ." J Thorac Cardiovasc Surg, 144(2), pp. 383-389.

[220] Ochiai, Y., Imoto, Y., Sakamoto, M., Kajiwara, T., Sese, A., Watanabe, M., Ohnob, T., and Joo, K., 2009, "Mid-Term Follow-up of the Status of Gore-Tex Graft after Extracardiac Conduit Fontan Procedure," Eur J Cardiothorac Surg, 36(1), pp. 63-68.

[221] Lee, C., Lee, C.-H., Hwang, S. W., Lim, H. G., Kim, S.-J., Lee, J. Y., Shim, W.-S., and Kim, W.-H., 2007, "Midterm Follow-up of the Status of Gore-Tex Graft after Extracardiac Conduit Fontan Procedure," Eur J Cardiothorac Surg, 31(6), pp. 1008-1012.

[222] Van Brakel, T. J., Schoof, P. H., De Roo, F., Nikkels, P. G. J., Evens, F. C. M., and Haas, F., 2014, "High Incidence of Dacron Conduit Stenosis for Extracardiac Fontan Procedure," J Thorac Cardiovasc Surg, 147(5), pp. 1568-1572.

[223] Nobile, F., and Vergara, C., 2008, "An Effective Fluid-Structure Interaction Formulation for Vascular Dynamics by Generalized Robin Conditions," SIAM J. Sci. Comput., 30(2), pp. 731–763.

[224] Moireau, P., Xiao, N., Astorino, M., Figueroa, C. A., Chapelle, D., Taylor, C. A., and Gerbeau, J.-F., 2012, "External Tissue Support and Fluid–Structure Simulation in Blood Flows," Biomech Model Mechanobiol, 11(1-2), pp. 1-18.

[225] Tricerri, P., Dedè, L., Deparis, S., Quarteroni, A., Robertson, A. M., and Sequeira, A., 2015, "Fluid-Structure Interaction Simulations of Cerebral Arteries Modeled by Isotropic and Anisotropic Constitutive Laws," COMPUT MECH, 55(3), pp. 479-498.

[226] Gee, M. W., F¨Orster, C., and Wall, W. A., 2009, "A Computational Strategy for Prestressing Patient-Specific Biomechanical Problems under Finite Deformation," Int. J. Numer. Meth. Biomed. Engng., 26(pp. 52-72.

[227] Hsu, M.-C., and Bazilevs, Y., 2011, "Blood Vessel Tissue Prestress Modeling for Vascular Fluid–Structure Interaction Simulation," FINITE ELEM ANAL DES, 47(6), pp. 593–599.

[228] Haggerty, C., Restrepo, M., Tang, E., De Zélicourt, D., Sundareswaran, K., Mirabella, L., Bethel, J., Whitehead, K., Fogel, M., and Yoganathan, A., 2014, "Fontan Hemodynamics from 100 Patient-Specific Cardiac Magnetic Resonance Studies: A Computational Fluid Dynamics Analysis " J Thorac Cardiovasc Surg, 148(4), pp. 1481-1489.